Numerical modeling of dry and water-laden gravitational flows for quantitative hazard assessment

Marc Peruzzetto

UNIVERSITE DE PARIS

Thèse préparée

à l'INSTITUT DE PHYSIQUE DU GLOBE DE PARIS

École doctorale STEP'UP - ED N°560

IPGP - Équipe de Sismologie

Numerical modeling of dry and water-laden gravitational flows for quantitative hazard assessment

par

Marc PERUZZETTO

présentée et soutenue publiquement le
4 Février 2021

Thèse de doctorat de Sciences de la Terre et de l'Environnement

dirigée par Anne Mangeney
& Gilles Grandjean

devant un Jury composé de :

Ancey Christophe Professeur (EPFL, Suisse)	Rapporteur
Kelfoun Karim Maître de conférences (LMV)	Rapporteur
Manzella Irene Lecturer (University of Plymouth, UK)	Membre
Labiouse Vincent Professeur (HEIA-FR, Suisse)	Membre
Vilotte Jean-Pierre Professeur (IPGP)	Président du Jury
Mangeney Anne Professeur (IPGP)	Directrice de thèse
Grandjean Gilles Directeur de Recherche (BRGM)	Directeur de thèse
Levy Clara Docteur (BRGM)	Co-encadrante

Contents

Abstract

In this work, we assess the possibility to use empirical thin-layer models to enhance propagation hazard estimation for gravitational flows. Thin-layer equations model the propagation of a flow on a topography and give its thickness, and its depth-averaged velocity. We test the SHALTOP numerical model with an empirical rheology described only one or two parameters, in order to facilitate its operational use. This approach is thus easier to use and computationally cheaper than models simulating the dynamics of each solid or fluid particle, and allows to model the dynamics and the geometry of the flows more finely than purely empirical models.

Three research issues are considered in this work. We first highlight the importance of a detailed description of the topography curvature, even with simple rheological laws. Topography curvature can indeed have a significant influence on the dynamics of rapid gravitational flows. It should thus be properly taken into account to calibrate correctly the models and estimate more precisely overflow hazards.

Then, we test the feasibility of using SHALTOP for propagation hazard quantification in two case studies. We first consider debris avalanches on the Soufrière de Guadeloupe volcano (Guadeloupe, Lesser Antilles), and then the combination of rock avalanches and subsequent debris flows in the Prêcheur river (Martinique, Lesser Antilles). In both cases, we use a wide variety of data (topographic, geophysical, geological, geomorphological, seismic, ...) to constrain simulation scenarios, calibrate the model and study potential future events.

Finally, we propose a methodology to estimate, thanks to numerical simulations, landslide travel distance as a function of destabilized volume. The resulting power law is site-specific. It is derived through a statistical analysis of a site-specific simulation database, with various volumes and rheological parameters. Through three case studies, we show that such a power law is associated to smaller uncertainties in comparison to purely empirical estimations, and models more accurately the dependence between the volume and the travel distance.

In the short term, this work contributes to adapt and test SHALTOP to allow its operational use for landslide hazard assessment. In the long term, our work contributes to enhancing landslide hazard maps and numerical tools for crisis management, by replacing purely empirical approaches by physically-based models. In this context, some scientific problems remain to be tackled, as the spatialization of uncertainty and the adaptation of models depending on the scale of the study (identified landslide, mountain slope or watershed).

Key-words: landslide, modeling, hazard, thin-layer, shallow-water, uncertainty

Résumé

Dans cette thèse, nous estimons la possibilité d'utiliser des modèles d'écoulement en couche mince de manière empirique pour améliorer la quantification des aléas gravitaires. Les équations d'écoulement en couche mince décrivent la dynamique d'un écoulement sur une topographie, à travers son épaisseur et sa vitesse moyennée sur l'épaisseur. Nous choisissons le modèle numérique SHALTOP avec une rhéologie empirique n'impliquant qu'un ou deux paramètres pour faciliter son utilisation opérationnelle. Il est ainsi plus simple d'utilisation et moins coûteux en temps de calcul que des modèles simulant la dynamique de chaque élément fluide ou solide, et permet de modéliser plus finement la dynamique et la géométrie de l'écoulement que des modèles purement empiriques .

Trois axes de recherche sont présentés dans cette thèse. Nous montrons d'abord l'importance, même pour des rhéologies simples, d'une description fine de la courbure de la topographie. Cette courbure peut avoir avoir une influence significative sur la dynamique d'écoulements rapides. Elle est donc importante pour calibrer correctement les modèles et estimer avec plus de précision les risques de débordement pour des écoulements chenalisés.

Dans un deuxième temps, nous évaluons les capacités de SHALTOP à quantifier la propagation sur des cas d'étude spécifiques. Nous considérons d'abord des avalanches de débris à la Soufrière de Guadeloupe, puis l'enchaînement d'avalanches de blocs et de laves torentielles dans la Rivière du Prêcheur, en Martinique. Dans les deux cas, nous combinons des données variées (topographiques, géophysiques, géologiques, géomorphologiques, sismiques, ...) afin de contraindre les scénarios de simulations, calibrer le modèle, et étudier de potentiels futurs événements.

Enfin, nous proposons une méthodologie pour estimer, à l'aide de simulations numériques, la distance de parcours d'écoulements gravitaires en fonction des volumes déstabilisés. La loi puissance obtenue est spécifique au site d'étude considéré : elle est obtenue par l'analyse statistique d'une base de données de simulations, avec des volumes et paramètres rhéologiques variés. A travers trois cas d'étude, nous montrons que la loi obtenue permet de réduire l'incertitude par rapport à des estimations purement empiriques, et de mieux modéliser la dépendance entre le volume et la distance de parcours.

A court terme, cette thèse contribue à adapter et tester SHALTOP pour permettre son utilisation opérationnelle pour des études d'aléas. A plus long terme, en remplaçant des approches purement empiriques par des méthodes plus physiques, nos travaux s'inscrivent dans la volonté d'améliorer les cartes d'aléas pour la propagation des glissements de terrain, ainsi que les outils numériques utilisés pour la gestion de crise. Dans ce contexte, des verrous scientifiques doivent encore être surmontés, comme la spatialisation des incertitudes et l'adaptation des modèles en fonction de l'échelle (glissement identifié, versant ou bassin versant).

Mots clés *: glissement de terrain, modélisation, aléa, couche mince, shallow-water, incertitude*

Remerciements

Je me souviens d'un jour de la première moitié de 2016, alors que j'étais en stage à Yogyakarta, en Indonésie, où je me demandais si je voulais faire un thèse, et sur quel sujet. C'était, pour être exact, le 3 Juin 2016. Je regarde les sujets de thèse proposés alors sur le site de l'IPG, et j'envoie un mail à Anne Mangeney et Jean-Christophe Komorowski pour leur dire que j'aimerais faire une thèse en lien avec l'estimation des risques gravitaires. Le 22 Juin suivant, Anne me répond qu'un sujet de thèse qu'"on" peut me proposer tournerait autour de l'évaluation des aléas gravitaires. Je ne le sais pas encore, mais derrière ce "on", il y a Gilles Grandjean, Clara Levy et Yannick Thiery.

Le sujet de thèse est donc né tandis que j'étais en Indonésie. Peut-être, déjà, une promesse de voyage ? Promesse tenue. Au premier sens du terme, puisque j'ai évolué entre l'IPGP à Paris et le BRGM à Orléans, et que mon travail m'amené en Martinique (quelle île...), en Champagne (pour un travail pas encore valorisé, mais tout de même très enrichissant au cœr des vignes, et quel spectacle magnifique en automne...), à Hong-Kong, à Vienne et même en Normandie pour aider à la mise en place du réseau RESIF. Voyage également scientifique et intellectuel : j'ai navigué sur la houle capricieuse de l'analyse tensorielle, accosté sur les sables parfois mouvants de la géotechnique, pris un peu de hauteur avec la photogrammétrie, emprunté les chemins incertains des statistiques, et enfin raconté mes aventures, avec quelques esquisses de tableaux géomorphologiques, et plus prosaïquement avec des vers non rimés en de l'ancestral Fortran.

Merci, donc, à mes encadrants pour ces voyages. Merci Anne pour ton refus inconditionnel de la fénéantise intellectuelle. Pour toi, rien n'est impossible, rien n'est infaisable, tout est seulement à faire. Grâce à cette philosophie, mon travail a gagné en précision et en exhaustivité, il te doit donc beaucoup. Merci, Gilles, de m'avoir ouvert les portes du BRGM. Ton recul et ton pragmatisme m'ont beaucoup aidé à me remettre sur les rails quand je me perdais dans les détails, oubliant la vision d'ensemble. Dès le départ, je voulais une thèse appliquée, je voulais des résultats utiles pour les experts travaillant sur les risques gravitaires. Tu as énormément contribué à ce que nos résultats scientifiques soient bien remis dans cette perspective.

Un grand merci également, évidemment, à Clara et Yannick, des encadrants de luxe ! Vous m'avez accompagné du début à la fin pour construire ma thèse, pour établir et analyser mes résultats, pour écrire le manuscrit et les articles. Vous m'avez initié au travail de terrain, aux subtilités de la géotechnique et de la géomorphologie, et au travail d'expertise du BRGM. Et enfin, vous avez quand même bien pris soin de moi, quand j'étais dans le dur, fatigué, éprouvé. Bref, un très grand merci à vous deux. C'était (et c'est toujours) un plaisir de travailler avec vous, j'espère que ça durera !

Beaucoup de personnes ont gravité autour de ma thèse et ont contribué aux résultats présentés ici. Merci à Christophe Ancey et Karim Kelfoun d'avoir accepté de relire le manuscrit : vos remarques et commentaires m'ont permis de l'améliorer et de préparer sereinement la soutenance, pour une présentation orale qui, j'espère, vous aura intéressés. Merci également aux autres membres du jury, Irene Manzella, Vincent Labiouse et Jean-Pierre Vilotte. Nos échanges lors de la soutenance

était très enrichissants, et je regrette que nous n'ayons pu discuter qu'en visio-conférence, Covid oblige... J'espère que nous pourrons échanger à nouveau de vive voix ! Merci aussi à Isabelle Thénévin, Olivier Maquaire et Jean-Christophe Komorowski pour leurs conseils et remarques lors des comités de thèse.

Le cœur de mon travail est l'utilisation de données de terrain pour contraindre et valider les simulations numériques. La récupération et l'exploitation de ces données de terrain est un travail que je n'aurais évidemment jamais pu réaliser seul. Un grand merci aux équipes des Observatoires Volcanologiques et Sismologiques et du BRGM de Martinique et de Guadeloupe pour leur aide, et en particulier à Benoit Vittecoq, Anne-Marie Lejeune, Yoann Legendre, Aude Nachbaur, Jean-Marie Saurel, Valérie Clouard et Fabrice Fontaine. Merci également à Sophie Lagarde, qui m'a accompagné sur le terrain et aidé pour toutes les mesures, et à Christophe Poinclou, du bureau d'études ANTEA, qui a pris le temps de m'expliquer les subtilités des essais géotechinques et la dilatance des sables. Même si le travail réalisé en Champagne n'est pas inclus dans ce manuscrit, j'y ai effectué plusieurs missions et les perspectives de recherche sur ce site ne manquent pas ! Merci donc à l'équipe du BRGM Grand-Est à Reims, et en particulier Pierre Pannet et Ysoline Hannion, pour leur accueuil et leur aide. Merci aussi à Antoine Petrelli pour une mission commune RESIF / glissement de terrain mémorable : de la science, du ping pong, et une belle rencontre avec un producteur indépendant de champagne !

Il me serait impossible de faire la liste exhaustive de toutes les personnes avec qui j'ai pu échanger et qui ont contribué à ce travail de thèse. Je tiens néanmoins à remercier spécialement Thomas Dewez qui m'a formé aux bases de la photogrammétrie et du traitement de nuages de points en 3D, Jérémy Rohmer qui m'a initié aux subtilités du monde des statistiques, et Martin Mergili qui m'a accueilli à Vienne, à BOKU, pour m'apprendre à utiliser le logiciel r.avaflow. Merci aussi à Sylvie Contamina et Claire Brugeron qui ont assuré le bon déroulement matériel de ma thèse, entre mes missions et mes allers-retours entre Paris et Orléans. La mise en forme du manuscrit doit énormément à Geneviève Moguilny, jamais avare de conseils sur l'utilisation de LaTeX et du cluster de calcul de l'IPGP !

Une belle science, c'est bien, un belle science dans un bon cadre de travail, c'est encore mieux. Merci donc à tous les doctorants de l'IPGP, à l'équipe de Sismologie de l'IPGP et à l'équipe de DRP/RIG du BRGM pour avoir rendu ces années agréables. Encore une fois, difficile d'être exhaustif... Une pensée particulière pour Virginie et Sylvain, mes premiers co-bureaux qui m'ont accueilli à l'IPG, pour Matthew et Mariano, leurs successeurs, pour Pauline et Alister, mes compagnons de thèse arrivés comme moi en Septembre 2017, et pour Hugo, mon papa de thèse, avec qui j'ai appris à jouer aux billes et qui a toujours été à mon écoute.

Enfin, une mention spéciale à tous ceux sans qui je ne serais pas là aujourd'hui. Ils sont nombreux, à commencer évidemment par Fred, Jammy et Sabine : je suis la génération C'est pas Sorcier*, ça ne s'invente pas ! Je n'aurais sans doute pas cet attrait pour les sciences sans eux, et sans tous les professeurs qui ont marqué ma scolarité, dès le CM2 (une année mémorable !). Je ne peux pas ne pas remercier mes professeurs de mathématiques et de physique de Terminale, qui m'ont fait découvrir ce que c'était vraiment que les mathématiques et les sciences expérimentales. Mon goût pour les géosciences n'est venu que plus tard, avec le fameux stage de géol des Mines, puis avec les cours de l'option Géosciences. De fil en aiguille, de stage en stage, j'en suis arrivé à la thèse. Merci donc à tous ceux qui m'ont créé ces opportunités, en particulier Hervé Chauris, Pascal Podvin, Anne Le Friant, Jean-Christophe Komorowski, Jean-Philippe Metaxian, François Beauducel, Alexandre Kazantsev.*

Et pour finir avec les personnes sans qui je ne serais pas là aujourd'hui, les plus évidentes et les plus importantes : Papa, Maman, du début à la fin, et pour la suite à venir, merci pour tout. Et bien sûr, Sandrine. Tu m'a accompagné, supporté, aidé, consolé. Pour tout cela, et toutes tes qualités, cette thèse, tu la mérites autant que moi.

Introduction

Context

Between 2004 and 2016, non seismically triggered landslides killed more than 55,000 people worldwide (Petley, 2012; Froude and Petley, 2018). Most of these landslides happened in mountainous areas in China and India during the monsoon season. Earthquakes also trigger fatal landslides (as in the case of the M. 7.9 earthquake in Wenchuan, China, Fan et al., 2019), but it is difficult to identify the cause of the death in the chaotic aftermaths of earthquakes (Petley, 2012). Landslides can also have a significant economic impact. In France, a highly publicized example is the Chambon landslide that partially destroyed the road between Grenoble and Briançon in May 2015. A new road could be opened only in December 2017 (Desrues et al., 2019). The coast of the construction of the new road, as well as the management of alternate solutions for the displacement of isolated population in the meantime, was at least 30 million euros for this single event (Echos, 2015).

Gravitational hazards are not specific to mountainous areas. Still in France, landslides occur for instance regularly on the hillsides of *Vallée de la Marne* and *Montagne de Reims*. They are rarely a threat to populations, but damage communication networks and vineyards (e.g. Pannet et al., 2015; Hannion and Hamman, 2018; Pannet, 2018).

Given the economic and human stakes, the study of landslides is important to assess correctly hazards and associated risks. Hazard is associated to the process itself, and combines the probability of occurrence of an event with its intensity (for instance, the velocity and/or the travel distance). The risk associates the hazard with its impact on exposed stakes, in regard of their economic value. The main steps of risk assessment for landslides are (Alexander, 2002; Glade and Crozier, 2005; Fell et al., 2008; Corominas et al., 2014):

1. Hazard characterization: What kind of landslides can be expected? In which range of volumes? What is the probability of occurrence? This step is mainly based on the inventory of past events in the study site.
2. Hazard cartography: where can landslides be initiated? How far can they go?
3. Quantification of intensity: what are the characteristics of landslides? If the focus is on propagation, hazard intensity is measured for instance by travel distance, velocity, dynamic pressure or deposited thicknesses. How is intensity related to the magnitude of the landslides, i.e. to the destabilized volume?
4. Analysis of stakes exposure: what is the probability that an infrastructure or a living quarter is affected by a landslide?
5. Analysis of vulnerability: What is the potential impact of a landslide of given magnitude on the exposed stakes? This is different from exposure analysis: for instance, a bridge can

be exposed to debris flow hazard, but will be threatened only in the case of high discharge events.

6. Integration of previous quantitative and qualitative, to derive a quantified risk assessment (QRA), in terms of economic costs and/or potential fatalities.

In this study, we focus on hazard assessment, that is, on the first three points of the previous list, and in particular on propagation assessment. Indeed, the mere study of gravitational hazards is already a complex research subject. Landslides can take various forms, like slope deformations, rapid collapses of mountainous or volcanic slopes, or debris flows (these phenomenons will be presented more thoroughly in Chapter 1). Such processes can of course follow one another during the evolution and the transformation of the landslide (e.g., because of the incorporation of water). Scales can also vary significantly. Destabilized volumes can range from a few m^3 for rockfalls, to several km^3 pour volcanic flank collapses. Landslides velocities also span a large range of magnitudes, from a few mm or cm per year for slope deformations, to several tens of meters per second for rock avalanches or debris flows. Thus, no unified framework exist for landslide hazard analysis.

In spite of significant progress over the past decades to better understand and describe the physical processes at stake (e.g. Corominas et al., 2014; Delannay et al., 2017), engineers and researchers studying landslides are also faced with methodological and practical issues. Indeed, it is sometimes difficult to characterize in details the geotechnical and hydrogeological properties of the geological formations that are destabilized, as well as the rheological properties of materials during propagation. If sampling, drilling, geophysical surveys and laboratory analyzes can be done to investigate a given landslide, the duration and financial cost of such measurement campaigns are sometimes incompatible with operational constraints. Besides, the spatial interpolation and/or the extrapolation of measures is complex and associated to major uncertainties (Thiery et al., 2020).

Quantitative gravitational hazard assessment must thus tackle scientific problems (understanding and modeling of physical processes), methodological problems (acquisition and interpretation of data, usage of predictive models at various scales, quantification and propagation of uncertainty), and operational constraints (limited temporal and financial resources). A milestone to solve these problems is the collaboration between academic and applied research institutes. This PhD project was developed in this perspective, as a result of the collaboration between the BRGM (Bureau des Recherches Géologiques et Minières, the French Geological Survey), whose expertise in natural hazards is often used by local authorities, and the IPGP (Institut de Physique du Globe de Paris), where a numerical model for gravitational flow propagation was developed (in collaboration with the Laboratoire d'Analyse et de Mathématiques Appliquées de l'Université Gustave Eiffel and the Ecole Normale Supérieure de Paris). It is precisely this need of skill and knowledge transfer between the academic and applied researches that raised my interest for this research topic. Indeed, it requires a global vision of the stakes and the understanding of various subjects to enable and justify the operational use of a numerical model. Thus, I had to acquaint myself with, for instance, differential calculus, field work and statistical analysis methods.

Objectives of the thesis

In this context, this PhD aims at assessing the usability of numerical models to quantify propagation hazard for gravitational flows, i.e. landslides whose propagation can be compared (in a first approximation), to flows. We focus in particular on rock avalanches, debris avalanches, and debris flows (see Chapter 1 for definitions).

We consider only thin-layer models, that is, models describing the propagation of a material layer whose thickness is small in comparison to its extent. In comparison to 3D models who aim at describing the dynamics of each fluid or solid particle, thin-layer models give only the thickness of the layer, and its averaged velocity. Thus, they are faster and easier to use, which is a significant advantage for an operational use. However, on the contrary to purely empirical methods, thin-layer models give better estimations of the dynamics and geometry of deposits. We will use the SHALTOP numerical model that has already been tested to reproduce granular flows at the scale of the laboratory (Mangeney-Castelnau et al., 2005; Mangeney et al., 2007b), as well as landslides at the field scale (e.g. Favreau et al., 2010; Levy et al., 2015; Brunet et al., 2017; Moretti et al., 2020a). In comparison to other thin-layer models (see McDougall (2017), Hungr et al. (2007) and Pastor et al. (2018a) for a review), SHALTOP can seem rather simple. Indeed, it does not model, for instance, erosion processes or two-phase flows (with a fluid and a solid fraction). Such processes are however difficult to model and constrain because they involve many parameters that must be fitted and require the use of ad-hoc (i.e. empirical) closure relations. As a good compromise, we choose to use a simplified description of the physical propagation processes, with only one or two rheological parameters. The latter are calibrated by reproducing documented events. This empirical approach allows to simplify the analysis and interpretation of results, and thus hazard assessment, while preserving in simulation the influence of topography on the landslide propagation. The problematic we will try to answer can thus be formulated as follows: **To what extent can thin-layer models be used empirically to quantify propagation hazard for gravitational flows?**

This question can be studied through three research axes that shape our work (Figure 0.1):

- What is the importance, in thin-layer models, of a detailed description of geometrical interactions between a landslide and the topography on which it propagates? How does it influence the topographic control on the flow dynamics?
- Can thin-layer models be used empirically with a limited number of rheological parameters to model realistic landslide scenarios?
- How can uncertainty be quantified and propagated in simulation results?

In the short term, this works contributes to assessing the practical modalities for using thin-layer models, and in particular SHALTOP, for landslide hazard assessment. In this perspective, SHALTOP has been adapted and modified to enhance its usability (in terms of modeled rheologies, simplicity of use and generation of unstable mass). Besides, the case studies, that will be presented hereafter, are associated to important stakes. Our simulations help characterize the associated gravitational hazard and can be used, in turn, for a preliminary risk assessment.

In the long term, this PhD contributes to developing a method where thin-layer models are used to derive hazard maps integrating uncertainties. Three problems must be tackled first: the propagation of uncertainty from measures to simulation results, the spatialization of uncertainty, and the change of scale (from the isolated landslide to the mountain slope or watershed). In this work, we address only the first point in a simplified framework. We consider cases where the landslide source area is identified, and propagate uncertainty only to the estimation of landslide travel distance. Deriving hazard maps for landslides thicknesses or maximum dynamic pressure is nevertheless an important objective. Such maps would be a major improvement to enhance gravitational hazards mitigation.

Structure of the thesis

The context of our study is presented into more details in Chapter 1. We present usual classification of landslides, along with physical processes controlling their propagation. We also give an overview of empirical, semi-empirical and numerical methods used to assess propagation hazard. Finally, we detail the main rheological laws used to model homogeneous one-phase flows in thin-layer models. The research directions are then considered, corresponding to the three questions listed above.

First is the question of the mathematical accuracy of thin-layer models. Even if the thin-layer equations are relatively simple, their formal derivation on complex topographies is not straightforward. This results of course from the difficulty to define rheological laws that are representative of physical phenomenons, but also from the complex mathematical tools that must be used to obtain the final equations. The first point is widely studied in the literature, as discussed in Chapter 1. The second point is, in comparison, less often considered: only few studies are dedicated to quantifying the importance of a rigorous mathematical derivation, in particular regarding the geometrical interactions between the flow and the topography on which it propagates. In Chapter 2, we detail the origin and effects of two topography curvature terms in thin-layer models. We quantify their influence on simulation results, by comparing simulations where they are properly taken into account, approximated or neglected. Thus, we identify situations where an incomplete topography curvature description lead to significant errors in numerical simulations, and thus to inaccurate hazard assessment.

Then, we test the possibility of using SHALTOP with simple rheological laws to reproduce documented events and to quantify the propagation hazard for future similar events. Two case studies with important stakes are considered. In Chapter 3, we consider a debris avalanche produced by a partial dome collapse from the Soufrière de Guadeloupe volcano (Guadeloupe, Martinique, Lesser Antilles). In Chapter 4 we study the combination of a rock avalanche and a subsequent debris flow in the Prêcheur river in Martinique, Lesser Antilles. In both case, the method is the same. We first a collect quantitative and qualitative information to constrain past landslides, and potential future events. This step is crucial to get realistic simulation scenarios. The originality of our approach lies in the aggregation of a wide variety of data (topographic surveys, geophysical measurements, geomorphological and geological observations, seismic recordings, ...). Rheological parameters are then calibrated empirically by reproducing documented events, and used to model forward prediction scenarios. By testing different rheological parameters and initial conditions, a sensitivity analysis is carried out.

In the case of Soufrière de Guadeloupe, relatively few quantitative data are available, but thin-layer models have already proven the ability to model debris avalanches in volcanic context (e.g. Mangeney et al., 2000b; Kelfoun and Druitt, 2005; Sosio et al., 2012). This case study thus enables to confirm this conclusion for SHALTOP, while improving gravitational hazard assessment in the Soufrière de Guadeloupe area.

The situation is more complex in the Prêcheur river, where SHALTOP is used to model very different phenomenons: a rock avalanche, and then a debris flow. As debris flows are two-phase flows, which do not lie in the theoretical validity frame of SHALTOP, our approach is even more empirical than in the Soufrière de Guadeloupe case. This is precisely the relevance of this case study, for we want to test if SHALTOP can be used empirically to model phenomenons that are, in theory, not meant to be described by its equations.

Finally, for landslide hazard assessment, quantifying uncertainty is important. As a matter of fact, the data collected on the field or in the litterature are uncertain, and the representativeness of models can be discussed. In this perspective, the previous parts focus on the reduction of

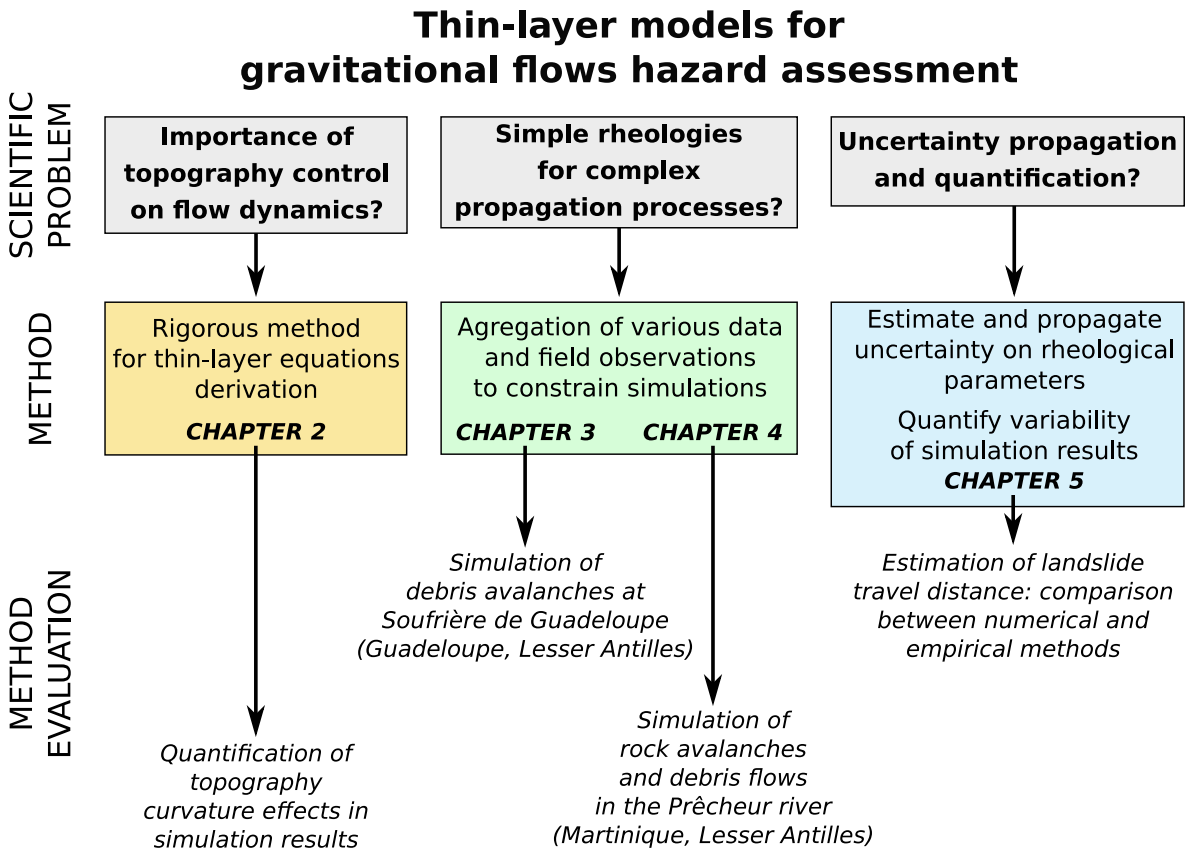

Figure 0.1: Scientific issues and structure of the thesis.

epistemic uncertainties, (that is, uncertainties that cannot be quantified as they result from an inappropriate description of the phenomenon), by ensuring the model equations are mathematically valid (Chapter 2), and by gathering various data to construct realistic simulation scenarios (Chapter 3 and 4). In the last part of this thesis (Chapter 5), we focus on the quantification of aleatory uncertainties (that can, precisely, be modeled and quantified), and on the possibility to reduce them with thin-layer models in comparison to purely empirical methods. This problem will be considered in the frame of power laws relating, for a given study site, the landslide travel distance to its volume. Such power laws can be derived empirically from landslide databases. The dispersion between the resulting power law and the data used to derive it can be used to estimate uncertainty, but results are not, in general, site-specific. To the contrary, numerical simulations take into account the topographic specificities of the study site, but uncertainty quantification is more complex. To solve this problem, we propose a method based on a database of site-specific simulations, with various rheological parameters and volumes. We test it on three different case studies: rock avalanches from the Samperre cliff, the Frank Slide (Canada), and the Fei Tsui Road debris slide (Hong-Kong)

Contexte

Entre 2004 et 2016, les mouvements gravitaires non liés à des séismes ont provoqué la mort de plus de 55 000 personnes dans le monde (Petley, 2012 ; Froude et Petley, 2018). La plupart d'entre eux se sont produit dans les régions montagneuses de la Chine et de l'Inde pendant les moussons. Les tremblements de terre sont aussi la source de glissements de terrains meurtriers (comme le tremblement de terre de magnitude M. 7,9 dans la région de Wenchuan, en Chine Fan et al., 2019), mais le dénombrement des pertes associées est complexe (Petley, 2012). Les glissements de terrain peuvent aussi avoir un impact économique significatif. Un exemple fortement médiatisé en France est le glissement du Chambon qui a provoqué la fermeture de la route reliant les villes de Grenoble à Briançon en Mai 2015, jusqu'à l'ouverture d'une nouvelle route en Décembre 2017 (Desrues et al., 2019). La construction de la nouvelle route, ainsi que la mise en place de solutions de déplacement alternatives en attendant, ont coûté plus de 30 million d'euros (Echos, 2015).

Les aléas gravitaires concernent aussi des reliefs moins escarpés que les massifs montagneux. Toujours en France, les coteaux de la vallée de la Marne et de la Montagne de Reims (Champagne), connaissent par exemple régulièrement des déstabilisations qui endommagent des routes et/ou des parcelles cultivées pour la vigne (e.g. Pannet et al., 2015 ; Hannion et Hamman, 2018 ; Pannet, 2018).

Compte tenu des enjeux économiques et humains, l'étude des glissements de terrain est importante pour évaluer correctement les aléas, et par suite les risques associés. L'aléa se rapporte au processus même en croisant la probabilité d'un événement avec son intensité (par exemple, la vitesse et/ou la distance de parcours du glissement de terrain). Le risque combine l'aléa avec son impact sur les enjeux exposés, au regard de leur valeur économique. Dans le cas des glissements de terrain, les principales étapes d'une analyse exhaustive de risque sont (Alexander, 2002 ; Glade et Crozier, 2005 ; Fell et al., 2008 ; Corominas et al., 2014) :

1. *La caractérisation de l'aléa : quels types de glissement de terrain sont attendus ? Quels volumes peuvent être déstabilisés ? Avec quelle probabilité d'occurrence ? Cette étape se base principalement sur l'inventaire des événements répertoriés sur la zone d'étude.*
2. *La cartographie de l'aléa : où les glissements de terrains peuvent-ils être initiés ? Jusqu'où peuvent ils aller ?*
3. *Quantification de l'intensité : quelles sont les caractéristiques des glissements de terrain ? Par exemple pour l'aléa de propagation, l'intensité est mesurée par la distance de parcours, la vitesses et/ou la pression dynamique, ou encore l'épaisseur des dépôts. Comment ces mesures de l'intensité sont-elles corrélées à la magnitude de l'événement, c'est à dire au volume du glissement de terrain ?*
4. *Analyse de l'exposition des enjeux : quel est la probabilité qu'une infrastructure ou un quartier d'habitation soient affectés par un glissement de terrain ?*
5. *Analyse de la vulnérabilité des enjeux : quel est l'impact potentiel d'un glissement de terrain de magnitude donnée sur les enjeux ? Cet aspect est différent de l'exposition : par exemple, un pont peut être fortement exposé à l'aléa de coulée de boue, mais son intégrité peut être menacée seulement en cas d'événement majeur.*
6. *Intégration des analyses précédentes, quantitatives ou qualitatives, pour obtenir une estimation quantifiée du risque en terme de coûts et/ou de victimes potentielles.*

Dans cette étude, nous nous concentrons sur l'étude de l'aléa, c'est à dire sur les trois premiers points de la liste précédente, et en particulier sur l'aléa de propagation. Bien que le choix de

*nos cas d'étude, qui seront décrits plus loin, ait été guidé par les enjeux associés, nous n'avons pas réalisé d'étude quantifiée des risques (*Quantitative Risk Assessment *en anglais). De fait, même sans aller jusqu'à l'évaluation des risques, l'analyse des aléas gravitaires est un sujet de recherche déjà complexe. En effet, les glissements de terrain peuvent prendre des formes très variées, allant de la déformation de pentes à la rupture brutale de versants de massifs montagneux ou volcaniques, en passant par les coulées de boue (ces différents termes seront définis plus précisément dans le Chapitre 1, en anglais). De tels processus peuvent bien sûr s'enchaîner lors de l'évolution et la transformation progressive d'un glissement de terrain (en raison, par exemple, de l'incorporation d'eau). Les échelles peuvent être aussi très différentes. Par exemple, les volumes mis en jeux peuvent aller de quelques* m^3 *pour les chutes de blocs, à plusieurs* km^3 *pour les déstabilisations de flancs d'édifices volcaniques. De même, les vitesses caractéristiques sont également très variables, de quelques mm ou cm par an pour des déformations de pentes, et jusqu'à plusieurs dizaines de mètres par seconde pour des avalanches de blocs ou les laves torrentielles. Ainsi, aucun cadre d'étude unifié n'existe, ce qui rend l'étude des aléas gravitaires très complexe.*

Malgré des progrès réalisés ces dernières décennies pour mieux caractériser les phénomènes physiques en jeu (e.g. Corominas et al., 2014), les ingénieurs, chercheurs et experts étudiant ces processus sont également confrontés à des problématiques pratiques et méthodologiques. De fait, il est parfois difficile de déterminer finement les caractéristiques géotechniques et hydrogéologiques des formations géologiques impliquées dans des déstabilisations, ainsi que les caractéristiques rhéologiques des matériaux lors de la propagation. Si des études ciblées sont possibles grâce à des prélèvements, des forages, des techniques géophysiques et des analyses en laboratoire, les coûts et la durée de telles campagnes de mesures sont parfois incompatibles avec les contraintes opérationnelles. Par ailleurs, l'interpolation spatiale des données récoltées est complexe et associée à des incertitudes importantes, quand la zone d'étude est étendue à un versant ou à un bassin versant (Thiery et al., 2020).

Cette problématique du changement d'échelle s'applique aussi aux méthodes utilisées pour évaluer l'aléa, où des méthodes purement quantitatives sont souvent inapplicables quand le site d'étude est très étendu. Par exemple, la modélisation numérique en 3 dimension des déformations d'un versant est complexe, mais envisageable si la géologie du site et les processus physiques en jeu sont suffisamment bien caractérisés. Néanmoins, une telle approche est inenvisageable à l'échelle du massif montagneux dans son ensemble : en plus de la difficulté d'obtenir d'obtenir des données topographiques, géologiques et géotechniques fiables à cette échelle, le temps de calcul peut s'avérer rédhibitoire. En pratique, des méthodes plus empiriques sont donc utilisées à ces échelles. Comme énoncé par Thiery et Terrier (2018), "il est préférable de disposer de quelques données de qualité et d'envisager un zonage basique [de l'aléa] qui pourra être justifié et probant plutôt qu'une multitude d'information de qualité médiocre et un zonage complexe avec de fortes incertitudes".

La quantification des aléas gravitaires fait ainsi face à des verrous scientifiques (compréhension et modélisation des processus physiques), méthodologiques (acquisition et interprétation des données, utilisation de modèles prédictifs à des échelles différentes, quantification de l'incertitude et de sa propagation), ainsi qu'à des contraintes opérationnelles (temporelles, financières). Pour apporter des solutions techniques à ces verrous, la collaboration entre le milieu de la recherche académique et celui de la recherche appliquée est fondamentale. C'est dans ce cadre que cette thèse a vu le jour, fruit de la collaboration entre le BRGM (Bureau des Recherches Géologiques et Minières), qui apporte régulièrement son expertise pour évaluer les risques gravitaires auprès de collectivités territoriales, et l'IPGP (Institut de Physique du Globe de Paris), où un modèle numérique de propagation des écoulements gravitaires a été développé (en collaboration avec le Laboratoire d'Analyse et de Mathématiques Appliquées de l'Université Gustave Eiffel et l'Ecole Normale Supérieure de Paris). C'est d'ailleurs ce besoin de transfert de compétences entre le

milieu académique et la recherche appliquée qui, personnellement, m'a incité à candidater à cette thèse. Il nécessite en effet une vision d'ensemble et l'appropriation de sujets variés pour permettre et justifier l'utilisation opérationnelle d'un modèle numérique. J'ai ainsi du me familiariser avec le calcul différentiel en mathématique, le travail de terrain ou encore les méthodes d'analyse statistique.

Objectifs de la thèse

*Dans ce contexte, l'objectif de cette thèse est d'évaluer la faisabilité d'utiliser des modèles numériques pour quantifier la propagation des écoulements gravitaires, c'est à dire des glissements dont la dynamique de propagation s'apparente à un écoulement. Nous nous intéressons en particulier aux avalanches de blocs ou de débris (*rock/debris avalanche *en anglais), et aux laves torrentielles (ou coulée de débris,* debris flow *en anglais).*

*Nous considérerons uniquement les modèles d'écoulement en couche mince, appelés par la suite "de couches minces" (*thin-layer models*, ou* shallow-water models *en anglais), c'est à dire des modèles décrivant la propagation d'un écoulement ou d'un glissement de terrain dont l'épaisseur est négligeable par rapport à son étendue. Par rapport à des modèles 3D décrivant, en première approximation, la dynamique de chaque particule de fluide et/ou de solide, les informations qu'ils fournissent concernent uniquement l'épaisseur des matériaux en mouvement, et leur vitesse moyennée (perpendiculairement à la topographie). Ces modèles intégrés sont donc plus simples d'utilisation, ce qui est un avantage majeur pour une utilisation opérationnelle. A l'inverse de modèles purement empiriques, ils permettent de simuler la dynamique et la géométrie des dépôts des glissements de terrain. Nous utiliserons ainsi le modèle numérique SHALTOP déjà testé à plusieurs reprises pour modéliser des écoulements granulaires à l'échelle du laboratoire (Mangeney-Castelnau et al., 2005 ; Mangeney et al., 2007b) et des glissements de terrains (e.g. Favreau et al., 2010 ; Levy et al., 2015 ; Brunet et al., 2017 ; Moretti et al., 2020a). En comparaison à d'autres modèles (voir par exemple McDougall, 2017 ; Hungr et al., 2007 ; Pastor et al., 2018a, pour une revue), SHALTOP peut sembler relativement simple, car il ne modélise pas, par exemple, les processus d'érosion ou la propagation d'écoulements bi-phasiques, contenant une fraction solide et un fraction liquide. Des tels processus sont néanmoins difficiles à modéliser et à contraindre, car ils impliquent un nombre importants de paramètres à déterminer et des lois empiriques ad-hoc. Nous prenons donc le parti d'utiliser une description simplifiée des processus de propagation, avec seulement un ou deux paramètres rhéologiques calibrés en reproduisant des événements documentés. Cette approche empirique permet de simplifier l'analyse et l'interprétation des résultats, et donc l'analyse de l'aléa, tout en préservant dans les simulations l'influence de la topographie sur la dynamique du glissement de terrain. La problématique à laquelle nous tenterons d'apporter des éléments de réponses peut ainsi être formulée de la manière suivante :* ***Dans quelle mesure les modèles numériques d'écoulements de couches minces peuvent-ils être utilisés de manière empirique pour quantifier la propagation des écoulements gravitaires ?***

Cette problématique peut se décliner en trois axes, qui structurent la thèse (Figure 0.1) :

- *Quelle est l'importance d'une description fine des interactions géométriques entre le glissement de terrain et la topographie, dans les modèles de couches minces, pour bien modéliser le contrôle de la topographie sur la dynamique des écoulements gravitaires ?*
- *Les modèles de couches minces peuvent-ils être utilisés avec un faible nombre de paramètres pour modéliser des scénarios réalistes de glissements de terrain ?*
- *Comment propager et quantifier l'incertitude dans les résultats des simulations ?*

A court terme, ce travail contribue à discuter les modalités d'utilisation des codes de couches minces, et en particulier de SHALTOP, pour réaliser des études d'aléas. En ce sens, le code SHALTOP a été adapté et modifié pour diversifier ses possibilités d'utilisation (en terme notamment de rhéologies modélisées, de simplicité d'utilisation et de génération des masses instables). Par ailleurs, les cas d'applications, présentés plus loin, présentent des enjeux importants. Ainsi, nos simulations permettent de mieux quantifier les aléas gravitaires associés. Les résultats pourront donc être utilisés, ensuite, pour une estimation préliminaire des risques.

A plus long terme, cette thèse donne des pistes pour construire une méthodologie de cartographie des aléas gravitaires utilisant des modèles de couches minces et intégrant les incertitudes d'estimation. Cet axe de recherche fait face à trois problèmes principaux : la propagation de l'incertitude des données d'entrées aux résultats des simulations, la méthodologie de spatialisation de l'incertitude, et le changement d'échelle (du glissement de terrain isolé au versant ou au bassin versant). Dans ce travail, nous apportons quelques éléments de réponses à la première problématique, sans aborder les deux dernières. Nous nous limitons à des cas d'étude où la zone source est identifiée, et ne considérons la propagation de l'incertitude que pour l'estimation de la distance de parcours des glissements de terrain. Nous ne considérons donc pas, par exemple, la géométrie des dépôts. L'obtention de carte d'épaisseurs ou de pression dynamiques maximales prenant intégrant l'incertitude, au moins d'une manière simplifiée, reste néanmoins un objectif important : de telles cartes seraient une réelle avancée pour améliorer la gestion des risques gravitaires.

Structure de la thèse

Le contexte de notre étude est défini plus précisément dans le Chapitre 1, où nous rappelons la catégorisation des mouvements gravitaires et les processus physiques contrôlant leur propagation. Nous y donnons également un aperçu des méthodes empiriques, semi-empiriques et numériques utilisées pour étudier et quantifier la propagation des glissements de terrain. Nous présentons également les principales lois rhéologiques utilisées pour modéliser des écoulements mono-phasiques, homogènes, dans les modèles de couche mince. Trois axes de développement sont ensuite considérés, répondant au trois problématiques énoncées précédemment.

Dans un premier temps se pose la question de la justesse mathématique des modèles de couches minces. Même si les équations finales restent relativement simples, la dérivation rigoureuse de ces équations pour des topographies complexes n'est pas évidente. Cela résulte bien sûr de la difficulté de déterminer une rhéologie représentative des processus physiques, mais aussi des outils mathématiques qui doivent être utilisés pour parvenir à la forme finale des équations. Le premier aspect est un sujet largement étudié dans la littérature, comme discuté dans le Chapitre 1. Le deuxième aspect est moins souvent considéré : peu d'études sont consacrées à l'importance d'une méthodologie mathématique rigoureuse, en particulier pour décrire finement les interactions géométriques entre le glissement de terrain et la topographie sur laquelle il se propage. Dans le Chapitre 2, nous détaillons l'origine et les effets de deux termes de courbure apparaissant des les équations des modèles de couches minces. Nous quantifions leur effets sur les résultats de simulations en comparant des simulations où ils sont pris en compte, négligés ou approximés. Ainsi, nous identifions les situations dans lesquelles une description incomplète de la courbure de la topographie peut induire des erreurs significatives dans les simulations numériques, et donc conduire à une estimation erronée des aléas.

Dans un second temps, nous évaluons la capacité de SHALTOP à reproduire des événements documentés et à quantifier l'aléa de propagation pour d'éventuels futurs événements semblables. Deux cas d'études avec des enjeux importants sont considérés : une avalanche de débris générée

par une déstabilisation partielle du dôme de la Soufrière de Guadeloupe (Chapitre 3), et l'enchaînement d'un effondrement de falaise et d'une coulée de débris dans la Rivière du Prêcheur, en Martinique (Chapitre 4). Dans les deux cas, la démarche est la même. Nous collectons d'abord des informations quantitatives et qualitatives pour contraindre au mieux les mouvements gravitaires passés et des scénarios de potentiels futurs événements. Cette étape est cruciale pour justifier les scénarios de modélisation, et l'originalité de notre approche réside dans l'utilisation de données variées (relevés topographiques, mesures géophysiques, observations géomorphologiques et géologiques, enregistrements sismiques...). Les paramètres du modèles SHALTOP sont ensuite calibrés empiriquement en reproduisant un ou plusieurs événements passés. Cette calibration permet de modéliser des événements futurs probables. En faisant varier les paramètres des simulations, et en considérant plusieurs scénarios différents, une analyse de sensibilité est finalement réalisée.

Dans les cas de la Soufrière de Guadeloupe, relativement peu de données quantitatives sont disponibles, mais les modèles de couches minces ont déjà montré leur capacité à modéliser des avalanches de débris en contexte volcanique (par exemple Mangeney et al., 2000b ; Kelfoun et Druitt, 2005 ; Sosio et al., 2012). Ce cas d'étude permet donc de confirmer cette conclusion pour SHALTOP, tout en améliorant la connaissance des aléas gravitaire pour la Soufrière de Guadeloupe.

La situation est plus complexe pour la Rivière du Prêcheur, où nous tentons d'utiliser SHALTOP pour modéliser des phénomènes aux caractéristiques physiques très différentes : une avalanche de blocs, puis la remobilisation des dépôts en une coulée de débris. La composante empirique de la modélisation est ainsi encore plus importante pour le Prêcheur que pour la Soufrière de Guadeloupe, puisque nous ne prenons pas en compte directement dans les équations les interactions entre fractions solides et liquides, alors qu'elles sont à priori importantes pour les coulées de débris. C'est précisément l'intérêt de ce cas d'étude, puisqu'il permet de juger si SHALTOP peut être utilisé empiriquement pour reproduire un phénomène qui, à priori, est hors du cadre de validité théorique de ses équations.

Pour l'évaluation des aléas gravitaires, l'estimation des incertitudes associée est importante, puisque les données servant à réaliser l'évaluation sont elles-mêmes incertaines, et que la représentativité des modèles est également approximative. En ce sens, les parties précédentes se concentrent sur la réduction des incertitudes épistémiques (c'est à dire les incertitudes non modélisables car liées à une description erronée du phénomène), en s'assurant de la validité mathématique des équations dans le Chapitre 2, et en synthétisant des données variées pour contraindre les scénarios de déstabilisation dans les Chapitres 3 et 4. Dans la dernière partie de cette thèse (Chapitre 5), nous nous intéressons plutôt à la quantification des incertitudes dites aléatoires (celles qui, justement, peuvent être modélisées), et à la possibilité de les réduire grâce à l'utilisation de modèles d'écoulement en couches minces, par rapport à des approches purement empiriques. Cette question sera étudiée dans le cadre de lois puissances estimant, pour un site donné, la distance de parcours d'un glissement de terrain en fonction de son volume. De telles relations peuvent être déduites empiriquement à partir de bases de données de glissements de terrain. La dispersion entre les lois puissance empiriques et les données utilisées pour les établir permet de quantifier l'incertitude des estimations, mais les lois obtenues ne sont en générale pas spécifiques au site d'étude. A l'inverse, l'utilisation de simulations numériques permet de prendre en compte les spécificités topographiques d'un site d'étude, mais la quantification des incertitudes est plus complexe. Nous proposons une solution basée sur des bases de données de simulations avec des volumes et des mobilités variées, spécifiques au site d'étude. Cette méthodologie est appliquée sur trois cas d'étude : les effondrements de la Falaise Samperre (Martinique), le Frank Slide *(Canada) et le* Fei Tsui Road debris slide *(Hong-Kong).*

Table of contents

Chapter 1

Gravitational flows: processes and models

1.1 Landslide types and processes

1.1.1 Landslides classification

Cruden (1991) defines a landslide as "the movement of a mass of rock, earth or debris on a slope". The term is however misleading, because it wrongly suggests that landslides are only associated to a sliding process along a rupture surface. For this reason, Varnes (1978) refers more broadly to "slope movements". In the following, we will mostly use the term "landslide", because it is widely used. However to describe more accurately the different kinds of landslides, more precise denominations are needed. Extending the pioneering work of Sharpe (1938), Varnes (1958) and Varnes (1978) proposed a classification of landslides based on the type of movement and on the type of material involved. It is summarized in Figure 1.1, with some examples sketched in Figure 1.2. A distinction is made between 5 main movement types:

- **Falls**: Detachment of a mass from a steep slope or a cliff, that starts propagating through free fall. It then bounces and rolls on the ground. Such events are common in mountainous areas (e.g. Roy et al., 2019), coastal cliffs (e.g. Benjamin et al., 2020) and volcanoes (Calder et al., 2005; Hibert et al., 2014; Durand et al., 2018; Kuehnert et al., 2020).

- **Topples**: Rotation of a mass around a pivot point located at its base (e.g. Schumm and Chorley, 1964; Alejano et al., 2010). This process can initiate slowly, but can lead eventually to failure and generation of, for instance, rockfalls.

- **Slides**: Displacement of a unit along one or several surfaces. For **rotational slides**, the sliding surface is concave, such that the unstable mass has a rotational movement around an axe roughly parallel to the slope. The downward movement of the upper section of the mass creates one or several, often vertical, head scarps. Examples of massive rotational slides involve the Maierato landslide in Italy (Guerricchio et al., 2012), the Villerville-Cricqueboeuf landslide in Pays d'Auge (Lissak et al., 2009), or the Rilly-la-Montagne landslide in Champagne (Marre, 1987), both in France. On the contrary, in **translational slides**, sliding occurs along a roughly planar surface along which the moving mass translates. A spectacular example of translational slide is given in Hungr et al. (2014), Figure 11 (Murazzano, Northern Italy).

TYPE OF MOVEMENT		TYPE OF MATERIAL		
		BEDROCK	ENGINEERING SOILS	
			Predominantly coarse	Predominantly fine
FALLS		Rock fall	Debris fall	Earth fall
TOPPLES		Rock topple	Debris topple	Earth topple
SLIDES	ROTATIONAL	Rock slide	Debris slide	Earth slide
	TRANSLATIONAL			
LATERAL SPREADS		Rock spread	Debris spread	Earth spread
FLOWS		Rock flow (deep creep)	Debris flow (soil creep)	Earth flow
COMPLEX		Combination of two or more principal types of movement		

Figure 1.1: Varnes' classification matrix of landslides by processes and types (USGS, 2004).

- **Spreading**: Movement is dominated by lateral extension, usually on near horizontal slopes. For instance in sensitive clay spreading, coherent blocks of clay spread by floating on a layer of liquefied clays (Locat et al., 2011).

- **Flows**: When the moving material disintegrates and/or displays important deformations, its dynamics can be compared to that of a flow. Thus, the disintegration of one or multiple rocks into multiple smaller fragments generates a granular flow (Hibert et al., 2014; Levy et al., 2015), debris avalanches or rock avalanches that propagates sometimes kilometers away from the destabilization areas (Korup et al., 2013; van Wyk de Vries et al., 2001). Such events are very fast, with velocities reaching tens of m s^{-1} as in the initial stage of the Mount Meager landslide (Guthrie et al., 2012; Allstadt, 2013). However, flows can also be much slower, as for some earthflows in plastic and ductile soils that generally advance no more than a few meters per hour (Picarelli et al., 2005). Creeping, which refers to the slow (a few cm per year) deformation of slopes, is included in the category of flow-like landslides by Varnes (1978), but Hungr et al. (2014) suggest another category is needed for such slow slope deformations. Finally, another type of flow-like landslide are debris flows, where saturated debris propagate rapidly (a few m s^{-1} to tens of m s^{-1}) in channels. This is a wide-spread hazard in mountainous areas (e.g. Remaître et al., 2011) but also on volcanoes where the remobilization of eruption materials by water generates *lahars* (Vallance and Iverson, 2015; Thouret et al., 2020). Debris flows are thus a subcategory of lahars, along with hyper-concentrated flows, as will be discussed in the next Section.

- **Complex**: When several of the previous processes occur in the same landslide. Cruden and Varnes (1996) use the word "complex" to characterize the type of activity of a landslide (in the sense that we can talk, for instance, of a "complex rotational slide"), but do not consider it anymore as a landslide category.

The second criterion to classify landslides is the type of materials involved. Varnes (1958) and Varnes (1978) identify two main categories:

- **Bedrock** or **rock**: Hard and intact materials that was not disturbed by soil movements before the landslide.

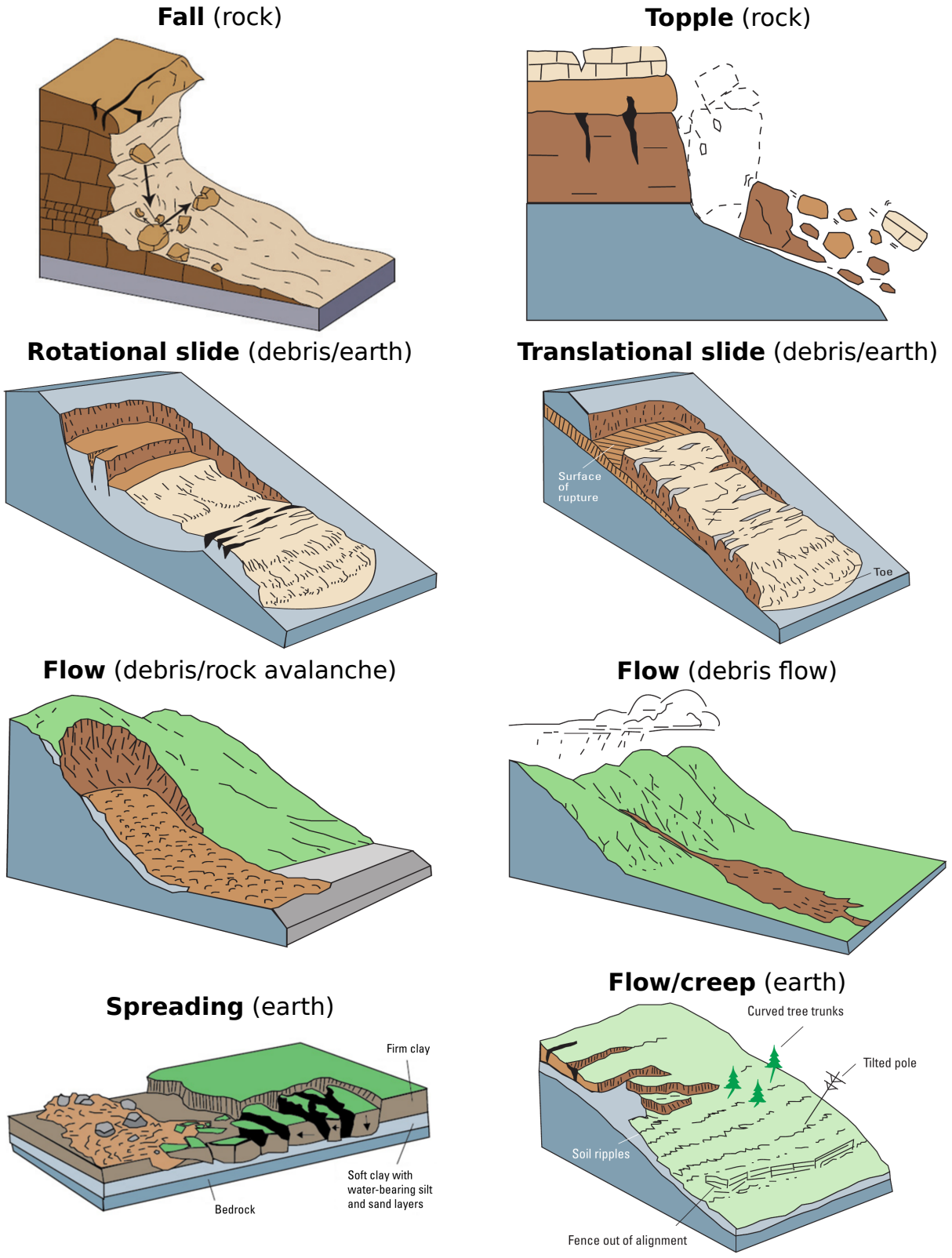

Figure 1.2: Classification of landslide processes, adapted from Highland and Bobrowsky (2008). Processes are given in bold. In parenthesis we give the type of material associated to each sketch. For flow-like landslide, we also give the names used in Figure 1.3.

- **Engineering soil**: Loose, unconsolidated or poorly cemented materials including rocks, organic materials, or minerals. The subcategory **debris** is used when the granulometry is relatively coarse: more than 20% of the fragments are greater than 2 mm. In the opposite case, the term **earth** is used.

Cruden and Varnes (1996) extended the aforementioned nomenclature to include a formal glossary of terms that can be used to characterize further the landslide process. They thus define different states of activity (e.g., active or inactive landslide), spatial distribution of activity (e.g. widening, retrogressive or confined), and styles (e.g. complex when multiple processes, such as slide and flows, occur in the same landslides, or multiple for the spatial repetition of similar movements). Additionally, they also list terms used to characterize the rate of movement (from extremely slow for velocities below 16 mm per year, to extremely rapid for velocities above 5 m s^{-1}) and water content (from dry to very wet).

Later on, Hungr et al. (2014) suggested an update of this classification. They argued that the full characterization of a landslide, as presented in the previous paragraph, can result in lengthy names. In turn, it is difficult for scientists to communicate about their work to public or private stakeholders, as well as to other scientists. Hungr et al. (2014) thus suggest that the designation of a landslide should be as simple as possible, and highlight the focus of the researcher, rather than explicit precisely all the processes at stake. For instance, the term "rock avalanche" is not formally included in the classification of Cruden and Varnes (1996). Following their nomenclature, the former should be referred as "rock flow", which is not a term widely used. Thus, Hungr et al. (2014) basically identify terms widely used in the literature to describe landslides and class them in the process/material type matrix used by Cruden and Varnes (1996). Besides, they add a process type, **slope deformation**, that refers to very slow processes (a few mm per year) affecting slopes.

The Varnes classification is today widely used (Highland and Bobrowsky, 2008; SafeLand, 2012), with sometimes some adaptations. For instance, Dikau et al. (1996) adapts the classification to lay emphasis on the rupture mechanisms and on their temporal evolution. (Leroueil et al., 1996) adds a third axe to the process/material matrice to include the current state of the landslide.

The works of Varnes (1958), Varnes (1978), Cruden and Varnes (1996) and Hungr et al. (2014) aim at classifying broadly landslides, taking into account within a single frame the initial deformation, the failure and the propagation processes. Of course, more refined classifications can be proposed if the focus is on one of them only. For instance, geotechnicians are particularly interested in the failure mechanisms, such that appropriate classifications for them include the geotechnical properties of the materials and geotechnical concepts, such as liquefaction (Hutchinson, 1988; Sassa, 1999). Flageollet (1989) uses another classification criterion, the main direction of movement, to differentiate between vertical collapses and subsidence, and horizontal movements (as in most other landslides).

On the contrary, if the focus is on the propagation of the landslide, it is worth highlighting the composition of the propagating materials in the classification scheme. Indeed, we may expect the latter to depend directly on the materials geotechnical and geomorphological properties. In this perspective, a simple distinction between rocks, soils or debris is not sufficient. Following Meunier (1991) and Meunier (1994), Coussot and Meunier (1996) suggest two classification criteria: the solid fraction type (fine and cohesive to coarse and non-cohesive) and proportion (dry to saturated materials). Such a classification is relevant and highly insightful for landslides that disintegrates during their propagation (that is, flow-like landslides), but not when the bulk moves relatively undisturbed and intact. This is illustrated by the mere fact that Coussot and Meunier (1996) refer to the latter case as "landslide", implying that in their perspective, debris avalanches or debris flows are not landslides. This is in contradiction with Cruden and Varnes

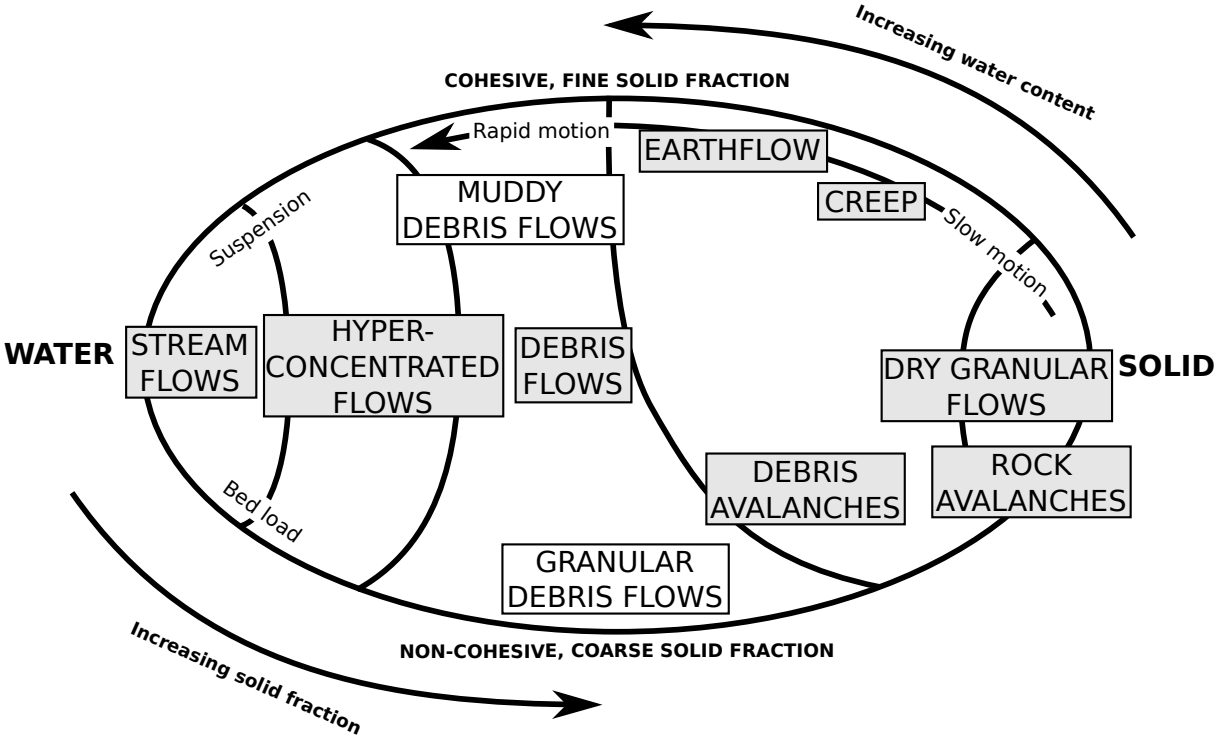

Figure 1.3: Classification of gravitational flows, adapted from (Coussot and Meunier, 1996). Grey rectangles match main types, white rectangle are debris flows subtypes.

(1996) and Hungr et al. (2014), highlighting the complexity of striking a common ground on the mere definition of "landslide".

1.1.2 Classification of flow-like landslides

Because our work focuses on flow-like landslides (that we will also call **gravitational flows**), let's elaborate further on the classification of Meunier (1991), Meunier (1994), and Coussot and Meunier (1996). A schematic representation of this classification is given in Figure 1.3, with some modifications in comparison to Coussot and Meunier (1996).

At one end of the spectrum, we find dry, non cohesive and coarse granular flows. Here, we use "coarse" to designate materials mainly composed of sand, gravels and boulders and thus with negligible clay fraction. In turn, the flow dynamics are mainly controlled by collision and friction between grains (Delannay et al., 2017). This is the case for **dry granular flows** generated by the disintegration of poorly cemented materials. They occur, for instance, in volcanic context where eruptive materials can form hundreds of meters high cliffs but shatter relatively easily after failure detached from the cliff. Examples include the Dolomieu Crater of Piton de la Fournaise volcano, Réunion island (Hibert et al., 2011; Durand et al., 2018) or the Samperre cliff, in Martinique, that we will study later on. When the flow is initiated by the destabilization of a large rock mass (up to several 100×10^6 m^3) and is made of large boulders and blocks (up to a few meters large), the name **rock avalanche**, or *sturzstrom*, is commonly used in mountainous context (Heim, 1932; Davies, 1982; Pirulli, 2009). In comparison, large destabilizations of volcanic edifices are commonly called **debris avalanches** (e.g. Glicken, 1996; Blahůt et al., 2019). The denomination debris avalanche also refers to the shallow-destabilizations of partly-saturated or saturated vegetated soils, most of the time after heavy rainfalls, as in the Vargas State, Venezueal, in 1999 (Hungr et al., 2014; Larsen and Wieczorek, 2006). Thus, debris avalanches may contain both fine and coarse materials, and are generally associated to a larger water content than rock

avalanches, due to precipitations or release of perched aquifers for volcanoes (Peruzzetto et al., 2019).

Large debris and rock avalanches (typically, larger than 10^6 m^3 and up to several 10^9 m^3) display surprinsingly long runouts. The mechanisms explaining this mobility increase with volume have been thouroughly discussed in the litterature. They include effects of excess pore pressure when fluids are trapped in the avalanche (Legros, 2006; Iverson et al., 2011) or lubrication by snow or ice (Delaney and Evans, 2014; Aaron and McDougall, 2019). However high mobilities are also observed for dry avalanches and other mechanisms have been suggested, such as fluidization by air (Hsu, 1975), acoustic fluidization (Johnson et al., 2016) or flash heating (Lucas et al., 2014) that reduces friction for high velocities (foor a review, see Korup et al., 2013; McDougall, 2017).

We can oppose these fast gravitational flows to **earthflows** and **creeping**. These movements are associated to the deformation of ductile soils. Until a threshold is reached, the presence of water in the material favors cohesion. However, increasing the water pore pressure progressively reduces internal friction and favors lubrication between solid grains, and thus deformations. While creeping is essentially related to slow (a few cm yr^{-1}) slope deformations (thus, its inclusion in flow-like landslides can be discussed, see (Hungr et al., 2014)), earthflows generally occur as surges with higher velocities (a few m hr^{-1}) triggered for instance by excess pore pressure and liquefaction.

Increasing the water content of gravitational flows often produces **debris flows**. Debris flows are common in mountainous areas, for instance in the Alpes, in Europe (e.g. Malet, 2003; Remaître, 2006; Quan Luna et al., 2012; Bel et al., 2015). This occurs, for instance, when debris avalanches or rock avalanches are channelized in rivers and/or incorporate water by flowing over glaciers and snow. The excess pore pressure favors partial liquefaction and thus enhance the mobility of the flow. The characteristic solid fraction of debris flows varies in the literature: Coussot and Meunier (1996) give weight solid fractions between 50 and 90%,Vallance and Iverson (2015) mention 60%, and Thouret et al. (2020) suggests values above 80%. In any case, solid fraction is high. A clear characteristic of debris flows is that there is no vertical separation between the solid and fluid phases that have similar velocities (although the fluid phase is slightly faster, see Vallance and Iverson, 2015). The physical process controlling the flow dynamics depend on the granulometry of the solid fraction. When there's a significant fraction of clays, viscous forces are predominant and the debris flow is referred to as a **muddy debris flow**. A main characteristic of such flows is their yield stress: flowing occurs only when shearing exceeds a critical value. This "toothpaste" behavior results, in particular, in the formation of levees at the front and on the sides of the flows (though this behavior is also observed for dry granular flow, see Mangeney et al. (2007b)). In comparison, when the debris flow is coarser with mainly sand, gravel and boulders, the predominant processes are the grain-to-grain interactions with collisions and friction: we refer to them as **granular debris flows**. Obviously, there is no clear-cut limit between muddy and granular debris flows: Scott et al. (1995) suggest for instance an empirical value for the clay fraction of 5%, below which the debris flow can be considered granular.

A decrease of solid fraction (typically, between 20% and 60% of volume, Thouret et al. (2020)) leads to the vertical separation of the solid and fluid phases. Coarse particles are transported at the base of the flow through bed load, while the fine particles remain in suspension. The resulting flow type is commonly referred to as **hyperconcentrated flows**. They differ from **stream flow**, for which the sediment load is further decreased.

Note that we slightly changed the classification suggested by Coussot and Meunier (1996) in their Figure 1. Indeed, their classification is meant to include both the initial deformation, rupture and propagation processes of flow-like landslides. In comparison, our focus is more on the propagation stage. We thus removed the category "landslide" whose generality is misleading, and replaced it by slow and cohesive gravitational flows: **earthflow** and **creep**. In the same

perspective, we do not consider that the absence of water is necessarily associated to stability. As a matter of fact, a dry granular flow is, by definition, both dry and mobile. We also associate the acceleration of motion with increased water content only to fine and cohesive materials, as a result of lubrication. Indeed, dry granular flows and rock avalanches can be very fast (several m s^{-1}) even without water.

Malet (2003) use a classification similar to that of Coussot and Meunier (1996), but goes into more details to clarify the meaning of "landslides" in this context. For him, it describes the transition between a dry and solid material, and water-laden and mobile debris flows. Thus, Malet (2003) suggests these movements display a transient nature between "slides", where deformation is concentrated along an interface, and "flows", where the whole moving layer displays important deformations. Hence the French term *glissement coulée*, whose literal translation "slide-flow" clearly illustrates the temporal succession of an initial slide and of the a subsequent flow. It has no direct equivalent in the Varnes classification, but can be referred to as creep, to describe slow deformations before rupture, or earthflow to describe landslides where flowing processes become predominant. This transition between static and flowing materials is very difficult to model because it demands a good understanding of the initial deformation and rupture processes, with soil mechanics, as well as the propagation processes.

In this study, we focus on the propagation of mobile flow-like landslides with a clear flowing behavior (that is, with important internal deformations), such as rock avalanches, debris avalanches and debris flows. In the following section, we present the main physical processes controlling propagation.

1.1.3 Main physical processes of gravitational flow propagation

There are still many challenges for characterizing the physical processes at stake in geophysical flows. Following Coussot and Ancey (1999) and Delannay et al. (2017), we can distinguish between the following mechanisms, depending on the solid fraction and on the shear rate of the flow.

- For very dilute flows (solid fraction below 1%), the dynamics are mainly controlled by the interstitial fluid (air or water), with hydro-dynamics and turbulence effects.
- For dilute flows (solid fraction between 10 and 50%) with high shear rates, the dynamics of the fluid are still the dominant process. For smaller shear rates (that is, for smaller deformations), binary collisions between grains can be described by kinetic theory. In its (maybe) simplest form, it uses the statistical distribution of velocities and positions of particles, and introduces a granular temperature that quantifies particles agitation. The resulting "granular gas" differ from "molecular gases" in the sense that collisions are not elastic, and thus dissipate energy.
- For dense flows (solid fraction above 50%), collisions can still occur but they are not binary and can last, such that a kinetic theory is no longer valid (in particular because the positions and velocities of different particles are no longer independent). Depending on the relative importance of particle-particle interactions and particle-fluid interactions, three regimes were suggested by Cassar et al. (2005):
  - Particle inertia dominated regime: interactions between grains are the main driving forces. Far small shear rates, they last a significant duration and the dynamics are well described by pure friction. When the shear rate increases, contact duration decreases and both friction and collisions must be accounted for. This is the case, for instance, in what we called granular debris flows.

- Viscous resistance dominated regime: the grains are slowed down by a viscous drag force proportional to the relative velocity of the fluid, in respect to the solid phase. The fluid phase movement is comparable to that of a fluid through a porous media. The excess pore pressure generated by non-zero relative velocities lubricates contacts between grains. Note that, as pointed out by Vallance and Iverson (2015), such effects can be significant even for very small relative velocities (e.g., 10^{-5} m s^{-1}).
- Fluid inertia dominated regime: viscosity is small, and the drag force applied on particles is controlled by inertial effects.

The variety of scales and processes makes it difficult to describe properly, and then model, gravitational flows. This is particularly true for the static-flowing transition: for instance, Remaître (2006) model the initiation and the propagation of debris flows with two different numerical codes. Even in the idealistic case where a model would describe gravitational flows correctly, it is in practice difficult to determine the right rheological parameters. In the case of muddy debris flows, the rheology of the fine fraction can be studied with rheometers to derive yield strength and viscosities, because small samples (about 1 cm^3) can be deemed representative of the matrice, at least in a first approximation. The situation is more complex for coarser debris flows for which appropriate rheometers should be tens of meters large (Coussot and Meunier, 1996) to accommodate for the coarse granulometry of the matrice. In turn, model calibration can be done by comparing prediction to field observations or flume-tests experiments (e.g. Iverson et al., 2011), but the resulting parameters are not necessarily representative of other events. Thus, the direct estimation of rheological parameters is still an open issue.

Besides, geophysical flows are transient by nature, in space and time. As a matter of fact, a debris avalanche can turn into a debris flow as it enters a ravine, while progressive dilution in the stream will eventually transform it into a hyper-concentrated flow, and then into a muddy stream flow. Similarly, at a given time, spatial variations of solid fraction between the sediment-laden front of a debris flow and its diluted tail results in very different dynamics and solid transportation processes. The transition between one fully-developed regime to another (for instance, particle inertia to viscous regime) is characterized by complex mechanisms that are not easy to include in models, such as the transition between static and dynamic states (Sibille et al., 2007; Prime et al., 2014a), or the dilation and compaction of dense and loose materials (Pailha and Pouliquen, 2009; Iverson, 2012; Bouchut et al., 2016). Eventually, debris flows are also characterized by episodic surges that can have multiple origins, as hydraulic instabilities (Zanuttigh and Lamberti, 2007), particular rheological properties (e.g., non-monotonic relations between the shear stress and shear rate, Coussot et al. (1993)), or pulsatile incorporation of solid materials through, for instance, bank erosion. All these process are very hard to include in one single rheological model. That is why Iverson (2003) talk about "the debris-flow rheology myth".

Another key problem that scientists must tackle in the perspective of modeling correctly geophysical flows is boundary conditions. In particular, the entrainment of materials along the bed of the flow can significantly increase the volume of debris avalanches and debris flows (e.g., from 150 to 1620 m^3 for the 2000 Tsing Shan debris flow in Hong Kong, Pirulli and Pastor, 2012). Nevertheless, this process is still poorly constrained. For instance, an empirical law classically used in numerical models relates the erosion rate to the flow momentum through a proportionality relation (McDougall and Hungr, 2005; Pirulli and Pastor, 2012). However, as pointed out by Iverson (2012), this may stand true only in situations where entrainment has no significant impact on the flow momentum, as in fluvial system. When this is no longer the case, erosion rates may actually be inversely proportional to the flow velocity (Iverson, 2012). As a matter of fact, the energy needed to accelerate sediments at rest to the flow velocity is, precisely, all the more important as the flow velocity is high. Lusso et al. (2017a) find that entrainment rate are inversely proportional to the strain rate (see their equation 9), which is compatible with

the conclusion of Iverson (2012), provided we approximate the strain rate by the average flow velocity divided by the flow thickness.

The pore pressure in the bed has presumably also a prominent role in controlling entrainment processes. By conducting experiments in flume tests, Iverson et al. (2011) show that entrainment of water saturated beds accelerates the flow, as a result of liquefaction that reduces friction at the base of the flow. However, for low pore pressure, the energy transfer required to entrain the static bed is not compensated by liquefaction, and the flow is decelerated. These results are in apparent contradiction with the experiments of Mangeney et al. (2010), where dry granular flows propagating on a dry erodible bed go further than on a non-erodible bed. Apart from different experimental set-up that could explain this difference, Mangeney (2011) suggest that low pore water pressure prevents liquefaction but enhance cohesion, while completely dry granular materials have no cohesion, and are thus more easily entrained. More details about erosion processes can be found in Iverson (2012), Pirulli and Pastor (2012), Iverson and Ouyang (2015) and Delannay et al. (2017). As pointed out by Bouchut et al. (2008), it is difficult to include formally bed erosion in numerical models, in a way that ensures energy is preserved.

This short overview of literature highlights the complexity of conducting detailed landslide hazard assessment, that is, "the spatial and temporal probability of occurrence of landslides in [a] target area, along with their mode of propagation, size and intensity" (Corominas et al., 2014). As discussed in the preamble, such an analysis involves the identification of unstable areas (i.e. susceptibility estimation), and the estimation of propagation hazard. As we focus only on the propagation, we will not detail the methods used to estimate landslide susceptibility, for which a good review can be found for instance in Glade and Crozier (2005), Fell et al. (2008), Corominas et al. (2014) and Reichenbach et al. (2018).

1.2 Empirical and semi-empirical models for propagation hazard assessment

Propagation hazard assessment relies on the estimation of the gravitational flow dynamics, for an event of given magnitude (i.e. volume). In its simplest form, it boils down to estimating the travel distance, but more detailed characterizations involves spatial estimation of the thickness of the flow and/or of the deposits, peak discharges, velocities and kinetic energy.

The evaluation of propagation can be done empirically. The most straightforward estimations are carried out by using geomorphological evidences and expert judgment, as for the French *Plan de Prévention des Risques* (PPR, Risk Prevention Schemes) (Thiery and Terrier, 2018; Hoblitt et al., 1998). Another more quantitative approach uses empirical relations between the landslide volume and geometrical characteristics of the deposits, including travel distance (or runout), affected area or width of propagation path (e.g. Legros, 2002; Lucas et al., 2014; Mitchell et al., 2019). To assess the intrinsic mobility of the landslide, the ratio between drop height and travel distance (called the Heim's ratio μ_H Heim, 1932; Hsu, 1975) is often used. The associated angle of reach is the angle of an imaginary line connecting the highest point of the landslide scar, to the furthest point reached by the landslide. It has been widely shown that μ_H decreases for larger landslide volumes (e.g. Corominas, 1996; Finlay et al., 1999; Lucas et al., 2014; Zhan et al., 2017; Mitchell et al., 2019; Strom and Abdrakhmatov, 2018; Brideau et al., 2019). However, μ_H is not an appropriate measure of mobility because it also describes purely geometrical effects (e.g. Finlay et al., 1999; Legros, 2002; Lucas et al., 2014). For instance, let's consider that mobility is controlled by the friction coefficient between the landslide and the topography. Then, for a given friction coefficient, an increase of volume is naturally associated to longer runouts, that are not necessarily compensated by higher drop heights in the same proportion. Then, μ_H will

be different, while the friction coefficient does not change. Thus, Lucas et al. (2014) proposed another indicator to estimate the intrisic mobility of landslides from field observations: the effective friction coefficient μ_{eff}. The expression of μ_{eff} is derived from the analytical solution of the dam-break problem and is, supposedly, a better estimate for the "real" friction coefficient.

For rockfalls, the shadow angle is preferred to the reach angle. The shadow angle (Evans and Hungr, 1993) is measured by considering the line joining the apex of the talus where rocks detached from a cliff fall, and the final position of the rock after bouncing and rolling on the ground. For debris flows, empirical relations have also established to estimate the peak discharge, planimetric and cross-section inundated areas from the event volume (Rickenmann, 1999; Iverson et al., 1998).

Although the dispersion around the fitted power laws is often large, it is easy to quantity the resulting uncertainty. This is typically done by considering a normal distribution of the residues between the power law and the data used to derive it. Besides, they remain relatively simple, which is key point when hazard assessment must be done quickly. Implementation of such empirical relations in Geographical Information Systems (GIS) softwares for hazard mapping are proposed, for instance, by Jaboyedoff and Labiouse (2003) for rockfalls, Iverson et al. (1998) and Berti and Simoni (2014) for debris flows, and Mitchell et al. (2019) for rock avalanches. However, this method cannot describe the full complexity of some events, such as flows with multiple channeling (Peruzzetto et al., 2019), overflows as in the Johnsons Landing debris avalanche (Marinelli et al., 2015; Pastor et al., 2018a), or erosion.

A statistical-empirical method was proposed by Fannin and Wise (2001) to model, in particular, the propagation of debris flows. It was called "volume-change method" by Hungr et al. (2005a) and Corominas et al. (2014). The propagation path is divided in "reaches" (i.e. sections) where erosion, deposition, or both, occur. The eroded and deposited mass are calculated as function of the width, length and slope of each section, after calibration on field observations. The modeled debris flow thus advances from one reach to another, until all the volume is deposited. This methods allows to derive probability that given travel distances are exceeded, but requires significant a priori knowledge of the channel where the debris flow propagates.

Recently, somehow more straight-forward semi-empirical methods have been developed: flow-routing algorithms (Wichmann and Becht, 2005; Horton et al., 2013). They use a random-walk algorithm to model possible propagation paths on a given Digital Elevation Model (DEM). Starting from a source point, such paths are constructed by progressing from one pixel to another, following probabilistic laws that take into account the slope gradient and the direction of propagation at the previous step. Velocities are estimated at each step empirically (with for instance a frictional model, see Horton et al., 2013), and iterations stop when a minimal value is reached. This process is repeated several times for each source point, which in turn yields a map of hundreds or thousands of possible propagating paths. This approach is fairly easy to apply (though of course parametrization must be considered with caution) and has met with significant success over the past years. Examples of application of the flow-routing algorithm Flow-R (Horton et al., 2013) include Pastorello et al. (2017), Melo and Zêzere (2017), and Kang and Lee (2018). However, flow-routing algorithms may fail to reproduce accurately spreading, multiple channeling and overflows of large rock and debris rock avalanches (Horton et al., 2013), and thus are primarily used to investigate debris flows. Besides, they are largely based on empirical relations, which is not sufficient to reproduce the complex processes at stake in actual landslides. Finally, and maybe most importantly, they do not model the thickness of the flow or of the deposits. Thus, they can be used for a first hazard assessment, but more refined modeling is needed to assess vulnerability.

1.3 Physically-based models for propagation hazard assessment

To estimate both the the travel distance and velocity of a landslide from a physically-based model, the simplest approach is to solve the momentum equation of a rigid block sliding on a 1D topography (i.e. given by a graph $z = z(x)$). Energy is thus dissipated by the force applied at the base of the block (Hungr et al., 2005a). A convenient representation of the results uses the energy line above the topography, defined by

$$z_E(x) = z(x) + \frac{Mv(x)^2}{g} + z_0, \tag{1.1}$$

where M is the mass of the block, $z(x)$ the altitude along the profile, $v(x)$ the velocity of the block, g the gravity field and z_0 the initial altitude of the block. The energy line $z_E(x)$ thus joins the initial position of the mass to its final position. When a Coulomb solid friction law is used, with a friction coefficient $\tan(\delta)$ (δ is the friction angle), the energy line is a straight line with slope $-\tan(\delta)$ (Hungr et al., 2005a). The simplicity of this approach allows to consider different laws to model the force applied at the base of the mass. For instance, it can be adapted to model rockfalls (Evans and Hungr, 1993). However, such methods remain largely empirical because the hypothesis of a rigid sliding block greatly simplifies the complexity of physical processes controlling the propagation of real landslides, as discussed previously.

However, the combined effects of particle collision and friction, or lubrication, advection and suspension in presence of an interstitial fluid, are difficult to model in a single framework (Andreotti et al., 2013; Delannay et al., 2017). Thus, current solutions for 3D-modeling (that is, when the dynamics of elementary volumes of fluid and/or of each solid particle are considered) often focus on reproducing one or two physical processes, but never all of them. Discrete element modeling (DEM) is now widely used to reproduce granular flows at the laboratory scale (Girolami et al., 2012; Windows-Yule et al., 2016). They can also be used to model fluid-particle interactions (Durán et al., 2012; Lefebvre-Lepot et al., 2015), which in turn can be applied to debris flow simulation (Zhao and Shan, 2013; Leonardi et al., 2014). Another approach is to consider a single-phase flow and solve the Navier-Stokes equations. Column collapse experiments are often used to test the resulting models (e.g. Lagrée et al., 2011; Ionescu et al., 2015; Martin et al., 2017; Lusso et al., 2017b), but real landslides can also be considered (Hu et al., 2015). The implementation of hybrid Eulerian-Lagrangian methods (Prime et al., 2014b; Ionescu et al., 2015; Lusso et al., 2017b; Koo et al., 2018) allows to model both large deformations (which is problematic using pure Lagrangian methods) and to track the material properties at the same time (which is difficult with Eulerian schemes as a result of numerical diffusion). In particular, this approach enables a fine description of the static-flowing transition (Prime et al., 2014b). However, these 3D models require huge computing resources. Most constitutive equations also depend on too many user-defined parameters, which is incompatible with the limited knowledge of the flowing material we have in practice.

The right balance between practical usage and physical modeling may have been reached, at least so far, by thin-layer models, also called shallow-water models. Their main assumption is that the flow (or landslide) extent is much larger than its thickness, so that the kinematic unknowns are reduced to two variables: the flow thickness and its depth-averaged velocity. The dimension of the problem is thus lower, allowing for relatively fast numerical computations. The first and simplest form of shallow-water equations was given by Barré de Saint-Venant (1871) for almost flat topographies. It was extended to curved 1D topographies (i.e. for topographies given by a 1D graph $z = z(x)$) for water flows by Dressler (1978) and Sivakumaran et al. (1983). The formulation was then adapted to model dry granular flows by Savage and Hutter (1991). This model has since been extended to real 2D topographies (i.e. given by a 2D graph $z = z(x, y)$). Some of the software products based on shallow-water equations are currently used for hazard

assessment to derive, for instance, maps of maximum flow height and velocity. Examples include RAMMS (Christen et al., 2010; Christen et al., 2012), 3d-DMM (GEO, 2011; Law et al., 2017), DAN3D (McDougall and Hungr, 2004; Moase et al., 2018) and FLO-2D (O'Brien et al., 1993). Various computational methods are used, in particular finite differences (O'Brien et al., 1993; Beguería et al., 2009; Kelfoun and Druitt, 2005), finite volumes (Mangeney et al., 2007b; Christen et al., 2010; Pirulli et al., 2007; Pudasaini, 2012) and Smoothed Particle Hydrodynamics (SPH) (McDougall and Hungr, 2004; Law et al., 2017; Pastor et al., 2009a). An example of promising developments include the writing of the shallow-water equations in each layer of a multi-layer flow, with an arbitrary number of layers (Fernández-Nieto et al., 2016). In particular, this makes it possible to describe any kind of velocity profile within the flow. Other research focuses include bed erosion along the flow path (Hungr, 1995; Bouchut et al., 2008; Iverson, 2012; Pirulli and Pastor, 2012; Fernández-Nieto et al., 2016; Fernández-Nieto et al., 2018) and the description of two-phase flows (e.g. Pudasaini, 2012; Bouchut et al., 2015; Bouchut et al., 2016; Pastor et al., 2018b; Iverson and George, 2014). Two international benchmarking exercises were carried out in 2007 and 2018 (Hungr et al., 2007; Pastor et al., 2018a) and confirmed the need for new developments in these directions as well as the importance of data acquisition so that model parameters can be fitted by direct rheological measurements or back-analysis.

In our work, we focus on one-phase thin-layer models. Using the numerical code SHALTOP (e.g. Bouchut and Westdickenberg, 2004; Mangeney et al., 2007b; Favreau et al., 2010; Moretti et al., 2015; Brunet et al., 2017; Peruzzetto et al., 2019), we evaluate their abilities and limits for propagation hazard assessment. In the following section, we will review into more details the different approaches used in the litterature to model one-phase thin-layer flows.

1.4 Rheologies for thin-layer models

The basic principle of all thin-layer models is to consider the local mass and momentum equations within the flow, and integrate them on the flow thickness to derive depth-averaged momentum and mass equations. As we will see in Chapter 2, this operation is not straight-forward when the topography on which the flow propagates is irregular. Here, we simply discuss rheological assumptions and the resulting depth-averaged equations on simple topographies. We focus on one-phase models, that all originate from the incompressible momentum and mass equations:

$$\partial_t \vec{U} + (\vec{U} \cdot \nabla_{\vec{X}})\vec{U} = -\vec{g} + \nabla \cdot \sigma, \tag{1.2}$$

$$\nabla_{\vec{X}} \cdot \vec{U} = 0, \tag{1.3}$$

where $\vec{U}(\vec{X})$ is the 3D velocity field, $-\vec{g}$ is the gravity, and σ is the Cauchy stress tensor. $\vec{X} = (\mathbf{X}, Z)$ is the cartesian coordinates system, with $\mathbf{X} = (X, Y)$. The base of the flow matches the topography and is given by a 2D surface $Z = b(\mathbf{X})$, with upward unit normal vector $\vec{n}$:

$$\vec{n} = \cos(\theta)\Big(-\frac{\partial b}{\partial X}, -\frac{\partial b}{\partial Y}, 1\Big) = \Big(-\mathbf{s}, \cos(\theta)\Big), \tag{1.4}$$

with

$$\cos(\theta) = \left(1 + \|\nabla_{\mathbf{X}} b\|^2\right)^{-\frac{1}{2}}, \tag{1.5}$$

$$\mathbf{s} = \cos(\theta)\nabla_{\mathbf{X}} b, \tag{1.6}$$

where θ is the slope angle. Note that for 1D-topographies parametrized by $Z = b(X)$, we have simply $\vec{n} = (\sin(\theta), \cos(\theta))$. The associated notations are given in Figure 1.4. The flow free surface is another 2D surface given by some function $F(\vec{X}, t) = 0$, with upward unit normal

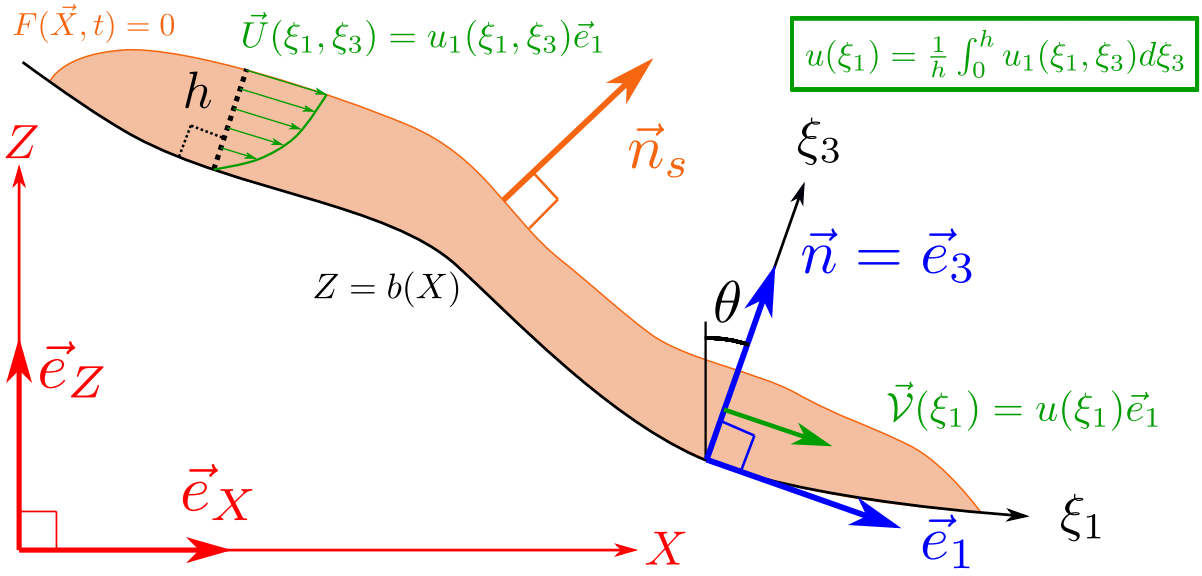

Figure 1.4: Notations used in the main body of the text for thin-layer models on 1D topographies given by $Z = b(X)$.

vector $\vec{n}_s$ and is assumed to be advected by the velocity field $\vec{U}$. These two boundary conditions read:

$$\vec{U}\cdot\vec{n}=0 \text{ at the bed,} \tag{1.7}$$

$$\partial_t F+\vec{U}\cdot\nabla_{\vec{X}}F=0 \text{ at the free surface.} \tag{1.8}$$

A traction free condition at the free surface is also commonly assumed at the surface of the material layer:

$$\sigma\vec{n}_s=\vec{0} \text{ at the free surface} \tag{1.9}$$

A slightly different and more general free surface condition is used in Bouchut and Westdickenberg (2004), where only the stress tangent to the layer surface is assumed to be null:

$$\sigma\vec{n}_s-(\vec{n}_s\cdot\sigma\vec{n}_s)\,\vec{n}_s=0 \text{ at the free surface.} \tag{1.10}$$

However, it does not change the final depth-averaged equations in comparison to other studies.

For the sake of clarity, and because formal derivations are actually scarce on general topographies (Bouchut and Westdickenberg, 2004; Luca et al., 2009b), we will consider thin-layer flows on 1D topographies given by a graph $Z = b(X)$. Indeed, as will be discussed in Chapter 2, the momentum equations must be integrated in the direction normal to the topography. As a matter of fact, the shallowness of landslides propagating on potentially steep slopes must be regarded in the direction normal to the topography. Moreover, the flow velocity is (at least in a first approximation) tangent to the topography. Thus the velocity in the normal direction is small. In order to translate this property it is appropriate to write these equations in a reference frame linked to the topography with one vector in the direction normal to the topography. This can be done relatively easily for 1D topographies (given by a 1D graph $Z = b(x)$) without complicating to much the equations, in particular because strain and stress tensors are aligned (that is, the principal stress directions coincide with velocity direction). It is however much more complex for general topographies.

Following the pioneering work of Savage and Hutter (1991) and the notations used in Chapter 2, we thus introduce for 1D topographies a topography reference frame with one unit vector $\vec{e}_1$ tangent to the topography, and a second unit vector $\vec{e}_3 = \vec{n}$ in the direction normal to the

topography (see Figure 1.4). The associated coordinate system is (ξ_1, ξ_3), with ξ_1 the curvilinear coordinate along the topography, and ξ_3 the distance to the topography. In this frame, the velocity has components $(u_1, 0)$, because it is tangent to the topography. The depth-averaged flow-velocity $\vec{\mathcal{V}}$ has components $(u, 0)$. Finally, the thickness of the material layer (measured in the direction normal to the topography) is h. With these notations, the classical conservative form of 1D thin layer equations as derived by Savage and Hutter (1991) is:

$$\partial_t h + \frac{\partial h}{\partial \xi_1} = 0, \tag{1.11}$$

$$\partial_t(hu) + \frac{\partial}{\partial \xi_1}(\alpha h u^2) + \frac{\partial}{\partial \xi_1}(\frac{1}{2} k g h^2 \cos(\theta)) = gh\sin(\theta) - T \tag{1.12}$$

where α is a shape factor used to describe non linear velocity profiles ($\alpha = 1$ is often used), and k a coefficient appearing when internal friction is considered, with a soil mechanics approach (see Section 1.4.2). The expression of the source term T depends on the constitutive equation for the stress tensor σ, which is needed to close the system of equations. Depending on the chosen constitutive equation, additional boundary conditions may also be required for the base of the flow. The rheological parameters arising in the expression of T are to a large extent empirical, because it is often impossible (or at least very difficult) to estimate them merely from geotechnical or rheological properties of the materials. They are thus most of the time calibrated by modeling the deposits or the dynamics of documented gravitational flows.

For one-phase thin-layer models, we can distinguish between four different approaches. The first one, which is used in SHALTOP, considers that the deviatoric stress tensor is null in the flow, that is, that off-diagonal terms of σ are zero ("hydro-static" approach). A second approach uses constant internal friction: it is not implemented in SHALTOP but is common in other thin-layer models. The third one considers a non constant internal friction through the $\mu(I)$-rheology. Finally, we will discuss another rheology and derivation used to model yield-stress fluids. The third and fourth rheologies were not used in this study, but I implemented them in SHALTOP during my PhD.

1.4.1 Hydrostatic pressure

In the most simple case, we can write the stress tensor $\sigma = -pI_3$. In turn, the pressure at the bottom of the material layer is proportional (in a first approximation) to the flow thickness, hence the designation "hydrostatic". It is misleading, in the sense that the layer is not static at all, but this name is nevertheless commonly used. As shown in (Bouchut and Westdickenberg, 2004) and explained in Chapter 2, this is enough to derive thin-layer equations. In particular, no friction must be imposed at the base of the flow. Indeed, no shearing occurs in the flow as the stress tensor is reduced to its diagonal terms, such that a friction boundary condition would not be coherent with the expression of σ.

Of course this is an over-simplification of real geophysical flows, in particular because in such models there is no energy dissipation. In order to have a more realistic model, it is thus relevant to introduce a dissipative term. The simplest way to do that is to introduce a friction boundary condition at the bottom of the flow, but as discussed in the previous paragraph the constitutive equations must then be changed. For flows on 1D topographies $Z = b(X)$, a solution is to assume that the expression of the stress tensor in the topography frame is:

$$\sigma = \begin{pmatrix} -p & \sigma_{13} \\ \sigma_{31} & -p \end{pmatrix}. \tag{1.13}$$

where $\sigma_{13} = \sigma_{31}$. It is then possible to formally introduce a condition on the stress tensor at the base of the flow using a frictional rheology:

$$\sigma\vec{n} - (\vec{n}\cdot\sigma\vec{n})\,\vec{n} = -\mu\frac{\vec{U}}{\|\vec{U}\|}(\vec{n}\cdot\sigma\vec{n})_+, \text{ at the base of the flow} \tag{1.14}$$

The latter equation simply states that stress component tangent to the topography (left hand side of (1.14)) is proportional to the stress component normal to the topography ($\vec{n}\cdot\sigma\vec{n}$) and is in the opposite direction of the velocity. The proportionality factor is the friction coefficient $\mu = \tan(\delta)$, with δ the associated friction angle. $(x)_+ = \max(0, x)$ is the positive part, needed to ensure that the flow is decelerated. The source term T in (1.12) then naturally arises for the depth-integration by taking into account the traction free condition at the surface and the bottom friction stress. The final momentum equation is:

$$\partial_t(hu) + \frac{\partial}{\partial\xi_1}(hu^2) + \frac{\partial}{\partial\xi_1}(\frac{1}{2}gh^2\cos(\theta)) = gh\sin(\theta) - h\mu(g\cos(\theta) + \gamma u^2), \tag{1.15}$$

where $\gamma = 1/R$ is the topography curvature in the propagation direction (R is the radius of curvature). For flows on 1D topographies $Z = b(X)$, y is:

$$\gamma(X) = \frac{\partial^2 b}{\partial X^2}\frac{1}{\left(1 + \left(\frac{\partial b}{\partial X}\right)^2\right)^{\frac{3}{2}}}. \tag{1.16}$$

For flows on complex 2D topographies $Z = b(X, Y)$, this method is not easy to formalize, because in this case the expression of $\nabla_{\vec{X}}\cdot\vec{U}$ in the topography coordinate system induces various and complex terms associated to the spatial variations of the topography reference frame. Besides, on 2D topographies, the principal stress directions are not necessarily aligned with the velocity (which is always the case, by construction, on 1D topographies). The ordering of terms after integration of the momentum equations is then difficult. To address this problem, Bouchut and Westdickenberg (2004) use the linear approximation of incompressible viscous newtonian fluids. In the cartesian reference frame, it reads:

$$\sigma = \sigma' - pI_3, \tag{1.17}$$

with

$$\sigma' = \nu\left(\nabla_{\vec{X}}\vec{U} + (\nabla_{\vec{X}}\vec{U})^t\right), \tag{1.18}$$

where ν is the kinematic viscosity.

To preserve mathematical formalism, Bouchut and Westdickenberg (2004) assume that ν is very small. This boils down to considering downslope shear flows, for which the only remaining terms in σ' in (1.18) are the derivative of the velocity (written in the topography frame) in the direction normal to the topography. Then, the bottom friction boundary condition (1.14) appears when the momentum equation along the flow depth are integrated, and we derive (1.15) for 1D topographies.

Thus, the formal approach proposed by Bouchut and Westdickenberg (2004) with a Newtonian description of the material dynamics and a negligible viscosity can be seen as an attempt to formalize mathematically the derivation on general topographies of classical thin-layer equations (that were previously derived for 1D topographies and extended not always rigorously to general topographies). The hypotheses on the flow rheology are thus chosen, to some extent at least, so that the final equations match the classical form of thin-layer equations. In this sense, they are indeed not necessarily compatible with field observations and laboratory experiments, and the friction coefficient μ must be calibrated by reproducing granular flows at the laboratory scale,

or gravitational flows at the field scale. However, so far, no model has been able to combine a rigorous mathematical derivation (in particular considering the complex spatial variations of topography) with a realistic constitutive equation. Besides, it is possible to define a friction coefficient μ that depends both on the material averaged velocity u and on the material layer thickness h. This allows to reproduce experimental evidence of friction increase for thin and/or fast flows (e.g. Pouliquen and Forterre, 2002; Mangeney et al., 2007b; Edwards et al., 2017). It is also possible to define μ such that the bottom stress has a similar form as the one derived for simple shear flows with a visco-plastic behavior (see Section 1.4.4).

1.4.2 Internal friction

In the hydrostatic derivation, the diagonal terms of the stress tensor are assumed to be equal. In their founding paper, Savage and Hutter (1991) use a different description of the stress state within the flow, but keep the same friction boundary condition (1.14). They argue that the material can be described by the Mohr-Coulomb theory. It is cohesionless, and can thus be characterized by an internal friction angle ϕ. As it is flowing, it is (supposedly) constantly verifying the Mohr-Coulomb yield criterion: there is plane element (not necessarily parallel to the bed) where the normal and shear stresses, respectively N and T, verify:

$$T = N\tan(\phi). \tag{1.19}$$

From classical geotechnical results, we thus have that on the Mohr Coulomb diagram (where N is the abcissa and T the ordinate) all other possible values of T and N (that is, for various plane element) span a circle centered on $N = 0$ and tangent to the line $T = N\tan(\phi)$ (see Figure 1.5). Besides, the bottom friction condition gives, for a plane element tangent to the topography, a relation between the bottom shear stress T_b and normal stress N_b:

$$T_b = N_b\tan(\delta). \tag{1.20}$$

At the bed, the normal and shear stress are given respectively by σ_{33} and σ_{13} because the stress tensor is written in frame linked to the topography. Thus, the circle giving the possible normal and shear stress in the material, for all possible plane element, is tangent to the line $T = N\tan(\phi)$ and passes through the point $(\sigma_{33}, \sigma_{13})$. There are two possible solutions, as shown in Figure 1.5. For a given circle, σ_{11} is the abcissa of the point symmetric to $(\sigma_{33}, \sigma_{13})$ in respect of the center of the circle (because $\sigma_{11} + \sigma_{33}$ is constant, whatever the orthonormal reference frame in wich σ is written). There are thus two possible values of σ_{11}, one for each circle: in one case, $\sigma_{11} > \sigma_{33}$, and in the other case $\sigma_{11} < \sigma_{33}$. Geometrical interpretation of the previous constraints yield:

$$\sigma_{33} = k_{act}\sigma_{11} \text{ or} \tag{1.21}$$

$$\sigma_{33} = k_{pass}\sigma_{11}, \tag{1.22}$$

with

$$k_{act} = 2\frac{1 - \sqrt{1 - (1 + \tan^2(\delta))\cos^2(\phi)}}{\cos^2(\phi)} - 1 < 1, \tag{1.23}$$

$$k_{pass} = 2\frac{1 + \sqrt{1 - (1 + \tan^2(\delta))\cos^2(\phi)}}{\cos^2(\phi)} - 1 > 1. \tag{1.24}$$

Following soil mechanics practices, k_{act} and k_{pass} are called the earth pressure coefficients. The "active" coefficient k_{act} is used when the granular material is elongated ($\partial_{\xi_3} u > 0$), and "passive" coefficient k_{pass} is used when the granular material is compressed ($\partial_{\xi_3} u < 0$). In turn, after the equations are integrated, the source T term in (1.12) becomes:

$$\partial_t(hu) + \frac{\partial}{\partial\xi_1}(hu^2) + \frac{\partial}{\partial\xi_1}(\frac{1}{2}k_{act/pass}gh^2\cos(\theta)) = gh\sin(\theta) - h\mu(g\cos(\theta) + \gamma u^2). \tag{1.25}$$

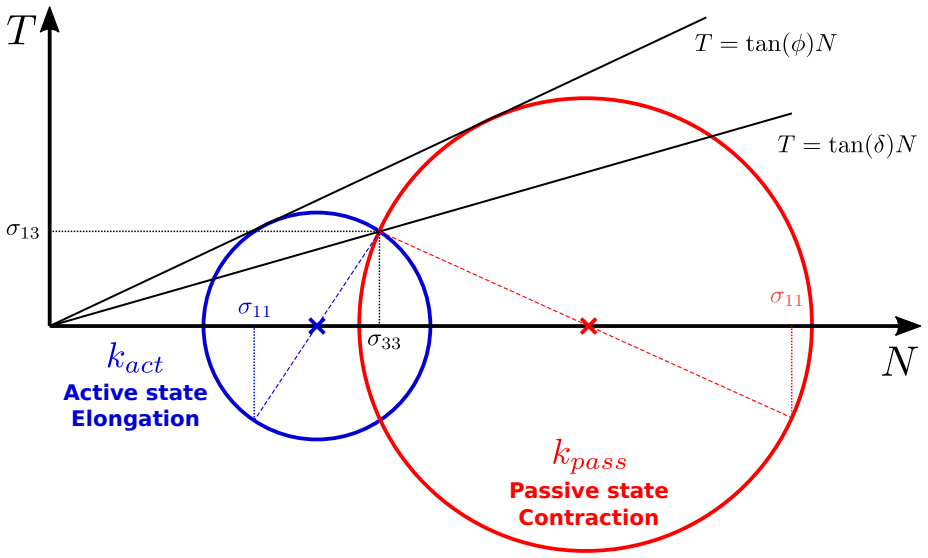

Figure 1.5: Geometrical relations in the Mohr-Coulomb diagram used to derive the stress tensor components with internal friction, for thin-layer flows propagating on 1D topographies $Z = b(X)$.

Apart from the fact that using static yield criteria can be questioned, as well as this non-linear response (e.g. Gray et al., 2003), the mere methodology used previously is difficult to extend to real topographies (i.e. given by $Z = b(X, Y)$). Indeed, when σ is a matrice of dimension 3, the shear and normal stresses are no longer constrained on the Mohr-Coulomb circle. If σ_1, σ_2 and σ_3 are the ordered main stresses (i.e. the eigen-values of the stress tensor σ), possible locations for normal and shear stress lie inside the circle intersecting the line $T = 0$ at the 2 main principal stresses σ_1 and σ_3, but outside the smaller circles given by σ_1 and σ_2, and by σ_2 and σ_3. Thus, the geometric considerations presented above no longer stand true. Besides, in a frame linked to the topography, the main stresses direction are not necessarily aligned with the velocity, thus it is difficult to derive explicit expression for the different terms of σ. In order to overcome these problems, it is convenient to assume that two of the three principle stresses are equal. To further simplify the equations, Hutter et al. (1993) and Gray et al. (1999) consider topographies with main slope in the x-direction, and velocities aligned with the main slope. It is then possible to compute the earth coefficients in the X and Y directions, to account for elongation and compression in these two directions. The resulting model is however not valid on general topographies as it is not invariant by rotation. A simple rotation invariant but isotropic formulation was proposed by Iverson and Denlinger (2001), and is now widely used in shallow-water models (e.g., Christen et al., 2010; Kelfoun and Druitt, 2005). It reads:

$$\bar{\sigma}_{11} = \bar{\sigma}_{22} = k_{act/pass}\bar{p}, \tag{1.26}$$

where $\bar{\sigma}_{11}$ and $\bar{\sigma}_{22}$ are the depth-averaged diagonal stress tensor components, in the down-slope and cross-slope directions, and $\bar{p}$ is the depth-averaged pressure. A more complete resolution can be found in Denlinger and Iverson (2004) who resolve the full stress state in the flow, but with significant numerical cost.

1.4.3 The $\mu(I)$-rheology

Over the past decade, the $\mu(I)$-rheology (e.g., GDR MiDi, 2004; Jop et al., 2006) has met with growing success to model granular flows. It was shown with dimensional arguments and numerical simulations that in 1D dense granular flows, the shear stress T is proportional to the

pressure p, following:

$$T = \mu(I)p, \tag{1.27}$$

$$I = \frac{\dot{\gamma}d}{\sqrt{p}}, \tag{1.28}$$

where I is the inertial number, $\dot{\gamma}$ is the shear rate, d the grain diameter, p the pressure (divided by the density, as before). I compares the characteristic time of deformation $T_{\dot{\gamma}} = 1/\dot{\gamma}$ to the characteristic time of grains rearrangements. Thus, high values of I characterize shear granular flows with strong velocity gradients, and low values of I represent quasi-static states where the the granular layer deforms slowly. Note that (1.27) is somehow similar to (1.19), in the sense that at the bottom of the flow, the normal stress component is given by the pressure p. However, while the internal friction coefficient $\tan(\phi)$ is constant, associated to the stability of the materials, $\mu(I)$ depends on the materials dynamics. The definitions (1.27) and (1.28) are extended by Jop et al. (2006) and Gray and Edwards (2014) to tensors:

$$\sigma' = \frac{\mu(I)p}{\|D\|}D, \tag{1.29}$$

$$I = \frac{2\|D\|d}{\sqrt{p}}, \tag{1.30}$$

with $D = \frac{1}{2}(\nabla_{\vec{X}}\vec{U} + (\nabla_{\vec{X}}\vec{U})^t)$, $\|D\| = \sqrt{\frac{1}{2}tr(D^2)}$. p and σ' are related to the stress tensor σ through:

$$\sigma = -pI_3 + \sigma'. \tag{1.31}$$

These constitutive equations are consistent with classical static analysis, in the sense that when $I \to 0$, the material will flow only if

$$\|\sigma'\| > \mu_s p, \tag{1.32}$$

where μ_s is a given friction coefficient (Jop et al., 2006).

For 1D simple shear flows on planes with inclination θ (i.e. for $Z = b(X) = \tan(\theta)X$), the velocity has components $(u_1, 0)$ in the topography reference frame and we can assume that the main velocity variations are along the flow depth, such that:

$$\frac{\partial u_1}{\partial \xi_3} \gg \frac{\partial u_1}{\partial \xi_1}. \tag{1.33}$$

In turn, if we assume $\partial u_1/\partial \xi_3 > 0$, we get:

$$\|D\| = \frac{1}{2}\frac{\partial u_1}{\partial \xi_3}. \tag{1.34}$$

In turn, following Gray and Edwards (2014), the ordering of the momentum equations in the thin layer approximation yields:

$$p = g\cos(\theta)(h - \xi_3), \tag{1.35}$$

$$\sigma'_{13} = g\sin(\theta)(h - \xi_3). \tag{1.36}$$

Replacing (1.36) in (1.29), we deduce that $\mu(I)$, and thus I, are constant throughout the depth of the material (once again, for steady uniform flows), with

$$\mu(I) = \tan\theta, \tag{1.37}$$

$$I = I_\theta. \tag{1.38}$$

With (1.35), (1.30) then becomes

$$\frac{\partial u_1}{\partial \xi_3} = \frac{I_\theta}{d}\sqrt{g\cos(\theta)}\,(h-\xi_3)^{\frac{1}{2}}\,, \tag{1.39}$$

which can be integrated to deduce a Bagnold velocity profile (assuming a no-slip condition at the base of the flow, which is more restrictive than the boundary condition (1.7)):

$$u_1(\xi_3) = \frac{2I_\theta}{3d}\sqrt{g\cos(\theta)}\Big[h^{\frac{3}{2}} - (h-\xi_3)^{\frac{3}{2}}\Big]. \tag{1.40}$$

The associated depth-averaged velocity is

$$u = \frac{2I_\theta}{5d}\sqrt{g\cos(\theta)}h^{\frac{3}{2}}, \tag{1.41}$$

which gives the expression of I_θ

$$I_\theta = \frac{5du}{2h\sqrt{gh\cos(\theta)}}. \tag{1.42}$$

It is also possible to derive explicitly the terms of σ', and the leading terms of σ'_{11}, σ'_{13} and σ'_{33}. As we assume the velocity is tangent to the topography, given the form of (1.29), we have immediately that $\sigma'_{33} = 0$. Following Gray and Edwards (2014) and Baker et al. (2016), we also have

$$\sigma'_{13} = \mu(I_\theta)g(h-\xi_3)\cos(\theta), \tag{1.43}$$

$$\sigma'_{11} = 2g\sin(\theta)\Big(\sqrt{h(h-\xi_3)} - (h-\xi_3)\Big)\frac{\partial h}{\partial \xi_1}. \tag{1.44}$$

Note that (1.43) is equivalent to (1.36) under the assumption $\mu(I) = \tan(\theta)$. However, using (1.43) allows to consider a wider range of situations, provided an explicit expression of $\mu(I)$. This will be discussed further on. Equation (1.44) can be integrated to derive the the depth-averaged value $\bar{\sigma}'_{11}$ of σ'_{11}:

$$\bar{\sigma}'_{11} = \frac{1}{3}g\sin(\theta)h\frac{\partial h}{\partial \xi_1}. \tag{1.45}$$

It is interesting to see that, given the Bagnold velocity profile that was previously computed, the latter equation can be written as a depth-averaged non-linear viscous law:

$$\bar{\sigma}'_{11} = \nu\sqrt{h}\frac{\partial u}{\partial \xi_1}. \tag{1.46}$$

with

$$\nu = \frac{5}{9}\frac{g\sin(\theta)}{I_\theta\sqrt{g\cos(\theta)}}. \tag{1.47}$$

The final step of the thin-layer equations derivation includes the integration along the layer thickness (that is over ξ_3) of $\partial\sigma'_{11}/\partial\xi_1$, which yields $\partial\bar{\sigma}'_{11}/\partial\xi_1$, and of $\partial\sigma'_{13}/\partial\xi_3$:

$$\int_0^h \frac{\partial \sigma'_{13}}{\partial \xi_3}d\xi_3 = \sigma'_{13}(\xi_3 = h) - \sigma'_{13}(\xi_3 = 0). \tag{1.48}$$

The traction free condition at the free surface gives $\sigma'_{13}(\xi_3 = h) = 0$. In the derivations described in previous sections, $\sigma'_{13}(\xi_3 = 0)$ was given by a bottom friction law. With the $\mu(I)$-rheology, we can instead use directly (1.43):

$$\sigma'_{13}(\xi_3 = 0) = \mu(I_\theta)gh\cos(\theta). \tag{1.49}$$

Thus, the final momentum thin-layer equation on u reads:

$$\partial_t(hu) + \frac{\partial}{\partial\xi_1}(hu^2) + \frac{\partial}{\partial\xi_1}(\frac{1}{2}gh^2\cos(\theta)) = gh\sin(\theta) - T, \tag{1.50}$$

with

$$T = \mu(I_\theta)gh\cos(\theta) - \frac{\partial}{\partial\xi_1}\Big(\nu h^{\frac{3}{2}}\frac{\partial u}{\partial\xi_1}\Big). \tag{1.51}$$

As before, the extension of these equations to flows on general topographies is not easy at all. Baker et al. (2016) derived a set of equations for granular flows propagating on plane topographies, i.e. given by a graph $Z = b(X, Y) = \tan(\theta)X$, with non negligible cross-slope velocities. In order to achieve this, they extended the non-linear viscous law (1.46) to:

$$\bar{\sigma}' = \nu\sqrt{h}\bar{D}, \tag{1.52}$$

with $\bar{D}$ the depth-averaged strain-rate tensor, $\bar{\sigma}'$ the depth-averaged deviatoric stress tensor, and ν is now a constant. The corresponding equations were implemented in the SHALTOP numerical code.

Note that in the previous derivations, we had $\mu(I) = \tan(\theta)$, and given the final form of the depth-averaged equations, $\mu(I)$ can be seen as a basal friction coefficient. In practice, this is verified in experiments for steady and uniform flows on inclined planes. Pouliquen and Forterre (2002) related empirically the basal friction coefficient (i.e., $\mu(I)$ or the slope angle) to granular flow velocity and thickness, following:

$$\mu = \mu_1 + (\mu_2 - \mu_1)\frac{1}{\frac{h\beta}{LF_r} + 1}, \tag{1.53}$$

where μ_1, μ_2, β and L are constants and $F_r = u/\sqrt{gh\cos\theta}$ is the Froude number. For slope inclinations $\tan(\theta) < \mu_1$ the granular flow stops, and accelerates if $\tan(\theta) > \mu_2$. We have shown that, for steady uniform flows without wall effects (Fernández-Nieto et al., 2018), $I = I_\theta$ is constant through the depth of the flow and is given by equation (1.42). We can write:

$$F_r = \frac{2hI_\theta}{5d}, \tag{1.54}$$

such that (1.53) becomes:

$$\mu(I) = \mu_1 + (\mu_2 - \mu_1)\frac{1}{\frac{I_0}{I_\theta} + 1}, \tag{1.55}$$

with $I_0 = (5\beta d)/(2L)$ a constant. This relation can then be used in the thin-layer equations, but, once again, this is formally valid only for steady uniform flows without wall effects, for a given range of slopes. Typically, $\mu(I) = \tan(\theta) = 0$ does not stand true for a flow on a flat topography, where such steady uniform law do not exist. Pouliquen and Forterre (2002) show that (1.53) and thus (1.55) are valid for high enough Froude numbers, when steady-uniform flows can develop. The critical value is β, that can be defined experimentally by fitting for steady-uniform granular flows a law:

$$\frac{u}{\sqrt{gh}} = \beta\frac{h}{h_{stop}(\theta)}, \tag{1.56}$$

where $h_{stop}(\theta)$ is the thickness of the deposits left by a steady-uniform flow with velocity u over a plan with inclination $\tan(\theta)$. For $F_r < \beta$, that is for flows with small velocities and/or important thicknesses, a transitional law must be found for μ, to reach the static friction coefficient μ_{start} above which the material starts flowing. This transitional behavior has a key role constraining the shape of the deposits (Mangeney et al., 2007b), and has been discussed for instance by

Pouliquen and Forterre (2002) and Edwards et al. (2017) (who introduce a more general form of (1.56)).

Even so, the derivation of the shallow-water equations with the $\mu(I)$-rheology heavily relies on the assumption that I is constant throughout the depth of the flow, from which $\mu(I) = \tan(\theta)$ is deduced. Thus, using these equations to model non steady uniform flows, or even steady flows with wall effects, can be questioned. Not to mention that, as for other rheologies, extending these equations to complex topographies is far from easy.

1.4.4 Visco-plastic flows

As discussed in Section 1.1.2, debris flows containing a significant solid fine fraction (typically, above 5 or 10%) have a significant viscous behavior and can be considered as yield stress fluids. Though we did not study such flows in this PhD, we deemed relevant to adapt the SHALTOP numerical code to model such flows, by modifying the source term T in (1.12). We follow Pastor et al. (2004) and Pastor et al. (2009a) who derive the expression of T. They consider thin-layer equations for non-newtonian fluids on 1D topographies. Keeping the notations of (1.13), they assume a linear variation of the shear stress σ_{13} from the bottom of the flow to the top, from which they deduce a velocity profile (note that the opposite was done for the $\mu(I)$-rheology, where the stress variations were deduced from the velocity profile). This linear variation, that can be seen as a first order approximation of the stress within the flow, reads:

$$\sigma_{13} = \sigma_B(1 - \xi_3/h), \tag{1.57}$$

where σ_B is the shear stress at the bottom of the flow. Then, a simple Bingham law also relates the shear stress to the strain-rate:

$$\sigma_{13} = \tau_y + \nu\frac{\partial u_1}{\partial \xi_3} \text{ for } \left|\frac{\partial u_1}{\partial \xi_3}\right| \geq 0, \tag{1.58}$$

$$\sigma_{13} \leq \tau_y \text{ for } \left|\frac{\partial u_1}{\partial \xi_3}\right| = 0, \tag{1.59}$$

where τ_y is the yield stress and ν is the kinematic viscosity. In the upper part of the flow (the plug), shear stress is inferior to the yield stress τ_y, and velocity is constant. In the lower layer, combining and integrating (1.57) and (1.58) yields a parabolic velocity profile:

$$u_1 = \frac{\tau_B}{h\nu}\left(h_s\xi_3 - \frac{\xi_3^2}{2}\right) \text{ for } \xi_3 < h_s, \tag{1.60}$$

$$u_1 = \frac{\tau_B h_S^2}{2h\nu} \text{ for } h_s \leq \xi_3 \leq h, \tag{1.61}$$

where h_s is the height of the plug (given from (1.57) and $\sigma_{13} = \tau_y$). The depth-average velocity u is then given by:

$$u = \frac{\tau_B h}{6\nu}\left(1 - \frac{\tau_y}{\tau_B}\right)^2\left(2 + \frac{\tau_y}{\tau_B}\right). \tag{1.62}$$

This equation provides a relation between the average velocity and the basal shear stress, that can in turn be used to close the system of equations. The roots of this third order polynomial are, however, not easy to estimate directly. The simplest method is to disregard terms in $(\tau_y/\tau_B)^3$, which in turn gives the bottom shear stress (and equivalently the source term T in (1.12)):

$$\tau_b = T = \frac{3}{2}\tau_y + 3\nu\frac{u}{h}. \tag{1.63}$$

This rheology models the behavior of visco-plastic flows: a minimum thickness is needed for the materials to flows, it remains static otherwise. Note that all quantities are divided by the material density: for instance the yield stress τ_y considered here is in Pa (kg m^{-3})$^{-1}$ and ν is the kinematic viscosity (i.e. the dynamic viscosity divided by density).

A generalization of this method was proposed by Pastor et al. (2009a) to model frictional-viscous fluids. They argue that instead of (1.58), the shear strength below the plug layer has the form:

$$\sigma_{13} = \tau_y + \mu_{CF} \left(\frac{\partial u_1}{\partial \xi_3} \right)^m + g \cos\theta (h - \xi_3) \tan\delta, \tag{1.64}$$

where δ is the friction angle, ρ the density, μ_{CF} is a material parameter and m is a parameter. The first two terms model visco-plastic behavior with non linear dependence between the shear stress σ_{13} and the shear rate $\dot{\gamma} = \frac{\partial u_1}{\partial \xi_3}$ (Herschel–Bulkley model). The last term adds a frictional behavior by using the pressure within the flow $p = g \cos\theta (h - \xi_3)$. Keeping the assumption of a linear variation along depth (1.57) for the shear stress σ_{13}, a velocity profile is again deduced, resulting again in an equation relating the averaged velocity to the basal shear stress τ_B. Note that with $m = 1$ and $\delta = 0$ we find back the Bingham model. On the contrary, $\mu_{CF} = 0$ and $\tau_y = 0$ yield a purely frictional rheology as in the previous section (without taking the curvature γ of the topography). For cohesionless materials ($\tau_y = 0$), $m = 2$ leads to:

$$\tau_b = T = gh \cos\theta \tan\delta + \frac{25}{4} \mu_{CF} \frac{u^2}{h^2}, \tag{1.65}$$

The quadratic term can be related to the empirical Voellmy's law (Voellmy, 1955; Salm, 1993), that is classically used is most thin-layer models to reproduce in particular snow avalanches and debris flows (McDougall, 2017):

$$\tau_b = gh \cos\theta \tan\delta + g \frac{u^2}{\xi}. \tag{1.66}$$

where ξ is a material parameter. Note that these derivations are only valid for simple 1D flows, and so far have only been empirically extended to flows on complex 2D topographies, by using the norm of the velocity instead of u and assuming the flow is going in the main slope direction.

1.5 Conclusion

As shown previously, gravitational movements are complex phenomena characterized by various physical processes controlling their initiation and their propagation. Current research topics thus span a wide range of domains, including for instance the objective zonation of susceptibility, the modeling of initial deformation and failure, the modeling of propagation, and the integration of all these processes to derive landslide hazard maps. The integration of estimated hazard with human and economic stakes in order to asses vulnerability and in turn risk is yet another field of research. In this work, we focus on the quantification of propagation for flow-like landslides such as rock avalanches, debris avalanches or debris flows: this includes the estimation of travel distance, but also of flow thickness and velocity.

As discussed in the previous sections, quantifying the propagation hazard is difficult for three main reasons:

- The physical processes at stake are sometimes difficult to describe, and thus to model.
- The physical characteristics of the materials needed to constrain simulations, may be difficult to constrain.

- In turn, the final propagation hazard assessment is associated to important uncertainties. Some of them cannot be modeled because they result from an inappropriate description of the phenomenon, when others can be estimated by quantifying the variability of some key elements (for instance, unstable volume or rheological parameters).

To address these problems, methods for propagation hazard assessments use empiricism and/or physically based models. Purely empirical methods are relatively easy to use and allow a rather simple uncertainty estimation, but only allow to characterize a few characteristics of the landslide, such as travel distance or peak discharges. In comparison, physically based models can simulate the full dynamics of the flow, but demand a strong a-priori on the rheology and, sometimes, important computing power. In turn, it is difficult to estimate rigorously the associated uncertainties. The right balance between these two kind of methods depend on the scale of the study site, on the data available to constrain simulations, and on temporal and financial operational constraints.

Over the past decades, thin-layer models have been increasingly used to simulate flow-like landslides because they are less complex than full 3D models simulating the dynamics of each elementary volume of fluid and/or solid particle, and still proved to reproduce correctly the dynamics and deposits of landslides. Even so, many different models exist to reproduce the variety of phenomena observed on the field: complex rheologies are needed to model complex flows, such as two-phase flows, but parameters are then difficult to calibrate. To the contrary, more simple rheologies (such as the Coulomb rheology with a hydro-static derivation) are more empirical, but make it possible to model more finely the geometrical control of topography on the flow propagation. Thus, there has been so far no unified approach for quantitative hazard assessment.

In this context, our objective is to assess the usability and the added value of thin-layer numerical models for propagation hazard assessment, in comparison to more empirical approaches. As we want our methods to be easily applied by practitioners in an operational context, we use a numerical model with fairly simple (and thus empirical) rheological laws and a limited number of parameters, but that includes a rigorous and precise description of the geometrical interactions between the topography and the flow. In this perspective, we will use the one-phase thin-layer model SHALTOP (e.g. Bouchut and Westdickenberg, 2004; Mangeney et al., 2007b; Favreau et al., 2010; Moretti et al., 2015).

In Chapter 2, we will first highlight the importance of a rigorous mathematical methodology to derive the thin-layer equations, even for simple rheologies. We will then test the ability of SHALTOP to model debris avalanches (on the Soufrière de Guadeloupe, Chapter 3), rock avalanches and debris flows (in the Prêcheur river, Chapter 4). Finally, in Chapter 5, we focus on the propagation and quantification of uncertainty in thin-layer simulations.

Chapter 2

Topography curvature effects in thin-layer models for fast gravity-driven flow without bed erosion

Context

As discussed thoroughly in the previous chapter, it is very difficult to include all the physical processes at stake in a gravitational flow in one single thin-layer model. A wide variety of models has been proposed instead (see Delannay et al. (2017) for a review). In most cases, the associated equations are derived for simple flows at the scale of the laboratory and are difficult to calibrate at the field scale. Thus, for hazard assessment, practitioners most commonly use models with semi-empirical rheologies that greatly simplify the physical processes, but use only few parameters which makes hazard assessment easier.

While numerous studies have focused on rheology description, only few have analyzed the importance of topography description in models. The following study contributes to fill this gap. In this perspective, its objective is not to develop a new set of equations that would reproduce more correctly observations. Instead, it aims at warning practitioners who use thin-layer models at the field scale about the potential influence of topography curvature effects on simulations results. This influence may not be negligible in some situations, and must thus be modeled accurately.

This study has been submitted to JGR: Earth Surface in March 2020 and was accepted in February 2021:

- **Peruzzetto M.**, Mangeney A., Bouchut F., Grandjean G., Levy C., Thiery Y., and Lucas A. *Topography Curvature Effects in Thin-Layer Models for Gravity-Driven Flows without Bed Erosion.* Journal of Geophysical Research: Earth Surface, submitted.

We reproduce here the submitted version of the article, from Section 2.1 to Section 2.7, as well as the abstract page 26. Appendices 2.A to 2.F are Supplementary Materials of the submitted article. Foot notes are not included in the article and were added following remarks of examiners.

Along with this work, I have also been involved more broadly in formal comparison exercises between the thin-layer model SHALTOP and other numerical models. Such exercises are important to assess the differences that can be expected between two simulations results, as a result of different methodological or numerical approaches. In 2007 and 2018, benchmarking exercises for

thin-layer models were organized by the JTC1, for the Workshop on Triggering and Propagation of Rapid Flow-like Landslides. I took part in the second one, and presented results during a seminar held in Hong-Kong. The corresponding conference paper, reproduced in Appendix A, is:

- **Peruzzetto, M.**, Mangeney A., Grandjean G., Levy, C., Thiery, Y., Bouchut, F. *Back-analysis of a rock avalanche and a debris flow with the SHALTOP code.* in Proceedings of the Second JTC1 Workshop on Triggering and Propagation of Rapid Flow-like Landslides, Hong-Kong (2018).

The 2007 and 2018 benchmarking exercises were interesting because they involved a large number of models (more than 10) and field-scale case studies. However, they yielded only partial conclusions on the origin of differences between codes, because the set-up of simulations and the presentation of results were not enough standardized. It is then difficult to compare rigorously results. In this perspective, the ongoing work:

- Gueugneau V., Charbonnier S., Esposti Ongaro T., de' Micheli Vitturi M., **Peruzzetto M.**, Patra A., Mangeney A., Kelfoun K., *Synthetic benchmarking of concentrated pyroclastic currents models*, Bulletin Of Volcanology. in prep.

compares simulations of pyroclastic currents carried out with 4 different thin-layer models, including SHALTOP, in a more unified framework. Similarly, the work

- Hugo M., Viroulet S., **Peruzzetto M.**, Mangeney A., Lagrée P.-Y., Popinet S. and Bouchut F. *Numerical simulations of granular column collapse: comparison between Navier-Stokes, discrete and thin-layer numerical simulations*, Physical Review E. in prep.

compares granular column collapse simulations carried out with the Navier-Stokes Gerris software, a Discrete Element Method numerical code, and SHALTOP. This comparison makes it possible to investigate, for instance, the different stopping processes. It also quantifies the extent to which thin-layer approximations involve errors in column collapses simulations, in comparison to models where equations are not depth-averaged.

Abstract

Depth-averaged thin-layer models are commonly used to model rapid gravity-driven flows such as debris flows or debris avalanches. However, the formal derivation of thin-layer equations for general topographies is not straightforward. The curvature of the topography results in a force that keeps the velocity tangent to the topography. Another curvature term appears in the bottom friction force when frictional rheologies are used. In this work, we present the main lines of the mathematical derivation for these curvature terms that are proportional to the square velocity. Then, with the SHALTOP numerical model, we quantify their influence on flow dynamics and deposits over synthetic and real topographies. This is done by comparing simulations in which these terms are exact, disregarded or approximated. With the Coulomb rheology, for slopes $\theta = 10°$ and for friction coefficients below $\mu = \tan(5°)$, neglecting the curvature force increases the simulated travel times by up to 10% and 30%, for synthetic and real topographies respectively. When the curvature in the friction force is neglected, the travel distance may be increased by several hundred meters on real topographies, whatever the topography slopes and friction

coefficients. We observe similar effects on a synthetic channel with slope $\theta = 25^\circ$ and $\mu = \tan(15^\circ)$, with a 50% increase of the kinetic energy. Finally, approximations of curvature in the friction force can break the non-invariance of the equations and decelerate the flow. With the Voellmy rheology, these discrepancies are less significant. Curvature effects can thus have significant impact for model calibration and for overflows prediction, both being critical for hazard assessment.

Contexte

Comme discuté dans le chapitre précédent, il est difficile d'inclure tous les processus physiques contrôlant la propagation des écoulements gravitaires, dans un seul modèle d'écoulement en couche mince. Une grande variété d'équations et de modèles différents existe donc (voir par exemple Delannay et al. (2017) pour une revue). Dans la plupart des cas, les équations sont obtenues pour des écoulements simples, à l'échelle du laboratoire et sont difficiles à calibrer pour des applications à l'échelle du terrain. Ainsi, pour ces applications, les rhéologies utilisées sont la plupart du temps semi-empiriques, et n'utilisent qu'un nombre limité de paramètres.

Si beaucoup d'études sont consacrées au développement de nouvelles rhéologies, peu s'intéressent à l'importance de la description de la topographie. L'étude suivante contribue à combler ce manque. Dans cette perspective, son objectif n'est pas de développer de nouvelles équations qui permettraient de reproduire correctement des observations. Son objectif est plutôt d'alerter les utilisateurs de modèles d'écoulement en couche mince pour des applications de terrain à propos de l'influence des effets de courbure de la topographie sur les résultats de simulations. Cette influence peut, dans certains cas, ne pas être négligeable, et doit donc être modélisée correctement.

Cette étude a été soumise à JGR : Earth Surface *en Mars 2020 et a été acceptée en Février 2021 :*

- ***Peruzzetto M.**, Mangeney A., Bouchut F., Grandjean G., Levy C., Thiery Y., and Lucas A.* Topography Curvature Effects in Thin-Layer Models for Gravity-Driven Flows without Bed Erosion. *Journal of Geophysical Research : Earth Surface, submitted.*

Nous reproduisons dans ce chapitre la version soumise de l'article, de la Section 2.1 à la Section 2.7, ainsi que le résumé en anglais page 26. Les Apendices 2.A à 2.F sont des ressources supplémentaires associées à l'article soumis. Les notes de bas de page ne sont font pas partie de l'article et ont été rajoutées suite aux retours des rapporteurs.

En parallèle de ce travail, je suis aussi impliqué plus largement dans des exercices de comparaison entre le modèle SHALTOP et d'autres modèles numériques. De tels exercices sont importants pour évaluer les différences qui peuvent être attendues entre deux simulations, en raison d'approches méthodologiques ou numériques différentes. En 2007 et 2018, des exercices de benchmarking entre modèles d'écoulement en couche mince ont été orgnisés par le JTC1, pour le Workshop on Triggering and Propagation of Rapid Flow-like Landslides. *J'ai pris part au second, et présenté les résultats lors d'un séminaire de restitution à Hong-Kong en 2018. La publication correspondant à la conférence est :*

- ***Peruzzetto, M.**, Mangeney A., Grandjean G., Levy, C., Thiery, Y., Bouchut, F.* Back-analysis of a rock avalanche and a debris flow with the SHALTOP code. *in Proceedings of the Second JTC1 Workshop on Triggering and Propagation of Rapid Flow-like Landslides, Hong-Kong (2018).*

Ces exercices de benchmarking de 2007 et 2018 ont été enrichissants car ils impliquaient un nombre important d'équipes internationales (plus de 10 chaque fois) et des cas d'étude de terrain. Toutefois, les conclusions de la comparaison n'étaient que partielles à cause d'un manque de standardisation des simulations, autant pour leur mise en oeuvre que pour la restitution des résultats. Il était donc compliqué de comparer rigoureusement les résultats. Dans cette perspective, le travail en cours :

- *Gueugneau V., Charbonnier S., Esposti Ongaro T., de' Micheli Vitturi M.,* ***Peruzzetto M.****, Patra A., Mangeney A., Kelfoun K.,* Synthetic benchmarking of concentrated pyroclastic currents models, *Bulletin Of Volcanology. in prep.*

compare des simulations d'écoulements pyroclastiques de 4 modèles d'écoulement en couche mince différents, dont SHALTOP, dans un cadre plus unifié. De manière similaire,

- *Hugo M., Viroulet S.,* ***Peruzzetto M.****, Mangeney A., Lagrée P.-Y., Popinet S. and Bouchut F.* Numerical simulations of granular column collapse : comparison between Navier-Stokes, discrete and thin-layer numerical simulations, *Physical Review E. in prep.*

compare des simulations d'écoulements granulaires secs réalisées avec le code numérique Gerris (qui résout les équations de Navier-Stokes), avec un code d'éléments discrets, et SHALTOP. Cette comparaison permet d'analyser, par exemple, les différentes manières dont l'arrêt de l'écoulement survient dans les différents codes. Elle permet aussi de quantifier les erreurs induites par l'approximation de couche mince, par rapport à des codes où les équations ne sont pas intégrées sur l'épaisseur de l'écoulement.

Résumé

Les modèles d'écoulement en couche mince sont couramment utilisés pour modéliser des écoulements gravitaires rapides, comme les laves torrentielles ou les avalanches de débris. Toutefois, la dérivation des équations associées sur des topographies quelconques n'est pas simple. La courbure de la topographie génère une force d'accélération qui assure que la vitesse de l'écoulement reste tangente à la topographie. Un autre terme de courbure apparaît dans dans la force de friction basale quand des rhéologies frictionnelles sont utilisées. Dans ce travail, nous présentons les étapes principales de la dérivation de ces termes de courbures, tous deux proportionnels au carré de la vitesse d'écoulement. Ensuite, avec le modèle numérique SHALTOP, nous quantifions leur influence sur la dynamique de l'écoulement sur des topographies synthétiques et réelles. Pour cela, nous comparons des simulations où ces termes sont exacts, négligés ou approximés. Avec la rhéologie de Coulomb, pour des pentes supérieures à $\theta = 10^\circ$ *et des angles de friction inférieurs à* $\mu = \tan(5^\circ)$*, négliger la force de courbure augmente les temps de parcours simulés de 10 et 30%, pour des topographies synthétiques et réelles respectivement. Quand le terme de courbure apparaissant dans la friction basale est négligé, la distance de parcours peut être augmentée de plusieurs centaines de mètres sur des topographies réelles, quelques soient les pentes et les angles de friction. Nous observons des effets similaires pour un chenal synthétique incliné de* $\theta = 25^\circ$ *et* $\mu = \tan(15^\circ)$*, avec une augmentation de 50% de l'énergie cinétique. Finalement, approximer le calcul des termes de courbure dans la friction basale peut rompre l'invariance par rotation des équations et ralentir l'écoulement. Avec la rhéologie de Voellmy, ces différences sont moins marquées. Une bonne prise en compte de la courbure de la topographie dans les équations est donc important pour calibrer correctement le modèle et pour mieux prédire les débordements. Ces deux points sont cruciaux pour l'estimation des aléas gravitaires.*

2.1 Introduction

The propagation of rapid gravity-driven flows (Iverson and Denlinger, 2001) occurring in mountainous or volcanic areas is a complex and hazardous phenomenon. A wide variety of events are associated with these flows, such as rock avalanches, debris avalanches and debris, mud or hyper-concentrated flows (Hungr et al., 2014). The understanding and estimation of their propagation processes is important for sediment fluxes quantification, for the study of landscapes dynamics. Besides, gravity-driven flows can have a significant economic impact and endanger local populations (Hungr et al., 2005b; Petley, 2012; Froude and Petley, 2018). In order to mitigate these risks, it is of prior importance to estimate the runout, dynamic impact and travel time of potential gravitational flows.

This can be done empirically, but physically-based modeling is needed to investigate more precisely the dynamics of the flow, in particular due to the first-order role of local topography. Over the past decades, thin-layer models (also called shallow-water models) have been increasingly used by practictioners. Their main assumption is that the flow extent is much larger than its thickness, so that the kinematic unknowns are reduced to two variables: the flow thickness and its depth-averaged velocity. The dimension of the problem is thus lower, allowing for relatively fast numerical computations. The first and simplest form of thin-layer equations was given by Barré de Saint-Venant (1871) for almost flat topographies. The 1D formulation (i.e. for topographies given by a 1D graph $Z = Z(X)$) for any bed inclination and small curvatures was derived by Savage and Hutter (1991). This model has since been extended to real 2D topographies (i.e. given by a 2D graph $Z = Z(X, Y)$). Some of the software products based on thin-layer equations are currently used for hazard assessment to derive, for instance, maps of maximum flow height and velocity. Examples include RAMMS (Christen et al., 2010; Christen et al., 2012), 3d-DMM (GEO, 2011; Law et al., 2017), DAN3D (McDougall and Hungr, 2004; Moase et al., 2018) and FLO-2D (O'Brien et al., 1993). A non exhaustive overview of some existing models used for field scale modeling is given in Table 2.1. Yavari-Ramshe and Ataie-Ashtiani (2016) and Delannay et al. (2017) give a more comprehensive review of thin-layer models. Current research focuses include modeling of multi-layer flows (Fernández-Nieto et al., 2018; Garres-Díaz et al., 2020), bed erosion along the flow path (Hungr, 1995; Bouchut et al., 2008; Iverson, 2012; Pirulli and Pastor, 2012) and the description of two-phase flows (e.g. Pudasaini, 2012; Rosatti and Begnudelli, 2013; Iverson and George, 2014; Bouchut et al., 2015; Bouchut et al., 2016; Pastor et al., 2018b).

In addition to the complexity of choosing realistic constitutive equations to model the flow physical properties, there is also a purely methodological difficulty in deriving the thin-layer equations for a complex topography, with acceleration forces arising from the curvature of the topography. Their influence in 1D thin-layer models was investigated by Hutter and Koch (1991), Greve and Hutter (1993) and Bouchut et al. (2003). Koch et al. (1994) investigated curvature effects for unconfined flows on simple 2D topographies. Their work was completed by Gray et al. (1999) and Wieland et al. (1999) for channelized flows in straight channels. Later on Pudasaini and Hutter (2003) and Pudasaini et al. (2003) considered flows in curved and twisted channels[1]. The generalization of curvature forces to general topographies was done by Bouchut and Westdickenberg (2004), Luca et al. (2009a) and Rauter and Tukovic (2018). To our knowledge, only one study focused on quantifying curvature effects in simulations on general topographies: Fischer et al. (2012) showed curtaure terms have a substantial effect for model calibration. However, it focuses on curvature terms in the bottom friction and does not consider other curvature terms that are independent from the chosen rheology.

In this work, we aim at quantifying more generally and precisely the influence of curvature terms

[1]Curvature effects have also been studied for several decades for snow avalanche modeling (e.g. Salm, 1967; Ancey, 1994)

Table 2.1: Non exhaustive list of 2D thin-layer models used at the field scale.

Model name	**Numerical scheme**	**Bed erosion**	**Two-phase flows**	**References**
MassMov2D	Finite Differences	-	-	(Beguería et al., 2009)
Flo-2D		-	-	(O'Brien et al., 1993)
Volcflow		x	-	(Kelfoun and Druitt, 2005)
SHALTOP	Finite Volumes	-	-	(Bouchut and Westdickenberg, 2004) (Mangeney et al., 2007b)
RAMMS		x	-	(Christen et al., 2010)
RASH3D		x	-	(Pirulli et al., 2007; Pirulli and Pastor, 2012)
r.avaflow		x	x	(Pudasaini, 2012; Mergili et al., 2017)
GeoClaw		-	-	(Berger et al., 2011; LeVeque et al., 2011)
D-Claw		-	x	(Iverson and George, 2014; George and Iverson, 2014)
Titan2D		-	x	(Patra et al., 2005; Pitman and Le, 2005)
TRENT-2D		-	x	(Armanini et al., 2009; Rosatti and Begnudelli, 2013)
DAN3D	SPH (Smoothed Particle Hydrodynamics)	x	-	(McDougall and Hungr, 2004)
GeoFlow_SPH		x	x	(Pastor et al., 2009b; Pastor et al., 2018b)
3d-DMM		x	-	(Kwan and Sun, 2007; Law et al., 2017)

in depth-averaged thin-layers simulations. This is important for practitioners using thin-layers models: we will identify situations (in terms of topographic settings and rheological parametrization) where curvature effects may significantly impact their simulation results, and thus are worth taking into account for hazard assessment. We focus on the modeling of single-phase incompressible flows, with an Eulerian description. We also disregard bed erosion and internal friction. The resulting equations may be over-simplified in comparison to the physical processes at stake in real geophysical flows. However, such equations are now widely used to simulate debris flows, debris avalanches and rock avalanches (Hungr et al., 2007; Pastor et al., 2018a). Thus, we deem important to assess quantitavely the importance of curvature terms for field applications. However, we acknowledge that it goes along with major uncertainties on the rheology and rheological parameters needed to reproduce correctly real gravity flows.

In the following section, we present the depth-averaged thin-layer equations for flows on complex topographies. We detail the derivation of two curvature terms: one that does not depend on the rheology and the other appearing in the bottom friction when a frictional rheology is used. We also introduce the SHALTOP numerical model (Mangeney et al., 2007b) and its modified version without curvature forces, that will be used to carry out simulations. The curvature terms will be formally analyzed and compared to previous studies in Section 2.3. Then, in Section 2.4, we illustrate for synthetic topographies the importance of taking into account curvature forces. Finally, in Section 2.5, we consider two real Digital Elevation Models, with a non-viscous debris flow in the Prêcheur river (Martinique, French Caribbean) and a potential massive debris avalanche from the Soufrière de Guadeloupe volcano (Guadeloupe, French Caribbean).

2.2 Modeling approach using thin-layer equations

Thin-layer equations model the propagation of a thin layer of fluid following the topography. As opposed to full 3D models, thin-layer models no longer simulate the movement of each solid or fluid element. Instead, they integrate their dynamics over a column of fluid in the direction normal to the topography and consider the mean flow velocity over this column. Although the resulting equations are relatively simple, their rigorous derivation is not straight-forward. As a matter of fact, the momentum and mass equations must first be written in a reference frame that allows a convenient integration. Its mere definition is difficult, not to mention the expression of the constitutive equations in the resulting coordinate system. In Appendix 2.B, we describe into details how curvature terms appear in the thin-layer equations derivation in Bouchut and Westdickenberg (2004). In the following, we will only present the chosen parametrization and the final equations.

2.2.1 Mass and momentum equations and boundary conditions

Most thin-layer models are based on the incompressible mass and momentum equations

$$\partial_t \vec{U} + (\vec{U} \cdot \nabla_{\vec{X}})\vec{U} = -\vec{g} + \nabla_{\vec{X}} \cdot \sigma, \tag{2.1}$$

$$\nabla_{\vec{X}} \cdot \vec{U} = 0, \tag{2.2}$$

where $-\vec{g}$ is gravity and σ the Cauchy stress tensor normalized by the flow density. $\vec{X} = (X, Y, Z)$ is the cartesian coordinate system associated with the orthonormal base $(\vec{e}_X, \vec{e}_Y, \vec{e}_Z)$. In the following we will write $\mathbf{X} = (X, Y) \in \mathbb{R}^2$ for the horizontal coordinates. In the following, 3D vectors will be identified by an arrow and 2D vectors will be in bold. For instance, $\vec{U}(\vec{X}) = (U_X, U_Y, U_Z) = (\mathbf{U}, U_Z)$ gives the components of the 3D velocity field in the cartesian reference frame. $\nabla_{\vec{X}}$ is the gradient operator.

The base of the flow matches the topography and is given by a 2D surface $Z = b(\mathbf{X})$, with upward unit normal vector $\vec{n}$ (Figure 2.1a for 1D topographies, Figure 2.1b for 2D topographies),

$$\vec{n} = c\Big(-\frac{\partial b}{\partial X}, -\frac{\partial b}{\partial Y}, 1\Big) = \Big(-\mathbf{s}, c\Big), \tag{2.3}$$

with

$$c = \cos(\theta) = \Big(1 + \|\nabla_{\mathbf{X}} b\|^2\Big)^{-\frac{1}{2}}, \tag{2.4}$$

$$\mathbf{s} = c\nabla_{\mathbf{X}} b, \tag{2.5}$$

where θ is the topography steepest slope angle. Along with boundary conditions detailed in Appendix 2.B, a constitutive equation for the stress tensor σ is needed to close the problem. The latter can be divided into pressure and deviatoric parts, namely

$$\sigma = \sigma' - pI_3, \tag{2.6}$$

with σ' the deviatoric stress tensor, p the pressure field (devided by the flow density) and I_3 the identity matrix. For scale analysis and to allow for a rigorous mathematical derivation, Bouchut and Westdickenberg (2004) chose a Newtonian approach with a linear stress constitutive equation

$$\sigma' = \nu\left(\nabla_{\vec{X}}\vec{U} + (\nabla_{\vec{X}}\vec{U})^t\right), \tag{2.7}$$

with ν the kinematic viscosity, that is assumed to be small (see Appendix 2.B). They furthermore imposed a friction boundary condition at the bed

$$\sigma\vec{n} - (\vec{n}\cdot\sigma\vec{n})\,\vec{n} = \mu\frac{\vec{U}}{\|\vec{U}\|}(-\vec{n}\cdot\sigma\vec{n})_+, \tag{2.8}$$

where $\mu = \tan(\delta)$ is the friction coefficient and δ is the friction angle. The key point here is the transformation of the equations in a convenient reference frame, in which they can be integrated.

2.2.2 Coordinate system and reference frame

The simplest way to derive the thin-layer equations is to use cartesian coordinates and integrate the Navier-Stoke equations along the vertical direction (Barré de Saint-Venant, 1871; Pitman et al., 2003; Berger et al., 2011). This is done in particular to model the propagation of tsunamis because the wavelength of waves is small in comparison to the water vertical depth and the main driving forces are horizontal pressure gradients (e.g. Berger et al., 2011; LeVeque et al., 2011). On the contrary, the shallowness of landslides propagating on potentially steep slopes must be regarded in the direction normal to the topography. Moreover, the flow velocity is (at least for a first approximation) tangent to the topography. Thus the velocity in the normal direction is small. In order to translate this property it is appropriate to write these equations in a reference frame linked to the topography with one vector in the direction normal to the topography. In Figure 2.1b, we give some reference frames used in previous studies. A proper definition is of prior importance, as the reference frame varies spatially. Spatial differential operators in the flow equations, with respect to this reference frame, will thus describe the spatial variations of the fluid thickness and velocity as well as the variations of the reference frame itself.

In order to characterize these variations, a functional relation must be found to relate the new coordinates to the cartesian coordinates, from which the spatial derivative operators in the new reference frame can be deduced. It is therefore somehow more natural and mathematically simple to first define the new coordinate system and to derive the associated reference frame, instead

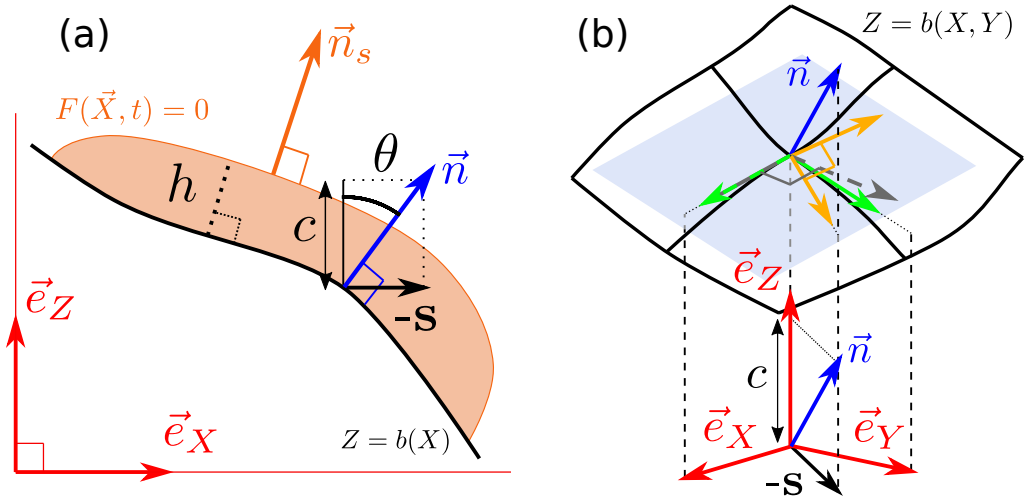

Figure 2.1: (a) Topography and flow description, for a 1D topography $Z = b(X)$. The orange area is the flow region, with thickness h in the direction normal to the topography. (b) 2D topography $Z = b(X, Y)$ description, with reference frames commonly used in the literature to derive thin-layer equations. Red arrows: Cartesian reference frame. Blue arrow: topography normal unit vector. $-\mathbf{s}$: main slope horizontal direction. All other arrows are in the topography tangent plane (blue plane). Green arrows: Christen et al. (2010). Dashed gray arrows: Mangeney-Castelnau et al. (2003). Orange arrows: Iverson and George (2014).

of the contrary. With this method, the reference frame may not be orthonormal but this does not entail any loss of generality or accuracy compared to models using an orthonormal reference frame.

The most straightforward way to localize a point M above the topography is to consider its projection M' on the topography, along the direction normal to the topography (Figure 2.2a). The point M, which has coordinates $\vec{X} = (X, Y, Z)$ in the cartesian reference frame, can then be localized with a new set of coordinates (x_1, x_2, x_3): $(x_1, x_2) = \mathbf{x}$ are the horizontal coordinates of M' in the cartesian reference frame and $x_3 = MM'$ is the distance to the topography (Figure 2.2a). Provided we remain in a sufficiently small neighborhood above the topography, this new coordinate system is non-ambiguous: one (and only one) triplet (x_1, x_2, x_3) can be associated with any point in this neighborhood and vice-versa. More formally, the link between the cartesian coordinates $\vec{X} = (\mathbf{X}, Z)$ and the new coordinates $\vec{x} = (x_1, x_2, x_3) = (\mathbf{x}, x_3)$ of a same physical point is given by:

$$(\mathbf{X}, Z) = \vec{X}(\mathbf{x}, x_3) = M' + x_3\vec{n} = \begin{pmatrix} \mathbf{x} \\ b(\mathbf{x}) \end{pmatrix} + x_3\vec{n}(\mathbf{x}). \tag{2.9}$$

As previously, $\vec{n} = \vec{n}(\mathbf{x})$ is the unit upward vector normal to the topography. The same coordinate system was used by Bouchut et al. (2003) for 1D topographies and Bouchut and Westdickenberg (2004) and Luca et al. (2009a) for 2D topographies. A more general formulation with a curvilinear coordinate system $\mathbf{x} = \mathbf{x}(\boldsymbol{\xi})$ is presented in Bouchut and Westdickenberg (2004). For instance, for 1D topographies, we can choose to locate M' by its curvilinear coordinates along the topography, instead of its cartesian X-coordinate (Savage and Hutter, 1991). For simplicity, we shall keep the Cartesian coordinate system to locate M'. However, this does not limit in any way the type of topographies that can be described in the model.

The reference frame $(\vec{e}_1, \vec{e}_2, \vec{e}_3)$ associated with the new coordinates $\vec{x} = (x_1, x_2, x_3)$follows coordinate lines, so we obtain, with the Einstein notation:

$$d\vec{X} = \vec{e}_i dx_i = \vec{e}_1 dx_1 + \vec{e}_2 dx_2 + \vec{e}_3 dx_3. \tag{2.10}$$

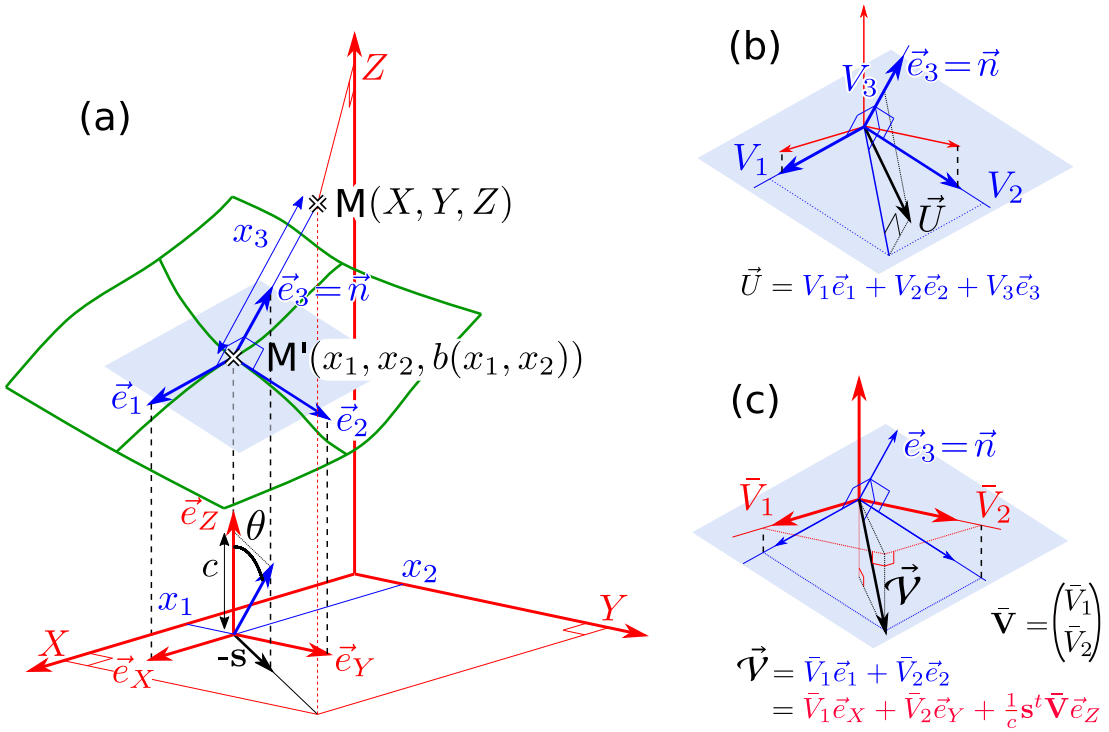

Figure 2.2: Notations and reference frames for the thin-layer equation derivations. (a) Coordinates of a material point M in the cartesian reference frame $(\vec{e}_X, \vec{e}_Y, \vec{e}_Z)$ (red arrows) are given by (X, Y, Z) and by (x_1, x_2, x_3) in the topography reference frame $(\vec{e}_1, \vec{e}_2, \vec{e}_3)$ (blues arrows). M' is the projection of M on the topography: it has cartesian coordinates $(x_1, x_2, b(x_1, x_2))$. $\vec{e}_3$ is the unit normal vector to the topography and $\vec{e}_1$, $\vec{e}_2$ are the projections parallel to $\vec{e}_Z$ of $\vec{e}_X$ and $\vec{e}_Y$ on the plane tangent to the topography (blue feature). (b) Parametrization of the physical velocity $\vec{U}$ of a material point in the topography reference frame. (c) Parametrization of the physical average velocity $\vec{\mathcal{V}}$ of the flow. $\vec{\mathcal{V}}$ is tangent to the topography and is parametrized in the cartesian reference frame (red) and in the topography reference frame (blue).

We therefore have, for instance, $\vec{e}_1 = \partial_{x_1}\vec{X}$. In this base, the velocity field has coordinates $\vec{V} = (V_1, V_2, V_3) = (\mathbf{V}, V_3)$, such that (Figure 2.2b):

$$\vec{U} = U_X\vec{e}_X + U_Y\vec{e}_Y + U_Z\vec{e}_Z = V_1\vec{e}_1 + V_2\vec{e}_2 + V_3\vec{e}_3. \tag{2.11}$$

We can show (see Appendix 2.B) that $\vec{e}_3 = \vec{n}$ and thus that V_3 is the topography normal component of the velocity (Figure 2.2b).

Note that in the previous equation, $\vec{U}$ must be seen as the physical 3D velocity of the fluid, in the sense that $\|\vec{U}\| = \left(U_X^2 + U_Y^2 + U_Z^2\right)^{\frac{1}{2}}$ is the real velocity. In comparison, $\vec{V}$ is only a parametrization of the velocity field. In particular, as the topography reference frame is in general not orthonormal, we have:

$$\|\vec{V}\| = \left(V_1^2 + V_2^2 + V_3^2\right)^{\frac{1}{2}} \neq \|\vec{U}\|. \tag{2.12}$$

It is not straightforward to replace $\vec{U}$ by $\vec{V}$ in the Navier-Stokes equations. This derivation can be found in Bouchut and Westdickenberg (2004), or in Luca et al. (2009a) with a different formalism. However, the resulting equations can be significantly simplified with the thin-layer approximations. In the following, we simply give the final thin-layer equations and analyze the resulting curvature terms. More details on the formal derivation and hypotheses are given in Appendix 2.B.

2.2.3 Thin-layer equations

In the thin-layer approximation, we describe the dynamics of a fluid layer with thickness $h(\mathbf{x})$. We assume this thickness to be small in comparison to the flow extent. Its physical depth-averaged velocity $\vec{\mathcal{V}}$ is tangent to the topography and thus can be written in the topography frame:

$$\vec{\mathcal{V}} = \bar{V}_1\vec{e}_1 + \bar{V}_2\vec{e}_2, \tag{2.13}$$

and has coordinates $(\boldsymbol{\mathcal{V}}, \mathcal{V}_3)$ in the cartesian coordinate system. We can show (see Appendix 2.B) that it is written in the cartesian reference frame:

$$\vec{\mathcal{V}} = \bar{V}_1\vec{e}_X + \bar{V}_2\vec{e}_Y + \frac{1}{c}\mathbf{s}^t\bar{\mathbf{V}}\vec{e}_Z. \tag{2.14}$$

We show that $\bar{V}_1\vec{e}_1$ and $\bar{V}_2\vec{e}_2$ are respectively the projections of $\bar{V}_1\vec{e}_X$ and $\bar{V}_2\vec{e}_Y$, on the topography-tangent plane, parallel to $\vec{e}_Z$ (Figure 2.2c).

The resulting equation for $\bar{\mathbf{V}} = (\bar{V}_1, \bar{V}_2)$ is given by:

$$\begin{aligned}\partial_t\bar{\mathbf{V}} + (\bar{\mathbf{V}}\cdot\nabla_{\mathbf{x}})\bar{\mathbf{V}} + (I_2 - \mathbf{s}\mathbf{s}^t)\nabla_{\mathbf{x}}\left(g(hc+b)\right) = \\ -c\left(\bar{\mathbf{V}}^t(\partial^2_{\mathbf{xx}}b)\bar{\mathbf{V}}\right)\mathbf{s} - \frac{\mu g c\bar{\mathbf{V}}}{\sqrt{\|\bar{\mathbf{V}}\|^2 + \left(\frac{1}{c}\mathbf{s}^t\bar{\mathbf{V}}\right)^2}}\left(1 + \frac{\bar{\mathbf{V}}^t(\partial^2_{\mathbf{xx}}b)\bar{\mathbf{V}}}{g}\right)_+.\end{aligned} \tag{2.15}$$

Two curvature terms, involving $\partial^2_{\mathbf{xx}}b$, appear in (2.15). One does not depend on the rheology (red term in (2.15)) and the other is included in the friction force (blue term in (2.15)). These terms arise from the expression of the pressure at the bottom of the flow (see Appendix 2.B). They will be interpreted in Section 2.3. Note that (2.15) is equivalent to equation (9.32) in Luca et al. (2009a). The viscosity ν does not appear in (2.15), because we chose it to be negligible, which allows for a rigorous mathematical derivation. To our knowledge, there exist no formal derivation of thin-layer equations with non negligible viscosity, an no assumption on the velocity profile, on general topographies.

The mass equation does not entail any curvature term. With the same formalism as in our development, Bouchut and Westdickenberg (2004) show that it reads :

$$\partial_t \left(\frac{h}{c}\right) + \nabla_{\mathbf{x}} \cdot \left(\frac{h}{c}\bar{\mathbf{V}}\right) = 0. \tag{2.16}$$

2.2.4 The SHALTOP numerical model

In order to investigate the influence of curvature forces in numerical simulations, we use the SHALTOP numerical model (Mangeney et al., 2007b). It has been used to reproduce both experimental dry granular flows (Mangeney et al., 2007b) and real landslides (Lucas and Mangeney, 2007; Favreau et al., 2010; Lucas et al., 2011; Lucas et al., 2014; Moretti et al., 2015; Moretti et al., 2020a; Brunet et al., 2017; Peruzzetto et al., 2019). We choose not to compare SHALTOP to another code that would not describe precisely the topography effects. We would not be able to tell whether discrepancies in results originate from curvature effects or, for instance, from the different numerical scheme. A proper benchmarking exercise would be needed, but is beyond the scope of this work. Instead we shall use the same code, but modify it in order to reflect several approximations or remove the curvature.

In SHALTOP, the flow equations are written in terms of the variable $\mathbf{u} = \bar{\mathbf{V}}/c$. This parametrization will be discuss later on. The corresponding momentum equation is:

$$\begin{aligned}\partial_t \mathbf{u} + c(\mathbf{u}\cdot\nabla_{\mathbf{x}})\mathbf{u} + \frac{1}{c}(Id - \mathbf{s}\mathbf{s}^t)\nabla_{\mathbf{x}}\left(g(hc+b)\right) \\ = -\frac{1}{c}\left(\mathbf{u}^t\mathcal{H}\mathbf{u}\right)\mathbf{s} + \frac{1}{c}\left(\mathbf{s}^t\mathcal{H}\mathbf{u}\right)\mathbf{u} - \frac{\mu g c \mathbf{u}}{\sqrt{c^2\|\mathbf{u}\|^2 + (\mathbf{s}^t\mathbf{u})^2}}\left(1 + \frac{c^2\mathbf{u}^t(\partial^2_{\mathbf{xx}}b)\mathbf{u}}{g}\right).\end{aligned} \tag{2.17}$$

with curvature terms colored as in (2.15). SHALTOP solves the conservative form of (2.17) with a finite-volume numerical scheme (see Mangeney et al. (2007b)

We will show in Section 2.3.1 that the curvature force (first two terms on the right-hand side of (2.17)) ensures the velocity remains tangent to the topography at all time. Thus, to model this effect, a tangent transport is applied (e.g. Knebelman, 1951). Considering the physical velocity $\vec{\mathcal{V}} = (c\mathbf{u}, \mathbf{s}^t\mathbf{u})$ in one cell with topography normal vectors $\vec{n}$, the transported velocity $\vec{\mathcal{V}}'$ in a neighboring cell with normal vector $\vec{n}'$ is computed with:

$$\vec{\mathcal{V}}' = \vec{\mathcal{V}} - \frac{\vec{\mathcal{V}}\cdot\vec{n}'}{1+\vec{n}\cdot\vec{n'}}\left(\vec{n}+\vec{n'}\right). \tag{2.18}$$

Since the curvature force involves the slope variations, for real data with small scale variations it is often necessary to slightly smooth the topography to avoid numerical instabilities. Indeed, when the topography radius of curvature is smaller than the flow thickness, lines normal to the topographies can cross within the flow. In turn the coordinate system defined in (2.9) is ambiguous: several coordinates (x_1, x_2, x_3) can be associated to a single physical point.

In SHALTOP, the friction coefficient μ can be a function of the flow thickness and velocity. We can thus change the expression of the bottom stress T as in other classical rheologies. For instance, in the semi-empirical Voellmy rheology (Voellmy, 1955; Salm, 1993), the bottom stress reads:

$$T = \rho h \mu (gc + \gamma\|\vec{\mathcal{V}}\|^2) + \rho g \frac{\|\vec{\mathcal{V}}\|^2}{\xi}, \tag{2.19}$$

with ρ the material density, γ the curvature along flow path (see next section for its computation) and ξ the turbulence coefficient. In numerical experiments (Sections 2.4 and (2.5)), we will

consider both the Coulomb and the Voellmy rheology that are classically used for field application due to the small number of parameters involved while being able to reproduce first order observations (e.g. Hungr et al., 2007; Lucas et al., 2014; McDougall, 2017).

2.3 Formal analysis of curvature terms

2.3.1 Interpretation of curvature terms

The curvature terms appearing in the derived thin-layer equations can be interpreted as acceleration forces in the non-Galilean reference frame linked to the topography. This appears more clearly when we write the depth-averaged equations for the 3D velocity $\vec{\mathcal{V}}$, in the cartesian reference frame:

$$\partial_t \vec{\mathcal{V}} + (\boldsymbol{\mathcal{V}} \cdot \nabla_{\mathbf{X}} \vec{\mathcal{V}}) = \vec{F}_g + \vec{F}_{\mathcal{H}} + \vec{F}_\mu, \tag{2.20}$$

with

$$\vec{F}_g = -\begin{pmatrix} Id - \mathbf{s}\mathbf{s}^t \\ c\mathbf{s}^t \end{pmatrix} \nabla_{\mathbf{X}}(g(hc+b)), \tag{2.21}$$

$$\vec{F}_{\mathcal{H}} = c(\boldsymbol{\mathcal{V}}^t \partial^2_{\mathbf{XX}} b \boldsymbol{\mathcal{V}})\vec{n} = \frac{1}{c^2}(\boldsymbol{\mathcal{V}}^t \mathcal{H} \boldsymbol{\mathcal{V}})\vec{n}, \tag{2.22}$$

$$\vec{F}_\mu = -\frac{\mu g c \vec{\mathcal{V}}}{\|\vec{\mathcal{V}}\|}\left(1 + \frac{\boldsymbol{\mathcal{V}}^t(\partial^2_{\mathbf{XX}} b)\boldsymbol{\mathcal{V}}}{g}\right)_+, \tag{2.23}$$

where $\mathcal{H} = c^3 \partial^2_{\mathbf{XX}} b$ is the curvature tensor. $\vec{F}_g$ represents the gravity and lateral pressure forces, $\vec{F}_\mu$ is the friction force and $\vec{F}_{\mathcal{H}}$ is the curvature force.

For a material point advected by the velocity field $\vec{\mathcal{V}}$, we can compute[1]

$$\frac{d}{dt}\left(\vec{\mathcal{V}} \cdot \vec{n}\right) = \left(\partial_t \vec{\mathcal{V}} + (\boldsymbol{\mathcal{V}} \cdot \nabla_{\mathbf{X}})\vec{\mathcal{V}}\right) \cdot \vec{n} + \vec{\mathcal{V}} \cdot \left((\boldsymbol{\mathcal{V}} \cdot \nabla_{\mathbf{X}})\vec{n}\right) \tag{2.24}$$

$$= \left(\partial_t \vec{\mathcal{V}} + (\boldsymbol{\mathcal{V}} \cdot \nabla_{\mathbf{X}})\vec{\mathcal{V}}\right) \cdot \vec{n} - c\boldsymbol{\mathcal{V}}^t \partial^2_{\mathbf{XX}} b \boldsymbol{\mathcal{V}}. \tag{2.25}$$

In the right-hand side of (2.24), we can use (2.20). As $\vec{F}_g \cdot \vec{n} = \vec{F}_\mu \cdot \vec{n} = 0$ and $\vec{F}_{\mathcal{H}} \cdot \vec{n} = c\boldsymbol{\mathcal{V}}^t \partial^2_{\mathbf{XX}} b \boldsymbol{\mathcal{V}}$, (2.24) becomes

$$\frac{d}{dt}(\vec{\mathcal{V}} \cdot \vec{n}) = 0. \tag{2.26}$$

In other words, the curvature force $\vec{F}_{\mathcal{H}}$ ensures that the flow velocity remains parallel to the topography, i.e. $\vec{\mathcal{V}} \cdot \vec{n} = 0$[2]. This force is normal to the topography and thus to the velocity and does no work: in the absence of gravity and friction, the material point would be advected on the topography at constant kinetic energy. Note that this acceleration force is still present, though the equations are written in the fixed cartesian coordinate system: that's because they arise in the intermediate step where the momentum equations are integrated in the direction normal to the topography. The Lagrangian form of equation (2.20) provides a direct expression

[1] (2.24) is obtained with $\frac{d}{dt}\left(\vec{\mathcal{V}} \cdot \vec{n}\right) = \frac{d\vec{\mathcal{V}}}{dt} \cdot \vec{n} + \vec{\mathcal{V}} \cdot \frac{d\vec{n}(\mathbf{X}(t))}{dt}$, where $\mathbf{X}(t)$ is the horizontal coordinates of the material point.

[2] Note that $\vec{\mathcal{V}} \cdot \vec{n} = 0$ is a necessary assumption to derive thin-layer equations, and not, stricly speaking, a physical reality. The cruvature force thus ensures that the final thin-layer equations are consistent with the assumptions made to derive them.

of the curvature along a flow path. As a matter of fact, if $M(t)$ is the position of a material point, we have[1]:

$$\dot{M}(t) = \vec{\mathcal{V}}, \tag{2.27}$$

$$\ddot{M}(t) = \partial_t \vec{\mathcal{V}} + \boldsymbol{\mathcal{V}} \cdot \nabla_{\mathbf{X}} \vec{\mathcal{V}}. \tag{2.28}$$

From classical analytical geometry results and using (2.20), the curvature of the topography along a flow path, γ, is thus given by

$$\gamma = \pm \frac{\left\| \dot{M} \wedge \ddot{M} \right\|}{\left\| \dot{M} \right\|^3} = c \frac{\boldsymbol{\mathcal{V}}^t \partial^2_{\mathbf{XX}} b \boldsymbol{\mathcal{V}}}{\|\vec{\mathcal{V}}\|^2}. \tag{2.29}$$

In the previous equation, we used (2.28) and (2.20), and the fact that $\vec{F}_{\mathcal{H}}$ is the only force which is not colinear to the velovity $\dot{M} = \vec{\mathcal{V}}$: other terms are canceled by the cross product operation. γ is positive for a convex topography and negative otherwise. We thus obtain the classical expression of a centripetal force

$$\vec{F}_{\mathcal{H}} = c(\boldsymbol{\mathcal{V}}^t \partial^2_{\mathbf{XX}} b \boldsymbol{\mathcal{V}}) \vec{n} = \gamma \|\vec{\mathcal{V}}\|^2 \vec{n}. \tag{2.30}$$

Note however that as for any acceleration force, the expression of the curvature force depends on the velocity parametrization. In the topography reference frame $(\vec{e}_1, \vec{e}_3, \vec{e}_3)$, the velocity components are given by $\vec{V}$. Provided we impose $V_3 = 0$, (2.15) describes the evolution of the 2D velocity field $\bar{\mathbf{V}}$ along the topography. The curvature force in this reference frame is exactly

$$\mathbf{F}^{\bar{V}}_{\mathcal{H}} = -c \left(\bar{\mathbf{V}}^t (\partial^2_{\mathbf{XX}} b) \bar{\mathbf{V}} \right) \mathbf{s}. \tag{2.31}$$

$\mathbf{F}^{\bar{V}}_{\mathcal{H}}$ has the direction of the main slope and can have a non-zero power ($\mathbf{F}^{\bar{V}}_{\mathcal{H}} \cdot \bar{\boldsymbol{V}} \neq 0$). As a matter of fact, in the absence of gravity and friction, the kinetic energy must remain constant, however it is given by $\|\vec{\mathcal{V}}\|^2 = \|\bar{\mathbf{V}}\|^2 + \left(\frac{1}{c} \mathbf{s}^t \bar{\mathbf{V}}\right)$ and not by $\|\bar{\mathbf{V}}\|^2$ which is not constant, explaining why the curvature force has a non-zero power in the topography reference frame.

2.3.2 Comparison with previous studies

Friction force

If we use (2.30) in (2.23) to introduce the curvature along flow path γ in the friction force, we get

$$\vec{F}_{\mu} = -\frac{\mu \vec{\mathcal{V}}}{\|\vec{\mathcal{V}}\|} \left(gc + \gamma \|\vec{\mathcal{V}}\|^2 \right)_+, \tag{2.32}$$

This is the classical expression of the friction force. In 1D (for $b = b(X)$), the derivation of γ is simple. Thus, most 1D thin-layer models (e.g. Savage and Hutter, 1991) include the curvature in the friction force. As shown in the previous section, the computation is less self-evident for real 2D topographies ($b = b(X, Y)$), in particular because the flow path must take into account velocity variations (see Appendix 2.C). The curvature term in the friction force is thus either neglected (O'Brien et al., 1993) or approximated. For instance, Pitman et al. (2003) use the curvature in the X and Y directions in the momentum equations for V_X and V_Y respectively. We could find only one reference (found in Fischer et al., 2012) to the exact curvature expression

[1]Strictly spealing, the Lagrangian formulation would give a trajectory $M = f(M_0, t)$, with M_0 the initial position of the particle. Here we consider M_0 as an initial condition, and not a variable. It is not necessary to use the complete Lagrangian formulation to derive the curvature along flow path.

mentioned above with a different numerical model than SHALTOP (that is based on the thin-layer equations derived previously). However, it is also possible to implicitly take into account this curvature by solving the equations for the pressure at the bottom of the flow, in addition to the flow thickness and velocity (Rauter and Tukovic, 2018, see next section).

If the curvature γ is positive, we see from (2.32) that neglecting the curvature decreases the bottom friction and accelerates the flow. The opposite effect is expected if γ is negative. On non-flat topographies, we can expect the flow to propagate on gradually decreasing slopes, at least in a first approximation. For instance, the longitudinal cross-sections of volcanoes are often modeled with an exponential fit (e.g. Mangeney-Castelnau et al., 2003; Kelfoun, 2011; Levy et al., 2015). The topography is thus "globally" convex and the curvature is positive at most points. Without the curvature term in the friction, we can thus expect landslides to go further than in the model including curvature.

The effect of approximating the curvature depends of course on the chosen approximation. In Appendix 2.C, we analyze these effects in some examples. In particular we can compute the curvature along topography in a straight direction given by the local velocity, that is, without taking into account changes in direction. If the flow is not moving in the main slope direction, then the curvature term will be over-estimated.

The numerical code Volcflow uses the following approximation (Karim Kelfoun, personnal communication),

$$\gamma = \gamma_x |\cos(\alpha)| + \gamma_y |\sin(\alpha)|, \tag{2.33}$$

where α is the angle between the horizontal component of the velocity and the X-axis. In our study, we shall test the approximation

$$\gamma = \gamma_x \cos^2(\alpha) + \gamma_y \sin^2(\alpha), \tag{2.34}$$

which is a more classical weighting as $\cos^2(\alpha) + \sin^2(\alpha) = 1$. In both cases, the model is no longer invariant by rotation. For instance, in the case of a flow confined to a channel, we show in Appendix 2.C that both approximations entail a deceleration of the flow in most realistic cases. When the channel is aligned with in the X or Y axes, the deviation from the exact equations is null, but significant differences can be expected otherwise. As the two previous approximations have similar effects, we will test only the second in the following. The effects of neglecting or approximating the curvature with (2.34) will be assessed in simulations in Sections 2.4 and 2.5.

Curvature force

The first detailed derivation of thin-layer equations for complex topographies was carried out by Savage and Hutter (1991) on 1D topographies. The curvature tensor $\mathcal{H}$ was reduced to a scalar κ, the curvature of the topography graph $Z = b(X)$. The curvature term is present in their final expression of the friction force, but no curvature force appears. That is however expected, given their parametrization. They use a curvilinear coordinate system (ξ, η), with η the distance from the topography (our coordinate x_3) and ξ the curvilinear coordinate along the topography graph. The associated orthonormal base is composed of the topography tangential vector $\vec{T}$ and of the topography normal vector $\vec{n}$. To be consistent with Savage and Hutter (1991), let us choose the new parametrization

$$\mathbf{u} = \frac{\bar{\mathbf{V}}}{c}. \tag{2.35}$$

This is equivalent to changing our topography reference frame to $(\vec{i}_1, \vec{i}_2, \vec{i}_3) = (c\vec{e}_1, c\vec{e}_2, \vec{e}_3)$, such that in 1D, $\vec{i}_1$ is the downslope unit vector and $(\vec{i}_1, \vec{i}_3)$ is an orthonormal base. With this

parametrization, the physical velocity is $(c\mathbf{u}, \mathbf{s}^t\mathbf{u})$ and its norm is

$$\|\vec{\mathcal{V}}\|^2 = \|c\mathbf{u}\|^2 + (\mathbf{s}^t\mathbf{u})^2. \tag{2.36}$$

Substituting (2.35) in (2.15), we can show that the momentum equation for $\mathbf{u}$ is (2.17), where the curvature force becomes:

$$\mathbf{F}^{\mathbf{u}}_{\mathcal{H}} = -\frac{1}{c}\left(\mathbf{u}^t\mathcal{H}\mathbf{u}\right)\mathbf{s} + \frac{1}{c}\left(\mathbf{s}^t\mathcal{H}\mathbf{u}\right)\mathbf{u}. \tag{2.37}$$

In comparison to (2.15), the new term $\frac{1}{c}\left(\mathbf{s}^t\mathcal{H}\mathbf{u}\right)\mathbf{u}$ comes from the computation of

$$(\bar{\mathbf{V}}\cdot\nabla_{\mathbf{X}})\bar{\mathbf{V}} = c(\nabla_{\mathbf{X}}(c\mathbf{u}))\mathbf{u}, \tag{2.38}$$

where $\partial_{\mathbf{X}}c$ appears. The curvature force is null when $\mathbf{s}$ and $\mathbf{u}$ are colinear (i.e. when the velocity is in the downslope direction). This is because in this case $\|\vec{\mathcal{V}}\| = \|\mathbf{u}\|$, so no correction needs to be applied to ensure energy is preserved. In particular in 1D, with this parametrization, no curvature forces appear in the equations.

Gray et al. (1999) derived thin-layer equations in a similar fashion. But instead of choosing a reference frame linked to the topography, they used a simpler reference surface with the constraint that the deviation from the topography is of the order $\mathcal{O}(\epsilon)$, where ϵ is the ratio of a characteristic height of the flow over its characteristic length. In thin-layer models, ϵ is assumed to be very small (see Appendix 2.B for a discussion on the ordering of the equations, and for the mathematical meaning of $\mathcal{O}()$). The same approach was used, for instance, by George and Iverson (2014). This in turn makes it possible to assume that the velocity component normal to the reference surface (and not normal to the topography) has magnitude $\mathcal{O}(\epsilon)$ and only the curvature of the reference surface needs to be accounted for. In Gray et al. (1999), this boils down to the curvature along the x-axis κ (see their equations (5.9) and (5.10)). With their ordering, it however disappears in the depth-averaged equations. The derivative of the curvature κ' also appears before the ordering of the equations in their work. It can also be found in the development of Bouchut and Westdickenberg (2004) when curvilinear instead of cartesian coordinates are considered (without changing the accuracy of the resulting equations).

Another fine description of the topography was made by Pudasaini and Hutter (2003) for flows confined in channels. The thalweg is described by a 3D parametric curve $\vec{R}(s)$ to which an orthonormal reference frame is associated with the Serret-Frénet formulas. Pudasaini and Hutter (2003) write the Navier-Stokes equations in this reference frame. The topography curvature is then rendered by the curvature κ and torsion τ of the thalweg $\vec{R}(s)$. However, they thus describe only a limited set of topographies, making a proper comparison with our model difficult.

Fischer et al. (2012) derive a curvature force by solving the Euler-Lagrange equations for a free point mass m with coordinates $\vec{X}(t) = (X_1(t), X_2(t), X_3(t))$ subjected to gravity and evolving on the topography in a fixed cartesian reference frame. With our notation, the Lagrangian reads

$$L = \frac{1}{2}m\|\vec{X}(t)\|^2 - mgX_3(t), \tag{2.39}$$

with the constraint

$$f(\vec{X}) = X_3(t) - b(X_1, X_2) = 0. \tag{2.40}$$

Solving this system yields

$$\frac{d^2\vec{X}}{dt^2} = -gc^2\begin{pmatrix}\nabla_{\mathbf{X}}b\\ \|\nabla_{\mathbf{X}}b\|^2\end{pmatrix} + c\left(\boldsymbol{\mathcal{V}}^t\partial^2_{\mathbf{XX}}b\boldsymbol{\mathcal{V}}\right)\vec{n} = -gc^2\begin{pmatrix}\nabla_{\mathbf{X}}b\\ \|\nabla_{\mathbf{X}}b\|^2\end{pmatrix} + \vec{F}_{\mathcal{H}}. \tag{2.41}$$

This is the Lagrangian form of the momentum equation (2.20), without the friction force $\vec{F}_\mu$ and lateral pressure forces in $\vec{F}_g$. Fischer et al. (2012) use (2.41) to justify the curvature term appearing in the friction force, but the curvature force $\vec{F}_\mathcal{H}$ is actually independent of the friction.

Rauter and Tukovic (2018) and Rauter et al. (2018) use an approach similar to that of Bouchut and Westdickenberg (2004). However, while we use the momentum equation for the topography-normal component of the velocity to get an explicit expression of the pressure, they keep this equation and consider the basal pressure as another unknown to be numerically estimated. This is equivalent to considering the basal pressure as a Lagrangian multiplier, respecting the constraint that the velocity is in the topography-tangent plane. With this method, Rauter and Tukovic (2018) do not need to explicitly describe the curvature. However, a rigorous derivation of their equations also requires complex differential calculations, in particular related to the definition of a gradient operator along the topography.

Now that we have detailed the origin of the curvature effects in thin-layer models, we will investigate their influence, in practice, in simulations. We will first consider simulations on synthetic topographies to identify situations where curvature effects significantly influences the results. We will then carry out simulations on real topographies.

2.4 Curvature effects in simulations with synthetic topographies

As shown in Section 2.3.1, the curvature force $\vec{F}_\mathcal{H}$ is needed to ensure that the flow velocity remains tangent to the topography. It is thus particularly important when the flow changes direction in twisted channels. As proposed by Gray and Hutter (1998), we create a synthetic topography with a channel composed of n_b successive bends, superimposed on a plane (Figure 2.3) with inclination $\theta = 10°$. The channel cross-section is a parabola (Figure 2.3b). At both extremities, there is a smooth transition between the end of the channel and the bottom plane (Figure 2.3a and 2.3c). The thalweg is a sinusoidal of amplitude A_b and period $L = 2.1$ m (black curve in Figure 2.3c). We define the ratio $\bar{\gamma} = A_b/(L/2)$, that can be seen as a non-dimensionalized bend curvature. This is detailed in Appendix 2.D, along with the exact mathematical definition of this synthetic topography and some precisions on the simulation set-up.

In the following, we will first investigate the effects of approximating curvature for a flow propagating in a straight channel (Section 2.4.1). We will then model flows in a channel with only one bend, with the Coulomb and the Voellmy rheologies and analyze how curvature affects the flow direction, velocity and kinetic energy (Section 2.4.2). For hazard assessment, however, it is convenient to synthesize the overall flow dynamics with a few simple characteristics. In Section 2.4.3, we will thus investigate curvature effects on the flow travel duration within the channel and on the maximal dynamic force, for various channel geometries and rheological parameters.

2.4.1 Curvature approximation and non-invariance by rotation

To demonstrate the importance of solving equations that are invariant by rotation, we first consider the propagation of a flow with the Coulomb rheology ($\mu = \tan(15°)$) and the Voellmy rheology ($\mu = \tan(15°)$ and $\xi = 2000$ m s^{-2}), in a channel without bends (that is, $A_b = 0$ m) and a slope inclination of $\theta = 10°$. As the flow propagates at the bottom of the channel, the curvature in the flow direction is, as a first approximation, zero. As a consequence, no curvature effects are expected. Changing the angle ϕ between the X-axis and the thalweg (see Figure 2.4a) should not change the flow dynamics. However, when we implement the approximation of the curvature (2.34) in the friction force, we lose the rotational invariance of the model and the flow

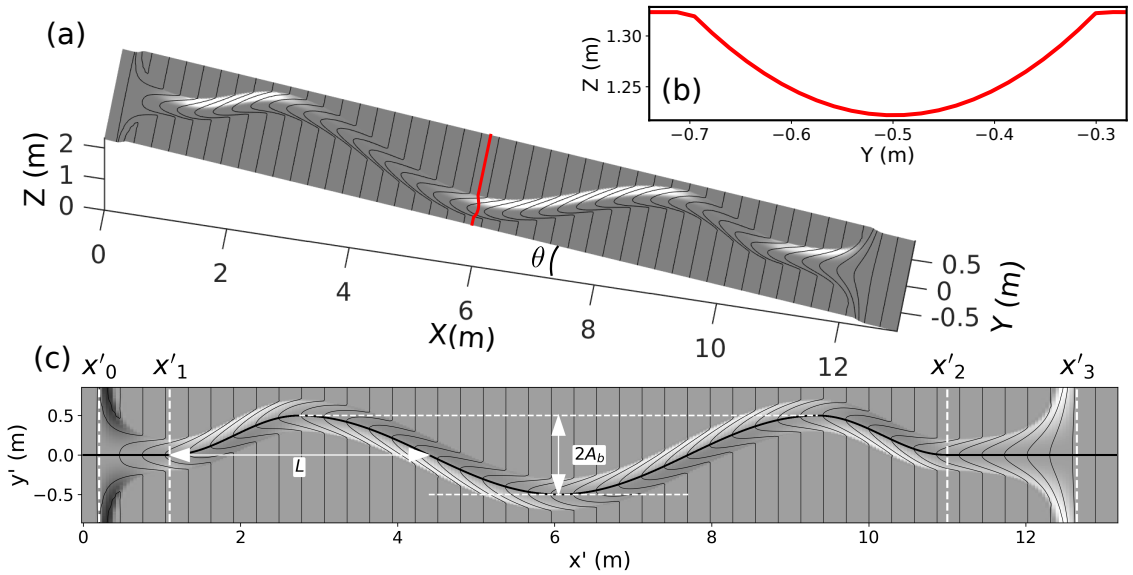

Figure 2.3: Synthetic topography with a twisted channel superimposed on a flat plane. (a) 3D view of the generated topography, in the fixed cartesian reference frame (b) Cross-section of the channel for $X = 6$ m (red curve in (a)). (c) Top view of the channel, with illustration of the parameters used to construct the topography (see Appendix 2.D). Here $L = 2.1$ m and $A_b = 0.5$ m. x' and y' are the curvilinear coordinates along the basal plane on which the channel is superimposed. The contour interval is 5 cm in both (a) and (b).

is slowed down when $\phi > 0$ (Figure 2.4b to 2.4e). For instance with $\phi = 45°$, after 0.5 s, the total kinetic energy is decreased by 20% and 15%, with the Coulomb (Figure 2.4a) and Voellmy rheology (Figure 2.4c) respectively. This directly impacts the travel distance, with 20% (Figure 2.4b) and 5% (Figure 2.4d) reductions respectively.

In the following, we will no longer consider the approximation of curvature in the friction force, and compare only simulations when it is properly taken into account (which is not numerically costly) or omitted. Comparisons with approximated curvature are however provided in the Supplementary Figures (Section 2.A) and will be referred to briefly.

2.4.2 Thicknesses, velocity and kinetic energy

Let us now construct a channel with one bend of amplitude $A_b = 0.5$ m (and thus $\bar{\gamma} = 0.48$). We will first consider the case where $\mu = 0$ in the Coulomb rheology. We thus model a pure fluid and can highlight the influence of the curvature force, independently of the curvature term appearing in the friction force. This is however unrealistic when considering real geophysical flows, as there is no energy dissipation. We will thus also consider $\mu = \tan(6°)$, which is a sensible friction coefficient for debris flow modeling (e.g. Moretti et al., 2015), and the Voellmy rheology that is commonly used to model such flows. To obtain insight on curvature effects for debris and rock avalanche modeling, we will finally model flows propagating on a steeper slope ($\theta = 25°$) with a higher friction coefficient $\mu = \tan(15°)$ (e.g. Moretti et al., 2020a).

Channel with slope $\theta = 10°$

For $\mu = 0$, the only acting forces are the curvature and gravity forces. The simulation results are displayed in Figure 2.5. As shown in Section 2.3.1, the curvature force horizontal component

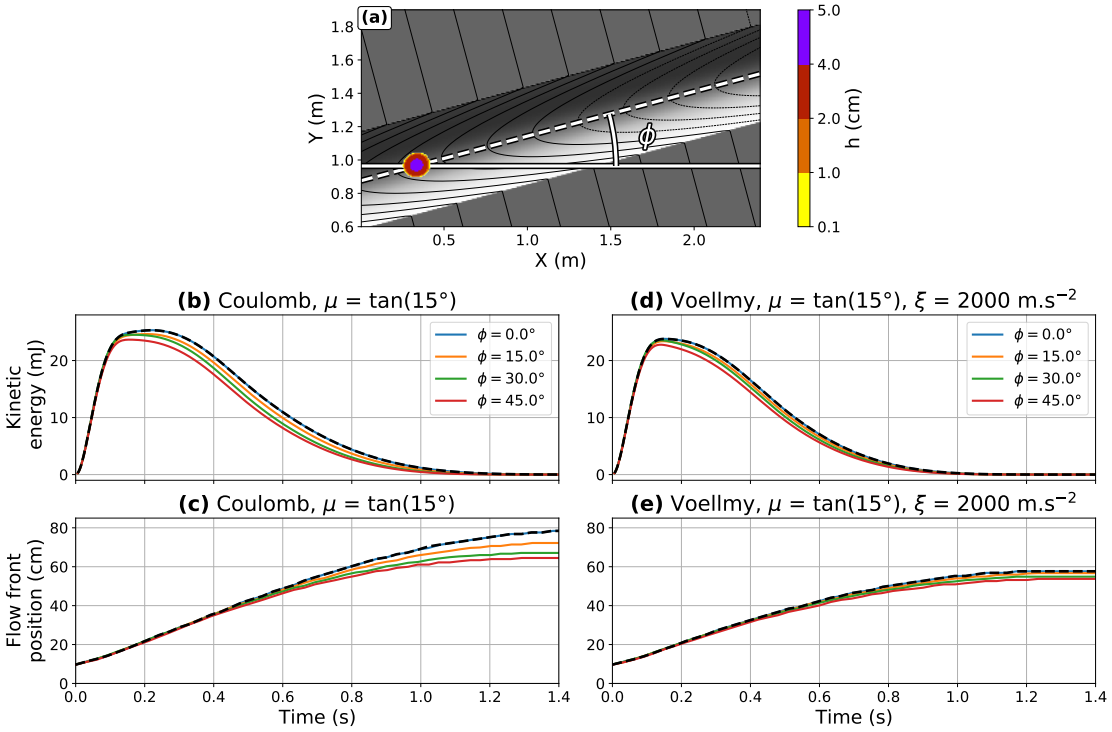

Figure 2.4: Modeling of a flow within a straight channel with inclination $\theta = 10°$. (a) Top view of the channel, with the initial mass (thickness is given by the color scale). ϕ is the angle between the channel direction (white dashed line) and the X-axis (white solid line). (b) and (c): Kinetic energy and flow front position, with the Coulomb rheology ($\mu = \tan(15°)$). Colored solid curves: results when the curvature term in the friction is approximated by weighting the curvature in the X and Y directions (see equation (2.34)), for different values of ϕ. Black dashed curves: result with the exact model, that does not depend on the channel orientation ϕ (up to small numerical errors, not shown here)as it should be. (d) and (e): Same as (b) and (c) but with the Voellmy rheology ($\mu = \tan(15°)$ and $\xi = 2000$ m s^{-2})

is in the steepest slope direction and thus tends to keep the flow at the bottom of the channel. This has a major impact on the flow direction at the exit of the channel (Figures 2.5a and 2.5b). It also results in a smoother increase of the flow velocity (Figure 2.5e, between 1 and 2 s), because without the curvature force, the flow bounces back and forth on the channels walls (Figures 2.5a and 2.5b). Thus, the effect of the curvature force cannot be neglected: its norm is indeed comparable to the norm of gravity and pressure forces when there are steep changes in the topography, as in the main bend and at the outlet of the channel (Supplementary Figures 2.A.1b and 2.A.1c). The maximum flow velocities are, however, of the same order: about 3 m s^{-1} at the outlet of the channel (Figures 2.5c and 2.5d).

In order to model debris flows more realistically, we now use a friction coefficient $\mu = \tan(6°)$. We can then analyze the influence of neglecting the curvature term in the friction force (Figures 2.6, $\vec{F}_\mu$=0). Because of friction, the flow is decelerated compared to the case without friction (only 2 m s^{-1} at the channel outlet). The curvature terms (both in friction and curvature forces), which are proportional to the square of velocity, are then only half as high as gravity and pressure forces (see Supplementary Figures 2.A.2b and 2.A.2d). However, neglecting the curvature force does still slow down the flow, with a 5% kinetic energy decrease at the channel outage (Figure 2.6i, $F_\mathcal{H}$=0). On the contrary, neglecting the curvature term in the friction force results in a slightly smaller friction force and thus increases the flow velocity (kinetic energy increased by 5% at the channel outage, Figure 2.6i, F_μ no curvature) and runout (e.g. Figures 2.6a and 2.6e). Approximating the curvature in the friction decelerates the flow, as expected (see Supplementary Figures 2.A.2 and 2.A.3).

In the literature, the empirical Voellmy rheology is also often used to model debris flows. We show in Supplementary Figures 2.A.4 and 2.A.5 that curvature effects have only limited influence with this rheology, which will be confirmed by further results.

Channel with slope $\theta = 25°$

The main slope of the channel and the parameters we have considered so far are reasonable estimates for modeling debris flows (e.g. Moretti et al., 2015). For debris and rock avalanches, it is more relevant to use steeper slopes and higher friction coefficients. In Figure 2.7, we investigate the curvature effects on a steeper slope ($\theta = 25°$) and for a higher friction coefficient $\mu = \tan(15°)$, which is still characteristic of mobile landslides (Pirulli and Mangeney, 2008). The impact of neglecting curvature terms is qualitatively similar to the previous case with $\mu = \tan(6°)$, but errors are amplified (see Supplementary Figures 2.A.6 and 2.A.7 for the simulations with approximated curvature in friction). In particular, neglecting the curvature term in the friction leads to a significant acceleration of the flow: at the channel outlet, the total kinetic energy is increased by 70% (Figure 2.8a, $F_\mathcal{H}$ exact and F_μ no curvature). It can be directly correlated to the 30% error induced on the friction in the channel bends, when curvature is not taken into account (Figures 2.8b and 2.8d).

In the above simulations, we have shown that the direction of the flow at the channel outlet can change significantly when curvature effects are not accounted for. That is of course of prior importance in hazard mapping. In order to characterize the flow dynamics, two other indicators can refine the hazard assessment analysis.

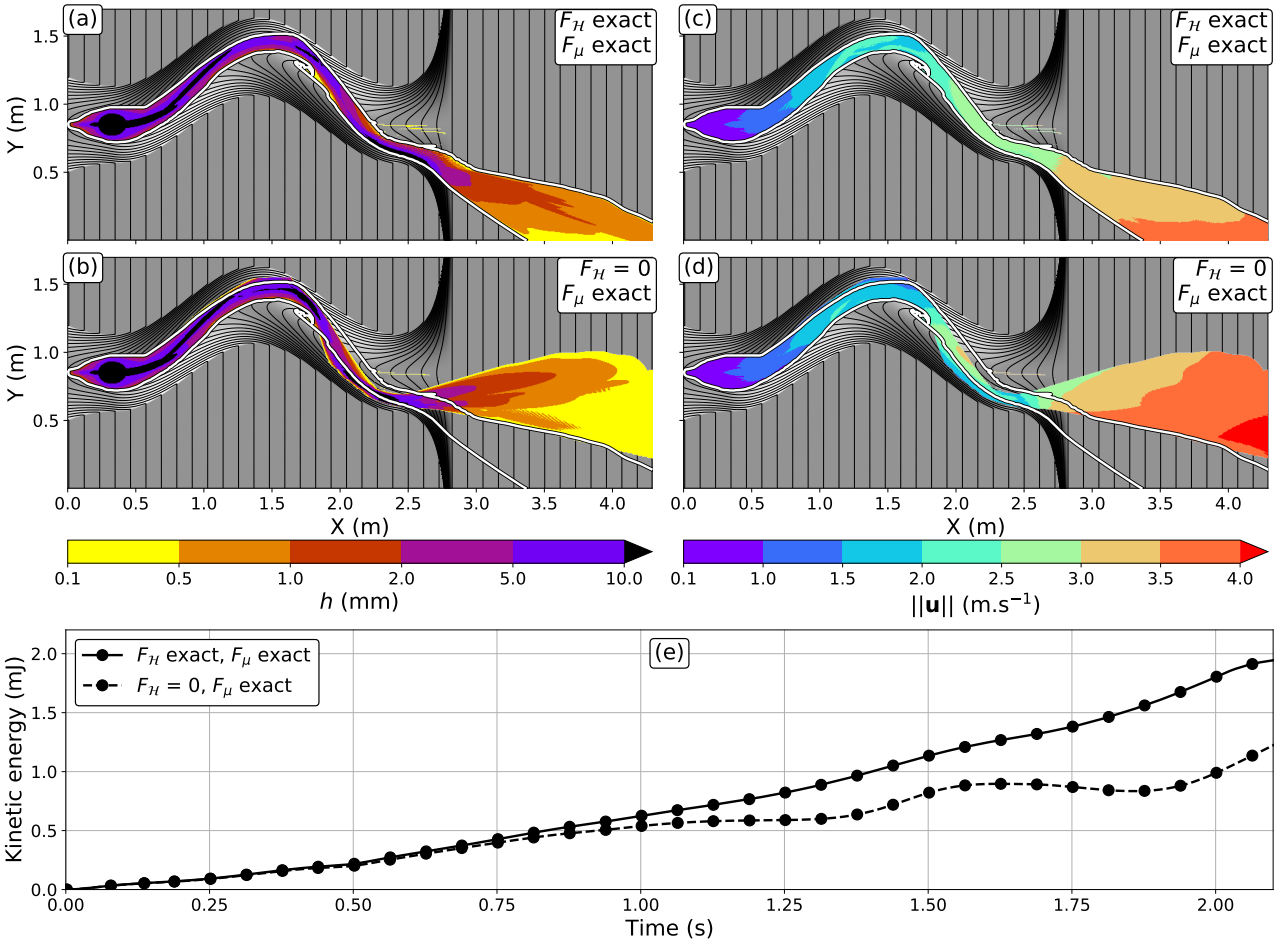

Figure 2.5: Flow simulation with the Coulomb rheology, $\mu = 0$ and a slope $\theta = 10°$. (a) and (c): with the curvature force ($F_{\mathcal{H}}$ exact). (b) and (d): without the curvature force ($F_{\mathcal{H}} = 0$). (a) and (b) give the maximum flow thickness during the simulation, (c) and (d) the maximum flow velocity. The white curve is the flow extent when the curvature force is taken into account. Simulation durations is 2.5 s. We give more details in Appendix 2.E on the derivation of maximum thickness and velocity maps.

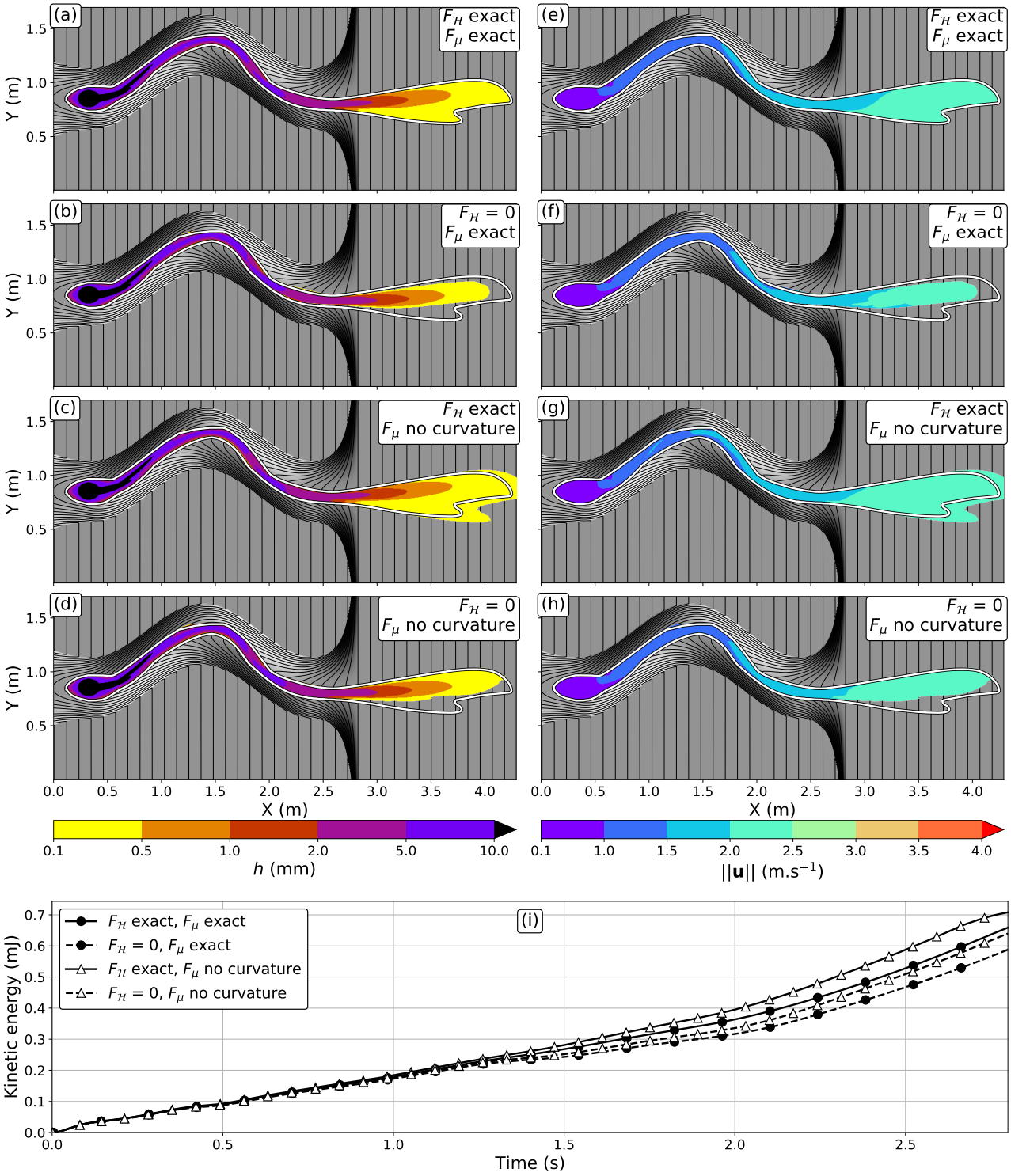

Figure 2.6: Flow simulation with the Coulomb rheology, $\mu = \tan(6°)$ and a slope $\theta = 10°$. The first column is the maximum flow thickness (a-d) and the second column is the flow maximum velocity (e-h), both after 2.8 s. Each subfigure displays the results of the simulation when the curvature force is taken into account ($F_{\mathcal{H}}$ exact) or neglected ($F_{\mathcal{H}} = 0$) and when the curvature in the friction is exact (F_μ exact) or neglected (F_μ no curvature). (a) and (e) are the simulation results in the reference case, with exact curvature terms: the corresponding flow extent (white line) is reported in all figures. The contour interval is 2 cm. (i) Kinetic energy in the different simulations.

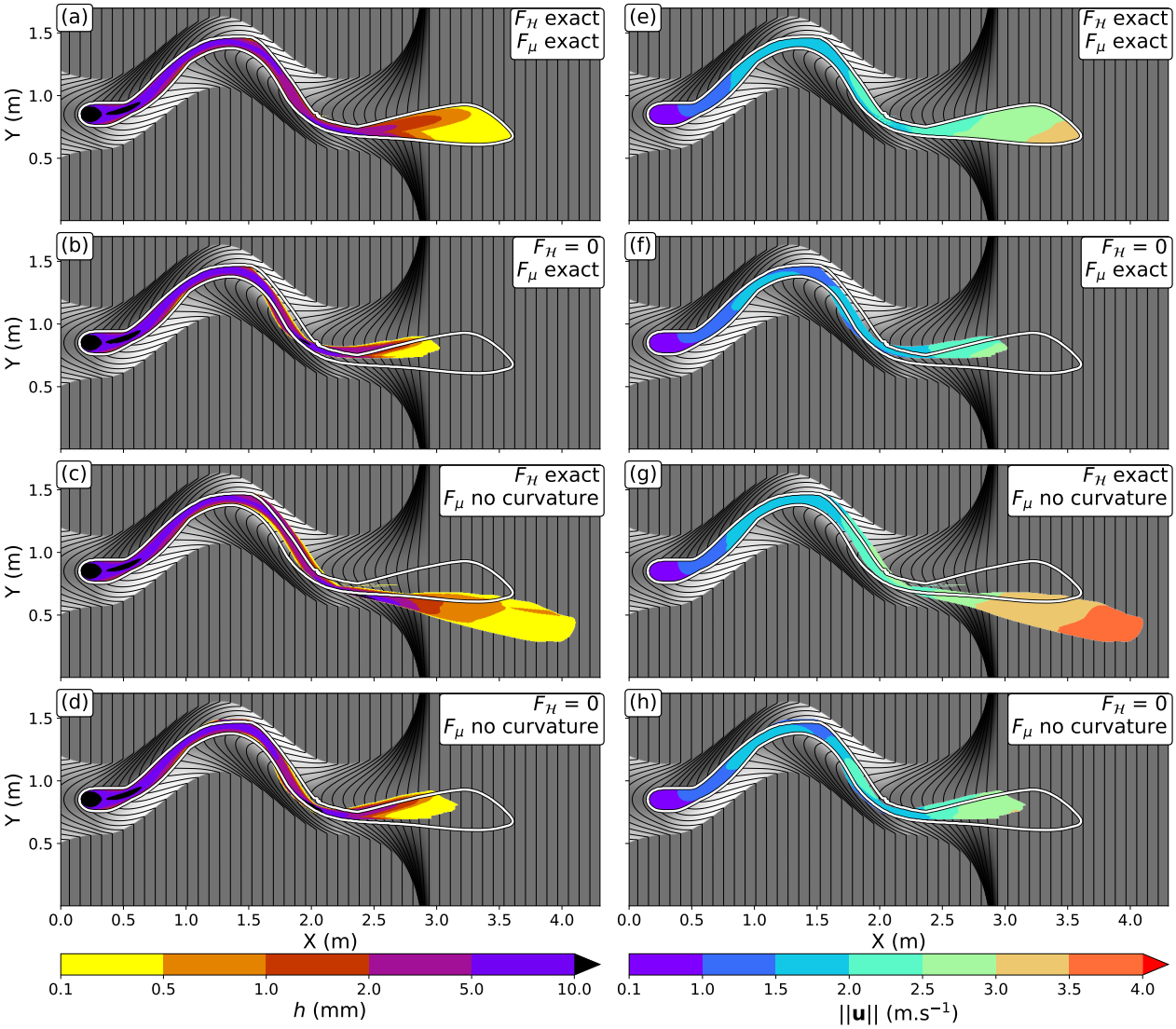

Figure 2.7: Same as Figure 2.6, but with the Coulomb rheology, $\mu = \tan(15^{\circ})$ and a slope $\theta = 25^{\circ}$. The contour interval is 4 cm. Simulation duration is 2.3 s. The kinetic energies are given in Figure 2.8.

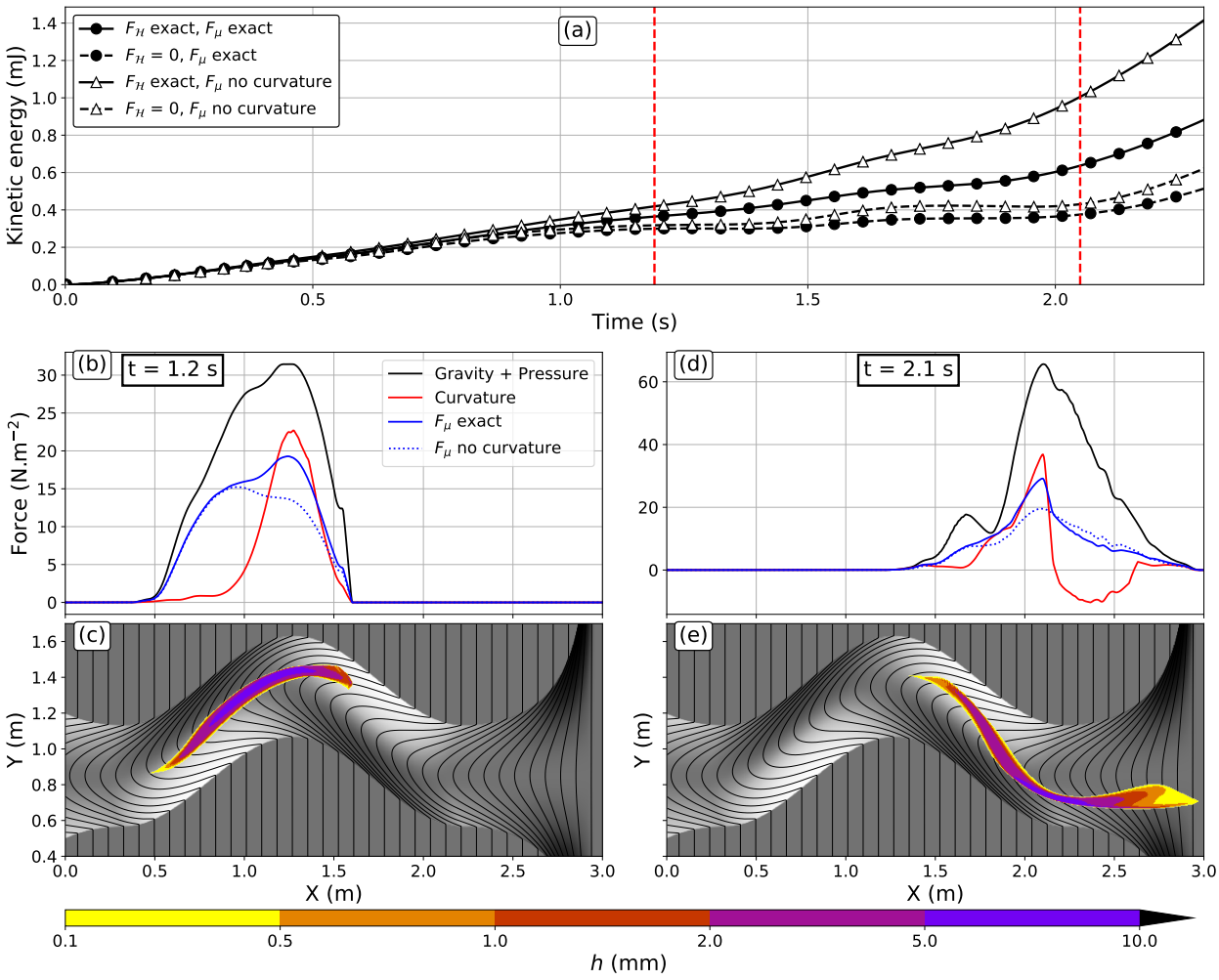

Figure 2.8: (a) Total kinetic energy of the flow with the Coulomb rheology, $\mu = \tan(15°)$ and a slope $\theta = 25°$. (b) For the simulation with exact curvature terms, maximum norm of gravity and pressure force ($\vec{F}_g^{\mathcal{V}}$, black curve), of the curvature force ($\vec{F}_{\mathcal{H}}^{\mathcal{V}}$, red curve, negative when $\vec{n} \cdot \vec{F}_{\mathcal{H}}^{\mathcal{V}} < 0$) and of the friction force ($\vec{F}_{\mathcal{H}}^{\mu}$, blue curves). The friction force is computed with the exact curvature term (F_μ exact) or when it is neglected (F_μ no curvature). The maximum is computed for a constant X coordinate, at t=1.2 s. (c) Flow thickness at t=1.2 s. (d) and (e): Same as (b) and (c), respectively, but for t=2.1 s. These two times are indicated by the red dashed vertical line in (a).

2.4.3 Travel time and maximum dynamic force

The flow travel duration within the channel is often a key indicator for hazard assessment. The second indicator is the maximum dynamic force F_d,

$$F_d = \max(\frac{1}{2}\rho h \|\vec{\mathcal{V}}\|^2) = \max(hP_d), \tag{2.42}$$

where P_d is the dynamic pressure. In the following we choose $\rho = 1500$ kg m^3 for the density: it acts only as a scaling factor. To obtain a more systematic analysis of the influence of curvature terms on these indicators, we keep only one bend, but try three different bend amplitudes: $A_b = 0$ m, $A_b = 0.25$ m and $A_b = 0.5$ m ($\bar{\gamma} = 0$, $\bar{\gamma} = 0.24$ and $\bar{\gamma} = 0.48$. Simulations are run in each configuration with the Coulomb and Voellmy rheologies, while varying the friction and turbulence coefficients.

Results are displayed in Figure 2.9 and summarized in Table 2.2. Unsurprisingly, for a straight channel, travel durations in the channel are very similar whatever the curvature description. There are however variations in the dynamic force (e.g. blues curves in Figure 2.9d), likely due to the initial spreading of the mass in all directions. When a bend is added ($A_b = 0.25$ m and $A_b = 0.5$ m), in the case of small friction coefficients and thus small friction forces, neglecting the curvature in the friction force has less effect than neglecting the curvature force (e.g. Figure 2.9a, $A_b = 0.5$ m for $\mu < \tan(6°)$). However the opposite occurs when the friction coefficient increases, as the friction force also increases. The error on maximum dynamic force is particularly high for fast flows, that is for small friction coefficients (e.g. for $A_b = 0.5$ m, up to 40% for $\mu = \tan(2°)$ and only 5% for $\mu = \tan(8°)$, Figure 2.9b). Note, however, that when we increase the length of the channel by adding successive bends, the effect of using incorrect curvature terms is amplified due to successive errors. We have for instance at most 5% discrepancies in travel durations with one bend and $\mu = \tan(6°)$, but up to 15% differences with 5 successive bends (see Table 2.2 and Supplementary Figure 2.A.8). With higher slope angles and friction coefficients corresponding to rock avalanches, the differences would be even more significant.

When we use the Voellmy rheology, as expected, differences in travel times are less striking: only 5% deviations for the flow travel time (Figure 2.9c), and 10% differences for the maximum dynamic force (Figure 2.9d).

We may wonder whether our observations on synthetic and simple topographies can be extrapolated to more realistic scenarios. In the next section, we thus carry out simulations on real topographies.

2.5 Curvature effects in simulations over real topographies

We chose two case studies for our simulations on real topographies: the simulation of debris flows in the Prêcheur river, in Martinique (French Caribbean) and the simulation of a debris avalanche on the Soufrière de Guadeloupe volcano, in Guadeloupe (French Caribbean)

2.5.1 Debris flow in the Prêcheur river

The Prêcheur river is located on the western flank of Montagne Pelée, an active volcano for which the last eruption dates back to 1932. Debris flows and hyper-concentrated flows occur regularly in this 6 km long river (Clouard et al., 2013; Nachbaur et al., 2019), with the risk of overflow into the Prêcheur village, at the mouth of the river (Aubaud et al., 2013; Quefféléan, 2018a). In

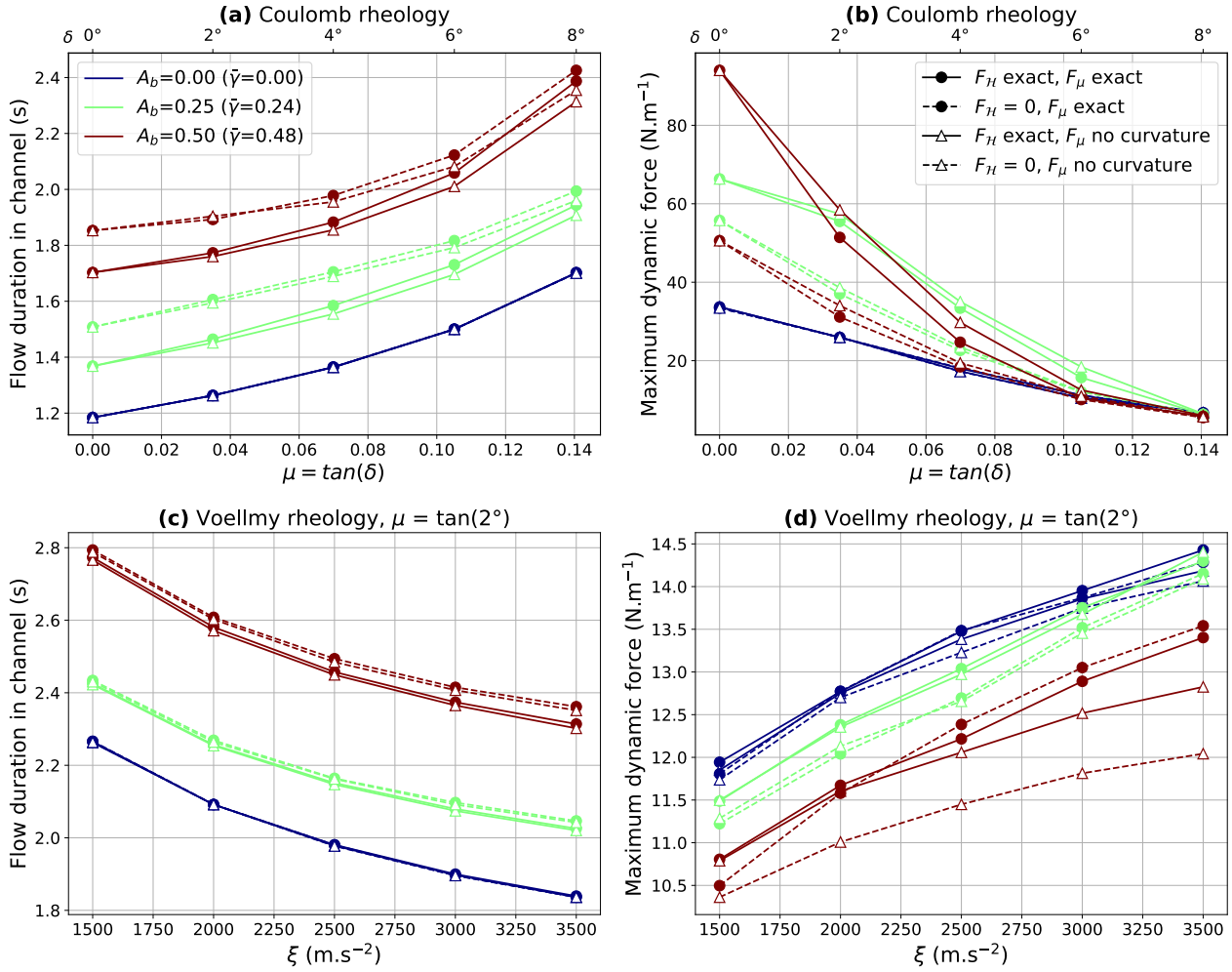

Figure 2.9: Simulation of a flow in a channel with slope $\theta = 10°$ and one bend with the Coulomb rheology (a and b) and the Voellmy rheology (c and d, with $\mu = \tan(2°)$). The bend amplitude A_b is either 0 m, 0.25 m or 0.5 m (respectively, blue, green and red curves).The corresponding non-dimensionalized curvature is $\bar{\gamma}$ The flow duration in the channel (a and c) and the maximum impact pressure (b and d) are plotted as functions of the friction coefficients for the Coulomb rheology (the top x-axis gives the corresponding friction angle) and as functions of the turbulence coefficient for the Voellmy rheology. Different situations are considered: when the curvature force is taken into account ($F_\mathcal{H}$ exact) or neglected ($F_\mathcal{H} = 0$) and when the curvature in the friction is exact (F_μ exact) or neglected (F_μ no curvature)

Table 2.2: Influence of curvature terms for synthetic topographies, with the Coulomb rheology, for different channel geometries with slope $\theta = 10°$ (lines, with A_b the channel bend amplitude) and friction coefficients (columns). The relative maximum deviation from the reference simulation with exact curvature is given for the flow duration in the channel (Δt, bold) and for the maximum dynamic force (F_d, italic). We specify which curvature term has the more prominent influence on the flow dynamics: the curvature force ($F_{\mathcal{H}}$) or the curvature in the friction (F_μ). n/a indicates indicates no simulation was done.

		$\mu = \tan(0°)$		$\mu = \tan(6°)$		$\mu = \tan(8°)$	
		Δt	F_d	Δt	F_d	Δt	F_d
$A_b = 0$ m		**0%**	*0%*	**0%**	*-5%*	**0%**	*0%*
$A_b = 0.25$ m	1 bend	**+10%**	*-15%*	**+5%**	*-25%*	**+2.5%**	*-5%*
		$F_{\mathcal{H}}$		$F_{\mathcal{H}}$		$F_{\mathcal{H}}, F_\mu$	
$A_b = 0.5$ m	1 bend	**+10%**	*-45%*	**+5%**	*+20%*	**-2.5%**	*+5%*
		$F_{\mathcal{H}}$		$F_{\mathcal{H}}, F_\mu$		F_μ	
	5 bends	not modeled		**+15%**[a] **-10%**[b]	*-60%*[a] *+135%*[b]	not modeled	
				F_μ			

[a] Differences for F_μ exact and $F_{\mathcal{H}} = 0$ neglected
[b] Differences for F_μ without curvature and $F_{\mathcal{H}}$ exact.

this context, numerical modeling can help constrain the prominent parameters controlling the flow dynamics and in turn be used for quantified risk assessment. However, a detailed analysis is beyond the scope of this paper. We only aim here to illustrate whether or not curvature effects have a significant impact on the flow dynamics. To that purpose, we release a hypothetical mass of 90,000 m^3 at the bottom of the cliff and model its propagation for 10 minutes, on a 5-meter Digital Elevation Model. We will first explore the possibility of overflows (Figures 2.10) in simulations with the Coulomb rheology. We will then conduct a more systematic analysis of curvature effects on the debris flow front position with the Coulomb and Voellmy rheologies and various rheological parameters, tracking the front position during the simulation with a thickness threshold of 1 cm (Figure 2.11). The results of approximating the curvature are displayed in Supplementary Figures 2.A.9 and 2.A.10.

Channel overflows with the Coulomb rheology

A critical point for hazard assessment is the possibility of overflows. In Figure 2.10, we show the maximum thickness of the flow in the Prêcheur river, simulated with the Coulomb rheology and $\mu = \tan(3°)$, which is representative of a highly mobile material. Keeping the curvature force but neglecting the curvature in the friction not only increases the runout, but also leads to multiple overflows (Figure 2.10c). Neglecting the curvature force partly compensates artificially this effect (Figure 2.10d). However, in this case, overflows dot not correspond to the ones modeled in the reference case(see Figure 2.10e and 2.10f, the white line is the extent of the flow in the simulation with exact curvature). Streaks outside the topography are artifacts explained in Appendix 2.E.

Flow front position and travel distance

We now track the flow front position as the flow propagates in the river. With the Coulomb rheology, the travel distance is increased by several hundred meters when the curvature in the friction force is neglected (Figure 2.11a, solid and dashed curves with triangles). This difference

may be reduced by choosing a thickness threshold higher than 1 cm. Nevertheless, it highlights the bias introduced by an improper curvature description. Curvature effects have a particularly strong influence in the upper part of the river which is narrow, twisted and with slopes above $\theta = 7°$ (see Figure 2.10): there are significant variations in the time needed by the flow to travel the first 1.5 km (Figure 2.11b). Depending on the friction coefficient, neglecting the curvature in the friction increases the flow velocity by 20 to 30% (Figure 2.11b, $F_{\mathcal{H}}$ exact, F_{μ} no curvature). This allows the flow to gain enough momentum to overrun flatter areas, whereas it remains stuck there in the reference case. To the contrary, neglecting the curvature force ($F_{\mathcal{H}} = 0$, F_{μ} exact) slows down the flow by 30 to 50%.

With the Voellmy rheology, the prominent factor impacting the flow dynamics is the curvature force (Figure 2.11d): without it, the flow needs up to 15% more time to travel the first 3 km. Further downstream, the delay between simulations is however constant (e.g. no more than 25 s with $\xi = 3500$ m s^{-2}, Figure 2.11c), which indicates once more that curvature effects affect the flow mainly in the upper part of the river.

2.5.2 Debris avalanche on the Soufrière de Guadeloupe volcano

Thin-layer numerical models are also commonly used to model the dynamics and emplacement of debris and rock avalanches, which are not confined to one channel as for debris flows. They usually involve bigger volumes (e.g. several million cubic meters) and spread on steeper slopes at least at their onset (e.g. Guthrie et al., 2012). In this section, we investigate the importance of curvature effects in simulations reproducing such events, studying the example of the Soufrière de Guadeloupe volcano, in Guadeloupe (French Caribbean). This volcanic edifice has a strong record of destabilization events, with at least 9 debris avalanches over the past 9,000 years (Boudon et al., 2007; Legendre, 2012). Peruzzetto et al. (2019) model the runout of a 90 $\times 10^6$ m^3 debris avalanche: this volume is consistent with the estimated volume (80 $\pm 40 \times 10^6$ m^3) of the 1530 CE debris avalanche. In order to reach the sea 9 km away from the volcano like the 1530 CE event, the friction coefficient $\mu = \tan(7°)$ had to be used (Figure 2.12a).

Using this friction coefficient and the same modeling set-up, we now model the debris avalanche emplacement by neglecting the different curvature terms (Figures 2.12b to 2.12f). The results of approximating the curvature are displayed in Supplementary Figure 2.A.11, and maximum kinetic energies in Supplementary Figure 2.A.12. When the curvature force is neglected, the most prominent difference is an excessive travel distance to the south (more than 1.5 km, Figure 2.12b, green rectangle). In some areas, spreading is less important, but only slightly (a difference of less than 200 m, Figure 2.12b, blue rectangle). Neglecting the curvature in the friction induces the most significant deviation from the reference simulation, with a generalized increase of the debris avalanche spreading (Figure 2.12c and 2.12d). In particular, the debris avalanche reaches the sea south of the Soufrière volcano, which is not predicted in the reference case (Figure 2.12a). Such differences are critical for tsunami hazard assessment.

2.6 Discussion

2.6.1 Importance of curvature effects for different rheologies

In our study, we derived curvature forces for the simplified case of a inviscid thin-layer flow. That is of course a simplification, as complex interactions between solid particles and between the solid and liquid phases can be expected (see Delannay et al. (2017) for a review). The formal

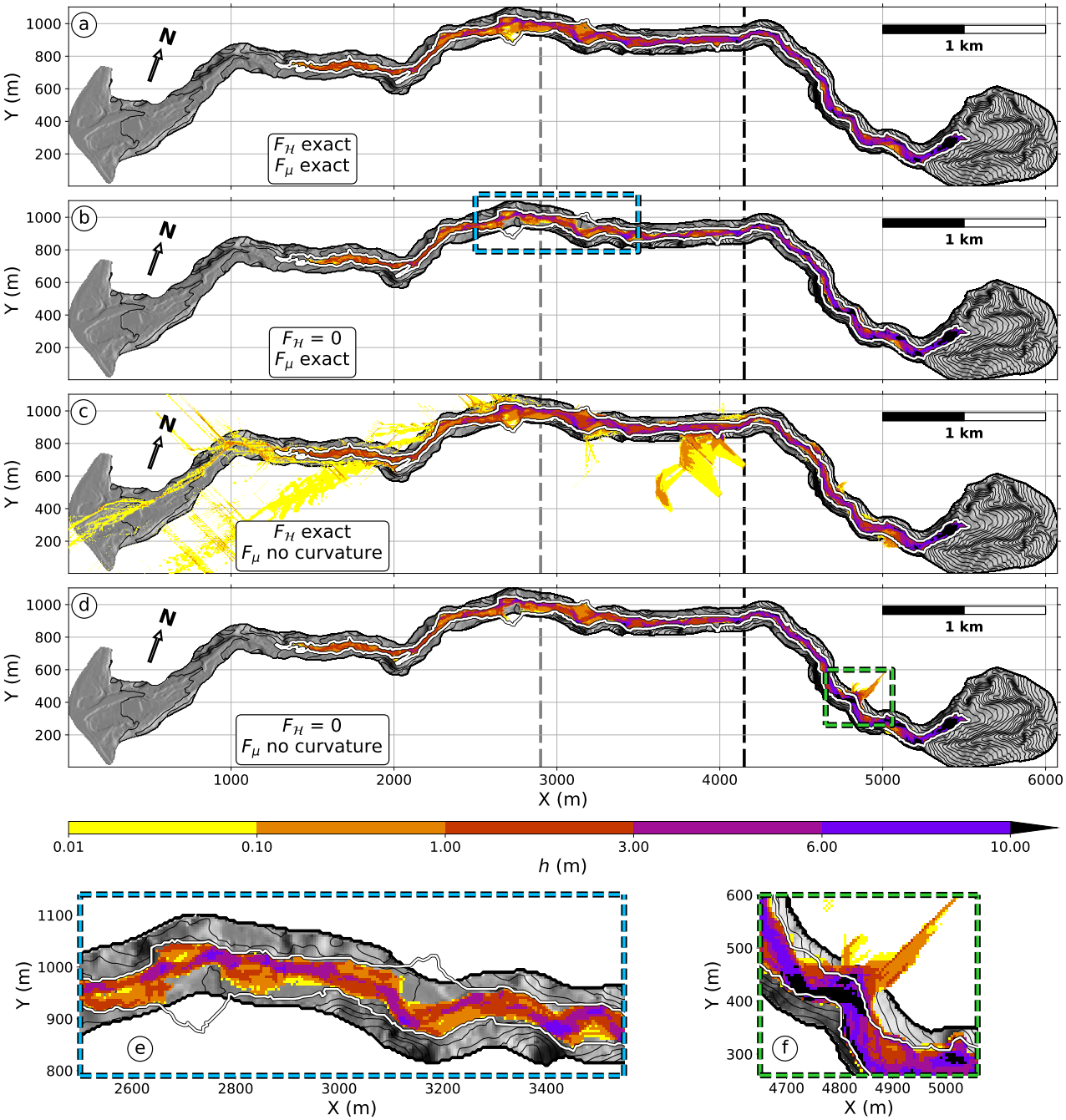

Figure 2.10: Maximum thickness of the flow simulated in the Prêcheur river with the Coulomb rheology and $\mu = \tan(3°)$. Each plot (a to d) displays the result of the simulation when the curvature force is taken into account ($F_{\mathcal{H}}$ exact) or neglected ($F_{\mathcal{H}} = 0$) and when the curvature in the friction is exact (F_{μ} exact) or neglected (F_{μ} no curvature). The simulation results in the reference case, with exact curvature terms, is given in (a). The corresponding flow extent (white curve) is reported in all figures. Green dashed rectangles (respectively blue dashed rectangles) indicate areas where the spreading is greater (respectively lesser) in other simulations, in comparison to the reference simulation (a). Zooms on these areas are given in (e) and (f). The contour step is 20 m.

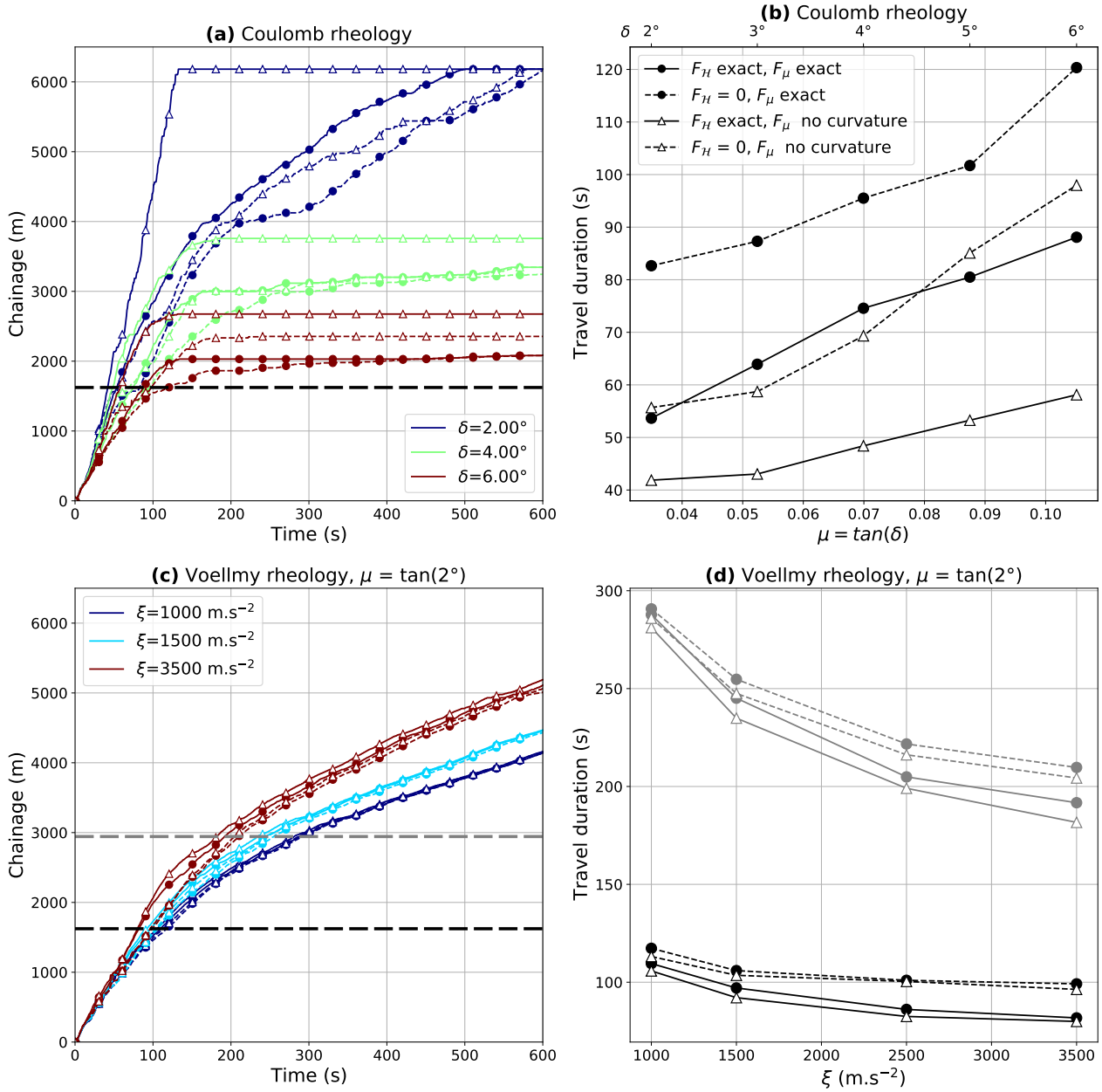

Figure 2.11: Simulations of debris flow in the Prêcheur river. Different situations are considered: when the curvature force is taken into account ($F_{\mathcal{H}}$ exact) or neglected ($F_{\mathcal{H}} = 0$) and when the curvature in the friction is exact (F_μ exact) or neglected (F_μ no curvature). (a) Flow front position with the Coulomb rheology. (b) Time needed for the flow to travel the first 1.6 km (black dashed line in (a)) with the Coulomb rheology, as a function of friction coefficient. (c) Flow front position with the Voellmy rheology and $\mu = \tan(2°)$. (d) Time needed for the flow to travel the first 1.6 km (black dashed line in (c)) and 2.9 km (gray dashed line in (c)) with the Voellmy rheology, as a function of turbulence coefficient.

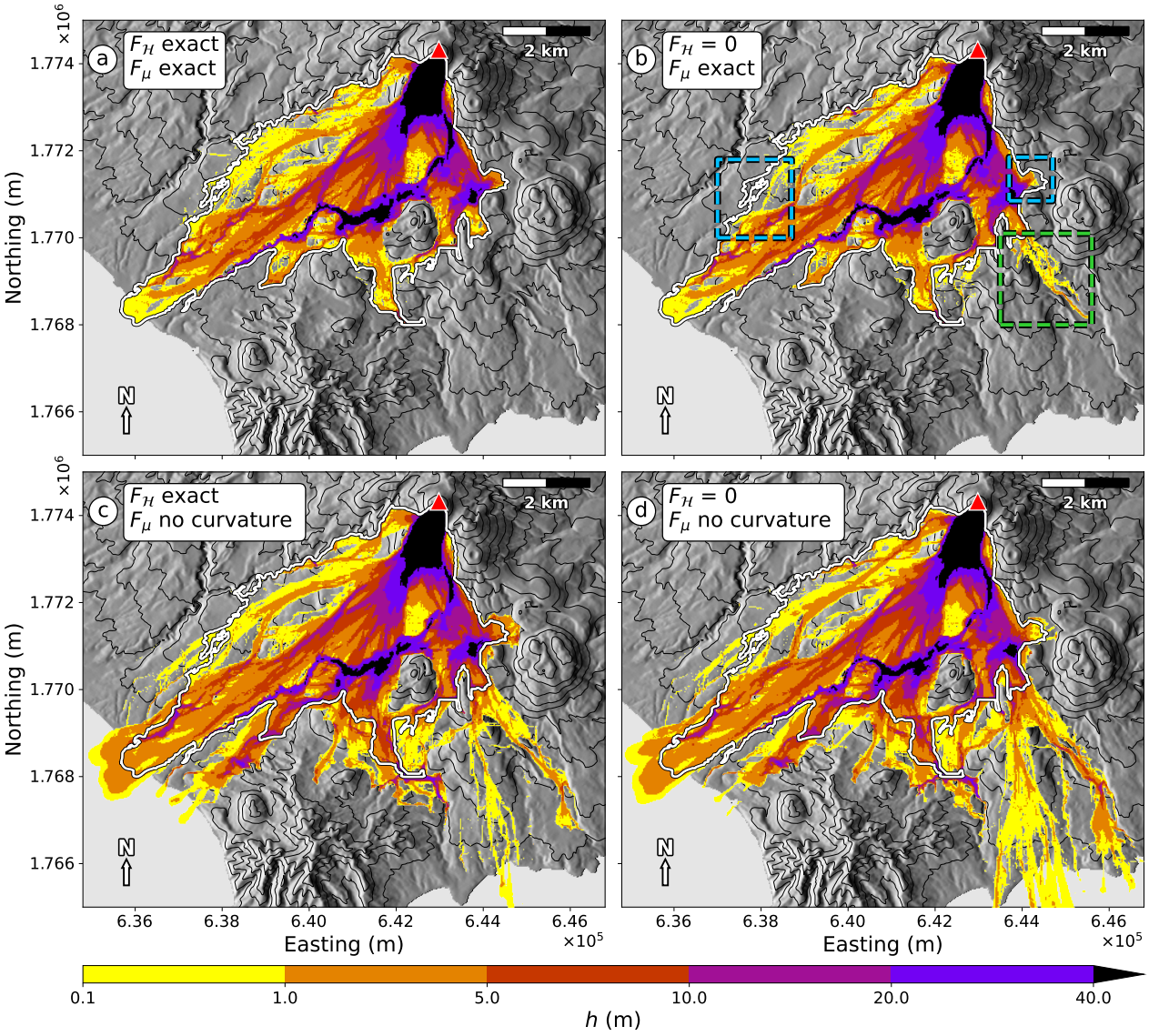

Figure 2.12: Maximum thickness of a hypothetical 90 $\times 10^6$ m^3 debris avalanche on the Soufrière de Guadeloupe volcano (French Caribbean). Each plot (a to f) displays the result of the simulation when the curvature force is taken into account ($F_{\mathcal{H}}$ exact) or neglected ($F_{\mathcal{H}} = 0$) and when the curvature in the friction is exact (F_μ exact) or neglected (F_μ no curvature). The simulation results in the reference case, with exact curvature terms, is given in (a) (Peruzzetto et al., 2019). The corresponding flow extent (white curve) is reported in all figures. Green dashed rectangles (respectively blue dashed rectangles) indicate areas where the spreading is greater (respectively lesser) in other simulations, in comparison to the reference simulation (a). The DEM is from IGN BDTopo, coordinates: WGS84, UTM20N. The contour interval is 100 m.

		Error max for channelized flow		**Error max for non-channelized flow**
		Synthetic topography	Prêcheur river	Soufrière de Guadeloupe
Coulomb	$\mu < \tan(5°)$	$F_{\mathcal{H}} = 0$	F_μ without curvature and $F_{\mathcal{H}}$ exact	n/a
	$\mu > \tan(5°)$	F_μ approximated	F_μ without curvature	F_μ without curvature
Voellmy		Limited influence of curvature effects		n/a

Table 2.3: Qualitative summary of the simulations results, with the different topographies (columns) and rheologies (lines). For the Coulomb rheology, we give the curvature description that gives the biggest error in comparison to simulations with the exact curvature. $F_{\mathcal{H}}$ refers to the curvature force and F_μ to the curvature in the friction force.

derivation of SHALTOP equations requires, for instance, that the kinematic viscosity is small (see Appendix 2.B), which can be questioned in practice for muddy debris flows. Pastor et al. (2004) and Pastor et al. (2009a) used the Bingham and Herschel-Bulkley theories to derive an implicit relation between the flow average velocity and the basal shear stress for simple shear flows on 1D topographies. Note that the resulting equations are similar to that of SHALTOP, provided we use an appropriate friction coefficient μ that depends on the thickness and on the flow velocity. A more comprehensive description of viscous flows is done by Pudasaini and Mergili (2019).

Historically, the first constitutive equations for 1D granular flows thin-layer models were linked to soil mechanics, with the introduction of an internal friction coefficient (Savage and Hutter, 1991; Gray et al., 1999). Some studies suggest that it is needed to model granular flows (Hungr, 1995; Gray et al., 1999; Pirulli et al., 2007). This is, however, difficult to extend to complex 2D topographies, requiring simplifications (Iverson and Denlinger, 2001) or on the contrary the resolution of the complete stress state within the flow (Denlinger and Iverson, 2004). Besides, Gray et al. (2003) show that a hydraulic approach without internal friction, as in our study, allows to reproduce accurately shock waves generated when granular materials flow around obstacles or over topography slope breaks.

Finally, the $\mu(I)$-rheology has been increasingly used over past years to model dry granular flows (e.g. GDR MiDi, 2004; Jop et al., 2006). Formal derivations have been done to derive its depth-integrated version but for simple topographies only (e.g. Gray and Edwards, 2014; Baker et al., 2016).

More generally, following the classification of thin-layer models done by Luca et al. (2009b), our study shows that curvature effects are important when there is limited resistance to shearing in the flow. However, we did not consider situations where resistance to shearing increases and/or stresses acting on topography perpendicular planes become significant (e.g., when an internal friction coefficient is used). In such cases, it is nevertheless difficult to concile both a fine decription of the topography and of the rheology. For instance, the velocity profile in the normal variable is in general unknown and evolves with the flow (Ionescu et al., 2015), such that assuming a velocity profile as in Luca et al. (2009b) may break down energy conservation. It becomes even more complex when we consider that the flow rheology can change during propagation (Iverson, 2003).

2.6.2 Importance of curvature effects in the Coulomb rheology

With the Coulomb rheology and without internal friction, our simulations show that curvature effects can be significant for fast flows (e.g. several m s^{-1}). For a given topography, the relative

importance of the curvature force and of the curvature within friction strongly depends on the friction coefficient μ (see Table 2.3): when it increases, the friction force (and thus the curvature term within friction) prevails over the curvature term. In the extreme case $\mu = 0$, there is no friction and the curvature force has a strong influence on the flow dynamics. The transition between these two regimes occurs between $\mu = \tan(6°)$ and $\mu = \tan(8°)$ in our simulations on synthetic topographies for a slope $\theta = 10°$. It is not clear how much these transition values depend on the flow path and on the topography itself: neglecting the curvature force in the Prêcheur river simulations entails a significant acceleration of the flow even for $\mu = \tan(2°)$. The latter is however artificially compensated for when the curvature force is also neglected for friction coefficient below $\tan(4°)$. This artificial compensation of two errors with competing effects (accelerating and decelerating the flow) is fortuitous and not at all a generality.

We did not focus on the effect of approximating the curvature in the friction force because it is actually straight-forward to implement the accurate curvature term. However, approximating the curvature does results in significant differences. On synthetic topographies with friction angles above $\mu = \tan(5°)$, the prominent error compared to the correct simulation is obtained when the curvature within friction is approximated (e.g., see Supplementary Figures 2.A.2, 2.A.6 and 2.A.7). However, on real topographies, the prominent error occurs when it is neglected (see Supplementary Figure 2.A.9 and 2.A.10 for the Prêcheur river, and Supplementary Figure 2.A.11 and 2.A.12 for Soufrière de Guadeloupe simulations). This difference may stem from the roughness of the terrain (which has locally high curvatures) that is not rendered in our smooth synthetic channel. Such local effects can then strongly affect the simulations results globally, impacting for instance the travel distance.

Reproducing the laboratory experiment from Iverson et al. (2004) yields similar conclusions as what we observed for synthetic and real topographies. In this experiment, a granular flow propagates in and irregular channel. We model it using friction coefficients calibrated by Lucas (2010) ($\mu = \tan(23°)$ in the channel and $\mu = \tan(26°)$ elsewhere). The channel is not significantly twisted: using the same notations as previously, we estimate a non-dimensionalized bend curvature $\bar{\gamma} = 0.15$. In comparison, we had $\bar{\gamma} = 0.48$ for our synthetic topographies. Thus, the flow path is rather straight in the channel and curvature effects are limited in the first 0.3 s of the simulations (see Supplementary Figure 2.A.14). However, the important slope break at the channel increases bottom friction when curvature is taken into account, and removing curvature accelerates the flow (see Supplementary Figure 2.A.15). Omitting the curvature force does change the final geometry of the mass but to a lesser extent. Indeed, the flow velocity remains globally in the direction of the topography slope. All these observations are in agreement with our results for synthetic channels. Future comparisons could be carried out by modelling experimental flows in twisted flumes, as in Scheidl et al. (2015).

Errors induced by inaccurate curvature description can be highly critical for model calibration. For instance, without curvature in friction, higher friction angles are needed to reproduce the previous experiments deposits (at least 3° higher, see Supplementary Figure 2.A.16). That could explain why, in the first JTC1 benchmarking exercise in 2007, SHALTOP used in many examples a lower friction coefficient than other thin-layer models (Hungr et al., 2007).

2.6.3 Limited influence of curvature effects in the Voellmy rheology

In the Voellmy rheology, an empirical turbulence term proportional to the square of velocity is added to the basal friction. It slows down the flow, but it also minimizes the relative importance of curvature effects (that are also proportional to the square of velocity) when there are sudden changes in the flow direction. As a result, there are only slight changes in the flow runout when curvature effects are not accounted for. This is clearly seen in our simulations, both on synthetic

and real topographies. In Appendix 2.F, we give an example of a back-analysis of a debris flow simulated with the Voellmy rheology. Neglecting the curvature force influences only slightly the results.

However, Salm (1993) actually suggests that the turbulence coefficient ξ is proportional to the mean distance between irregularities on the topography. This distance can be seen as an estimate of the local topography radius of curvature. In the same perspective, in their guide book to avalanche modeling, Salm et al. (1990) advise choosing higher turbulence coefficients on rough topographies than on smooth topographies. More recently, Gruber and Bartelt (2007) calibrated a spatially varying turbulence coefficient by back-analysis of snow avalanches. As Fischer et al. (2012) point out, the resulting map of turbulence coefficients is strongly correlated to the topography curvature. This suggests that the Voellmy rheology, or at least the Voellmy rheology with a turbulence coefficient correlated to the local topography curvature, might be a way of taking into account curvature effects empirically. However the resulting model cannot correctly reproduce the complexity of the interaction between the flow and the topography, in particular because the curvature force depends on the velocity direction and not only on its norm.

2.6.4 Importance of local curvature effects for overflows and runup estimations

For smooth topographies and channelized flows, we can expect some hazard indicators, such as the travel distance and the impacted area, to vary evenly when the simulation parameters span their variation ranges. This is no longer the case when the flow manages to overflow topographic barriers. Such non-linear behaviors and threshold effects are highly critical for hazard assessment and complicate hazard mapping (Mergili et al., 2018). They cannot be described by simple laws relating, for instance, the travel distance to the initial unstable volume (e.g. Lucas et al., 2014; Mitchell et al., 2019).

In our study, when we disregarded the curvature force in the simulation of the debris avalanche on Soufrière de Guadeloupe volcano, part of the material managed to overrun a plateau and enter a ravine. It could then spread much further (about 1.5 km, see Figure 2.12b). Such a behavior is however not systematic. For channelized flows, the curvature force tends to maintain the flow at the bottom of the channel, whereas it would otherwise bounce back and forth on its walls and potentially overflow the channel. However, in the long run, the curvature force allows the flow to move faster because it does not dissipate energy boucing back and forth on the channel banks. If a sudden twist is encountered further down, the flow may in turn have enough energy to overflow the channel banks, which would not be the case without the curvature force. We could reproduce such a situation in the Prêcheur river, with the Coulomb rheology and $\mu = \tan(2°)$ (see Supplementary Figure 2.A.13).

Local curvature effects are thus worth taking into account when considering debris flow runup against steep slopes (Iverson et al., 2016) and on the outer bank of a channel bend (Scheidl et al., 2015). In the latter case, the runup (that is, the elevation difference between the inner and outer boundaries of the flow in the channel, as measured in the field) can be related to the flow velocity (Prochaska et al., 2008; Scheidl et al., 2015). The runup and/or the deduced velocity can then be used to fit rheological parameters in thin-layer simulations. As they describe the dynamics of the flow in locations where we can expect strong curvature effects, the resulting best-fit parameters may depend significantly on whether or not these curvature effects are properly described in the model, even with the Voellmy rheology.

2.7 Conclusion

In this work, we show how an incorrect derivation of the thin-layer equations can lead to the omission of two curvature terms, originating from the expression of the pressure at the bottom of the flow. The first one, the curvature force, does not depend on the rheology and ensures that the flow velocity remains tangent to the topography. The second one appears in the bottom friction force (and thus only when frictional rheologies such as Coulomb or Voellmy are used). They are both proportional to the square of the flow velocity, but also depend on the velocity orientation and topography curvature tensor.

We have carried out simulations on synthetic and real topographies to highlight the influence of these curvature terms in thin-layer numerical simulations, with the code SHALTOP (see Table 2.3). The curvature terms are all the more important when the flow is fast (typically, several m s^{-1} to tens of m s^{-1}), that is for low friction coefficients and/or steep slopes.

For flows propagating in twisted channels modeled with the Coulomb rheology, the curvature force tends to maintain the flow at the bottom of the channel. Thus, neglecting it favors bouncing on the channel walls and reduces the propagation velocity. For instance, in the case of the upper section of Prêcheur river where slopes are higher than $\theta = 7°$, omitting the curvature force in simulations reduces the average velocity of channelized flow by 30%, for friction coefficients below $\mu = \tan(6°)$. Simulated overflows then differ, which is critical for hazard assessment.

Approximating the curvature in the friction force can break the rotational invariance of the model and slow down the flow. Neglecting the curvature in friction decreases the norm of the friction force and thus accelerates the flow, when the latter propagates from steep to more gentle slopes. It results in the most important errors when the flow velocity is in the main slope direction, and more generally on real topographies. For instance, in the case of the simulation of a debris avalanche on the Soufrière de Guadeloupe, travel distances are increased by several hundred meters. We observe similar effects on a synthetic channel with slope $\theta = 25°$ and $\mu = \tan(15°)$, with a 50% increase of the kinetic energy. Though such effects can sometimes be artificially compensated for by also neglecting the curvature force, it is not at all systematic and thus both terms need to be properly taken into account for correct model calibration.

Though we have focused on debris flows and debris avalanches modeling, our results could apply to other geophysical flows, such as moutain river stream flows (Borthwick and Barber, 1992; Churuksaeva and Starchenko, 2015) and concentrated and dilute pyroclastic currents (Komorowski et al., 2013; Kelfoun et al., 2017). Curvature effects may also be important for modeling landslide-generated tsunamis, for which the thin-layer equations must be integrated in the direction normal to the topography for the landslide, and in the vertical direction for the fluid layer (Ma et al., 2013; Delgado-Sánchez et al., 2019).

Note that strong curvature effects may also be an inherent limitation of thin-layer models. Indeed, curvature forces are particularly strong when the topography curvature is high, as for instance in a narrow channel. However, in this case, the thin-layer assumption may no longer be valid. In order to discriminate between real curvature effects and numerical artifacts, comparisons with full 3D models where no approximations are done on the layer thickness could be conducted. Yet such comparisons exercises may prove difficult (e.g. Pirulli et al., 2018).

Of course, our results must also be considered in regard of the rheology uncertainty, which is sometimes large. We believe future research should focus on both the developement of accurate physically-based rheologies with constrained realistic parameters, and on methodologies to properly describe topography effects. Such studies are complementary to, in turn, develop a model uniting both aspects.

Appendix

2.A Supplementary Figures

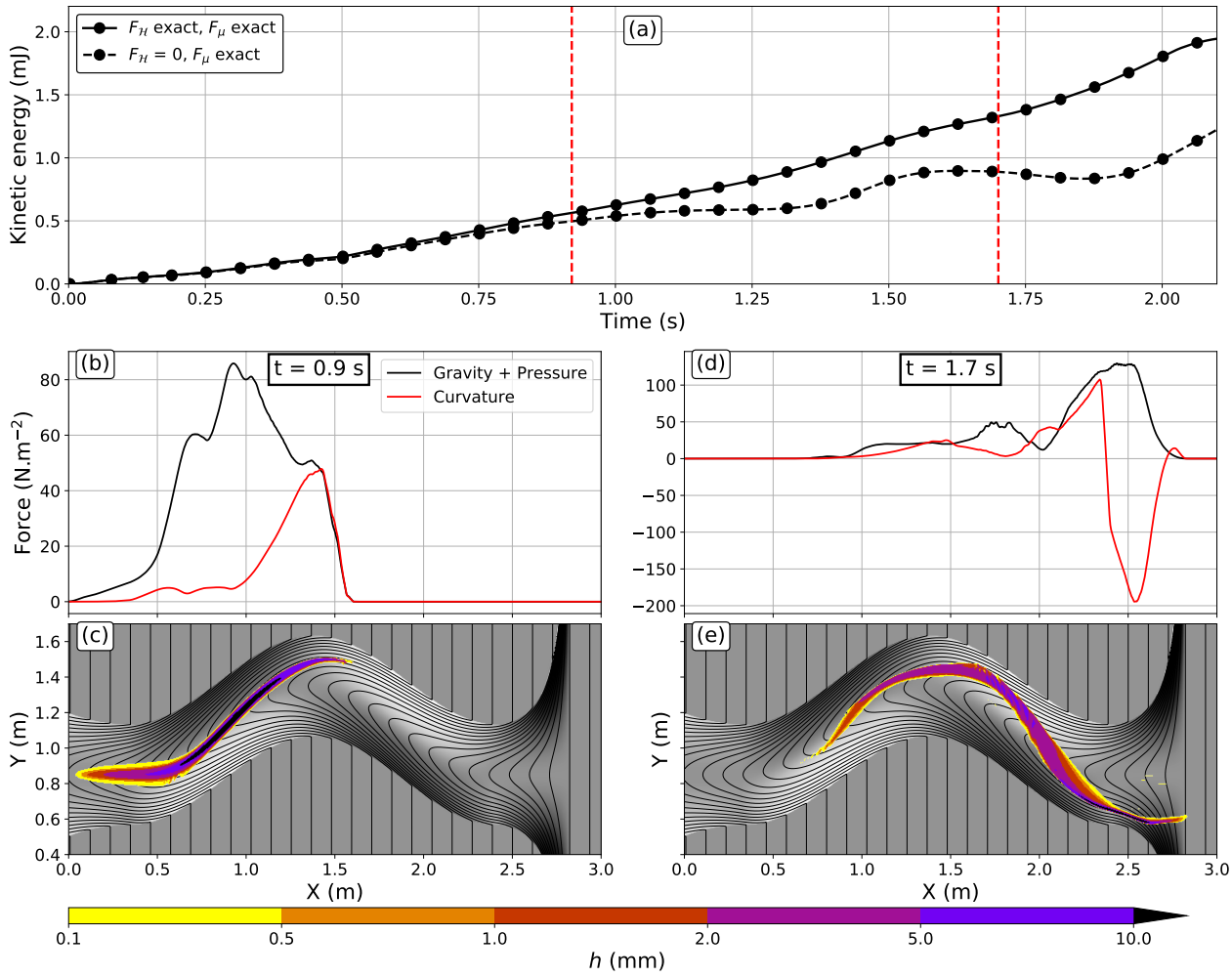

Figure 2.A.1: (a) Total kinetic energy of the flow with a Coulomb rheology, $\mu = 0$ and a slope $\theta = 10°$. (b) For the simulation with exact curvature terms, maximum norm of gravity and pressure force ($\vec{F}_g$, black curve) and of the curvature force ($\vec{F}_{\mathcal{H}}$, red curve, negative when $\vec{n} \cdot \vec{F}_{\mathcal{H}} < 0$). The maximum is computed for a constant X coordinate, at t=0.9 s. (c) Flow thickness at t=0.9 s. (d) and (e): Same as (b) and (c), respectively, but for t=1.7 s. These two times are indicated by the red dashed vertical line in (a).

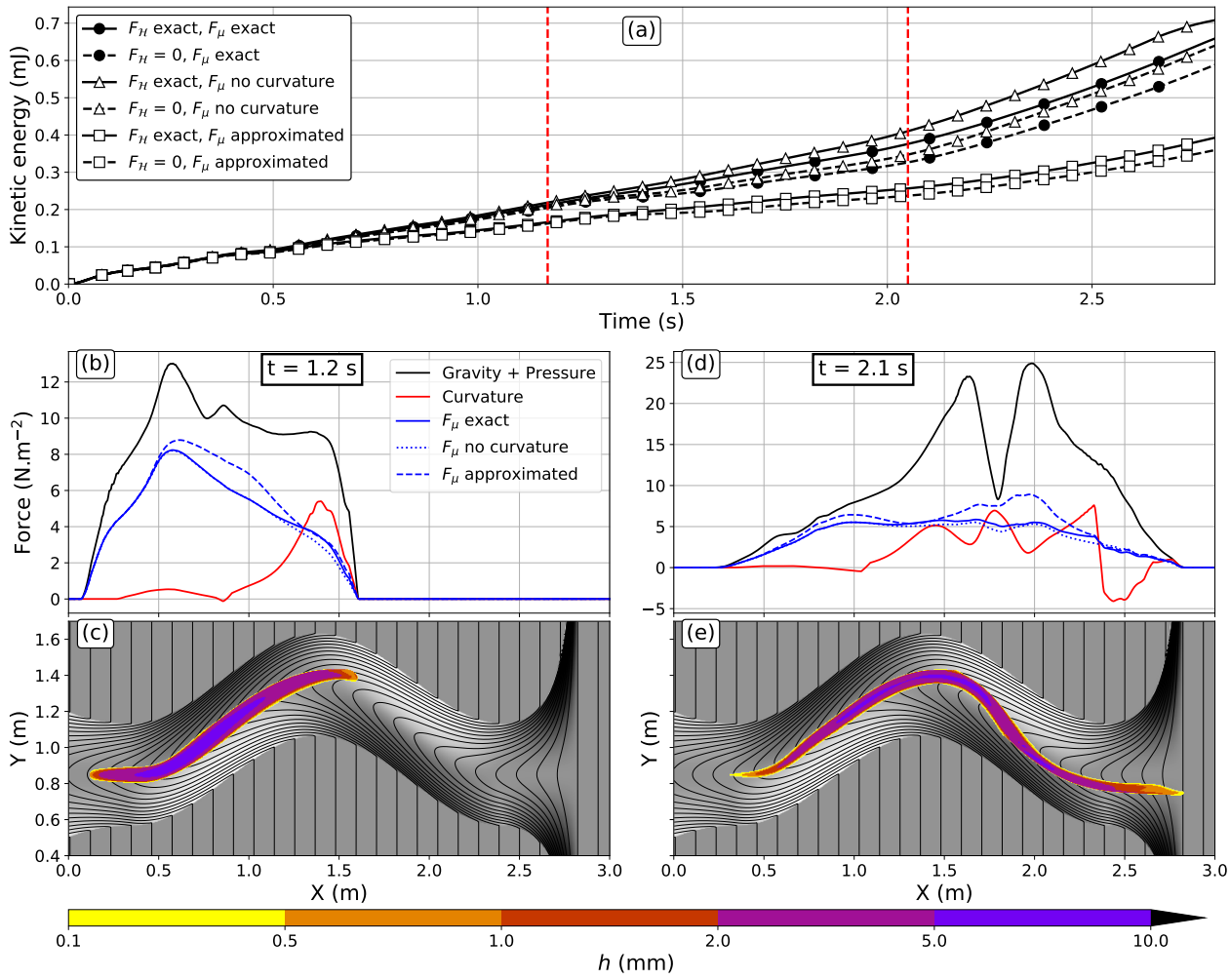

Figure 2.A.2: (a) Total kinetic energy of the flow with the Coulomb rheology, $\mu = \tan(6°)$ and a slope $\theta = 10°$. (b) For the simulation with exact curvature terms, maximum norm of gravity and pressure force ($\vec{F}_g^{\mathcal{V}}$, black curve), of the curvature force ($\vec{F}_\mathcal{H}^{\mathcal{V}}$, red curve, negative when $\vec{n} \cdot \vec{F}_\mathcal{H}^{\mathcal{V}} < 0$) and of the friction force ($\vec{F}_\mathcal{H}^{\mu}$, blue curves). The friction force is computed with the exact curvature term (F_μ exact), its approximation (F_μ approximated) and when it is neglected (F_μ no curvature). The maximum is computed for a constant X coordinate, at t=1.2 s. (c) Flow thickness at t=1.2 s. (d) and (e): Same as (b) and (c), respectively, but for t=2.1 s. These two times are indicated by the red dashed vertical line in (a).

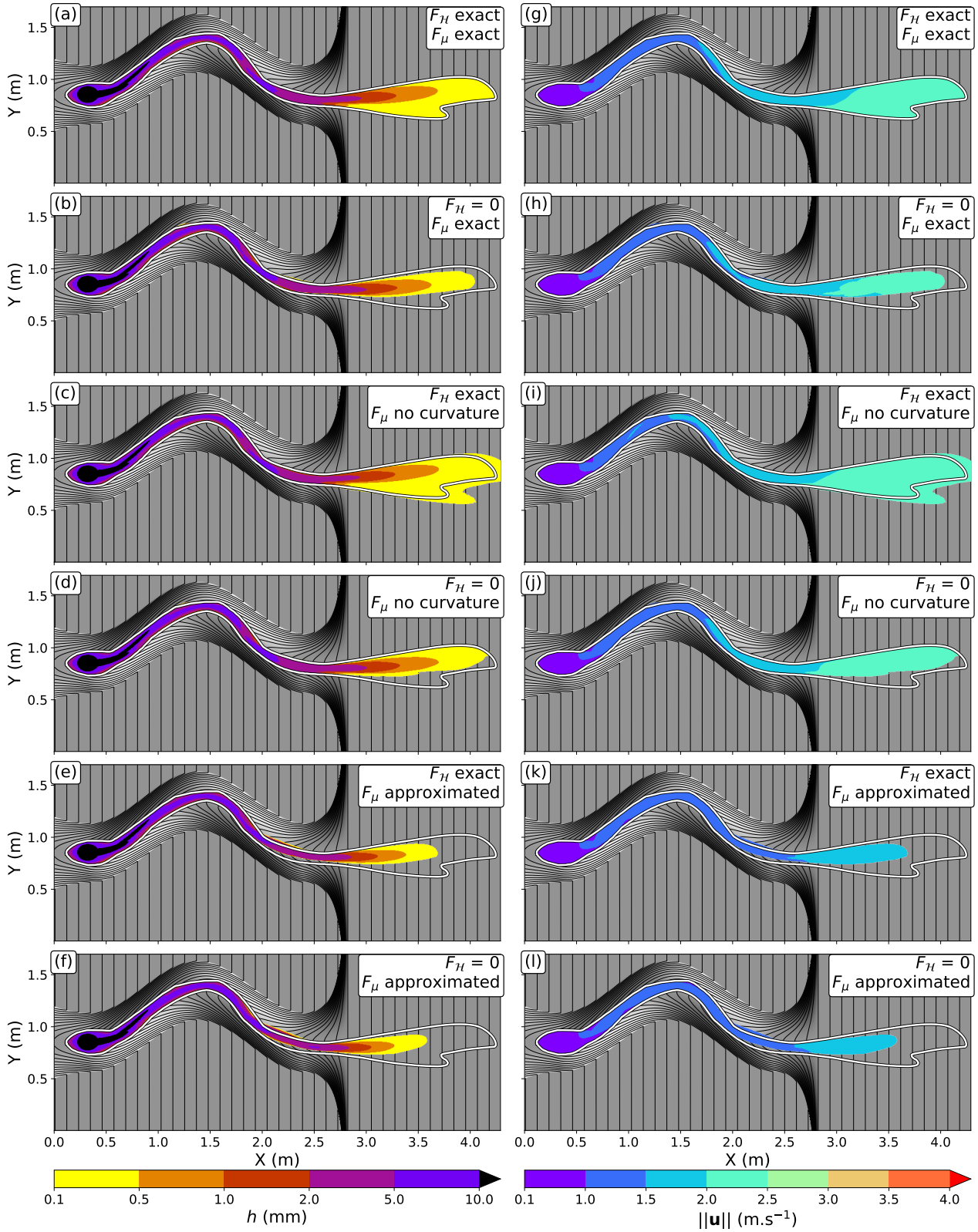

Figure 2.A.3: Flow simulation with the Coulomb rheology, $\mu = \tan(6°)$, and a slope $\theta = 10°$. (a-f) Maximum flow thickness. (g-l) Maximum flow velocity. (a) and (g) are the simulation results in the reference case, with exact curvature terms: the corresponding flow extent (white curve) is reported in all figures. The contour interval is 2 cm. Simulation duration is 2.8 s.

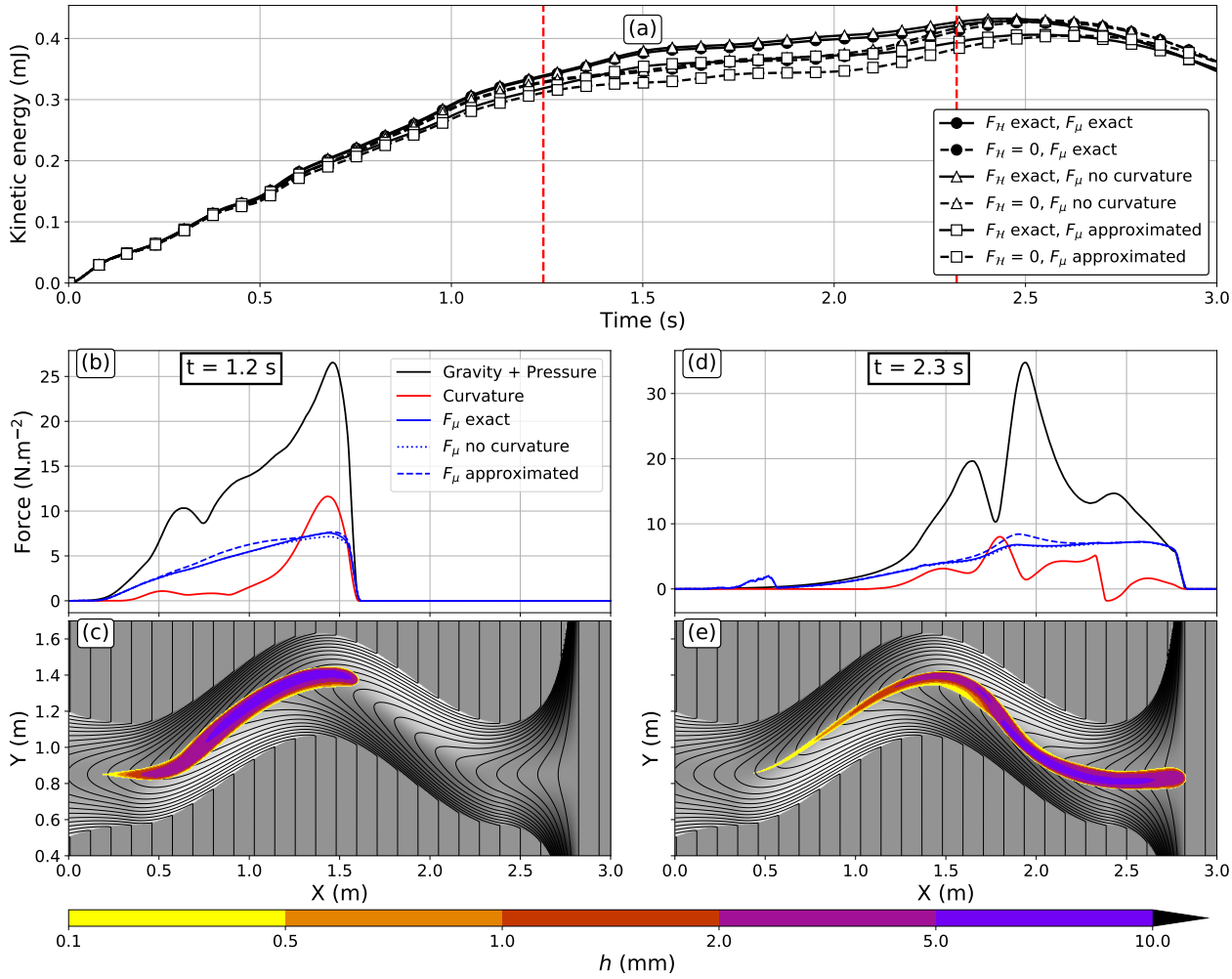

Figure 2.A.4: Same as Supplementary Figure 2.A.2 but with the Voellmy rheology, $\mu = \tan(2°)$, $\xi = 3500m\ s^{-2}$ and a slope $\theta = 10°$. The friction force in (b) and (d) includes the Voellmy turbulence term. (b) and (c): t=1.2 s. (d) and (e):t=2.3 s.

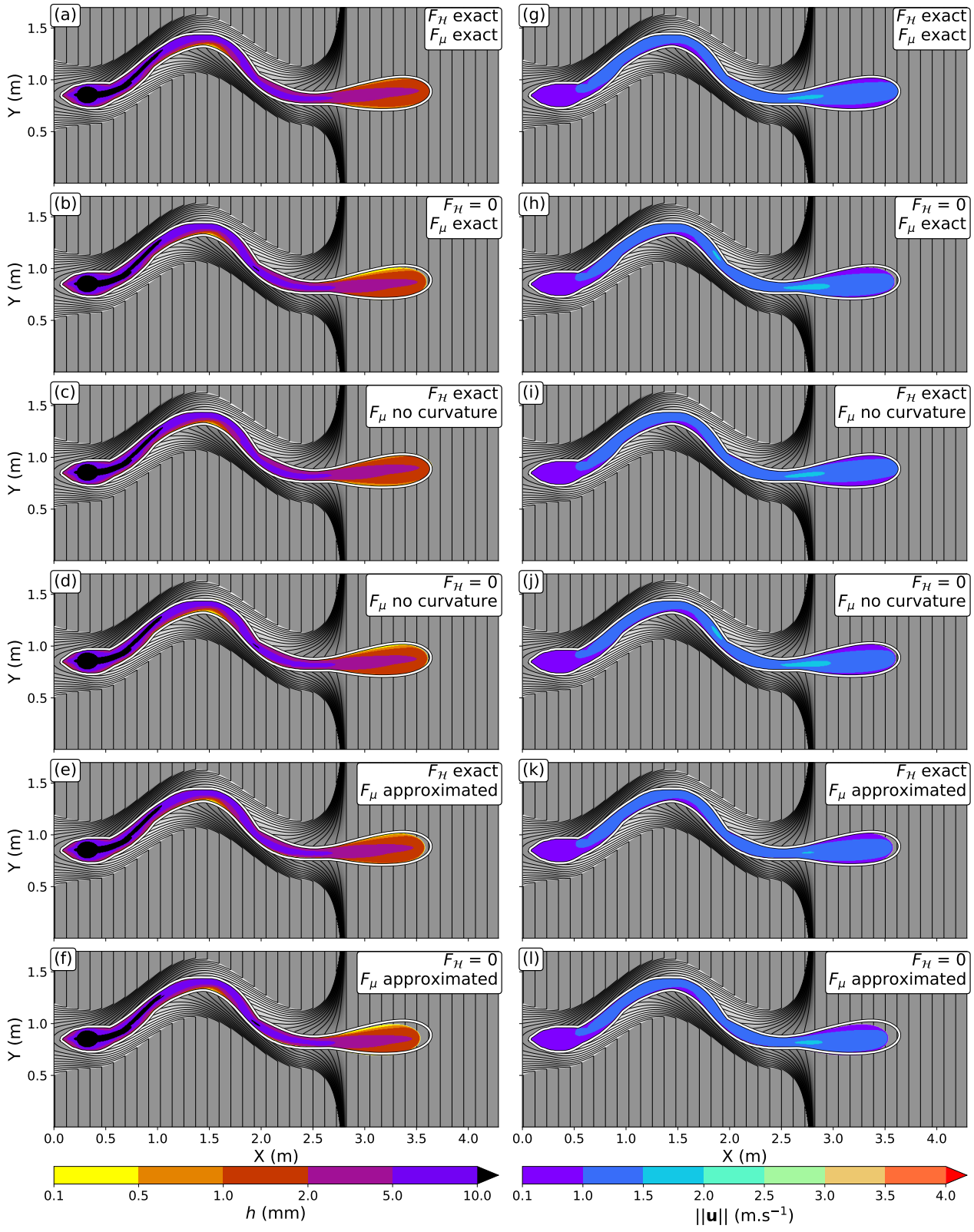

Figure 2.A.5: Flow simulation with the Voellmy rheology, $\mu = \tan(2°)$, $\xi = 3500$ m s^{-2} and a slope $\theta = 10°$. (a-f) Maximum flow thickness. (g-l) Maximum flow velocity. (a) and (g) are the simulation results in the reference case, with exact curvature terms: the corresponding flow extent (white curve) is reported in all figures. The contour interval is 2 cm. Simulation duration is 3.0 s.

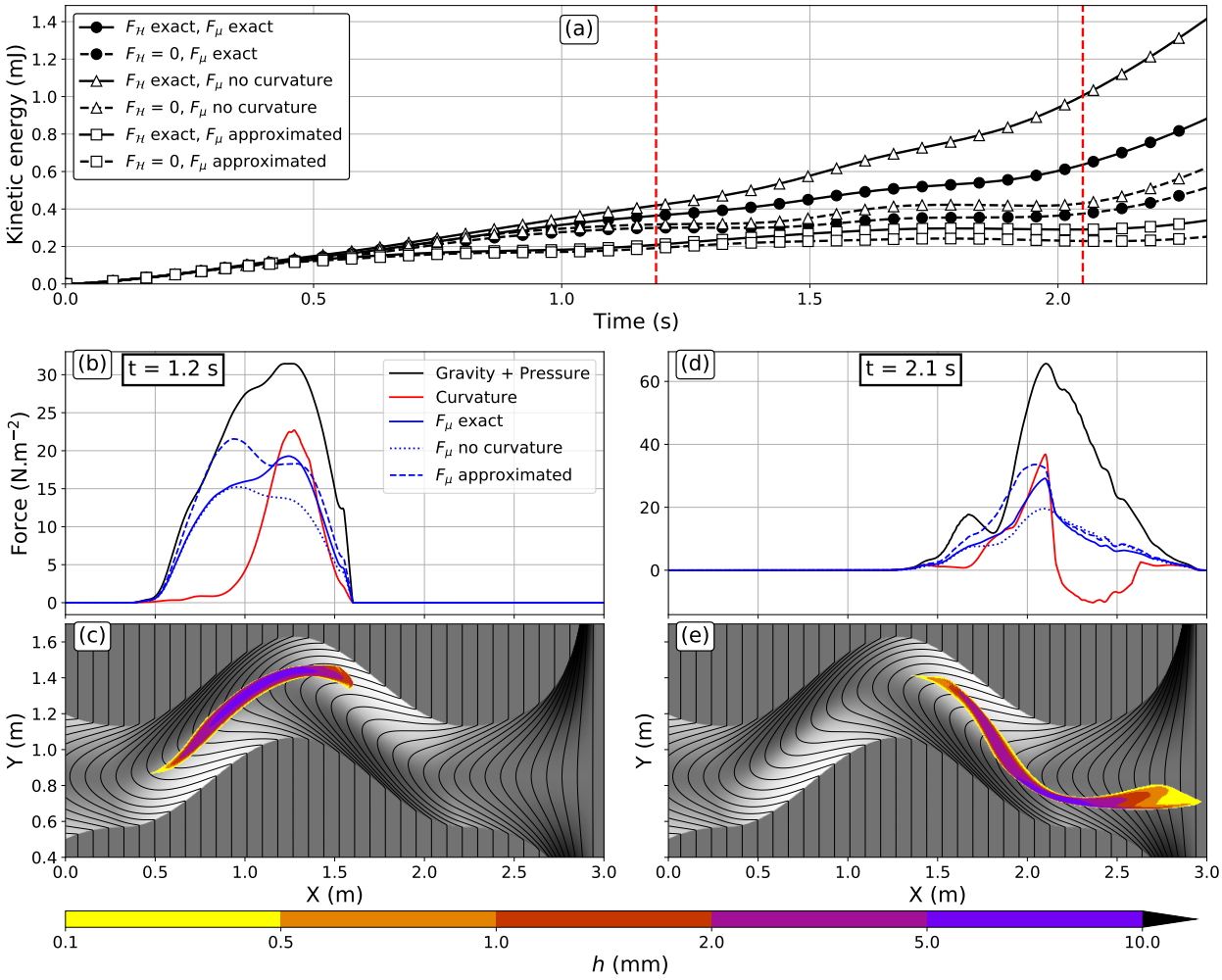

Figure 2.A.6: Same as Supplementary Figure 2.A.2 but with the Coulomb rheology, $\mu = \tan(15°)$, and a slope $\theta = 25°$. (b) and (c): t=1.2 s. (d) and (e):t=2.1 s.

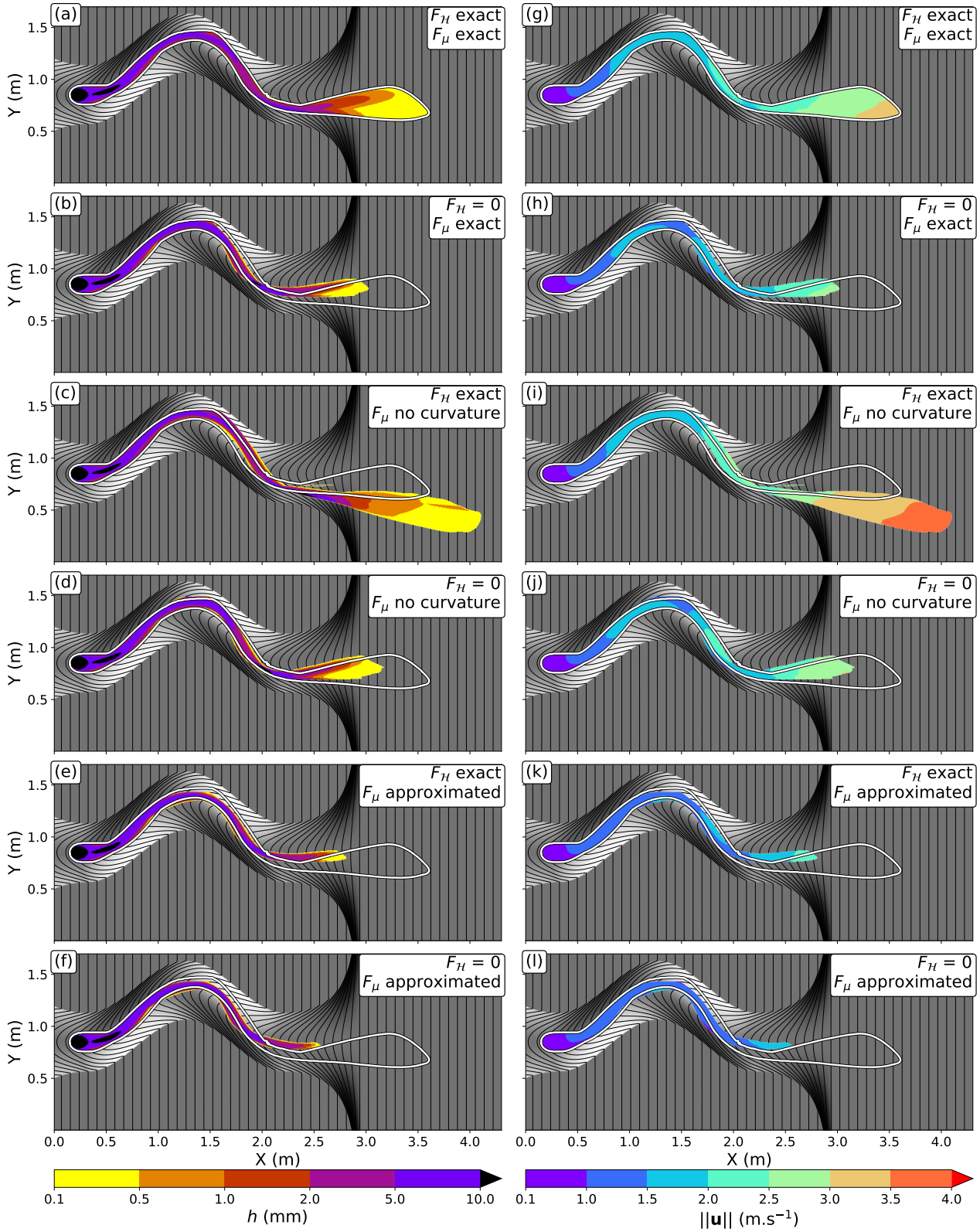

Figure 2.A.7: Flow simulation with the Coulomb rheology, $\mu = \tan(15°)$, and a slope $\theta = 25°$. (a-f) Maximum flow thickness. (g-l) Maximum flow velocity. (a) and (g) are the simulation results in the reference case, with exact curvature terms: the corresponding flow extent (white curve) is reported in all figures. The contour interval is 2 cm. Simulation duration is 2.3 s.

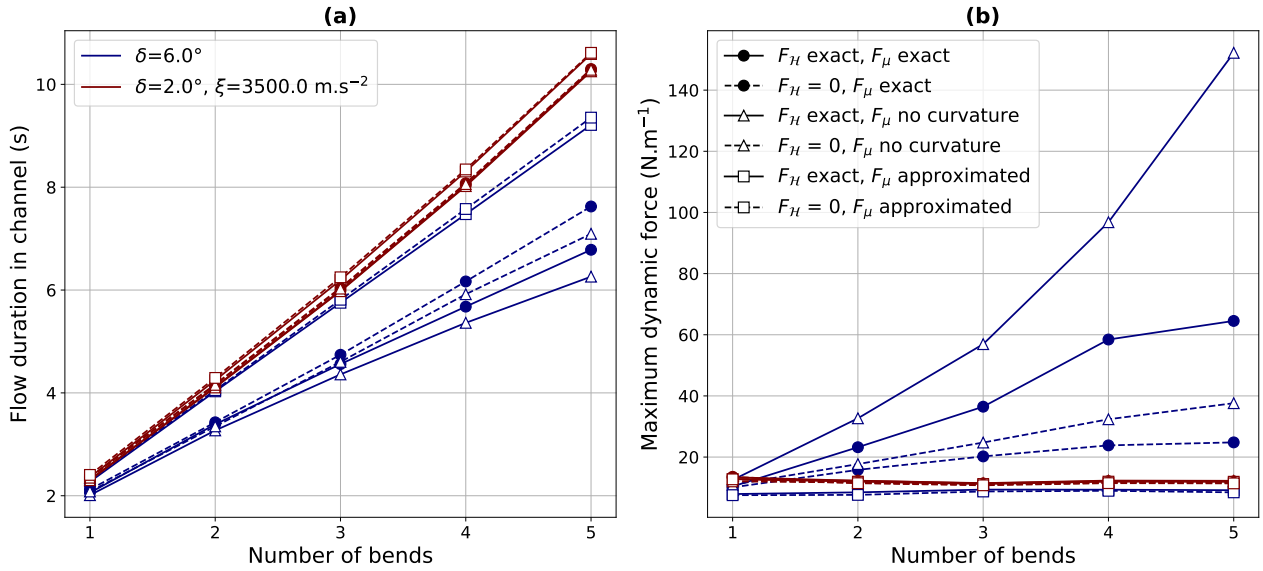

Figure 2.A.8: Simulations of a flow in a channel with slope $\theta = 10°$, a bend amplitude A_b =0.5 m, with the Coulomb rheology ($\mu = \tan(6°)$, blue curves) and the Voellmy rheology ($\mu = \tan(6°)$, $\xi = 3500\text{m s}^{-2}$, red curves). The flow duration in the channel (a) and the maximum impact pressure (b) are plotted as functions of the number of bends. Different situations are considered: when the curvature force is taken into account ($F_{\mathcal{H}}$ exact) or neglected ($F_{\mathcal{H}} = 0$) and when the curvature in the friction is exact (F_μ exact), neglected (F_μ no curvature) or approximated (F_μ approximated).

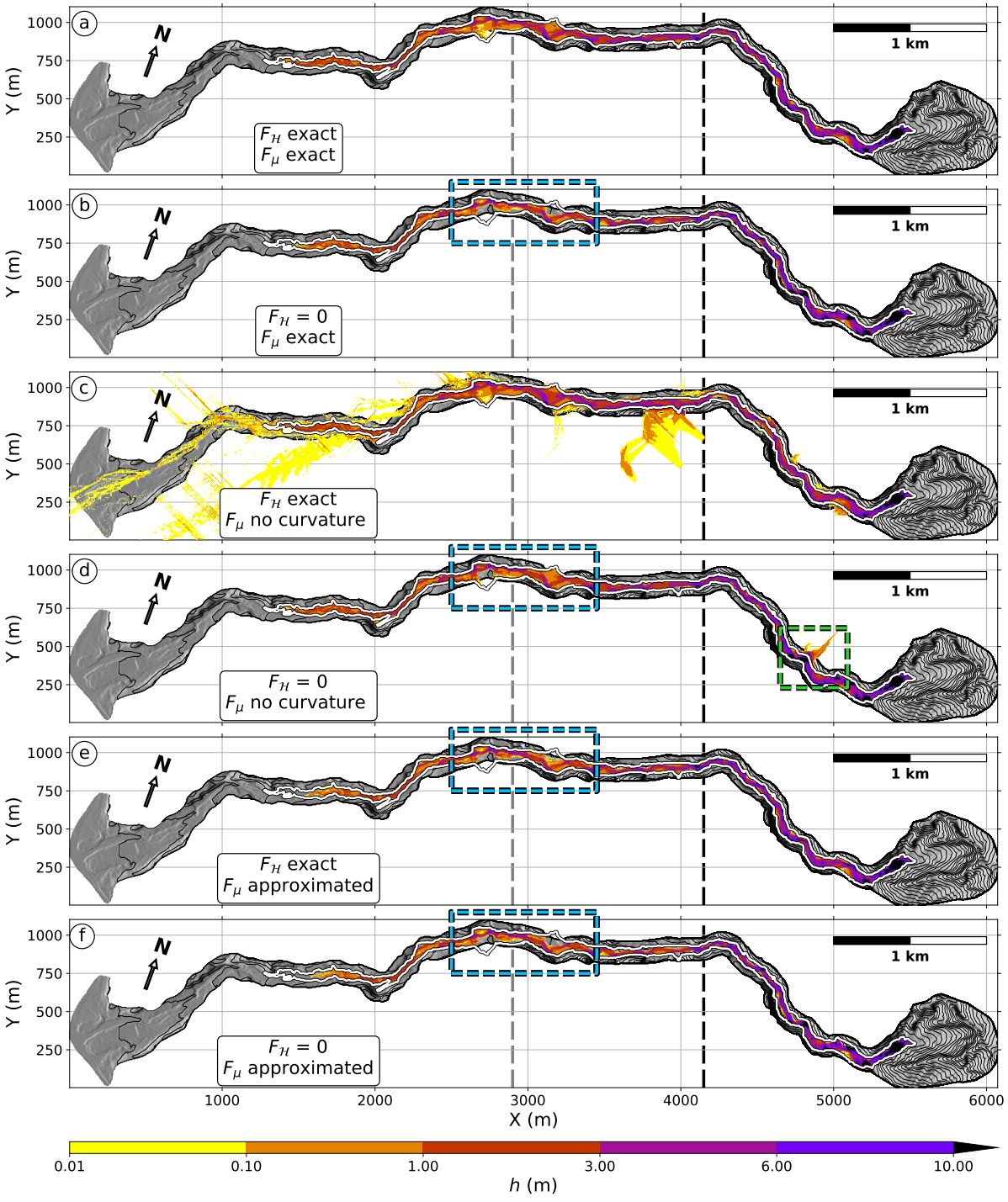

Figure 2.A.9: Maximum thickness of the flow simulated in the Prêcheur river with the Coulomb rheology and $\mu = \tan(3°)$. Each plot (a to f) displays the result of the simulation when the curvature force is taken into account ($F_{\mathcal{H}}$ exact) or neglected ($F_{\mathcal{H}} = 0$) and when the curvature in the friction is exact (F_μ exact), neglected (F_μ no curvature) or approximated (F_μ approximated). The simulation results in the reference case, with exact curvature terms, is given in (a). The corresponding flow extent (white curve) is reported in all figures. Green dashed rectangles (respectively blue dashed rectangles) indicate areas where the spreading is greater (respectively lesser) in other simulations, in comparison to the reference simulation (a). The contour step is 20 m.

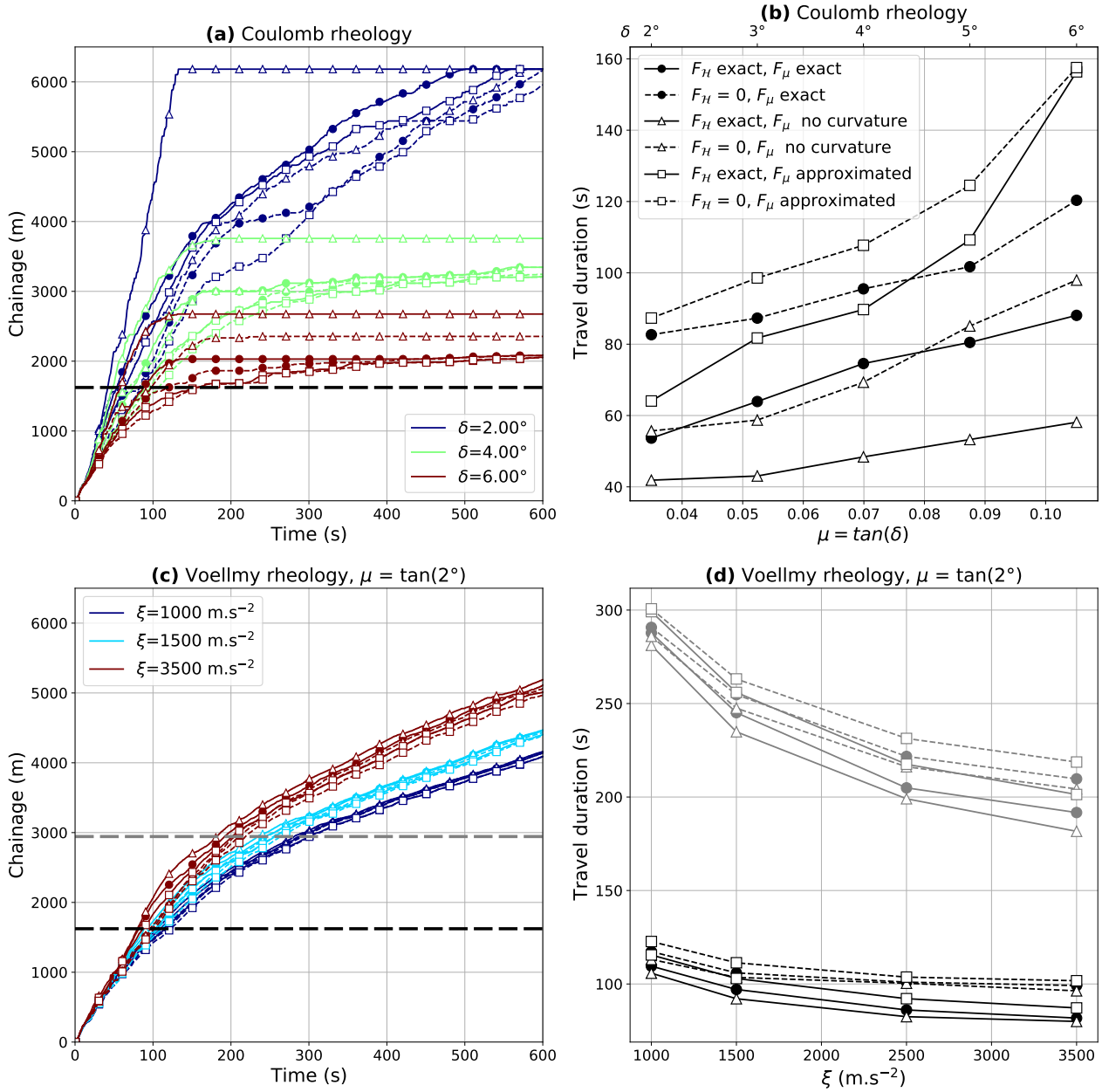

Figure 2.A.10: Simulations of debris flow in the Prêcheur river. Different situations are considered: when the curvature force is taken into account ($F_{\mathcal{H}}$ exact) or neglected ($F_{\mathcal{H}} = 0$) and when the curvature in the friction is exact (F_μ exact), neglected (F_μ no curvature) or approximated (F_μ approximated). (a) Flow front position with the Coulomb rheology. (b) Time needed for the flow to travel the first 1.6 km (black dashed line in (a)) with the Coulomb rheology, as a function of friction coefficient. (c) Flow front position with the Voellmy rheology and $\mu = \tan(2°)$. (d) Time needed for the flow to travel the first 1.6 km (black dashed line in (c)) and 2.9 km (gray dashed line in (c)) with the Voellmy rheology, as a function of turbulence coefficient.

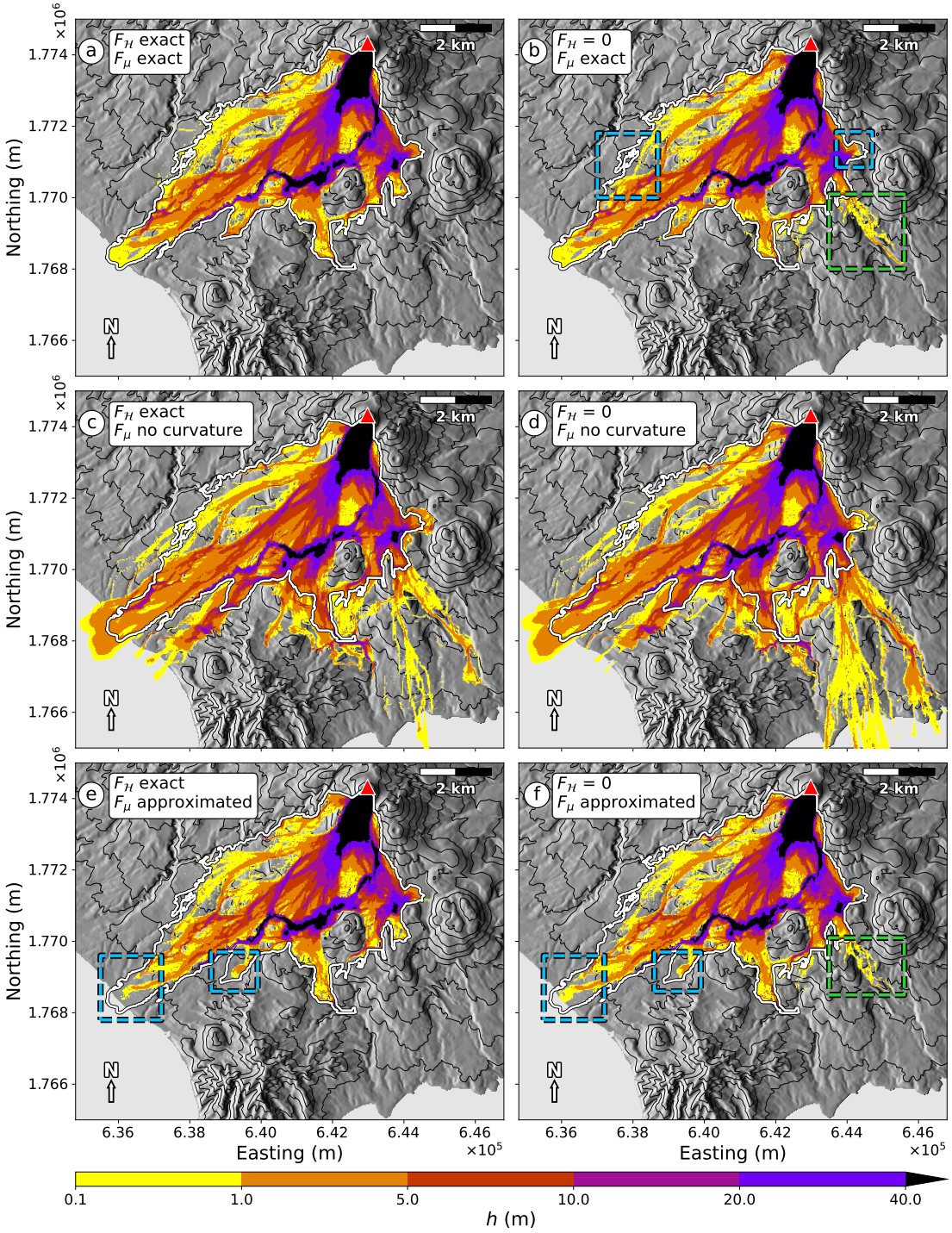

Figure 2.A.11: Maximum thickness of a hypothetical 90 $\times 10^6$ m^3 debris avalanche on the Soufrière de Guadeloupe volcano (French Caribbean). Each plot (a to f) displays the result of the simulation when the curvature force is taken into account ($F_{\mathcal{H}}$ exact) or neglected ($F_{\mathcal{H}} = 0$) and when the curvature in the friction is exact (F_μ exact), neglected (F_μ no curvature) or approximated (F_μ approximated). The simulation results in the reference case, with exact curvature terms, is given in (a) (Peruzzetto et al., 2019). The corresponding flow extent (white curve) is reported in all figures. Green dashed rectangles (respectively blue dashed rectangles) indicate areas where the spreading is greater (respectively lesser) in other simulations, in comparison to the reference simulation (a). The DEM is from IGN BDTopo, coordinates: WGS84, UTM20N. The contour interval is 100m.

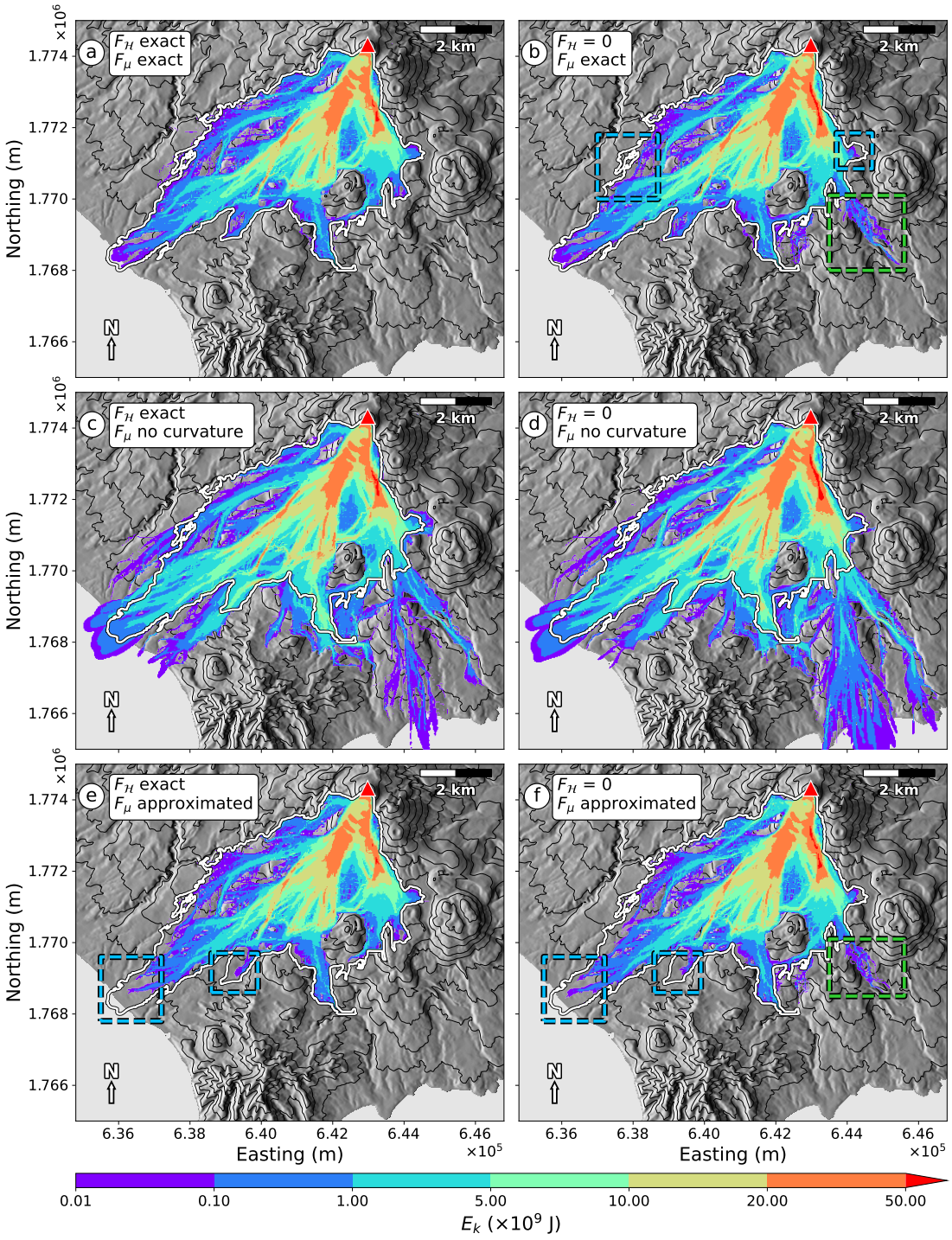

Figure 2.A.12: Same as Supplementary Figure 2.A.11, but with the simulated maximum kinetic energies.

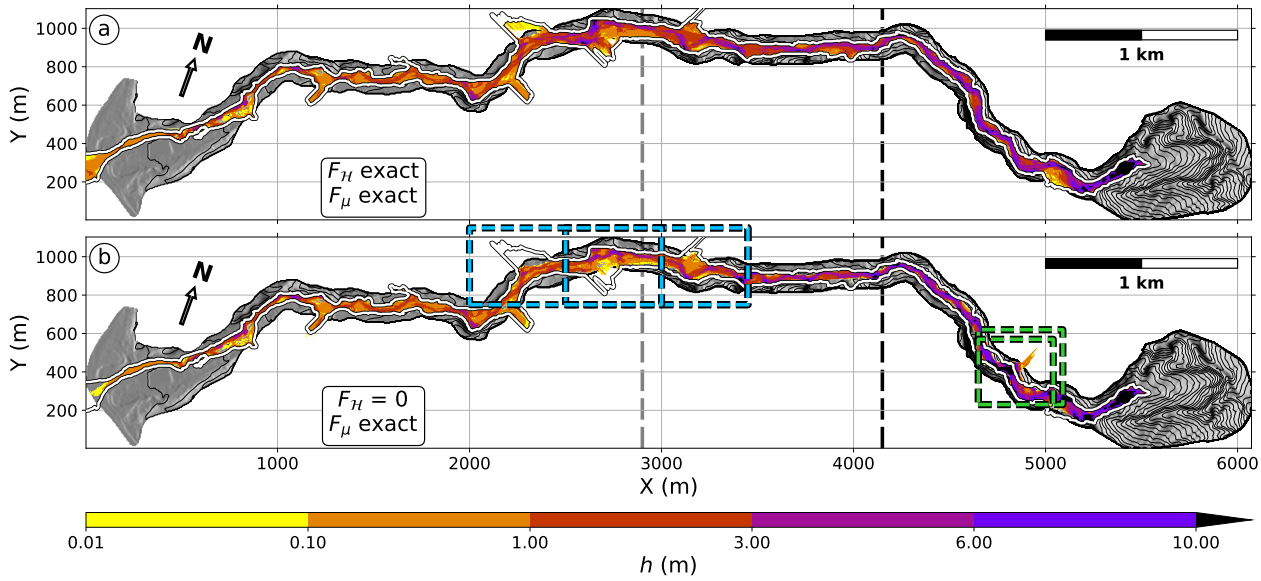

Figure 2.A.13: Maximum thickness of the flow simulated in the Prêcheur river with the Coulomb rheology and $\mu = \tan(2°)$. (a) Curvature and friction forces are exact. Maximum flow extent (white line) is reported in (b). (b) Curvature force is neglected but the friction force is exact. Green dashed rectangles (respectively blue dashed rectangles) indicate areas where the spreading is greater (respectively lesser) in other simulations, in comparison to the reference simulation (a). The contour step is 20 m.

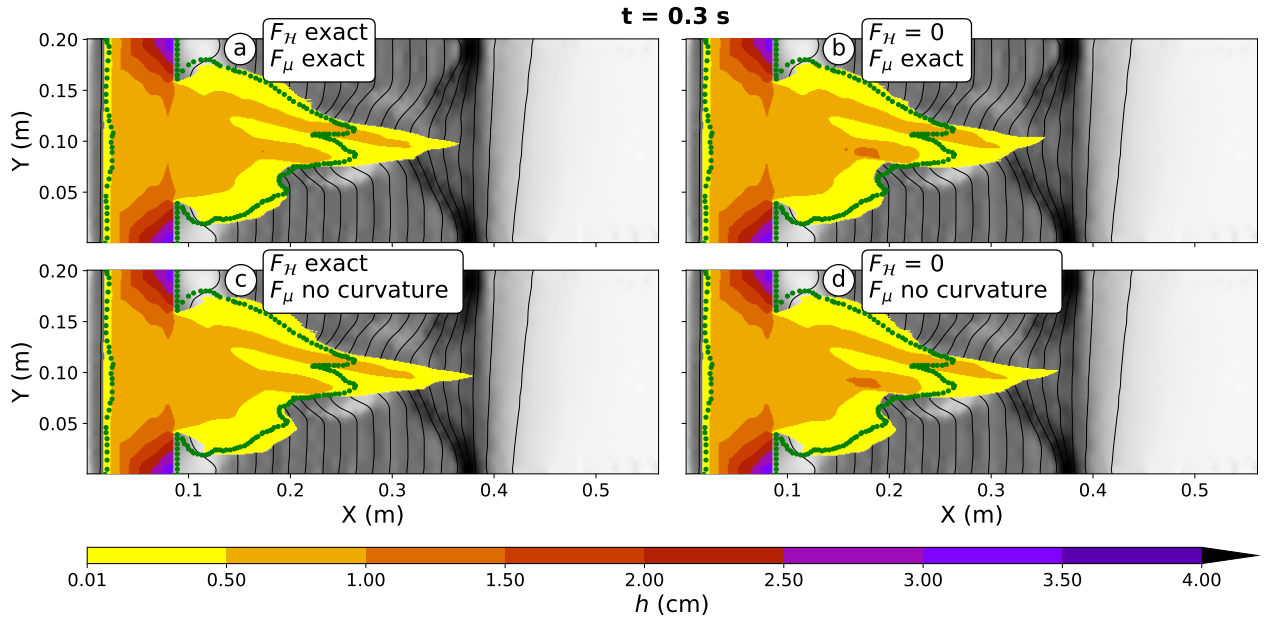

Figure 2.A.14: Simulation of the experimental set-up of Iverson et al. (2004). Colore scale: thickness of simulated flow, at $t = 0.3$ s. Green dotted line: contour of the deposits in the experiment. Each plot (a to d) displays the result of the simulation when the curvature force is taken into account ($F_{\mathcal{H}}$ exact) or neglected ($F_{\mathcal{H}} = 0$) and when the curvature in the friction is exact (F_μ exact) or neglected (F_μ no curvature). We use $\mu = \tan(23°)$ in the channel and $\mu = \tan(26°)$ elsewhere, as in Lucas (2010).

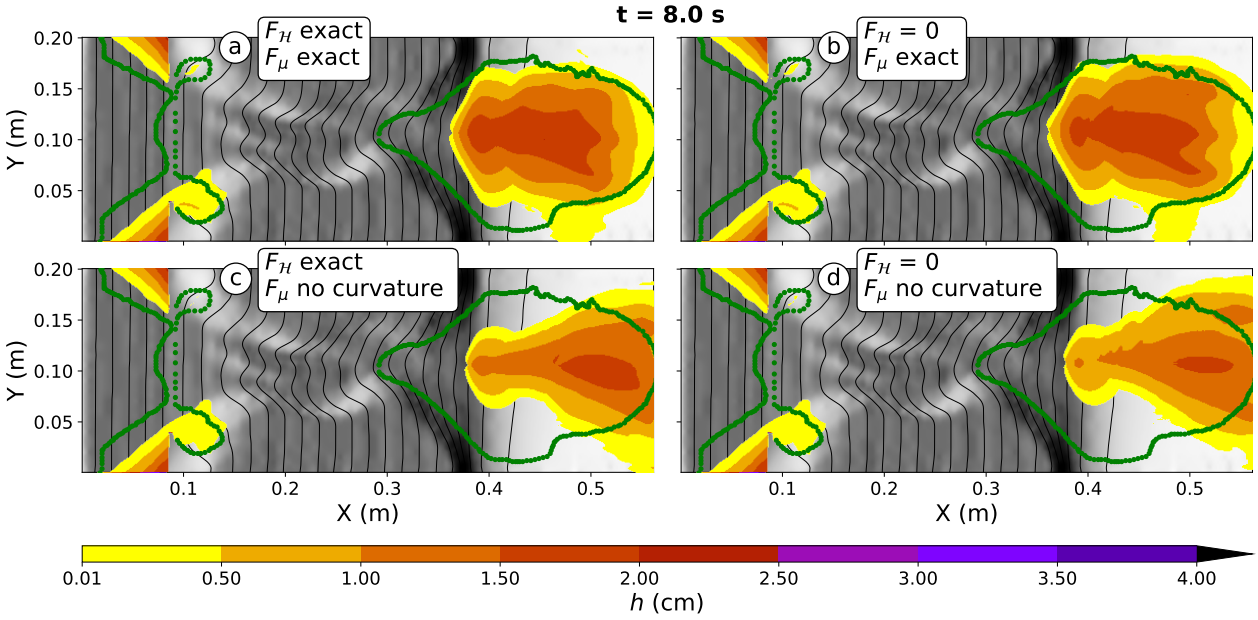

Figure 2.A.15: Same as Supplementary Figure 2.A.14, but for $t = 8.0$ s.

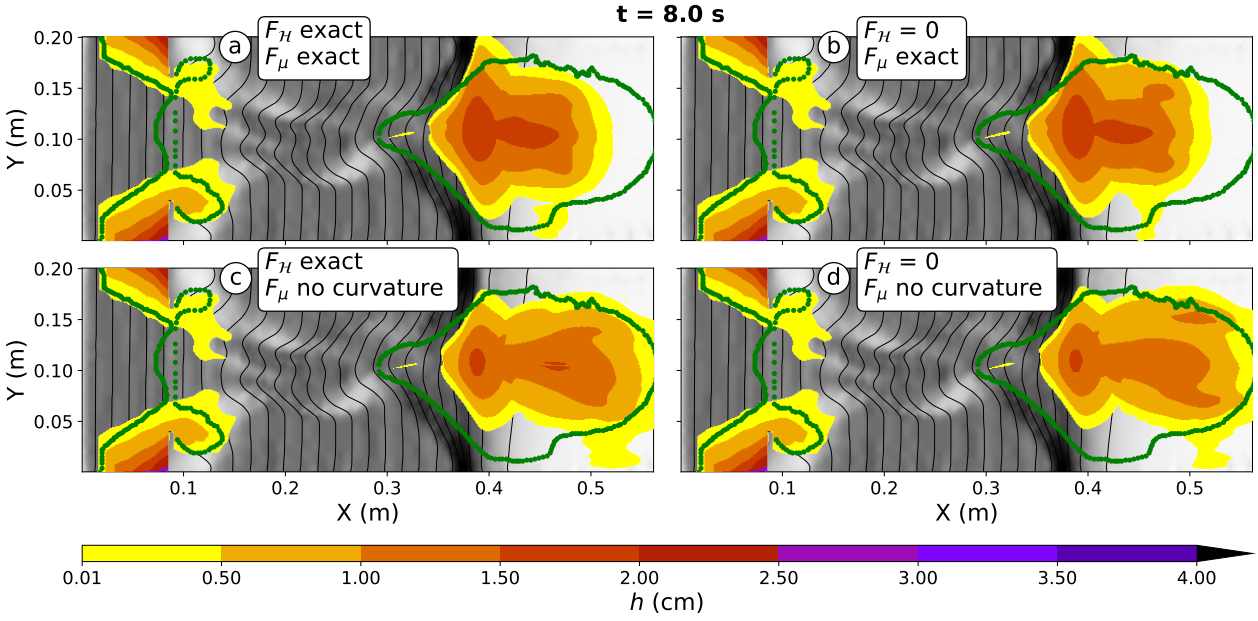

Figure 2.A.16: Same as Supplementary Figure 2.A.14, but for $t = 8.0$ s, $\mu = \tan(26°)$ in the channel and $\mu = \tan(29°)$ elsewhere.

2.B Derivation of SHALTOP thin-layer equations

2.B.1 Navier-Stokes equations

We detail here the derivation of the thin-layer equations, starting from the Navier-Stokes equations:

$$\partial_t \vec{U} + (\vec{U} \cdot \nabla_{\vec{X}})\vec{U} = -\vec{g} + \nabla_{\vec{X}} \cdot \sigma, \tag{2.43}$$

$$\nabla_{\vec{X}} \cdot \vec{U} = 0, \tag{2.44}$$

Notations are given in the main body of the article. The flow free surface is a 2D surface given by some time dependent equation $F(\vec{X}, t) = 0$, with upward unit normal vector $\vec{n}_s$ (Figure 1a), and is assumed to be advected by the velocity field $\vec{U}$. The two associated boundary conditions read

$$\vec{U} \cdot \vec{n} = 0 \text{ at the bed,} \tag{2.45}$$

$$\partial_t F + \vec{U} \cdot \nabla_{\vec{X}} F = 0 \text{ at the free surface.} \tag{2.46}$$

Denoting by $(n_t, \vec{n}_s)$ a time-space normal to the free surface (which means that $\vec{n}_s = \nabla_{\vec{X}} F / \|\nabla_{\vec{X}} F\|$, $n_t = \partial_t F / \|\nabla_{\vec{X}} F\|$), condition (2.46) can also be written as $n_t + \vec{U} \cdot \vec{n}_s = 0$. A traction free condition at the free surface is commonly assumed,

$$\sigma \vec{n}_s = \vec{0} \text{ at the free surface.} \tag{2.47}$$

We have written for σ:

$$\sigma = \sigma' - pI_3, \tag{2.48}$$

with σ' the deviatoric stress tensor, p the pressure field (devided by the flow density) and I_3 the identity matrix. Bouchut and Westdickenberg (2004) chose a Newtonian approach with a linear stress constitutive equation

$$\sigma' = \nu \left(\nabla_{\vec{X}} \vec{U} + (\nabla_{\vec{X}} \vec{U})^t \right), \tag{2.49}$$

with ν the kinematic viscosity. Besides, we furthermore impose a friction boundary condition at the bed

$$\sigma \vec{n} - (\vec{n} \cdot \sigma \vec{n})\, \vec{n} = \mu \frac{\vec{U}}{\|\vec{U}\|} (-\vec{n} \cdot \sigma \vec{n})_+, \tag{2.50}$$

However, other closing equations may be chosen, as discussed in Setcion 6.1 in the main body of the article. Nevertheless, it is difficult to reconcile fine descriptions of both the topography and the rheology. Indeed, for 1D topographies, we can reasonably assume that the main stress directions are normal and tangent to the topography. As the velocity is also along the main slope direction, this greatly simplifies the expression of the stress tensor in a reference frame linked to the topography. This is no longer the case for real topographies, as the flow can go in the cross-slope direction (for instance, in the bend of a channel). It is very difficult to rigorously take into account this variability when integrating the equations to derive the thin-layer equations. In order to preserve the mathematical formalism, simplifications are therefore needed. In this perspective, using a fluid dynamics approach as in Bouchut and Westdickenberg (2004) may be physically incorret, but it facilitates the formal derivation of the equations in a frame linked to the topography, as will be shown in the next section. Besides, it also simplifies the ordering, as the only parameter for the internal rheology is the viscosity ν, as will be shown in Section 2.B.3.

2.B.2 Coordinate system

We introduce a coordinate system $(x_1, x_2, x_3) = (\mathbf{x}, x_3)$ related to the cartesian coordinate system $(X, Y, Z) = (\mathbf{X}, Z)$ through:

$$(\mathbf{X}, Z) = \vec{X}(\mathbf{x}, x_3) = \begin{pmatrix} \mathbf{x} \\ b(\mathbf{x}) \end{pmatrix} + x_3 \vec{n}(\mathbf{x}). \tag{2.51}$$

The vectors of the reference frame $(\vec{e}_1, \vec{e}_2, \vec{e}_3)$ associated with the new coordinates $\vec{x} = (x_1, x_2, x_3)$ have the same direction as coordinate lines, so we obtain, with the Einstein notation:

$$d\vec{X} = \vec{e}_i dx_i = \vec{e}_1 dx_1 + \vec{e}_2 dx_2 + \vec{e}_3 dx_3. \tag{2.52}$$

We therefore have, for instance, $\vec{e}_1 = \partial_{x_1} \vec{X}$. Introducing the Jacobian matrix A of (2.51):

$$A = \partial_{\vec{X}} \vec{x} = \begin{pmatrix} \partial_X x_1 & \partial_Y x_1 & \partial_Z x_1 \\ \partial_X x_2 & \partial_Y x_2 & \partial_Z x_2 \\ \partial_X x_3 & \partial_Y x_3 & \partial_Z x_3 \end{pmatrix}, \tag{2.53}$$

$$A^{-1} = \partial_{\vec{x}} \vec{X} = \begin{pmatrix} \partial_{x_1} X & \partial_{x_2} X & \partial_{x_3} X \\ \partial_{x_1} Y & \partial_{x_2} Y & \partial_{x_3} Y \\ \partial_{x_1} Z & \partial_{x_2} Z & \partial_{x_3} Z \end{pmatrix}, \tag{2.54}$$

$\vec{e}_i$ is thus the i-th column of A^{-1}. By computing A^{-1}, we can deduce that $\vec{e}_3$ is exactly $\vec{n}$, the unit vector normal to the topography (Figure 2a), and that $\vec{e}_1$ and $\vec{e}_2$ are orthogonal to $\vec{n}$. However, the base $(\vec{e}_1, \vec{e}_2, \vec{e}_3)$ is in general not orthogonal. In this base, the velocity field has coordinates $\vec{V} = (V_1, V_2, V_3) = (\mathbf{V}, V_3)$:

$$\vec{U} = U_X \vec{e}_X + U_Y \vec{e}_Y + U_Z \vec{e}_Z = V_1 \vec{e}_1 + V_2 \vec{e}_2 + V_3 \vec{e}_3. \tag{2.55}$$

From the latter equation, we can deduce

$$\vec{V} = A\vec{U}, \tag{2.56}$$

$$V_3 = \vec{U} \cdot \vec{n}. \tag{2.57}$$

Therefore, V_3 is the topography normal component of the velocity (Figure 2b).

It is not straightforward to replace $\vec{U}$ by $\vec{V}$ in the Navier-Stokes equations, because it involves the Jacobian matrix A that varies along the topography and along the depth of the flow. This derivation can be found in (Bouchut and Westdickenberg, 2004), or in (Luca et al., 2009a) with a different formalism. However, the resulting equations can be significantly simplified with the thin-layer approximations.

2.B.3 Assumptions for ordering

In the thin-layer approximation, we describe the dynamics of a fluid layer with thickness $h(\mathbf{x})$. We introduce the aspect ratio $\epsilon = H/L$, where H is the typical thickness of the fluid and L its extent along the topography, and the topography curvature tensor $\mathcal{H} = c^3 \partial^2_{\mathbf{XX}} b$,

$$\mathcal{H} = c^3 \begin{pmatrix} \frac{\partial^2 b}{\partial X^2} & \frac{\partial^2 b}{\partial X \partial Y} \\ \frac{\partial^2 b}{\partial X \partial Y} & \frac{\partial^2 b}{\partial Y^2} \end{pmatrix}. \tag{2.58}$$

The underlying rationale to derive the thin-layer equations consists in comparing terms in the Navier-Stokes equations to the aspect ratio ϵ (which is itself small) and neglect the smallest

ones. Such comparisons are done with the mathematical notations $\mathcal{O}()$ and $o()$. For instance, $h = \mathcal{O}(\epsilon)$ can be understood as "h has at most the same order of magnitude as ϵ" and $h = o(\epsilon)$ means "h is much smaller than ϵ". We use also the notation $h \sim \epsilon$, which means that h has exactly the same order of magnitude as ϵ. With this formalism, we will accept to neglect terms that are of magnitude $\mathcal{O}(\epsilon^2)$ in the non-conservative form of the momentum equation and terms of magnitude $\mathcal{O}(\epsilon^3)$ in the depth-integrated mass conservation equation. To get these final approximate equations, we make the following assumptions:

(a) The fluid layer is thin, i.e. $\epsilon \ll 1$ and $h \sim \epsilon$ and thus $x_3 = \mathcal{O}(\epsilon)$ within the flow layer. This is in practice often valid, with geophysical flows that are sometimes several kilometers long and only several meters or tens of meters thick.

(b) The slope curvature is small, i.e. $\mathcal{H} = \mathcal{O}(\epsilon)$ or equivalently $\partial_{\mathbf{x}}\mathbf{s} = \mathcal{O}(\epsilon)$. This assumption is easily satisfied in open areas, but can be problematic, at least locally, for irregular topographies.

(c) The velocity $\mathbf{V}$ is almost constant in the material layer. This assumption will be discussed further on.

(d) The velocity in the direction normal to the topography, that is $\vec{U} \cdot \vec{n} = V_3$, is of the order $\mathcal{O}(\epsilon)$.

(e) The friction coefficient μ has magnitude $\mathcal{O}(\epsilon)$ and it is also $\mathcal{O}(\nu/\epsilon)$. In reality, we use $\mu < \tan(6°) = 0.11$ for mobile debris flows. For dry and massive landslides, empirical relations (e.g. Lucas et al., 2014) show that μ decreases with increasing destabilized volumes. For instance, we may have $\mu = \tan(11°) = 0.20$ for 1 km^3 landslides and $\mu = \tan(19°) = 0.34$ for 1×10^6 m^3 landslides. For even smaller landslides (Hibert et al., 2011; Levy et al., 2015) and granular flows experiments (Mangeney et al., 2007b), typical friction coefficients reach $\mu = \tan(25°) = 0.47$ or even $\mu = \tan(30°) = 0.58$.

(f) The material kinematic viscosity ν has magnitude $o(\epsilon^2)$. For example, the viscosity of water is 10^{-6} m^2 s^{-1}. The dynamic viscosity of mudflows is estimated with rheometers (e.g. O'Brien et al., 1993; Malet et al., 2002; Sosio and Crosta, 2009) and/or by modeling back-analysis (McArdell et al., 2003) and ranges from 1 to 100 Pa s. Assuming a density of 2000 kg m^{-3}, the associated kinematic viscosity ranges from 5×10^{-4} m^2 s^{-1} to 5×10^{-2} m^2 s^{-1}.

The last assumption may thus be an over-simplification in the case of muddy debris flows, which can be very viscous. However, thin-layer models for viscous flows have been so far properly derived only for simple topographies (Pastor et al., 2015; Baker et al., 2016). Extending them to real topographies requires important simplifications, such that the resulting equations are very similar to the ones we will derive here: only the basal shear stress changes (Pastor et al., 2015). However, in our equations, we can use a friction coefficient μ that depends on the flow thickness and velocity. By choosing it correctly, we can thus reproduce other rheologies classically used in thin-layer models, including the Bingham rheology for viscous flows.

On account of boundary condition (2.45), assumption (d) can actually be derived from (a) (see Bouchut and Westdickenberg, 2004). Moreover, the assumption (c) can take several forms. The simplest expression is

$$\mathbf{V}(t, \vec{x}) = \bar{\mathbf{V}}(t, \mathbf{x}) + \mathcal{O}(\epsilon^2), \tag{2.59}$$

but a more general form is

$$\mathbf{V}(t, \vec{x}) = \bar{\mathbf{V}}(t, \mathbf{x}) + \mathbf{V}^1(t, \mathbf{x})(x_3 - \frac{h(t, \mathbf{x})}{2}) + \mathcal{O}(\epsilon^2). \tag{2.60}$$

In the second approximation, we assume that the deviation from a linear velocity profile is only of the order $\mathcal{O}(\epsilon^2)$. Bouchut and Westdickenberg (2004) show that both approximations yield the same system of averaged equations. The velocity $\bar{\mathbf{V}}$ can be seen as a parametrization of the average flow velocity, or of the velocity at the middle of the fluid layer, in the plane tangent to the topography (Figure 2b). That is equivalent to within an error in $\mathcal{O}(\epsilon^2)$. For simplicity, in the following, we will consider only the approximation expressed in equation (2.59).

In the next section, we will use the above assumptions to simplify the expression of the topography reference frame and in turn the relation between the cartesian coordinates $\vec{U}$ and the new coordinates $\vec{V}$ of the velocity field. The spatial differential operators can also be written more simply. This makes it possible to write the Navier-Stokes equations in the topography coordinate system, from which we will deduce the thin-layer equations.

2.B.4 Derivation of the thin-layer equations

Using the thin-layer assumptions, we can derive a relatively simple expression for the topography reference frame. With assumptions (a) and (b), we can show that the Jacobian matrix A (recall that A^{-1} columns give the cartesian coordinates of the topography reference frame vectors) reads

$$A = \begin{pmatrix} I_2 - \mathbf{s}\mathbf{s}^t & c\mathbf{s} \\ -\mathbf{s}^t & c \end{pmatrix} + \mathcal{O}(\epsilon^2), \tag{2.61}$$

$$A^{-1} = \begin{pmatrix} I_2 & -\mathbf{s} \\ \frac{1}{c}\mathbf{s}^t & c \end{pmatrix} + \mathcal{O}(\epsilon^2). \tag{2.62}$$

Note that the reference frame is constant throughout the depth of the material layer (within errors in $\mathcal{O}(\epsilon^2)$). As mentioned above, the base $(\vec{e}_i)_{i\in[1,3]}$ is, in general, neither orthogonal nor orthonormal. Indeed, we have $G_{ij} = \vec{e}_i \cdot \vec{e}_j \neq \delta_{ij}$, where δ_{ij} is the Kronecker symbol. The matrix G_{ij} is thus not diagonal,

$$G = A^{-t}A^{-1} = \begin{pmatrix} I_2 + \frac{1}{c^2}\mathbf{s}\mathbf{s}^t & 0 \\ 0 & 1 \end{pmatrix} + \mathcal{O}(\epsilon^2) = \begin{pmatrix} M^{-1} & 0 \\ 0 & 1 \end{pmatrix} + \mathcal{O}(\epsilon^2), \tag{2.63}$$

where we introduced

$$M = I_2 - \mathbf{s}\mathbf{s}^t = \left(I_2 + \frac{1}{c^2}\mathbf{s}\mathbf{s}^t\right)^{-1}. \tag{2.64}$$

Note however that $\vec{e}_1$ and $\vec{e}_2$ are respectively the projections of the cartesian base vectors $\vec{e}_X$ and $\vec{e}_Y$, on the topography-tangent plane, parallel to $\vec{e}_Z$ (Figure 2a). They thus have the same horizontal direction but not the same norm as the reference frame chosen for instance by Christen et al. (2010).

With the thin-layer approximation, we obtain the following relation between $\bar{\mathbf{V}}$ and $\vec{U}$,

$$\|\vec{U}\|^2 = \|\bar{\mathbf{V}}\|^2 + \left(\frac{1}{c}\mathbf{s}^t\bar{\mathbf{V}}\right)^2 + \mathcal{O}(\epsilon^2).$$

Note that even with the thin-layer approximation, $\|\bar{\mathbf{V}}\|$ is not the physical velocity norm $\|\vec{U}\|$.

The Navier-Stokes equations (2.43) and (2.44) must now be transformed to derive equations for $\vec{V}$, the velocity in the topography reference frame. For this, we must express the gradient and the divergence operators in the topography reference frame. This can be done using the

Christoffel symbols and classical tensor algebra results, as in Gray et al. (1999). Bouchut and Westdickenberg (2004) instead compute the differential operators directly using the chain rule,

$$\nabla_{\vec{X}} \cdot \vec{U} = \frac{1}{J}\partial_i(J\, V_i), \tag{2.65}$$

$$A\left((\vec{U}\cdot\nabla_{\vec{X}})\vec{U}\right) = (\vec{V}\cdot\nabla_{\vec{x}})\vec{V} - \vec{\Gamma}(\vec{V}), \tag{2.66}$$

where $J = \det(A^{-1}) = \frac{1}{c} + \mathcal{O}(\epsilon^2)$ and

$$\vec{\Gamma}(\vec{V}) = -A\left(V_l \partial_l(A^{-1})\right)\vec{V}, \tag{2.67}$$

with $\partial_l = \partial_{x_l}$. After rewriting and further calculations, in the case of inviscid derivations (i.e. $\sigma = -pI_3$), the momentum equation in the flow becomes

$$\partial_t \bar{\mathbf{V}} + (\vec{V}\cdot\nabla_{\vec{x}})\bar{\mathbf{V}} + M\nabla_{\mathbf{x}}\left(p + g(x_3 c + b)\right) = \mathbf{\Gamma}(\vec{V}), \tag{2.68}$$

$$\partial_t V_3 + (\vec{V}\cdot\nabla_{\vec{x}})V_3 + \partial_{x_3} p + gc = \Gamma_3(\vec{V}). \tag{2.69}$$

With the thin-layer assumption, using the expression for $\mathbf{V}$ in (2.59) or (2.60) and the average flow velocity $\bar{\mathbf{V}}$, the source terms $\mathbf{\Gamma}(\vec{V})$ and $\Gamma_3(\vec{V})$ are given by

$$\Gamma_3(\vec{V}) = -c\bar{\mathbf{V}}^t(\partial^2_{\mathbf{xx}} b)\bar{\mathbf{V}} + \mathcal{O}(\epsilon^2) = \mathcal{O}(\epsilon), \tag{2.70}$$

$$\mathbf{\Gamma}(\vec{V}) = \Gamma_3(\vec{V})\mathbf{s} + \mathcal{O}(\epsilon^2). \tag{2.71}$$

As $V_3 = \mathcal{O}(\epsilon)$, the momentum equation for the normal velocity V_3, (2.69), becomes

$$p = c(g + \bar{\mathbf{V}}^t\partial^2_{\mathbf{xx}} b\bar{\mathbf{V}})(h(t,\boldsymbol{x}) - x_3) + \mathcal{O}(\epsilon^2) = \mathcal{O}(\epsilon). \tag{2.72}$$

Substituting in (2.68), we obtain, still in the hydrostatic case, the thin-layer momentum equation for $\bar{\mathbf{V}}$,

$$\partial_t \bar{\mathbf{V}} + (\bar{\mathbf{V}}\cdot\nabla_{\mathbf{x}})\bar{\mathbf{V}} + (I_2 - \mathbf{s}\mathbf{s}^t)\nabla_{\mathbf{x}}\left(g(hc+b)\right) = -c\big(\bar{\mathbf{V}}^t(\partial^2_{\mathbf{xx}} b)\bar{\mathbf{V}}\big)\mathbf{s} + \mathcal{O}(\epsilon^2). \tag{2.73}$$

Note that we only integrated the momentum equation over the direction normal to the topography (2.69), from which we derived the expression of the pressure within the flow (2.72). When we inject this expression in (2.68), we directly obtain the momentum equation for the average velocity (2.73), without further integration. These results are of course obtained from the approximations presented in Section 2.B.3 and the expression of the velocity (2.59) (or (2.60), see section 3.3.2 in Bouchut and Westdickenberg, 2004). However, if we now include the deviatoric stress (2.49) in the Navier-Stokes equations, we have to integrate formally the momentum equation over the direction normal to topography (2.68), along the flow depth.

The details of the derivations are given in Bouchut and Westdickenberg (2004). The key point is the computation of $\nabla_{\vec{X}}\cdot\sigma'$ as a function of $\vec{V}$ and $\vec{x}$, which is not straightforward. It is simplified by assuming simple shear flows where the predominant terms are the velocity derivatives in the direction normal to the topography, $\partial_{x_3}\vec{V}$. The integration of the momentum equation for V_3 then gives the same expression of p as in (2.72). However the integration of the momentum equation for $\mathbf{V}$ leads to two new terms including $\partial_{x_3}\mathbf{V}$ at the surface and at the base of the flow. The traction free boundary condition at the surface eliminates one of them and the friction condition at the base results in a new source term S that must be added to the right-hand side of (2.73),

$$\begin{aligned} S &= -\frac{\bar{\mathbf{V}}}{h\|\vec{U}\|}\left(\mu p_{bottom} + \mu\ \mathcal{O}(\nu)\right)_+ \\ &= -\frac{\bar{\mathbf{V}}}{\|\vec{U}\|}\left(\mu\left(gc - \Gamma_3(\vec{V})\right) + \frac{\mu}{h}\ \mathcal{O}(\epsilon^2) + \frac{\mu}{h}\ \mathcal{O}(\nu)\right)_+ . \end{aligned} \tag{2.74}$$

To be consistent with the case without friction, we want $\frac{\mu}{h}\,\mathcal{O}(\epsilon^2)$ and $\frac{\mu}{h}\,\mathcal{O}(\nu)$ to be of the order of $\mathcal{O}(\epsilon^2)$. As h has magnitude ϵ, we need at least $\nu = \mathcal{O}(\epsilon^2)$ and $\mu = \mathcal{O}(\epsilon)$ (more formally, by integrating the conservative form of the Navier-Stokes equations, the friction source term is in terms of hS, and we avoid the division by h, that can be problematic when h is small). In practice, Bouchut and Westdickenberg (2004) choose $\nu = o(\epsilon^2)$ and $\mu = \mathcal{O}(\frac{\nu}{\epsilon}) = o(\epsilon)$, which is more restrictive but necessary to properly derive the equations. In both cases however, the term $\mu\Gamma_3(\vec{V})$ has magnitude $\mathcal{O}(\epsilon^2)$, as the leading error terms, and could thus be neglected. For real landslides, the restriction $\mu = o(\epsilon)$ or $\mu = \mathcal{O}(\epsilon)$ is nevertheless hardly realistic and greater velocities can be expected. In turn, $\mu\Gamma_3(\vec{V})$ may well be greater than $\mathcal{O}(\epsilon^2)$. Though it is difficult to quantify how it compares to other terms that are also neglected, it may be interesting to keep it.

The resulting equation for $\bar{\mathbf{V}}$ is finally given by

$$\begin{aligned}\partial_t\bar{\mathbf{V}} + (\bar{\mathbf{V}}\cdot\nabla_{\mathbf{x}})\bar{\mathbf{V}} + (I_2 - \mathbf{s}\mathbf{s}^t)\nabla_{\mathbf{x}}\left(g(hc+b)\right) = \\ - c\left(\bar{\mathbf{V}}^t(\partial^2_{\mathbf{xx}}b)\bar{\mathbf{V}}\right)\mathbf{s} - \frac{\mu g c\bar{\mathbf{V}}}{\sqrt{\|\bar{\mathbf{V}}\|^2 + \left(\frac{1}{c}\mathbf{s}^t\bar{\mathbf{V}}\right)^2}}\left(1 + \frac{\bar{\mathbf{V}}^t(\partial^2_{\mathbf{xx}}b)\bar{\mathbf{V}}}{g}\right)_+ + \mathcal{O}(\epsilon^2). \quad (2.75)\end{aligned}$$

We dot not detail here the derivation of the mass equation, a it does not entail any curvature term. With the same formalism as in our development, Bouchut and Westdickenberg (2004) show that it reads :

$$\partial_t\left(\frac{h}{c}\right) + \nabla_{\mathbf{x}}\cdot\left(\frac{h}{c}\bar{\mathbf{V}}\right) = \mathcal{O}(\epsilon^3). \quad (2.76)$$

2.C Curvature approximation in friction forces

In this section, we analyze the effect of approximating the curvature term in the friction force. This term is taken into account in most models, but not always accurately. As in the main body of the article, we choose the following parametrization of the velocity,

$$\vec{\mathcal{V}} = c\left(u, u_t, \frac{\partial b}{\partial x}u + \frac{\partial b}{\partial y}u_t\right) = (c\mathbf{u}, \mathbf{s}\cdot\mathbf{u}). \tag{2.77}$$

The angle α gives the velocity direction, such that $\mathbf{u} = \|\mathbf{u}\|(\cos(\alpha), \sin(\alpha))$. The expression of the basal friction force reads

$$\vec{T_f} = \rho h \mu (g\cos(\theta) + \gamma(\mathbf{u}))\frac{\vec{\mathcal{V}}}{\|\vec{\mathcal{V}}\|}, \tag{2.78}$$

with ρ the material density, h the thickness of the material layer in the direction normal to topography and $\gamma(\mathbf{u})$ a curvature term. From the previous sections, we have

$$\gamma(\mathbf{u}) = \gamma\|\vec{\mathcal{V}}\|^2 = \mathbf{u}^t\mathcal{H}\mathbf{u}. \tag{2.79}$$

Note that in order to practically compute the curvature along the flow path, velocity variations must be taken into account. To illustrate this, let us consider a line tangent to the topography, passing through a point $(x_0, y_0, b(x_0, y_0))$ in a fixed direction (cu, cu_t), with as previously $c = \cos(\theta)$. The resulting curve $M(t)$ is given by

$$M(t) = (x_0 + tcu, y_0 + tcu_t, b(x_0 + tcu, y_0 + tcu_t)), \tag{2.80}$$

$$\dot{M}(t) = (cu, cu_t, cu\partial_x b + cu_t\partial_y b), \tag{2.81}$$

$$\ddot{M}(t) = (0, 0, c^2u^2\partial_{xx}b + 2c^2uu_t\partial_{xy}b + c^2u_t^2\partial_{yy}b). \tag{2.82}$$

The associated curvature is

$$\gamma_1 = \pm\frac{\left\|\dot{M}(t)\wedge\ddot{M}(t)\right\|}{\left\|\dot{M}(t)\right\|^3} = \frac{\sqrt{u^2+u_t^2}}{\|\vec{\mathcal{V}}\|^3}\mathbf{u}^t\mathcal{H}\mathbf{u}. \tag{2.83}$$

We thus have an approximation $\gamma_1(\mathbf{u}) = \gamma_1\|\vec{\mathcal{V}}\|^2$ of $\gamma(\mathbf{u})$,

$$\gamma_1(\mathbf{u}) = \sqrt{\frac{\|\mathbf{u}\|^2}{\cos^2(\theta)(\|\mathbf{u}\|^2 + \|\mathbf{u}\|^2\|\nabla b\|^2\cos^2(\alpha_b))}}\gamma(\mathbf{u}). \tag{2.84}$$

where α_b is the angle between $\mathbf{u}$ and the steepest slope direction. After some further transformations we obtain

$$\gamma_1(\mathbf{u}) = \frac{1}{\sqrt{1-\sin^2(\theta)\sin^2(\alpha_b)}}\gamma(\mathbf{u}). \tag{2.85}$$

We have not taken into account the velocity variations and we observe that this approximation yields an over-estimation of the curvature term and decelerates the flow. $\gamma_1(\mathbf{u})$ an $\gamma(\mathbf{u})$ are equal when the topography is flat or when the flow direction is aligned with the steepest slope.

We will now demonstrate the importance of using the full curvature tensor to compute the curvature. As

$$\mathcal{H} = \begin{pmatrix}\mathcal{H}_{xx} & \mathcal{H}_{xy}\\ \mathcal{H}_{xy} & \mathcal{H}_{yy}\end{pmatrix} = \cos^3(\theta)\begin{pmatrix}\partial_{xx}b & \partial_{xy}b\\ \partial_{xy}b & \partial_{yy}b\end{pmatrix}, \tag{2.86}$$

is symmetric, it has two eigen-values λ_1 and λ_2. We introduce the angle β giving the principal directions of curvature, such that the unit eigen-vectors associated with λ_1 and λ_2 are respectively

$$\mathbf{f_1} = (\cos(\beta), \sin(\beta)), \qquad \mathbf{f_2} = (-\sin(\beta), \cos(\beta)). \tag{2.87}$$

From the previous relations we easily deduce

$$\mathcal{H}_{xx} = \lambda_1 \cos^2(\beta) + \lambda_2 \sin^2(\beta), \tag{2.88}$$
$$\mathcal{H}_{yy} = \lambda_1 \sin^2(\beta) + \lambda_2 \cos^2(\beta), \tag{2.89}$$
$$\mathcal{H}_{xy} = (\lambda_1 - \lambda_2) \sin(\beta) \cos(\beta). \tag{2.90}$$

With these notations, the curvature term $\gamma(\mathbf{u})$ reads

$$\gamma(\mathbf{u}) = \mathcal{H}_{xx} u^2 + 2\mathcal{H}_{xy} u u_t + \mathcal{H}_{yy} u_t^2 = \|\mathbf{u}\|^2 \left(\lambda_1 \cos^2(\alpha - \beta) + \lambda_2 \sin^2(\alpha - \beta)\right). \tag{2.91}$$

Let us now approximate, wrongly, the curvature along the flow path with two expressions,

$$\gamma_2 = \mathcal{H}_{xx} \cos^2(\alpha) + \mathcal{H}_{yy} \sin^2(\alpha), \tag{2.92}$$
$$\gamma_3 = \mathcal{H}_{xx} |\cos(\alpha)| + \mathcal{H}_{yy} |\sin(\alpha)|. \tag{2.93}$$

We can also consider the curvatures in the x and y directions, respectively γ_x and γ_y,

$$\gamma_x = \frac{\partial_{xx} b}{(1 + (\partial_x b)^2)^{\frac{3}{2}}} = \frac{\mathcal{H}_{xx}}{\left(1 - \sin^2(\phi) \sin^2(\theta)\right)^{\frac{3}{2}}}, \tag{2.94}$$
$$\gamma_y = \frac{\partial_{yy} b}{(1 + (\partial_y b)^2)^{\frac{3}{2}}} = \frac{\mathcal{H}_{yy}}{\left(1 - \cos^2(\phi) \sin^2(\theta)\right)^{\frac{3}{2}}}, \tag{2.95}$$

where ϕ is the angle of the steepest slope direction,

$$\cos\phi = -\frac{\partial_x b}{\|\nabla b\|}, \qquad \sin\phi = -\frac{\partial_y b}{\|\nabla b\|}. \tag{2.96}$$

As previously, we can weight γ_x and γ_y to estimate the curvature in the velocity direction,

$$\gamma_4 = \gamma_x \cos^2(\alpha) + \gamma_y \sin^2(\alpha), \tag{2.97}$$
$$\gamma_5 = \gamma_x |\cos(\alpha)| + \gamma_y |\sin(\alpha)|. \tag{2.98}$$

In the main body of the article, we tested the influence of the approximation γ_4 on the flow dynamics. Note that if $\mathcal{H}$ were a scalar, the exact curvature along the flow path would be (see (2.79))

$$\gamma = \mathcal{H} \frac{\|\mathbf{u}\|^2}{\|\vec{\mathcal{V}}\|^2}. \tag{2.99}$$

We could thus consider adding a multiplicative factor $\|\mathbf{u}\|^2/\|\vec{\mathcal{V}}\|^2$ in the expressions (2.92), (2.93), (2.97), (2.98) of γ_2, γ_3, γ_4 and γ_5. Though this would provide a better estimate, it is not intuitive. We thus choose to keep the previous expressions, which seem more "natural", especially when considering the curvature along the x and y directions.

There is no simple way to determine under what conditions these approximations result in an acceleration or a deceleration of the flow. Note however that they are not invariant by rotation, as they depend on the orientation α of the velocity. We can however look at a simple albeit realistic case, when a flow is confined at the bottom of a ravine. We assume the ravine is aligned with the steepest slope, as well as one of the eigen-vectors of $\mathcal{H}$, say $\mathbf{f_1}$, so that $\alpha_b = 0$ and $\alpha = \beta = \phi$. In particular we then have $\|\mathbf{u}\| = \|\vec{\mathcal{V}}\|$. As the ravine cross-section is convex,

the eigen-value associated with the other eigen-vector is positive: $\lambda_2 \geq 0$. Similarly, the sign of λ_1 depends on the convexity or concavity of the ravine longitudinal profile, i.e. the thalweg. Typically, if the slope locally increases, $\lambda_1 < 0$.

In the following we will evaluate the influence of each approximation of the curvature on the dynamics of the flow. If the estimated curvature term is higher than $\gamma(\mathbf{u}) = \lambda_1 \|\mathbf{u}\|^2$, then the flow is decelerated. Otherwise, it is accelerated.

2.C.1 Approximation γ_2

Let us first consider the approximation $\gamma_2(\mathbf{u}) = \gamma_2 \|\vec{\mathcal{V}}\|^2$. With the chosen configuration, it simplifies to

$$\gamma_2(\mathbf{u}) = \gamma(\mathbf{u}) + 2\|\mathbf{u}\|^2(\lambda_2 - \lambda_1)\sin^2(\alpha)\cos^2(\alpha). \tag{2.100}$$

As $\lambda_2 > 0$, the approximation γ_2 results in an over-estimation of the curvature when $\lambda_2 > \lambda_1$. On the other hand, the flow is accelerated when $\lambda_1 > \lambda_2 > 0$, that is when the thalweg slope suddenly decreases.

2.C.2 Approximation γ_3

The detailed development is more complex for the approximation γ_3. As $\gamma_3(\mathbf{u}) = \gamma_3 \|\vec{\mathcal{V}}\|^2$ is $\pi/2$-periodic for α, we can consider only $\alpha \in [0, \pi/2]$. Simple trigonometric transformations then yield

$$\gamma_3(\mathbf{u}) = \left(\frac{\sqrt{2}}{2}(3\lambda_1 - \lambda_2)\cos(\alpha - \frac{\pi}{4}) + \sqrt{2}\cos^3(\alpha - \frac{\pi}{4})(\lambda_2 - \lambda_1) \right) \|\mathbf{u}\|^2. \tag{2.101}$$

Introducing $r = \lambda_1/\lambda_2$ and $\tilde{\alpha} = \alpha - \pi/4 \in [-\pi/4, \pi/4]$, we get

$$\gamma_3(\mathbf{u}) = \lambda_2 \|\mathbf{u}\|^2 \left(\frac{\sqrt{2}}{2}(3r - 1)\cos(\tilde{\alpha}) + \sqrt{2}(1 - r)\cos^3(\tilde{\alpha}) \right). \tag{2.102}$$

As this function is even in $\tilde{\alpha}$, we can limit the analysis to $\tilde{\alpha} \in [0, \pi/4]$. Moreover we have

$$\frac{d\gamma_3(\mathbf{u})}{d\tilde{\alpha}} = -\lambda_2 \|\mathbf{u}\|^2 \sin(\tilde{\alpha}) K(\tilde{\alpha}, r), \tag{2.103}$$

with

$$K(\tilde{\alpha}, r) = \frac{\sqrt{2}}{2}(3r - 1) + 3\sqrt{2}(1 - r)\cos^2(\tilde{\alpha}). \tag{2.104}$$

If $r \leq 1$ (i.e. $\lambda_1 \leq \lambda_2$), $K(\tilde{\alpha}, r) \geq \sqrt{2}$ and $\gamma_3(\mathbf{u})$ decreases between $\tilde{\alpha} = 0$ and $\tilde{\alpha} = \pi/4$. We then have

$$\gamma_3(\mathbf{u}) \geq \gamma_3(\mathbf{u})|_{\tilde{\alpha}=\pi/4} = \lambda_1 \|\mathbf{u}\|^2. \tag{2.105}$$

If $r > 1$ (i.e. $\lambda_1 > \lambda_2$), $K(\tilde{\alpha}, r) \in [\frac{\sqrt{2}}{2}(5 - 3r), \sqrt{2}]$. Thus for $r \leq \frac{5}{3}$ (i.e. $\lambda_1 \leq \frac{5}{3}\lambda_2$), we also have $\gamma_3(\mathbf{u}) \geq \lambda_1 \|\mathbf{u}\|^2$. On the other hand, if $r > \frac{5}{3}$, there is an angle $\tilde{\alpha_0} \in [0, \pi/4]$ such that $K(\tilde{\alpha_0}) = 0$. $\gamma_3(\mathbf{u})$ then increases for $\tilde{\alpha} \in [0, \tilde{\alpha_0}]$ and decreases for $\tilde{\alpha} \in [\tilde{\alpha_0}, \pi/4]$. Moreover, we have

$$\gamma_3(\mathbf{u})|_{\tilde{\alpha}=0} = \frac{\sqrt{2}}{2}(r + 1)\lambda_2 \|\mathbf{u}\|^2 = \frac{\sqrt{2}}{2}(\lambda_1 + \lambda_2)\|\mathbf{u}\|^2 \tag{2.106}$$

$$\gamma_3(\mathbf{u})|_{\tilde{\alpha}=\pi/4} = \lambda_1 \|\mathbf{u}\|^2. \tag{2.107}$$

Thus, if $r \leq \sqrt{2}+1$ (i.e. $\lambda_1 \leq (\sqrt{2}+1)\lambda_2$), $\gamma_3(\mathbf{u}) \geq \lambda_1 \|\mathbf{u}\|^2$ and the flow is decelerated.

We can thus conclude that the approximation γ_3 will decelerate the flow if $\lambda_1 \leq (\sqrt{2}+1)\lambda_2$. Otherwise, it depends on the channel direction. However, $\lambda_1 > (\sqrt{2}+1)\lambda_2$ can hardly be found more than locally in a realistic channel as it corresponds to a sudden flattening of the channel thalweg.

2.C.3 Approximations γ_4 and γ_5

Once again in the channel configuration, we compute for $\gamma_4(\mathbf{u}) = \gamma_4 \|\vec{\mathcal{V}}\|^2$ and $\gamma_5(\mathbf{u}) = \gamma_5 \|\vec{\mathcal{V}}\|^2$

$$\gamma_4(\mathbf{u}) = \|\mathbf{u}\|^2 \left[\lambda_1 \left(\frac{\cos^4(\alpha)}{\left(1-\sin^2(\alpha)\sin^2(\theta)\right)^{\frac{3}{2}}} + \frac{\sin^4(\alpha)}{\left(1-\cos^2(\alpha)\sin^2(\theta)\right)^{\frac{3}{2}}} \right) + \lambda_2 \sin^2(\alpha)\cos^2(\alpha) \left(\frac{1}{\left(1-\sin^2(\alpha)\sin^2(\theta)\right)^{\frac{3}{2}}} + \frac{1}{\left(1-\cos^2(\alpha)\sin^2(\theta)\right)^{\frac{3}{2}}} \right) \right], \quad (2.108)$$

$$\gamma_5(\mathbf{u}) = \|\mathbf{u}\|^2 \left[\lambda_1 \left(\frac{\cos^3(\alpha)}{\left(1-\sin^2(\alpha)\sin^2(\theta)\right)^{\frac{3}{2}}} + \frac{\sin^3(\alpha)}{\left(1-\cos^2(\alpha)\sin^2(\theta)\right)^{\frac{3}{2}}} \right) + \lambda_2 \sin(\alpha)\cos(\alpha) \left(\frac{\sin(\alpha)}{\left(1-\sin^2(\alpha)\sin^2(\theta)\right)^{\frac{3}{2}}} + \frac{\cos(\alpha)}{\left(1-\cos^2(\alpha)\sin^2(\theta)\right)^{\frac{3}{2}}} \right) \right]. \quad (2.109)$$

In comparison to γ_2 and γ_3, the curvature approximations depend on the slope angle θ, which makes a rigorous analysis difficult. This is illustrated in Figures 2.C.1 and 2.C.2, where we plot for various slope angles the difference between the exact curvature term $\gamma(\mathbf{u})$ and $\gamma_4(\mathbf{u})$ and $\gamma_5(\mathbf{u})$ respectively. Note that for $\theta = 0°$, we have $\gamma_2(\mathbf{u}) = \gamma_4(\mathbf{u})$ and $\gamma_3(\mathbf{u}) = \gamma_5(\mathbf{u})$. For small slope angles, the difference between the approximations and the exact curvature term is positive when $\lambda_1/\lambda_2 < 0$, whatever the channel direction α. However, when $\theta > 60°$ and $\theta > 40°$ (for γ_4 and γ_5 respectively), if $\lambda_1/\lambda_2 > 0$, the flow is decelerated. We were unable to derive the different situations analytically or generally.

However we can identify graphically (Figure 2.C.3) the values of λ_1/λ_2 and θ for which the flow is always accelerated (dark blue area) or decelerated (dark red area). In particular, we can deduce graphically that the approximations γ_4 and γ_5 will always decelerate the flow if $\lambda_1/\lambda_2 \in [-2, 1]$. We may expect that the situation $\lambda_1/\lambda_2 \notin [-2, 1]$, in the case of a channel, will be met only locally along the thalweg. However, even if $\lambda_1 < -2\lambda_2$, the flow will still be slowed down if $\theta < 60°$ and $\theta < 40°$, for γ_4 and γ_5 respectively. Even for higher slope angles, if $\lambda_1 > -6\lambda_2$, the flow is slowed down in more than 50% of channel orientations.

We can thus expect the approximations γ_4 and γ_5 to decelerate the flow in most situations. This is, in practice, verified on real topographies, as illustrated in the main body of the article.

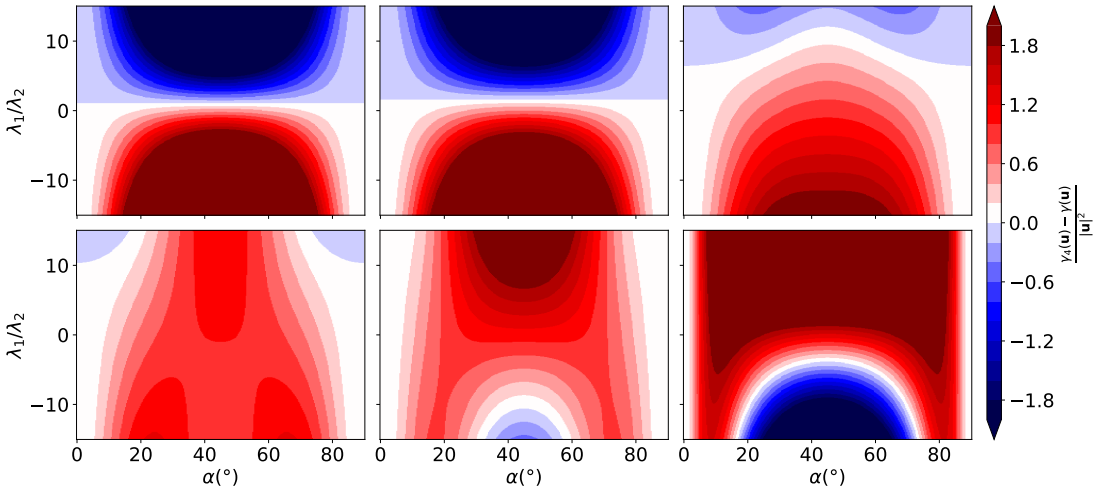

Figure 2.C.1: Normalized difference between the approximated $\gamma_4(\mathbf{u})$ and exact $\gamma(\mathbf{u})$ curvature terms, for (a) $\theta = 0°$, (b) $\theta = 30°$, (c) $\theta = 55°$, (d) $\theta = 60°$, (e) $\theta = 65°$, (f) $\theta = 80°$, plotted as a function of the channel orientation α and of the main curvature ratio λ_1/λ_2. For $\theta = 0°$, $\gamma_4 = \gamma_2$. A positive difference (white and red colors) induces a deceleration of the flow, a negative difference (blue colors) an acceleration.

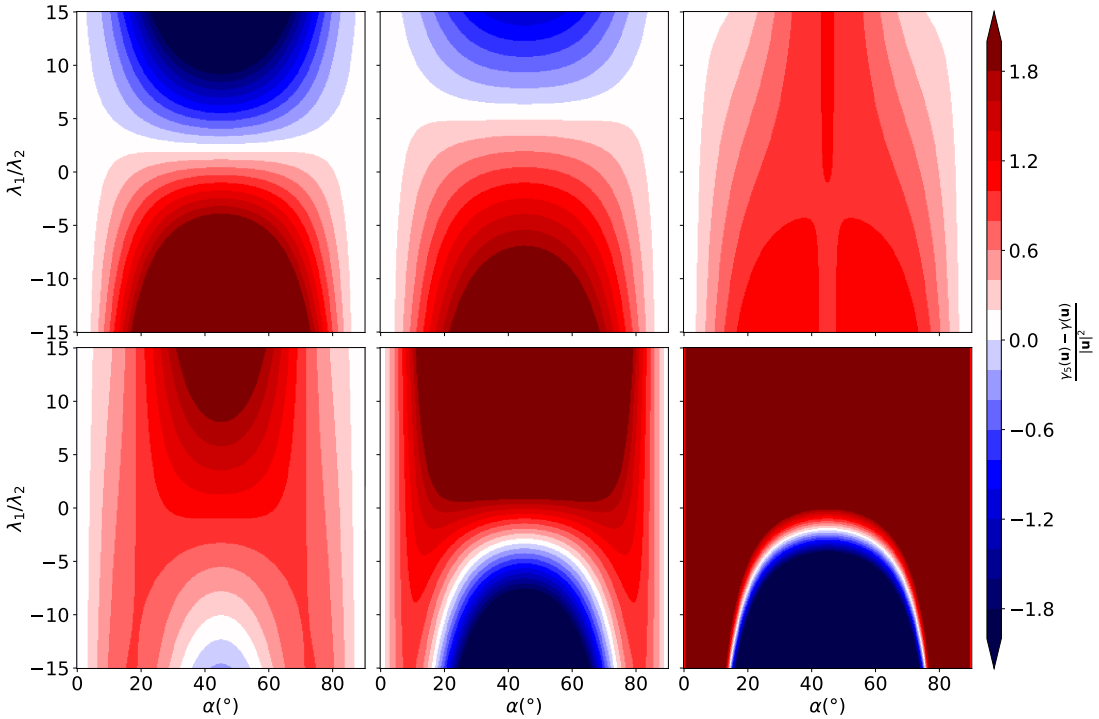

Figure 2.C.2: Normalized difference between the approximated $\gamma_5(\mathbf{u})$ and exact $\gamma(\mathbf{u})$ curvature terms, for (a) $\theta = 0°$, (b) $\theta = 30°$, (c) $\theta = 40°$, (d) $\theta = 50°$, (e) $\theta = 60°$, (f) $\theta = 80°$, plotted as a function of the channel orientation α and of the main curvature ratio λ_1/λ_2. For $\theta = 0°$, $\gamma_5 = \gamma_3$. A positive difference (white and red colors) induces a deceleration of the flow, a negative difference (blue colors) an acceleration.

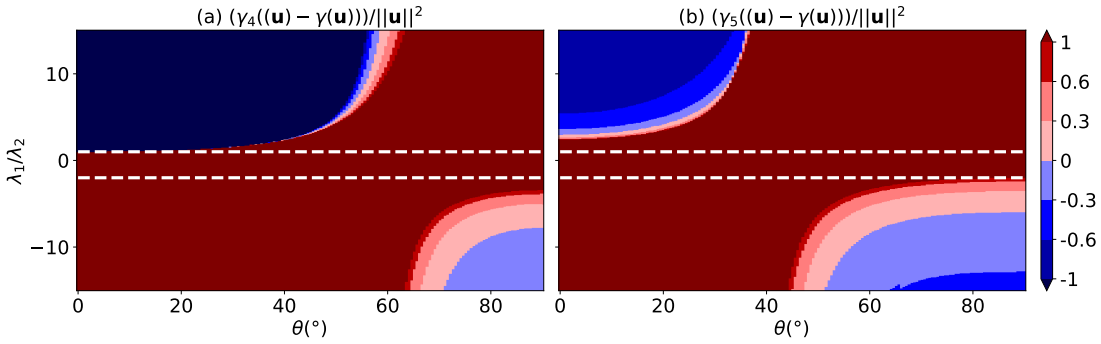

Figure 2.C.3: Sign of the difference between the approximated and exact curvature terms, depending on the slope angle θ and the main curvature ratio λ_1/λ_2. (a) $\gamma_4(\mathbf{u}) - \gamma(\mathbf{u})$. (b) $\gamma_5(\mathbf{u}) - \gamma(\mathbf{u})$ The color scale is $p_1 - p_2$, where p_1 and p_2 are the percentage of α values giving a positive and a negative difference, respectively. $p_1 - p_2 = 0$ means the flow is accelerated for 50% of α values and decelerated for the remaining 50%. The dashed curves delimit the area where $\lambda_1/\lambda_2 \in [-2, 1]$ and where the difference is always positive (and thus where the approximations decelerate the flow).

2.D Supplementary Note 3: Synthetic topography generation

We define a basal reference surface S_B in the fixed cartesian reference frame by $z = z_B(x, y)$. The upward unit normal vector is

$$\vec{n}_B = \frac{1}{\sqrt{1 + (\partial_x z_B)^2 + (\partial_y z_B)^2}}(-\partial_x z_B, -\partial_y z_B, 1). \tag{2.110}$$

Taking $z_B = z_B(x)$, we then have $dz_B/dx = \tan\theta$ and we consider θ to be constant, i.e. the reference surface is a plane. We then construct a curvilinear coordinate system on this surface by

$$x'(x, y) = \int_0^x \sqrt{1 + (\partial_x z_B(\tau, y))^2} d\tau = \frac{x}{\cos\theta}, \tag{2.111}$$

$$y'(x, y) = y. \tag{2.112}$$

The third coordinate, z', is the surface normal distance from a point to the surface. The channel itself is constructed between x'_1 and x'_2 and has n_b bends, such that each bend has length $L = (x'_2 - x'_1)/n_b$. Defining the amplitude A_b of the bends, the thalweg is given by $y' = f_t(x')$, with

$$f_t(x') = 0 \qquad \text{if } x' < x'_1 \text{ or } x' > x'_2, \tag{2.113}$$

$$f_t(x') = \frac{A_b}{2} + \frac{A_b}{2}\cos\left(-\frac{2\pi}{L}\left(x' - x'_1 - \frac{L}{2}\right)\right) \qquad \text{if } x' \in [x'_1, x'_1 + \frac{L}{2}], \tag{2.114}$$

$$f_t(x') = A_b \cos\left(\frac{\pi}{L}\left(x' - x'_1 + \frac{L}{2}\right)\right) \qquad \text{if } x' \in [x'_1 + \frac{L}{2}, x'_2 - \frac{L}{2}], \tag{2.115}$$

$$f_t(x') = (-1)^{n_b+1}\left[\frac{A_b}{2} + \frac{A_b}{2}\cos\left(\frac{2\pi}{L}\left(x' - x'_2 + \frac{L}{2}\right)\right)\right] \qquad \text{if } x' \in [x'_2 - \frac{L}{2}, x'_2]. \tag{2.116}$$

We construct the channel cross-section as a truncated parabola centered on the thalweg,

$$z' = z'_B(x', y') = \min(\frac{R}{2}, \beta(x')(y' - f_t(x'))^2), \tag{2.117}$$

where R is the curvature radius of the cross-section at the channel bottom. With x'_0 and x'_3 giving the transition length before and after the channel, $\beta(x')$ is given by

$$\beta(x') = 0 \qquad \text{if } x' < x'_0 \text{ or } x' > x'_3, \tag{2.118}$$

$$\beta(x') = \frac{3}{2R}\left(\frac{x' - x'_0}{x'_1 - x'_0}\right)^2 - \frac{1}{R}\left(\frac{x - x'_0}{x'_1 - x'_0}\right)^3 \qquad \text{if } x' \in [x'_0, x'_1], \tag{2.119}$$

$$\beta(x') = \frac{1}{2R} \qquad \text{if } x' \in [x'_1, x'_2], \tag{2.120}$$

$$\beta(x') = \frac{3}{2R}\left(\frac{x' - x'_3}{x'_2 - x'_3}\right)^2 - \frac{1}{R}\left(\frac{x - x'_3}{x'_2 - x'_3}\right)^3 \qquad \text{if } x' \in [x'_2, x'_3]. \tag{2.121}$$

For any point M_B on the reference surface, points M on the final synthetic topography are thus given by

$$M = M_B + z'_B \vec{n}_B. \tag{2.122}$$

In the main body of the article we introduced the ratio $\bar{\gamma} = A_b/L$. This expression arises from the expression of the curvature of the channel thalweg, $\gamma(x')$, that we compute with:

$$\gamma(x') = \frac{|f''_t(x')|}{\left(1 + (f'_t(x'))^2\right)^{\frac{3}{2}}}. \tag{2.123}$$

The maximum curvature is obtained in the bend at, for instance, $x' = x'_1 - L/2$. The associated curvature is

$$\gamma = \frac{\pi^2 A_b}{L^2}. \tag{2.124}$$

Considering a reference case where $A_b = L/2$ where the bend amplitude is half the period of the sinusoid, we non-dimensionalize γ following:

$$\bar{\gamma} = \frac{\pi^2 A_b}{L^2}\frac{2L^2}{\pi^2 L} = \frac{2A_b}{L}, \tag{2.125}$$

which is the expression used in the main body of the article. In our simulations, the initial mass, at the beginning of the channel, is a truncated spherical dome above the topography. Its projection on the topography is approximately a circle of radius 9 cm and the dome has a maximum height of 5 cm. For the simulations of Section 4.1 we used a regular grid with a constant horizontal spacing of 8 mm. In Section 4.2 the grid step is 5 mm, and in Section 4.3 it is 7 mm (because we wanted to increase computation velocity, as numerous simulations are done).

2.E Supplementary Note 4: Comments on numerical simulations.

We give here some details on numerical simulation set-up and results processing to help interpret correctly Figures 5, 7, 8 and 10.

Maximum thickness and velocities are derived from successive snapshots recorded during the simulation. To derive Figures 5, 7 and 8, we use snapshots recorded every 0.01 s. When the flow is fast, the flow extent may change significantly between two successive snaphots, resulting in artifacts when the final flow extent is drawn (e.g. in Figure 5a between X=1.5 and X=2.0). Besides, we do not represent thicknesses below 0.1 mm in Figures 5, 7 and 8: in turn, some part of the maximum thickness velocities maps may appear disconnected from the main flow path (e.g. in Figure 5a).

The Digital Elevation Model used to carry out simulations in the Prêcheur river is relatively narrow around the Figure, as can be seen in Figure 10. However, it is necessary in SHALTOP to fgive numeric values for altitudes in the whole simulation grid. Setting an arbitrary value (for instance, 0 or 9999) would create strong topography gradients around the river. This can be problematic, because the code is not able to deal with flows on almost vertical slopes. Thus, the topography around the river was reconstructed iteratively by averaging altitudes in successive neighborhoods of the DEM, until the whole grid was filled. The resulting topography is not realistic around the initial data (hence we do not show it in figures), but the transition between the real DEM and the reconstructed topography is smooth enough to avoid numerical issues. The streaks observed when the flow overflows the Prêcheur river correspond to propagation on this artificial topography.

2.F Supplementary Note 5: Back-analysis of a debris flow: the 2008 Yu-Tung debris flow

The Second JTC1 Workshop on the Triggering and Propagation of Rapid Flow-like Landslides was held in Hong Kong in December 2018. One of its key components was a benchmarking exercise for landslide dynamics and runout modeling. One of the events that participants were asked to reproduce was a debris flow that occurred in June 2008 above Yu Tung Road in Hong Kong following heavy rainfalls (Figure 2.F.1). The flow front velocity could be estimated at some locations from super-elevation data and visual observations (Pastor et al., 2018a). With SHALTOP, the Voellmy rheology proved to be the most efficient rheology to reproduce these observed velocities: the back-analysis results, with all precise curvature terms, are given in Figure 2.F.2 a and b ((Peruzzetto et al., 2018a)). Here we investigate the effects on the back-analysis of neglecting the curvature force and approximating the curvature in the friction force.

As proposed by Peruzzetto et al. (2018a), for each set of parameters, the flow front position and velocities were computed for different thickness thresholds. However they derived the RMS only from the differences between observed and modeled velocities, at the chainages (i.e. horizontal distance from the source of the landslide) where measures were done. Thus, they do not take into account possible errors on these positions. This is particularly critical for the velocity measurement at the onset of the flow, when it is accelerating: a slight increase in chainage leads to sharp flow front velocity increase. For this reason, Peruzzetto et al. (2018a) did not take into account the first observed velocity in their RMS computation. This is not acceptable if we want to investigate the influence of curvature effects, as we can expect them to be highest at the beginning of the flow, when the flow enters the channel. Therefore, we use here a different method to compute the RMS.

We first compute μ_y, σ_y, the mean and standard deviations of the N observed velocities v_i (that is, the y coordinates of crosses in Figure 2.F.2 a). Similarly, μ_x, σ_x are the mean and standard deviations of the chainages x_i where these velocities were measured (that is, the x coordinates of crosses in Figure 2.F.2 a). We thus have a set of standardized observed data

$$X_i = \frac{x_i - \mu_x}{\sigma_x}, \qquad Y_i = \frac{v_i - \mu_y}{\sigma_y}. \tag{2.126}$$

For each simulation and chosen thickness threshold, the simulated flow front velocity v^s is given by a function f of the chainage x, that can be numerically estimated by interpolation. Similarly, the standardized flow front velocity $Y = (v^s - \mu_y)/\sigma_y$ is given by a function F of the standardized flow front position $X = (x - \mu_x)/\sigma_x$. We can thus compute the distances d_i between the observations (X_i, Y_i) and the graph $Y = F(x)$. The relative RMS is then computed as

$$RMS = \frac{1}{N} \sum_i d_i. \tag{2.127}$$

Comparing the results of the inversion for the rheological parameters with and without the curvature force (respectively, Figure 2.F.2 b and d), we see that neglecting the curvature force increases the uncertainty. The inverted parameters are nevertheless comparable. Comparing now the inverted flow front velocities,(Figure 2.F.2 c), as expected, the most significant differences are at the onset of the flow. As in the synthetic case without friction, the flow bounces forth and back on the channel walls, leading to a velocity increase that is less smooth than in the reference case. Further downstream, velocities are nevertheless similar.

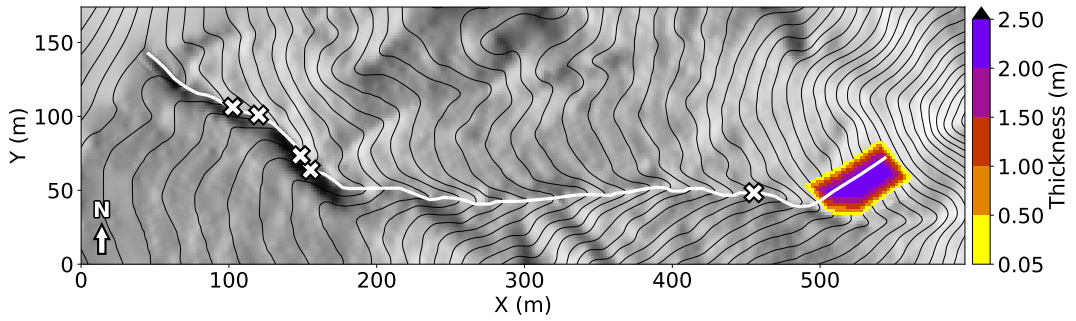

Figure 2.F.1: 2008 Yu Tung Road debris flow topography and initial mass. The white curve is the thalweg of the channel, along which chainage is measured (see Figure 2.F.2). White crosses are locations where the flow front velocity was measured. The contour interval is 5 m.

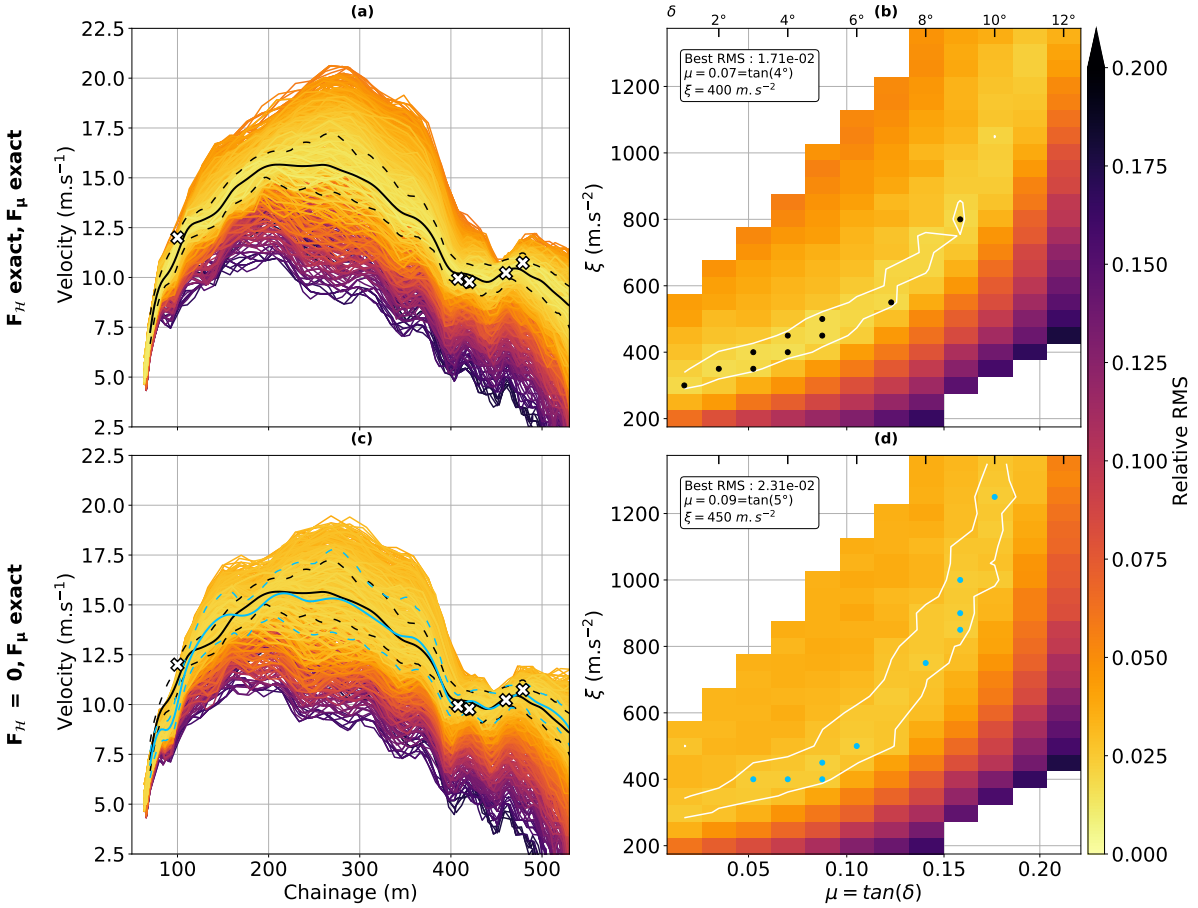

Figure 2.F.2: Simulations of the 2008 Yu Tung debris flow, with curvature forces (a and b) and without curvature forces (c and d), with a Voellmy rheology. For each pair of parameters (μ, ξ), position of the flow is derived for different thickness thresholds (5 to 40 cm, with a 5 cm step). The resulting flow front velocity is plotted against chainage (a and c). Curve color gives the relative RMS between observed (white crosses) and simulated velocities. The RMS averaged over all thresholds is given in (b) and (d). The best ten pairs of parameters are indicated by points (bigger dots indicate a relative RMS smaller than 1.9%. The cyan and black solid curves (a and c) are the mean flow front velocities for these parameters, respectively with and without curvature forces. Dashed curves are the minimum and maximum velocities, with the same color code.

Chapter 3

Thin-layer models for debris avalanches hazard assessment

Context

The previous chapter focused on demonstrating the importance of a rigorous methodology to derive the thin-layer equations. We will now investigate how thin-layer models can be used in practice at the field scale when few data are available to constrain simulations parameters and simulations scenarios. In such situations, the objective is not to derive precise hazard maps because the associated uncertainties are not easy to quantify. Instead, we aim at quantifying the main characteristics of the gravitational flow for a set of realistic simulation scenarios, after model calibration on documented events. Simulation scenarios are constrained by aggregating geological, geophysical and geomorphological data. This allows in particular to identify the most exposed areas and provide stakeholders with a first approximation of expected flow thicknesses, velocities and dynamic pressure.

Our first case study is the Soufrière de Guadeloupe volcano (Martinique, Lesser Antilles). Due to its current hydrothermal unrest and a long record of partial dome collapse, it is important to investigate the consequence of the debris avalanche produced by such an event, if it were to happen again. Although simulations are not easy to constrain due to incomplete data, the propagation of the avalanche is relatively easy to simulate (taking into account, of course, the simplified assumptions of the thin-layer model) because it is a single event, with an instantaneous initiation (in a first approximation at least). The situation is more complex in the Prêcheur river, our second case study, as it will be shown in Chapter 4.

The work on the Soufrière de Guadeloupe volcano was initiated in 2014 during a part-time research internship at the IPGP, while I was a student at MINES ParisTech. It was completed at the beginning of my PhD, and is the subject of a paper published in 2019:

- **Peruzzetto, M.**, Komorowski, J.-C., Le Friant, A., Rosas-Carbajal, M., Mangeney, A., and Legendre, Y.. *Modeling of Partial Dome Collapse of La Soufrière of Guadeloupe Volcano: Implications for Hazard Assessment and Monitoring.* Scientific Reports 9, no. 1 (2019).

In this Chapter we reproduce this article, from Section 3.1 to Section 3.5. The associated abstract is given page 94. Appendix 3.A is a Supplementary material of the article.

In Chapter 4, we will investigate if SHALTOP can be used in an even more empirical way to model debris flows, though we are outside the theoretical validity frame of SHALTOP equations. In the same perspective, I have been more broadly involved in landslide modeling at the field scale, in various geomorpholigcal contexts. In particular, the study

- Poulain, P., Le Friant A., Mangeney, A., Viroulet, S., Fernández Nieto E.D., Castro Diaz M., **Peruzzetto, M.**, Bouchut, F., and Grandjean, G. *Submarine Granular Flows and Generated Tsunami Waves: From Laboratories Experiments to Numerical Simulations of Montagne Pelée Flank Collapses.* Journal of Geophysical Research: Earth Surface, submitted.

investigate the possibility to use empirically SHALTOP to model submarine gravitational flows. Laboratory expriments are first considered, with granular flows that are either dry, immersed or that enter water. A real case scenario is then considered, with the propagation of historical massive debris avalanches originating from Montagne Pelée volcano (Martinique, Lesser Antilles) on land and in the sea. Results are compared to simulations with the HYSEA shallow-water model (Synolakis et al., 2009; Macías et al., 2015; González-Vida et al., 2018). This model is based on the work of Fernández-Nieto et al. (2008) and explicitely takes into account the fluid and granular layers. However, it does not model accurately topography curvature effects. This study shows that both model reproduce rather well deposits, but fail to model the dynamics of the flow.

SHALTOP was also tested in a non terrestrial context. The paper

- Guimpier, A., Conway, S.J., Mangeney, A., Lucas, A., Mangold N., **Peruzzetto, M.**, Pajola M., et al. *Dynamics of Recent Landslides (<20 My) on Mars Insights from High-Resolution Topography on Earth and Mars and Numerical Modelling.* Planetary and Space Science, submitted.

uses SHALTOP to model the deposits of Martian landslides. Geomorphological observations are coupled to numerical simulations to investigate the propagation processes of three landslides. Two of them present geomorphological characteristics of dry rock avalanches and can be modeled with SHALTOP and a frictional rheology for dry granular flows. This rheology fails to reproduce the deposits of the third landslide which indicates that it may be associated to different mass wasting processes, as confirmed by geomorphological evidence. This event has indeed similar characteristics to those of mudflows on Earth. Thus, this study contributes to better understanding gravitational processeses on Mars.

Abstract

Over the past 9,150 years, at least 9 flank collapses have been identified in the history of La Soufrière of Guadeloupe volcano. On account of the volcano's current unrest, the possibility of such a flank collapse should not be dismissed in assessing hazards for future eruptive magmatic as well as non-magmatic scenarios. We combine morphological and geophysical data to identify seven unstable structures (volumes ranging from 1×10^6 m^3 to 100×10^6 m^3), including one that has a volume compatible with the last recorded flank collapse in 1530 CE. We model their dynamics and emplacement with the SHALTOP numerical model and a simple Coulomb friction law. The best-fit friction coefficient to reproduce the 1530 CE event is $\tan(7°) = 0.13$, suggesting the transformation of the debris avalanche into a debris flow, which is confirmed by the texture

of mapped deposits. Various friction angles are tested to investigate less water-rich and less mobile avalanches. The most densely populated areas of Saint-Claude and Basse-Terre, and an area of Gourbeyre south of the Palmiste ridge, are primarily exposed in the case of the more voluminous and mobile flank collapse scenarios considered. However, topography has a prominent role in controlling flow dynamics, with barrier effects and multiple channels. Classical mobility indicators, such as the Heim's ratio, are thus not adequate for a comprehensive hazard analysis.

Contexte

Dans le chapitre précédent, nous avons montré qu'une méthodologie rigoureuse est nécessaire pour établir les équations d'écoulement en couche mince. Nous allons maintenant voir comment elles peuvent être utilisées, en pratique, à l'échelle du terrain quand relativement peu de données sont disponibles pour contraindre les paramètres et les scénarios de simulation. Dans de telles situations, l'objectif n'est pas d'obtenir des cartes d'aléas précises, parce que les incertitudes associées ne sont pas aisées à quantifier. Ainsi, vous voulons plutôt quantifier les principales caractéristiques de l'écoulement gravitaire pour une gamme de scénarios de simulations réalistes, après avoir calibré le modèle sur un événement passé. Les scénarios de simulation sont définis grâce à l'agrégation de données géologiques, géophysiques et géomorphologiques. Cela permet en particulier d'identifier les zones les plus exposées, et de fournir aux collectivités et autres parties prenantes une première estimations des épaisseurs, vitesses et pressions dynamiques.

Notre premier cas d'étude est la Soufrière de Guadeloupe, dans les Petites Antilles. Compte tenu de la réactivation hydrothermale du volcan et de la mise en évidence de déstabilisations passées, il est important d'évaluer les conséquences d'une potentielle future déstabilisation. Même si les simulations se sont pas faciles à contraindre, la propagation de l'avalanche de débris reste relativement facile à modéliser parce qu'il s'agit d'un événement unique, initié de manière instantanée. La situation est plus complexe pour la rivière du Prêcheur, comme nous le verrons dans le Chapitre 4.

Ce travail sur la Soufrière de Guadeloupe a été initié en 2014 pendant un stage de recherche à mi-temps à l'IPGP, pendant que j'étais étudiant à MINES ParisTech. Il a été finalisé au début de ma thèse, et a donné lieu à un papier publié en 2019 :

- ***Peruzzetto, M.**, Komorowski, J.-C., Le Friant, A., Rosas-Carbajal, M., Mangeney, A., and Legendre, Y.*. Modeling of Partial Dome Collapse of La Soufrière of Guadeloupe Volcano : Implications for Hazard Assessment and Monitoring. *Scientific Reports 9, no. 1 (2019).*

*Nous reproduisons cet article dans ce chapitre, de la Section 3.1 à la Section 3.5. Le résumé anglais (*abstract*) est donné page 94. L'appendice 3.A est une ressource supplémentaire (*Supplementary materials*) associée à l'article.*

Dans le Chapitre 4, nous verrons si SHALTOP peut être utilisé de manière encore plus empirique pour modéliser des laves torrentielles, bien que ce phénomène soit théoriquement hors du cadre de validité des équations. Dans la même perspective, j'ai été plus largement impliqué dans des études modélisant des déstabilisations gravitaires, dans des contextes géomorphologiques variés. En particulier, l'étude

- *Poulain, P., Le Friant A., Mangeney, A., Viroulet, S., Fernández Nieto E.D., Castro Diaz M., **Peruzzetto, M.**, Bouchut, F., and Grandjean, G.* Submarine Granular Flows and Generated Tsunami Waves : From Laboratories Experiments to Numerical Simulations of Montagne Pelée Flank Collapses. *Journal of Geophysical Research : Earth Surface, submitted.*

teste la possibilitié d'utiliser SHALTOP (toujours empiriquement) pour modéliser des écoulements gravitaires sous-marins. Des expériences de laboratoire sont dans un premier temps considérées, avec des écoulements granulaires secs, immergés ou entrant dans l'eau. Un cas d'étude réel est ensuite étudié, avec la propagation d'avalanches de débris massives de la Montagne Pelée en Martinique (Petites Antilles), sur terre puis sous la mer. Les résultats sont comparés à ceux

du code d'écoulement en couche mince HYSEA (Synolakis et al., 2009 ; Macías et al., 2015 ; González-Vida et al., 2018). Ce code, basé sur les travaux de Fernández-Nieto et al. (2008), prend explicitement en compte la présence d'une couche liquide et d'une couche granulaire, mais ne décrit pas la topographie aussi précisément que SHALTOP. Les deux modèles parviennent à reproduire relativement bien les dépôts des écoulements, mais sont moins précis pour la dynamique.

SHALTOP a aussi été testé pour des glissements de terrain sur d'autres planètes que la Terre. Le papier

- *Guimpier, A., Conway, S.J., Mangeney, A., Lucas, A., Mangold N.,* ***Peruzzetto, M.****, Pajola M., et al.* Dynamics of Recent Landslides (<20 My) on Mars Insights from High-Resolution Topography on Earth and Mars and Numerical Modelling. *Planetary and Space Science, submitted.*

utilise SHALTOP pour modéliser les dépôts de trois glissements de terrain martiens. Ces simulations sont couplées à des observations géomorphologiques pour étudier les processus de propagation de ces glissements de terrain. Deux d'entre eux présentent des caractéristiques géomorphologiques d'avalanches de blocs, et peuvent en effet être simulés avec SHALTOP et une rhéologie frictionnelle adaptée à des écoulements gravitaires secs. Au contraire, cette même rhéologie ne permet pas de modéliser les dépôts du troisième glissement, ce qui indique que d'autres processus sont associés à sa mise en place. Cela est d'ailleurs confirmé par des marqueurs géomorphologiques semblables à ceux de coulées de boue sur terre. Ainsi, cette étude contribue à mieux comprendre les processus gravitaires sur Mars.

Résumé

Au cours des 9150 dernières années, au moins 9 déstabilisations de flanc ont été identifiées dans l'histoire du volcan la Soufrière de Guadeloupe. Compte-tenu de son activité actuelle, l'éventualité d'une nouvelle déstabilisation de ce type doit être prise en compte pour de futurs épisodes d'éruptions magmatiques ou non-magmatiques. Nous associons des données géomorphologiques et géophysiques pour identifier sept structures instables (volumes allant de 1×10^6 m^3 *à* 100×10^6 m^3 *, dont une qui a un volume compatible avec la dernière déstabilisation de 1530 CE. Nous modélisons la dynamique et les dépôts des avalanches de débris générées avec SHALTOP, et une simple loi frictionnelle de Coulomb. Le coefficient de friction permettant de reproduire l'événement de 1530 CE est* $\tan(7°) = 0.13$*. Cela suggère que l'avalanche de débris s'est transformée en lave torrentielle, ce qui est confirmé par la texture des dépôts cartographiés. Différents coefficients de friction sont testés pour étudier des avalanches moins riches en eau, et donc moins mobiles. Les zones les plus densément peuplées de Saint-Claude et Basse-Terre, et un quartier de Gourbeyre au sud du Plateau du Palmiste, sont exposées principalement par les avalanches de débris les plus volumineuses et les plus mobiles. Toutefois, la topographie joue un rôle primordial et contrôle fortement la dynamique de l'avalanche, avec des barrières topographiques et de multiples chenalisations. Des indicateurs de mobilité classiques, comme le ratio de Heim, ne sont donc pas suffisants pour réaliser une étude complète de l'aléa gravitaire.*

3.1 Introduction

3.1.1 La Soufrière of Guadeloupe volcano

The Guadeloupe archipelago is located in the northern part of the Lesser Antilles arc that resulted from subduction of the North and South American plates under the Caribbean plate. This process initiated volcanism about 40 Ma ago (Bouysse et al., 1990) . Activity of the inner arc in the last 3 Ma built seven volcanic complexes on the island of Basse-Terre (Guadeloupe), progressing from north to south (Boudon, 1988; Komorowski et al., 2005; Samper et al., 2009; Ricci et al., 2017).

La Soufrière of Guadeloupe is an andesitic active volcano. It belongs to the 0.445 Ma old Grande Découverte-La Soufrière volcanic complex (Boudon, 1988; Komorowski et al., 2005) and is located about 2 km north of the town of Saint-Claude where about 10 000 people live (Figure 3.1). Successive eruptions and erosion phases built a complex and steep landscape (see Figure 3.1 for the following geographic names). To the south and south-west, old massive lava flows (Parnasse Plateau, Palmiste plateau) and eruptive centers (Morne Goyavier, La Citerne, Morne Graine Verte, Gros Fougas) partially protect inhabited areas. They are cut by numerous ravines, such as the Ravine de la Citerne and the Ravine Blanche. Three main rivers have their source in the vicinity of La Soufrière volcano: Le Galion and Rivière Noire flow south-west twoards the cities of Saint-Claude and Basse-terre, and the Rivière du Grand Carbet heads east.

At least 15 Holocene magmatic eruptions (9 lava dome eruptions and 6 explosive plinian to sub-plinian eruptions) have been identified. Phreatic and hydrothermal activity is also recurrent, along with partial edifice collapses. Over the last 9,150 years, at least 9 debris-avalanches occurred, mainly to the south-west, and reached a distance of 9-15 km from the dome (Komorowski et al., 2005; Boudon et al., 2007; Komorowski, 2008; Legendre, 2012). The last magmatic eruption, in 1530 CE, started with a partial flank-collapse of $80 \pm 40 \times 10^6$ m^3. It then produced sub-plinian tephra fallout, a lava dome, and pyroclastic density currents from column and dome collapse (Legendre, 2012; Komorowski, 2008; Boudon et al., 2008; Komorowski et al., 2008). In addition, recent studies have shown that a small magmatic eruption occured in 1657 $\pm$ 20 years Cal. CE (Legendre, 2012). Since 1635 CE, 6 phreatic explosions have been witnessed (Feuillard et al., 1983; Boudon, 1988; Komorowski et al., 2005; Rosas-Carbajal et al., 2016). The most recent and violent one took place in 1976-1977 and led to the evacuation of more than 70 000 people (Feuillard et al., 1983; Boudon, 1988; Komorowski et al., 2005; Hincks et al., 2014). It may have been triggered by a small intrusion of magma that did not reach the surface (Feuillard et al., 1983; Villemant et al., 2005; Boichu et al., 2011; Villemant et al., 2014).

La Soufrière is monitored by the Guadeloupe Volcanological and Seismological Observatory (OVSG-IPGP), and has shown over the last two decades an increasing unrest (Komorowski et al., 2005; Villemant et al., 2014; Moretti et al., 2018; Moretti et al., 2020b). Shallow seismicity has been progressively increasing, as has the temperature of some acid-sulfate thermal springs (Villemant et al., 2005; Villemant et al., 2014; Moretti et al., 2018; Moretti et al., 2020b). Fumarolic activity has also strengthened, leading to a partial restriction of access to the dome in 1999 (Komorowski et al., 2005). In February and April 2018, three seismic swarms mainly composed of hybrid volcano-tectonic earthquakes released a total seismic energy of about 90 GJ (OVSG-IPGP, 2018a; OVSG-IPGP, 2018b; Moretti et al., 2018; Moretti et al., 2020b). Such an energy release had not been measured for 40 years. Furthermore, near-field deformations, including inflation (3-7 mm/year) and flank basal spreading (7-10 mm/year), are recorded (OVSG-IPGP, 2018a; OVSG-IPGP, 2018b; Moretti et al., 2018; Moretti et al., 2020b).

The past history of La Soufrière volcano of Guadeloupe, its structure, its deformation, its well-developed hydrothermal system, and the current activity constitute factors that favor a future

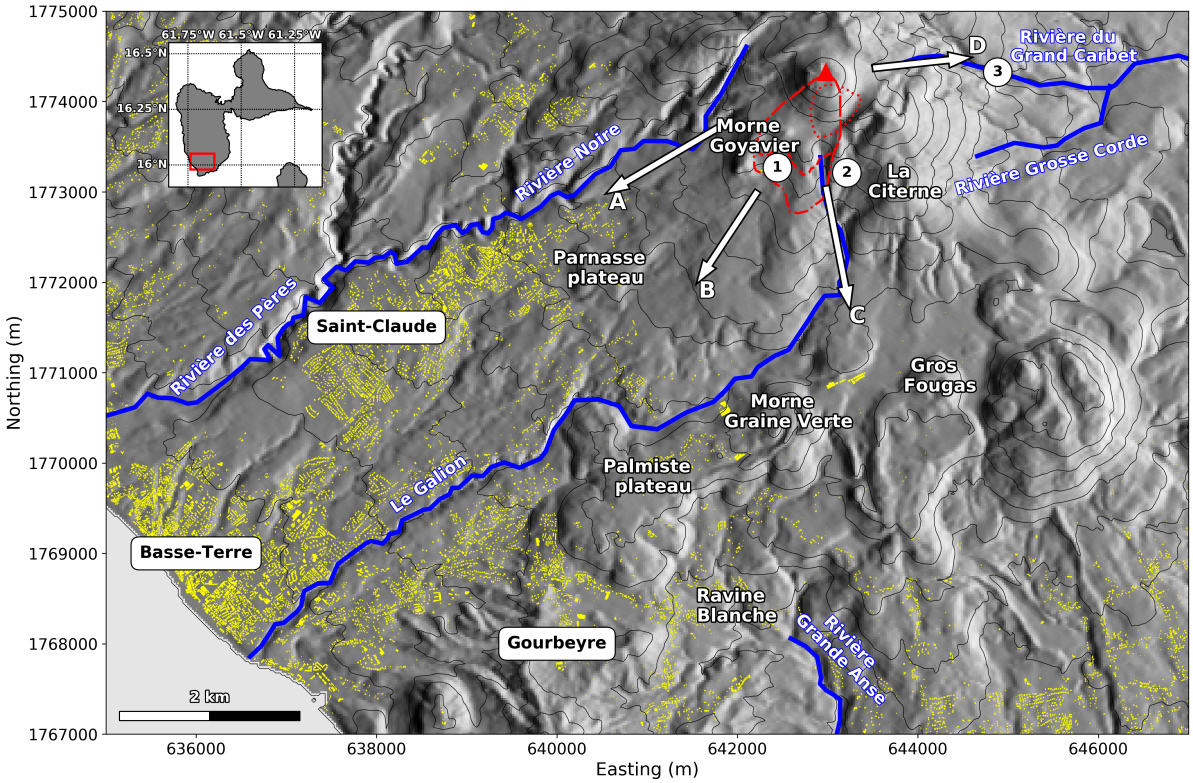

Figure 3.1: Rivers and main topographic features around La Soufrière of Guadeloupe volcano (red triangle), along with the three main cities (Saint-Claude, Basse-Terre and Gourbeyre). The upper left insert features the Guadeloupe island, with the red rectangle matching the extent of the map. ① Ravine des Bains Jaunes, ② Ravine de la Citerne, ③ Second Carbet waterfall. Arrows A, B, C and D identify the main flow pathways discussed in the main body of the text. Yellow patches are buildings (data from IGN BDAlti). The lateral extent of some initial unstable volumes is displayed with the red lines. Dashed-dotted line: *topA2* and *midA2* scenarii ; dashed line: *topA1_inf* and *topA1_sup* scenarii ; dotted line: *dolomieu* scenario. The DEM is from IGN BDTopo, coordinates: WGS84, UTM20N. The contour interval is 100 m.

instability, as observed on many other volcanoes (Harnett et al., 2019). Thus, we are concerned with the consequences of slope failure involving the current lava dome. Instability could be significantly enhanced as a result of magma or hydrothermal pressurisation (Voight, 2000), intense volcanic seismicity, a strong local-to-regional earthquake (e.g. 21 st November 2004 Mw=6,3 earthquake (Feuillet et al., 2011)), or extreme rainfall (Casita-style collapse (Vries et al., 2000)). Such failure could trigger rock avalanches or debris avalanches depending on material water content (Hungr et al., 2014). Mixing of hydrothermal fluids (Rosas-Carbajal et al., 2016; Komorowski et al., 2005) with the rock avalanches could promote their transition into mobile debris flows if they become saturated and are channelised in ravines. This would significantly enhance their mobility and would engender major risks to population, infrastructure and network, depending on the volume of collapsed material. To address this problem, we investigated different scenarios based on the current geological and geophysical knowledge of La Soufrière of Guadeloupe volcano.

3.1.2 Dome structure and fluid circulation

Thorough geological surveys have investigated the eruptive history of La Soufrière volcano (Komorowski et al., 2005; Komorowski, 2008; Boudon et al., 2008; Legendre, 2012). The current dome of La Soufrière (Figure 3.2) volcano is composed both of andesite lava and pyroclastic deposits (Boudon et al., 2008; Komorowski et al., 2008). These have been altered over centuries by fluid circulation (Salaün et al., 2011), and have an average bulk density of 1800 kg/m^3 (Brothelande et al., 2014).

Using self-potential measurements, resistivity tomography and density muon radiography, several studies over the last decades have shown the extensive structural and textural heterogeneity of the dome (Nicollin et al., 2006; Nicollin et al., 2007; Lesparre et al., 2012; Coutant et al., 2012; Lesparre et al., 2014; Brothelande et al., 2014; Rosas-Carbajal et al., 2016; Rosas-Carbajal et al., 2017). Since the last magmatic event, successive phreatic eruptions have led to the creation of numerous fractures (Figure 3.2) that constitute major structural discontinuities favouring the circulation of meteoric and acid hydrothermal fluids (Villemant et al., 2014). The dome is thus divided between dense and relatively unaltered areas, and more fragile parts with active fumaroles and hydrothermal fluid circulation, especially in the south-east of the dome (Nicollin et al., 2006; Lesparre et al., 2014).

Perched reservoirs have been identified (Lesparre et al., 2014; Rosas-Carbajal et al., 2016), including one just beneath the fractures opened during the 1976-1977 eruption (Feuillard et al., 1983). This reservoir is the source of fumaroles located along these fractures, and of two acid ponds. It may also be involved in the massive water resurgence that occurred in 1976-1977 and in previous phreatic and hydrothermal historical eruptions (Komorowski et al., 2005; Rosas-Carbajal et al., 2016). The presence of a basal hydrothermalised layer has long been inferred (Nicollin et al., 2006; Nicollin et al., 2007). The self-potential positive anomaly in the south-west basal part of the dome identified in previous studies (Brothelande et al., 2014) can be interpreted as structural evidence of the hydrothermal activity linked to the basal layer. Recent 3D electrical tomography (Rosas-Carbajal et al., 2016) confirms the presence of highly conductive regions inside the dome linked to fluid reservoirs and to the circulation of hot, acidic fluids. The most prominent feature is a massive, listric, conductive body beneath the south-west part of the dome, sloping to the south, with inferred conductivity values higher than 0.1 S.m^{-1} (A1, orange area in Figure 3.3). It contains a well defined sub-region with conductivity higher than 1 S.m^{-1} (A2, red area in Figure 3.3) starting under the lava dome summit and Tarissan pit, descending south and ending horizontally at the base of the dome where several thermal springs are active in the upper Galion River (Figure 3.2). This fluid-saturated and mechanically weakened area

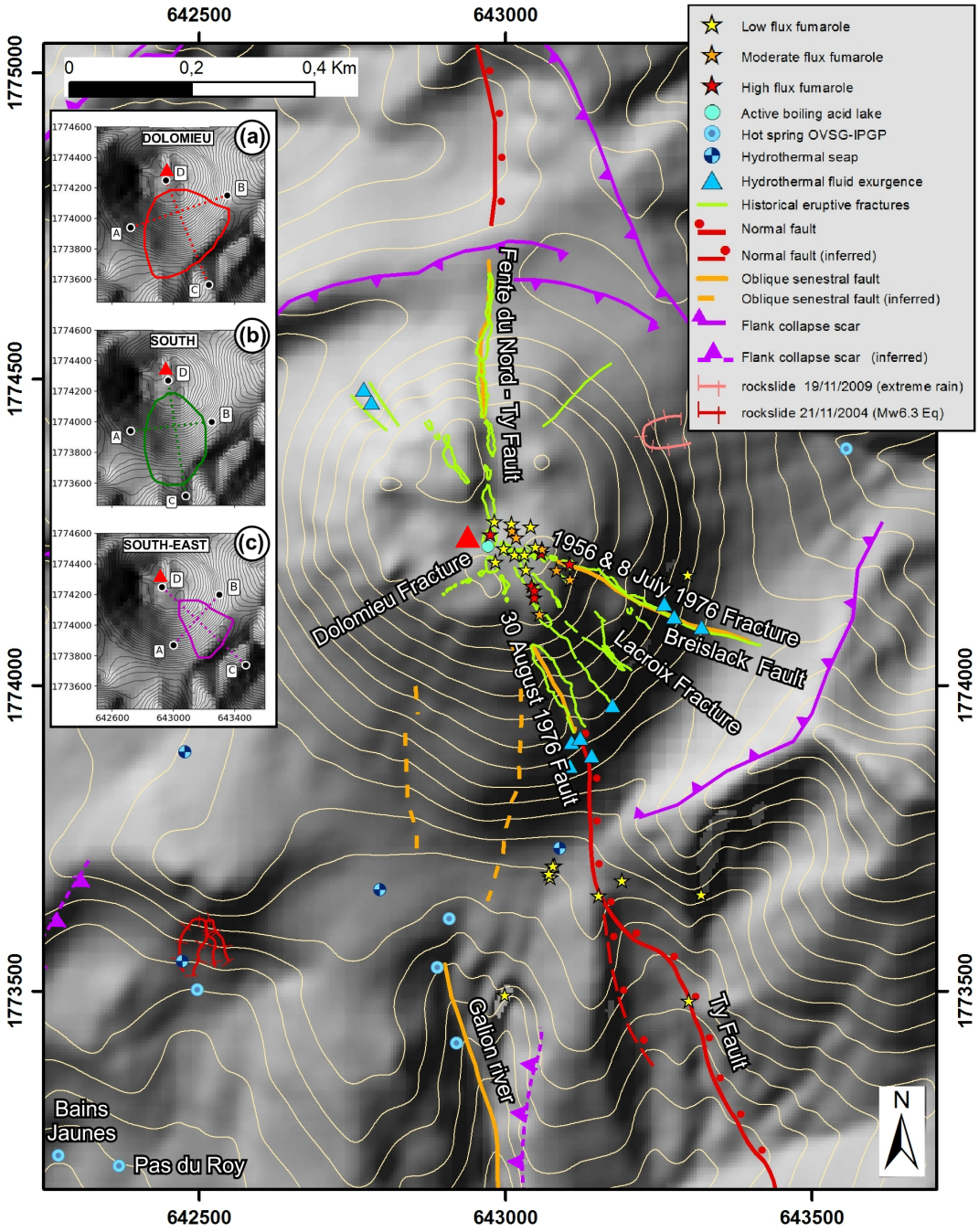

Figure 3.2: La Soufrière of Guadeloupe lava dome. Main structures of the lava dome and surface manifestations of the active hydrothermal system are displayed. Inserts: (a), (b) and (c) are the collapse structure outline for the *dolomieu*, *south*, *south-east* scenarios respectively (Figure 3.4). The red triangle is a reference for the center of the dome (Tarissan crater). The DEM is from GeoEye Ikonos 2005-11-25 acquired image processed by Latitude Geosystems, the map was created with the Arcgis software, coordinates: WGS84, UTM20N. The contour interval is 25 m.

can be related to the trend of the SW flank of the dome, that has been shown, by continuous monitoring, to be moving horizontally to the south above the conductive bodies at about 7-10 mm/year (OVSG-IPGP, 2018a; OVSG-IPGP, 2018b; Moretti et al., 2018; Moretti et al., 2020b). We interpret it as basal flank spreading over a decollement surface (Rosas-Carbajal et al., 2016; OVSG-IPGP, 2018a; OVSG-IPGP, 2018b; Moretti et al., 2018; Moretti et al., 2020b). We are concerned that this basal spreading could trigger shallow or deep-seated landslides (Morgan and McGovern, 2005). The geometry and intrinsic mechanical weakness of these fluid-saturated areas suggest they might be relevant candidates for unstable regions in case of massive partial dome collapse. Indeed, the presence of such a low strength layer at the base of the dome likely contributes to the inherent instability of the edifice. (Komorowski, 2008; Lesparre et al., 2012; Reid, 2004; Rosas-Carbajal et al., 2016). This hypothesis may be supported by the history of Holocene edifice collapse and systematic emplacement of debris avalanches to the south and south- west (Komorowski et al., 2005; Le Friant et al., 2006; Boudon et al., 2007; Komorowski, 2008; Legendre, 2012), that is, in the same direction as the listric, highly conductive bodies A1 and A2.

Along with this active hydrothermal system, the dome is affected by several tectonic active faults (Figure 3.2): in particular the Ty fault runs through the dome from the south-east to the north (Feuillet et al., 2002; Mathieu et al., 2013). The repeated measurement of the width of the 30^{th} August 1976 fracture and of the Fente du Nord (northern section of the Ty fault), using caliper measurements on a 3D metal rod fissurometer, has demonstrated a subsidence and sinistral movement of a few millimetres over the last 35 years on either side of the Ty fault (Rosas-Carbajal et al., 2016; OVSG-IPGP, 2018a). Although the amplitude remains moderate, on the order of 3-10 mm/year (OVSG-IPGP, 2018a; Moretti et al., 2018; Moretti et al., 2020b), these data confirm the potential structural instability of the dome.

3.1.3 Collapse scenarios

The stability of volcanic edifices has been thoroughly studied since the dramatic Mount St Helens flank collapse in 1980, but is often hard to assess correctly due to the lack of geotechnical data (Voight, 2000). Stability is classically studied with Limit Equilibrium Methods, with Finite Element (Schaefer et al., 2013) or Finit Difference (Hürlimann et al., 2000; Apuani et al., 2005) numerical schemes. In our case, however, such an analysis is complex due to the lack of data. We therefore define the collapse scars with geometric, geological and geophysical constraints only.

A review of the phenomena associated with 3 and perhaps 4 of the historical non-magmatic hydrothermal eruptions indicates that small collapses within hydrothermally active areas of the dome were associated with small laterally-directed explosions and with rock avalanche flows, with a runout of 1-2 km (Komorowski et al., 2005; Hincks et al., 2014; Rosas-Carbajal et al., 2016). Given the current instability conditions of the dome as well as the current unrest conditions, this scenario of a relatively small destabilization is the most critical and urgent scenario to investigate and to model. However, a more catastrophic destabilization, involving the basal hydrothermal layer, should not be excluded, as it is consistent with past and more voluminous events associated with magmatic eruptions of the last 10 000 years at La Soufrière (Komorowski et al., 2005; Komorowski, 2008; Legendre, 2012).

We thus consider 7 scenarios and summarize their characteristics in Table 3.1. We first constrain 4 deep-rooted collapse geometries with the main conductive bodies A1 and A2 (Figure 3.3, Rosas-Carbajal et al., 2016). Their lateral extent matches the extent of the A1 body. Their longitudinal profiles feature different shapes: *topA1_sup* (48×10^6 m^3) follows the top of the A1 conducting body, *topA1_inf* (53×10^6 m^3) is similar but displays a flatter profile, *topA2* (93×10^6 m^3) is constrained by the top of the A2 body, and *midA2* (110×10^6 m^3) cuts through A2.

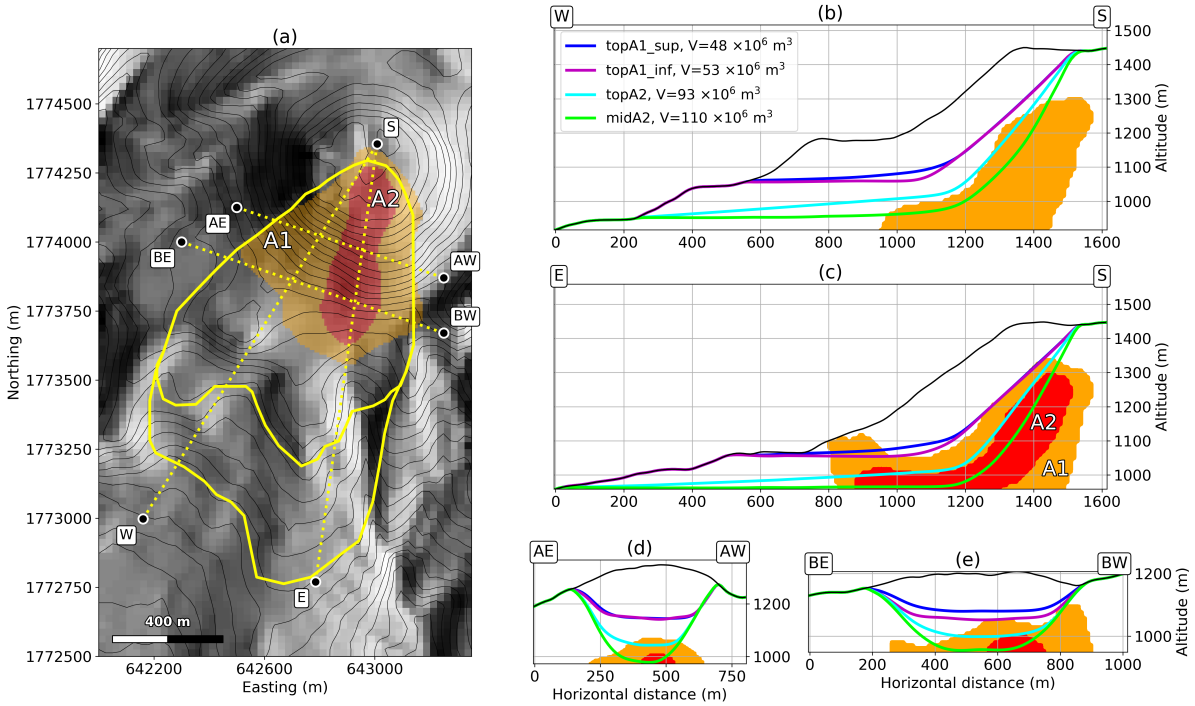

Figure 3.3: Collapse geometries of deep rooted scenarios. The inner yellow contour in (a) is the extent of *topA1_sup* and *topA1_inf* scenarios, the outer yellow contour is the extent of *topA2* and *midA2* scenarios. In (b), (c), (d), (e), longitudinal and transverse cross-sections of the initial (black line) and post-collapse (colored lines) topographies are given. The A1 (Rosas-Carbajal et al., 2016) conducting body (orange area) and A2 (Rosas-Carbajal et al., 2016) conducting body (red area) are seen from above in (a), and within cross-sections in (b), (c), (d) and (e). Cross-sections extents and directions are given by the corresponding letters S, W, E, AE, AW, BE, BW in (a). The DEM is from IGN BDTopo, coordinates: WGS84, UTM20N. The contour interval is 20 m.

We then consider 3 superficial geometries for unstable regions with volumes ranging from 1 × 10^6 m^3 to 10 × 10^6 m^3 (Figure 3.4). The *south-east* scenario (1.1 × 10^6 m^3) is one of the most plausible scenario as it lies entirely within the area showing the current fumarolic unrest, between the 30^{th} August 1976 fault (southern limit), and the 1956 - 8^{th} July 1976 eruptive fractures (northern limit). They are controlled by oblique sinistral fault motion on the Ty and Breislack faults respectively (Figure 3.2). The *south* scenario (7.1 × 10^6 m^3) extends from the Lacroix fracture to a hypothetical structure linking the Dolomieu fracture to the positive self-potential anomaly identified in previous studies (Brothelande et al., 2014) and discussed previously. The *dolomieu* scenario (9.7 × 10^6 m^3) shares this western limit, but goes further to the east to the 1956 - 8th July 1976 eruptive fractures.

3.1.4 SHALTOP numerical model

In order to simulate the emplacement of the resulting debris avalanche we solve the shallow-water equations, with the main assumptions being that the avalanche is homogeneous and that its thickness is much smaller than its characteristic length. Several numerical models exist to solve these equations, such as Volcflow (Kelfoun and Druitt, 2005) and DAN3D (Hungr and McDougall, 2009), which have been both used to model volcanic flank collapse (Kelfoun and Druitt, 2005; Sosio et al., 2012). RAMMS (Christen et al., 2010; Christen et al., 2012) and r.avaflow (Mergili

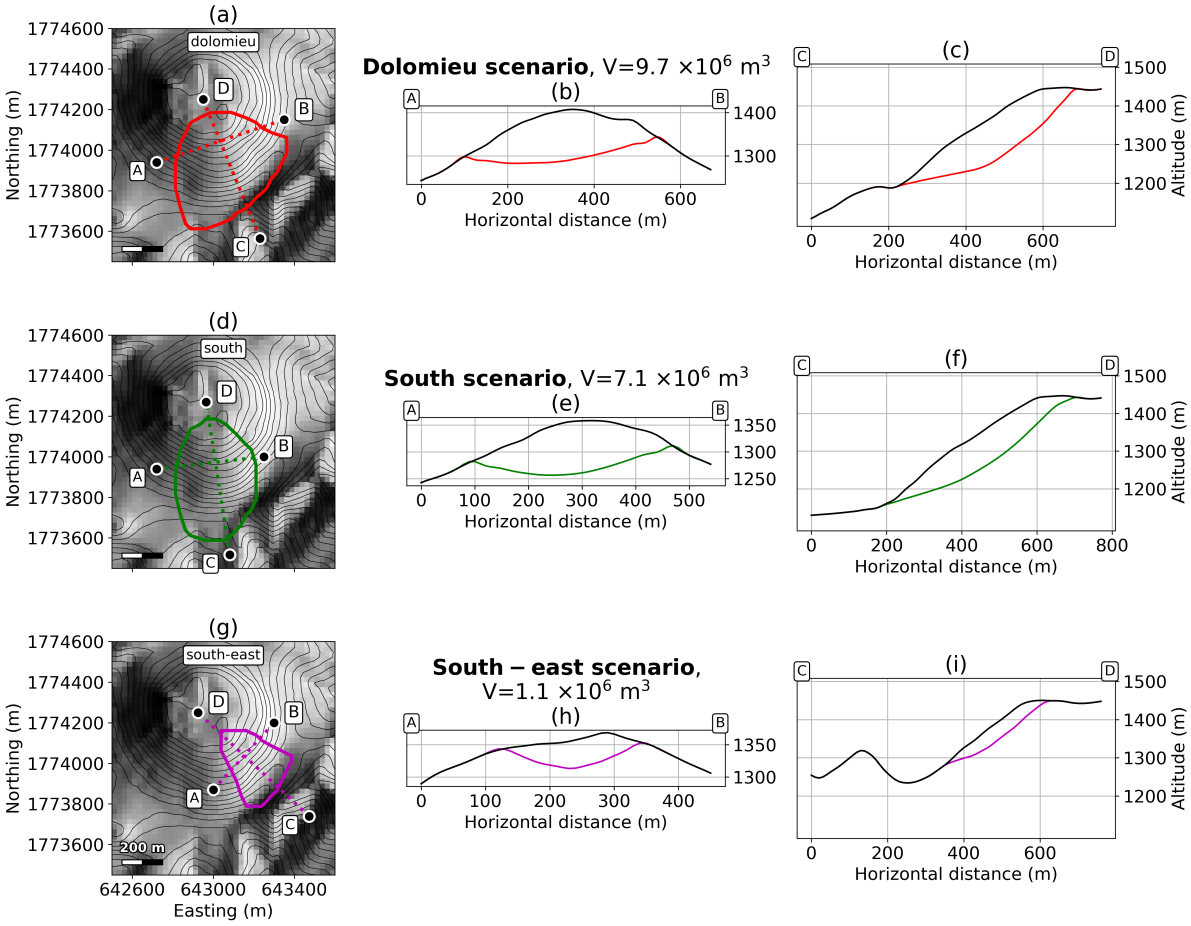

Figure 3.4: Collapse geometries of superficial scenarios. (a), (d) and (g) respectively display the extent of *dolomieu*, *south* and *south-east* scars. (b) and (c), (e) and (f), and (h) and (i) are crossections of the initial (black line) and post-collapse (colored line) topographies, respectively for *dolomieu*, *south* and *south-east* scenarios. Cross-sections extents are indicated by the letters A, B, C, D. The DEM is from IGN BDTopo, coordinates: WGS84, UTM20N. The contour interval is 20 m.

Scenario name	***south-east***	***south***	***dolomieu***	***topA1_sup***	***topA1_inf***	***topA2***	***midA2***
INITIAL CONDITIONS CHARACTERIZATION							
Scar geometry	superficial			deep-seated			
Most likely forcing	Intense rainfall, earthquake, phreatic eruption			magmatic eruption			
Relative probability of occurrence	high			low			
Volume ($\times 10^6$ m^3)	1.1	7.1	9.7	48	53	93	110
Proportion in A1 **Proportion in A2**	0%			1% 0%	1.5% 0%	8% 0.5%	11% 2.5%
Empirical $\mu_{\mathbf{eff}}$ $\delta_{\mathbf{eff}}$	0.34 18.6°	0.29 16.4°	0.29 16.0°	0.25 14.3°	0.25 14.2°	0.24 13.6°	0.24 13.4°
SIMULATION RESULTS							
Best-fit for the 1530 CE deposits	-			-		$\delta = 7°$	-
Material trapped in the scarp	no			yes			
Large lateral spreading of the flow	no	if $\delta \leq 10°$		if $\delta \leq 10°$			
Flow reaches Basse-Terre	no			if $\delta = 7°$			
Flow reaches coast	no			no		if $\delta = 7°$	
Flow reaches Saint-Claude	no	if $\delta \leq 10°$		if $\delta \leq 10°$			

Table 3.1: Main characteristics and results of the different simulated scenarios. The proportion of the volume contained in A1 without A2, and in A2, is given in percentage. μ_{eff} is computed following the Lucas law (Lucas et al., 2014) $\mu_{eff} = V^{-0.0774}$ where V is the volume of the unstable material and $\mu_{eff} = tan(\delta_{eff})$. In the part of the table "simulation results", δ is the friction angle needed in the simulations to have the result described in the first column.

et al., 2017) numerical models are also commonly used to model debris avalanches and debris flows. In our study we used the SHALTOP numerical model (Bouchut et al., 2003; Bouchut and Westdickenberg, 2004; Mangeney et al., 2007b) that has already been tested on several natural cases (Moretti et al., 2012; Lucas et al., 2014; Brunet et al., 2017) and experiments (Mangeney et al., 2007b). It describes a continuous and homogeneous granular flow over a 3D topography. The equations are depth-averaged and numerically solved by taking into account the spatial and temporal variations of the flow thickness and mean velocity, as well as topography curvature. The model calculates the flow thickness in the direction normal to the topography as well as the two-dimensional depth-averaged flow velocity. Processes that would lead to density variations, such as expansion, contraction or incorporation of air and water, are dismissed. Bed erosion is also neglected. Finally, we use a frictional rheology to model the interaction between the flow and the topography, as it has been proven to reproduce the main features of natural landslides (Lucas et al., 2014; Kuo et al., 2009; Moretti et al., 2015). Furthermore, a previous benchmark of rheological laws Sosio et al. (2012) concluded that the frictional rheology yields better results than Bingham or Voellmy rheologies for modeling large volcanic landslides. In depth-averaged models with friction rheologies, the empirical friction coefficient $\mu_S = tan(\delta)$, with δ the friction angle, can be seen as a phenomenological representation of the dissipation during the flow (Mangeney et al., 2007b). It can be constant or depend on the flow thickness and velocity, as for instance in the Pouliquen law (Pouliquen and Forterre, 2002). We choose to a use constant friction as it has proved to produce conclusive results (Sosio et al., 2012), and limits the number of unknown parameters.

For each scenario, simulations are run with various friction angles. We first use a value of 7° that best reproduces the deposits of the 1530 CE event (see following section), and is consistent with previous simulations of dome collapse of La Soufrière of Guadeloupe (Le Friant et al., 2006). This friction angle is typical of debris-flow modeling (Moretti et al., 2015). It thus corresponds to a highly mobile and mechanically weak material, as characterized for instance the historical non-magmatic volcanic debris avalanches that occurred at Ontake in 1984 (Endo et al., 1989; Voight and Sousa, 1994) and Bandai San in 1888 (Siebert et al., 1987; Nakamura and Glicken, 1988). In order to investigate drier and less mobile debris avalanches, we also use an empirical relation (Lucas et al., 2014) relating the friction angle to the volume involved. For our scenarios, the resulting friction angle ranges from 13° to 20°. Finally, we have also considered intermediate values of 10° and 12° to investigate the sensitivity of the simulated deposit to the friction angle.

3.2 Results

3.2.1 1530 CE collapse equivalent (*topA2* scenario)

The 1530 CE debris avalanche volume was estimated at 80±40 × 10^6 m^3 (Komorowski, 2008; Boudon et al., 2008; Legendre, 2012). Its mapped extent, deduced from field observations (Komorowski, 2008; Boudon et al., 2008; Legendre, 2012), is shown in Figure 3.5 with the white dashed line. The estimated volume is consistent with our *topA2* scenario. In order for our modelled scenario to reach the sea like the 1530 CE collapse, we had to use a friction friction angle $\delta = 7°$. In comparison, the friction angle derived from the empirical law of Lucas (Lucas et al., 2014) is $\delta = 13.6°$. However, our best-fit friction angle is in good agreement with the value $\delta = 8°$ that was used to simulate with SHALTOP the debris flow part of the Mount Meager landslide in a previous study (Moretti et al., 2015). The dynamics from our simulation are given in Figure 3.5 and the final deposits in Figure 3.6 (g). Three flow paths are clearly visible (Figure 3.1 and 3.5 e, arrows A, B and C). Geographical references are shown in Figure 3.1.

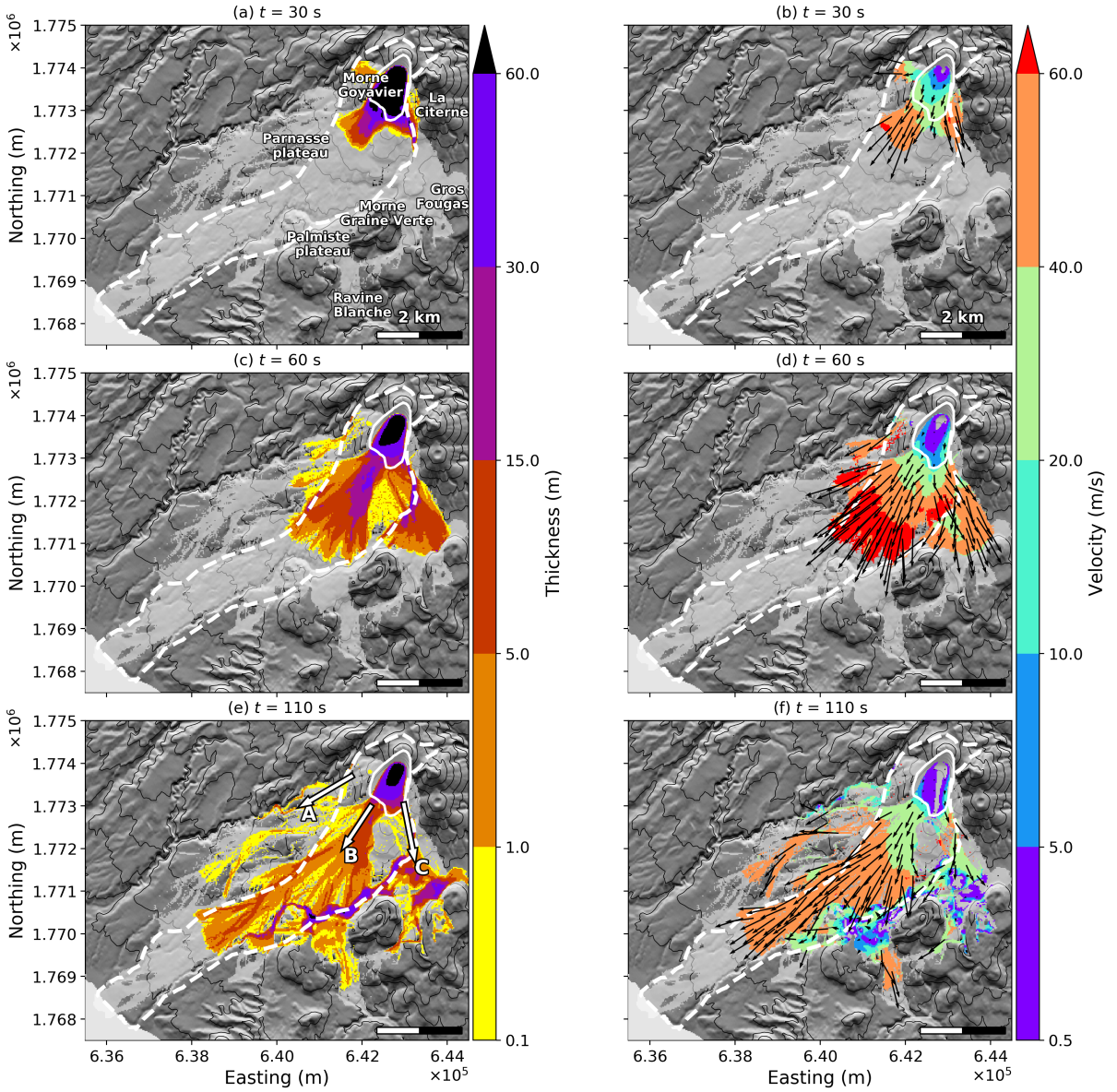

Figure 3.5: *topA2* simulation. Snapshots of flow thickness (a, c, e) and velocity (b, d, f) for the *topA2* scenario and $\delta = 7°$, at t=30 s (a, b), t=60 s (c,d) and t=110 s (e, f). Black arrows give the flow velocity direction. The light grey area features the flow path in the simulation, i.e. the total covered area. The white dashed line is the mapped extent of the 1530 CE collapse deposits (Boudon et al., 2008; Komorowski, 2008; Legendre, 2012). The white plain line is the extent of the initial unstable volume in our simulation. Arrows A, B and C are the main flow directions, as in Figure 3.1. The DEM is from IGN BDTopo, coordinates: WGS84, UTM20N. The contour interval is 100 m.

The first flow path (Figure 3.1 and 3.5 e, arrow A) heads directly south-west between Morne Goyavier and the Rivière Noire ravine. It involves only small thicknesses (less than 1 meter 110 s after collapse, Figure 3.5) but threatens the northern parts of Saint-Claude village. If the 1530 CE collapse had a similar behavior in this area, its thin deposits may have been easily eroded. Indeed, they have never been identified in the field.

The main feature, which is consistent with identified deposits of the 1530 CE event, is the material that spreads from Bain Jaunes (Figure 3.1, ①) towards Basse-Terre (Figure 3.1 and 3.5 e, arrow B). The flow is first partially channelled in the Ravine des Bains Jaunes and adjacent ravines (Figure 3.1, ①). However, because it subsequently encounters no massive topographic barriers apart from the Parnasse lava flow to the north and the Galion ravine to the south, it produces deposits of limited thickness (up to 5 meters) with a large lateral extension. The flow is characterized by high velocities (70 m/s 60 seconds after collapse, 50 m/s 110 seconds after the collapse). The thickness of the distal deposits (up to 5 meters, Figure 3.6 (g)) is, furthermore, in agreement with the deposit thickness observed in the field (see Appendix A). The flow first spreads radially, but after 110 seconds the main flow front, about 500 meters wide, runs on the northern side of Galion River down to the sea which is reached after 200 seconds. This part of the flow is particularly fast and could generate jetted flow as described in the literature (Heim, 1932; Hsu, 1975) in historically observed rock avalanches (sturztroms). Such effects cannot, however, be modeled with SHALTOP, for which the flow is assumed to follow the topography closely.

The rest of the flow (Figure 3.1 an 3.5 e, arrow C) is first channelized in the Galion river and in the Ravine de la Citerne (Figure 3.1, ②), and bounces back and forth between the high walls of the ravines before filling and overspilling it (thickness up to 80 meters). It then spreads radially to the south of La Citerne scoria cone, into an area between the Morne Graine Verte and the Gros Fougas scoria cones further south. 110 seconds after collapse, the associated flow front has almost entirely stopped, except for a small patch that overpasses a notch in the Palmiste plateau, allowing it to flow to the south towards parts of Gourbeyre village. Although no desposits were found here for the 1530 CE event, older deposits have been identified in this area (Komorowski, 2008; Legendre, 2012).

3.2.2 All scenarios

Final deposits for all scenarios are displayed in Figures 3.6 and 3.7 for deep-rooted and superficial collapses respectively, with $\delta = 7°$, $\delta = 10°$ and Lucas friction angles. Results are summarized in Table 3.1. The aforementioned pathways (Figure 3.1, arrows A, B and C) can be identified in all scenarios.

The part of the modeled debris avalanches heading south-west towards Saint-Claude (Figure 3.1, arrows A) does not cross the deep Rivière Noire canyon in any simulation. This natural barrier and the prominent Parnasse lava flow, that forms a massive topographic barrier on the eastern boundary of Saint-Claude thus channel the avalanche flow towards Saint-Claude and the northern quarters of Basse-Terre.

The second flow path (Figure 3.1, arrow B) generates widespread deposits and is visible in all scenarios. For δ=7°, it stops only a few hundreds meters away from the sea in the *topA1_sup* and *topA1_inf* scenarios, while the material enters the sea in *topA2* and *midA2* scenarios. In these four scenarios, still with δ=7°, a small volume overtops the Palmiste plateau in its central part and enters Ravine Blanche.

The third flow path (Figure 3.1, arrow C), generated by the material entering the Galion river, is present in all the scenarios. For friction angles above 10°, the debris avalanche overspills the Galion river but stops between Morne Graine vert and Gros Fougas in all scenarios. Only

for δ=7°, the flow comes to rest against the southern edge of the Palmiste lava plateau in the north-east periphery of Gourbeyre. In the three biggest scenarios, it enters Ravine Blanche.

The last flow path (Figure 3.1, arrow D) is only seen in the *dolomieu* and *south-east* scenarios. This flow is generated by the material released in the active hydrothermal part of the dome between Fracture Lacroix and 8^{th} July 1976 fracture, as only the *dolomieu* and *south-east* scenarios include material in this area. The flow heads towards the east and is first mainly contained in the Rivière du Grand Carbet (Figure 3.1). For δ=7°, it then spreads in a flatter area about one kilometer after the second Chute du Carbet waterfall (Figure 3.1, ③) at the junction with the Grosse Corde River.

3.2.3 Final deposits main characteristics

In Figure 3.8 we summarize the main characteristics of the debris avalanche deposits resulting from the different modelled scenarios. For the seven collapse geometries, of varying volume, and for three friction angles (7°, 10°, 12°), we plot: runout (distance between scar highest point and deposit front), covered area, mobile volume (i.e. material leaving the scarp), Heim's ratio (μ_H) and effective friction coefficient (μ_{eff}). The Heim's ratio (Heim, 1932) is defined as $\mu_H = H/\Delta L'$, where H and $\Delta L'$ are respectively the difference in altitude and horizontal distance between the highest point of the original mass and the lowest point of the deposit. The effective friction coefficient was derived theoretically for a dam-break scenario (Lucas et al., 2014) and is defined by:

$$\mu_{eff} = tan(\theta) + \frac{H_0}{\Delta L}, \tag{3.1}$$

where θ is the mean slope angle along the flow course, H_0 the maximum material thickness at the onset of the collapse and ΔL the length travelled by the flow front (see section Methods).

As expected, lower friction angles involve longer runouts (Figure 3.8 a) and greater deposit areas (Figure 3.8 b). For $\delta = 7°$ a consistent trend can be seen with increasing volume. However for $\delta = 12°$ and $\delta = 10°$, the runout does not significantly vary between the *dolomieu*, *topA1_inf* and *topA1_sup* scenarios, while the deposit area is almost twice as large for *topA1_inf* and *topA1_sup* in comparison to *dolomieu*. This feature highlights the strong control of topography on the emplacement of the debris avalanche deposits. Topographic barriers slow down the flow front in the main flow direction and favor lateral spreading. For the four collapse geometries of largest volume, a significant part of the material remains blocked within the collapse structure due to its almost flat distal basal slope (Figure 3.3 b and c): for *midA2* and $\delta = 12°$, only a volume of 30×10^6 m^3 leaves the structure while more than 100×10^6 m^3 is initially destabilized (Figure 3.8 c). The *topA2* geometry leads to a larger mobile volume even though it is more superficial. As a matter of fact, bigger collapses involve deeper scars, thus expanding the area of the collapse basal surface with a flat slope that cannot be overrun by a pure cohesionless collapse. This hence favors blockage of material within the structure and reduces the truly mobile portion of the collapse volume.

The Heim's ratios of the modelled deposits are systematically lower than effective friction coefficients (Figure 3.8 d). Both overestimate the friction coefficient used in Shaltop. While Heim's ratios seem to reach a constant value for unstable volume bigger than 10×10^6 m^3, effective friction coefficients show a sharp increase for $\delta = 10°$ and $\delta = 12°$. It has been shown that μ_{eff} can be a better approximation of the real friction coefficient (Lucas et al., 2014) for simple coherent landslides but that does not seem to be the case here, for landslides made of multiple flows. These discrepancies illustrate the impossibility of using simple indicators whose theoretical validity stands only for simple coherent landslides, to describe more complex phenomena characterized by multiple channelizations and complex topographies.

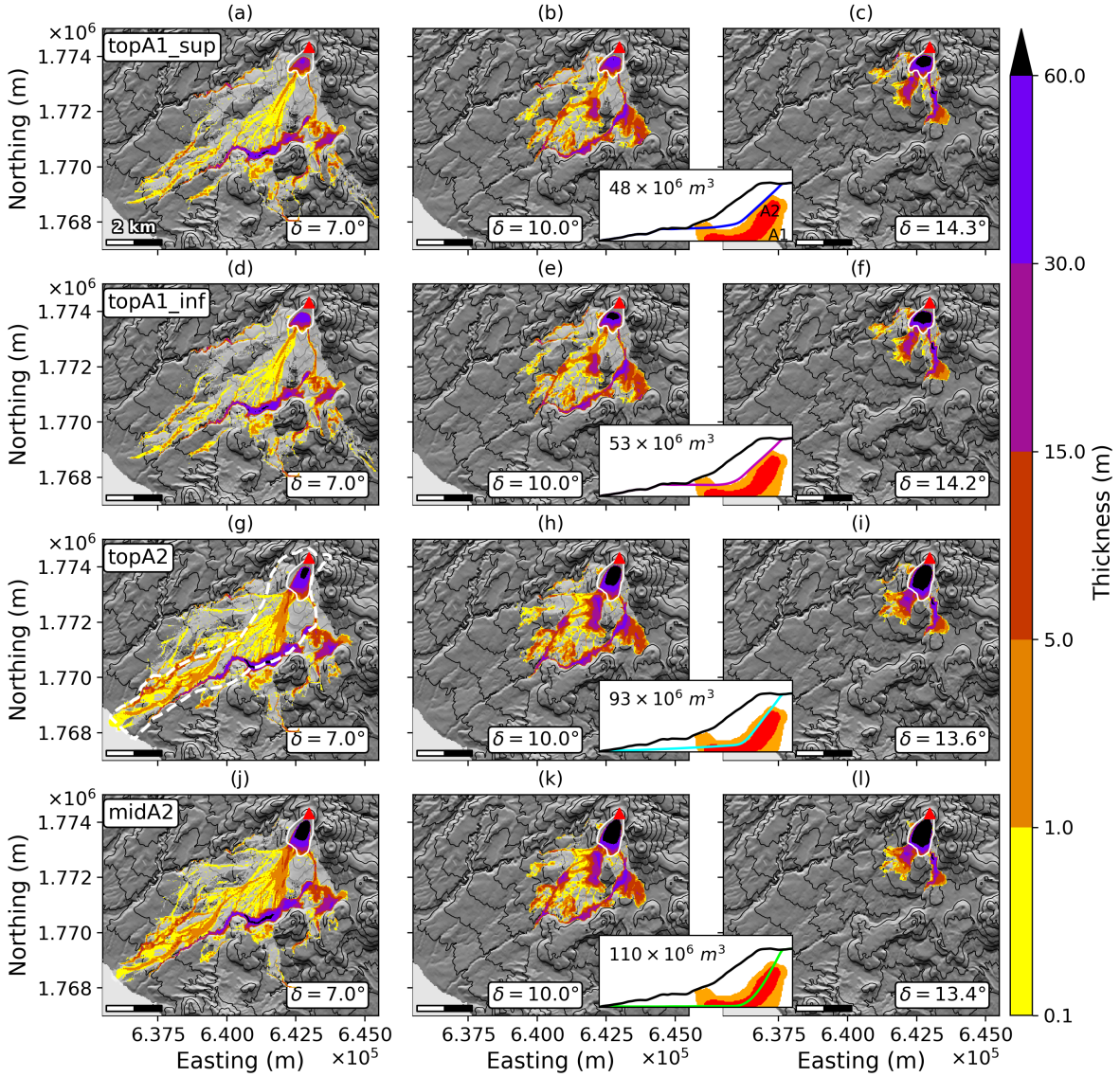

Figure 3.6: Final deposits for deep-rooted scenarios. *topA1_sup* (a-c), *topA1_inf* (d-f), *topA2* (g-i) and *midA2* (j-l) scenarios, with $\delta = 7°$ (a, d, g, j), $\delta = 10°$ (b, e, h, k) and the friction angle derived from Lucas' law (c, f, i, l, Lucas et al., 2014). Colorscale gives thicknesses in meters. The light grey area features the flow path in the simulation, i.e. the total covered area. The white plain line is the extent of the initial unstable volume. The red triangle marks the summit of La Soufrière volcano. The insert in each row displays the unstable volume and a profile of the scarp for each scenario: it is a copy of Figure 3.3c where only the relevant scar has been kept. The DEM is from IGN BDTopo, coordinates: WGS84, UTM20N. The contour interval is 100 m.

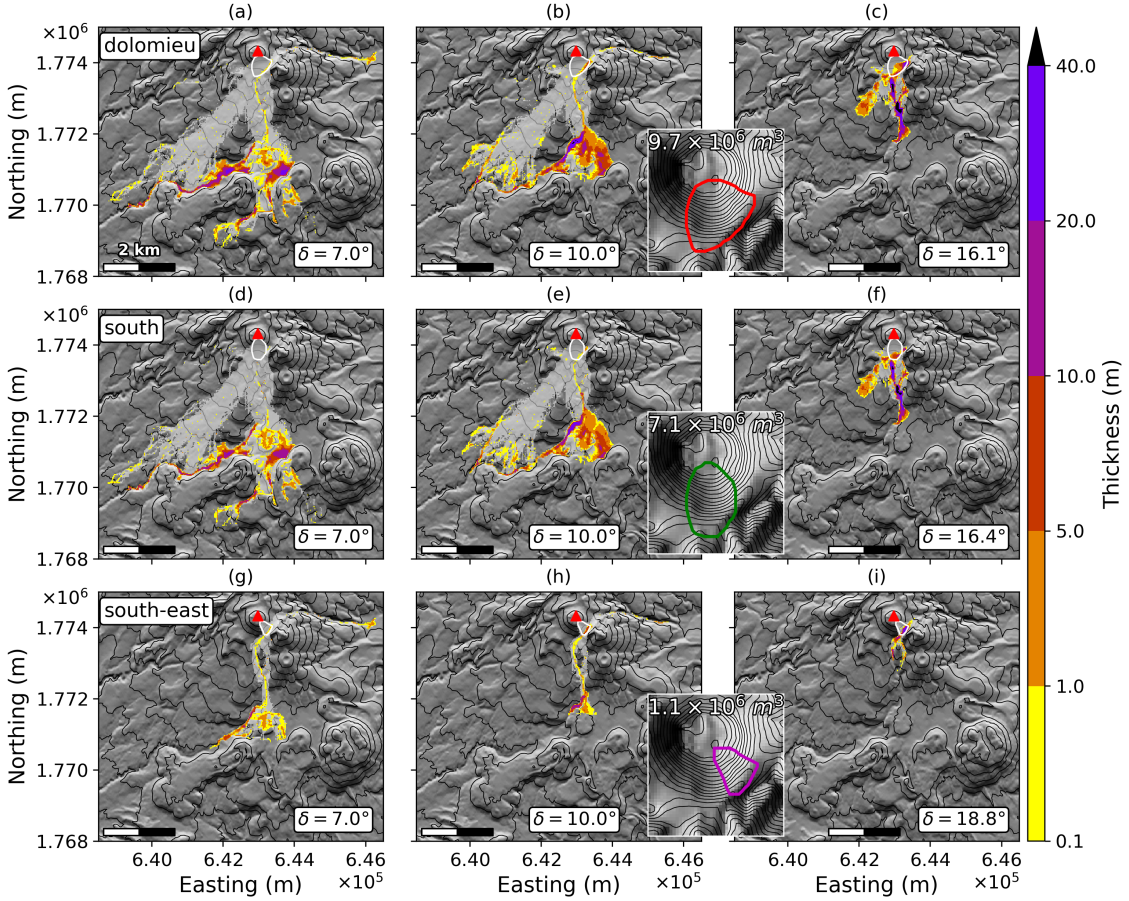

Figure 3.7: Final deposits for the superficial scenarios. *dolomieu* (a-c), *south* (d-f) and *south-east* (g-i) scenarii, with $\delta = 7°$ (a, d, g), $\delta = 10°$ (b, e, h) and the friction angle derived from Lucas' law (c, f, i, Lucas et al., 2014). The light grey area features the flow path in the simulation, i.e. the total covered area. The white plain line is the extent of the initial unstable volume. The red triangle marks the summit of La Soufrière volcano. The inserts in each row are close-ups on the dome showing the extent of the initial unstable volume and its volume for each scenario: they are copies of Figures 3.4 a, d and g. The DEM is from IGN BDTopo, coordinates: WGS84, UTM20N. The contour interval is 100 m for the main maps, and 20 m for the inserts.

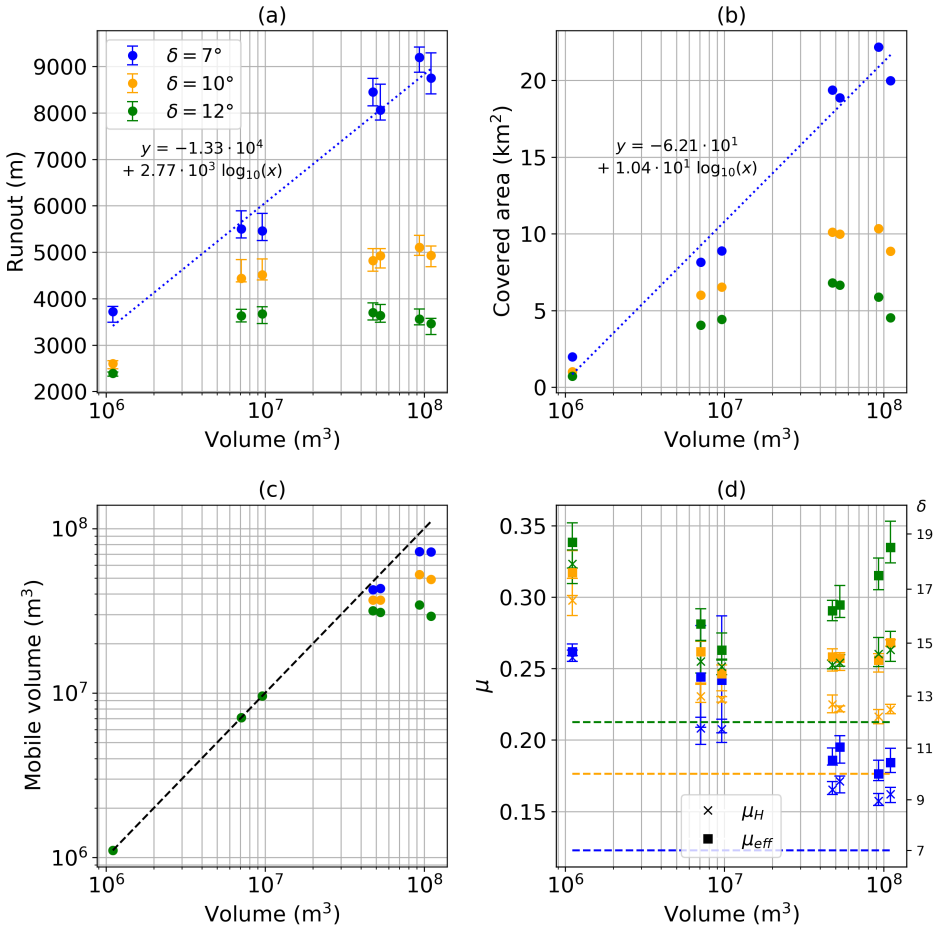

Figure 3.8: Main characteristics of debris avalanche deposits. Tested scenarios are categorized by unstable volume, with $\delta = 7°$ (blue), $\delta = 10°$ (orange) and $\delta = 12°$ (green). (a) Runout, i.e. maximum distance between the highest point in the scar prior to collapse and flow front. (b) Covered area. (c) Mobile volume, i.e. volume of the material leaving the scar (d) Heim's ratio (crosses) and effective friction coefficient (squares). Values on the right y-axis are the angles δ in degrees, matching μ on the opposite axis, such that $\mu = tan(\delta)$. Colored lines are the friction coefficients matching the tested friction angles. Error bars in (a) and (d) display the maximum, minimum and mean value derived following the methodology presented in the body of the text. The blue dashed lines in (a) and (b) are the best logarithmic fits derived for $\delta = 7°$, with their matching equation indicated on the plots.

3.3 Discussion

In the case of the biggest collapse geometries, the strongly concave post-collapse topographies are associated to important deposit thicknesses. The shallow-water assumption is thus not valid as the thickness is not negligible in comparison to the initial flow extent, and we cannot expect our model to properly describe the initiation phase of the collapse. However, at least two reasons justify the use of shallow-water models. First, full 3D models demand significant computing resources and are time-consuming, while each of our simulations was run in less than 4 hours, which is a major advantage to carry out multiple simulations with various geometries and parameters for risk analysis. Secondly, previous studies have shown that shallow-water models can indeed reproduce real landslide deposits (Lucas et al., 2011; Lucas et al., 2014; Zhao et al., 2014; Brunet et al., 2017; Kuo et al., 2009).

Nevertheless complex topographies can favor threshold effects: for some paths to be taken by the debris avalanches, the scar geometry must have a minimum extent and/or define a minimum destabilized volume. For instance, including the material between the Lacroix and the 1956 - 8th July 1976 fractures in *dolomieu* and *south-east* scenarios enables some material to enter the Rivière du Grand Carbet, while no flow is modelled there in the *south* scenario whose eastern collapse boundary is only a few tens of meters west of Lacroix fracture. The overtopping of Palmiste lava Plateau, observed in the *topA2* scenario and not in the *midA2* scenario, is another example of such a threshold effect.

Whether topographic barriers are crossed or not strongly depends on the volume of mobile material and on the friction coefficient. To illustrate this, simulations were run for the *dolomieu* and *topA2* scenarios with friction angles varying between 7° and 16° (i.e. friction coefficients between 0.12 and 0.29). Their characteristics are shown in Figure 3.9. The *dolomieu* scenario's scar is steep enough to enable all the material to flow (Figure 3.9 c). On the contrary, the truly mobile volume continually decreases in the *topA2* scenario as μ_S increases. For $\mu_S > 0.2 = tan(11.3°)$, the topography constrains the flow: although the mobile volume is bigger in *topA2* than in *dolomieu* scenario, runouts are similar (Figure 3.9 a) and spreading is more important in *topA2* (Figure 3.9 b). For $\mu_S < 0.2$, both scenarios reach a smoother area west of the Palmiste Plateau. However in the *dolomieu* scenario, there is only little mobile material left, so that it becomes blocked in the Galion river and small valleys (Figure 3.7). On the contrary, in the *topA2* scenario enough material is available to prevent confinement and the flow can propagate more easily (Figure 3.6).

Finally, the difference between the friction coefficients μ_S used in the simulations, μ_{eff} and μ_H is clearly seen in Figure 3.9 d. In contrast to the case of landslides that dot not feature multiple channelizations (Lucas et al., 2014), μ_H over-estimates μ_S but for $\mu_S > 0.19 = tan(10.8°)$ the bias is almost constant and seems not to depend on the scenario (Figure 3.9 d).

The values of friction angles to be used in numerical simulation remain subject to debate. Lucas' empirical law (that was derived for almost dry debris avalanches) yielded good fits in other volcanic contexts (Mount St. Helens and Soufrière Hills, Zhao et al., 2014) where seismic data was used to constrain the simulation parameters. However in our case the value $\mu_S = tan(7°)$ used to reproduce an analogue of the 1530 CE event is much lower than the Lucas empirical value of $\mu_{eff} = tan(13.6°)$. This suggests a strong mobility of the debris avalanche that could be explained by the presence of water. Indeed, such a low friction angle ($\delta = 8°$) was needed with the same SHALTOP model to reproduce debris flows (Moretti et al., 2015). This is consistent with the 1530 CE event that is characterized in the field by deposits (Komorowski, 2008; Legendre, 2012) by a well-developed muddy textural facies (Appendix A). The transition between a debris avalanche and debris flow emplacement mechanism occurs about 5 km from the source and about half-way along the total runout distance. Water could thus have a prominent role in controlling

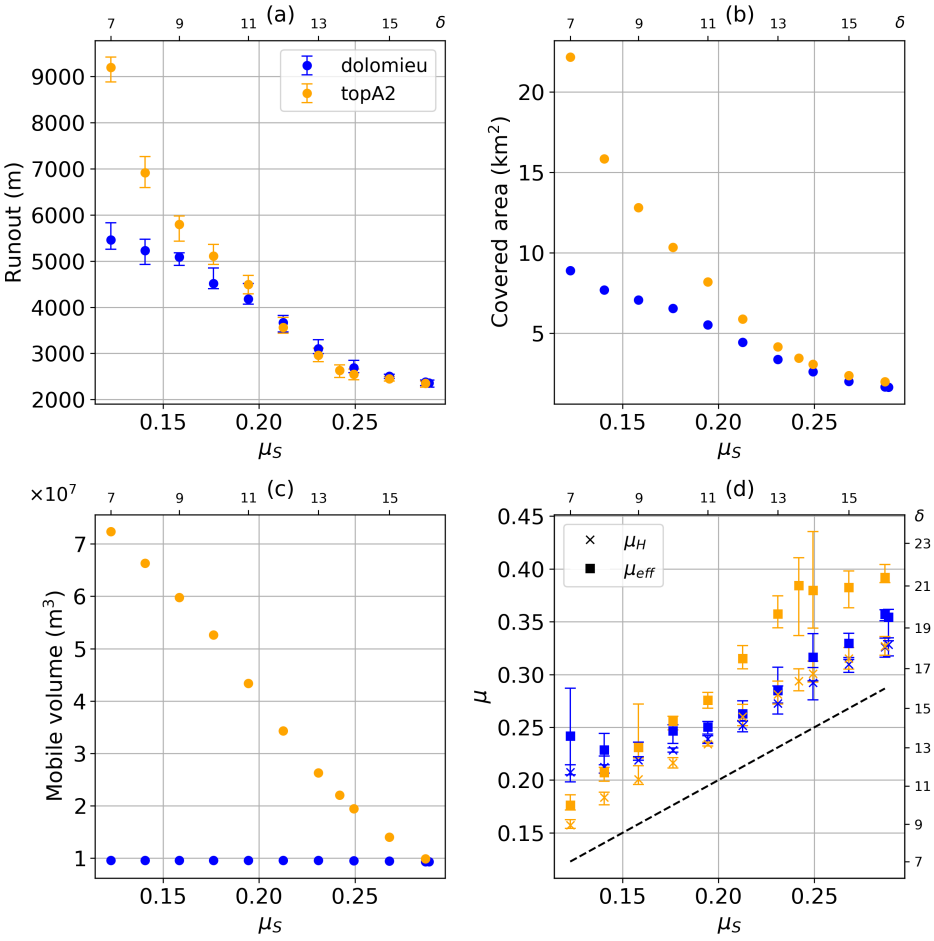

Figure 3.9: Main characteristics of debris avalanche deposits for the *dolomieu* (blue) and *topA2* (orange) scenarios. Varying friction coefficient are tested (from $\delta = 7°$ to $\delta = 16°$). (a) Runout, i.e. maximum distance between the highest point in the collapse structure prior to collapse and flow front. (b) Covered area. (c) Mobile volume, i.e. volume of the material leaving the collapse structure (d) Heim's ratio (crosses) and effective friction coefficient (squares). Values on the right y-axis in (d) and top x-axis are the angles δ in degrees, matching μ on the opposite axis, such that $\mu = tan(\delta)$. Error bars in (a) and (d) display the maximum, minimum and mean value derived following the methodology presented in the body of the text.

the dynamics of future partial flank collapse and debris avalanche mobility, particularly for the deep rooted landslides cutting through the highly conductive fluid-saturated bodies A1 and A2. For instance, more than 13% of the collapsing volume of the *midA2* scenario lies within these bodies (Table 3.1). But there are numerous other sources of water in the La Soufrière of Guadeloupe volcano, such as perched aquifers inside the lava dome (Lesparre et al., 2014), shallow depth reservoirs of hydrothermal fluids (Lesparre et al., 2014; Brothelande et al., 2014; Rosas-Carbajal et al., 2017), depressurized deep rising hydrothermal fluids (Rosas-Carbajal et al., 2016; Lesparre et al., 2012), rivers and extreme rainfall. This is typical of the volcanic context. For instance, the debris avalanche of August 2012 on Tongariro (Procter et al., 2014; Lube et al., 2014) and the 1998 debris avalanche on Casita volcano (Sheridan, 1980; Vries et al., 2000; Scott et al., 2005) both initiated as debris avalanches but later transformed into more mobile and devastating debris flows, mostly in their distal part.

3.4 Conclusion

Our modelling of geologically and geophysically constrained partial collapse scenarios at La Soufrière of Guadeloupe provides key insights on the propagation dynamics and controlling factors of the resulting debris avalanches. Back calibration of the last flank collapse in 1530 CE and field evidence from deposit textures suggest such an event could be highly mobile due to the presence of water in the flow. Multiple simulations of debris avalanches were carried out with various initial geometries constrained by morphological and geophysical data, as well as different friction angles. Four main trends were identified for the flows as they are channelled by the topography, with two different dynamics. Part of the flow fills the ravines and stops quickly while another part reaches open areas where it spreads with high velocities and limited thicknesses. We show that the initial collapse geometry plays a major role in our model in retaining material upslope and thus controlling the volume effectively leaving the collapse structure. For the biggest collapse geometries, friction coefficients below 0.2 (i.e. friction angles below 11°) increase the mobile volume and favor overtopping of topographic barriers by the flow.

In these simulations, the northern and eastern parts of Saint-Claude are the most exposed inhabited areas. They could be impacted even by shallow small-volume partial dome collapse (our dolomieu and south scenarios) if water is incorporated in the debris avalanche, increasing its mobility. In the case of a major dome collapse, the mixing of the altered material with perched ground water and hydrothermal fluids could threaten Basse-Terre, with the propagation of a relatively thin but rapid flow. Gourbeyre is at first sight well protected by the Palmiste plateau but massive collapse and/or mobile flows could threaten its eastern periphery. However, in the most probable event of a small collapse from the most active part of the dome (our *south-east* scenario), the material should be mainly confined in the ravines and impact only remote areas. Nevertheless, all the material accumulated in the ravines could form temporary dams and be easily remobilized as debris flows or mud flows long after the initial landslide, thus endangering urban areas all along the rivers. The Rivière des Pères, the Galion river, the Rivière du Grand Carbet and the Rivière Grand Anse (heading to the south towards Trois Rivières) would be particularly exposed.

Given the current unrest of La Soufrière of Guadeloupe volcano, the work initiated in this study must be continued in order to improve risk assessment associated with a partial dome collapse. In particular, a limit stability analysis would help constrain the unstable volumes in the dome. Numerous simulations randomly sampling a range of model parameters could also be developed to produce probabilistic debris avalanche innundation maps.

3.5 Methodological highlights

3.5.1 Scar geometries

The three superficial collapse structures were constructed using an interface specifically developed for that purpose. Starting from a 25-meter DEM of the intact lava dome, the surface to be modified was defined from geological constraints. The z-value of a series of control points within this surface was then manually modified, the rest being interpolated with the MATLAB TriScatteredInterp function and the natural interpolation method. The collapse structure was then smoothed with a moving average.

The four deep rooted collapse structures were constructed with a similar approach. Control points were given along 5 longitudinal profiles, one being the profile displayed in Figure 3.3c (used as reference). 30 points were then generated for each profile along a Beziers curve passing through all control points. Finally, the 150 resulting points (plus some manually added points to refine the interpolation) were used to interpolate the scar with a multiquadric radial basis function.

In both cases, the thickness of the initial unstable volume was given in each point of coordinates (x, y) by:

$$h = \cos(\theta)(z_{init} - z_{scar}), \tag{3.2}$$

where z_{init} is the altitude of the initial DEM, z_{scar} the altitude of the DEM including the collapse structure, and θ the local slope angle. The volume of destabilized material is computed with:

$$V = \sum_{i,j} (z_{init}(i,j) - z_{scar}(i,j))\, dx\ dy, \tag{3.3}$$

where $dx = dy = 25\ m$ and the indexes (i, j) indicate the position on the 25-meter DEM.

3.5.2 Computation of runout, Heim's ratio and effective friction coefficient

The metrics we use are shown in Figure 3.10. For a given simulation, we first derive the map of the maximum flow thickness for the entire simulation and draw the contour line corresponding to a 10 cm thickness. We then compute the geographical distance $\Delta L'$ to the upper point of the collapse structure (Figure 3.10, point A) along this line and identify all local maximums. We keep only the point with the global maximum distance d_{max}, and all points further than $0.9d_{max}$ (Figure 3.10, points C). We then derive straight profiles along topography from A to C, passing through the lowest point of the collapse geometry (Figure 3.10, point B). Runout (i.e. $\Delta L'$), μ_H and μ_{eff} are computed for all these profiles, yielding a variability estimation that is displayed with error bars in Figures 3.8 and 3.9.

Appendix

3.A Field evidence of the 1530 CE debris avalanche

The field evidence for the 1530 CE debris avalanche of La Soufrière, collected between 1994 and 2008, has been partially discussed in previous works, such as Komorowski (2008), Boudon et al. (2008) and Legendre (2012). Figure 3.A.1 was produced from a compilation and new

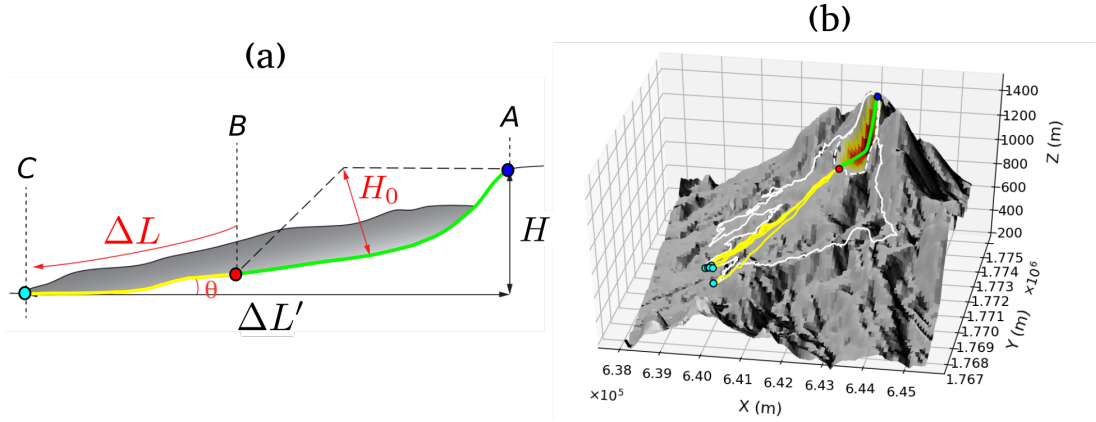

Figure 3.10: Computation of μ_H and μ_{eff}. (a) Landslides metrics in 2D (after Lucas et al., 2014). A (blue point) and B (red point) are respectively the highest and lowest points of the initial mass. C (cyan point) is the flow front position. H_0 is the initial mass maximum thickness. H and $\Delta L'$ are respectively the difference in altitude and horizontal distance between A and C. ΔL is the length traveled by the front flow, i.e. the length of the yellow curve. θ is the mean local slope between A and C, i.e. the mean local slope of the joint yellow and green curves. The Heim's ratio is $\mu_H = H/\Delta L'$, and the effective friction coefficient is $\mu_{eff} = tan(\theta) + H_0/\Delta L$. (b) Landslides metrics in 3D, for the *topA2* scenario with $\delta = 10°$. Color code of lines and points matches (a). The white line is the deposit extent, the dashed white line is the collapse scar extent. Colorscale in the collapse geometry matches the initial mass thickness (from yellow to red). Points A and B are uniquely defined. Points C are chosen as explained in the main body of the text. The DEM is from IGN BDTopo, coordinates: WGS84, UTM20N.

interpretation of these data in terms of location, thickness and textural facies of the identified deposits. The co-existence of deposits showing a typical debris avalanche facies with those showing a muddy debris-flow facies is striking and highlights both the complexity and mobility of the overall flow. Although localized deposits with a debris flow facies were found only 850 meters away from the summit in Ravine Tarade, all other occurrences of debris flow facies are located between a distance of 5.6 km from source in the north-eastern periphery of Basse-Terre and the Caribbean sea. The occurrences of deposits with debris avalanche facies furthest from source are located north of the Palmiste Plateau about 5.6 km from source. The 1530 CE partial edifice collapse may thus initially emplaced a debris avalanche with only localized debris flows in the vicinity of the volcano. After travelling between 3.6 and 5.6 kilometers south-west, it transformed into a massive thick debris flow given its initial elevated water content and reached the sea. A precise comparison with our simulation is complex due to the uncertainty on the initial conditions of the 1530 CE debris avalanche, and on the topography that may have changed since the event. In particular, the 1530 CE debris avalanche deposits seem to be thicker near the mouth of The Galion river than in our simulation. However in the area of Basse-Terre, the orders magnitude of mapped and simulated thicknesses are similar.

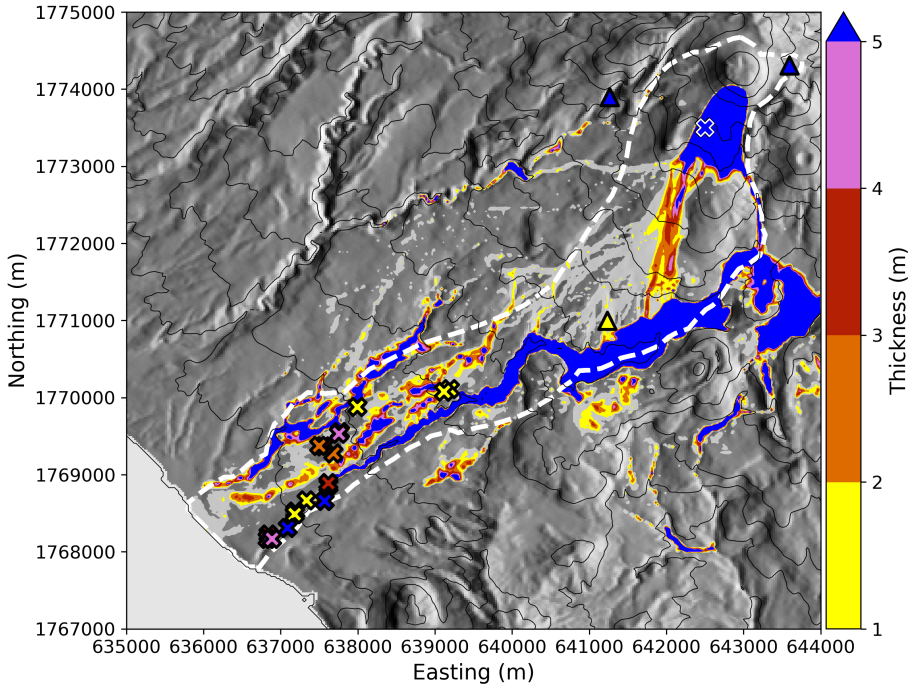

Figure 3.A.1: Comparison between observed and simulated deposits for the 1530 CE debris avalanche. Deposits identified on the field with debris avalanche facies are marked with triangles, and deposits with debris flow facies are marked with crosses. The color of the symbols indicates the thickness of the deposits. The white dashed line is the estimated extent of the deposits. The simulated deposits of the *topA2* scenario with $\delta = 7°$ are displayed with the same colorscale. The light grey area matches the flow path in the simulation. The DEM is from IGN BDTopo, coordinates: WGS84, UTM20N. The contour interval is 100 m.

Chapter 4

Thin-layer models for rock avalanches and subsequent debris flows hazard assessment

Context

In comparison to the Soufrière de Guadeloupe case study, the case of the Prêcheur river (Martinique, Lesser Antilles) is more complex because it combines two different phenomena: and initial rock avalanche from the Samperre cliff, upstream the river, and the remobilization of deposits as debris flows or hyperconcentrated flows (also called lahars in volcanic context). We will try to model them with a single code, SHALTOP, changing only the rheological parameters. Thus, we use SHALTOP empirically to model debris flows, which is in theory outside it validity framework. Given the complexity of modeling precisely such flows, for which the main physical processes may change during propagation, and between the front and the tail of the flow, we focus on high discharge debris flows initiated by instantaneous or very quick remobilization of a debris reservoir. Such events display, presumably, less temporal and spatial rheological variations as they are less diluted along the river. Contrary to potential dome collapse of the Soufrière de Guadeloupe volcano that threaten several cities, in the case of the Prêcheur river stakes are limited to the Prêcheur village, at the mouth of the river. However, the historical recurrence of destructive debris flows makes it important to address this hazard. In 2010, a high-discharge debris flow flooded a quarter of the Prêcheur village, at the mouth of the river. In 2018, a new episode of combined cliff collapses and lahars raised concerns that such a destructive event could occur once again.

The work presented in this chapter results from the combined efforts of the IPGP and BRGM to better characterize the hazards in the river catchment. Both institutions, with the local BRGM antenna and the OVSM (Observatoire Volcanologique and Sismologique de Martinique), are involved in monitoring the river. The OVSM maintains a network of seismic stations used to identify rock avalanches and debris flows, and trigger alarms in the Prêcheur village whenever a significant increase of flow height is detected. Alarms are also triggered by a pendulum system. The BRGM installed cameras that help characterizing the river bed evolution. These data, as well as helicopter flights, are used to help stakeholders understanding hazards and guide risk mitigation. Thus, in 2018, a report from the ONF (Office National des Forêts) focused on lahars, and suggested planning measures to limit overflow hazards in the Prêcheur village (Quefféléan, 2018a). Later on, a report from the BRGM analyzed possible future destabilization scenarios for the Samperre Cliff (Nachbaur et al., 2019). In this perspective, our work can be seen as a

synthetic study to analyze both phenomena (cliff destabilization and high discharge lahars) in a single framework. It will be continued in a post-doc at the BRGM, and will result in a report delivered to local authorities.

The methodology we use for the Prêcheur river here is the same as in the previous chapter, even though it is adapted to the type of available data. We aggregate a wide variety of observations to constrain simulation scenarios and characterize observed events, calibrate the model by back-analysis, and use the results to model a forward-prediction scenario. In comparison to the Soufrière de Guadeloupe case study, more data are actually available (with, for instance, successive topographic surveys), but the phenomena are more complex, such that all available data are necessary to justify the simulation scenarios and hypotheses. We thus use, for instance, granulometric curves to justify the choice of the rheological law. Seismic recordings are also used to estimate the travel time of observed debris flows.

This chapter is the base of an article that was submitted in February 2021 to *Engineering Geology*. Significant modifiations have been included to reduce its length:

- Peruzzetto, M., Levy C., Thiery, Y. , Grandjean G., Mangeney A., LejeuneA.-M., Nachbaur A., et al. *Simplified simulation of rock avalanches and subsequent debris flows with a single thin-layer model. Application to the Prêcheur river (Martinique, Lesser Antilles).* Engineering Geology, submitted.

We give in Figure 4.1 the main questions and problematics that must be tackled in this chapter, when analyzing the sediments transfer from the Samperre cliff to the sea, with the initial rock avalanche, the remobilization of the deposits as lahars, and their evacuation in the sea. Each step (lines in Figure 4.1) is characterized by physical processes (orange boxes), for which modeling solutions must be found (black boxes). We constrain the propagation processes by field work and agregation of existing data, and test numerical solutions for modeling the propagationth with SHALTOP by reproducing past events. We will also estimate, when possible, the volume involved in potential future rock avalanches from the cliff, and lahars (red boxes). Figure 4.1 will be completed at the end of this chapter.

Abstract

In this work, we assess the possibility of modeling a rock avalanche, and the subsequent remobilization of the deposits as a high discharge debris flow, with a single one-phase thin-layer numerical code, SHALTOP. The back-analysis of past events and the construction of a forward prediction scenario are often complex because little quantitative data are available to constrain precisely the simulation set-up and rheological parameters. Using the Prêcheur river and the Samperre cliff (Martinique, Lesser Antilles) as case studies, we focus on extreme events with highest potential impact on populations and infrastructures. We use geological and geomorphological data, topographic surveys, seismic recordings and granulometric analysis to define realistic scenarios and reproduce the main characteristics of documented events. The calibrated rheological parameters are then used to model the emplacement of a possible 1.5×10^6 m^3 cliff collapse, with the Coulomb rheology and a friction coefficient $\mu_S = \tan(14°) = 0.25$. The resulting deposits are remobilized as a high-discharge debris flow with the Coulomb rheology and $\mu_S = \tan(2°)$ or $\mu_S = \tan(3°)$, or with the Voellmy rheology with a turbulence coefficient $\xi = 500$ m s^{-2}. The initial geometry of the reservoir has little impact on the flow dynamics, in particular with the Voellmy rheology. However, a progressive release modeled with a constant source discharge slows down the flow and limits overflows, in comparison to instantaneous releases. By combining different source mechanisms and rheological parameters, our simulations

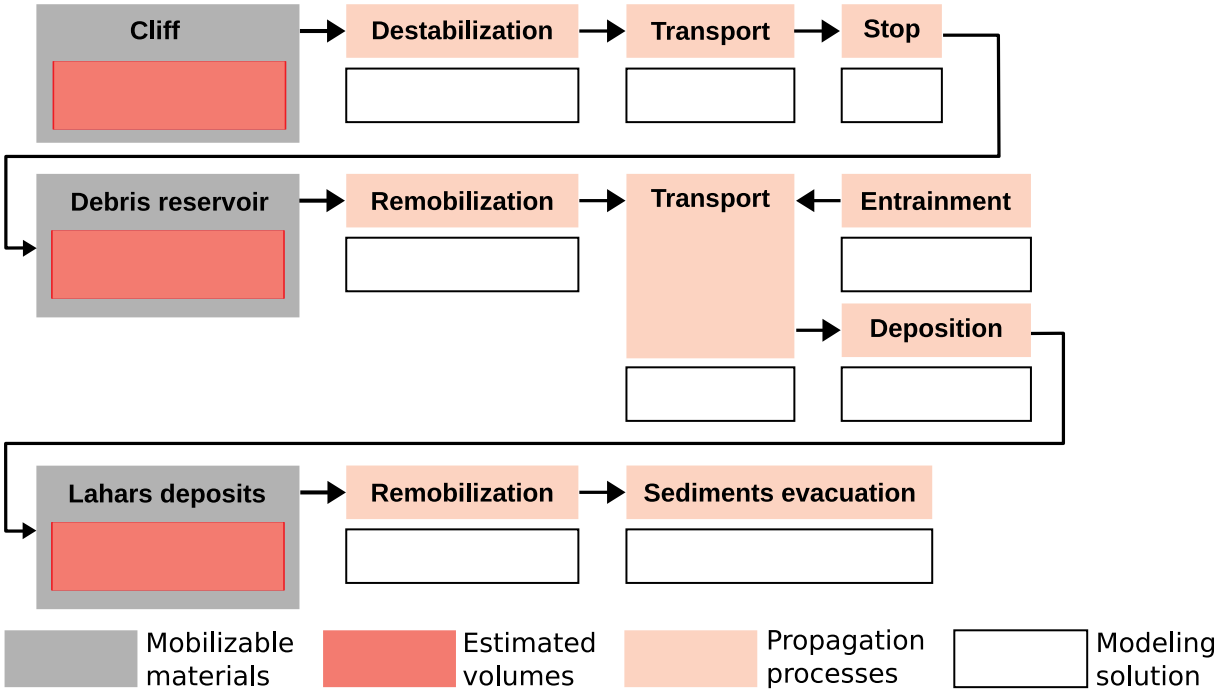

Figure 4.1: Incomplete diagram of sediment transfer processes, from the Samperre Cliff to the sea, along with modeling solutions.

could reproduce empirically the range of flow velocities deduced from seismic recordings for the most important lahars of 2009 and 2010. This study should be completed by two-phase flow thin-layer modeling to investigate the dynamics of hyper-concentrated flows, as well as the influence of erosion and deposition on inundation hazard. Nevertheless, our results already pave the way to improved real-time monitoring and early-warning systems.

Contexte

Par rapport au cas d'étude de la Soufrière de Guadeloupe, le cas de la Rivière de Prêcheur (Martinique, Petites Antilles) est plus complexe car il combine deux phénomènes distincts : une avalanche de blocs sur la Falaise Samperre, en amont de la Rivière, et la remobilisation des dépôts en laves torrentielles ou écoulements hyper-concentrés (aussi appelés lahars en contexte volcanique). Nous allons tenter de les modéliser avec le même code SHALTOP, en changeant seulement les paramètres rhéologiques. Ainsi, nous utilisons SHALTOP en dehors de son cadre de validité théorique. Par ailleurs, compte tenu de la complexité de modéliser de tels écoulements, nous nous concentrons sur des événements extrêmes, c'est à dire des laves torrentielles à fort débit initiées par une remobilisation instantanée ou très rapide du réservoir de débris en pied de falaise. Un tel événement présente, à priori, moins de variabilités spatiales (entre le front et la queue de l'écoulement) et temporelles, car le lahar est moin rapidement dilué dans la rivière. Contrairement à la Soufrière de Guadeloupe qui menace plusieurs villes, les enjeux dans la rivière du Prêcheur sont limités au village du Prêcheur, à son embouchure. Toutefois, la récurrence de laves torrentielles dangereuses rend important l'étude de l'aléa. En 2010, une lave torrentielle a ainsi inondé un quartier du village. En 2018, une nouvelle phase de la déstabilisation de la falaise Samperre a eu lieu, sans, heureusement, provoquer de pertes humaines ou matérielles.

Le travail présenté ici résulte des efforts combinés du BRGM et de l'IPGP pour mieux caractériser les aléas dans le bassin versant du Prêcheur. Ces deux institutions, via l'antenne Martinique du BRGM et l'OVSM (Observatoire Volcanologique et Sismologique de Martinique) sont impliquées dans la surveillance de la rivière et de la falaise. L'OVSM est responsable de la maintenance du système d'alerte, comprenant des géophones et un système pendulaire, qui servent à déclencher une sirène en cas de montée du niveau de l'eau. Grâce au réseau de capteurs sismiques installés sur la Montagne Pelée, l'OVSM détecte également en temps réel les effondrements de la Falaise Samperre. L'installation de caméras à faible fréquence d'acquisition par le BRGM permet de suivre l'évolution du lit de la rivière. Ces données, ainsi que des survols réguliers de la rivière, permettent de mieux caractériser les aléas et de suggérer des orientations pour la gestion des risques. Ainsi, en 2018, un rapport de l'Office National de Fôrets (ONF) s'est concentré sur les lahars et les aménagements envisageables pour limiter les risques de débordement (Quefféléan, 2018a). En 2019, le BRGM s'est lui concentré sur l'identification des mécanismes de déstabilisation de la Falaise et des volumes encore instables (Nachbaur et al., 2019). Cette étude tente de faire une synthèse des deux aléas (avalanche de blocs et laves torrentielles massives) dans un cadre d'étude unifié. Elle sera poursuivie pendant un post-doc au BRGM, qui donnera lieu à un rapport rendu à la DEAL Martinique.

La méthode que nous utilisons pour la rivière du Prêcheur est la même que dans le chapitre précédent, mais elle est adaptée aux types de données disponibles. Par rapport au cas de la Soufrière de Guadeloupe, plus de données sont disponibles (avec par exemple, des relevés topographiques successifs), mais les phénomènes étudiés sont plus complexes. Ainsi toutes les données disponibles sont nécessaires pour justifier les scénarios et les hypothèses de simulation. Par exemple, nous utilisons des analyses granulométriques pour justifier le choix de la loi rhéologique. Des enregistrements sismiques sont également utilisés pour estimer les temps de parcours des laves torrentielles.

Ce chapitre est une première version d'un article qui a été soumis à Engineering Geology *en Février 2021. Des modifications importantes ont été faites pour réduire la taille de l'article :*

- *Peruzzetto, M., Levy C., Thiery, Y. , Grandjean G., Mangeney A., LejeuneA.-M., Nachbaur A., et al.* Simplified simulation of rock avalanches and subsequent debris flows with a single thin-layer model. Application to the Prêcheur river (Martinique, Lesser Antilles). *Engineering Geology, submitted.*

Dans la Figure 4.1, nous identifions les problèmes principaux qui se posent dans ce chapitre pour comprendre les mécanismes de transfert des sédiments, de la Falaise Samperre jusqu'à la mer. Chaque étape (lignes dans la Figure 4.1) est caractérisée par des processus physiques (rectangles oranges) pour lesquels des solutions de modélisation doivent être cherchées (rectangles noirs). Nous identifierons les différents processus à l'aide du travail de terrain et l'agrégation de données déjà existantes, et testerons les solutions numériques en reproduisant un événement passé. Nous estimerons aussi, quand c'est faisable, les volumes impliqués dans de futures avalanches de blocs et laves torrentielles (rectangles rouges). La Figure 4.1 sera complétée à la fin de ce chapitre.

Résumé

Nous évaluons la possibilité de modéliser une avalanche de blocs et la remobilisation des dépôts en de puissantes laves torrentielles, avec un seul code d'écoulement en couche mince, SHALTOP. La calibration du modèle et la construction des scénarios de modélisation prédictifs sont souvent rendues complexes par le manque de données quantitatives. En utilisant la Rivière du Prêcheur et la Falaise Samperre comme cas d'étude, nous nous concentrons sur des événements extrêmes, ayant l'impact le plus important sur les populations et les infrastructures. Nous utilisons des données géologiques et géomorphologiques, des relevés topographiques, des enregistrements sismiques et des analyses granulométriques pour construire des scénarios de simulations réalistes, et reproduire les caractéristiques principales d'événements passés. La calibration des paramètres rhéologiques permet ensuite de modéliser les dépôts d'une potentielle avalanche de blocs de 1.5×10^6 m^3*, avec la rhéologie de Coulomb et* $\mu_S = \tan(14°) = 0.25$*. Ces dépôts sont ensuite remobilisés pour générer une lave torrentielle, avec la rhéologie de Coulomb et* $\mu_S = \tan(2°)$ *ou* $\mu_S = \tan(3°)$*, ou avec la rhéologie de Voellmy et un coefficient de turbulence* $\xi = 500$ $m\ s^{-2}$*. A volume fixé, la géométrie initiale du réservoir a relativement peu d'influence sur la dynamique de l'écoulement, en particulier avec la rhéologie de Voellmy. Toutefois, par rapport à une remobilisation instantanée, une remobilisation progressive (avec un débit source constant) ralentit la propagation et limite les débordements. En combinant différents paramètres rhéologiques et mécanismes d'initiation, nos simulations permettent de retrouver empiriquement la gamme de temps parcours mesurée grâce aux enregistrements sismiques, pour les principaux lahars de 2009 et 2010. Cette étude pourrait être complétée par la simulation d'écoulements bi-phasiques pour essayer de modéliser des écoulement hyper-concentrés, ainsi que l'influence de l'érosion et de la déposition dans la partie avale du Prêcheur sur les risques de débordement. Nos résultats ouvrent toutefois déjà des perspectives intéressantes d'amélioration de la surveillance en continu, ainsi que des systèmes d'alerte.*

4.1 Introduction

The remobilization by water of old or recent volcanic material, during or even long after an eruption, generates sediment-laden flows called lahars that travel in gullys and rivers tens to hundreds of kilometers away from the volcano (Vallance and Iverson, 2015; Thouret et al., 2020). Thus, they are sometimes major threats for the populations and infrastuctures. Non eruptive lahars can be correlated to landslides that create loose debris reservoirs. This happened several times over the past decades in the Prêcheur river, in Martinique (Lesser Antilles) (Clouard et al., 2013; Aubaud et al., 2013). Hazard assessment studies considering both the landslide that creates the reservoir and its remobilization as lahars are difficult, because these are two distinct and different phenomena.

The initial landslide can take various forms, as debris or rock avalanches. Lahars can propagate as hyperconcentrated flows (HFs) or debris flows (DFs). In the following, we will thus talk about lahar to refer to both DFs and HFs. We define DFs as homogeneous mixtures of water and granulated rocks with volumetric solid fraction higher than 60%, similar velocities for the solid and fluid phases and densities above 1800 kg m^{-3} (Coussot and Meunier, 1996; Vallance and Iverson, 2015; Thouret et al., 2020). In comparison, HFs feature solid fractions between 20% and 60%, a vertical separation of the two phases and densities below 1800 kg m^{-3}. When the fluid fraction is further increased, the flow becomes a muddy streamflow, where fine particles (silts and clays) are suspended in the stream and coarser grains are carried along the stream bed. We may expect that the remobilization of a small amount of solid materials will produce HFs, while fast remobilization by liquefaction of a large debris reservoir will turn into a DF (Vallance and Iverson, 2015). However, lahars dynamics vary with space and time, with bulking and dilution controlling the volumetric solid fraction. The excess pore water pressure, resulting from difference in velocities between solid and fluid phases, favors partial liquefaction and slows down the settling of solid grains. On the contrary, friction between grains dissipates kinetic energy (Vallance and Iverson, 2015). Because of the combination of all these process, a DF initiated in the upper section of a river may well turn into HF at its tail because of dilution and settling, while its front increases it solid content due to bed erosion. Further dilution downstream can then transform completely the DF into a HF (for a conceptual view of such a process, see Figure 2 in Thouret et al. (2020)).

Over the past decades, thin-layer models have been increasingly used to study these phenomena (see McDougall (2017) for a general review, and Thouret et al. (2020) for lahar modeling). Their main assumption is that the landslide thickness is small in comparison to its lateral extent. In turn, the flow description boils down to its thickness and its thickness-averaged velocity. In their simplest form, they describe an homogeneous flow and dissipate energy solely by considering a stress applied at the base of the flow. Such models proved to reproduce well rock and debris avalanches, and debris flows (Hungr et al., 2007; Pastor et al., 2018a). Some numerical codes also model, for instance, two-phase flows (Iverson and George, 2014; Bouchut et al., 2015; Bouchut et al., 2016; Mergili et al., 2017; Pastor et al., 2018b), three-phase flows (fluid, coarse solid fraction, fine solid fraction Pudasaini and Mergili, 2019), and erosion along flow path (Iverson, 2012; Pirulli and Pastor, 2012). However, these developments rely often on empirical relations with parameters difficult to constrain and/or are not yet adapted to flows on complex topographies.

In the following, we will use the one-phase thin-layer model SHALTOP (Bouchut et al., 2003; Bouchut and Westdickenberg, 2004; Mangeney-Castelnau et al., 2005; Mangeney et al., 2007a), that has been used extensively to model gravitational flows at the field scale(e.g. Pirulli and Mangeney, 2008; Favreau et al., 2010; Lucas et al., 2014; Moretti et al., 2012; Moretti et al., 2015; Moretti et al., 2020a; Peruzzetto et al., 2019). SHALTOP is semi-empirical in the sense that rheological parameters are calibrated by reproducing past events. However, in comparison

to purely empirical methods that rely only on observations, it solves the momentum equations to model the dynamics of the flow the complex geometrical interactions between the flow and the topography.

In this work, we test the feasibility of using SHALTOP to model both a rock avalanche and the debris flows produced by the subsequent remobilization of the deposits. To our knowledge, the combined simulation of both phenomena, which is required for comprehensive hazard assessment, is rarely done with single-phase thin-layer models. Multi-phase models can be used (e.g. Mergili et al., 2020), but involve more parameters which makes their operational use more difficult. Because they have the highest potential impact on infrastructures and populations, we focus on extreme events (avalanches of volumes $> 1 \times 10^6$ m^3, and high discharge DFs). We choose the Prêcheur river as study site, where such events are documented and where large DFs threaten a village at the mouth of the river (Figure 4.2). A wide variety of data is available, but only part of these data is quantitative, which makes it difficult to constrain precisely simulations. Our methodology is summarized in Figure 4.3. We use topographic surveys, geological and geomorphological observations to construct realistic initial conditions for our simulations. The rheological parameters are then calibrated by reproducing documented events (2 rock avalanches and 1 high-discharge DF). For rock avalanches, runout is given by aerial photopgraphs and an insight on their dynamics is provided by seismic data. For DFs, the rheology is constrained by the granulometry and morphology of deposits. We estimate areas flooded by DFs with aerial photographs, and travel times with geophones recordings. Using the calibrated rheological parameters, we can then consider forward-prediction simulation scenarios. We first model a possible future avalanche, and remobilize instantaneously the simulated deposits to produce a DF. Then, to explore the influence of DF initiation mechanism, we we also use a constant discharge as source term to model progressive materials remobilization, instead of an instantaneous release.

In Section 4.2 we present in more details our study site, Prêcheur river, along with the events we use to calibrate our model. Then in Section 4.3, we explain how we constrain the initial conditions of rock avalanches and DFs simulations. In Section 4.4, we present into more detatils the SHALTOP numerical model. Section 4.5 gives the results of model calibration, and Section 4.6 the results of forward prediction simulations. Finally, we discuss these results in Section 4.7, and conclude in Section 4.8.

4.2 Data

The Prêcheur river catchment is located west of Montagne Pelée volcano in Martinique, Lesser Antilles (Figure 4.2a). Since the 1902 eruption, this volcano has be been continuously monitored by the Martinique Volcanologic and Seismologic Observatory (OVSM). Both seismic and fumarolic activities have remained low since the last 1928-1932 eruption, with only one significant seismic swarm in 1987 (Hirn et al., 1987; Boudon et al., 2005). The Samperre cliff is located about 2 km north-west of the summit, at the source of the Samperre river (Figure 4.4a). About 2.5 km downstream, the latter joins the Prêcheur river whose source is located between Montagne Pelée and the Samperre cliff. At the mouth of the river, 7 km downstream the Samperre cliff, the Prêcheur village (Figure 4.4b) is built on the river alluvial fan and hosted 1300 inhabitants in 2017 (INSEE, 2020). The bridge (Figure 4.4b) is the only access to the northern part of the village. In Figure 4.5, we give a conceptual view of the Prêcheur catchment, summarizing the sediments types and initiation processes for lahars and rock avalanches.

In the following we present the available data to constrain simulations of rock avalanches from the Samperre Cliff (Section 4.2.1). Simulations scenarios for rock avalanches are given by topographic surveys, and geological/geomorpholigical interpretation of the cliff setting (Section 4.2.1).

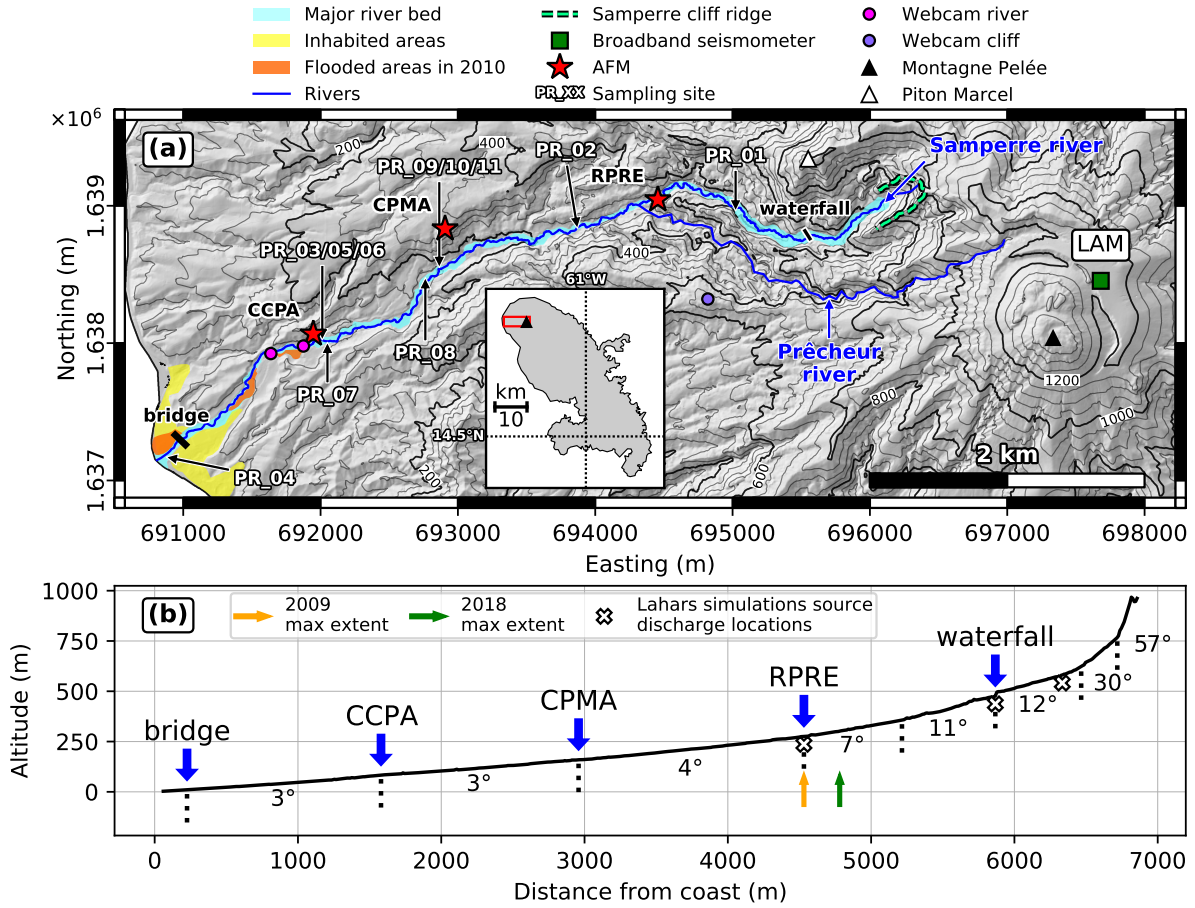

Figure 4.2: Prêcheur river map and section. (a) Map of the Prêcheur river. The 1 m DEM in the river area is from Helimap 08/2018, and from IGN 03/2010 elsewhere. Coordinates: WGS84 UTM20N (b) River cross-section, from the river mouth (left) to the Samperre cliff (right). Green and red arrows: estimated deposits extents after the 2009 and 2018 Samperre rock avalanche episodes, respectively. White crosses: source areas for debris flow simulations with imposed discharge. Average slopes are given for each section between dotted vertical black lines. Horizontal and vertical scales differ.

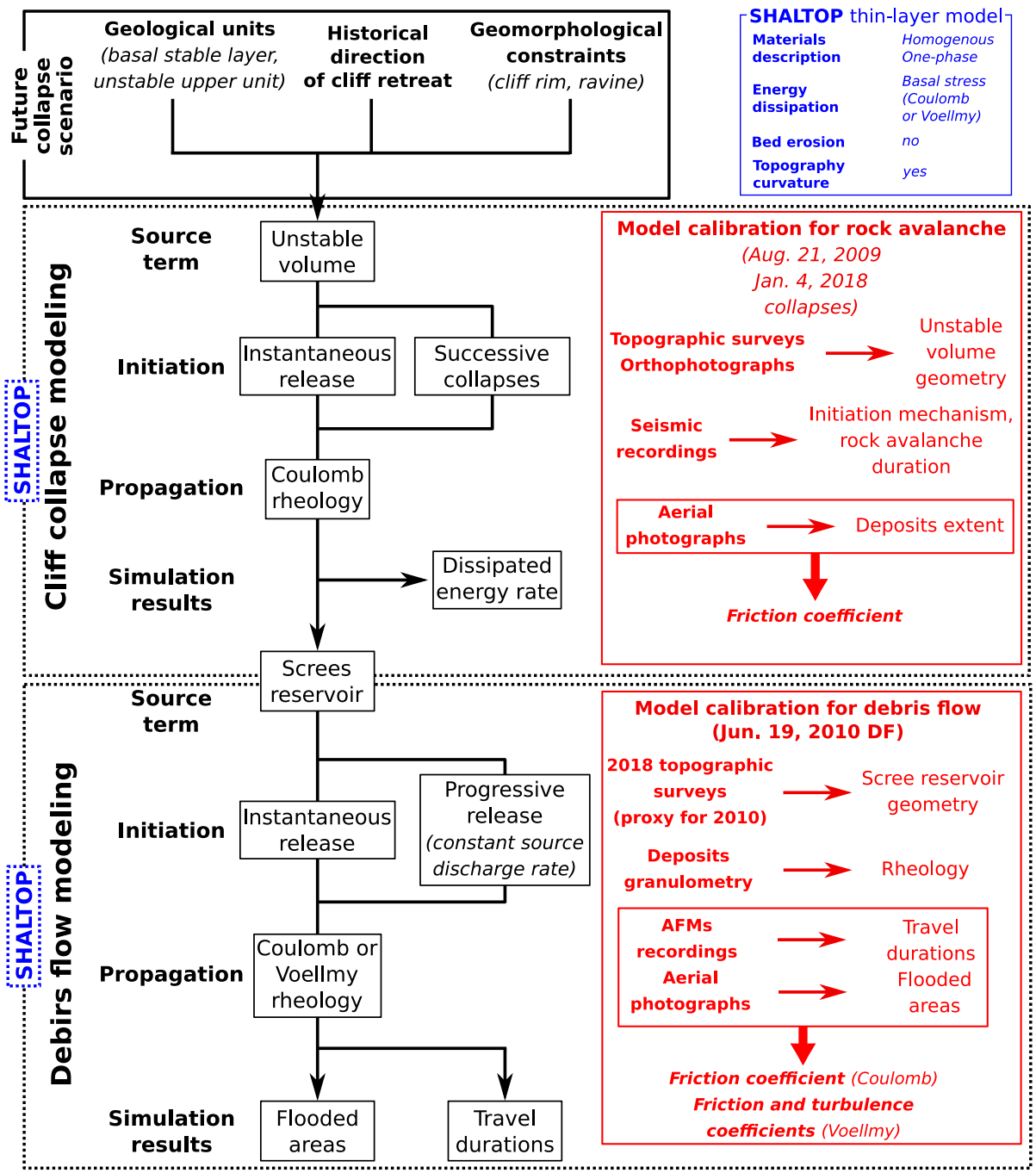

Figure 4.3: Modeling strategy for sand/rock avalanche and subsequent debris flow simulation. We indicate the data used to construct a forward prediction scenario (top panel), and the data used for model calibration (red panels).

Figure 4.4: 2018 views of the Samperre cliff and Prêcheur village. (a) Feb. 2, 2018 view of the cliff, after the main destabilizations. The dust cloud generated minor collapse is visible on the right side of the cliff: the rocks rapidly disintegrate to form a granular flow. (b) Mar. 30, 2018. Helicopter view of the prêcheur village, constructed on the alluvial fan of the Prêcheur river, with a central view of the bridge.

Calibration of rheological parameters is done by reproducing the Aug. 21, 2009 and Jan. 2, 2018 rock avalanches.

In Section 4.2.2, we present in more details the Prêcheur river catchment. We give a geomorphological description of the river as well as the monitoring system that was used to characterize DF events. The granulometric data and field observations used to constrain the rheology in simulations are also described. Finally, we will also present the June 19, 2010 DF used for calibrating the model parameters.

These data are summarized in Figure 4.6, where we provide a chronology of the main rock avalanches and DFs/HFs that occurred between 2009 and 2019, along with the available monitoring and warning system.

4.2.1 Rock avalanches from the Samperre cliff

Geological setting

Over the past 40 years, the Samperre cliff has produced at least 4 episodes of massive destablizations in 1980, 1997-1998 (Aubaud et al., 2013), 2009-2011 (2.1×10^6 m^3, Clouard et al., 2013) and 2018-2019 (5×10^6 m^3, Quefféléan, 2018a; Nachbaur et al., 2019). Since 1975, the occurence and relative magnitude of collapse events is systematically inferred from the seismic network maintained by the OVMP (Aubaud et al., 2013; OVSM-IPGP, 2020). However, another collapse episode is inferred from testimonies in the early 1950s (Aubaud et al., 2013). Thus, the cliff rim retreated by 250 m between 1988 and 2018 (Nachbaur et al., 2019). Its evolution between March 2010 and August 2018 is given in Figure 4.7a.

As it is impossible to get near the Samperre cliff, its geotechnical characteristics are unknown and a precise monitoring system would be complex to set up. However, In August 2018, the acquisition of LIDAR data and aerial photographs allowed for the construction of a textured 3D model of the cliff. These new data, along with historical aerial views, allow completing the geological interpretation of the cliff (Nachbaur et al., 2019), in addition to previous studies (Mathon and Barras, 2010; Clouard et al., 2013).

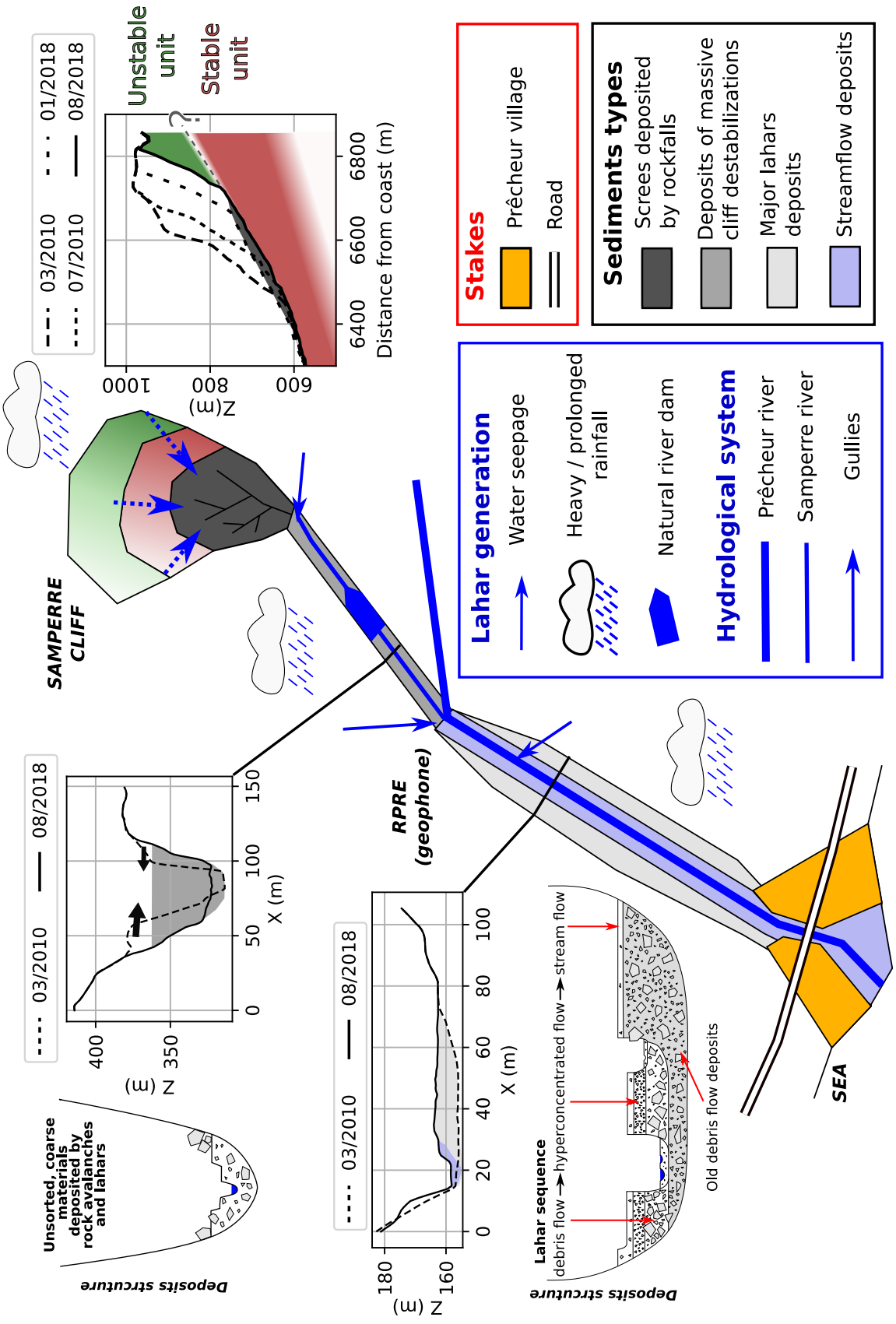

Figure 4.5: Conceptual view of the catchment geomorphology, with sediments types and deposits structure, and lahar initiation processes.

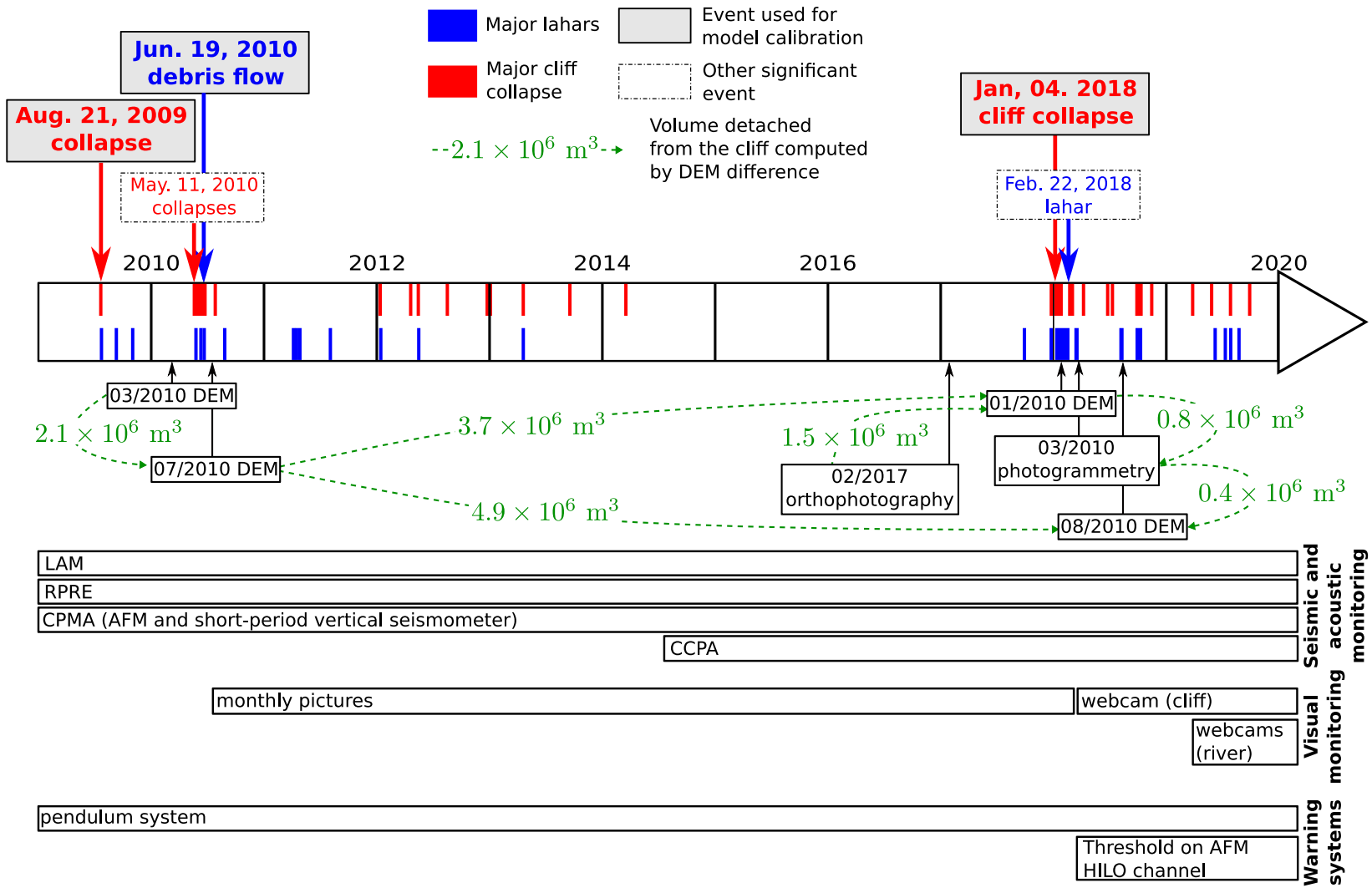

Figure 4.6: Chronology of destabilisations on the Samperre cliff and lahars in the Prêcheur river, between 2009 and 2019, along with monitoring and warning systems.

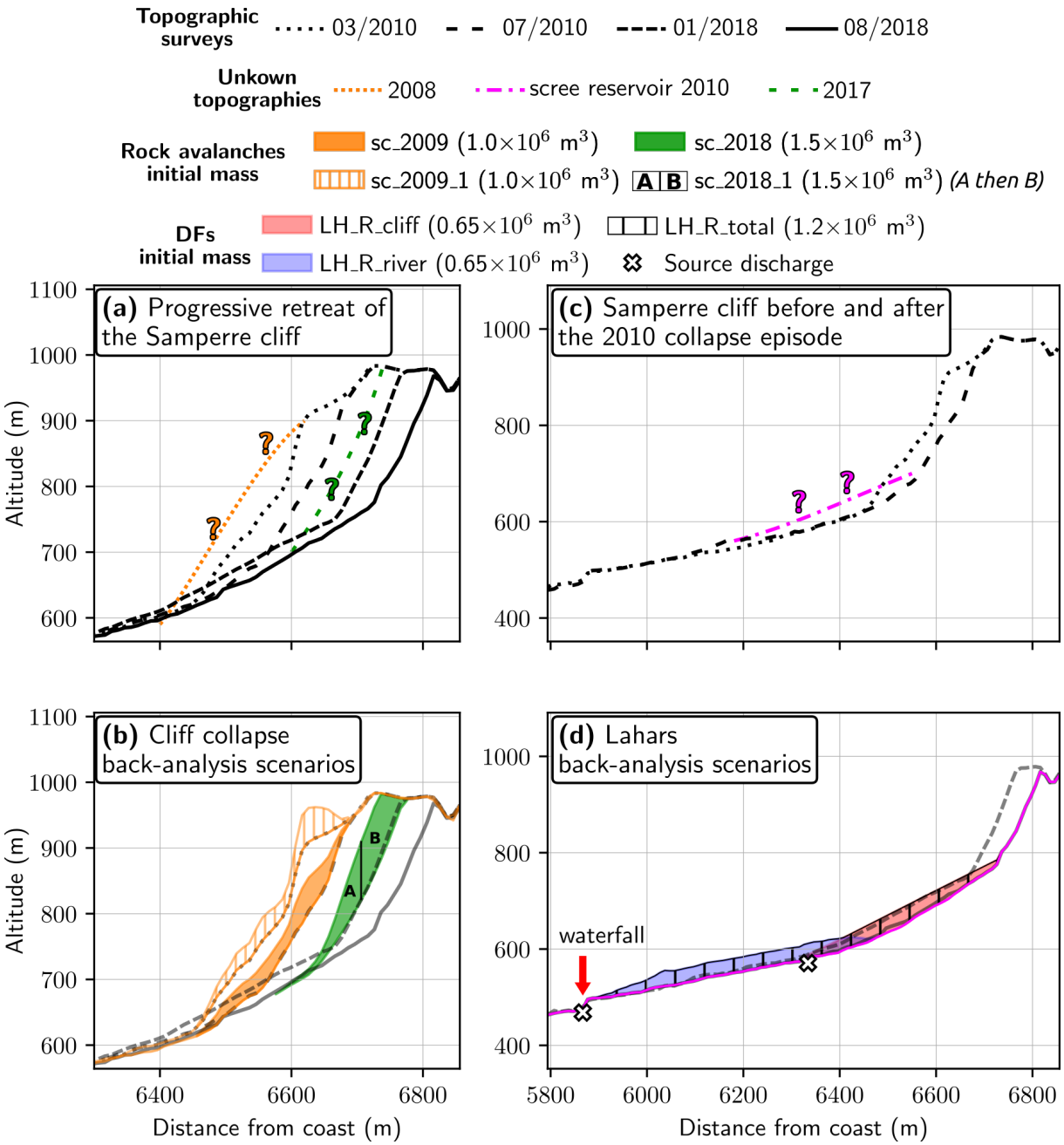

Figure 4.7: Samperre Cliff longitudinal cross-section with topographic surveys and initial mass in simulation. (a) Progressive retreat of the cliff between 2009 and 2018. (b) Initial mass for the *sc_2009* and *sc_2018* rock avalanche scenarios. (c) Topograpgy before (03/2010 DEM) and after (07/2010 DEM) the May 2010 main collapse episode. At the time of the 07/2010 topographic survey, the collapse deposits (purple dashed line) had already been washed away. Its geometry is thus unknown. (d) Simulation scenarios to reproduce the Jun. 19, 2010 lahar. The 01/2018 topographic survey is used as a proxy to reconstruct the surface of the reservoir at the bottom of the cliff (*LH_R_cliff* scenario, red patch). A smoothed version of the 08/2018 topography (purple line) is the bottom layer in the simulation. The *LH_R_total* is constructed by adding 30 m of material (from the gully bottom) in the major river bed (see Figure 4.2a). White crosses indicate source areas for simulation with imposed source discharges.

On the northern side of the cliff, an ochre basal unit, already seen in 2010, was further exposed in 2018 (Figure 4.8a, red patch). Nachbaur et al. (2019) interpret it as hydrothermal volcanic deposits emplaced before the major 25 km^3 flank collapse (D1) event that occurred 216 kyrs ago (Le Friant et al., 2003; Boudon et al., 2007; Germa et al., 2011; Brunet et al., 2017). This massive collapse may have actually occurred as a succession of smaller (about 5 km^3) debris avalanches (Brunet et al., 2017). As the cliff is located within the destabilization structure, they could either be the surface of the flank collapse scar, or of a mega-block transported by the debris avalanche. On the opposite side of the cliff, a bottom layer of old and light pyroclastic deposits is visible (Figure 4.8a, orange patch). Nachbaur et al. (2019) suggest they were emplaced after the D1 flank-collapse. The associated eruptive activity could be either the formation of the Piton Marcel dome (Figure 4.2a, grey triangle) following the flank collapse, or the edification of the old Pelée volcano, between 126 kyrs BP and 25 kyrs BP (Germa et al., 2011; Le Friant et al., 2003). Both the pre-D1 ochre basal unit and the lower pyroclastic deposits seem to have remained stable over the past decade: the cliff progressively retreated along their surface.

Most of the upper part of the cliff, which collapsed during the 2010 and 2018 destabilization crisis, is constituted of a 100 to 200 meter succession of pyroclastic deposits, with dark grey to brownish colors (Figure 4.8a, pink patch). The interface with the basal stable layer is marked by a clear slope break, as well as several water seepages (Nachbaur et al., 2019). Finally, the 2018 destabilizations unveiled a white, probably andesitic, 30 m thick lava flow at the top of the cliff (Figure 4.8a, blue patch), estimated at 12 kyrs BP by Nachbaur et al. (2019). It is capped by a thin layer of pumice deposits (Figure 4.8a, yellow patch) emplaced during Montagne Pelée plinian P1 eruption dated 1285±25 yr CE by Nachbaur et al. (2019). This layer is probably the one identified after the 2010 destabilizations on the north-east side of the cliff by Mathon and Barras (2010) and Clouard et al. (2013).

Because of the fluid circulations identified between the stable basal layer and the less consolidated pyroclastic materials, Nachbaur et al. (2019) and Clouard et al. (2013) suggest the bottom part of these latter formations is progressively weakened until it collapses (at least for the 2010 and 2018 collapse sequences). The cliff rim then retreats as a consequence of gravitational readjustments (Aubaud et al., 2013). During such episodes most destabilizations involve limited volumes (up to 10-100 $\times 10^3$ m^3), but larger events (1 to 2 $\times$ 10^6 m^3) can be expected. Once destabilized, the pyroclastic materials disintegrate quickly (see Figure 4.4a) and generate rock avalanches, as observed in other volcanic contexts (Hibert et al., 2011; Levy et al., 2015; Durand et al., 2018). Their travel distance seldom exceeds a few hundreds meters. However, some of the biggest rock avalanches reach the RPRE station (Figure 4.2a) about 2 km downstream. In recent years, the most important ones occurred in 2009-2010 and 2018.

Aug. 21, 2009 rock avalanche

On Aug. 21, 2009 at 14:12 UTM, a major rock avalanche occurred, following 23 smaller rock avalanches in the previous 30 days. It was not preceded by intense precipitations (only 2 mm in the previous 24h, Clouard et al., 2013). The avalanche was recorded by all seismic stations of the Montagne Pelée's surveillance network in a radius of about 10 km as a 4 min long event, with most of the energy in the first 170 s (Figure 4.9a). From aerial inspection, deposits could be mapped down to RPRE (Figure 4.2a and 4.2b, green arrow.), about 2 km away from the cliff (Clouard et al., 2013). Unfortunately, only the post-collapse cliff morphology could be mapped, thanks to a LIDAR survey carried by IGN in March 2010. No significant destabilization occurred in between. Clouard et al. (2013) estimate nevertheless the order of magnitude of the 2009 collapse volume to be 1 $\times$ 10^6 m^3.

A new phase of destabilizations started on May 8 2010, with a paroxysm on May 11 (47 collapses

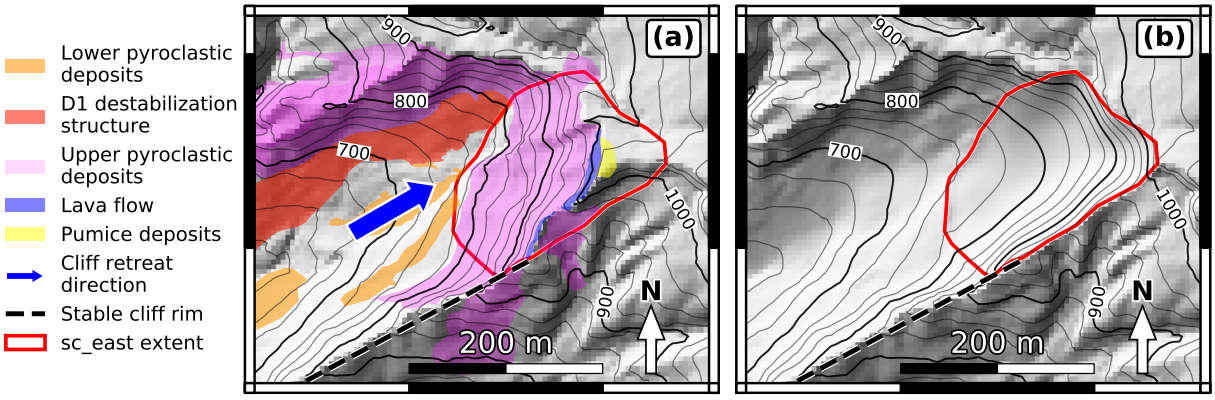

Figure 4.8: Samperre cliff geology and *sc_east* scenario. (a) Cliff topography in August 2018 with main geological units (Nachbaur et al., 2019). (b) Modified 08/2018 topography with the scar from the potential rock avalanche (*sc_east* scenario). The unstable volume is 1.9×10^6 m^3.

in one day, Clouard et al., 2013). Thanks to a new LIDAR acquisition in July 2010, Clouard et al. (2013) estimated the total collapsed volume between March and July 2010 to 2.1×10^6 m^3. In comparison to the 2009 crisis, the rock avalanche deposits extended only a few hundreds meters away from the cliff toe (approximately, right most white cross in Figure 4.2b), presumably because the rock avalanche occurred as successive small destabilizations rather than one major event as in 2009.

Because we have a risk conservative approach, we will model only the 2009 event that occurred in one main single phase and displayed a long runout. However, the screes reservoir resulting from the 2010 crisis will be used to model the initiation of the Jun. 19, 2010 destructive debris flow.

Jan. 2, 2018 rock avalanche

After the main May 2010 collapse crisis, smaller rock avalanches kept occurring on the cliff until 2014 (see Figure 4.6) resulting in up to 50 m retreat of the rim between 2010 and 2017 (Nachbaur et al., 2019). On Jan. 2, 2018, after a particularly rainy wet season, a new sequence of destabilization started. Its main phase lasted about two month, but episodic gravitational readjustments occurred until October 2019. This crisis culminated on Jan. 4, 2018 with one main event that will be reproduced to calibrate simulation rheological parameters.

It was recorded widely on the seismic network and lasted about 2 minutes (Figure 4.10). From helicopter overflight, it is estimated to have reached the river bend just upstream RPRE (Figure 4.2b, orange arrow). Several topographic surveys help characterize this collapse event (see Figure 4.7a). On Jan. 19, 2018, a photogrammetric 3D model of the cliff gives the early evolution of the cliff as well as the debris reservoir accumulated at the cliff toe. On Mar. 8, 2018, a helicopter overflight allows the fortuitous acquisition of a new photogrammetric model. However, as neither the flight plan nor the picture acquisition were meant to be used for such a purpose, the resulting model is of relative poor quality. Finally a LIDAR acquisition over the whole river Aug. 17, 2018 gives the full extent of the cliff retreat (with, in comparison, only minor destabilizations occurring afterwards). By comparing each Digital Elevation Model (DEM) to the July 2010 DEM, we get the following estimations of collapsed volumes (see Figure 4.6):

- Between July 2010 and Jan, 19. 2018: 3.4×10^6 m^3. Quefféléan (2018a) gets a higher 3.7×10^6 m^3 estimation. The discrepancy may arise from the presence of screes at the cliff toe that makes the estimation more complex.

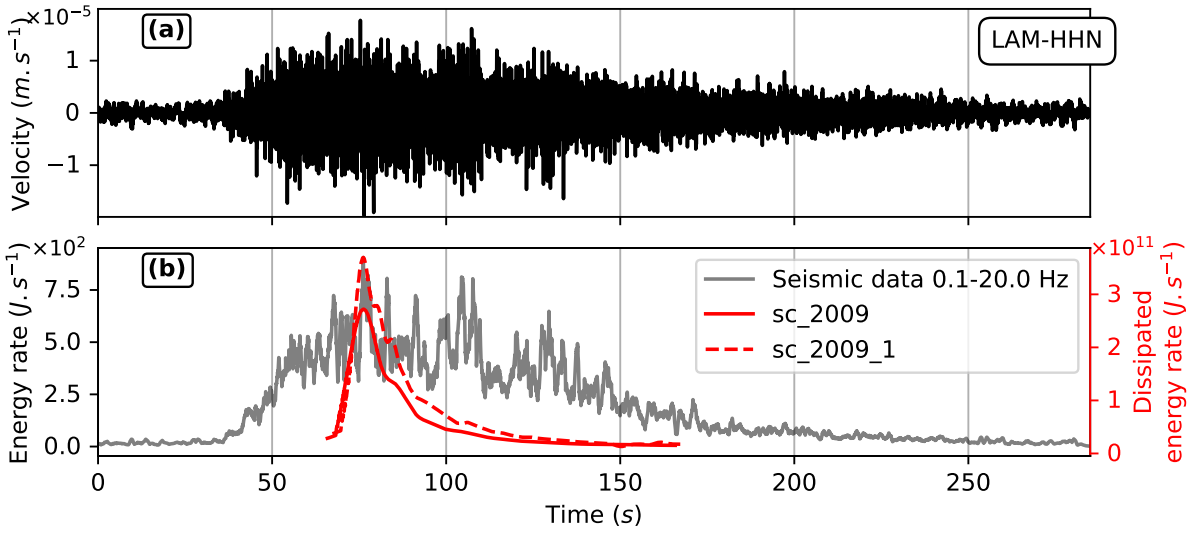

Figure 4.9: Seismic recordings of the Aug. 21, 2009 Samperre rock avalanche. (a) Signal recorded at station LAM, northern component. (b) Grey line: Seismic energy rate at station LAM. Red lines: energy dissipated during the *sc_2009* scenario (plain line, $\mu_S = \tan(11°) = 0.19$), and the *sc_2009_1* scenario (dashed line, $\mu_S = \tan(12°) = 0.21$). Grey and red lines are aligned for their maximums to match.

- Between Jan. 19, 2018 and Mar. 8, 2018: 0.8×10^6 m^3.
- Between Mar. 8, 2018 and August 2018: 0.4×10^6 m^3.

Our 4.9×10^6 m^3 estimation of the total collapsed volume between July 2010 and August 2018 is consistent with Quefféléan (2018b) (5×10^6 m^3). Besides, by comparing the Jan. 19, 2018 and August 2018 surveys, we could estimate the screes reservoir volume, at the bottom of the cliff, to 0.4×10^6 m^3. This reservoir had indeed been washed away by the time of the August 2018 LIDAR acquisition. Several factors explain the difference with the 3.7×10^6 m^3 volume estimated previously. Firstly, the avalanche deposits were not limited to the cliff bottom but reached the bend just above RPRE (Figure 4.2a). Secondly, as mentioned before, the cliff did undergo several collapse episodes between 2010 and 2018. By reconstructing a synthetic topography that is constrained by the 2017 cliff rim as seen on ortho-photographs, we estimate that the volume that actually collapsed in the first days of January 2018 may rather be 1.5×10^6 m^3 (see the definition of the *sc_2018* scenario in section 4.3.1). Finally, a few lahars had already occurred between Jan. 2, 2018 and Jan. 19, 2018 and thus started carrying off the avalanche deposits.

4.2.2 DF in the Prêcheur river

Geomorpholocial context

The watershed drained by the Prêcheur river is about 6.2 km^2 (Aubaud et al., 2013). Its baseflow discharge does not exceed 2 m^3 s^{-1}, but in case of extreme cyclonic events it may reach up to 150 m^3 s^{-1} (Aubaud et al., 2013). Its main affluent is the Samperre river, but other small and intermittent torrents join it.

Following Quefféléan (2018a), the river can be divided in two main sections. The first one is the Samperre river branch, down to its junction with the Prêcheur river. It is very narrow (down to 10 m) and steep-walled (more than 70 m at some locations). Average slopes are

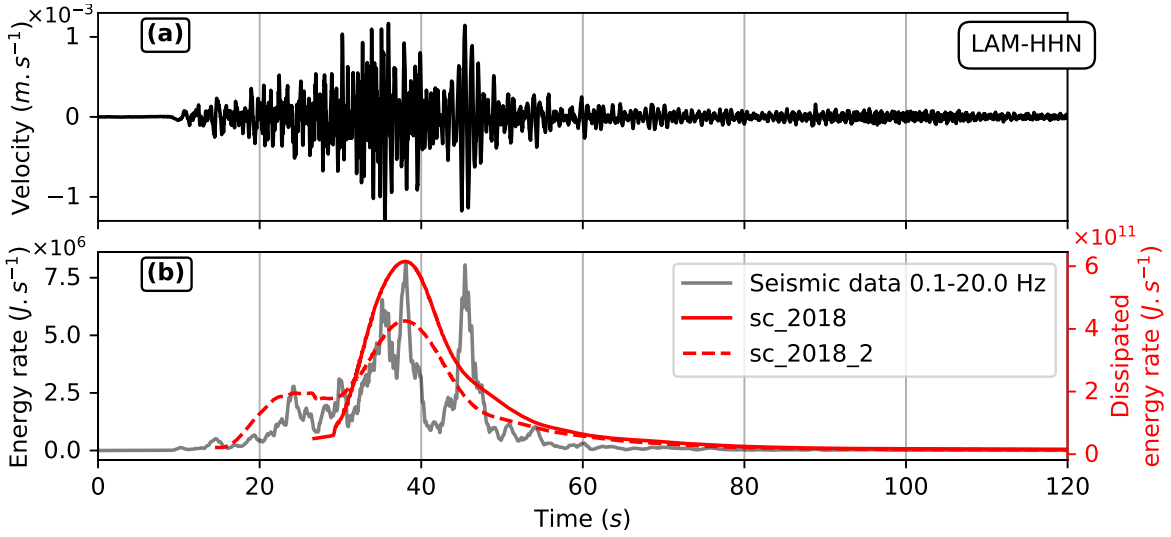

Figure 4.10: Seismic recordings of the Jan. 4, 2018 Samperre rock avalanche. (a) Signal recorded at station LAM, northern component. (b) Grey line: Seismic energy rate at station LAM. Red lines: energy dissipated during the *sc_2018* and *sc_2018_1* scenarios (plain and dashed lines respectively), with friction coefficient $\mu_S = \tan(14°) = 0.25$. Grey and red lines are aligned for their maximums to match.

between 7° and 12° in the last 2 km. Further upstream, slope increases up to 30° at the cliff foot (Figure 4.2b). Such slopes favor the remobilization of rock avalanches deposits, suggesting the most powerful DFs are generated in this part of the river. However the remobilization mechanism of the screes is not fully constrained. On aerial photographs from the 2018-2019 crisis, the absence of collapse scars in the debris reservoir points to progressive gullying rather than instantaneous remobilization. However, Lalubie (2013) suggest instantaneous liquefaction could also trigger DFs. Such an hypothesis is coherent with the high discharge and velocities observed during the destructive June 2010 DF, that had completely drained the screes at the cliff toe (see Section 4.2.2). Another major source of DF is river daming from river bank instabilities. Subsequent breaching can produce debris flows, as on Jun. 9, 2019.

In the second section of the river, from the Samperre river / Prêcheur river junction down to the river mouth, the river cuts through relatively poor resisting materials, such as pumices deposits (Meunier, 1999; Quefféléan, 2018a). As a result, the river bed progressively widens (from 30 m to 60 or 70 m) and flattens, with 3° to 4° slopes. Thus, it is mainly a deposition area for debris flows, with meter-sized blocks scattered on the river bed. The conditions in which these deposits could be further remobilized by subsequent lahar (DFs or HFs) are not clear. Given the small slopes, DFs are unlikely to be generated in this section of the river, but the extent to which HFs could develop there is still an open question. In normal streamflow conditions, the water course meanders through the unconsolidated sandy deposits, forming terraces, some them several meters high (Figure 4.12c). Though the river bed is wide, the banks are sometime steep and small landslides develop all along the river. However, in most place, they are not large enough to dam the whole river.

Initiation processes for lahars are given in Figure 4.5. In Figure 4.11a, we summarize the locations where DFs, HFs and SFs can be initiated. Figure 4.11b gives the expected evolution of a DF initiated in the upper section of the river.

The Prêcheur village is constructed on the alluvial fan of the river. The outlet position is also mobile, with 80 to 100 m variations in the stream direction over the last 40 years (Quefféléan, 2018a). The river mouth has undergone important variations since 1950: after an important

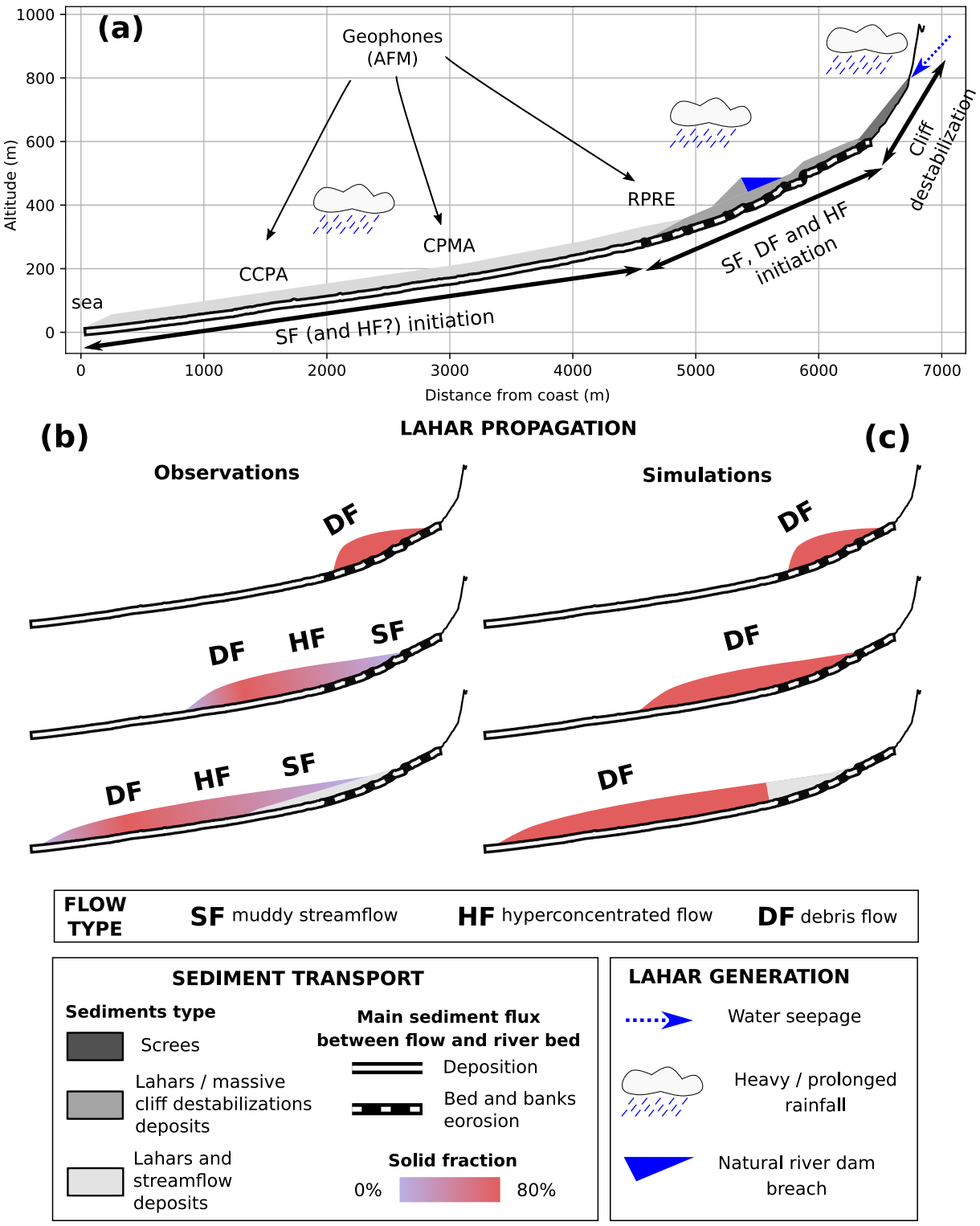

Figure 4.11: Cross-section of the Samperre and Prêcheur river, from the Samperre cliff to the sea (a), with a conceptual view of lahars processes (b) and our modeling solution (c).

lahar reported by Prêcheur inhabitants in the early 1950s, the river mouth was more than 330 m wide at its outlet and about 90 m wide at the actual location of the bridge (Aubaud et al., 2013; Quefféléan, 2018a). With the banks progressively anthropized and the installation of blocks to protect the village, the outlet is now only 80 m wide, and the river bed is 30 m wide below the bridge. In order to mitigate the overflow hazard which is enhanced by the reduction of the river bed width, the river bed is actively cleared after major lahars by quarry companies.

Prêcheur river monitoring: AFMs and webcams

In order to monitor the Prêcheur river and detect lahars, a short-period one-component seismic station was installed in 1979 at the CPMA site (Figure 4.2a) by the OVSM. In 1998, 2001 and 2014, three geophones, called Acoustic Flow Monitoring (AFM) sensors (LaHusen, 2005), were installed at CPMA, RPRE and CCPA respectively. AFM system, developed at the Cascades Volcano Observatory (LaHusen, 1998) is the most common monitoring lahar system. It is currently installed on active volcanoes (e.g. Pinatubo (Marcial et al., 1996), Merapi (Lavigne et al., 2000), Ruapehu (Cole et al., 2009) and Tungurahua (Jones et al., 2015)). Acoustic signals are processed on site by the digitizer, and three records are recovered in real-time by the OVSM: FULL (10-300 Hz, low gain), HILO (10-100 Hz, high gain) and HIHI (100-300 Hz, high gain). HILO and HIHI records allow monitoring the normal streamflow of the river but are saturated by large events due to their high gain. The latter are thus better analyzed with the FULL record. Values span between 0 and 4000 mV, but are usually below 350 mV for HIHI and HILO channels and 50 mV for FULL channel in normal streamflow conditions. In 2010, sampling interval was 10 min and 5 min in normal conditions for CPMA and RPRE respectively, but was reduced to 1 min when the HILO channel exceeded 500 mV at CPMA and 1000 mV at RPRE. From 2019, the replacement of digitizers allowed to decrease the sampling interval to 20 s. Finally, a rain gauge with 5 mm resolution was also installed in CPMA in 2000.

The first warning system was set up at the RPRE station in 1999, consisting of several cables with different lengths hanging vertically above the river. An increase of water level is detected by inclinometers on the top of each cable. When two sensors are activated, an alarm is automatically triggered in the Prêcheur village. As the most powerful lahars sometimes rip of cables, a threshold on the HILO channel of the AFMs was also defined in 2010 to trigger automatically an alarm in the Prêcheur village.

Following the 2018 rock avalanches and lahar crisis, two Solarcams were installed in 2019 by the BRGM (Bureau de Recherches Géologiques et Minières) in the lowest section of the river, and another one upstream, facing the cliff, to monitor the scree reservoir (pink and purple dots in Figure 4.2). Pictures are automatically recovered every 15 min. Though it is not enough to record lahar dynamics, it enables a detailed monitoring of the river bed sedimentary load. As we calibrate our thin-layer model on a DF that occured in 2010, we do not use these cameras.

Granulometry of lahar deposits

In order to characterize the rheology of the lahars, we collected 11 samples of lahars deposits for granulometry analysis, at 5 sites along the river, from its outlet to about 5.5 km upstream. To our knowledge, it is the first time such a sampling is done: Meunier (1999) only analyzed the granulometry of streamflow deposits at the river mouth, and Lalubie (2013) similarly recovered one sample only at 80 m altitude (presumably near the CCPA station). More generally, on-site sampling is rarely carried out to constrain numerical simulations. Although they cannot be used directly to calibrate simulation parameters, they help better understand the physical process controlling the dynamics of the flow.

We recovered lahar deposits by digging a rectangular parallelepiped in exposed terrace outcrops. On site 20 mm sieving was performed to recover at least 5 kg of material, with the mass fraction of grains larger than 20 mm measured on site as well. Granulometric curves as well as an example of sampling site are presented in Figure 4.12. All samples contain mainly sand, gravel and boulders, with less than 4% of silts and clays (diameter d<0.1 mm). When comparing to the granulometric envelopes derived by Bardou et al. (2003) in alpine context, our samples fit neither the "friction-viscous" nor the "viscoplastic" envelopes, whose fine fraction is more important (between 5% and 20% of clay, Figure 4.12a). This suggest that in the Prêcheur river, DFs dynamics are controlled by collision and friction between grains. The difference with the corresponding envelope in Figure 4.12 may be explained by the different context in which the deposits were emplaced. Our results are more consistent with the grading ranges of Semeru volcano lahars deposits presented by Dumaisnil et al. (2010), in particular for hyper-concentrated flow and granular flow deposits (Figure 4.12b). In their study, granular flows should be understood as DFs with only little silts and clays, such that collision and friction between grains are the main driving forces. Pallares et al. (2015) also find DF deposits with less than 10% silt and sand.

The distinction between DF deposits and HF deposits is not easy as each one can evolve into the other one. Following Dumaisnil et al. (2010) we can associate finer grading range (mainly sand and gravel) to HFs (as for sampling sites PR-02, PR-04, PR-05 and PR-07) and coarser, unsorted deposits to DFs (as for sampling sites PR-01 and PR-06).

As mentioned in the introduction, we focus on the modeling of DFs: their high solid concentration increases their impact pressure on infrastructure and thus their destructive power. Besides, the homogeneous mixing of solid and fluid phases makes them easier to model with one-phase thin-layer models. However, only high magnitude events have DFs dynamics all the way downstream (at least at their front), as otherwise dilution and sediments settling will transform a DF into a HF. Such a high magnitude DF occurred on Jun. 19, 2010: we will use it to calibrate our model.

The Jun. 19, 2010 debris flow

After the main collapse episodes of May 11, 2010, the first lahar occurred on May, 14. Two lahars, on May 16 and 17, triggered the RPRE pendulum alert system (Aubaud et al., 2013). 5 small to medium amplitude lahars were recorded in late May and early June. On Jun. 19, at 7:30 UTM and after a non exceptionnal tropical wave, a high discharge DF ripped of the pendulum warning system and flooded the Abymes quarter in the Prêcheur village (Figure 4.13). We will reproduce this event to calibrate rheological parameters for DF simulations, using geophones records to constrain travel time, visual observations to identify flooded areas, and granulometric analyses to choose an appropriate rheological law.

AFMs records enable the identification of two initial relatively small amplitude surges, with the main phase (that we will try to model) occurring between 8:30 and 9:00 UTM (Figure 4.14a and b). The 3000 mV peak value registered at CPMA is particularly high: in all the other lahars that occurred in 2009 and 2010, it exceeded 1000 mV on a few occasions only. The signal amplitude then progressively decreased until 11:00 UTM. A last small surge can be spotted at 11:30 UTM, lasting about 30 min (Figure 4.14b). As pointed out by Aubaud et al. (2013), the triggering rainfall was not particularly strong (11 mm in 1h40), but the main surge was preceded by 1 hour long 30 mm precipitations (as recorded in CPMA station, Figure 4.14b). This surge was particularly fast: the peak amplitude was recorded with only 2 to 3 min intervals at RPRE then at CPMA (Figure 4.14a). Given the 1.5 km distance between the two stations, it yields an average velocity of 30 to 45 km hr^{-1} (8 to 13 m s^{-1}). The extent and location of overflows is given in Figure 4.2a (south-western most orange patch). Two other significant deposition areas are also reported on the river left bank (Figure 4.2a, orange patches between the bridge and

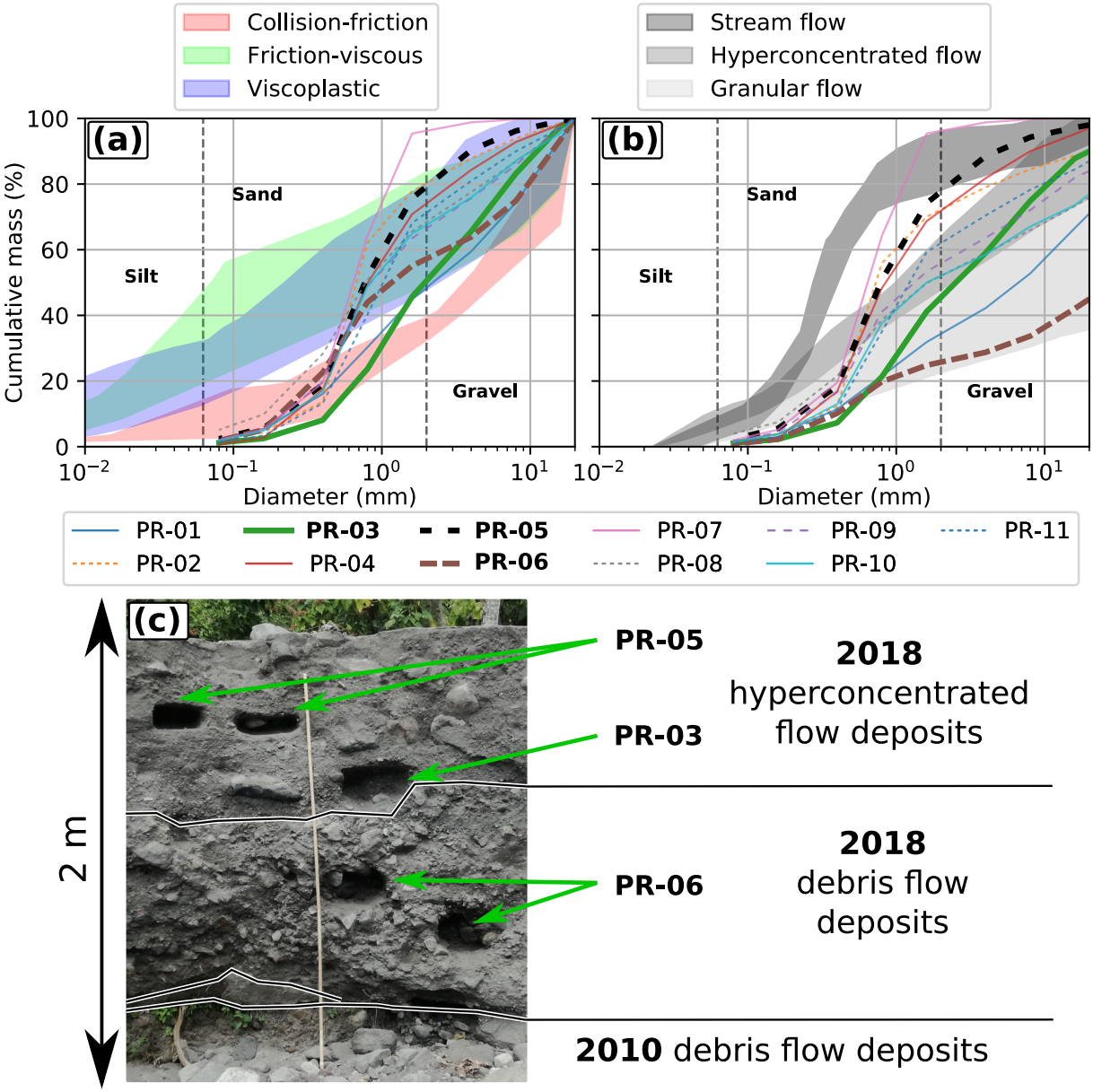

Figure 4.12: Granulometry of lahar deposits. (a) Lines: granulometry of samples, with boulders larger than 2 cm removed. Colored patches: granulometric envelopes from Bardou et al. (2003) associated to flow rheologies, in alpine context. (b) Lines : granulometry of the whole sample. Grey patches: Granulometric envelopes from Dumaisnil et al. (2010), for lahars deposits on the Semeru volcano, Indoenisa. (c) Example of sampling site. Granulometric curves of the samples are given in bold in (a) and (b). See Figure 4.2a for the location of sampling sites.

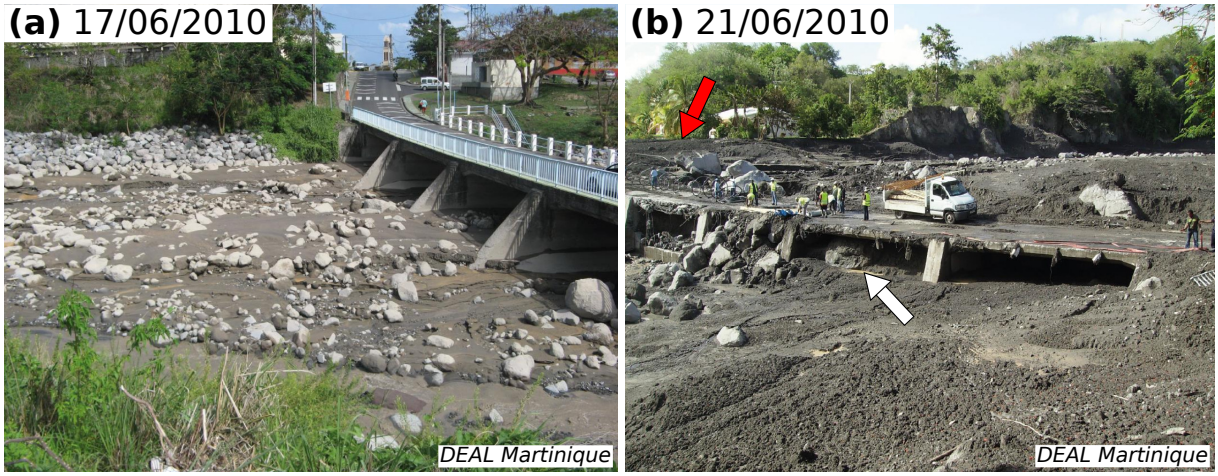

Figure 4.13: Prêcheur river bridge, before and after its destruction in June 2010. (a) Jun. 17, 2010. View of the bridge two days before the Jun. 19, 2010 DF, looking upstream. Previous lahars had already filled the river bed. (b) Jun. 19, 2010. View of the Prêcheur bridge after the Jun. 19, 2010 DF that flooded the Prêcheur village. Note the boulders below the bridge damming the river (white arrow). The overflow took place just upstream the bridge, on the right river bank (red arrow).

CCPA). On Jun. 20, a new high-discharge lahar was generated. In combination to the Jun. 19, DF, it completely washed away the screes reservoir at the bottom of the cliff. Indeed, the scree reservoir was still visible during helicopter overflight on Jun. 15, but had disappeared on Jun. 25.

The Jun. 19 lahar is described as a DF by Mathon and Barras (2010) and Laigle and Macabies (2010). Its velocity, as well as the screes washout at the cliff toe, suggest it may have been triggered by the instantaneous or at least very quick remobilization of the screes, in what Lalubie (2013) called a liquefaction triggered lahar. From visual observation of its dynamics, as well as from the presence of small side lobes on the river banks (see Figure 4.15) not higher than a few tens of centimeters, we can infer that it had a slightly more viscous behavior than the 2018 lahars, for which such lobes were not observed. It is confirmed by the granulometry of the PR-08 sample that we associate to 2010 deposits: it features the highest fine fraction. However, as discussed previously, it remains low: only 5% of clays and silts within the 20 mm fraction, and less than 4% of the total flowing sediment. Even if water circulation may have washed away part of the fine fraction since 2010 (Dumaisnil et al., 2010), what must be actually considered is the clay fraction, which will be even less than the previous percentages (that accounts for both clays and silts). Besides, though side-lobes are typical of visco-plastic, yield-stress fluids (Coussot et al., 1993), they can also be observed for dry granular flows (Mangeney et al., 2007b).

In the following, we explain how all these data are used to define realistic initial conditions for rock avalanche and DF simulations.

4.3 Simulation scenarios: initial conditions and topography

To define the initial mass that will be released at the beginning of the simulation, we use topographic surveys. As mentioned previously, 4 DEMs with 1 meter resolution are available, acquired in March 2010, July 2010, January 2018 and August 2018. They will be further referred to as 03/2010, 07/2010, 01/2018 and 08/2018 DEMs. As the 08/2018 DEM is the most detailed one, simulations were thus carried out on this DEM, with small patch of screes identified at the cliff

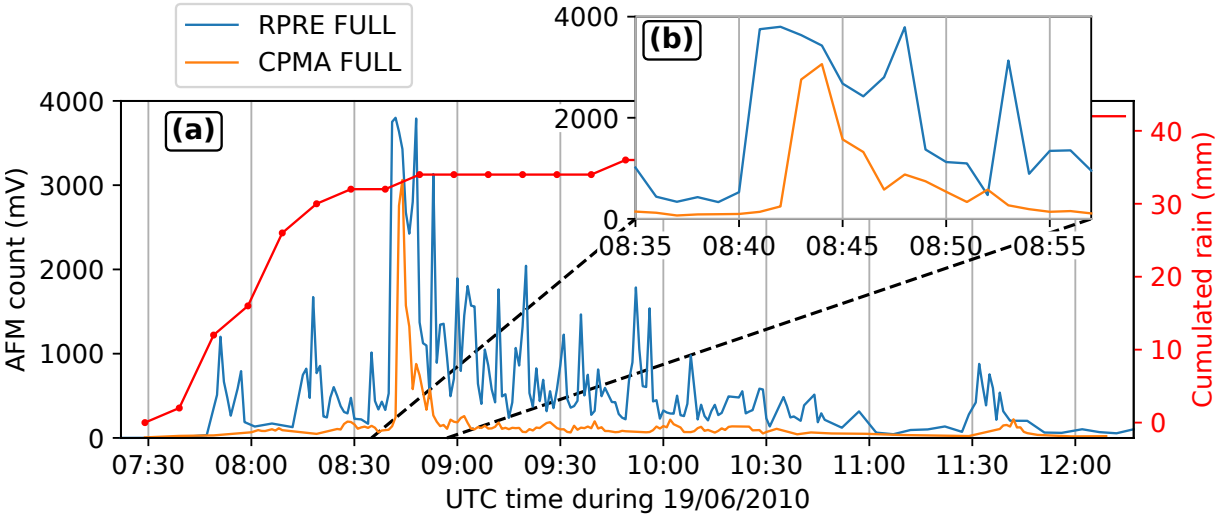

Figure 4.14: AFMs recordings of the Jun. 19, 2010 lahar from RPRE and CPMA. (a) Full event recording, with cumulated pluviometry recorded in CPMA. The black dashed line locates the main event ploted in (b). (b) Main phase of the lahar, with the main DF surge. Time is in hours, UTM.

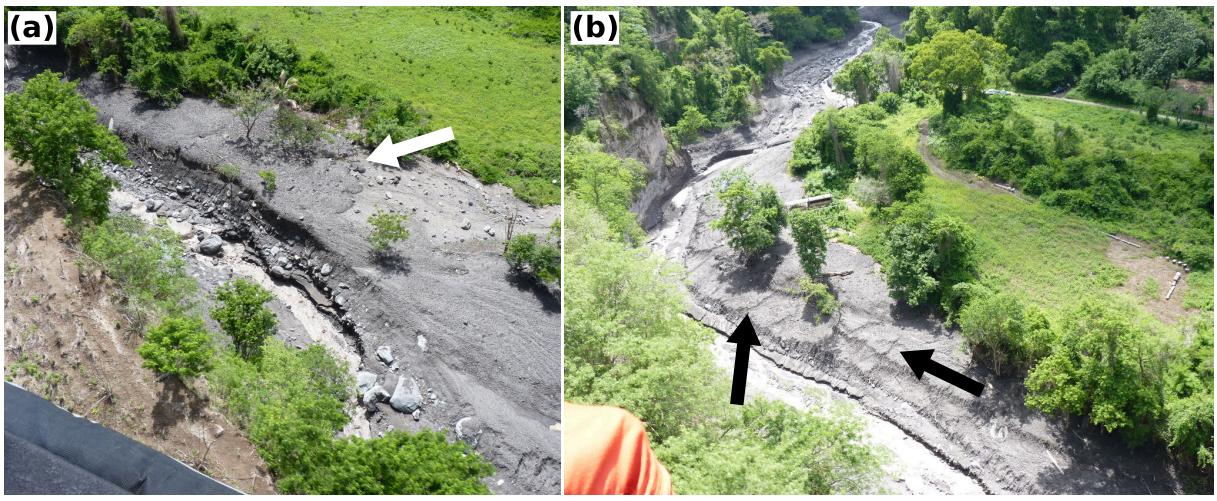

Figure 4.15: Jun. 25 2010 overflight of the Prêcheur river, after the Jun. 19, and Jun. 20 lahars. Both pictures ((a) and (b)) were taken between RPRE and the bridge. Black and white arrows point at deposits side lobes discussed in the main body of the thesis.

	sc_2009	*sc_2009_1*	*sc_2018*	*sc_2018_1*	*sc_east*
Purpose	Reproduce Aug. 21, 2009 collapse		Reproduce Jan. 4, 2018 collapse		Forward prediction
Sensitivity analysis		Mass geometry and topography		Initiation mechanism	
Data to constrain initial mass	Volume only		2017 orthophotographs 01/2018 DEM		08/2018 DEM geoloogy geomorphology
Volume ($\times 10^6$ m^3)	1		1.5	0.8, then 0.7	1.9
$\mu_{\mathbf{eff}} = \mathbf{V}^{-0.0774}$	$0.34 = \tan(18.9°)$		$0.33 = \tan(18.4°)$		$0.34 = \tan(18.9°)$
Initiation	Instantaneous		Instantaneous	2 collapses 13 s apart	Instantaneous
μ_S	$0.19 = \tan(11°)$	$0.21 = \tan(12°)$	$0.25 = \tan(14°)$		$0.25 = \tan(14°)$
Travel distance (m)	1550		1800		1630

Table 4.1: Rock avalanches scenarios. Travel distances are measured from the cliff bottom (right most white cross in Figure 4.2b).

toe removed by manual modification of contour lines. Only one simulation was carried out on the 03/2010 DEM to investigate the influence of topography on simulations results (*sc_2009_1*, see Section 4.3.1). DEMS are re-interpolated to 5 m for rock avalanche simulations and 10 m for DFs simulations because higher resolutions demand too much computational power.

The topography in the Samperre cliff sector is however adapted to each simulation scenario to take into account the progressive retreat of the cliff and define realistic geometries for initial unstable volumes. This is done by using the successive topographic surveys, along with the geologic and geomorphologic observations presented in the previous sections. In the following, we explain into more details how we construct the rock avalanche and DFs simulations scenarios, that will be used to calibrate rheological parameters (Section 4.3.1 and 4.3.2). We then present the construction of forward prediction simulation scenarios 4.3.3. The corresponding rock avalanches simulation scenarios are given in Table 4.1, and DF simulation scenarios in Table 4.2. The initial unstable masses are also presented in Figure 4.7.

4.3.1 Scenarios for rock avalanche back-analysis

Aug. 21, 2009 rock avalanche

As discussed previously, there is no topographic survey of the Samperre cliff available before the 2009 destabilization crisis. Thus, we cannot constrain the collapse geometry, though we do have an estimation of the volume (1×10^6 m^3 Clouard et al., 2013)). As a consequence, we define our initial volume as the difference between 03/2010 and 07/2010 DEMs, and uniformly scale resulting heights to get a final volume of 1.0×10^6 m^3. This is our *sc_2009* scenario (Figure 4.7b, orange patch). The rock avalanche is propagated on the 07/2010 DEM in the cliff area, and on the 08/2018 DEM further downstream. The resulting unstable volume shape is not representative of a real destabilization geometry, but several studies suggest that the initial mass geometry has little influence on runout simulated with thin-layer models (e.g. Lucas et al., 2011). However, to investigate the influence of bottom topography on the results, we will also propagate the avalanche on the 03/2010 DEM (*sc_2009_1*). In this case the initial mass is constructed as previously, but is added on the 03/2010 DEM.

Jan. 4, 2018 rock avalanche

In order to define the unstable volume involved in the Jan. 4, 2018 destabilization, we use the cliff rim position (as seen on February 2017 orthophotographs) to reconstruct a synthetic cliff

		LH_R_cliff, *LH_R_river*	*LH_R_total*	*sc_east*	*LH_R_cliff*, *LH_R_waterfall*, *LH_R_RPRE*
Purpose		Reproduce Jun. 19, 2010 DF		Forward prediction	Influence of source mechanism
Initial reservoir location		Cliff toe or river	Cliff toe and river	Deposits of cliff collapse *sc_east* simulation	n.a.
Volume ($\times 10^6$ m^3)		0.65	1.2	1.9	0.65 / 1.2
Initiation		Instantaneous remobilization			Imposed discharge rate at the cliff toe, waterfall or RPRE.
RPRE-CPMA (1.6 km)	**Δt (min)**	**1** (4)	*1* (3.5)	2.5 (3.5)	**3.5** / *3.5*
	vel. (m s^{-1})	**26.5** (6.5)	*26.5* (7.5)	10.5 (7.5)	**7.5** / *7.5*
RPRE-bridge (4.3 km)	**Δt (min)**	**7.5** (15)	*5.5* (12)	6.5 (12)	**11.5** / *10*
	vel. (m s^{-1})	**9.5** (5)	*13* (6)	11 (6)	**6** / *7*
Inundated area ($\times 10^4$m^2)	**Left bank**	**2** (1)	*8.5* (6)	8 (6)	**1** / *4.5*
	Right bank	**1.5** (3)	*3.5* (4)	3.5 (4)	**1** / *2.5*

Table 4.2: Debris flow simulation scenarios characteristics and main results. Simulations results are given for $\mu = \tan(2°)$ and the Coulomb rheology, and for the Voellmy rheology in parenthesis (with $\xi = 500$ m s^{-2}). Travel duration Δt is measured by picking the onset of discharge increase. Results are given with a 10 min source discharge duration for *LH_R_cliff*, *LH_R_waterfall*, and *LH_R_RPRE*. Colors highlight values to be compared, between instantaneous release and progressive release simulations.

topography, as it may have been before the 2018 destabilization crisis (Figures 4.16b and 4.7b). This is done by defining a set of longitudinal and transverse cross-sections on the 07/2010 DEM, changing the corresponding profiles with cubic splines, and interpolating the DEM in between, to finally reconstruct the cliff edge as it was in February 2017.

The post-collapse topography is given by the 01/2018 DEM that was manually modified to remove the screes reservoir at the cliff bottom. The 1.5×10^6 m^3 unstable volume is then defined as the difference between these two reconstructed topographies. This is our *sc_2018* scenario (Figure 4.7b, green patch). To investigate the influence of retrogressive destabilizations on runout prediction, we construct a *sc_2018_1* scenario (Figure 4.17) . In this simulation a 0.8×10^6 m^3 volume is first released at the cliff bottom (A in Figure 4.17a), and the rest (B in Figure 4.17a) collapses 13 s later. This delay corresponds to the initial duration of the seismic signal before the seismic energy starts increasing sharply (see Figure 4.10b).

4.3.2 Scenarios for DF back-analysis

In this section we present the simulations scenarios that were used to perform the back-analysis of the high-discharge Jun. 19, 2010 DF. Their main characteristics are given in Table 4.2.

As the screes reservoir at the cliff toe had already been washed away by the time of the 07/2010 DEM, there are no data to constrain the reservoir geometry (see Figure 4.7c for the pre and post collapse DEMs), apart from aerial photographs. To the contrary, the reservoir can be clearly identified on the 01/2018 DEM. As a result, we use the 2018 reservoir as a proxy for the 2010 reservoir. The corresponding scenario will be called *LH_R_cliff* scenario. It involves only 0.65×10^6 m^3 of materials, which is less than a third of the collapsed volume estimated by Clouard et al. (2013). Thus, we also carry out simulations with supplementary material added in the river, down to the waterfall (*LH_R_total* scenario). Moreover, we will discuss the

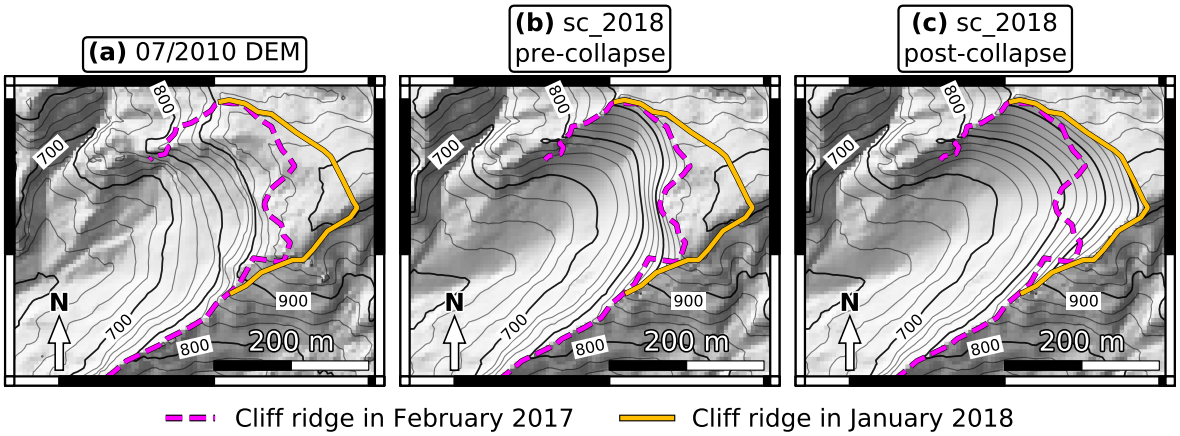

Figure 4.16: Reconstruction of the pre 2018 collapse cliff geometry for *sc_2009* scenario. (a) Cliff in July 2010. (b) Synthetic reconstruction of the cliff topography based on the 2017 cliff rim (top of *sc_2009* unstable volume). (c) Cliff on Jan. 19, 2018 modified to remove deposits at the cliff bottom.

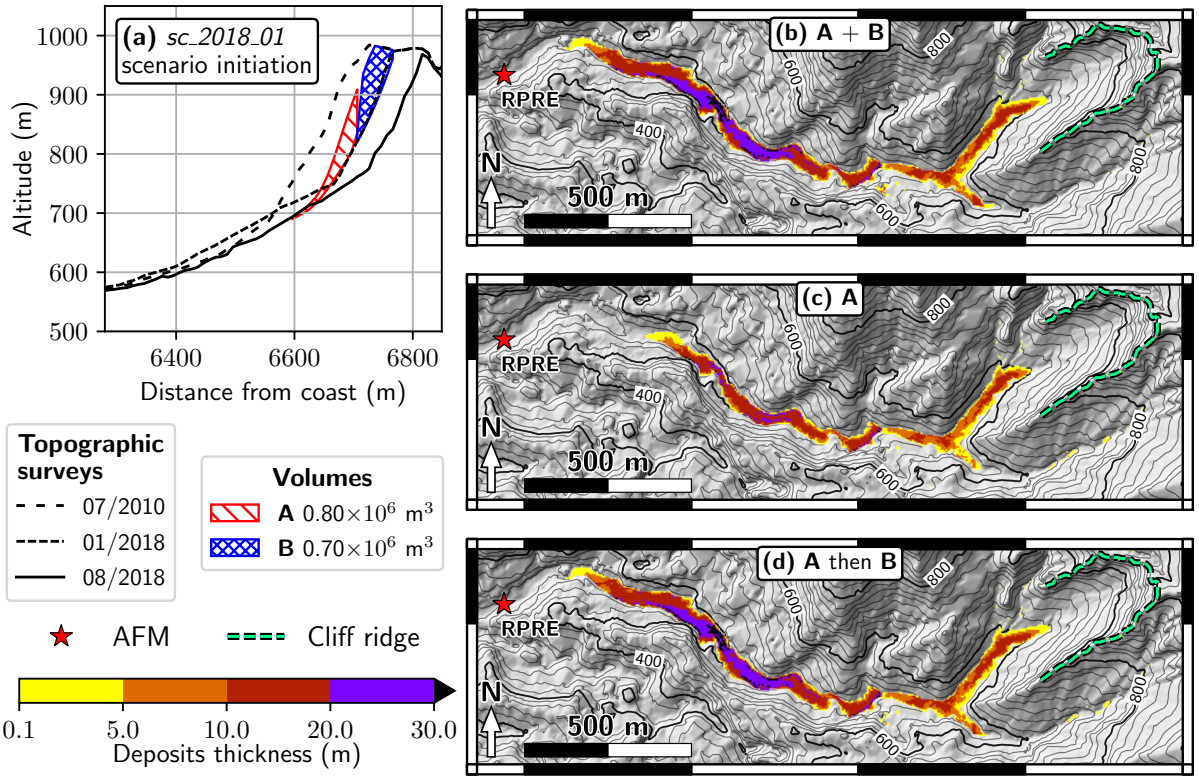

Figure 4.17: *sc_2018_2* scenario, with two successive collapses. (a) Black lines: topographic surveys. Red hatched patch (A): first initial 0.8×10^6 m^3 collapse. Blue hatched patch (B): second 0.7×10^6 m^3 collapse, 13 s after initiation. (b) Final deposits of *sc_2018* scenario, with A and B collapsing at once. (c) Final deposits when A only collapses. (d) Final deposits of the *sc_2018_1* scenario, with A collapsing, followed by B 13 s later. All simulations are done with the Coulomb rheology and $\mu_S = \tan(14°) = 0.25$. Green dashed line: Samperre cliff rim. Topography in (b), (c) and (d) is the 08/2018 DEM. Thick contour interval is 100 m.

influence of the initial reservoir geometry by constructing a reservoir in the river, without any deposits at the cliff bottom (*LH_R_river* scenario). In each case, we consider an instantaneous remobilization of the the reservoir.

On the 01/2018 photogrammetric model, we fit in the CloudCompare software a 27° dipping plane to the surface of the screes reservoir. The fit is good, with a RMS of 2.1 m, when the reservoir is about 120 m large and 340 m long. The reservoir geometry is thus rather simple and we can expect that the 2010 reservoir shared the same characteristics, as the materials involved are similar. The difference between this plane and the 08/2018 DEM (with, once again, remaining deposits removed) provides us with the initial 0.65×10^6 m^3 mass of the *LH_R_cliff* scenario (Figure 4.7d, red patch). To investigate other initial conditions we create another 600 m long reservoir in the river, between the cliff bottom and the waterfall (which is an upper estimation of the maximum distance reached by the rock avalanches in 2010). In this section, we fill the main river bed with up to 30 m thick deposits, which is a reasonable estimate of thicknesses estimated during helicopter flights and is also consistent with rock avalanche simulation results. Thicknesses linearly increase in the first 90 meters and linearly decrease in the last 150 meters, yielding a 0.65×10^6 m^3 final reservoir (Figure 4.7d, blue patch). The corresponding simulation is referred to as *LH_R_river* scenario. By combining the river reservoir and the cliff reservoir, we obtain the *LH_R_total* scenario (1.2×10^6 m^3, Figure 4.7d, hatched patch).

4.3.3 Forward-prediction scenarios for rock avalanche and subsequent debris flow

In a first forward prediction scenario, we will model the propagation of a possible future rock avalanche, and the subsequent instantaneous remobilization of the simulated deposits to produce a DF (*sc_east* scenario. We use the geological an geomorphological data given in Section 4.2.1 to constrain the initial unstable mass in the cliff. Following its historical retreat direction (Nachbaur et al., 2019), we infer that the north-west part of the cliff is the most likely candidate for future large collapses (Figure 4.8a and b, red line). Following Nachbaur et al. (2019), the western limit is constrained by the contact between the unstable upper pyroclastic deposits (Figure 4.8a, pink patch), and the stable basal units (Figure 4.8a, orange and red patch). This contact is marked by a clear slope break. We match the northern extent of the unstable volume with the gully running behind the Samperre Cliff (Figure 4.2a). Finally, for the south-east limit, we extend the actual cliff rim towards the north-east: over the past decades, it has constantly progressed in this direction (Figure 4.2a and 4.2b, black dashed line).

In this simulation scenario, the simulated deposits will be instantaneously remobilized to model a subsequent high discharge DF. However, given the relative poor constraints we have on DF initiation, it is relevant to also consider DF simulations where the release is not instantaneous. To empirically assess the effect of progressive remobilization, we impose a constant discharge during 10 or 20 min on an area of approximately 300 m^2 in the river. This could also reproduce, to some extent at least, DF initiation by progressive breaching of river dams. Note, however, that the flow has no initial velocity in the source area: the discharge rate controls only the amount of material that is added at each time step.

Source discharge areas are located either at the cliff bottom (*LH_D_cliffl* scenario), at the waterfall (*LH_D_waterfall* scenario) or at the RPRE station (*LH_D_RPRE* scenario). Corresponding locations are given by white crosses in Figure 4.2b. To facilitate the comparison with DF simulations with instantaneous remobilization (*LH_R_total*, *LH_R_cliff* and *LH_R_river*), the released volumes are the same: 0.65×10^6 m^3 or 1.2×10^6 m^3.

Now we have presented the initial conditions of our simulation scenarios, we will introduce the thin-layer model SHALTOP, that we use to model the propagation of rock avalanches and DFs.

4.4 Numerical model

4.4.1 Shaltop numerical model

The SHALTOP numerical code simulates the dynamics and emplacement of flows on general topographies (Bouchut et al., 2003; Bouchut and Westdickenberg, 2004; Mangeney-Castelnau et al., 2005; Mangeney et al., 2007b). It has been successfully tested to reproduce both real landslides (e.g. Moretti et al., 2015; Brunet et al., 2017; Peruzzetto et al., 2018b) and laboratory experiments (Mangeney et al., 2007b). In SHALTOP, the layer moving on the topography is considered homogeneous. Energy is dissipated through a force applied at the base of the flow, in the opposite direction of the flow velocity. In its simplest form, this force derived from the solid friction Coulomb rheology, such that the basal stress T is:

$$T = \mu_S \rho h (g \cos(\theta) + \gamma u^2), \tag{4.1}$$

where $\mu_S = \tan(\delta)$ is the friction coefficient and δ the friction angle, ρ is the flow density, h the flow thickness, g the gravity field, θ the local slope angle, γ the curvature along flow path and u the velocity norm. Using the Coulomb rheology to model rock and debris avalanches, it has been shown that the friction coefficient μ_S needed to model observed deposits decreases as the volume of the avalanche increases (Lucas et al., 2014). Typical friction coefficients thus range from $\tan(30°) = 0.58$ for granular flow experiments, $\tan(20°) = 0.36$ for 0.5×10^6 m^3 landslides and $\tan(11°) = 0.20$ for 1 km^3 debris avalanches. However, such values were derived for rock and debris avalanches with little water content. In comparison, water-laden flows are more mobile, and empirical friction coefficients below $\tan(7°) = 0.12$ may be needed to model them (Moretti et al., 2015; Peruzzetto et al., 2019).

For snow avalanche and debris flow modeling, the empirical Voellmy rheology is also commonly used (Salm, 1993; Hungr et al., 2007; Pastor et al., 2018a). It introduces a turbulence term proportional to the square velocity:

$$T = \mu_S \rho h (g \cos(\theta) + \gamma u^2) + \rho g \frac{u^2}{\xi}, \tag{4.2}$$

where ξ is the turbulence coefficient. Friction coefficients used in the Voellmy rheology to model DFs are usually below $\tan(10°) = 0.18$, which is necessary to propagate the DF on gentle slopes. For such friction coefficients, turbulence coefficients span 100 to 1000 m^2 s^{-1}. Zimmermann et al. (2020) find however a more constrained range, from 100 to 500 m^2 s^{-1}. However, it is sometimes difficult to constrain both parameters by back-analysis, as various couples (μ_S, ξ) may provide similar results (e.g. Peruzzetto et al., 2018a).

We model rock avalanches with the Coulomb rheology, as it proved to reproduce correctly real landslides deposits (e.g. Lucas and Mangeney, 2007; Favreau et al., 2010; Lucas et al., 2014; Yamada et al., 2018; Peruzzetto et al., 2019; Moretti et al., 2020a). For the back-analyses, friction coefficients were tested between $\mu_S = \tan(10°) = 0.18$ and $\mu_S = \tan(20°) = 0.36$.

DFs were simulated both with the Coulomb rheology the Voellmy rheology, with friction coefficients equal to $\tan(2°) = 0.03$, $\tan(3°) = 0.05$, $\tan(4°) = 0.07$ (with higher values, the flow would stop before it reaches the Prêcheur village). Turbulence coefficients ξ range from 100 m s^{-2} to 500 m s^{-2} as realistic values were constrained by Zimmermann et al. (2020) within that range. Influence of further increasing ξ is investigated with the Coulomb rheology, as it is equivalent to choosing infinite values for ξ. As discussed previously, we assume the DF is homogeneous, and use the same rheological law in the whole DF, without considering possible dilution and sediments settling at its tail. In Figure 4.11b and 4.11c, we compare schematically what may be expected in reality, and our empirical approach.

In the following section, we explain how simulation results are processed and compared to field data and observations. In turn, his comparison makes it possible to calibrate the simulation rheological.

4.4.2 Simulation output processing

Cliff collapse simulations are primarily calibrated with the travel distance observed during aerial reconnaissance. Following Schneider et al. (2010) and Levy et al. (2015), we also compare the dissipated energy rate P_{SH} during the simulation to the seismic energy rate P_s (see Figures 4.9b and 4.10b). This allows to see if the simulated duration of of the rock avalanche is similar to the duration of the generated signal, which is a good proxy for the actual duration of the rock avalanche (Levy et al., 2015). Temporal variations of P_{SH} and P_s can also help characterizing the dynamics of the rock avalanche, and in particular determining if the initial collapse happened in one or several successive steps. We define P_{SH} as:

$$P_{SH} = -\frac{d}{dt}\left(E_k + E_p\right), \tag{4.3}$$

with E_k the total flow kinetic energy and E_p the total flow potential energy. This is equivalent to computing the energy dissipated by the basal friction force. P_S is computed with the 0.1-20 Hz filtered seismic signal recorded on the LAM station, about 1300 m away from the cliff. Following Vilajosana et al. (2008), Levy et al. (2015) and Durand et al. (2018), the seismic energy E_S is:

$$E_S = 2\pi r \rho h c e^{\alpha r} \int_{t=t_{init}}^{t=t_{final}} \left(u_E^2 + u_N^2 + u_Z^2\right) dt, \tag{4.4}$$

where we assumed a point-source and an isotropic and homogeneous medium. We also consider that seismic surface waves dominate the signal. The parameters are $r = 1300$ m the distance to the signal source, $h = 250$ m the thickness of the layer in which waves propagate, $c = 1300$ m s^{-1} the group seismic wave velocity, and $\alpha = 4.2 \times 10^{-4}$ m^{-1} an attenuation parameter. In reality, α, h and c are frequency dependent. Besides, much more complex topographic corrections should be needed (Kuehnert et al., 2020). But Levy et al. (2015) find no major difference between the energy integrated over successive frequency bands and the energy computed directly as in (4.4), when the frequency band includes the frequencies concentrating most of the energy (in our case, around 1 Hz). Furthermore, we are more interested in trends than absolute values. Thus, we simply define P_S as

$$P_S = \frac{dEs}{dt} = 2\pi r \rho h c e^{\alpha r} \left(u_E^2 + u_N^2 + u_Z^2\right). \tag{4.5}$$

Lowess smoothing (Seabold and Perktold, 2010) is applied to the resulting time series.

Lahar simulations are calibrated by quantifying the flooded area in the Prêcheur village (i.e., in the yellow patches in Figure 4.2a), disregarding flow thicknesses below 0.1 m. We also compute travel durations between RPRE and CPMA, and RPRE and the Prêcheur bridge. This is done by deriving discharge time series at each position, and picking either the increase onset, or the maximum. Discharges are computed along river perpendicular sections.

4.5 Model calibration results

In this section we will first describe the back-analysis results for the rock avalanches (Section 4.5.1) and DF simulations(Section 4.5.2). Then, we will analyze the forward prediction simulation results, where we model a potential future rock avalanche and the remobilization as DF of the resulting deposits (Section 4.6). Results are summarized in Table 4.1 and 4.2.

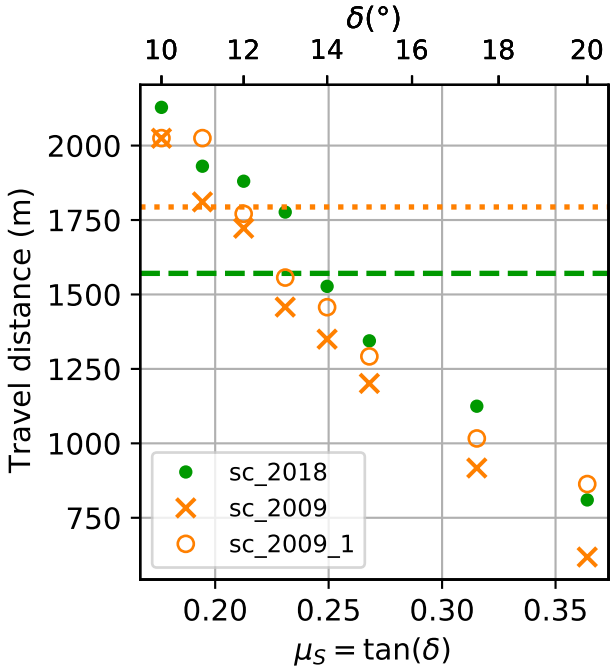

Figure 4.18: Simulation results for the *sc_2009* (orange crosses), *sc_2009_1* (orange circles) and *sc_2018* (green dots) rock avalanche scenarios, for various friction coefficients $\mu_S = \tan(\delta)$. Travel distances are measured from the cliff toe (right most white cross in Figure 4.2b) along the river stream. Error bars (computed by considering 1 to 10 m thickness thresholds, to locate the extent of the deposits) are not displayed, but are at most twice the size of the markers.

4.5.1 Samperre rock avalanches back-analysis

The travel distance of the *sc_2009*, *sc_2009_1* and *sc_2018* rock avalanche scenarios are displayed in Figure 4.18 (orange crosses, orange dots and green dots respectively). The best-fit friction coefficients to reproduce the Aug. 21, 2009 observations (dotted orange line in Figure 4.18) are $\mu_S = \tan(11°) = 0.19$ and $\mu_S = \tan(12°) = 0.21$ for the *sc_2009* and *sc_2009_1* scenarios respectively. The *sc_2009_1* simulations (same volume as *sc_2009*, but different initial geometry) display slightly higher runouts than the *sc_2009* simulations (maximum increase of 200 m, compare orange circles and crosses in Figure 4.18). The Jan. 4, 2018 deposits extent (dashed green line in Figure 4.18) is best reproduced with $\mu_S = \tan(14°) = 0.25$. For this friction coefficient, the final deposits extent and geometry of the *sc_2018_1* scenario (where the initial unstable volume is released in two phases) are very similar to the *sc_2018*'s deposits (compare Figures 4.17b and Figures 4.17d).

With the best-fit friction coefficients, the main phase of the *sc_2009* and *sc_2009_1* avalanches last about 70 s, which is much less then the 170 s main phase of the Aug. 21, 2009 collapse (compare red and grey lines in Figure 4.9b). Moreover, the cigar-shape clearly seen in the seismic signal is not reproduced by the simulations dissipated energy rate: it displays a sharp 10 s increase followed by a progressive decrease. In comparison, seismic signal and modeled flow durations are more consistent for the Jan. 4, 2018 event (about 60 s and 80 s for the main phase respectively, see Figure 4.10b). The flow dissipated energy rate reproduces correctly the main seismic energy increase phase (Figure 4.10b, at 30 s), but fails to reproduce the signal complexity, with successive energy peaks. Results are slightly improved in the *sc_2018_1* scenario where the mass is released in two successive steps, 13 s apart (Figure 4.10b, red dashed line).

Thicknesses and velocities for the *sc_2018* scenario with $\mu_S = \tan(14°) = 0.25$ are given in

Figure 4.19 and Figure 4.20. In the first 30 s, the flow is locally more than 40 m thick, with front velocities between 30 and 40 m s^{-2}. After 100s, thicknesses do not exceed 30 m with velocities lower than 20 m $^{-1}$. While most of the energy is dissipated after 100 s (Figure 4.10b, red plain line), at that time the flow front is still about 500 m away from its final resting position. Afterwards, 600 s are still needed for the front to stop.

4.5.2 Debris flow back-analysis

Instantaneous reservoir remobilization: *LH_R_cliff* and *LH_R_river*

In the *LH_R_cliff* scenario, the Voellmy rheology with $\mu_S = \tan(2°)$ and $\xi = 500$ m s^{-2}, and the Coulomb rheology with $\mu_S = \tan(2°)$ and $\mu_S = \tan(3°)$, reproduce correctly the flooded areas, with thicknesses in the village mostly below 1 m (Figure 4.21a-e). Small overflows on the left bank within inhabited areas are modeled with all rheologies though they were not observed in 2010. The most important overflow is obtained with Coulomb and $\mu_S = \tan(2°)$ (Figure 4.21d, 20,000 m^2). Still on the left river bank but more upstream, other 2010 overflow areas are modeled correctly (Figure 4.21a-c, green outlines between the bridge and CCPA). With Voellmy, the area flooded in 2010 on the right river bank (about 20,000 m^2) is over-estimated with $\mu_S = \tan(2°)$ and under-estimated with $\mu_S = \tan(3°)$ (see Figure 4.21e). With Coulomb and $\mu_S = \tan(3°)$, the total flooded area on the right bank is consistent with observations (Figure 4.21e, right-most orange cross), but the shape of the flooded zone does not match in-situ observations (Figure 4.21b, compare green outline with yellow deposits on the right bank). In comparison, Coulomb and $\mu_S = \tan(2°)$ yield more realistic results (Figure 4.21c and 4.21e, right most blue circle).

The Jun. 19, 2010 DF travel duration between RPRE and CPMA (1.5 km) is estimated from AFMs recordings between 1 and 4 min. When picking the maximum discharge time at these locations in simulations, only the Coulomb rheology with $\mu_S = \tan(2°)$ could reproduce a 4 min interval (Figure 4.21f, blue plain line). The second and third smallest interval are 5 min (Voellmy, $\mu_S = \tan(2°)$ and $\xi = 500$ m ^{2}) and 5 min 20 s (Coulomb, $\mu_S = \tan(3°)$). For these 3 simulations, the corresponding flow durations between RPRE and the Prêcheur bridge (4,3 km) vary between 10 and 24 min (Figure 4.21g). With Voellmy and $\mu_S = \tan(2°)$, travel durations between RPRE and CPMA is at most 6 min, and 20 min between RPRE and the Prêcheur bridge. With a slightly higher friction coefficient ($\mu_S = \tan(3°)$), the flow is slowed down (at most 8 min are needed to reach CPMA).

Picking discharge onsets instead of discharge maximums decreases travel durations. For instance, with $\mu_S = 2°$ and the Voellmy rheology, the travel duration between RPRE and CPMA is decreased by 1 min (Figure 4.21f, compare blue plain and dashed lines). These effects are amplified when greater distances are considered. Thus, with $\mu_S = \tan(3°)$, picking onsets instead of maximums increase travel durations between RPRE and CPMA by 1 to 2 min, and travel durations between RPRE and the bridge by 10 min (Figure 4.21f-g, compare orange plain and dashed lines).

The *LH_R_river* scenario involves a similar volume as the *LH_R_cliff* scenario, but with the reservoir located further downstream. It does not change significantly the results (see Figure 4.22). As mentionned previously, the 0.65×10^6 m^3 volume involved in the *LH_R_cliff* and *LH_R_river* scenarios is small in comparison to the volume that actually collapsed the the Samperre during the May 2010 destabilization crisis (2.1×10^6 m^3, Clouard et al., 2013). Thus, we also consider a larger 1.2×10^6 m^3 screes reservoir at the cliff bottom that extends down to the waterfall.

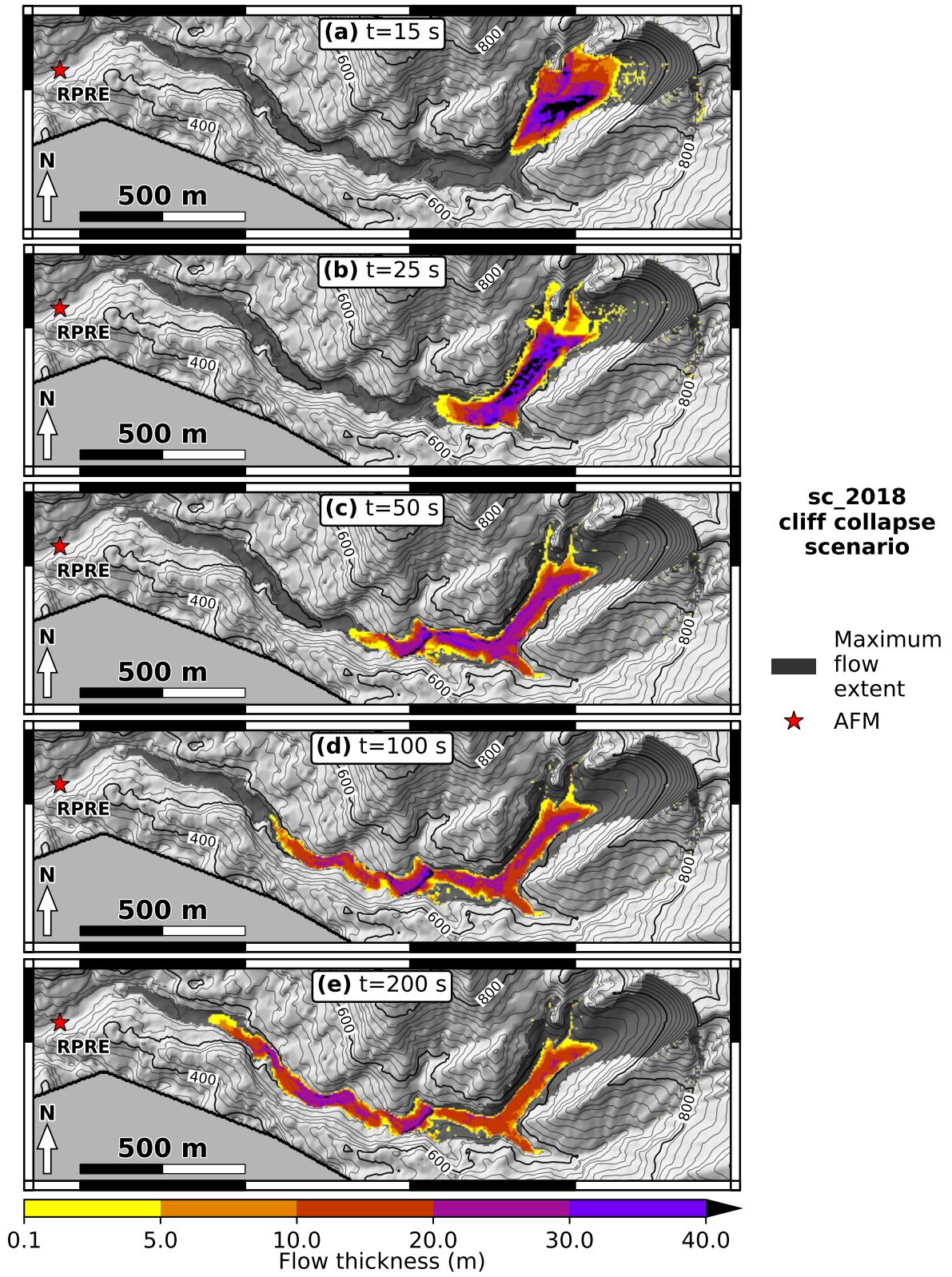

Figure 4.19: *sc_2018* simulation with Coulomb rheology and $\mu_S = \tan(14°) = 0.25$. Flow thickness is given at (a) $t = 15$ s, (b) $t = 25$ s, (c) $t = 50$ s and (d) $t = 100$ s.

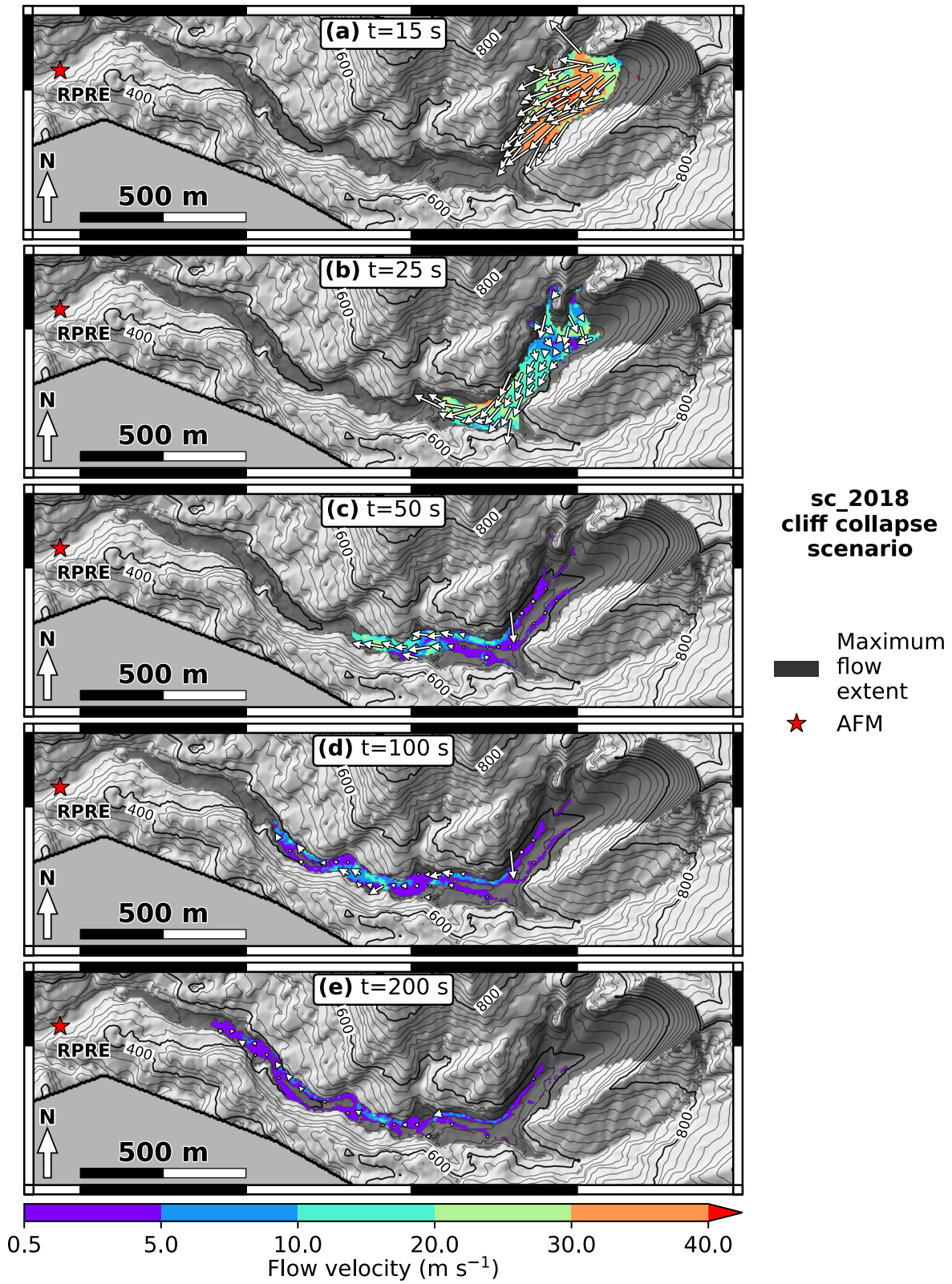

Figure 4.20: *sc_2018* simulation with Coulomb rheology and $\mu_S = \tan(14°) = 0.25$. Flow velocity is given at (a) $t = 15$ s, (b) $t = 25$ s, (c) $t = 50$ s and (d) $t = 100$ s. Small white arrows give flow velocity direction.

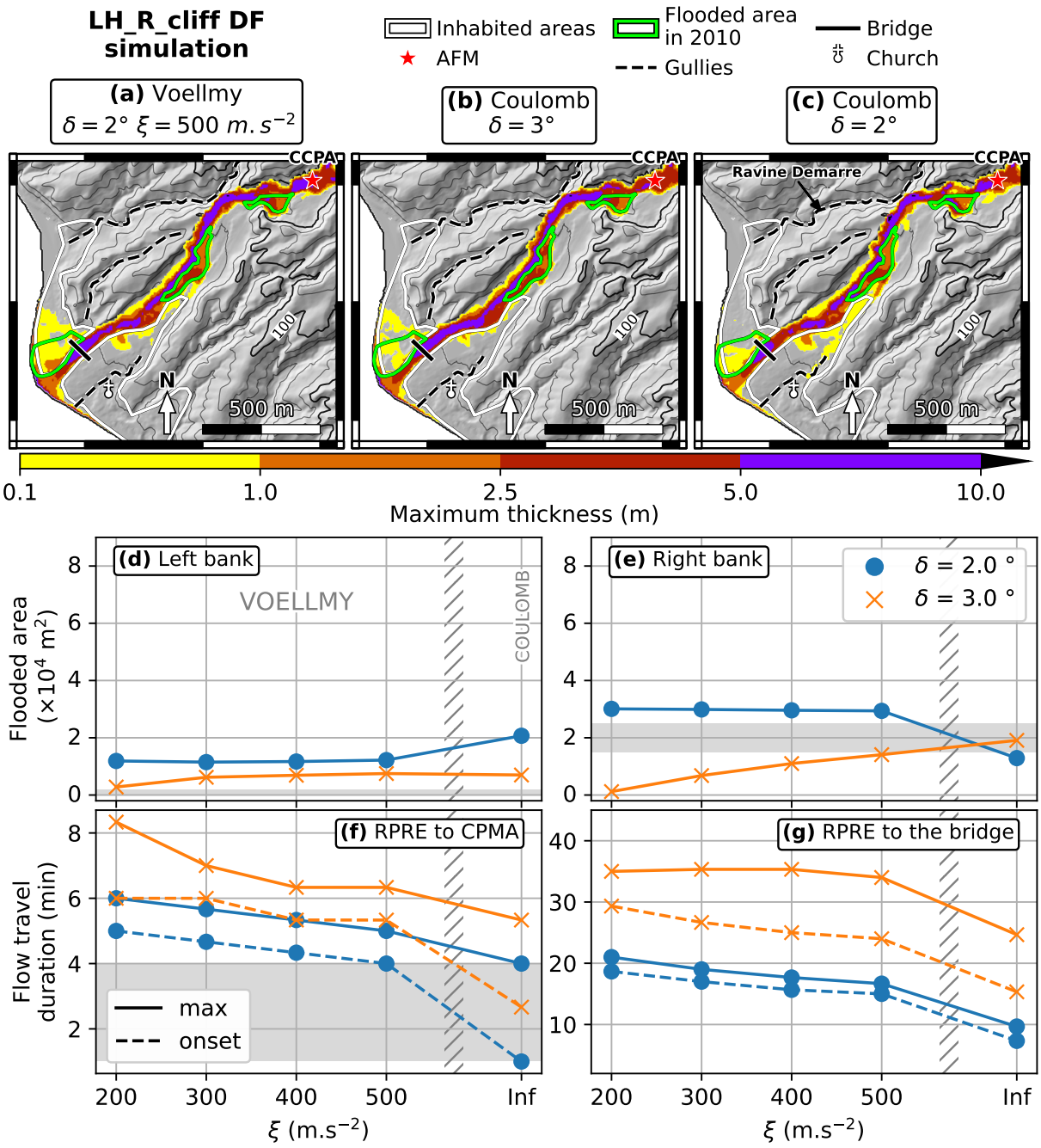

Figure 4.21: Simulation results for the *LH_R_cliff* scenario. (a) Maximum flow thickness with the Voellmy rheology, $\mu_S = \tan(2°) = 0.03$ and $\xi = 500$ m s^{-2}. (b) Maximum flow thickness with the Coulomb rheology and $\mu_S = \tan(3°) = 0.05$. (c) Maximum flow thickness with the Coulomb rheology and $\mu_S = \tan(2°) = 0.03$. Topography is the 08/2018 DEM. Each point in (d), (e), (f) and (g) is a simulation result, with friction coefficient given by line color and turbulence coefficients given by the x-coordinate. Left of hatches is for the Voellmy rheolgy, right is for the Coulomb rheology (equivalent to infinite turbulence coefficient). (d) Flow travel duration between RPRE and CPMA (about 1.6 km). They are measured by picking the maximum of the discharge at each location (plain line), or the onset of the discharge increase(dashed line). (e) Flow travel duration between RPRE and the Prêcheur bridge (about 4.3 km). (f) Area flooded on the left river bank, within inhabited areas. (g) Area flooded on the right river bank, within inhabited areas. Grey patch give observations ranges for the Jun. 19, 2010 DF.

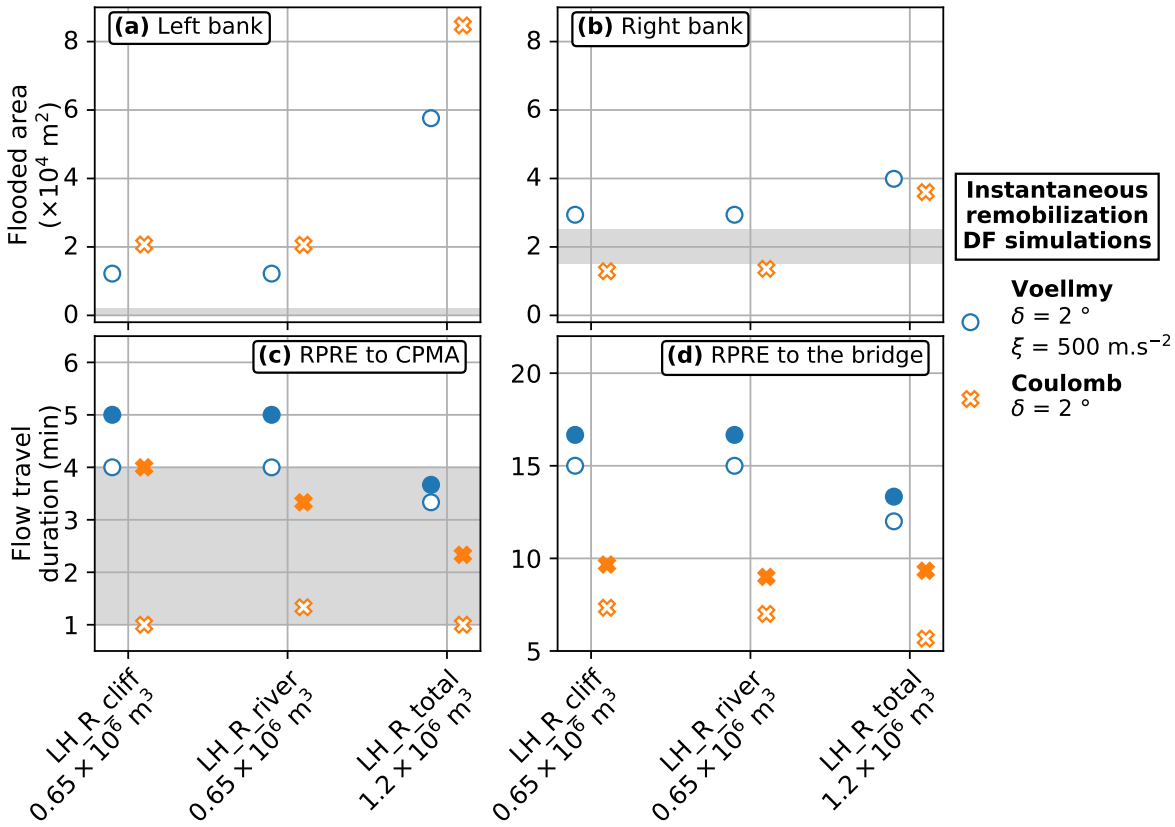

Figure 4.22: Comparison between the *LH_R_cliff*, *LH_R_river* and *LH_R_total* scenarios (see abscissa). (a) Area flooded in the Precheur village, left bank. (b) Area flooded in the Prêcheur village, right bank. (c) Travel durations between RPRE and CPMA. (d) Travel durations between RPRE and the bridge. Filled markers: durations measured by picking discharge maximum. Empty markers: durations measured by picking the onset of discharge increase. Grey patch give observations ranges for the Jun. 19, 2010 DF.

Instantaneous reservoir remobilization: *LH_R_total*

In comparison to the *LH_R_cliff* scenario, observed flooded areas are largely over-estimated in the *LH_R_total* scenario (Figure 4.23a-e), which indicates the *LH_R_cliff* scenario is more realistic. With the Voellmy rheology, 40,000 and 60,000 m^2 are flooded in inhabited areas on the left bank for $\mu_S = \tan(3°)$ and $\mu_S = \tan(2°)$ respectively, whatever the turbulence coefficient ξ (only about 10,000 m^2 in *LH_R_cliff* scenario). In particular, the flow follows a small gully in the Prêcheur village, on the northern side of the church (Figure 4.23a-b, black dashed line near the cross), which was not observed in 2010. Both $\mu_S = \tan(2°)$ and $\mu_S = \tan(3°)$ yield a 40,000 m^2 flooded area on the right bank (Figure 4.23e) that largely exceeds observations (Figure 4.23a-c, green line). Results are similar with the Coulomb rheology and $\mu_S = \tan(3°)$, but $\mu_S = \tan(2°)$ results in a large overflow: the alluvial fan is completely flooded (Figure 4.23c). Besides, the DF manages to run over the river right bank about 400 m downstream CCPA, and enters two adjacent gullys (Figure 4.23c, black dashed lines on the northern side of the river). One of these gullies drives the flow back to the alluvial fan. Less material enters the other gully, the Ravine Demarre, but it then heads towards the northern quarter of the Prêcheur village which is not reached in other simulations.

Voellmy rheology with $\mu_S = \tan(2°)$ and $\xi = 500$ m s^{-2}, as well as Coulomb rheology with $\mu_S = \tan(2°)$ and $\mu_S = \tan(3°)$, give travel durations between RPRE and CPMA smaller than 4 min (Figure 4.23f), which is consistent with observations. The DF covers the distance between RPRE and the bridge in 17 to 30 min with $\mu_S = \tan(3°)$, and in 10 to 17 min with $\mu_S = \tan(2°)$ (Figure 4.23g, orange and blue plain lines respectively). The effect of measuring durations with the onset of discharge increase instead of maximums is similar to simulations with the *LH_R_cliff* scenario.

From the previous simulations, we have shown that the instantaneous remobilization of 0.65×10^6 m^3 modeled with the Coulomb or Voellmy rheology could reproduce the main characteristics (travel duration between RPRE and CPMA and flooded areas) of the Jun. 19, 2010 DF. The remobilization of a higher volume leads to an over-estimation of flooded areas, but yields a better match with observed travel durations. We will now use the rheological parameters derived from the previous rock avalanche and DF simulations for the forward prediction scenarios.

4.6 Forward-prediction simulations results

4.6.1 Possible future collapse and subsequent DF

A forward prediction simulation is done with the *sc_east* scenario, where 1.9×10^6 m^3 collapse from the cliff. We use the Coulomb rheology with $\mu_S = \tan(14°) = 0.25$, which is the best-fit friction coefficient that reproduced the Jan. 4, 2018 event in the *sc_2018* simulation. Given the uncertainty related to the volume involved in the Aug. 21, 2009 event, we choose not to use the associated back-analyzed friction coefficient. The final deposits of the simulated rock avalanche of the *sc_east* scenario are similar to the *sc_2018* simulation with the same friction coefficient, as they extend only a few tens of meters further downstream (Figure 4.24a). Their maximum thickness is about 30 m.

This reservoir is then used as a source term for the propagation of the DF. We use instantaneous remobilization, as it proved to reproduce results coherent with observations for the *LH_R_cliff* scenario (in particular for flooded areas) and the *LH_R_total* scenario (in particular for the travel durations). We test three rheologies: the Voellmy rheology with $\mu_S = \tan(2°)$ and $\xi =$

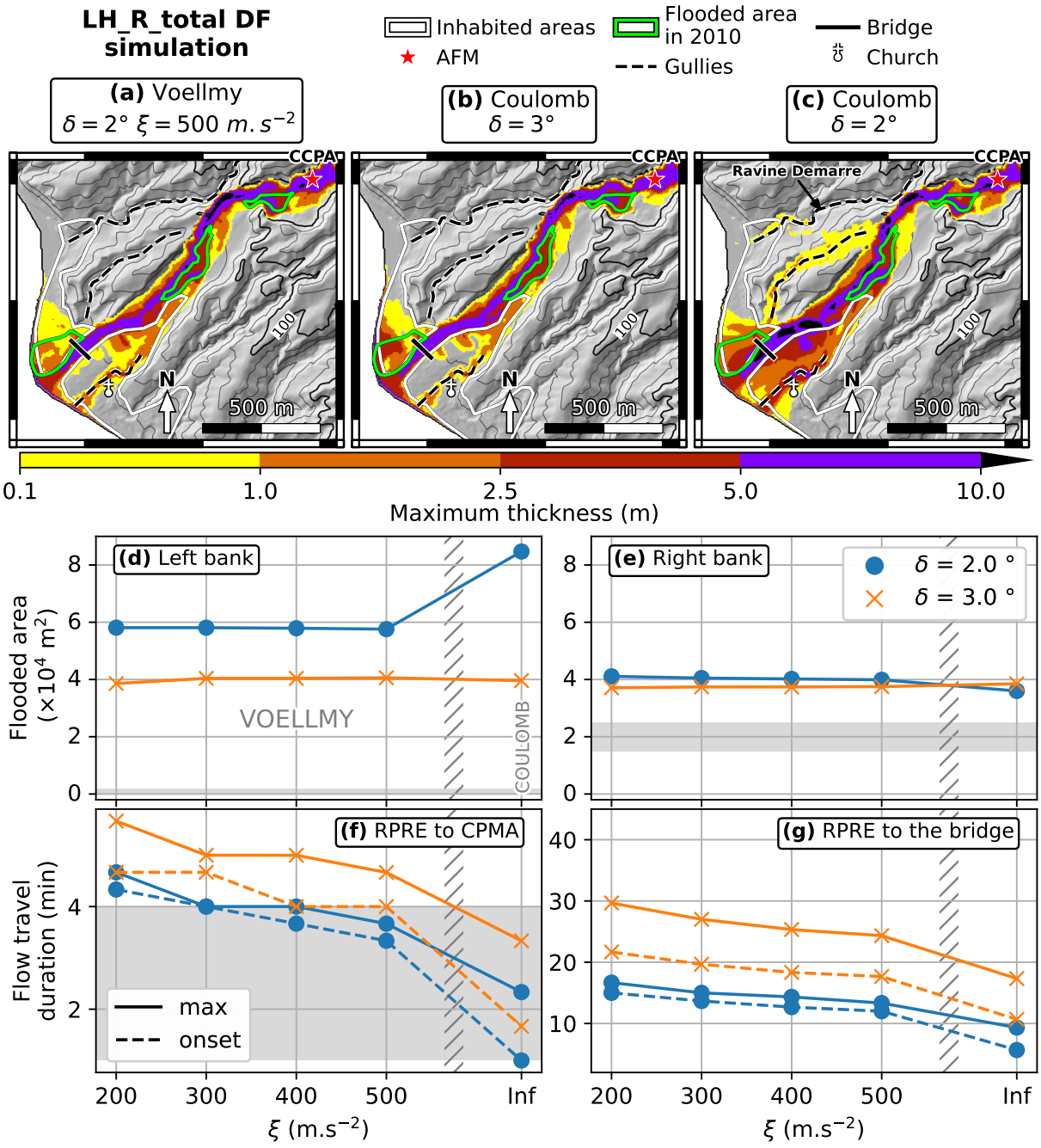

Figure 4.23: Simulation results for the *LH_R_total* scenario. See Figure 4.21 for legend.

500 m s^{-2}, and the Coulomb rheology with $\mu_S = \tan(2°)$ or $\mu_S = \tan(3°)$. The corresponding disharges are given in Figure 4.24b, 4.24c and 4.24d.

With the Voellmy rheology, the travel durations and flooded areas are very similar to results derived in the *LH_R_total*. However, the DF velocity is reduced by about 10% when the Coulomb rheology is used (see Table 4.2). As a matter of fact, the initial mass is spread more broadly in the river bed, such that the flow front accelerates on a shorter distance. This effect is not observed with Voellmy because the turbulent retarding term in (4.2) prevents the flow from accelerating indefinitely. Peak discharges at RPRE vary between 4,000 and 6,000 m^3 s^{-1}: this is coherent with field observations in other contexts, for this range of volumes (see Figure 2 in Rickenmann, 1999). With Coulomb and $\mu_S = \tan(3°)$, some of the flowing material stops before it reaches the sea, such that the peak discharge at the bridge does not exceed 400 m^3 s^{-1}. To the the contrary, $\mu_S = \tan(2°)$ increases mobility, and peak discharges reach almost 1000 m^3 s^{-1} with the Voellmy rheology Figure 4.24c), and more than 1600 m^3 s^{-1} with the Coulomb rheology (before the DF overflows the river bed, Figure 4.24d).

4.6.2 DF with progressive initiation

We investigate here the influence of the initiation mechanism on the DF dynamics in simulations. in Figure 4.25, we compare the results of releasing instantaneously the screes reservoir as in the *LH_R_cliff* scenario, to simulations where we impose a constant source discharge during $\Delta t = 10$ or 20 min at the foot of the reservoir location (*LH_D_cliff* scenario). The total released volume remains the same. In comparison to the instaneous release, $\Delta t = 10$ min reduces by half the flooded area on the left bank. It is almost not flooded for $\Delta t = 20$ min (Figure 4.25a). With this discharge duration, inundations on the right bank are also halved (Figure 4.25b). Finally, every 10 min increase in the discharge duration produces a 2 min and 5 min increase of the travel duration between RPRE and CPMA, and between RPRE and the bridge respectively (Figure 4.25c-d). Here travel durations are measured by picking the onset of discharge increase, because no clear maximum can be identified when we impose a constant discharge in the source area. For a given released volume, the location of the source discharge area has in comparison little influence on the results (Figure 4.26, comparison between *LH_D_cliffl*, *LH_D_waterfall* and *LH_D_RPRE* scenarios). The main difference is obtained when the DF is initiated at RPRE: it needs 1 min less to reach CPMA, and then the bridge.

4.7 Discussion

In this section we will first discuss the results of rock avalanche modeling (Section 4.7.1). Then, we will tackle the complex issue of DF modeling (Section 4.7.2). Our DF simulations were calibrated on an extreme high-discharge event: we may wonder to what extent we could also reproduce smaller DFs (Section 4.7.3). Finally, we will discuss the implications of our work for hazard assessment (Section 4.7.4).

4.7.1 Rock avalanche modeling

Comparison with empirical estimations of runout

Lucas et al. (2014) estimate the mobility of landslides through the effective friction coefficient μ_{eff}. μ_{eff} differs from the traditional angle of reach (or Heim's ration) μ_H: while μ_H depends

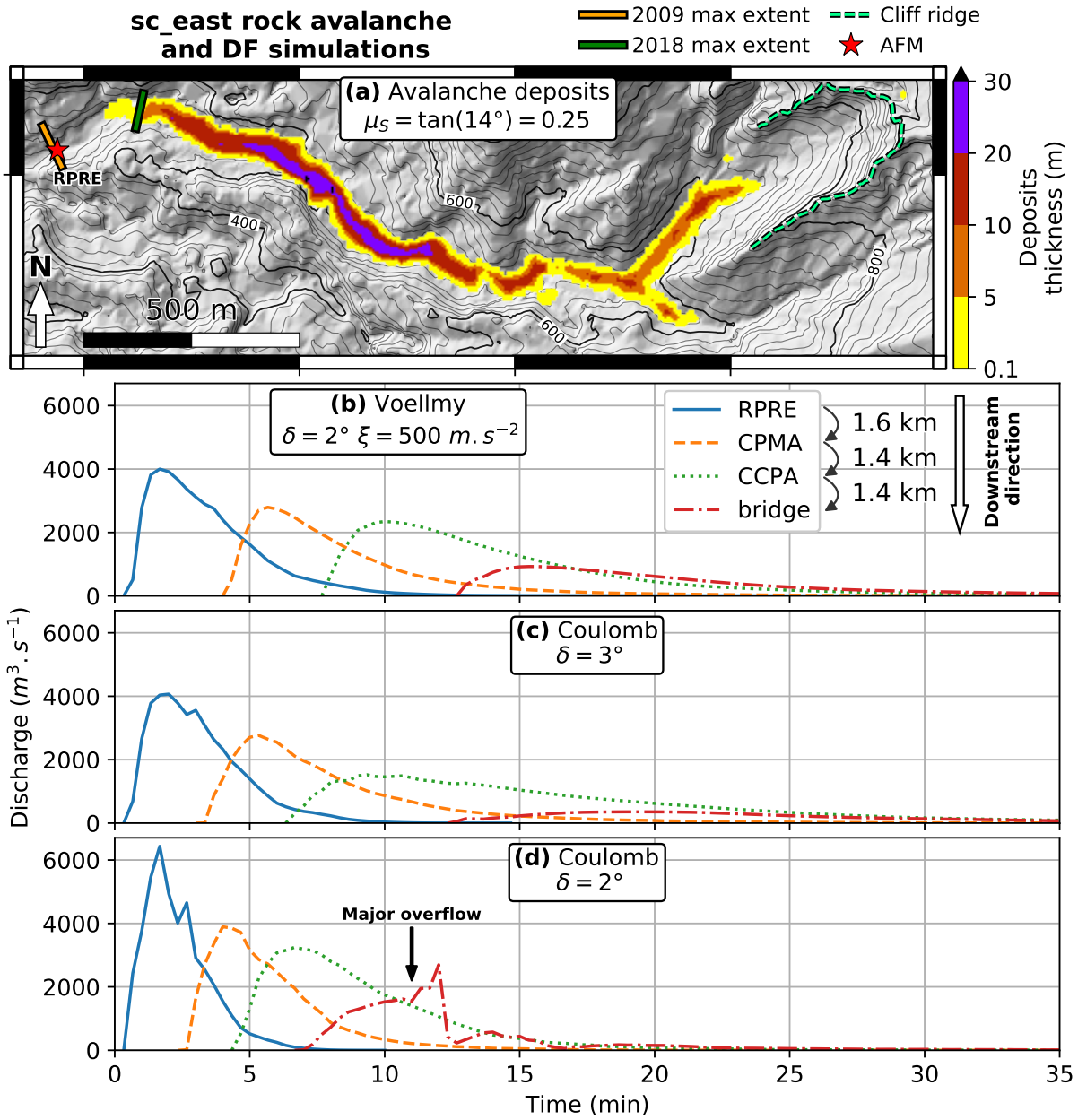

Figure 4.24: Results of the *sc_ east* rock avalanche scenario and subsequent DF. (a) Final deposits of the rock avalanche, modeled with Coulomb and $\mu_S = \tan(14°) = 0.25$. The topography is the 08/2018 DEM. (b), (c) and (d): Simulated discharges at RPRE, CPMA, CCPA and the bridge. (b) Voellmy rheology, $\mu_S = \tan(2°)$ and $\xi = 500$ m s^{-2}. (c) Coulomb rheology, $\mu_S = \tan(3°)$. (d) Coulomb rheology, $\mu_S = \tan(2°)$. Strong variations in (d) for discharge at the bridge result from major overflows around the bridge.

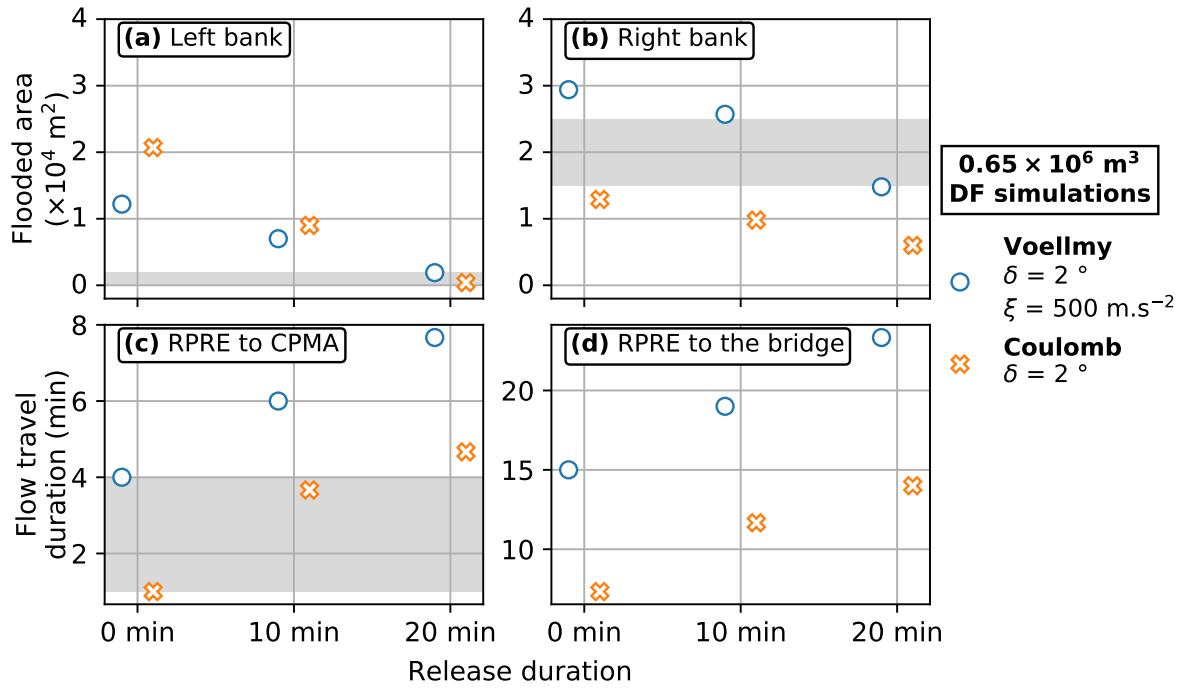

Figure 4.25: Comparison between the *LH_R_cliff* and *LH_D_cliff* scenarios. The released volume is always 0.65×10^6 m^3, but release is either instantaneous, or lasts 10 or 20 min (see abscissa). (a) Area flooded in the Precheur village, left bank. (b) Area flooded in the Prêcheur village, right bank. (c) Travel durations between RPRE and CPMA. (d) Travel durations between RPRE and the bridge. Durations are measured with discharge onsets. Grey patches are observations for the Jun. 19, 2010 DF.

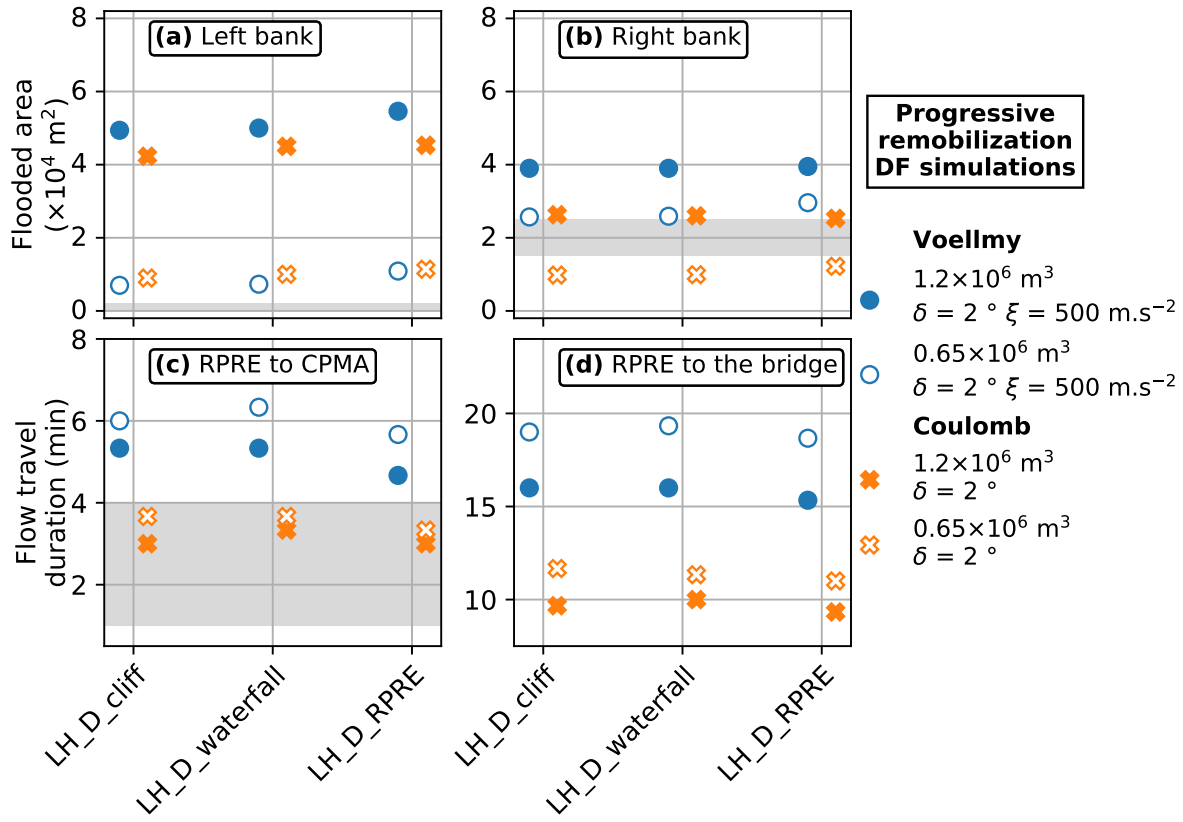

Figure 4.26: Results of the *LH_D_cliff*, *LH_D_waterfall* and *LH_D_RPRE* scenarios (see abscissa). Release duration is 10 min. (a) Area flooded in the Precheur village, left bank. (b) Area flooded in the Prêcheur village, right bank. (c) Travel durations between RPRE and CPMA. (d) Travel durations between RPRE and the bridge. Durations are measured with discharge onsets. Grey patches are observations for the Jun. 19, 2010 DF.

only on the landslide runout, μ_{eff} takes also the initial mass geometry into account. We have:

$$\mu_{eff} = \tan(\theta) + \frac{H_0}{\Delta L}, \tag{4.6}$$

$$\mu_H = \frac{H}{\Delta L'}, \tag{4.7}$$

with θ the topography average slope along flow path, H_0 the maximum height of the initial mass and ΔL the landslide travel distance along topography from the scar toe. H (drop height) and $\Delta L'$ are respectively the difference in altitude and horizontal distance between the upper scar and furthest deposits location (see supplementary in Lucas et al., 2014). The expression (4.6) of μ_{eff} is derived from the analytical solution of thin-layer dam-break (Mangeney et al., 2000a). Lucas et al. (2014) use a database of terrestrial and non-terrestrial landslides with a small amount of water to estimate empirical relations relating μ_H and μ_{eff} to the landslide volume V:

$$\mu_{eff} = V^{-0.0774}, \tag{4.8}$$

$$\mu_H = 1.2V^{-0.089}. \tag{4.9}$$

When we apply theses relation to the 2009 and 2018 Samperre rock avalanches, we get values between $\tan(18.5°) = 0.33$ and $= \tan(19.5°) = 0.35$ for both μ_H and μ_{eff}. This is in good agreement with the values we compute directly from observations, using (4.6) and (4.7) (between $= \tan(19°) = 0.34$ and $= \tan(19.5°) = 0.35$ for both μ_H and μ_{eff}).

In comparison, in the simulations we used friction coefficients between $\mu_S = \tan(11°) = 0.19$ and $\mu_S = \tan(14°) = 0.25$ to reproduce observed travel distances. It has been shown that μ_H cannot be used to estimate directly the flow mobility, because it describes also purely geometrical effects (e.g. Lucas and Mangeney, 2007; Staron and Lajeunesse, 2009; Lucas et al., 2014). The latter are corrected by the more complex definition of μ_{eff}, such that it proved to better estimate the friction coefficient μ_S needed to reproduce real landslides (Lucas et al., 2014). It seems not to be the case in our study, but large uncertainties are actually associated to (4.6). For instance, using Supplementary Table 4 in Lucas et al. (2014), we deduce a 95% confidence interval [0.25 - 0.45] for μ_{eff}, for the 2018 event. However, Peruzzetto et al. (2019) also find that μ_{eff} over-estimates μ_S. As the expression (4.6) was derived for flows on constant slopes, it may no longer be valid for flows on complex topographies when the flow follows bended channels.

One or multiple successive collapses?

We found that modeling successive collapses helps reproduce, to some extent at least, the complexity observed in the Jan. 4, 2018 seismic signal, without changing significantly the runout. Because SHALTOP models one-phase/one-layer flows, it should be noted that in the *sc_2018_1* scenario, the second avalanche is assumed to be mixed with the first one as soon as they join. As a result, we do not model the possible development of a two-layer flow, with the second avalanche propagating above the first one. As the latter flattens the topography, such a mechanism could enhance mobility.

However, the fact that for a given volume, the initiation mechanism has little influence on the travel distance is consistent with results from (Moretti et al., 2015) who model the 2010 Mount Meager landslide, with 1, 2 or 3 successive collapses. For our simulations, one possible explanation is that the initial kinetic energy of the avalanche is dissipated quickly (in the first 25 s to 50 s (see Figure 4.20a-b), because the avalanche is blocked at the inlet of the gully. The latter is indeed too narrow for the flow to enter it at once. Then, the rock avalanche can move further downstream only if relatively small friction coefficients are used in the simulations. In turn, the final travel distance may then depend more on the friction coefficient and on the volume

of material available to fill the river asperities, than on the initial position of or destabilization process.

Nevertheless, such an analysis may be valid for large collapses only. In May 2010, destabilizations occurred as a succession of 47 successive events in the first day (Clouard et al., 2013). Given the estimated 2.1×10^6 m^3 total volume, this suggests an average volume of 50,000 m^3 per event (certainly less, as collapses kept occurring in the following days). Following Lucas et al. (2014), friction coefficients around $\mu_S = \tan(23°) = 0.42$ are needed to model the propagation of such volumes. In turn, these small granular avalanches stop in the vicinity of the cliff toe. In comparison, larger granular flows are modeled with lower friction coefficients (in our case, less than $\tan(15°) = 0.27$). The physical process enhancing the mobility of large landslides are still debated: they include flash heating (Lucas et al., 2014), granular agitation at the base of the flow (Bartelt et al., 2007), and acoustic fluidization (Johnson et al., 2016) (e.g. see Korup et al. (2013) for a review).

We infer that the mechanism of the Aug. 21, 2009 rock avalanche is different from both the January 2018 and May 2010 destabilizations. As a matter of fact, it occurred in one single main event and the recorded seismic signal is very different from those recorded on Jan. 4, 2018 (see Figure 4.9 and Figure 4.10). Its cigar-shaped envelope is similar to signals of granular flows in Dolomieu crater, on Piton de la Fournaise volcano in Réunion island (Hibert et al., 2014; Durand et al., 2018). We suggest it may have been initiated as a progressive retrogressive collapse. Such a process cannot be modeled with SHALTOP, where the initiation is instantaneous. It could however be empirically reproduced by imposing a constant source discharge, as we did for DF simulations.

4.7.2 DF modeling

DF initiation: gully erosion or liquefaction?

As for rock avalanches, thin-layer models equations cannot reproduce the physical processes at stake during the initiation of DFs. In mountainous areas, DFs are often initiated as multiple local destabilizations of unconsolidated and water-laden debris on steep slopes. As they shear, increased pore-water pressure promote liquefaction, and in turn the disintegration of the debris (Iverson, 1997; Iverson, 2014). However, the process aforementioned is commonly associated to debris flows in mountainous areas occurring after heavy rainfalls, such as in Vargas state, Venezuela, in 1999 (Larsen and Wieczorek, 2006).

The instability of the reservoir could thus be controlled by sand dilatancy properties (Bolton, 1986; Yin and Chang, 2013). If it is in a loose state it will undergo compaction under shearing, leading to the increase of pore pressure and in turn destabilization. Such a mechanism require undrained conditions, which might be possible at the reservoir bottom due to water resurgences, even without major precipitations. For instance, Chen et al. (1995) show that water supply at the base of an unstable mass triggers larger failure than water supply from the surface. A detailed geotechnical analysis of the screes reservoir would be necessary to better constrain its destabilization process, all the more so as previous studies have shown instabilities in granular materials can occur both in loose and dense sands, and in drained and undrained conditions (e.g. Wanatowski et al., 2010). However, for safety reasons, it is impossible to sample the reservoir screes, and only the lahars deposits can be used as proxys. Geotechnical analysis of some of the samples recovered in the river was carrid out (uni-axial tests). Interpretation and exploitation of these results is beyond the scope of this work, but could help investigate the stability of the screes reservoir.

As discussed previously, the high discharges observed during the Jun. 19, 2010 DF as well as the relative short duration of its main phase (about 10 min, see Figure 4.14a) suggest an instantaneous or at least very fast initiation. However, for smaller DFs, the respective importance of screes destabilization and gully erosion/entrainment by runoff in the DF initiation is difficult to constrain. For instance, McGuire et al. (2017) suggest that post wildfires debris flows are more likely generated by mass failure of sediments in the river than progressive bulking, but the nature of the solid materials is different than in our case. Cascading and entrainment processes, with a small amount of material progressively gaining momentum as it flows over an erodible bed, have been observed both for dry granular flows (Mangeney et al., 2010; Viroulet et al., 2019) and for flows on water-laden beds with high pore pressure (Iverson et al., 2011).

Modeling such processes is not easy. We used constant source discharges to investigate the influence of progressive material release. However, the extent to which this strategy allows to model the dynamics of a DF initiated by progressive gully-erosion or runoff is hard to quantify. To answer this question, more data is needed to characterize DF initiation. Comparisons with more realistic initiation models could also be carried out. Recent studies have proposed integrated models to simulate multiple rainfall induced debris flows at the catchment scale, with rainfall runoff, infiltration, shallow-destabilizations and entrainment (Shen et al., 2018; Bout et al., 2018; Hong et al., 2019). The applicability of such models to the specific case of the Prêcheur river is nevertheless uncertain, in particular because of water seepage at the cliff toe that are difficult to constrain and model. Besides, they rely on many parameters that are difficult to constrain.

DF propagation: erosion

As discussed previously, we have not considered entrainment in our simulations. Apart from the influence such a process could have for the DF initiation, we may expect it also influences the DF dynamics further downstream. In particular, the upper river section above RPRE is narrow and steep-walled, with slopes between 7° and 12°, such that it is prone to bed (from previous lahars deposits) and lateral erosion. It is however difficult to constrain numerically. The most commonly used erosion/deposition law relates erosion rate to flow momentum hu: (McDougall and Hungr, 2005; Pirulli and Pastor, 2012):

$$\frac{\partial b}{\partial t} = Ehu, \tag{4.10}$$

where b is the altitude of the bed, h the flow thickness, u the flow velocity and E is a positive empirical coefficient. Assuming an exponential increase of the landslide volume from its initial value V_i to its final value V_f over the length of the landslide path L, McDougall and Hungr (2005) propose the following estimation of E:

$$.E = \frac{ln(V_f/V_0)}{L} \tag{4.11}$$

Such a law makes it possible to empirically reproduce the sometimes drastic increase of flowing material (e.g., from 150 to 1620 m^3 for the 2000 Tsing Shan debris flow in Hong Kong, Pirulli and Pastor, 2012). However, as suggested by Iverson (2012), proportionality between erosion rate and velocity may stand true only in situations where entrainment has no significant impact on the flow momentum, as in fluvial system. When this is no longer the case, Iverson (2012) show that erosion rates are actually inversely proportional to the flow velocity. A similar conclusion is reached by Lusso et al. (2017a). As a matter of fact, the energy needed to accelerate sediments at rest to the flow velocity is, precisely, all the more important as the flow velocity is high. In turn, relations as in (4.10) lead to thin-layer equations (Bouchut et al., 2008) that do not conserve energy. Iverson (2014) give an overview of existing erosion and deposition models in

thin-layer models and specify the necessary requirements for mass and momentum conservation at the static-flowing interface, highlighting the mere methodological complexity of deriving a physically based model.

In our case, on account of the previous discussion, we may expect the high velocity at the onset of the Jun. 19, 2010 DF to limit its erosive power, at least at its front. However, this stands true only at the flow bottom and in the frame of laminar flows as in the development of Iverson (2012). If large blocks bulge out in the flow, resulting turbulences could create pressure drag and thus enhance entrainment. Inflexion points along the stream with sudden decrease of the slope may also favor erosion (Hu et al., 2016; Li et al., 2018). Besides, DFs experiments in flumes show that bank erosion may actually have a greater impact on DF dynamics than mere bed erosion (Lyu et al., 2017).

Given the gentle slope in the lower section of the river below RPRE (less than 4°), the main process at stake is supposedly deposition. However, the extent to which previous lahar deposits could be entrained is still unclear and difficult to quantify, as only the final deposits can be mapped. In order to estimate the conditions (in particular, DF velocity, height, solid content, and bed pore pressure) under which entrainment could occur on such gentle slopes, further analyses are needed with, for instance, flume tests and/or permanent on site instrumentation. The cameras installed downstream RPRE could help adress this issue, but other footage further upstream (for instance near CPMA) would provide key data on the DF evolution. More quantitative measurements demand the installation of sensors, such as pressure sensors or load cells (Arattano and Marchi, 2008). However, their installation and maintenance would be difficult because is it complex to access the river.

Nevertheless, such data would be a prerequisite to try and model precisely erosion along the river. As a matter of fact, entrainment in numerical model is at least partly empirical. Thus, it strongly depends on an a-priori knowledge experts in charge of in situ observations have about erosion areas and erodible thicknesses.

DF propagation: dilution and deposition

As we focused on high discharge events that display DF characteristics all along the Prêcheur river, we disregarded smaller events whose progressive dilution turns them into HFs with a vertical separation between the solid and fluid phases as they reach the Prêcheur village. We should also consider with caution the simulated velocities and thicknesses of the DF's tail where dilution is likely to change the flow rheology.

We can thus wonder whether deposits are well modeled in our simulations. A first estimation can be given by comparing the 03/2010 and 07/2010 DEMs. Because the river is very narrow in its upper section it could not be mapped properly and a detailed sedimentary balance is difficult to establish. However when we consider only the lower section (starting 400 m downstream the junction between the Prêcheur and Samperre river), we find that approximately 0.46×10^6 m^3 were deposited by the lahars between March and July 2010. Similarly, we compute a 0.37×10^6 m^3 volume deposited between July 2010 and August 2018, supposedly by the 2018 lahars. This stands for about 20% of the 2.1×10^6 m^3 that collapsed in 2010, the rest being evacuated in the sea or deposited upstream. The real percentage is actually higher, because some of the deposits had already been washed away by normal streamflow. But this could be counter-balanced by bank and bed erosion that are not accounted for in the 2.1×10^6 m^3. Both effects are nevertheless difficult to estimate. In comparison, in our *LH_R_cliff* and *LH_R_total* scenario, we model final deposits in the same area of 0.04×10^6 m^3 with the Coulomb rheology and $\mu_S = \tan(2°)$, and 0.12×10^6 m^3 with the Voellmy rheology, $\mu_S = \tan(2°)$ and $\xi = 500$ m s^{-2}. Thus, the

deposited volumes differ significantly from the 2010 and 2018 observations, whatever the initial volume (0.65×10^6 m^3 and 1.2×10^6 m^3). A more thorough comparison should take into account the influence of the river bed morphology, but this already suggests that deposition process may not be properly modeled.

This is of prior importance to investigate more precisely overflow hazards, as it closely linked to the river bed filling level. Numerical modeling with multi-phase shallow water models, such as *D-Claw* (George and Iverson, 2014; Iverson and George, 2014), *r.avaflow* (Mergili et al., 2017; Pudasaini and Mergili, 2019) or *GeoFlow_SPH* (Pastor et al., 2018b), could help investigate such effects. However, as discussed in the introduction, the associated equations are generally not fitted to complex topographies, but this would be less problematic in the lower section of the river that displays gentle slopes (less than 4°) and a wider river bed than upstream RPRE. Thus, future research could focus on using these models to investigate more deeply deposition process in the lower section of the river, without modeling explicitly the DF initiation (for instance, by using an hydrograph at RPRE as a source term).

Another key physical process that we do not model is the dilution of the DF as it reaches the sea. As we do not have bathymetric data, the altitude in the sea is set to 0 and we let the material flow freely through the grid boundary. Provided bathymetric data is available, the interaction between sea water and the DF can, in theory, be empirically modeled with two-phase models (Pudasaini and Mergili, 2019). We may however expect some process, such as the the transformation of the DF into a turbidity current (Elverhøi et al., 2000), not to be properly simulated. To our knowledge, research has mainly focused on understanding the generation of tsunamis by debris flows (e.g. Walder and Watts, 2003; de Lange et al., 2020), rather than on the influence of debris flow dilution in a large water body on the upstream dynamics.

4.7.3 Comparison between DF simulations and other documented events

Using the inventory of lahars made by Aubaud et al. (2013), we recovered the records from RPRE's and CPMA's AFMS of the 8 strongest lahars between September 2009 and August 2010 (classified as "strong" or "very strong" by Aubaud et al., 2013). DFs and HFs cannot be differentiated. By manually picking the maximums of the FULL channel on each AFM, for each surge during the lahar, we could derive a set of travel durations between the two stations (Figure 4.27a). Average travel durations decrease for increasing peak FULL values at RPRE: when the latter are higher than 3000 mV, lahars need no more than 7 min to go from RPRE to CPMA. However, when RPRE FULL records are about 1000 mV, travel duration span from 2 to 15 min. Any further interpretation is nevertheless complicated by the picking uncertainty, as sampling interval is only 1 min and the identification of maximum couples in RPRE and CPMA is sometimes difficult.

In our simulations, such variations in travel durations could be modeled by using different initial conditions and rheological parameters (Figure 4.27b-c). We find that high discharges at RPRE (more than 5000 m^3 s$-$1) are associated to travel durations between RPRE and CPMA spanning from 2.5 min to 5 min, while a discharge of 2500 m^3 s$-$1 yield durations spanning from 5 min to 12 min (Figure 4.27b). Such an effect is also observed when travel durations are computed by picking discharge onsets instead of discharge maximums (Figure 4.27c). For simulations with the Voellmy rheology, changing rheological parameters only slightly changes the modeled discharge but entails important variations in travel durations. Discharge are thus mainly controlled by the initial condition (i.e. the simulation scenario, for instance see vertically aligned stars and circles in Figure 4.27b and 4.27c). To the contrary, with the Coulomb rheology, a same simulation scenario will produce different discharges depending on the friction coefficient (e.g. stars with dashed circle in Figure 4.27b).

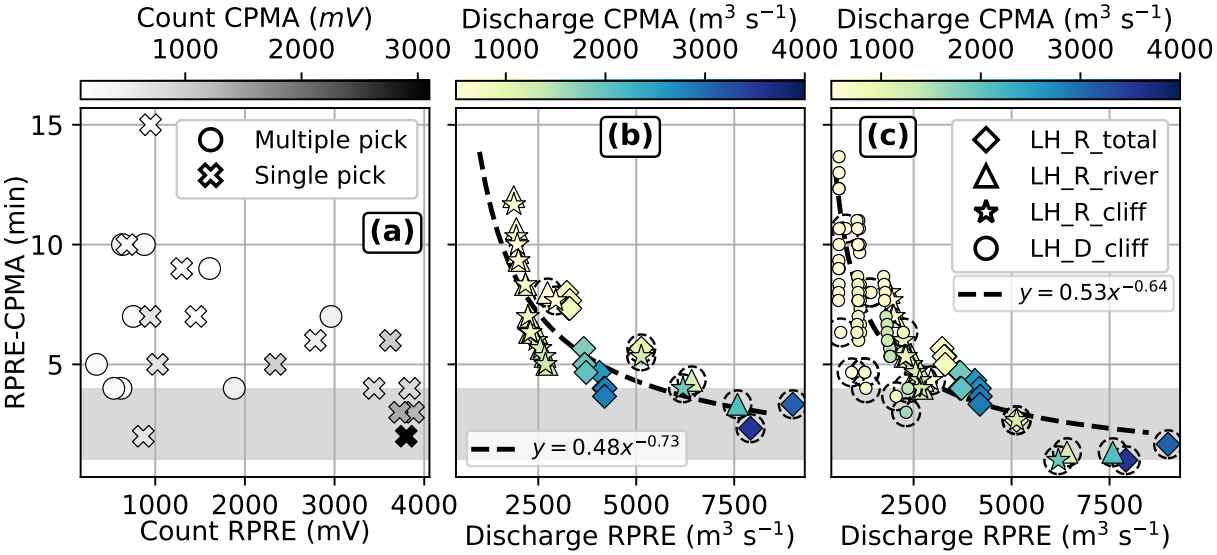

Figure 4.27: Flow travel durations between RPRE and CPMA deduced from AFMs recordings and simulations. (a) Dephasing between RPRE and CPMA FULL channel maximum, as a function of RPRE FULL channel maximum. Greyscale gives CPMA FULL channel. Picking was done manually for lahars with "strong intensity" between 2009 and 2011, from the database of Aubaud et al. (2013). Crosses: match between RPRE and CPMA FULL maximum is unambiguous. Circles: Uncertain pick, with multiple maximums in FULL CPMA possibly matching one maximum in FULL RPRE. (b) Dephasing between maximum discharges at RPRE and CPMA in simulation, as a function of maximum discharge at RPRE. Colorscale gives maximum discharge at CPMA. Symbols give the simulation scenario. Dashed black circles indicate simulations where the Coulomb rheology was used (Voellmy otherwise). Friction coefficient is $\mu_S = \tan(2°)$, $\mu_S = \tan(3°)$ or $\mu_S = \tan(4°)$. Turbulence coefficients range from 100 to 500 m s^{-2}. Dashed black line is the power law regression. (c) Same as (b) but with dephasing measured by picking the onset of discharge increase. Grey patch give observations ranges for the Jun. 19, 2010 DF.

This comparison shows that the range of travel durations (from RPRE to CPMA) measured for the most important lahars in 2009 and 2010 can be empirically reproduced by choosing different rheological parameters and source terms in DF simulations. This preliminary analysis should be completed by using a catalogue of more recent lahars: their dynamics can be more precisely contrained thanks to the CCPA AFM that was installed in 2014. Results could be then used for operationnal hazard assessment.

4.7.4 Towards hazard management

Prediction of rock avalanche and DF occurrence

Given its remote location, it is very hard to monitor the Samperre cliff. Samples of materials supposedly sharing the same characteristics as those composing the cliff could help characterize its geotechnical properties. In particular, though the cliff basal layer associated to ancient flank collapse seems not to have moved over the past decades, its stability should be further investigated. As a matter of fact, its ochre color suggests strong hydrothermal alteration. A more detailed study of the hydrogeological setting of the cliff would also help constrain the instability mechanisms. Finally, geomorphological and geological analysis of adjacent gullys could also point at other potentially unstable slopes.

In order to try and predict the occurrence of DFs, further investigations need to be done to better characterize the initiation process and the respective role of meteoric and seepage water, depending on the DF morphology. The latter can be deduced from deposits analysis and/or visual observations. Then and only then may it be possible to estimate DF occurrence hazard, provided i) a real-time estimation of the sedimentary stock in the river, ii) spatio-temporal precipitation data in the previous days/weeks, iii) a hydrogeological conceptual model of the Prêcheur river watershed. The latter may prove particularly difficult to construct in practice as the result of the impossibility to access most of the river sources. Besides, because of unconstrained underground water circulations,the hydrogeological and topographic watershed may well be different.

Though counter-examples exist, most lahars in the Prêcheur river are associated to rainfall events. To characterize the critical rainfall conditions that can trigger a lahar (and in particular a DF), it is common to define site-specific thresholds on rain intensity and duration from empirical observations (e.g. Marra et al., 2016; Staley et al., 2017; Bel et al., 2017). Some attempts have also been made to compute these rain intensity-duration thresholds with physical modeling of runoff (Berti and Simoni, 2005; Tang et al., 2019) and/or shallow destabilizations (Berti and Simoni, 2005; Papa et al., 2013). So far, no such threshold could be derived for the Prêcheur river catchment: lahars are associated to both light and heavy rains (Ville et al., 2015). However, this study did not take into account the volume of loose materials available at the cliff toe and in the upper section of the river. These latter data are difficult to constrain, but it is essential to consider them when investigating correlations between precipitations and lahars occurrences. Such an analysis is however difficult, as there are important spatial variations of precipitations intensity around the Montagne Pelée, at the scale of a few hundred meters. For instance, while the annual mean precipitation is about 1,000 mm yr^{-1} on the west coast of Martinique, it sometimes exceeds 10,000 yr^{-1} at the summit of Montagne Pelée (Aubaud et al., 2013). Thus, the pluviometry recorded at CPMA may not be representative of precipitations near the cliff

Flood hazard mapping

Deriving flood hazard maps is one of the most critical point of hazard assessment as subsequent land management may have long lasting impact on the population, with construction restrictions or even resettlement (Crittenden and Rodolfo, 2002; Bowman and Henquinet, 2015). In our simulations, no simple relation between flooded areas in inhabited areas and mobility could be established from our simulations. On the one hand, more material will reach the Prêcheur village when smaller friction coefficients and/or higher turbulence coefficients are used. On the other hand, low friction coefficients in simulations favor the evacuation of debris in the ocean. Such competing effects can be observed in our simulations: in the *LH_R_cliff* scenario, when we increase the turbulence coefficient (up to infinite values for the Coulomb rheology), the flooded area on the river right bank expands for $\mu_S = \tan(3°)$ and lessens for $\mu_S = \tan(2°)$.

The possibility that DFs overflow the river banks further upstream and enter adjacent gullies is another major concern. Quefféléan (2018a) suggest that the rocky edge separating the Prêcheur river from the Ravine Demarre, a few hundred meters downstream CCPA, could be overflowed (or even destroyed) by high discharge DFs. Such a situation is reproduced in our *LH_R_total* simulation with Coulomb and $\mu_S = \tan(2°)$. However, the over-topping of river banks is a highly non-linear phenomenon, with thresholds effects (Mergili et al., 2018; Peruzzetto et al., 2019), such that their modeling with thin-layer models should be considered with caution.

Thus, given the uncertainties associated to the numerical model and the partial knowledge we have in practice of DFs, it may prove difficult to derive quantitative flood maps merely from simulations results. Such maps must also consider the appreciation by experts of their realism, based on field observations (e.g. Moase et al., 2018). However, simulations results should not

either be dismissed. As a matter of fact, they can provide key insight on possible overflow scenarios that were not identified during field work. For instance, we have shown that in the case of en extreme high discharge DF, part of the flow may enter the gully between the Prêcheur river and the Ravine Demarre (Figure 4.23c). Such a scenario had not been considered by Quefféléan (2018a), and could be further investigated in future field works. Numerical modeling can also guide works in the river bed to mitigate overflow hazard: simulations can assess, at least qualitatively, the impact of river bed carving and/or protection works. This could be done by manually modifying the DEM on which simulations are run.

Real-time monitoring and early warning

So far, alarms have been triggered in the Prêcheur village when the flow height increases and activates the pendulum system at RPRE and/or when a threshold level is exceeded on the FULL channel of RPRE's AFM. Though efficient, this system sometimes results in false positive alarms when, for instance, the pendulum system is activated by debris or branches falling from the banks or when the DF undergoes dilution and reaches the Prêcheur village without endangering neither the population nor the infrastructures. A more thorough analysis of AFM and seismic stations recordings, could help characterize the DF discharge and sediment bed transport (e.g. Burtin et al., 2008; Roth et al., 2016; Anthony et al., 2018), and thus its rheology. Such analyzes need, however, a calibration step, with additional sensors measuring directly these characteristic. But instrumenting the river is in practice difficult.

Numerical modeling may help compensate for this lack of data. We derive in Figure 4.27b and 4.27c a power law giving the flow travel duration between RPRE and CPMA as function of the modeled peak discharge at RPRE. If we manage to better quantify the relation linking AFM peak values to records dephasing between RPRE and CPMA, it will be then possible to combine these results to estimate peak discharges from AFM recordings. In a first approximation, this could be done by assuming AFM peak values match peak discharges, as we have done in this study. However, the seismic energy radiated by flows also depends on the sediment bed transport. As DFs sometimes display particle segregation at their front (Vallance and Iverson, 2015), AFM peak value may precede peak discharges.

More generally speaking, provided a database of simulation with various rheologies and initial conditions, statistical analyzes can provide in turn simple relations between the main characteristics of the lahars. Though the construction of the database is computationally demanding, the results can then be used very quickly for real-time monitoring. For instance, we could derive linear relations between the travel durations from RPRE to CPMA, and from RPRE to the bridge (Figure 4.28). Another example is given in Figure 4.29 where we compare simulated discharges at RPRE and CPMA, to flooded areas on the left and right river banks. We find that flooded areas are better correlated to the discharge at CPMA than at RPRE. Such observations could help improve the monitoring of the Prêcheur river by identifying locations where data acquisition is the most relevant.

4.8 Conclusion

In this work, we have modeled a rock avalanche, and the subsequent remobilization of the deposits as a high discharge debris flow, with a single thin-layer numerical code, SHALTOP. It is a physically-based model that simulates the propagation of a flow on a complex topography, but it is used here empirically by using a maximum of two rheological parameters. They are calibrated by reproducing real events, which then allows to investigate possible future events. In our case

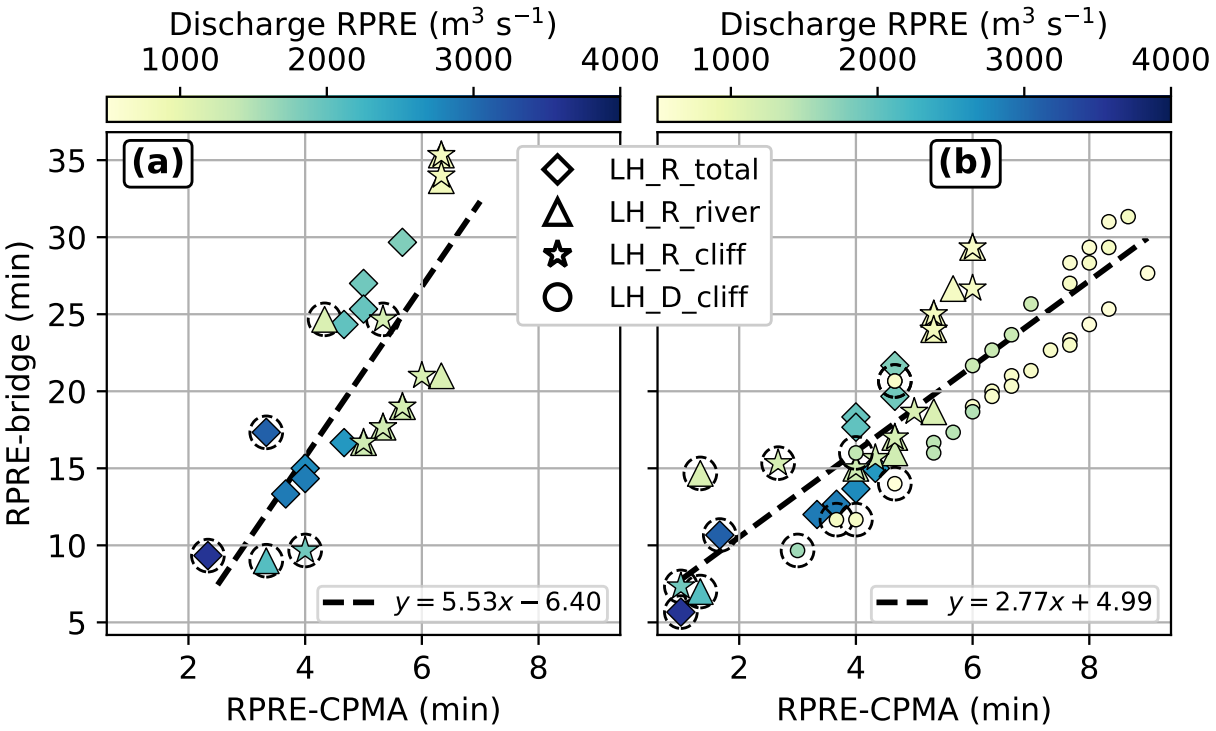

Figure 4.28: Travel durations between RPRE and CPMA, and RPRE and the bridge. (a) Dephasing between maximum discharges at RPRE and the bridge in simulations, as a function of dephasing between maximum discharges at RPRE and CPMA. Colorscale gives maximum discharge at RPRE. Simulation scenario is given by the symbology. Dashed black circles indicate simulations where the Coulomb rheology was used (Voellmy otherwise). Friction cofficient is $\mu_S = \tan(2°)$ or $\mu_S = \tan(3°)$. Turbulence coefficients range from 100 to 500 m s^{-2}. Dashed black line is a linear fit. (b) Same as (a), but with dephasing measured by picking the onset of discharge increase.

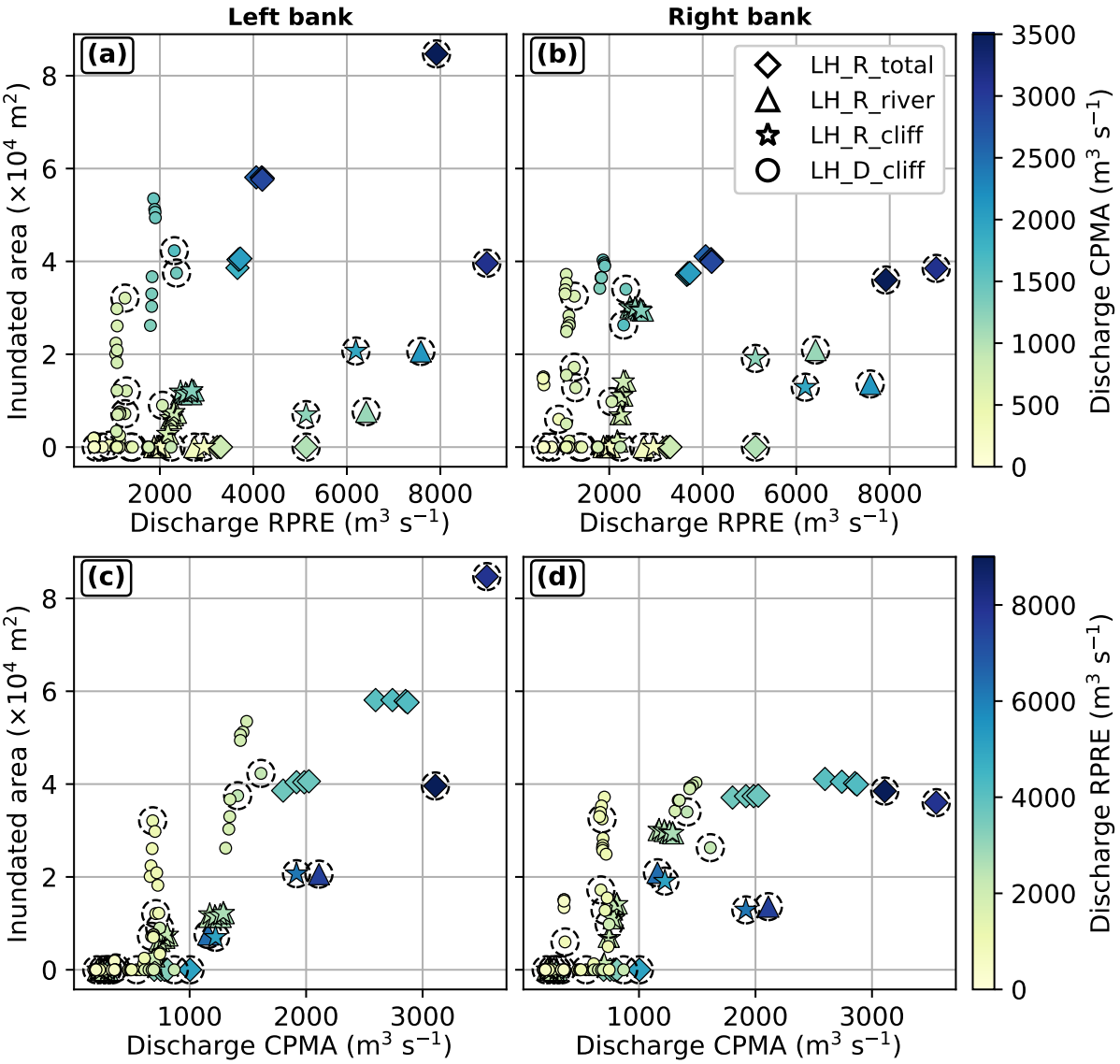

Figure 4.29: Simulated flooded area depending on discharge. (a) Flooded are on the left bank vs peak simulated discharge at RPRE. (b) Flooded are on the right bank vs peak simulated discharge at RPRE. (c) Flooded are on the left bank vs peak simulated discharge at CPMA. (d) Flooded are on the right bank vs peak simulated discharge at CPMA. Colorscale gives maximum discharge at CPMA in (a) and (b), and at RPRE in (c) and (d). Note x-axis scale in (a) and (b) is different from (c) and (d). Simulation scenario is given by the symbology. Dashed black circles indicate simulations where the Coulomb rheology was used (Voellmy otherwise). Friction cofficient is $\mu_S = \tan(2°)$, $\mu_S = \tan(3°)$ or $\mu_S = \tan(4°)$. Turbulence coefficients range from 100 to 500 m s^{-2}.

study, the Prêcheur river catchment in Martinique, the back-analysis of past events and the construction of a forward prediction scenario are made complex because little quantitative data is available to constrain precisely the simulation set-up and rheological parameters. However, we show that combining a wide variety of information (geological and geomorphological data, topographic surveys, seismic recordings and granulometric analysis of materials) makes it possible to define realistic scenarios and reproduce the main characteristics of documented events.

In Figure 4.30, we complete Figure 4.1 with what field work and agregation of various data told us about the processes transfering sediments from the Samperre Cliff to the Cliff. We also highlight the different modeling solutions that were chosen. The two main processes, rock avalanches and debris flows, are modeled separately. To calibrate avalanche simulations, we reproduce the Aug. 21, 2009 (1.0×10^6 m^3) and Jan. 4, 2018 (1.5×10^6 m^3) Samperre rock avalanches runouts with the Coulomb rheology. We found best-fit friction coefficients between $\mu_S = \tan(11°) = 0.19$ and $\mu_S = \tan(14°) = 0.25$, respectively.

The calibration of debris flows simulation is done by reproducing the destructive Jun. 19, 2010 DF that flooded the Prêcheur village. By releasing instantaneously a 0.65×10^6 m^3 reservoir at the bottom of the cliff, we could reproduce both the observed travel durations and flooded areas. With the Coulomb rheology, a low friction coefficient is needed ($\mu_S = \tan(2°)$). The Voellmy rheology with turbulence coefficients above 500 m $^{-2}$ also yields conclusive results. With a larger reservoir (1.2×10^6 m^3), the flow velocity is increased, allowing for an even better match with observations, but the flooded area expands to an extent that was not observed in 2010. By exploring different source terms, we show that the initial reservoir geometry has little influence on the DF simulation result. However, when we consider progressive remobilization of materials by imposing a constant discharge as source term, the flooded area is reduced (by 50% or even 100% for a 20 min constant source discharge), as well as the flow travel duration (10 min longer between RPRE station and the Prêcheur village, for a 20 min constant source discharge).

Using the back-analyzed rheological parameters, geological and geomorphological constraints, we could model an hypothetical 1.9×10^6 m^3 future collapse of the cliff. The resulting deposits are then remobilized instantaneously to generate a DF. We model an average velocity of 11 m s^{-1} on the 4.3 km long river section between RPRE and the outlet. With Coulomb and $\mu_S = \tan(2°)$, the discharge rate is almost 2,000 m^3 s^{-1} at the bridge. It drops down to 1,000 m^3 s^{-1} with the Voellmy rheology, $\mu_S = \tan(2°)$ and $\xi = 500$ m s^{-2}.

Thus, we show that SHALTOP can be used to model both rock avalanches and high discharge debris flows, at least in a first approximation. We suggest the dynamics of the debris flow front, which displays a high solid fraction and little vertical separation between the solid and fluid phases, are rather well modeled. In turn, we may be relatively confident in the modeled flow front velocity. However, erosion and deposition processes as well as progressive dilution affect the tail of the DF. Thus, flood maps should be analyzed with caution. However, they do provide a key insights on the most exposed areas and on potential overflows locations.

This work contributes to assessing the usability of thin-layer models for hazard assessment, particularly in complex cases where the deposits of an initial rock avalanche are remobilized by debris flows. We also show how various data can be aggregated and used to constrain simulations scenarios and parameters. In the case of the Prêcheur river, future research should focus on modeling more finely the DFs dynamics in the lower part of the river to assess more accurately flood hazard, for instance with two-phase thin-layer models. Further data acquisition and analysis is also of prior importance to help better characterize the DFs occurring in the river, and in turn calibrate simulations parameters.

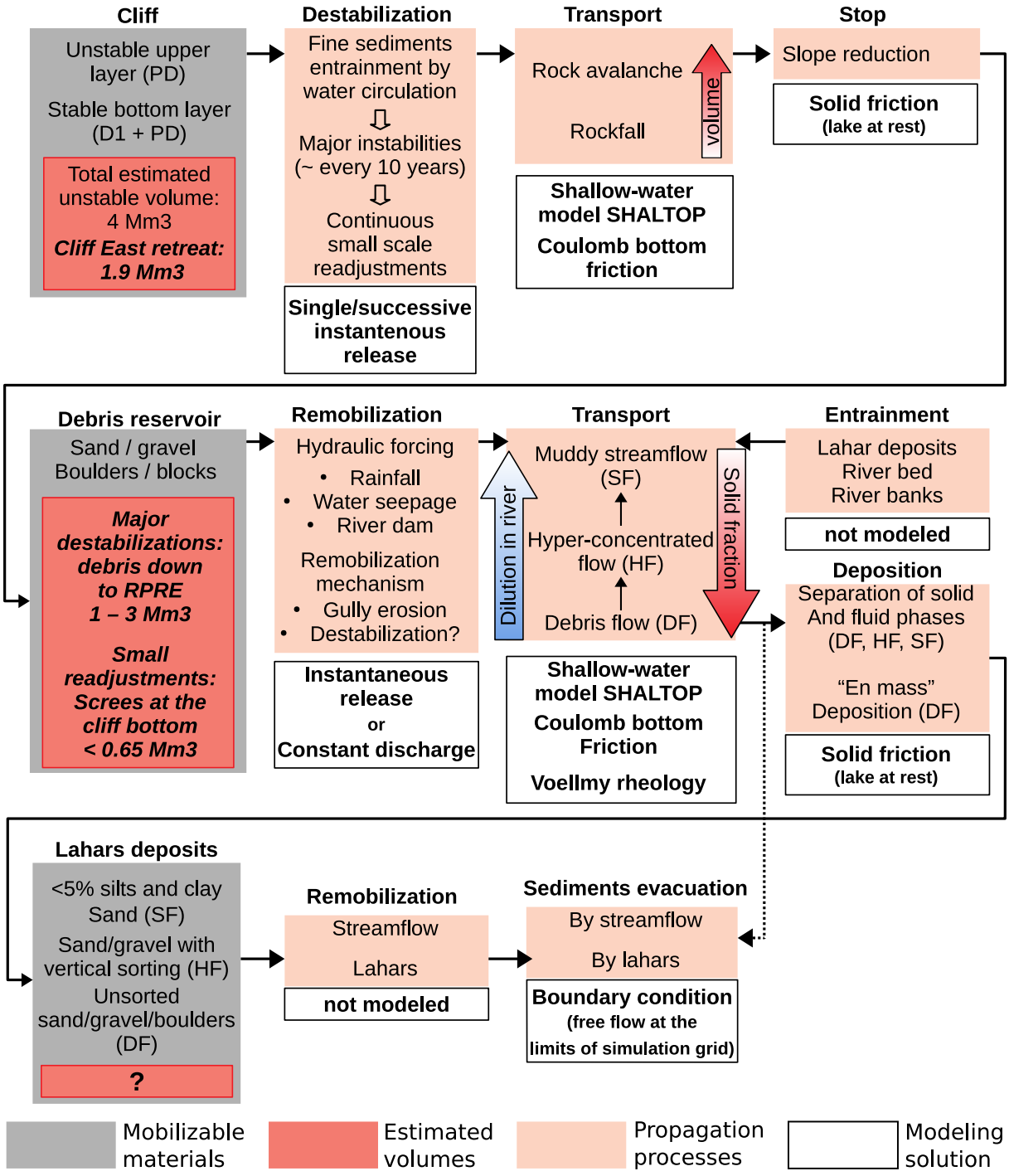

Figure 4.30: Diagram of sediment transfer processes, from the Samperre Cliff to the sea, along with modeling solutions.

Chapter 5

Thin-layer models for operational runout hazard assessment: comparison with empirical estimations

Context

In the previous two chapters, we have shown how thin-layer models (in particular SHALTOP) can be used in combination with a wide variety of data and field observations to reproduce gravitational flows. A cautious analysis of data is needed to define realistic simulations scenarios and interpret correctly the simulation results. Thus, these studies are not straight-forward, in the sense that the method must be adapted to the considered case study, depending on the available data. This can be time consuming, which is not always compatible with short delays given to practitioners. Besides, the communication of the results to stakeholders must also be done carefully, because uncertainty is not quantified and relies on the expert judgement that is thus inseparable from the results. In turn, the map showing the results of one simulation can be misleading if it is not commented to stress the underlying assumptions and uncertainties.

In this context, the last chapter of this thesis focuses on quantifying the uncertainty associated to simulation results. We propose a methodology to estimate, on a given study site, landslide travel distance as a function of volume, with thin-layer numerical models and an explicit quantification of uncertainty. The basic principle of our approach is to construct for a given site a database of simulations, with various volumes and rheological parameters. The relation between the simulation input (volume and rheological parameter) and output (travel distance) is then modeled by a statistical law (in our case, a power law). This allows to estimate travel distances for volumes and parameters not used in the simulation database. Note that a similar approach had already been introduced in the previous two chapters: for instance, for the debris flow simulations in the Prêcheur river, we have derived power laws giving the flow travel time as a function of discharge. We will formalize this method to include, in particular, uncertainty quantification.

It is true that we considerably simplify the problem, in particular because the final estimation is not spatialized: we will not derive hazard maps. However, even in this simplified framework, it is not straight-forward to estimate rigorously the uncertainty. Besides, considering simple travel distance estimations allows to interpret more easily results, and compare them to purely empirical estimations.

The work presented here was published in a special issue of *Geosciences*: *Landslides and Granular Flows on Earth*.

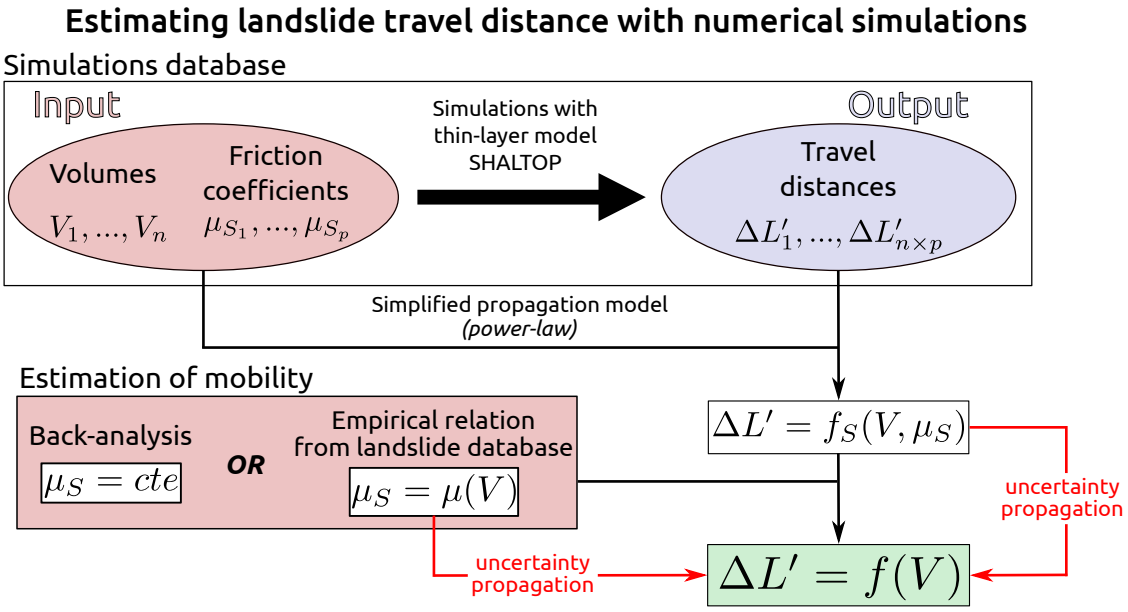

Figure 5.1: Methodology for landslide travel distance estimation with thin-layer models

- **Peruzzetto, M.**, Mangeney, A., Grandjean, G., Levy, C., Thiery, Y., Rohmer, J., and Lucas, A., *Operational Estimation of Landslide Runout: Comparison of Empirical and Numerical Methodologies*. Geosciences, 2020.

In this Chapter, we reproduce this paper, from Section 5.1 to Section 5.5. The associated abstract is given page 174. The appendices of this chapter (Appendice 5.A to 5.D) are appendices of the article.

In Figure 5.1, we give the graphical abstract of the paper that explains our method.

Abstract

A key point of landslide hazard assessment is the estimation of their runout. Empirical relations linking angle of reach to volume can be used relatively easily, but they are generally associated to large uncertainties as they do not consider the topographic specificity of a given study site. On the contrary, numerical simulations provide more detailed results on the deposits morphology, but their rheological parameters can be difficult to constrain. Simulating all possible values can be time consuming and incompatible with operational requirements of rapid estimations. We propose and compare three operational methods to derive power laws relating the landslide travel distance to the destabilized volume. The first one relies only on empirical relations, the second one on numerical simulations with back-analysis, and the third one combines both approaches. Their efficiency is tested on three case studies : the Samperre cliff collapses in Martinique, Lesser Antilles (0.5 to 4×10^6 m^3), the Frank Slide rock avalanche (36×10^6 m^3) and the Fei Tsui debris slide in Hong Kong (0.014×10^6 m^3). Purely numerical estimations yield the smallest uncertainty, but the uncertainty on rheological parameters is difficult to quantify. Combining numerical and empirical approaches allows to reduce the uncertainty of estimation by up to 50%, in comparison to purely empirical estimations. But it may also induces a bias in the estimation, though observations always lie in the 95% prediction intervals. We also show that empirical estimations fail to model properly the dependence between volume and travel distance, particularly for small landslides ($< 0.02 \times 10^6$ m ^{3}).

Contexte

Dans les deux chapitres précédents, nous avons montré comment SHALTOP peut être utilisé avec des mesures et des observations de terrain pour reproduire et étudier des écoulements gravitaires. Une analyse minutieuse des données est nécessaire pour construire des scénarios réalistes, et interpréter correctement les résultats des simulations. Ainsi, de telles études peuvent être complexes, car la méthodologie doit être adaptée à chaque cas d'étude en fonction des données disponibles. Cela peut nécessiter beaucoup de temps, ce qui n'est pas toujours compatible avec les impératifs opérationnels. Par ailleurs, la communication des résultats aux parties prenantes doit également être faite avec précaution parce que l'incertitude n'est pas quantifiée et est directement liée à un jugement d'expert, qui est ainsi indissociable des résultats. Ainsi, la carte montrant le résultat des simulations peut être trompeuse si elle n'est pas commentée pour expliquer et souligner les hypothèses faites, et les incertitudes sous-jacentes.

C'est dans cette perspective de quantification des incertitudes associées aux résultats de simulations que s'inscrit ce dernier chapitre. Nous allons proposer une méthodologie pour estimer, pour un site donné, la distance parcourue par un écoulement gravitaire en fonction du volume, à l'aide de modèles d'écoulement en couche mince et en prenant en compte les incertitudes. Le principe de base de notre approche est de construire, pour un site donné, une base de données de simulations avec des volumes et des paramètres rhéologiques variés. La relation entre les paramètres d'entrée (volume et paramètre rhéologique) et les sorties de la simulation (la distance de parcours) est ensuite modélisée par une loi statistique (dans notre cas, une loi puissance). Cela permet d'estimer les distances de parcours pour des volumes et paramètres non présents dans les simulations initiales. En fait, une approche similaire a déjà été utilisée dans les chapitres précédents, quand nous avons déduit, par exemple, une loi puissance donnant le temps parcours d'une lave torrentielle en fonction de son débit. Nous allons formaliser cette méthode pour y inclure, en particulier, la quantification de l'incertitude.

Il est vrai que nous simplifions considérablement le problème de la quantification des incertitudes, en particulier parce que nous ne considérons pas la spatialisation des incertitudes : nous ne calculerons pas de cartes d'aléas. Toutefois, même dans ce cadre simplifié, il n'est pas simple de propager de manière rigoureuse l'incertitude. Par ailleurs, considérer simplement l'estimation des distances de parcours permet d'interpréter plus facilement les résultats, et de les comparer à des estimations purement empiriques.

Le travail à donné lieu à un papier publié dans un numéro spécial de Geosciences *:* Landslides and Granular Flows on Earth *:*

- ***Peruzzetto, M.**, Mangeney, A., Grandjean, G., Levy, C., Thiery, Y., Rohmer, J., and Lucas, A.*, Operational Estimation of Landslide Runout : Comparison of Empirical and Numerical Methodologies. *Geosciences, 2020.*

*Nous reproduisons dans ce chapitre ce papier, de la Section 5.1 à la Section 5.5. Le résumé en anglais associé (*abstract*) est donné page 174. Les appendices de ce chapitre (Appendice 5.A à 5.D) sont des appendices de l'article.*

*Dans la Figure 5.1, nous donnons le résumé graphique (*graphical abstract*) de l'article qui explique et résume la méthodologie.*

Résumé

*Un point clé de l'évaluation des aléas gravitaires est l'estimation de leur distance de parcours. Des relations empiriques reliant l'angle d'atteinte (*angle of reach *en anglais) peuvent être utilisées relativement facilement, mais sont en général associées à de fortes incertitudes puisqu'elles ne prennent en compte ni les spécificités topographiques du site d'étude, ni les caractéristiques des matériaux. A l'inverse, les simulations numériques donnent plus de détails sur la morphologie des dépôts, mais leurs paramètres rhéologiques peuvent être difficiles à contraindre. La simulation de toutes les valeurs possibles est coûteuse en temps de calcul, et parfois incompatible avec les exigences opérationnelles d'estimation rapide. Nous proposons et comparons trois méthodes opérationnelles pour obtenir des lois puissance reliant la distance de parcours au volume déstabilisé. La première s'appuie uniquement sur des relations empiriques, la deuxième sur des simulations numériques avec calibration des paramètres, et la troisième combine les deux approches. Leur efficacité est testée sur trois cas d'étude : des avalanches de blocs de la falaise Samperre en Martinique dans les Petites Antilles (0.5 to* 4×10^6 m^3*), l'avalanche de blocs de* Frank Slide *(*36×10^6 m^3*), et le glissement de terrain de Fei Tsui Road à Hong-Kong (*0.014×10^6 m^3*). Les estimations purement numériques donnent les incertitudes les plus faibles, mais l'incertitude sur les paramètres rhéologiques est difficile à quantifier. En combinant les approches numériques et empiriques, l'incertitude est réduite jusqu'à 50%, en comparaison des estimations purement empiriques. Mais dans ce cas, l'estimation peut être biaisée, même si les observations des trois cas d'études sont toujours comprises dans l'intervalle de confiance à 95%. Finalement, nous montrons que les estimations empiriques ne parviennent pas à modéliser correctement la dépendance entre le volume et la distance de parcours, en particulier pour les petits glissements de terrain (*$< 0.02 \times 10^6$ m^3*).*

5.1 Introduction

Landslide hazard assessment is the estimation of the probability that an area is impacted by a landslide of given intensity during a given period of time (Corominas et al., 2014; Thiery et al., 2017). It relies on the evaluation of landslide susceptibility (i.e. the likelihood that a given type of landslide occurs in a given area) and intensity. The definition of intensity depends on the propagation mechanism (Corominas et al., 2014), but generally includes the runout (or travel distance), the velocity and volume of the landslide. These characteristics are commonly estimated from empirical relations (in most case, power laws) depending on the landslide volume (e.g. Corominas, 1996; Legros, 2002; Lucas et al., 2014; Zhan et al., 2017; Mitchell et al., 2018; Strom and Abdrakhmatov, 2018; Brideau et al., 2019). However, in order to get more insight on the landslide dynamics, physical model must be used. The most simple one is the rigid sliding block model for which an analytical solution can be derived (Hungr et al., 2005a). Analytical solutions for one-dimensional dam-break problems have also been proposed in (Mangeney et al., 2000a), and used for instance in Lucas et al. (2014) to estimate landslide travel distances. Flow routing algorithms implemented in Geographic Information Systems (GIS) softwares combine probabilistic methods and semi-empirical energy dissipation laws to reproduce multiple channelling and mass spreading (Wichmann and Becht, 2005; Horton et al., 2013). Nevertheless, physically-based numerical modeling is needed to reproduce the complex mechanisms governing landslide propagation. 3D modeling allows to describe precisely the interactions between fluid and/or solid particles (Leonardi et al., 2014; Prime et al., 2014b; Hu et al., 2015) but is often computationally costly and relies on many user-defined parameters, which are in practice difficult to estimate.

In comparison, thin-layer models (also commonly called shallow-water models) integrate the momentum equations over the flow thickness of fast-propagating landslides, whose thickness is negligible in comparison to their extent. Thus, the state variables are reduced to the flow thickness and thickness-averaged velocity and simulations can be run faster than full 3D models. In their most simple form, the shallow-water equations describe the evolution of a homogeneous flow and use a solid Coulomb friction law to model the interaction between the topography and the flow, through a friction coefficient $\mu_S = \tan(\delta)$. The stress applied at the base of the flow can also be modeled with the Voellmy rheology that includes a turbulence term (Salm, 1993; McDougall, 2017), or the Bingham rheology for yield-stress fluids (Pastor et al., 2004). More complex shallow-water models include, for instance, erosion and deposition along flow path (McDougall and Hungr, 2005; Pirulli and Pastor, 2012) and two-phase flows with dilatancy effects (Iverson, 2014; Bouchut et al., 2015; Bouchut et al., 2016; Pudasaini and Mergili, 2019).

In this work, we aim at developing and comparing methodologies to estimate the travel distance of rapid gravity-driven flows (Iverson and Denlinger, 2001; Lucas et al., 2014; McDougall, 2017) depending on their volume. The resulting relations must be simple enough to be used operationally by practitioners. They can be established simply by using mobility indicators such as the Heim's ratio μ_H or the effective friction coefficient μ_{eff} (Lucas et al., 2014):

$$\mu_H = \frac{H}{\Delta L'}, \tag{5.1}$$

$$\mu_{eff} = \tan(\theta) + \frac{H_0}{\Delta L}. \tag{5.2}$$

H is the drop height, $\Delta L'$ the horizontal travel distance along flow path, θ the average slope along flow path, H_0 the initial mass maximum height and ΔL the travel distance along topography from the collapse scar toe (Figure 5.2). μ_{eff} is less straight-forward to use than μ_H as it takes into account the geometry of the initial mass, which is not always easy to estimate.

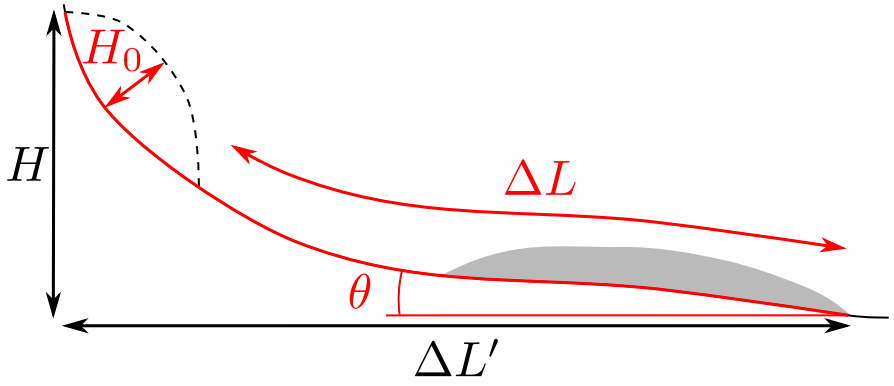

Figure 5.2: Parametrization of landslide mobility, with notations from Lucas et al. (2014). Dashed line: initial mass. Grey shaded are: final landslide deposits. H is the drop height, $\Delta L'$ the horizontal travel distance. H_0 is the mass initial thickness, ΔL the travel distance along topography from the landslide scar toe, and θ is the average slope angle along the flow path. The notations in red are used for μ_{eff}, and in black for μ_H.

empirical estimations relating the landslide volume to μ_H or μ_{eff} rely on large datasets that are not, in general, site specific. Thus, the particular topographic setting of a given study site is not taken into account. This often results in large uncertainties that are however relatively simple to evaluate from the residuals between the fitted model and the observations.

In comparison, numerical modeling and in particular shallow-water models are commonlyused to carry out site-specific hazard analysis (e.g. Hussin et al., 2012; Mergili et al., 2018; Peruzzetto et al., 2019). But many simulations (up to 1,000 or even 10,000) are needed to perform a rigorous probabilistic hazard analysis (e.g. Rohmer and Foerster, 2011). Besides, estimating parameters can be difficult, or at least time consuming and costly, which is often incompatible with operational constraints where hazard assessment must be carried out quickly. Rheological parameters can be estimated by back-analysis when previous events are documented, but the extent to which results can be used for forward prediction is hard to constrain (Mergili et al., 2018). Rheological parameters can also be empirically deduced from mobility indicators. In particular, the effective friction coefficient μ_{eff}, whose definition differs from the Heim's ratio μ_H as it takes into account the initial mass geometry, proved to be a relatively good estimation of the friction coefficient μ_S needed to model observed deposits (Lucas et al., 2014).

In this context, the extent to which numerical modeling can improve the estimation of landslide runout in comparison to empirical approaches, has, to our knowledge, never been quantified. To answer this question, we will derive site-specific power laws relating the horizontal travel distance $\Delta L'$ to the unstable volume V, using a purely empirical approach, a numerical approach and combining empirical data with numerical modeling. Empirical data is drawn from two landslides databases (Lucas et al. (2014), and Corominas (1996) and Mitchell et al. (2019)). Numerical modeling is carried out with the SHALTOP shallow-water numerical model (Mangeney-Castelnau et al., 2005; Bouchut and Westdickenberg, 2004; Mangeney et al., 2007b). We will use a simple Coulomb friction law that proved, with SHALTOP, to reproduce successfully real landslides deposits (Lucas et al., 2007; Lucas et al., 2014; Moretti et al., 2015; Yamada et al., 2018; Peruzzetto et al., 2019; Moretti et al., 2020a). Besides, this rheology involves a single parameter, which simplifies uncertainty analysis. We compare the prediction and associated uncertainties for three documented case studies: rock/sand avalanches from the Samperre cliff in Martinique, Lesser Antilles, the Frank Slide rock avalanche in Canada and the Fei Tsui Road debris slide in Hong-Kong.

5.2 Materials and Methods

5.2.1 Data

We present here the case studies on which methods of travel distance estimations will be compared. Empirical methods are based on empirical estimations of mobility deduced from landslide databases. In comparison, numerical methods rely on site-specific simulation databases.

Case studies

In this work we focus on three landslide case studies, spanning a large range of volumes and runouts. Their characteristics are summarized in Table 5.1.

Destabilizations from the Samperre cliff, in Martinique, Lesser Antilles, involve volumes between 1 and 4×10^6 m^3 (Clouard et al., 2013; Nachbaur et al., 2019) that propagate on a complex topography (Figure 5.3a and 5.3b). As they detach from the cliff, old pyroclastic materials erupted from the nearby Montagne Pelée volcano desegregate rapidly and the landslide propagates as a granular avalanche. Massive destabilizations occur roughly every 10 years, as in 2009 and 2018 (Clouard et al., 2013; Nachbaur et al., 2019) and travel about 2 km in the Samperre torrent that has its source at the cliff toe (Figure 5.3c). The stream flows in a narrow (no more than 40 m wide) and steep-walled (up to 70 m high banks) ravine that confines laterally the avalanche. The volume involved in the August 2009 collapse is estimated at 1×10^6 m^3 in Clouard et al. (2013). In 2018, the main destabilization phase occurred in early January, and involved at most 3.7×10^6 m^3 (Quefféléan, 2018a), as deduced from 1-m Digital Elevation Models (DEMs) comparisons between July 2017 (LiDAR) and mid-January 2018 (photogrammetric reconstruction). However, considering the cliff retreat between these two dates, we estimate a smaller 1.5×10^6 m^3 volume (see Appendix 5.B).

In comparison, the Frank Slide rock avalanche features a larger volume: 36×10^6 m^3. It is more easily constrained than the Samperre destabilizations, because it consisted in a single event that occurred in 1902 on the east face of Turtle Moutain in western Alberta, Canada (Figure 5.4a and 5.4b). It involved mainly Paleozoic limestones that slid along the dipping bed of Turtle Mountain anticline (Benko and Stead, 1998). The rock avalanche covered approximately 2.6 km^2 and traveled about 3 km (from the rear scar) without confinement. The scar displays 30° to 60° slopes, but the topography flattens quickly at the mountain toe. The rock avalanche then ran slightly uphill on the other side of the valley with slopes no higher than 3° (Figure 5.4c).

The 1995 Fei Tsui Road debris slide case-study differs significantly from the previous ones (Figure 5.5). It occurred in Hong-Kong after intense rainfalls: more than 1,300 mm in the preceding month and 230 mm in the preceding 12 hours (GEO, 1996). It involved 14,000 m^3 of debris, which is unusually high for landslides in Hong-Kong (Knill, 1996; GEO, 1996). The debris slide originated form a 30 m high cut slope in moderately to highly weathered volcanic materials, with the base of the scar following a kaolinite-rich altered tuff layer. It is assumed that the development of a 1 to 4 m high perched aquifer above the kaolinite-rich layer favored the initiation of the landslide as a translational slide. As a result of low cohesion values (GEO, 1996), the material then desegregated rapidly. The debris slide traveled about 65 m (30 m from the scar toe) with limited spreading, with some of the deposits piled up against the corner of a building.

		Samperre cliff collapses (Clouard et al., 2013; Aubaud et al., 2013) (Nachbaur et al., 2019)	Frank Slide rock avalanche (Benko and Stead, 1998)	Fei Tsui Road debris Slide (GEO, 1996; Knill, 1996)
DOCUMENTED EVENT	Volume (V)	1×10^6 m^3 (2009) 1.5×10^6 m^3 (2018)	35×10^6 m^3	14×10^3 m^3
	$\mu^1_{eff}(V)$	$\tan(18.5°) = 0.33$ (2009) $\tan(18.0°) = 0.32$ (2018)	$\tan(14.4°) = 0.26$	$\tan(24.7°) = 0.46$
	Observed horizontal travel distances ($\Delta L'$)	2,100 m (2009) 2,000 m (2018)	3,200 m	65 m
	Best-fit friction coefficient μ_S	$\tan(13°) = 0.23$	$\tan(11°) = 0.19$	$\tan(26°) = 0.49$
SIMULATION DATABASE	Range of volumes V	0.25×10^6 m^3 to 3.7×10^6 m^3	10×10^6 m^3 to 70×10^6 m^3	5×10^3 m^3 to 30×10^3 m^3
	Range of friction coefficients μ_S	$\tan(10°) = 0.18$ to $\tan(35°) = 0.70$	$\tan(7°) = 0.12$ to $\tan(23°) = 0.42$	$\mu_S = \tan(20°) = 0.36$ to $\mu_S = \tan(32°) = 0.62$
	Simulation grid size	585×151	201×201	97×117
	Simulation grid resoultion	5 m	20 m	1 m
	Number of simulations	165	137	91
	Maximum duration for one simulation	12 hours	30 min	10 min

Table 5.1: Description of the case studies considered in this work. We give the characteristics of the documented landslides and of the simulation databases. $\mu^1_{eff}(V)$ gives the effective friction coefficient estimated from the landslide volume, using the power law deduced for *DB1* (see Figure 5.6b). For the Samperre case study, we give the estimated volumes and travel distances for the 2009 and 2018 collapses (date in brackets).

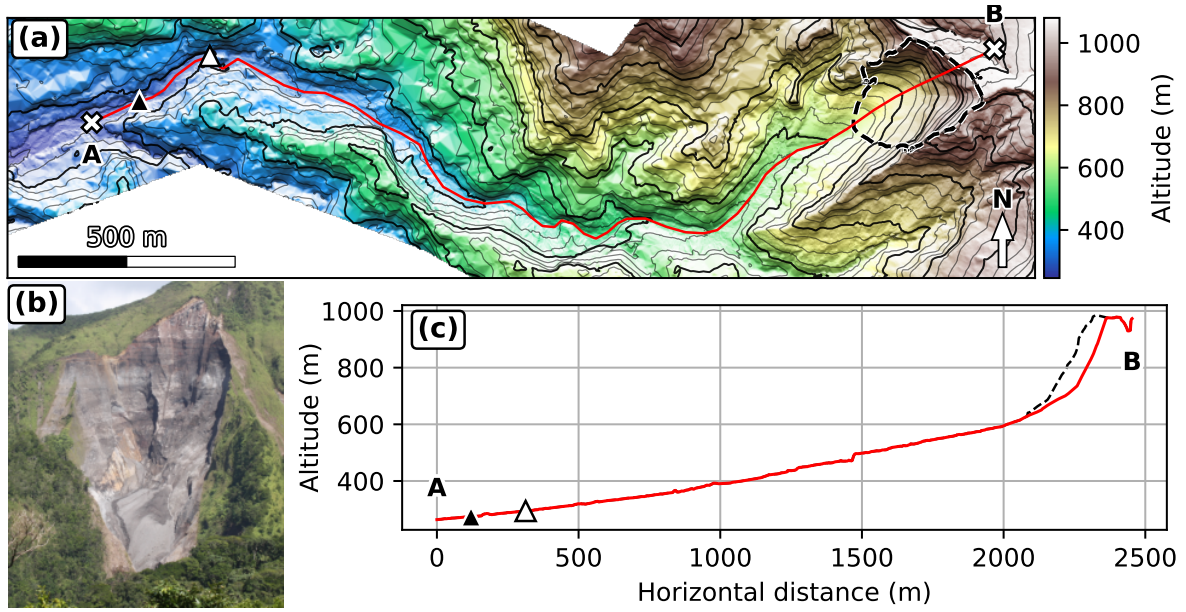

Figure 5.3: Samperre cliff destabilizations. (a) August 2018 topography, 1 m DEM. Black dashed outline: extent of the destabilized area (difference between 2010 and 2018 DEMs). Bold contour interval is 100 m. Red line: cross-section along which travel distances are measured. Black triangle: observed travel distance in 2009. White triangle: observed travel distance in 2018. (b) Picture of the Samperre cliff (black dashed outline in (a)) taken in February 2018 (OVSM). (c) Cross-section along red line in (a). Red line: Post-collapse topography with deposits removed. Black dashed line: Topography in July 2010. Black and white triangles are reported from (a).

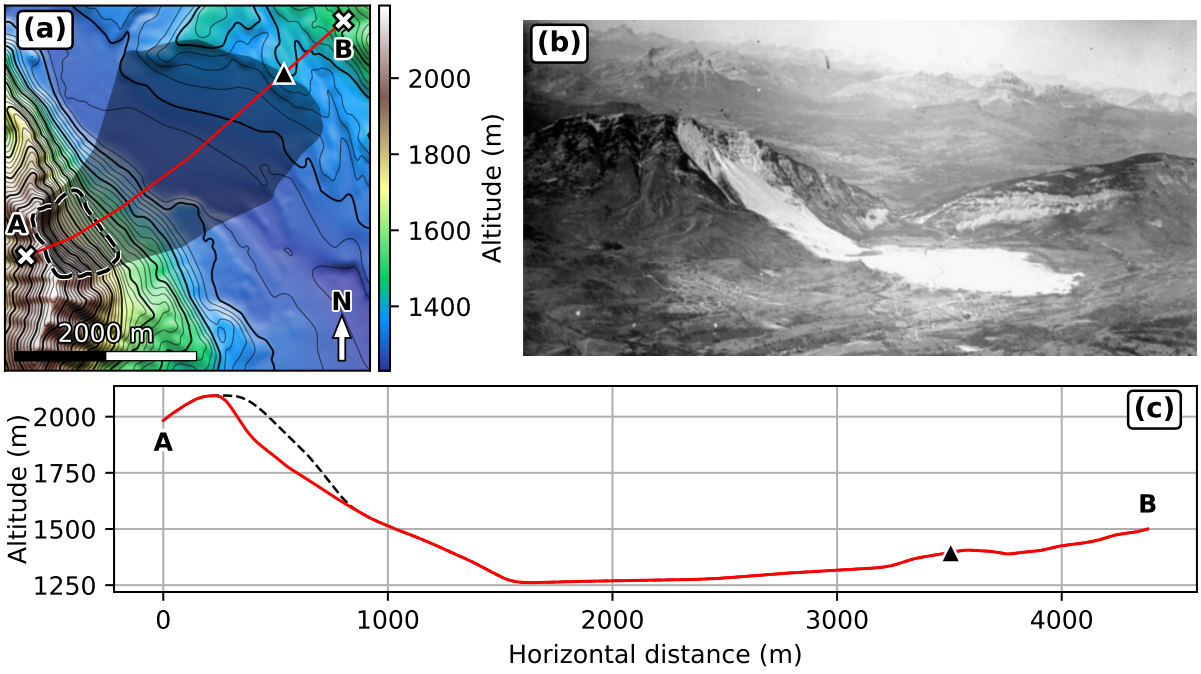

Figure 5.4: Frank Slide rock avalanche. (a) Post collapse topography with deposits removed, 20 m DEM. Black dashed outline: landslide scar. Dark area: observed landslide extent. Bold contour interval is 100 m. Red line: cross-section along which travel distances are measured. Black triangle: Observed travel distance. (b) Picture of the Frank Slide, taken in 1922 (Canada. Dept. of National Defence / Library and Archives Canada / PA-052095). (c) Cross-section along red line in (a). Red line: Post-collapse topography with deposits removed. Black dashed line: Reconstructed pre-collapse topography. Black triangle: observed deposit extent.

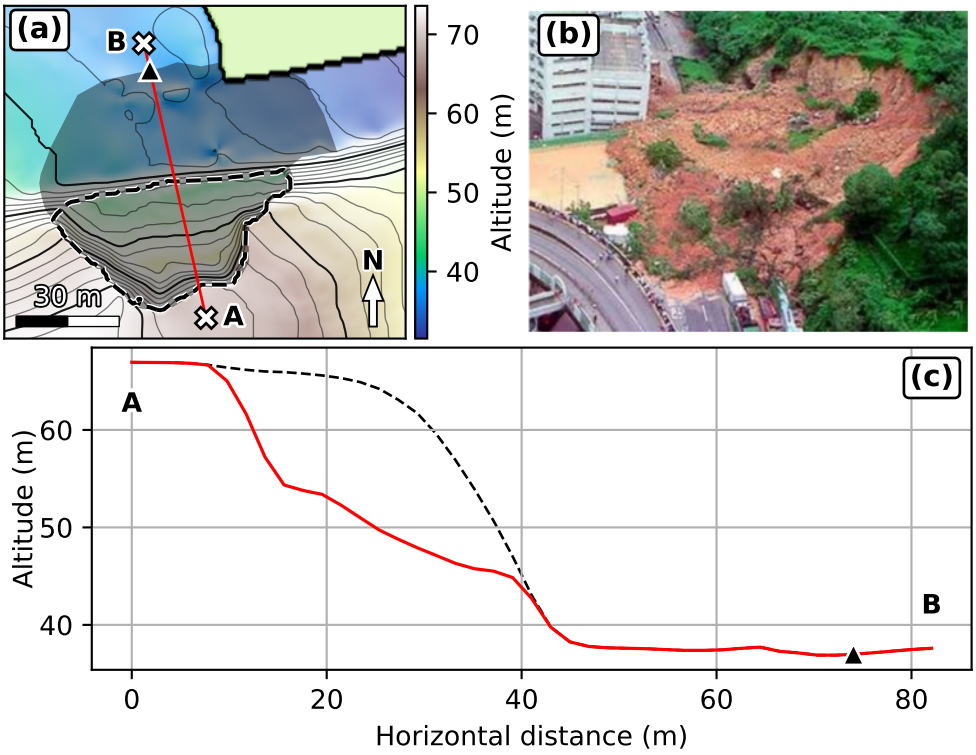

Figure 5.5: Fei Tsui Road debris slide. (a) Post collapse topography with deposits removed, 1 m DEM. Black dashed outline: landslide scar. Dark area: observed landslide extent. Bold contour interval is 10 m. Red line: cross-section along which travel distances are measured. Dark triangle: Observed travel distance. (b) Picture of Fei Tsui Road debris slide (GEO, Hong-Kong). (c) Cross-section along red line in (a). Red line: Post-collapse topography. Black dashed line: Reconstructed pre-collapse topography with deposits removed. Black triangle: observed deposit extent.

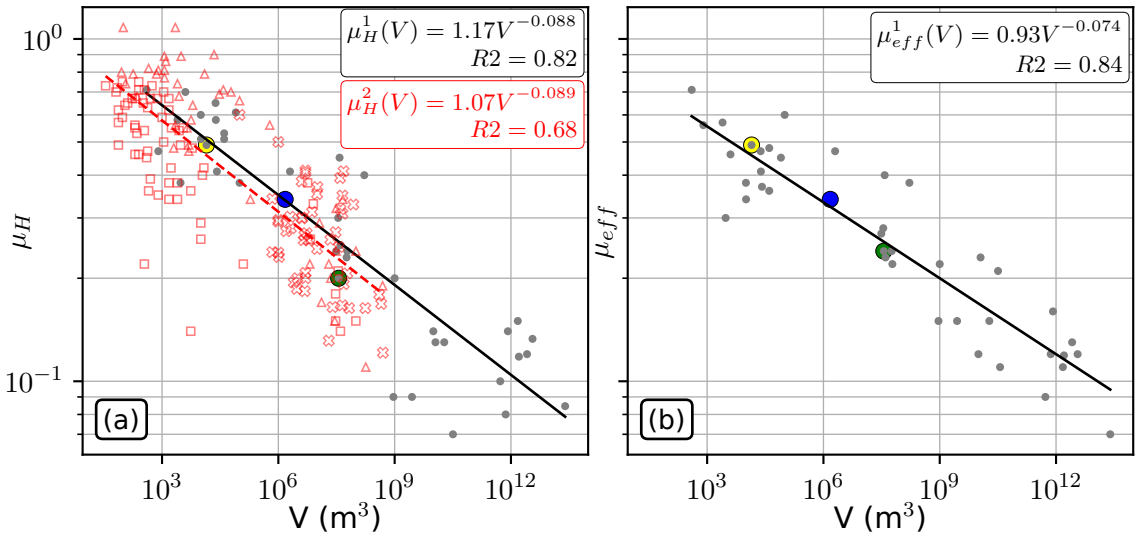

Figure 5.6: Empirical landslide databases. (a) μ_H as a function of landslide volume V. Grey circles: *DB1*. Red marker: *DB2*. Squares: rockfalls and rock avalanches from Corominas (1996). Triangles: debris flow, debris slides and debris avalanches from Corominas (1996). Crosses: Rock avalanches from Mitchell et al. (2019). Black line: power law regression result for *DB1* (equation given in black). Red dashed line: power law regression result for *DB2* (equation given in red). (b) μ_{eff} as a function of landslide volume V, for *DB1*. Black line: power law regression result for *DB1* (equation given in black). Yellow circle: observations for Fei Tsui Road debris slide. Blue circle: observations for the most import destabilization of the Samperre cliff in 2018. Green circle: observations for the Franks Slide.

Landslide databases

We use two databases to estimate empirically travel distances. The first one (*DB1*) is drawn from Lucas et al. (2014). It includes 43 dense and rapid landslides from Earth, Mars, Iapetus (Saturn's satellite) and Io (Jupiter's satellite). Both the Frank Slide and the Fei Tsui Road debris slide are included in *DB1*. The second database (*DB2*) combines 44 rockfalls, rock avalanches, debris flows, debris slides and debris avalanches drawn from Corominas (1996), as well as 49 rock avalanches drawn from Mitchell et al. (2019).

From these databases we fit two power laws relating μ_H to the landslide volume V: $\mu_H = \mu_H^1(V)$ for *DB1* and $\mu_H = \mu_H^2(V)$ for *DB2*. Only *DB1* could be used to derive a relation between μ_{eff} and V, $\mu_{eff} = \mu_{eff}^1(V)$, because the field observations required to compute μ_{eff} are not available in *DB2*. The regression results are given in Figure 5.6. More details on the regressions quality are available in Table 5.A.1. Note that our power law $\mu_{eff}^1(V)$ differs from the power law derived in Lucas et al. (2014) because we fit a power law $\mu_{eff} = \alpha V^{\beta}$ without constraining α, while in Lucas et al. (2014), $\alpha = 1$ is imposed.

Simulation databases

For each case study, we construct a simulation database with the SHALTOP shallow-water numerical code (Mangeney-Castelnau et al., 2005; Bouchut and Westdickenberg, 2004; Mangeney et al., 2007b). This is done by considering multiple initial unstable geometries and friction coefficients μ_S. For each case study, we model destabilized volumes ranging from one third to about twice the volumes involved in documented events. The range of tested μ_S encompasses realistic coefficients estimated from expert knowledge, in regard of the volumes considered. In

particular, the value $\mu_{eff} = \mu^1_{eff}(V)$ (with V the volume of the real landslide, see Table 5.1) is also tested: it has been shown to be a good estimate of the friction coefficient μ_S needed to reproduce the landslide dynamics and deposits (Lucas et al., 2014; Moretti et al., 2015; Yamada et al., 2018). The lowest value μ_S is also constrained by practical considerations: for small μ_S, the landslide does not stop within the simulation grid and no travel distance can be measured. The main characteristics of the simulations are given in Table 5.1.

For the Samperre cliff case study, several topographic surveys were carried out over the years: they allow to quantify the evolution of the cliff after collapses episodes, but no data are available to constrain precisely individual events. Thus, we have inferred a total of 10 initial volumes/geometries spanning volumes from 0.25×10^6 m^3 to 3.7×10^6 m^3: two of them are used to reproduce the August 2009 (1×10^6 m^3) and January 2018 1.5×10^6 m^3 major events. More details about the definition of collapse scenarios are given in Appendix 5.B. Friction coefficients are chosen between $\mu_S = \tan(10°) = 0.18$ and $\mu_S = \tan(15°) = 0.27$ every 1°, and every 2.5° up to $\mu_S = \tan(35°) = 0.70$. This results in a total of 165 simulations. The best-fit friction coefficients used in simulation to reproduce the travel distance of the 2010 and 2018 events are $\tan(11°) = 0.19$ and $\tan(14°) = 0.25$, respectively. Given the relative poor constraints we have on the 2010 event, in particular in term of initial geometry (see Appendix 5.B), we suggest the second fit is more accurate. Thus, we will use in the following intermediate value $\tan(13°) = 0.23$ that is closer to the 2018 event back-analysis.

For the Frank Slide and Fei Tsui Road case studies, simulations are run on 20 and 1 meter DEMs respectively. They were provided (along with the initial mass of the past landslides) for the First JTC1 Benchmarking Exercise (Hungr et al., 2007). In comparison to the Samperre case study, we use a more simple way of simulating various volumes. Indeed, we simply scale uniformly the heights of the real destabilized mass to explore larger and smaller volumes. For the Frank Slide, in addition to the real 36×10^6 m^3 landslide, we test 7 other volumes from 10 to 70×10^6 m^3, every 10×10^6 m^3. Friction coefficients are taken between $\mu_S = \tan(7°) = 0.12$ and $\mu_S = \tan(23°) = 0.42$, every 1°. This amounts to 137 simulations. The best-fit friction coefficient used in simulation to reproduce observed deposits resulting from the historical 36×10^6 m^3 landslide is $\tan(11°) = 0.19$, as in Lucas et al. (2007).

For the Fei Tsui Road debris slide, we test volumes between 5,000 and 30,000 m^3, every 5,000 m^3, and the real 14,000 m^3 volume. Friction coefficients are chosen between $\mu_S = \tan(20°) = 0.36$ and $\mu_S = \tan(32°) = 0.62$ every 1°, resulting in 91 simulations. The best-fit friction coefficient used in simulation to reproduce the 2018 14×10^3 m^3 debris slide is $\mu_S^{fit} = \tan(26°) = 0.49$, as in Lucas et al. (2007).

Simulations are run on the S-CAPAD DELL cluster of the IPGP, on CPU Power Edge C6220, PowerEdge R720xd or PowerEdge R730xd nodes. 128 nodes were thus available, each one with 16 cores. In turn, simulations could be run simultaneously (one simulation per core). Each simulation lasts between 10 min (in the Fei Tsui Road case study) and 12 hours (in the Samperre case study). Note that the total number of simulations remains small in comparison to what would be needed for a thorough analysis of uncertainty (at least 1,000 simulations, e.g. Rohmer and Foerster, 2011). Nevertheless, it is compatible with time constraints met by practitioners who must carry out quick hazard assessment.

For each case study, we use the simulations results to compute site-specific power laws relating the horizontal travel distance $\Delta L'$ to the initial volume V and the friction coefficient μ_S: $\Delta L' = f_S(V, \mu_S)$. For each simulated deposits, we can also compute the resulting μ_{eff} from (5.2). For clarity, values derived from simulations results will be noted $\tilde{\mu}_{eff}$, while μ_{eff} refers to values deduced from real landslides. Their definition is however the same. In turn, we can compute another power law relating $\Delta L'$ to V and $\tilde{\mu}_{eff}$: $\Delta L' = g_S(V, \tilde{\mu}_{eff})$. The data used to derive f_S and g_S are given in Supplementary Materials.

5.2.2 Estimation of horizontal travel distances

We use three different methods to estimate the horizontal travel distance $\Delta L'$ directly from the landslide volume V. They are summarized in Figure 5.7. We use empirical data from *DB1* or *DB2*, site-specific numerical simulations or a combination of the two. For the sake of clarity and simplicity, we do not explicit the functions that will be mentioned hereafter. It can be any kind of statistical model fitted to the landslide travel distance databases, or to the numerical simulations results, provided the associated uncertainties can be estimated. In this work, we use power law relations that are fitted by transforming the variables on a logarithm scale and by fitting a linear regression model using Ordinary Least Square (OLS) regressions (see more details in Appendix 5.C). Thus, the final relation relating $\Delta L'$ to V has the form:

$$\Delta L' = \alpha V^{\beta}, \tag{5.3}$$

where the coefficients α and β depend on the studied site and on the chosen methodology.

Empirical runout estimation

For a given study site, we choose a profile along which travel distances will be measured, in the main direction of propagation of observed landslides (red lines in Figures 5.4a, 5.4c, 5.3a, 5.3c, 5.5a and 5.5c). Provided an origin is chosen, a ratio $\tilde{\mu}_H = H/\Delta L'$ can be computed for each point along the profile. Thus, we do not need to run simulations. However, in practice, it is convenient to compute $\tilde{\mu}_H$ for the points that are reached by landslides in our simulations. As the modeled stopping points span a large portion of the profile, it is equivalent to choosing manually points along profiles and the resulting relation does not depend on the simulations. Besides, for the Samperre cliff simulations in particular, this allows to take directly into account the variability of the profile, as we consider different collapse geometries.

If the topography is convex, which is the case in our three case studies, it is possible to invert the previous relation to derive $\Delta L'$ from $\tilde{\mu}_H$: $\Delta L' = \Delta L'(\tilde{\mu}_H)$. Note that $\tilde{\mu}_H$ is computed geometrically. We relate it to realistic landslide mobilities by choosing $\tilde{\mu}_H = \mu_H$, where μ_H is the Heim's ratio measured on real landslides. Using the volume dependent relations deduced from the empirical databases *DB1* and *DB2*, $\mu_H = \mu_H^1(V)$ and $\mu_H = \mu_H^2(V)$, we get:

$$\Delta L' = \Delta L'(\tilde{\mu}_H) = \Delta L'(\mu_H^1(V)), \tag{5.4}$$

$$\Delta L' = \Delta L'(\tilde{\mu}_H) = \Delta L'(\mu_H^2(V)), \tag{5.5}$$

which we will write more simply

$$\Delta L' = f_{emp}^1(V), \tag{5.6}$$

$$\Delta L' = f_{emp}^2(V). \tag{5.7}$$

In comparison, it is more difficult to use μ_{eff} for direct empirical estimation as its definition includes a more complex topography description (the mean slope along flow path) and the initial geometry and volume (through the initial height H_0). Thus, it is not straight-forward to invert (5.2) to get a relation $\Delta L' = \Delta L'(\mu_{eff}, V)$. However, this can be done through simulations, as will be explained in Section 5.2.2.

Not that we could also have used empirical power laws $\Delta L' = F_{emp}(V)$ derived directly from landslide databases, and apply them directly on each case study. We choose not to, because such a method does not yield a site-specific power law. In comparison, μ_H can be deemed to be, in a first approximation, a good mobility indicator, that can then be used on a chosen site. We will however compare in Section 5.4.3 relations $\Delta L' = F_{emp}(V)$ found in the literature, to the site-specific laws derived in this study.

Numerical runout estimation

The travel distance can also be estimated without using empirical mobility indicators. For each study site, we derived from the simulation results a statistical relation $\Delta L' = f_S(V, \mu_S)$. As we want our final relation to depend only on V, we must choose a value for μ_S. It can be done by modeling a past landslide for which both the initial volume and the travel distances are known. By choosing for μ_S the best-fit friction coefficient μ_S^{fit}, and assuming that it does not depend on the landslide volume, we then get a function that only depends on volume:

$$\Delta L' = f_S(V, \mu_S^{fit}) = f_S^{fit}(V) \tag{5.8}$$

However, if no past event is available for back-analysis, we can use empirical observations.

Numerical/empirical runout estimation

In the relation $\Delta L' = f_S(V, \mu_S)$ deduced from a simulation database, we can choose μ_S as a function of the volume. As a matter of fact, it has been shown that lower friction coefficients are needed to model larger landslides. This can be done by back-analysis of multiple events with various volumes on a same site, but we do not have enough data for that. The other possibility is to consider that the empirical mobility indicators μ_{eff} and μ_H are good estimates for μ_S and setting respectively $\mu_S = \mu_H^1(V)$, $\mu_S = \mu_H^2(V)$ or $\mu_S = \mu_{eff}^1(V)$. Combining these relation with $\Delta L' = f_S(V, \mu_S)$, we derive the volume dependent relations:

$$\Delta L' = f_{S,\mu_H}^1(V) = f_S(V, \mu_H^1(V)), \tag{5.9}$$
$$\Delta L' = f_{S,\mu_H}^2(V) = f_S(V, \mu_H^2(V)), \tag{5.10}$$
$$\Delta L' = f_{S,\mu_{eff}}^1(V) = f_S(V, \mu_{eff}^1(V)). \tag{5.11}$$

Another possibility is not to consider μ_S, and use only the simulations results. As a matter of fact, we can compute for each simulated landslide the mobility indicators $\tilde{\mu}_H$ and $\tilde{\mu}_{eff}$. The $\tilde{}$ indicates that they are given by simulation results, when μ_H and μ_{eff} are computed using data from historical landslides. Their respective geometrical definitions are however the same.

From the simulation database, we can thus estimate a relation $\Delta L' = \Delta L'(\tilde{\mu}_H)$, which is the same as for empirical runout estimation (see Section 5.2.2). To be consistent with the definition (5.2) of μ_{eff} that includes both the initial mass geometry and the travel distance, we derive from the simulations results a relation $\Delta L' = g_S(V, \tilde{\mu}_{eff})$. This is done with the tuples $(\tilde{\mu}_{eff}, V)$ for which $\tilde{\mu}_{eff}$ lies within the 95% prediction interval of the empirical relation $\tilde{\mu}_{eff} = \mu_{eff}^1(V)$. Other tuples are deemed to be unrealistic. Finally, we use $\tilde{\mu}_{eff} = \mu_{eff}^1(V)$ in $\Delta L' = g_S(V, \tilde{\mu}_{eff})$ to derive the relation:

$$\Delta L' = g_{S,\mu_{eff}}^1(V) = g_S(V, \mu_{eff}^1(V)) \tag{5.12}$$

5.2.3 Estimation of uncertainty

To derive the uncertainty associated to the estimation of the travel distance, we use the dispersion between observed values and values predicted by power laws, and the uncertainty on the power law coefficients. Classical results of linear regression can be used to derive prediction intervals for a given power law, taking both these aspects into account (see Appendix 5.C). However, it is not straight-forward to extend these results for nested power laws, when the result of one is the input of another. Indeed, the final expression of the runout involves the sum and product

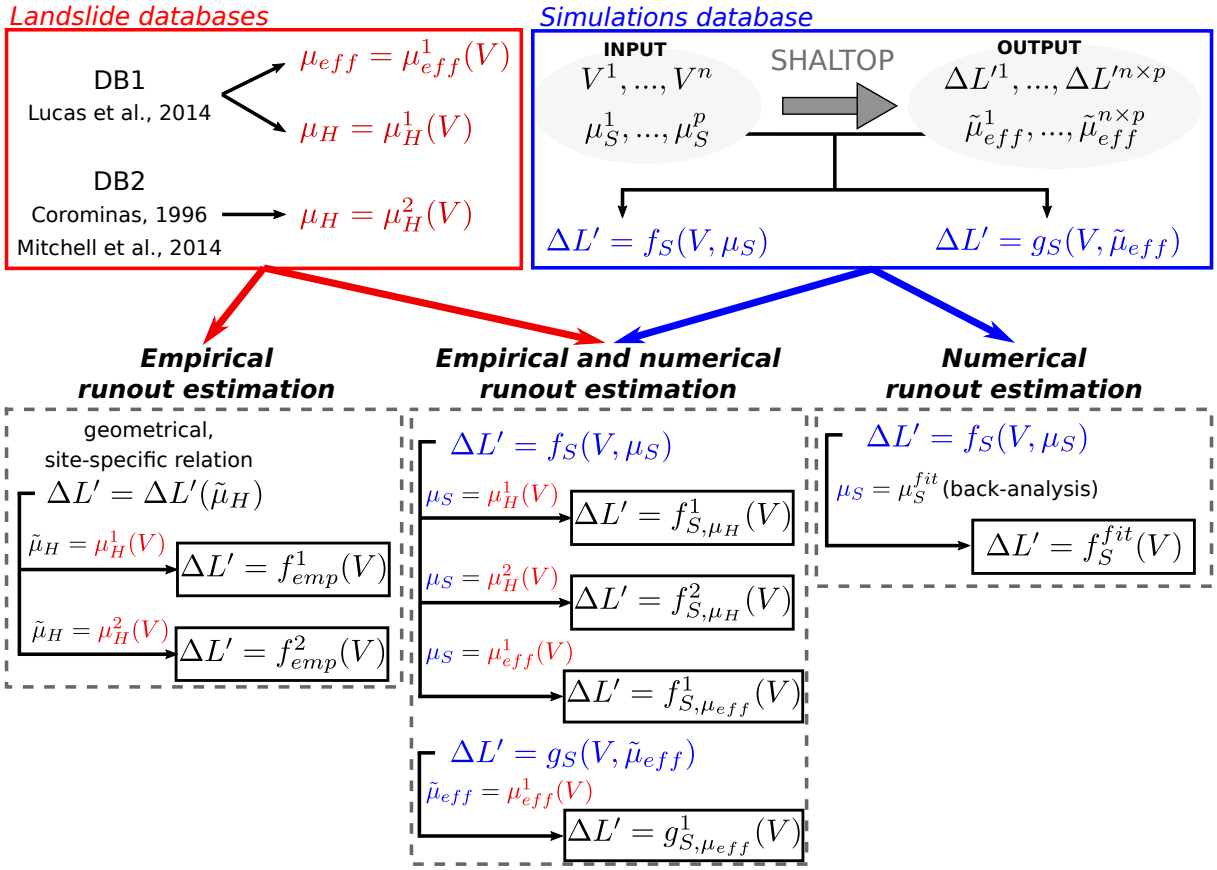

Figure 5.7: Methodologies to derive volume dependent relations for travel distance estimation. The superscripts ^{1} and ^{2} refer to the empirical database that is used for a given relation (*DB1* and *DB2* respectively). In this study, all functions are power laws.

of random variables that are not independent. Thus, it is not easy to derive formally the final probability density function. Instead, we derive numerically prediction intervals by computing 4,000 estimations with coefficients and/or residues of each power law drawn randomly (following probabilistic laws whose parameters are given by the regression). We then derive the 95% prediction interval from the 2.5th and 97.5th percentiles. More details are given in Appendix 5.C.

The normalized standard deviation σ_V of the estimation $\Delta L'(V)$, for a given volume V, is defined as:

$$\sigma(V) = \sqrt{\frac{1}{n}\sum_{i=0}^{n}\left(\frac{\hat{\Delta L}'(V) - \hat{\Delta L}_i'(V)}{\hat{\Delta L}'(V)}\right)^2}, \tag{5.13}$$

where $\hat{\Delta L}'(V)$ is the direct estimation from the best-fit power law, and $\hat{\Delta L}_i'(V)$ are n random estimates. We define the total standard deviation over a range of different volumes V_j as

$$\sigma = \frac{1}{m}\sum_{j=1}^{m}\sigma(V_j). \tag{5.14}$$

We choose $m = 50$ volumes V_j sampled regularly in logarithmic scale between the minimum and maximum simulated volumes. When we use back analysis for travel distance estimation in $\Delta L' = f_S^{fit}(V)$, we also take into account for σ the uncertainty on the best fit friction coefficient $\mu_S^{fit} = \tan(\delta_S^{fit})$. This is done by drawing random values of δ_S ($\mu_S = \tan(\delta_S)$) with a normal distribution of mean δ_S^{fit} and standard deviation 1°. This value is chosen because it matches the interval between two successive tested values of δ_S in simulations, in the neighbourhood of the best-fit friction angle.

5.3 Results

In this section, we will first present the results of the different power laws that were computed in this study, from empirical data or from simulations results. Then, we will compare, for each case study, the different final estimations $\Delta L' = \Delta L'(V)$ giving directly the travel distance as a function of the unstable volume V.

5.3.1 Quality of power law regressions

In this work, we have used simple power laws to derive statistical models both from empirical databases and simulations results. Their quality can be at first hand assesed from the adjusted R2, but other indicators are needed to assess the reliability of uncertainty estimation. The details of the statistical analyses, with the coefficients and quality indicators, are given in Table 5.A.1. The behaviour of residuals depending on predicted values is given in Appendix (Figure 5.A.1 and Figure 5.A.2).

The site-specific power laws are associated to very good $R2$: 0.91 for $g_S(V, \tilde{\mu}_{eff})$ for the Samperre case study, and more than 0.97 for other power laws. In comparison, empirical power laws feature $R2$ values between 0.68 (for *DB2*) and 0.84 (for *DB1*). $g_S(V, \tilde{\mu}_{eff})$ and $f_S(V, \mu_S)$ have a Variance Inflation Factor (VIF) below 1.08, which is a good indication that the explanatory variables are not linearly correlated and that the OLS regression is robust (in the sense that the inversion problem is well-constrained). The linearity hypothesis (that is, the validity of using a linear model to represent the link between the logarithm of the runout with the predictor variables) is also relatively well verified, with residues relatively well centered around 0 (Figure 5.A.1 and

5.A.2). However, we do see for the Frank Slide case study slightly concave and convex shapes for the residuals curve (Figure 5.A.2d, 5.A.2e, 5.A.2f). In turn, the hypothesis of homoscedasticity of residuals (that is, that the deviation from the regression result is similar for all predictions) is not verified in the Frank Slide case study (p-value of the Breush-Pagan test below 0.04). Finally, while the hypothesis that the distribution of residuals follows a normal law is well verified for all empirical power laws $\mu_H^1(V)$, $\mu_H^2(V)$ and $\mu_{eff}^1(V)$, it can be questioned for the site-specific power laws, in particular for $\Delta L' = \Delta L'(\tilde{\mu}_H)$ and $\Delta L' = f_S(V, \mu_S)$ (p-values of the Jarque-Bera test below 0.15).

5.3.2 Estimation of travel horizontal travel distances

In Table 5.2 we summarize the different power laws $\Delta L' = \alpha V^\beta$ that were derived to estimate travel distances with different methodologies. In the following we compare the estimation results for each case study.

Samperre cliff case study

Estimations of travel distances for the Samperre cliff case study are given in Figure 5.8 and Figure 5.9. The empirical estimation f_{emp}^1 (that uses directly μ_H and *DB1*) is in good agreement with observations (Figure 5.8a), but f_{emp}^2 (derived from *DB2*) slightly over-estimates them (Figure 5.8c). When we use simulations results with μ_S approximated from μ_H or μ_{eff} (f_{S,μ_H}^1, f_{S,μ_H}^2, $f_{S,\mu_{eff}}^1$ in Figure 5.8b, 5.8d, 5.8f respectively), the observed travel distance is systematically under-estimated by at most 40%. Finally the empirical/numerical estimation $g_{S,\mu_{eff}}$ is in almost perfect agreement with the back-analysis estimation f_S^{fit} (Figure 5.8e) and thus with the observations. The exponent β is 0.14 for the empirical estimations, and varies between 0.24 and 0.33 for the empirical/numercial and numerical estimations (Table 5.2).

Observations lie within the 95% prediction intervals of all estimations (black dashed lines in Figure 5.8). These intervals delimit the values predicted by the statistical models in 95% of the cases, given the estimated uncertainties (See Appendix 5.C). These intervals are always very large, which can be correlated to high values of the normalized standard deviations in travel distance estimations, σ (see Table 5.2). Indeed, we have $\sigma = 0.6$ for empirical estimations, which means that the standard deviation of estimations amounts to 60% of the direct prediction of the power law, when uncertainties are not taken into account. Using Shaltop reduces σ to 0.4 in empirical/numerical estimations with $\mu_S = \mu_H$, and even 0.3 when we choose $\mu_S = \mu_{eff}$. When the best-fit friction coefficient is used, σ drops down to 0.13 (see Table 5.2). In turn, the 95% prediction interval for f_S^{fit} is 2 to 3 times smaller than for other power laws.

As described in Section 5.2.2, the final empirical and empirical/numerical estimations of runout uses a first empirical power law, whose result is used in a second site-specific power law. By adding uncertainty in the first or in the second power law, or in both (see Appendix 5.C), we see that most of the uncertainty comes from the empirical relation giving μ_H or μ_{eff} as a function of volume. This is illustrated in Figure 5.9, where we see that the total uncertainty is almost the same when we consider uncertainty on both power laws (blue bars from "Both power laws") or on the empirical relation only (blue bars from "Empirical power law"): the difference is less than 2%. Besides, most of the uncertainty can be recovered by considering only the deviation between the best-fit power laws, and the data used to derive them. In comparison, the uncertainty on the power law coefficients increases σ by at most 3% (compare orange and green bars in Figure 5.9). This can be expected, as we compute σ for volumes within the range of simulated volumes. If we considered larger or smaller volumes, the uncertainty on coefficients would have more significant effects.

Methodology		Empirical database	Estimation name	Samperre Cliff $\Delta\bar{L}'$ (m)	β	σ_β	σ	Frank Slide $\Delta\bar{L}'$ (m)	β	σ_β	σ	Fei Tsui $\Delta\bar{L}'$ (m)	β	σ_β	σ
Empirical	with μ_H only	DB1	$\Delta L' = f^1_{emp}(V)$	1667	0.141	0.011	*0.63*	2908	0.064	0.005	*0.24*	57	0.092	0.007	*0.37*
		DB2	$\Delta L' = f^2_{emp}(V)$	1994	0.143	0.008	*0.61*	3169	0.065	0.004	*0.24*	64	0.094	0.005	*0.35*
Empirical/ numerical	$\mu_S = \mu_H$	DB1	$\Delta L' = f^1_{S_{\mu_H}}(V)$	967	0.329	0.011	*0.42*	2725	0.094	0.006	*0.21*	62	0.388	0.006	*0.20*
		DB2	$\Delta L' = f^2_{S_{\mu_H}}(V)$	1100	0.330	0.010	*0.41*	2940	0.095	0.005	*0.21*	66	0.389	0.005	*0.19*
	$\mu_S = \mu_{eff}$	DB1	$\Delta L' = f^1_{S_{\mu_{eff}}}(V)$	1027	0.313	0.011	*0.32*	2724	0.085	0.005	*0.17*	66	0.380	0.005	*0.16*
	with μ_{eff} only	DB1	$\Delta L' = g^1_{S_{\mu_{eff}}}(V)$	1588	0.240	0.017	*0.45*	4486	0.283	0.010	*0.35*	92	0.392	0.007	*0.18*
Numerical	Back-analysis	n.a.	$\Delta L' = f^{fit}_S(V)$	1620	0.227	0.009	*0.13*	3245	0.037	0.004	*0.07*	63	0.335	0.004	*0.03*

Table 5.2: Estimations of travel distance $\Delta L'$ depending on destabilized volume V, following a power law $\Delta L' = \alpha V^\beta$. We give the value of the exponent β along with the standard deviation of its estimation σ_β, and the normalized standard deviation σ of the prediction $\Delta L'$ see (5.13) and (5.14). $\Delta\bar{L}'$ is the averaged predicted travel distance for volumes between the minimum and maximum volumes used in the simulation databases, in each case study.

Frank Slide case study

The results for the Frank Slide case study are presented in Figure 5.10. The main conclusions are similar to the Samperre case study. The direct empirical estimations predict correctly the observed travel distance (Figure 5.10a and 5.10c). Using μ_H and μ_{eff} as input values for μ_S in simulations, the observed travel distance are under-estimated by at most a 15% (Figure 5.10b, 5.10d and 5.10f, compare blue rectangle and black line).

However, on the contrary to the Samperre case study, the estimation $g_{S,\mu_{eff}}$ is significantly different from the other estimations. It predicts a travel distance that is about twice the observed travel distance (Figure 5.10e). The power law exponent $\beta = 0.33$ is also significantly different: we get only $\beta = 0.065$ for f^1_{emp} and f^2_{emp}, $\beta = 0.1$ for empirical/numerical estimations, and $\beta = 0.045$ for the back-analysis estimation. Finally, $g_{S,\mu_{eff}}$ is associated to larger uncertainties, with $\sigma = 0.35$. It is even more than the uncertainty for empirical estimations, $\sigma = 0.24$. As for the Samperre case study, the latter is improved by empirical/numerical estimations, though less significantly ($\sigma = 0.21$ for f^1_{S,μ_H} and f^2_{S,μ_H}, and $\sigma = 0.17$ for $f^1_{S,\mu_{eff}}$). Once again, the back-analysis estimation f^{fit}_S yields the most precise estimation, with $\sigma = 0.07$.

The analysis of uncertainty propagation (see Figure 5.A.3) yields similar conclusions as in the Samperre case study.

Fei Tsui Road case study

The results for the Fei Tsui case study are presented in Figure 5.11. As previously, the direct empirical estimations are coherent with observations (Figure 5.11a and 5.11c). The estimation f^1_{emp}, that uses the database *DB1*, only slightly under-estimates the estimation by about 10%. When μ_{eff} and μ_H are used to estimate μ_S in numerical simulations, the observations are all well reproduced (Figure 5.11b, 5.11d and 5.11f). To the contrary, the estimation with $g_{S,\mu_{eff}}$ over-estimates the real travel distance by 45%.

A major difference between the empirical estimations and other estimations is the value of the power law exponent β. For f^1_{emp} and f^2_{emp} we compute $\beta = 0.09$, but we get $\beta = 0.38$ or $\beta = 0.39$ for empirical/numercial estimations. A similar value ($\beta = 0.34$) is derived for the back-analysis estimation f^{fit}_S.

Finally, as for the Samperre cliff case study, numerical simulations allow to reduce significantly the estimation normalized standard deviation σ. When σ is more about 0.35 for empirical estimations, it is reduced to less than 0.20 with empirical/numerical estimations (down to 0.16 with $f^1_{s,\mu_{eff}}$). f^{fit}_S yields the smallest standard deviation, with $\sigma = 0.03$.

The analysis of uncertainty propagation (see Figure 5.A.4) yields similar conclusions as in the Samperre and Frank Slide case studies.

5.4 Discussion

5.4.1 Uncertainty of travel distances estimation

Uncertainty reduction with numerical models

A major result of this work is that combining empirical estimations with numerical simulations reduces the standardized standard deviation σ of estimations. The smallest uncertainty is de-

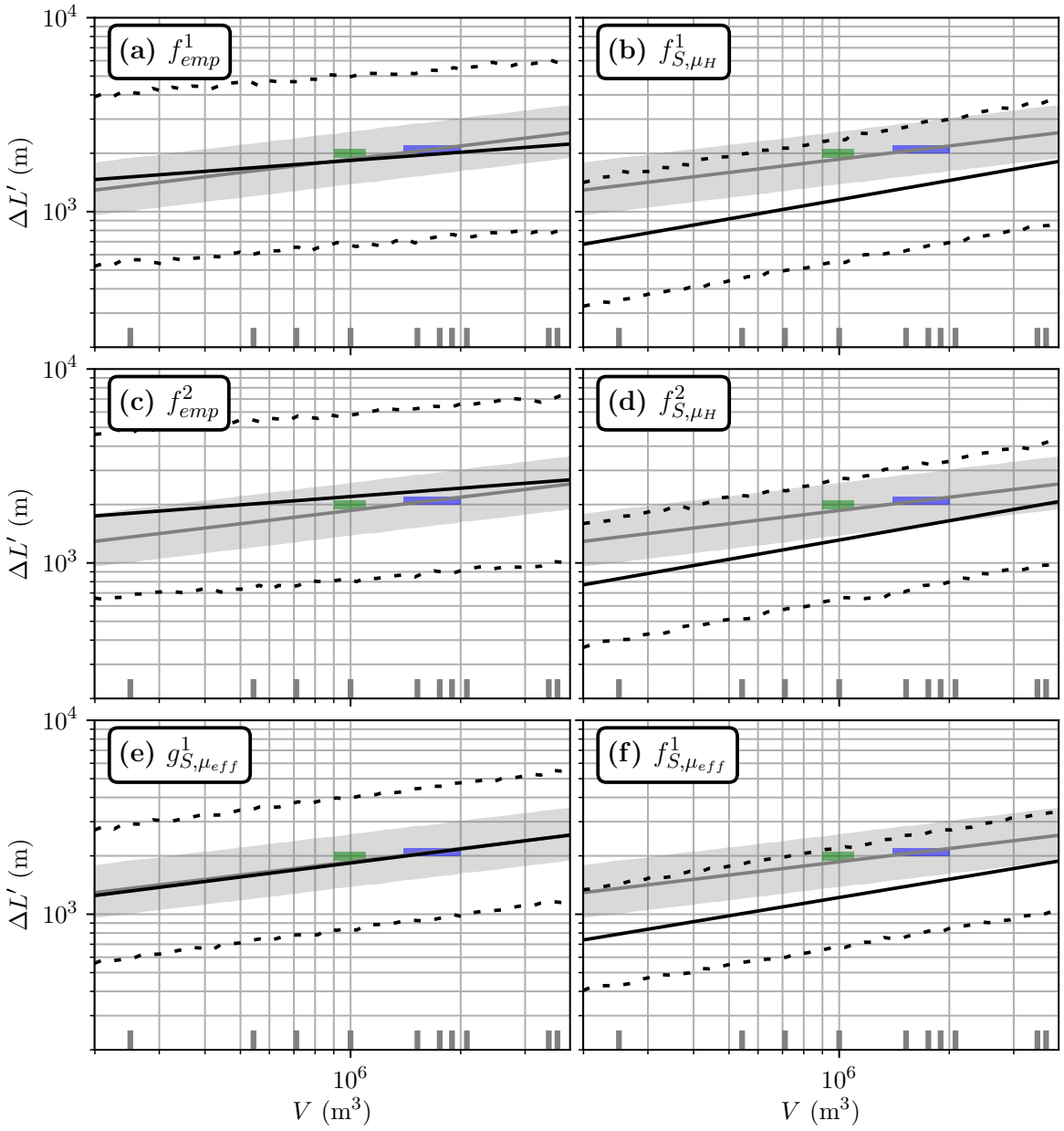

Figure 5.8: Travel distance estimated from volume for the Samperre case study. Green and blue rectangles: estimations of volumes and travel distances for the 2009 and 2018 collapses, respectively. Grey line: numerical estimation from back-analysis (f_S^{fit}), with $\mu_S = \tan(13.5°) = 0.24$. The grey area is the upper and lower limits of the 95% prediction intervals derived for $\mu_S^{fit} = \tan(13° \pm 2°)$. Thick grey dashes: simulated volumes. (a) Estimation with f^1_{emp}. (b) Estimation with f^1_{S,μ_H}. (c) Estimation with f^2_{emp}. (d) Estimation with f^2_{S,μ_H}. (e) Estimation with $g^1_{S,\mu_{eff}}$. (f) Estimation with $f^1_{S,\mu_{eff}}$. Black lines are direct estimates, dashed lines give the 95% prediction interval.

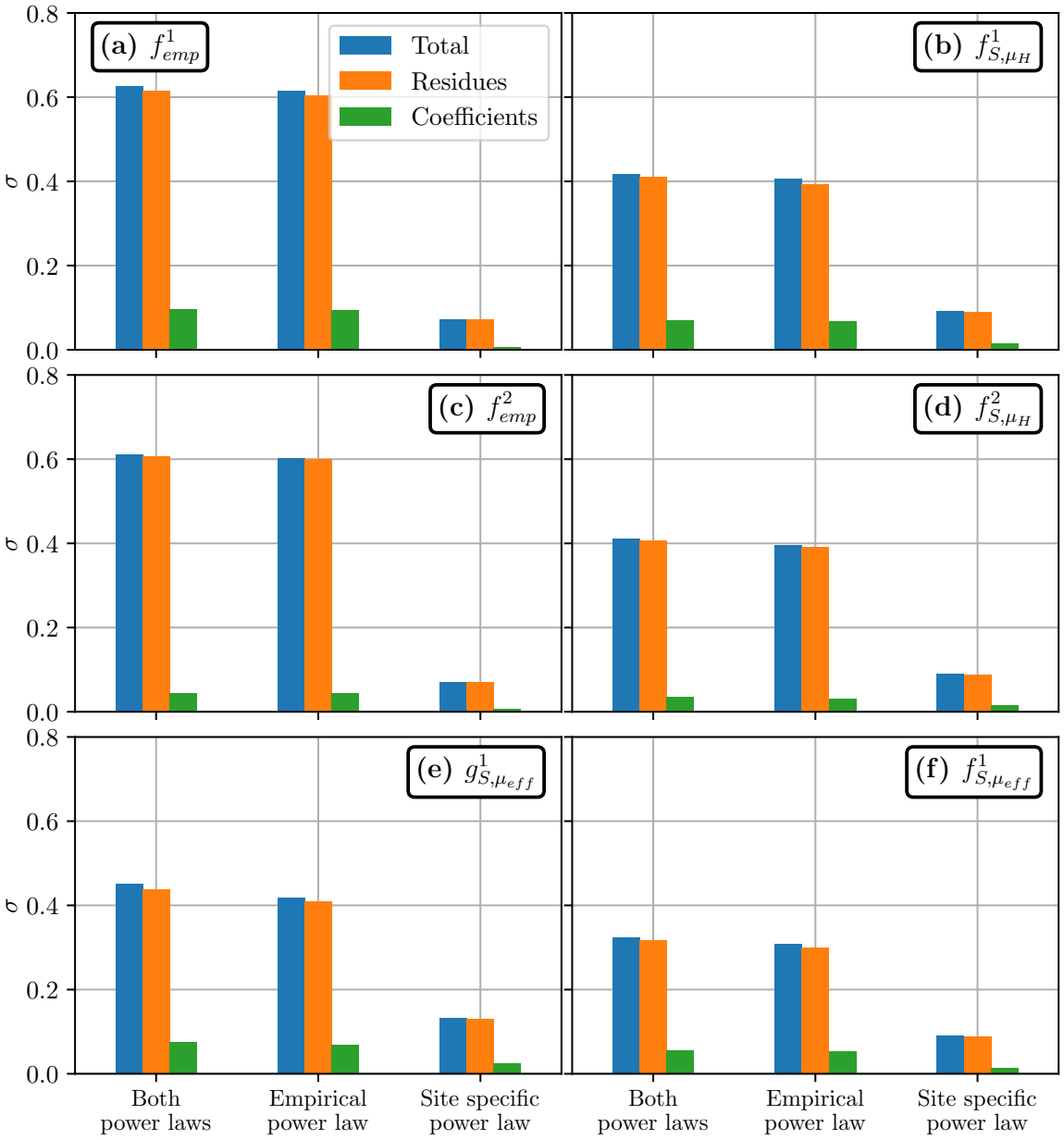

Figure 5.9: Uncertainty in travel distance estimation for the Samperre cliff case study, measured by the normalized standard deviation σ (see main body of the text). σ is computed by drawing randomly the power laws coefficients (green bars), the residuals (orange bars), or both (blue bars). As each estimation is the combination of two power laws, we consider uncertainties on the first power law derived from empirical databases (middle bars), on the second power law that is derived for the topography and simulation (right bars), or on both (left bars). (a) Estimation with f^1_{emp}. (b) Estimation with f^1_{S,μ_H}. (c) Estimation with f^2_{emp}. (d) Estimation with f^2_{S,μ_H}. (e) Estimation with $g^1_{S,\mu_{eff}}$. (f) Estimation with $f^1_{S,\mu_{eff}}$

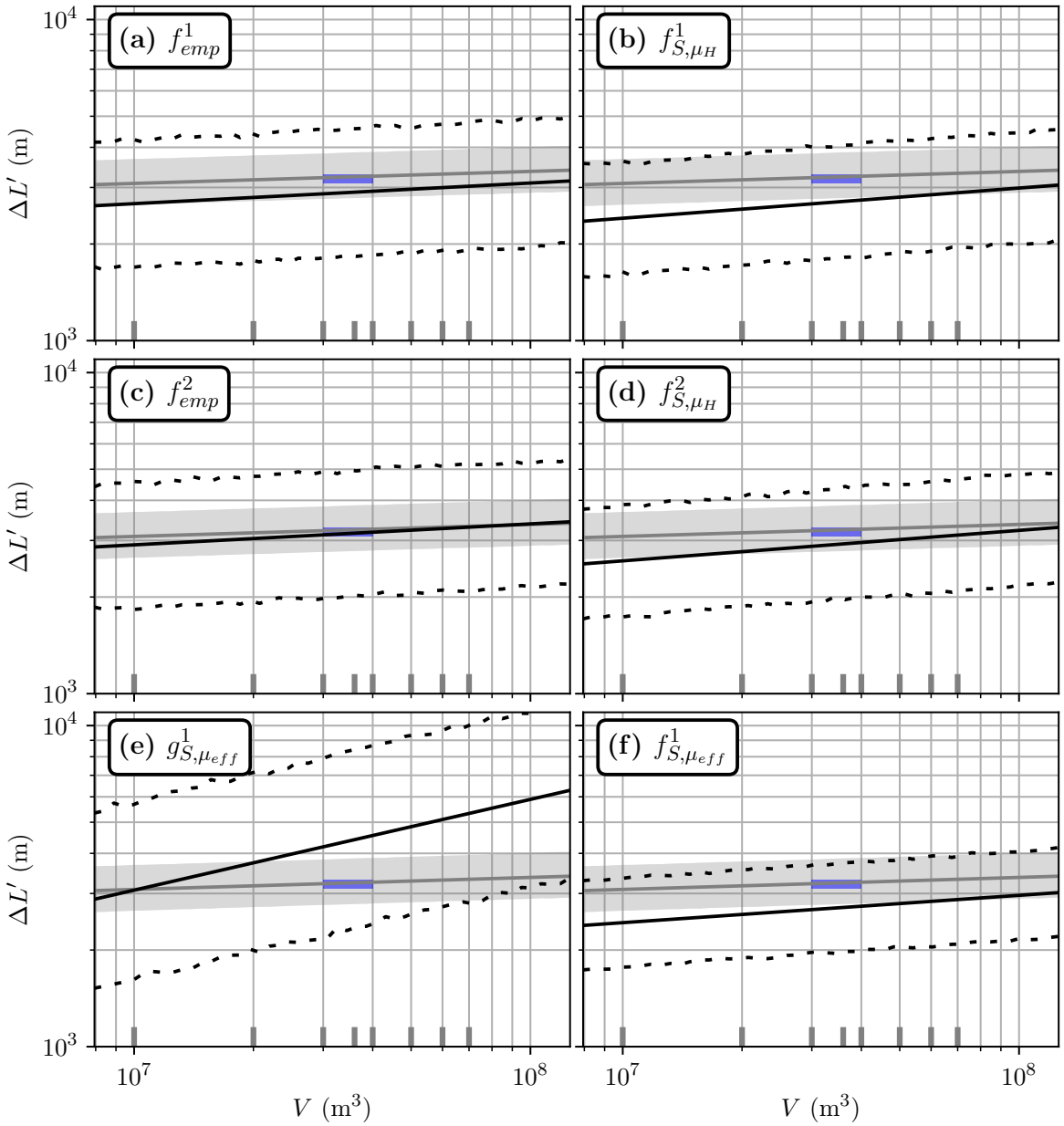

Figure 5.10: Travel distance estimated from volume for the Frank Slide case study. Blue rectangle: estimations of volumes and travel distances for the documented event. (a), (b), (c), (d), (e) and (f), and symbols are the same as for Figure 5.8.

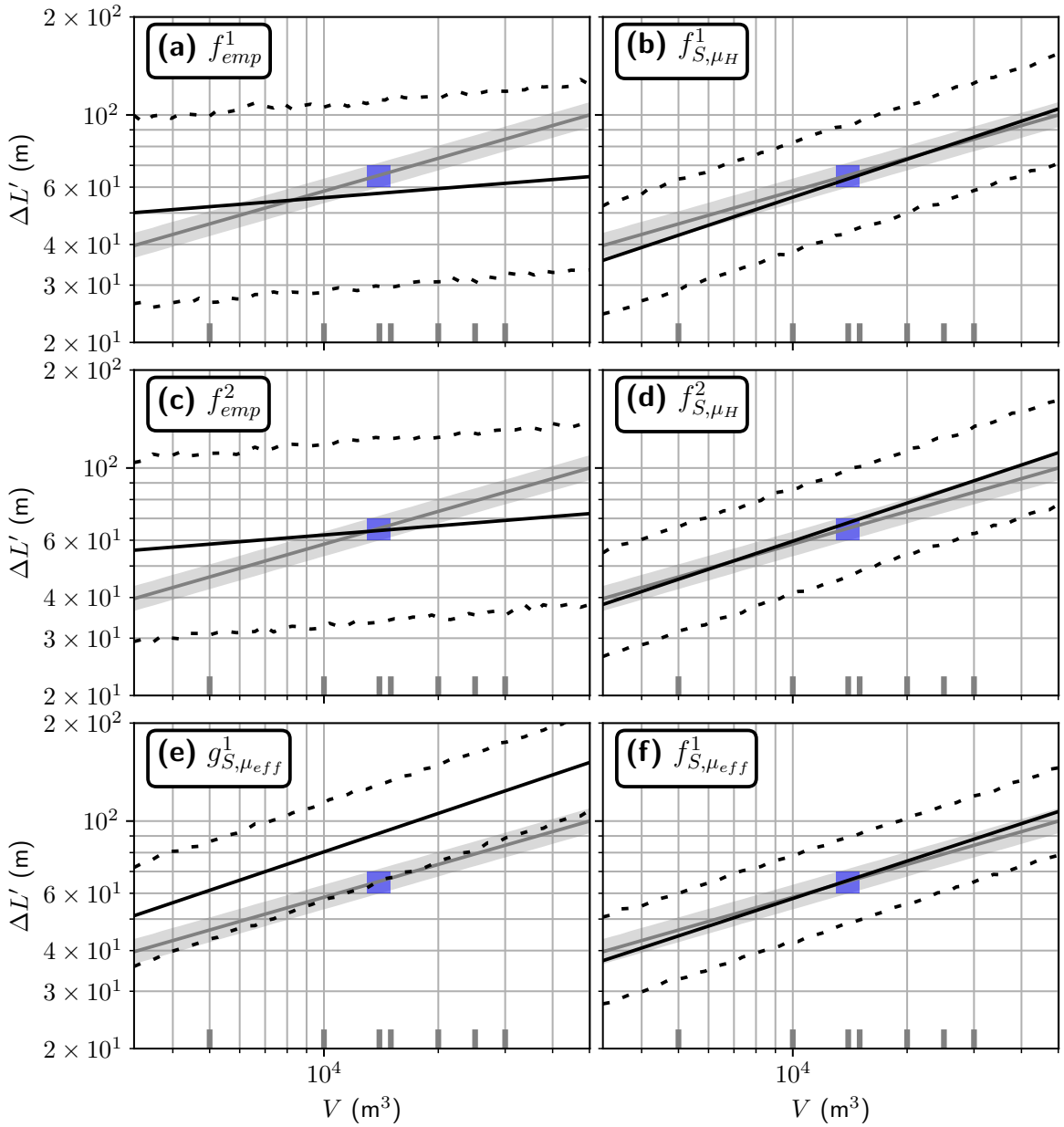

Figure 5.11: Travel distance estimated from volume for the Fei Tsui Road case study. Blue rectangle: estimations of volumes and travel distances for the documented event. (a), (b), (c), (d), (e) and (f), and symbols are the same as for Figure 5.8.

rived by using back-analysis and a constant friction coefficient, but it is difficult to quantify the uncertainty on the best-fit friction oefficient μ_S^{fit}. As shown by Mergili et al. (2018), the extent to which it can be used for other landslides is not clear, even considering similar volumes and propagation paths.

This reduction is all the more important as the volumes considered are small. By setting $\mu_S = \mu_H^1(V)$ or $\mu_S = \mu_H^2(V)$ in $\Delta L' = f_S(V, \mu_S)$, σ is reduced by 12.5% for the Frank Slide and by 43% for the Fei Tsui Road case study. A similar trend is observed with $\mu_S = \mu_{eff}^1(V)$ (reductions by 29% and 54% respectively). This can be directly correlated to the exponents of $\tilde{\mu}_H$ in $\Delta L'(\tilde{\mu}_H)$, whose absolute values are systematically higher than the exponents of μ_S in $f_S(V, \mu_S)$ (see Table 5.A.1). In turn, uncertainty on μ_H or μ_{eff} results in less deviation in the final empirical/numerical estimations, in comparison to the purely empirical estimation (see Appendix 5.D).

We may argue that as the site-specific power laws do not always verify the hypotheses of OLS regressions, the associated uncertainty estimation (and thus the observed reduction of uncertainty afore-mentionned) is not relevant. However, the estimation of the coefficients of the power laws does not depend on these hypotheses, such that the argument presented in the previous paragraph still stands true. Besides, the residuals of the site-specific power laws are at most between -0.1 and 0.1 (in logarithmic scale), while they range from -0.3 to 0.3 for the empirical power laws (compare Figure 5.A.1 and Figure 5.A.2). In turn, even if real uncertainty of site specific laws is higher than what we estimate, it will still be less than the uncertainty associated to empirical, non site-specific power laws. Thus, improving the quality of empirical/numerical travel distance estimations should be done primarily by improving the quality of the empirical power laws.

Uncertainty related to dispersion in empirical power laws

Empirical laws can be improved by considering a database of landslides sharing similar characteristics with the case study. For instance, if we construct *DB2* by taking only the debris flows, debris slides and debris avalanches from Corominas (1996), we derive a new relations $\mu_H = \mu_H^{2*}(V)$ with $R2 = 0.8$ that can be used for the Fei Tsui Road case study (see Figure 5.A.5 and Figure 5.A.6). As a result, the standard deviation σ of the travel distance estimation f_{emp}^{2*} is about 0.25. In comparison, we had $\sigma = 0.35$ for f_{emp}^2 (that is, when we included rockfalls and rock avalanches in *DB2*). But removing rockfalls and rock avalanches from *DB2* also leads to a 15% over-estimation of the observed travel distance (though it remains in the 95% prediction interval).

Although regrouping landslides by type may increase the quality of the fit, associated $R2$ hardly exceeds 0.9 (e.g. no more than 0.85 in Lucas et al. (2014), less than 0.5 in Strom and Abdrakhmatov (2018), less than 0.2 in Mitchell et al. (2019), and less than 0.8 in Legros (2002)). In Corominas (1996), combining both landslide types and geometrical characteristics of the propagation (i.e. whether the landslide is laterally or frontally obstructed) allows to derive power laws with $R2$ values between 0.65 and 0.92. Further improvements of the quality of empirical power laws may demand to express more finely the characteristics of the topography upon which the landslide propagates.

Uncertainty related to topography description

To estimate more finely the travel distance in empirical relations, it may be worth using statistical model that do not depend only on the volume. For instance in Mitchell et al. (2019), a relation

$$\Delta L' = a_0 10^{a_3 C} V^{a_1} H^{a_2} \times 10^{\epsilon}, \tag{5.15}$$

is derived from a database of rock avalanches, with $R2 = 0.8$. Here, C is an indicator variable with $C = 1$ if lateral confinement is observed, and $C = 0$ otherwise. In comparison, with the same data, they derive a power law $\mu_H = a_0 V^{a_1}$ with $R2 = 0.2$ only. In our work, combining their data with the data of Corominas (1996) allows to increase the $R2$ to 0.68 because the resulting database *DB2* spans a wider range of volumes.

By estimating the probabilistic distribution of the residues ϵ in (5.15), it is then possible to estimate, for a given topography and volume, the probability that the landslide goes further than a chosen point M on the topography. This is done by considering the difference ϵ_M between the travel distance $\Delta L'_M$ associated to the point M, and the travel distance predicted by the power law:

$$\epsilon_M = log_{10}\left(\frac{\Delta L'_M}{a_0 10^{a_3 C} V^{a_1} H_M^{a_2}}\right). \tag{5.16}$$

Then the probability that the travel distance $\Delta L'$ exceeds $\Delta L'_M$, given a volume V, a drop height H_M and a confinement indicator C is:

$$P(\Delta L' > \Delta L'_M) = P(\epsilon > \epsilon_M), \tag{5.17}$$

which can be computed if the distribution of ϵ is known. This methodology could be applied in our case: in particular, it allows to skip the derivation of the site-specific relation $\Delta L' = \Delta L'(\tilde{\mu}_H)$. However, it should be adapted to consider the uncertainty on the power law coefficients, which was not done in Mitchell et al. (2019). Besides, using the landslide drop height H as an explanatory variable may favor multi-linearity, as H is correlated to V. For instance in Legros (2002), a power law $H = a_0 V^{a_1}$ with $R2 = 0.7$ was derived for volcanic landslides.

A fine description of topography, as well as of the initial unstable mass, is also needed to estimate empirically the friction coefficient μ_S of a given landslide. In our empirical/numerical methodologies of travel distance estimations, we used μ_H and μ_{eff}. The relevance of this choice is discussed in the next section.

5.4.2 Are μ_H and μ_{eff} good estimates of μ_S?

Comparison with empirical data in Lucas et al. (2014) shows a good correlation between μ_{eff} and μ_S over a wide range of volumes. This is not in exact agreement with our results, because we needed $\mu_S < \mu^1_{eff}(V)$, as well as $\mu_S < \mu^1_H(V)$ and $\mu_S < \mu^2_H(V)$, to reproduce the Samperre cliff collapse and the Frank Slide respectively. In simulations, when comparing μ_S to $\tilde{\mu}_{eff}$ and $\tilde{\mu}_H$ (Figure 5.12), we find almost systematically that $\tilde{\mu}_H$ and $\tilde{\mu}_{eff}$ over-estimate μ_S by up to 30%. This is in agreement with results of Peruzzetto et al. (2019). The only exception is the Fei Tsui Road case study where we have $\tilde{\mu}_H < \mu_S$ for $V > 15,000$ m ^{3} (Figure 5.12e).

As already discussed in the literature (e.g. Lajeunesse et al., 2006; Legros, 2002; Finlay et al., 1999; Lucas et al., 2014), the Heim's ratio μ_H can't be considered as a good proxy for the real basal friction coefficient of the landslide. Indeed, the reduction of μ_H with increasing volumes results from real friction reduction (in the sense that a lower friction coefficient μ_S is needed to model larger landslide) but also from purely geometrical effects. This is illustrated in our simulations in the Samperre and Fei Tsui Road case studies: when the volume V is increased but μ_S remains constant, μ_H is reduced (see Figures 5.12a and 5.12e).

This should be supposedly corrected for with μ_{eff} whose expression (5.2) was derived analytically to match μ_S (Lucas et al., 2014). However, though $\tilde{\mu}_{eff}$ is almost constant for various volumes and a given μ_S in the Fei Tsui Road case study (Figures 5.12f), it increases with volume in

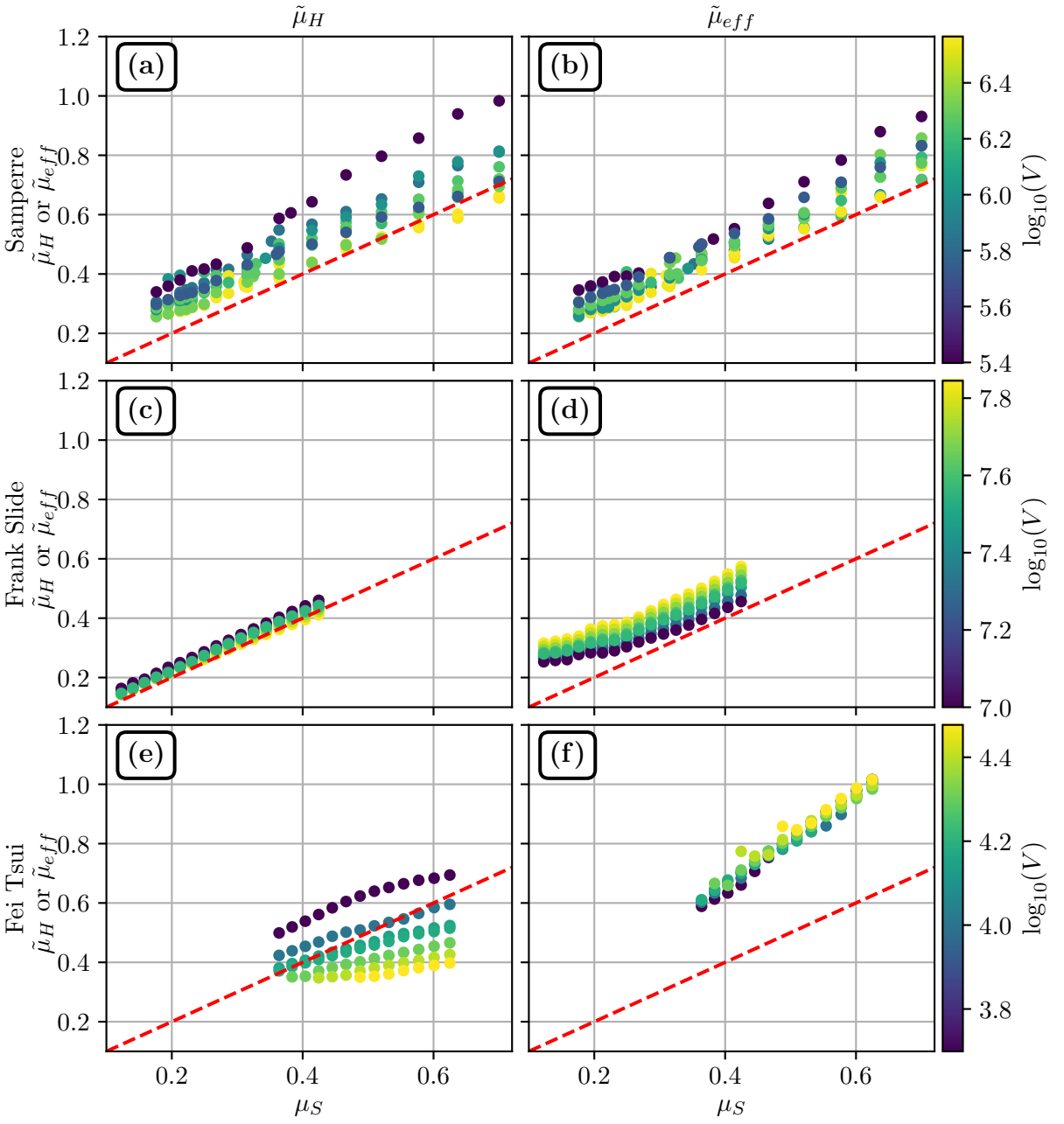

Figure 5.12: $\tilde{\mu}_{eff}$ and $\tilde{\mu}_H$ computed from simulations results, plotted against μ_S. (a) and (b) $\tilde{\mu}_H$ against μ_S and $\tilde{\mu}_{eff}$ against μ_S (respectively) for the Samperre case study. (c) and (d) $\tilde{\mu}_H$ against μ_S and $\tilde{\mu}_{eff}$ against μ_S (respectively) for the Frank Slide case study. (e) and (f) $\tilde{\mu}_H$ against μ_S and $\tilde{\mu}_{eff}$ against μ_S (respectively) for the Fai Tsui debris slide case study. Color scale gives the volume (in logarithmic scale) of the simulation. The red dashed lines correspond to $\mu_H = \mu_S$ and $\mu_{eff} = \mu_S$.

the Frank Slide case study (Figures 5.12d), but on the contrary decreases with volume in the Samperre case study (Figures 5.12b). This may be explained by the fact that, for the Frank Slide case study, the increase of initial volume favors lateral spreading, such that in (5.2), the increase of the initial maximum thickness H_0 is not compensated by an increase of the travel distance along topography ΔL. The opposite happens in the Samperre case study, where the landslide is laterally confined in a narrow gully.

These results highlight the complexity of defining simple mobility estimations that can be computed from landslide deposits and be used as proxys for the friction coefficient μ_S. In particular, the description of topography is not easy. The analytical development leading to the definition of μ_{eff} in Lucas et al. (2014) was done for landslides on 1D planar surfaces (that is, on a 1D topography given by a graph $z = \tan(\theta)x$). Thus, it does not take into account lateral spreading that can limit travel distance: it has been observed empirically that lateral confinement increases travel distances (Strom and Abdrakhmatov, 2018; Mitchell et al., 2019). Besides, the propagation of landslides on complex topographies with non constant slope is not predicted either. In Lucas et al. (2014), the formal expression of μ_{eff} is extended empirically to non constant slopes by considering the average slope θ along the landslide path. As discussed previously, it proved to yield conclusive results at the scale of the database, but it may not be precise enough when considering forward prediction in a specific case study.

Indeed, when we try using μ_{eff} directly to estimate travel distances (that is, with the function $\Delta L' = g_S(V, \tilde{\mu}_{eff})$), we get somehow unstable results. Though the estimation is good for the Samperre Cliff (Figure 5.8e), high uncertainties are obtained for the Frank Slide case study. In the latter case, the dependence to volume seems also over-estimated in comparison to other estimations (Figure 5.10e). Finally for the Fei Tsui Road case study, the observed travel distance is over-estimated by 45%.

Thus, further investigations are needed to try and derive formulas relating landslides deposits and topography geometry to μ_S. This could be done by modeling the propagation of landslides on synthetic topographies with, for instance, a slope break or an exponential profiles, and analyze the correlations between $\tilde{\mu}_H$ and $\tilde{\mu}_{eff}$ derived from simulations results, and μ_S.

Another possibility is to disregard empirical mobility estimations, and consider instead directly the friction coefficient μ_S needed to reproduce each event from a database of at least, typically, 30 landslides, which is necessary to evaluate correctly uncertainty. The resulting relation $\mu_S = \mu_S(V)$ could be then used directly in the function $\Delta L' = f_S(V, \mu_S)$ derived from site-specific simulations. The systematic back-analysis of mapped landslides has been done for instance in Aaron and McDougall (2019) and Zimmermann et al. (2020) but with the Voellmy rheology. We could find only one example of such studies with the Coulomb rheology in Brideau et al. (2019), but for a small range of volumes (between 0 and 10,000 m^3) and 1D simulations (i.e. along profiles, not on real topographies). Note that the relation $\mu_S = \mu_S(V)$ may depend on the numerical code used to derive it: although thin-layer models solve roughly similar equations, differences in equations (in particular related to the description of internal stress) and numerical implementations can affect the results. For instance, we found a best-fit friction coefficient $\mu_S^{fit} = \tan(11°)$ for the Frank Slide, but $\mu_S^{fit} = \tan(14°)$ is obtained in Pirulli and Mangeney (2008), and $\mu_S^{fit} = \tan(11°)$ in Hungr and Evans (1996)

In any case, a good estimation of μ_S is important, because it will influence the final estimation of travel distance, and in particular the dependence to volume.

5.4.3 Dependence between travel distance and volume

In our final estimations of travel distance $\Delta L' = \alpha V^{\beta}$, the dependence to volume is measured by β. It varies significantly depending on the methodology and on the case study. In empirical/numerical estimations, β is increased in comparison to purely empirical estimations, all the more so as volumes are small. For instance in the Frank Slide case study, the exponent β of empirical estimations f^1_{emp} and f^2_{emp} is 20% below the exponent β of $f^1_{S,\mu_{eff}}$ (where we set $\mu_S = \mu^1_{eff}(V)$). In the Fei Tsui Road case study, it is 75% below (see Table 5.2). This shows that μ_H does not model properly the influence of the initial volume on the final travel distance, particularly for small landslides.

The influence of initial volume on travel distance is indeed all the more important as we consider small landslides with limited travel distances. This is illustrated by comparing the exponents of V and μ_S in the function $\Delta L' = f_S(\mu_S, V)$ (see Table 5.A.1 and Appendix 5.D). For the Fei Tsui Road case study, volumes variations represents 20% of the total variance of travel distances, the rest being attributed to variations of μ_S. For the Samperre and Frankslide case studies, this proportion drops down to 3.7% and 0.3% respectively. This is not rendered in the empirical relations $\mu^1_H(V)$ and $\mu^2_H(V)$, explaining why f^1_{emp} and f^2_{emp} under-estimate the dependance to volume in comparison to empirical/numerical estimations.

These observations also explain why, in the Fei Tsui Road case study, the dependence to volume are similar between the empirical/numerical estimations of travel distance and the purely numerical estimations where we use the back-analyzed value μ^{fit}_S of μ_S. We have indeed $\beta = 0.38$ or $\beta = 0.39$ in the former estimations, and $\beta = 0.34$ for f^{fit}_S, with a constant friction coefficient derived by back-analysis. In comparison, for the Frank Slide case study, the exponent β in f^{fit}_S is less than half the exponent in f^1_{S,μ_H}, f^2_{S,μ_H} and $f^1_{S,\mu_{eff}}$. Indeed, in this case, the travel distance depends mainly on the friction coefficient μ_S, such that choosing a constant value of μ_S instead of a volume dependent value has more impact than in the Fei Tsui Road case study.

These results may seem contradictory with empirical power laws $\Delta L' = F_{emp}(V)$ derived directly from landslide databases. The exponent β varies between 0.25 and 0.39 in Legros (2002) and does not seem to depend on the range of volumes considered. In Lucas et al. (2014), $\beta = 0.22$ for $V < 10^6$ m^3, $\beta = 0.28$ for $V > 10^8$ m^3 and $\beta = 0.35$ for all volumes. One possible explanation to the difference between these values and the ones of our study is that, for the Frank Slide and Fei Tsui Road simulations, our initial unstable mass were constructed by simply scaling the heights of the documented landslide to obtain different volumes, without changing the scar geometry. Though it was shown that the initial scar geometry has little influence on the landslide runout (Lucas et al., 2011), it may be worth investigating more realistic initial settings.

However, our empirical estimations $\Delta L' = f^1_{emp}(V)$ and $\Delta L' = f^2_{emp}(V)$ also display exponents β significantly different, between 0.06 and 0.13, whereas $\beta > 0.2$ for F_{emp}. The discrepancies in volume dependencies are thus not related only to numerical issues. It may rather be related to the fact that f^1_{emp} and f^2_{emp} are site-specific relations, while F_{emp} is not as it uses observations of V and $\Delta L'$ on different topographies. In turn, it may be possible that aggregating the observations of landslides on various topographies yields an exponent β close to 0.33, as predicted by analytical results for landslides propagating on constant slopes (Lucas et al., 2014). However, considering each topography separately may well result in topography-specific values for β, different from 0.33.

5.5 Conclusions

In this work, we derived operational and site-specific power laws to predict the horizontal travel distance $\Delta L'$ of a landslide from its volume V. Such simple relations are indeed of prior importance for landslide hazard assessment, in particular for crisis management when travel distance estimations must be provided quickly by practitioners. We have compared three methodologies to derive such power laws, using i) a purely empirical approach, ii) a database of simulations along with the back-analysis of a documented event, and iii) combining an empirical estimation of mobility with simulations.

We show that:

1. The best results, in terms of prediction uncertainty, are obtained with numerical estimations of travel distances, with friction coefficient deduced from back-analysis. The standard deviation of estimations is indeed less than half the standard deviation of empirical/numerical estimations, and less than 30% the standard deviation of purely empirical estimations. However, the uncertainty on the back-analysis results are asserted, to some extent, in an expert way. In turn, comparison with other methodologies should be done with caution.

2. Combining numerical modeling with empirical estimations of μ_H and μ_{eff} reduces the uncertainty of estimation by about 50%, in comparison to purely empirical estimations. The smallest uncertainties are obtained by using μ_{eff} to estimate the simulation friction coefficient μ_S. However, setting $\mu_S = \mu_H$ or $\mu_S = \mu_{eff}$ results, in 2 out of the 3 tested case studies, in an under-estimation of observed travel distances.

3. When we relate the effective friction coefficient μ_{eff} observed on real landslides, to the effective friction coefficient $\tilde{\mu}_{eff}$ computed from simulations results, the resulting estimations of travel distance displays large uncertainties (even larger than empirical estimates) and/or over-estimates observations. This could be explained by the fact that the analytic expression of μ_{eff} and $\tilde{\mu}_{eff}$ was derived for constant slopes, such that their definition on complex topographies is not straight-forward.

4. Numerical simulations allow to better characterize the respective influence of initial volume and physical mobility (as measured with μ_S) on the final travel distance, for a given topography. We show that for large landslide (i.e. for volumes $> 1 \times 10^6$ m^3), the travel distance depends mainly on μ_S, while for small landslide (i.e. for volumes $< 5 \times 10^5$ m^3) the initial volume V has a more prominent role. This is not rendered in empirical estimations of travel distances, for which the dependence of travel distance to volume is under-estimated, all the more so as small volumes are considered.

The milestone of our work is the construction of a simulation database, where various landslide volumes, collapse geometries and mobilities are tested. The definition of the initial unstable masses can be time consuming, especially when little information is available to constrain collapse geometries. This aspect may be the main practical difficulty to tackle in the perspective of using our methodology for operational hazard assessment, especially in a regulatory framework. Indeed, though the statistical analysis of results must be interpreted with caution, its implementation can be automated to a large degree. In comparison, the methodology for constructing initial geometries relies, at least to some extent, on expert judgment. It must be easy enough to be reproducible and applied in a reasonable time, but must also provide realistic collapse scenarios. Further work, including applications to other case studies, is needed to better constrain the right balance between these two requirements. In any case, our study proves the relevance of using numerical simulations to improve empirical estimations of travel distances for operational use.

In this work, we have used only power laws which are easy to manipulate, but other non-parametric models, such as the General Additive Models (e.g. Wood, 2017), could be used when linear regression models are not valid. Further research should also focus on the estimation of the friction coefficient μ_S to be used in simulations. This could be done by systematic back-analysis of a landslide database, and/or by adapting the definition of landslide mobility indicators, such as μ_{eff}, to take into account the topography more precisely. However, we may expect that significant uncertainties will remain, as a result of the partial knowledge we have in practice of the process at stake during the landslide propagation. Thus, expert judgments are valuable to assess the representativeness of results. The selection, evaluation and aggregation of such judgments (e.g. Hathout et al., 2019) could also help constrain the estimation of runout.

To conclude, let's note that the information in our simulation databases are greatly simplified for the purpose of this study, as we focused only on the estimation of travel distances. However, we could also extract thicknesses and dynamic pressure maps for various volumes as done for instance in tsunami hazard assessment (Aniel-Quiroga et al., 2018). The quantification of spatial uncertainty is however difficult and requires tools more complex than our simple power laws.

Appendix

5.A Supplementary Table and Figures

		$\mathbf{a_0}$	$\mathbf{a_1}$	$\mathbf{a_2}$	B-P	J-B	R2	VIF
$\mu_H = \mu_H(V) = 10^{a_0} V^{a_1}$	DB1	0.0691± 0.1107	-0.0875± 0.0135	n.a.	0.23	0.29	0.82	n.a.
	DB2	0.0287± 0.0530	-0.0889± 0.0099	n.a.	0.20	0.18	0.68	n.a.
$\mu_{eff} = \mu_{eff}(V) = 10^{a_0} V^{a_1}$	DB1	-0.0335± 0.0872	-0.0739± 0.0105	n.a.	0.98	0.83	0.84	n.a.
$\Delta L' = \Delta L'(\tilde{\mu}_H) = 10^{a_0} \tilde{\mu}_H^{a_1}$	Samperre	2.5291± 0.0128	-1.6113± 0.0328	n.a.	0.07	0.01	0.98	n.a.
	Frank Slide	3.0274± 0.0069	-0.7345± 0.0120	n.a.	0.01	0.00	0.99	n.a.
	Fei Tsui Road	1.4496± 0.0031	-1.0543± 0.0089	n.a.	0.99	0.00	1.00	n.a.
$\Delta L' = f_S(V, \mu_S) = 10^{a_0} V^{a_1} \mu_S^{a_2}$	Samperre	1.1697± 0.1061	0.2275± 0.0172	-1.1557± 0.0317	0.40	0.00	0.97	1.00
	Frank Slide	2.7682± 0.0566	0.0374± 0.0075	-0.6460± 0.0119	0.04	0.05	0.99	1.00
	Fei Tsui Road	0.2373± 0.0347	0.3346± 0.0078	-0.6103± 0.0266	0.78	0.14	0.99	1.03
$\Delta L' = g_S(V, \mu_{eff}) = 10^{a_0} V^{a_1} \mu_{eff}^{a_2}$	Samperre	1.7719± 0.1751	0.1287± 0.0293	-1.5085± 0.0904	0.00	0.12	0.91	1.05
	Frank Slide	1.4650± 0.1070	0.1872± 0.0133	-1.2926± 0.0446	0.01	0.30	0.97	1.08
	Fei Tsui Road	0.3313± 0.0406	0.3407± 0.0097	-0.6919± 0.0442	0.02	0.12	0.99	1.01

Table 5.A.1: Results of the intermediate power laws. We give the coefficients along with the 95% confidence interval. We also indicate the adjusted $R2$ and the p-values of the Jarque-bera test (J-B, normality of residuals hypothesis) and of the Breush-Pagan test (B-P, homoscedasticity hypothesis). Low p-values (typically, less than 0.05) indicate that the hypothesis is not verified. The Variance Inflation Factor (VIF) measures colinearity between a_1 and a_2.

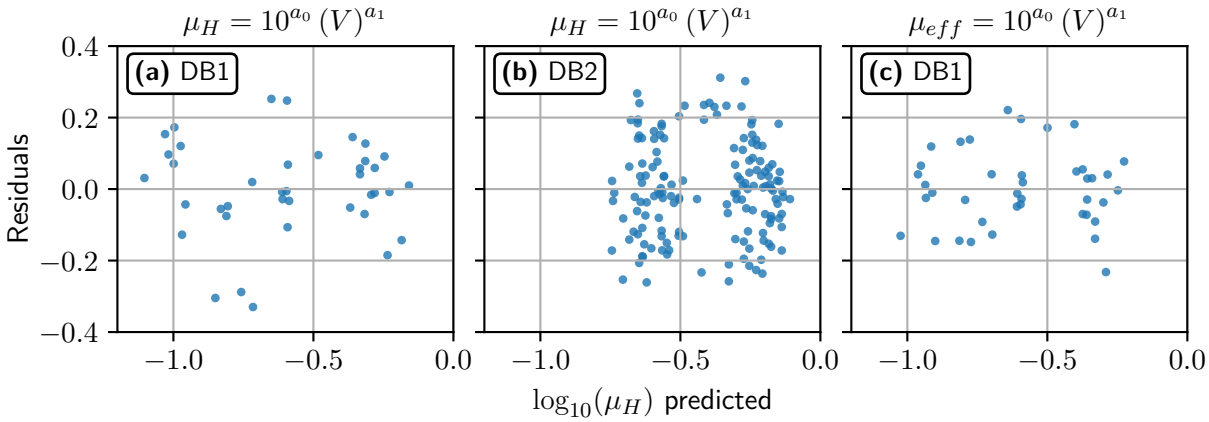

Figure 5.A.1: Residuals VS predicted values for the different power laws deduced from empirical databases. The axis scale is logarithmic. (a) $\mu_H = \mu_H^1(V)$, with *DB1*. (b) $\mu_H = \mu_H^2(V)$, with *DB2*. (c) $\mu_H = \mu_{eff}^2(V)$, with *DB1*.

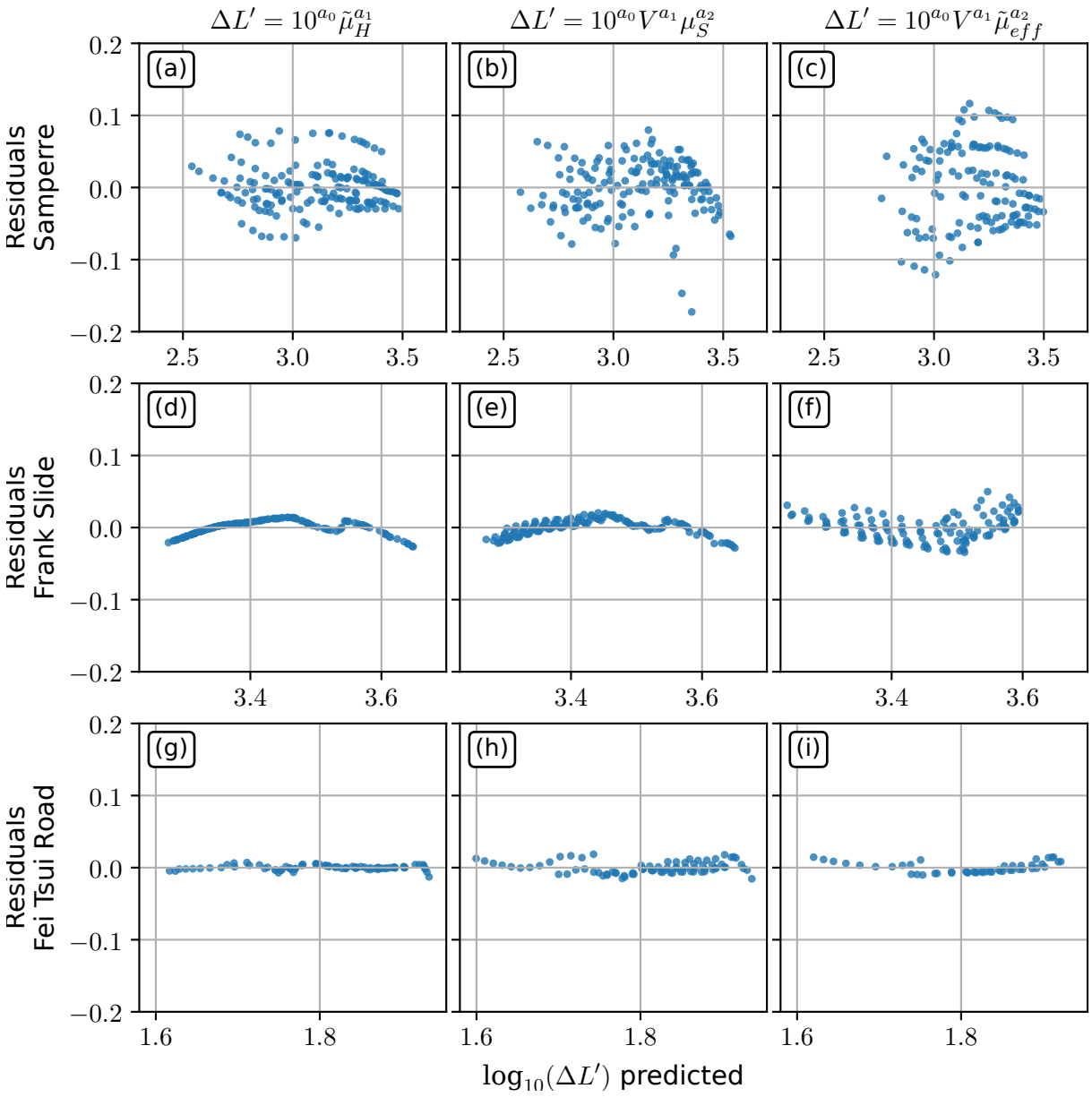

Figure 5.A.2: Residuals VS predicted values for the different power laws deduced for each case study. The axis scale is logarithmic. Each line refers to a case study, and each column to a law. (a), (b) and (c): $\Delta L' = \Delta L'(\tilde{\mu}_{eff})$, $\Delta L' = f_S(V, \mu_S)$ and $\Delta L' = f_S(V, \tilde{\mu}_{eff})$ respectively for the Samperre cliff case study. (d), (e) and (f): $\Delta L' = \Delta L'(\tilde{\mu}_{eff})$, $\Delta L' = f_S(V, \mu_S)$ and $\Delta L' = f_S(V, \tilde{\mu}_{eff})$ respectively for the Frank Slide case study. (g), (h) and (i): $\Delta L' = \Delta L'(\tilde{\mu}_{eff})$, $\Delta L' = f_S(V, \mu_S)$ and $\Delta L' = f_S(V, \tilde{\mu}_{eff})$ respectively for the Fei Tsui Road debris slide case study.

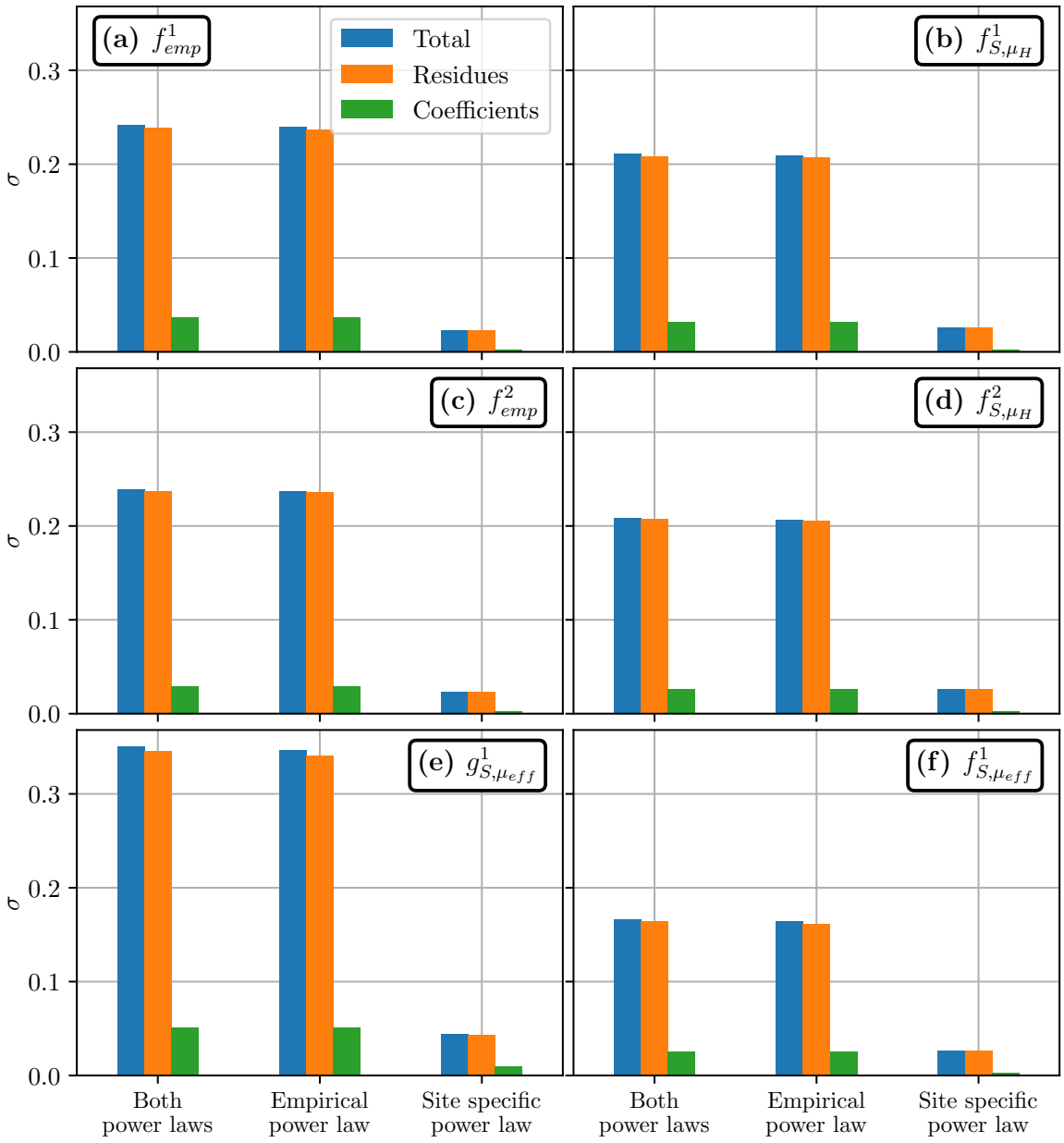

Figure 5.A.3: Uncertainty in travel distance estimation for the Frank Slide cliff case study. (a), (b), (c), (d), (e) and (f), and symbology are the same as for Figure 5.9.

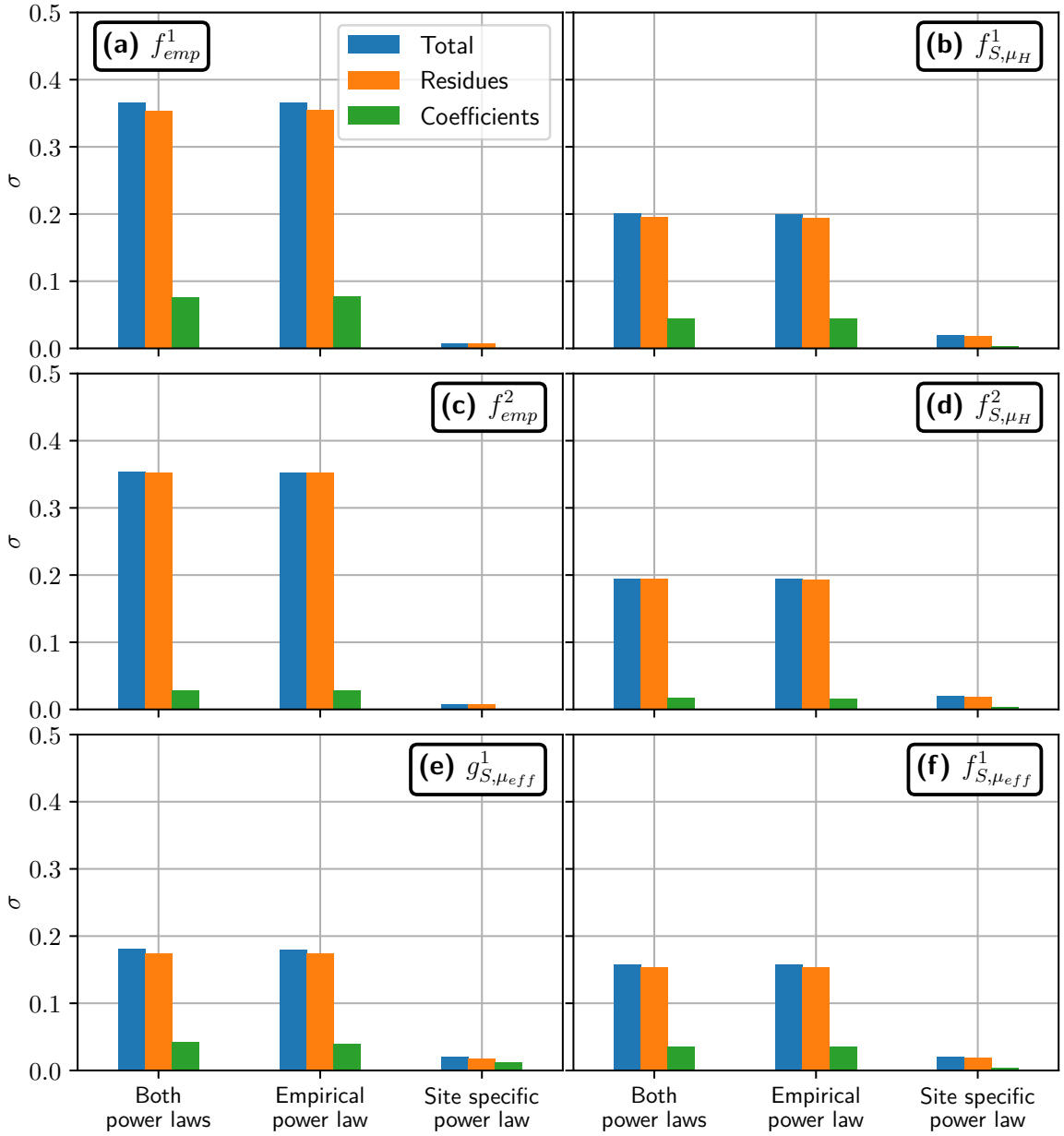

Figure 5.A.4: Uncertainty in travel distance estimation for the Fei Tsui Road cliff case study. (a), (b), (c), (d), (e) and (f), and symbology are the same as for Figure 5.9.

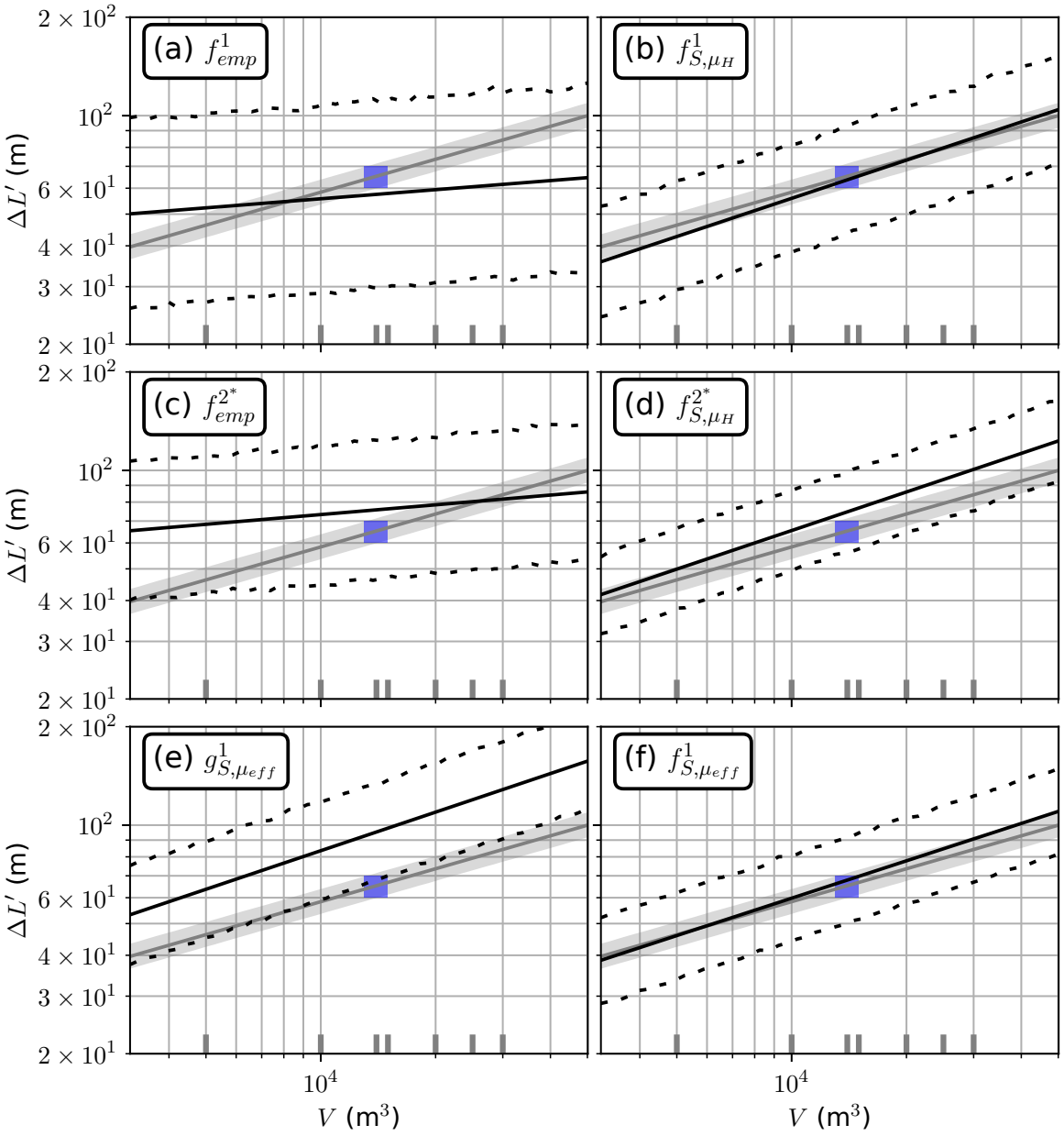

Figure 5.A.5: Travel distance estimated from volume for the Fei Tsui Road case study, and a variation of *DB2* with only debris flows, debris avalanches and debris slides. The corresponding travel distance estimations are marked with the super-script $^{2^*}$. Notations are otherwise the same as in the main body of the article. Green and blue rectangles: estimations of volumes and travel distances for the 2009 and 2018 collapses, respectively. Grey line: Numerical estimation from back-analysis (f_S^{fit}), with $\mu_S^{fit} = \tan(26°) = 0.49$. The grey area is the upper and lower limits of the 95% prediction intervals derived for $\mu_S = \tan(13.5° \pm 2°)$. Thick grey dashes: simulated volumes. (a) Estimation with f^1_{emp}. (b) Estimation with f^1_{S,μ_H}. (c) Estimation with $f^{2^*}_{emp}$. (d) Estimation with $f^{2^*}_{S,\mu_H}$. (e) Estimation with $g^1_{S,\mu_{eff}}$. (f) Estimation with $f^1_{S,\mu_{eff}}$. Black lines are direct estimates, dashed lines give the 95% prediction interval.

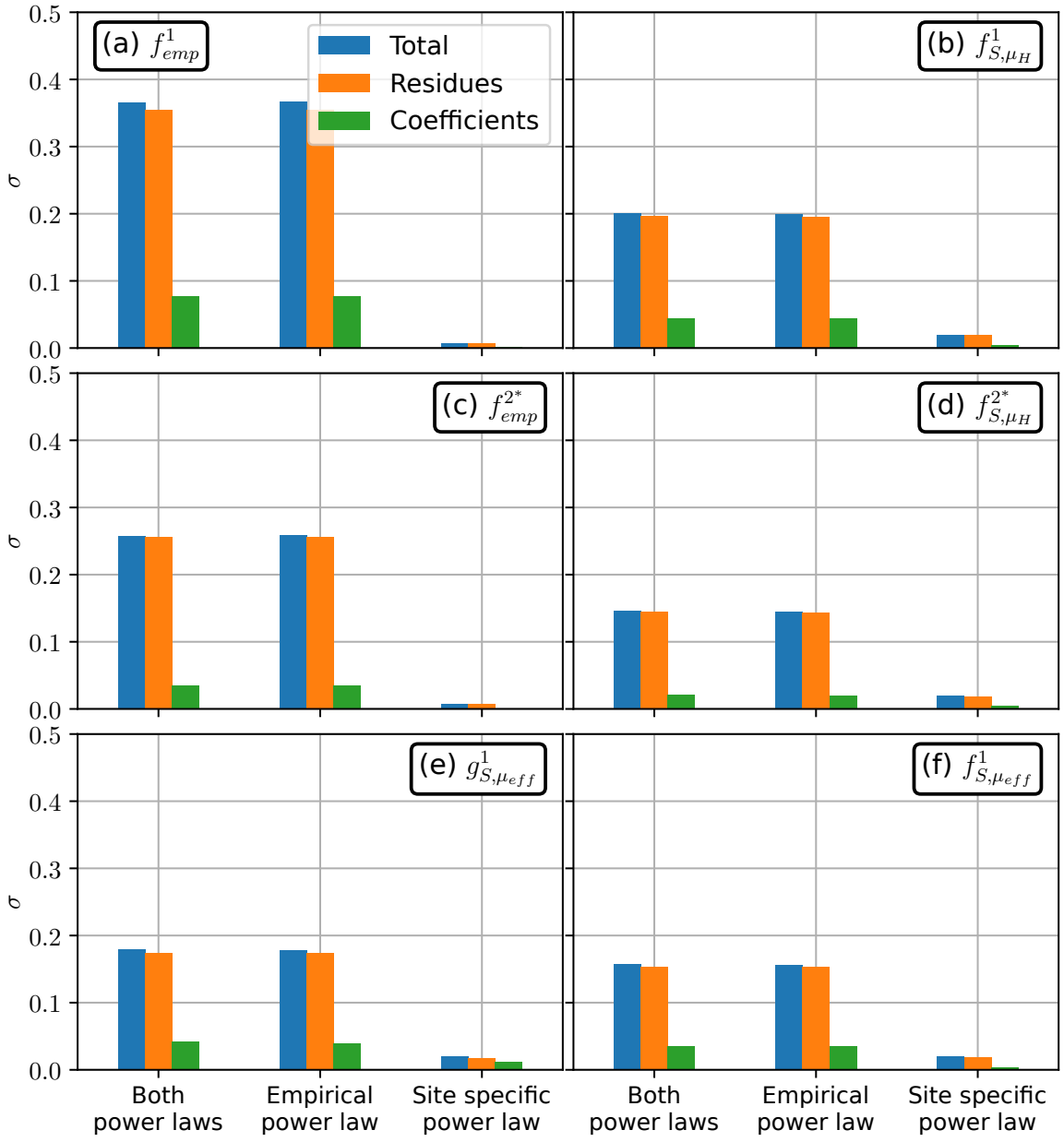

Figure 5.A.6: Uncertainty in travel distance estimation for the Fei Tsui Road cliff case study, and a variation of *DB2* with only debris flows, debris avalanches and debris slides. The corresponding travel distance estimations are marked with the super-script $^{2^*}$. Notations are otherwise the same as in the main body of the article. (a), (b), (c), (d), (e) and (f), and symbology are the same as for Figure 5.9.

5.B Simulation database for the Samperre cliff case study

The Samperre cliff destabilizations occurred in several successive steps, such that the available topographic surveys of March 2010, July 2010, January 2018 and August 2018 do not allow an exact reconstruction of the destabilized volumes. The volume of the major 2009 cliff collapse was estimated to 1×10^6 m^3 (Clouard et al., 2013), but the scar geometry is unknown. Thus, we reconstruct empirically the initial mass by scaling the difference between the March and July 2010 DEMs (before and after another major destabilization episode) to obtain a 1×10^6 m^3, which is the estimated volume involved in the August 2009 collapse. The avalanche propagation is then modeled on the July 2010 DEM. Another documented destabilization took place in January 2018. We estimate its volume at 1.5×10^6 m^3 from the difference between the January 2018 DEM, and a synthetic reconstruction of the cliff in 2017 (constrained by the cliff rim as observed on ortho-photographs). The resulting mass is propagated on the January 2018 DEM. We generate other initial geometries as follows:

- By taking the difference between the March and July 2010 DEMs. The resulting 2.1×10^6 m^3 mass is propagated on the July 2010 DEM. It is also scaled uniformly to consider a smaller volumes (250,000 m^3).
- By taking the difference between the July 2010 and January 2018 DEMs, resulting in a 3.7×10^6 m^3 initial mass that is released on the Januray 2018 DEM. Three intermediate synthetic topographies are also considered, yielding three other volumes (0.71×10^6 m^3, 1.8×10^6 m^3 and 3.5×10^6 m^3).
- By considering two possible future destabilizations on the eastern and northern side of the cliff (1.9×10^6 m^3 and 0.5×10^6 m^3 respectively). The resulting avalanche is propagated on the August 2018 DEM.

Thus, we run simulations for a total of 10 initial volumes/geometries. Note that the different DEMs on which the simulations are run differ near the cliff as a result of its progressive retreat, but the Samperre river, where the avalanches propagate, did not significantly vary. The DEMs are all re-interpolated to 5 m.

5.C Power law derivation and uncertainty estimation

We use the *statsmodel* python package (Seabold and Perktold, 2010) to derive power laws, through Ordinary Least Square (OLS) linear or multi-linear regressions (Kraemer and Sonnberger, 1986). Fitting a power law $y = ax^b$ is indeed equivalent to fitting a linear model $\log(y) = \log(a) + b\log(x)$ For $\mu_H = \mu_H^1(V)$, $\mu_H = \mu_H^2(V)$ and $\mu_{eff} = \mu_{eff}^1(V)$, a first OLS regression is carried out and outliers (points whose residue have a Student p-value lower than 0.025) are removed. A new OLS regression is then carried out. The quality of the linear regression is primarily given by the coefficients confidence interval and the adjusted $R2$. Note that a rigorous estimation of uncertainty should take into account both the dispersion between the data and the best-fit, and the uncertainty on the best-fit linear model coefficients. For instance, let's assume we have set of data $(x_1, ..., x_n)$ (e.g. observed volumes) and $(y_1, ..., y_n)$ (e.g. travel distances), for which we want to derive a linear model of the form:

$$y_i = ax_i + b + \epsilon_i, \tag{5.18}$$

where the ϵ_i are the residues. Then the OLS regression will find $\hat{a}$ and $\hat{b}$ such that $\sum \epsilon_i^2$ is minimal. If the residues have a normal distribution that does not depend on x or y, and are

centered on 0, then for a new value $x^\star$, we can derive a confidence interval around the best-fit estimate:

$$y^\star = \hat{a}x^\star + \hat{b} \pm t_{n-2}s_y, \tag{5.19}$$

where s_y is the standard deviation of the residuals and t_{n-2} is a coefficient that depends on the number n of observations and on the level of confidence. It is derived from the Student law with $n-2$ degree of freedom. However, such an interval does not take into account the uncertainty on the estimations $\hat{a}$ and $\hat{b}$ and thus has no real statistical meaning.

On the contrary, if we disregard the uncertainty on residues but consider the uncertainty on coefficients, we derive the confidence interval:

$$y^\star = \hat{a}x^\star + \hat{b} \pm t_{n-2}s_y\sqrt{\frac{1}{n} + \frac{(x^\star - \bar{x})^2}{(n-1)s_x^2}}, \tag{5.20}$$

where $\bar{x}$ is the mean of the x_i, and s_x^2 their estimated variance. This interval has a given probability (e.g. 95%) of containing $ax^\star + b$, where a and b are the "real" coefficients (remember the OLS regression provides only estimations $\hat{a}$ and $\hat{b}$). Note that the interval is all the more large as $x^\star$ is further away from the samples x_i.

If we now combine the uncertainty on the coefficients estimation and the dispersion of the data around the best fit, we get the prediction interval:

$$y^\star = \hat{a}x^\star + \hat{b} \pm t_{n-2}s_y\sqrt{1 + \frac{1}{n} + \frac{(x^\star - \bar{x})^2}{(n-1)s_x^2}}. \tag{5.21}$$

The resulting interval has a given probability of containing the real value $y^\star = ax^\star + b + \epsilon^\star$ estimated with the real coefficient a and b and taking into account a residue $\epsilon^\star$ that follows a centered normal law with standard deviation s_y.

The previous formulas are derived for simple linear regressions but can be extended to multi-linear regressions. However, the derivation of confidence and prediction intervals for nested linear fits (that is, when the prediction of a linear model is used as input of another linear model) is not straight-forward. Thus, we derive them numerically by computing 4,000 estimations: the coefficients and/or the residues of the successive linear models are drawn randomly following normal laws whose parameters are given by the OLS regression results. To get for instance a 95% interval, we then identify the 2.5th and 97.5th percentiles.

If we consider for instance the empirical estimation of travel distance $\Delta L' = f^1_{emp}(V)$, it uses successively two power laws:

$$\tilde{\mu}_H = 10^{\alpha_1}V^{\beta_1} \times 10^{\epsilon_1}, \tag{5.22}$$

$$\Delta L' = 10^{\alpha_2}\tilde{\mu}_H^{\beta_2} \times 10^{\epsilon_2}, \tag{5.23}$$

where α_1, β_1, α_2, β_2 are coefficients estimated by the regression and ϵ_1 and ϵ_2 are residues. The total uncertainty (i.e. prediction interval) for a given volume is obtained with random draws on α_1, β_1, α_2, β_2, ϵ_1 and ϵ_2. We can also consider only the best-fit values of the power laws coefficients and draw only ϵ_1 and ϵ_2, or to the contrary disregard dispersion and draw only α_1, β_1, α_2 and β_2. Finally we can distinguish between the uncertainties specific to each power law by drawing only α_1, β_1 and ϵ_1, or only α_2, β_2 and ϵ_2.

The previous methodology can be deemed to represent correctly real uncertainties only if certain conditions are met:

- There is indeed a linear relation between the input (x) and output values (y). This can be verified with the Harvey-Collier test that evaluates to what extent the slope of the linear regression changes when data points are recursively added. In practice, we could not implement this test in a satisfactory manner, because results proved to depend strongly on the order in which points were added. Thus, we evaluate linearity graphically with the graph of residuals: if they have concave or convexe shapes, then the hypothesis of linearity can be questionned (Figure 5.A.1 and 5.A.2).
- The residuals have a normal distribution. This is can be verified with the Jarque-Bera test.
- The residuals are homoscedastic: they do not depend on the value y predicted by the linear model. In other words, the dispersion between the linear fit and the predicted value is the same for all predicted values. Graphically, this means the scatter plot of residuals against predicted value does not have a cone shape. This is quantitatively assessed with the Breush-Pagan test.
- For multi-linear regressions, the explanatory input variables are not linearly related. This can be assessed by computing the Variance Inflation Factor (VIF) for each associated coefficient. High VIF (typically above 5 or 10) indicate strong linear correlations

5.D Propagation of uncertainty in power laws

Let's consider a power law that was derived with OLS regression.

$$z = ax^b y^c. \tag{5.24}$$

We want to quantify how uncertainties on x and y will impact the estimation of z. In a first approximation (that is, without considering the uncertainty on the estimation of a, b and c), this can be done by considering the first order development:

$$(1+\alpha)^\gamma \simeq 1 + \gamma\beta, \tag{5.25}$$

that stands true if $\alpha \ll 1$. In turn, if we consider small relative variations ϵ_x and ϵ_y of, respectively, x_0 and y_0, we compute the first order approximation:

$$a\left((1+\epsilon_x)x_0\right)^b \left((1+\epsilon_y)y_0\right)^c \simeq ax_0^b y_0^c (1+b\epsilon_x)(1+c\epsilon_y), \tag{5.26}$$

$$\simeq z_0(1+b\epsilon_x+c\epsilon_y), \tag{5.27}$$

where $z_0 = ax_0^b + y_0^c$. If we now assume ϵ_x and ϵ_y follow some uncorrelated random laws with known variances $V(\epsilon_x)$ and $V(\epsilon_y)$, the ratio R_x of the variance of the error on z linked to error on x, over the total variance of the error on z, is:

$$R_x = \frac{V(b\epsilon_x)}{V(b\epsilon_x + c\epsilon_y)} = \frac{b^2 V(\epsilon_x)}{b^2 V(\epsilon_x) + c^2 V(\epsilon_y)}. \tag{5.28}$$

If we further assume $V(\epsilon_x) = V(\epsilon_y)$, we get:

$$R_x = \frac{b^2}{b^2 + c^2}. \tag{5.29}$$

Similarly, we derive:

$$R_y = \frac{c^2}{b^2 + c^2}. \tag{5.30}$$

Conclusion

In this work, we have assessed the usability of thin-layer models for gravitational flows hazard assessment. In this perspective, we chose the SHALTOP numerical model with a limited number of rheological parameters (one or two), which simplifies its operational usage. These parameters are calibrated by reproducing previous events, which means the numerical code is used empirically. However, it includes a rigorous description of the geometrical interactions between the flow and the topography: it allows a more detailed modeling of the topographic control on the flow dynamics. The question is thus: to what extent can SHALTOP be used empirically to study gravitational flows and quantify related hazards?

Our work was structured along three research focus that are summarized in Figure 6.1. First, we analyzed the importance of a rigorous mathematical derivation of the equations, even for simplified rheological laws. It is indeed necessary to model correctly the geometrical interactions between the flow and the topography, and in turn topography curvature effects. As we showed in Chapter 2, correct thin-layer equations include two curvature terms. The first one is independent from the rheology and ensures that the flow velocity remains tangent to the topography. In particular, it tends to accelerate channelized flows by maintaining them at the bottom of the channel. The second curvature term appears in the expression of the pressure at the bottom of the flow, and generally slows down the flow when frictional rheologies are used. By comparing simulations where these curvature terms are exact, to simulations where they are approximated or neglected, we showed that discrepancies are particularly important for fast flows (steep slopes and/or low friction coefficients with the Coulomb rheology). Incorrect curvature description can thus lead to under-estimate the velocity of channelized flows. On the contrary, we showed that the spreading of unconfined flows can be drastically over-estimated when curvature is neglected in frictional rheologies. Thus, curvature terms are important for model calibration, to ensure that the calibrated rheological parameters do not result from an improper topography description and can be used in different topographic contexts. Curvature effects are also essential to estimate as accurately as possible overflows, which is capital for hazard assessment.

Having demonstrated the mathematical robustness of SHALTOP, we then proved its ability to reproduce debris avalanches, rock avalanches and debris flows, even with simplified rheologies, and help quantify related hazards. To that end, we aggregated a wide variety of data (topographic and geophysical surveys, geomorphological observations, seismic recordings, ...) to constrain the simulation scenarios, calibrate rheological parameters and simulate forward prediction scenarios. In Chapter 3, we studied debris avalanches on the Soufrière de Guadeloupe volcano (Guadeloupe, Lesser Antilles). Model calibration on a past event highlighted the strong mobility of the debris avalanche in comparison to other events with similar volume, that we relate to the presence of water in the materials. By testing different initial collapse geometries and rheological parameters we showed that only massive and mobile destabilizations of the dome threaten the city of Basse-Terre, 6 km away from the volcano. However, the outskirts of Saint-Claude, which are closer from the volcano, are more exposed. In Chapter 4, we considered a more complex case study, with the combination of rock avalanches and the subsequent remobilization of deposits as debris flows. In

this case, our approach is all the more empirical, because SHALTOP equations were not derived to model two-phase flows. However, SHALTOP is able to reproduce the main characteristics of extreme events (i.e. high discharge debris flows). We could thus quantify the areas exposed to overflows, and estimate travel times for a forward prediction scenario.

In the Soufrière de Guadeloupe and Prêcheur river case studies, although simulations do give precious insights on the dynamics of the gravitational flows, they cannot be used to derive hazard maps integrating uncertainty. Indeed, the simulation results are too spatially and temporally detailed to allow for a simple propagation and quantification of uncertainty. Uncertainty is nevertheless a key point in the perspective of using thin-layer models for operational hazard assessment. Thus, in Chapter 5, we addressed this problem in a rather simple framework: the estimation of travel distance as a function of volume. For a given study site, this estimation is done by analyzing with statistical tools a database of simulations (including various initial volumes and rheological parameters). By calibrating or estimating empirically rheological parameters we could then derive a simple power law, relating the travel distance to the unstable volume. Using three case studies, we showed that such a method allows to reduce the uncertainty of estimation, in comparison to purely empirical methods, in particular when model calibration is possible. We also show that the dependence between travel distance and volume is better modeled with numerical simulations. However, further works are needed to help constrain rheological parameters when calibration is not possible.

Our results suggest three main axes of development for further research. First, we have shown that a fine description of topography in thin-layer equations is necessary to model correctly the geometrical interactions between the flow and the topography, but only in the case of "hydrostatic" flows with basal friction. A detailed description of topography is yet to be introduced in thin-layer models for more complex rheologies. Secondly, while we could use a wide variety of data to constrain our simulations, in particular in the case of the Prêcheur river, the acquisition and processing of more observations and quantitative data would allow a more systematic characterization of gravitational flows. It would then be possible to evaluate more quantitatively, with statistical methods, the agreement between simulations and observations. For instance, the systematic estimation of debris flow discharge or flow thicknesses in the Prêcheur river would be precious data to calibrate the model. It would be then possible to use simulations to improve monitoring, by deriving relations relating, for instance, the travel time or flooded area to the flow height.

Finally, we have used relatively simple statistical tools to aggregate and simplify simulations results. The resulting relations have the advantage of being easy to implement and use for quantitative hazard assessment. However, they cannot be used to spatialize hazard, if we want to construct hazard maps integrating the uncertainty on simulation parameters, and on the position and/or geometry of the initial mass. In this perspective, meta-models could be powerful, albeit complex, tools. They are statistically-based models derived from computer experiments. Their construction can be computationally intensive with thousands of simulations, but it is then relatively easy (at least in theory) to estimate a simulation result for a new set of input parameters, without having to actually run the simulation. In this sense, our power laws relating travel distance to unstable volumes and friction coefficient in Chapter 5 could be seen as very simple meta-models. More complex meta-models may be used to estimate spatially peak discharges and velocities, or even the contour of the impacted area. They could also improve monitoring by updating, in near real-time, hazard maps (or at least expected flow characteristics in exposed areas), depending on information available to characterize hazards. These information could be, in the case of the Prêcheur river, flow height in the uper section of the river, or volume estimations of the scree reservoir at the bottom of the Samperre cliff.

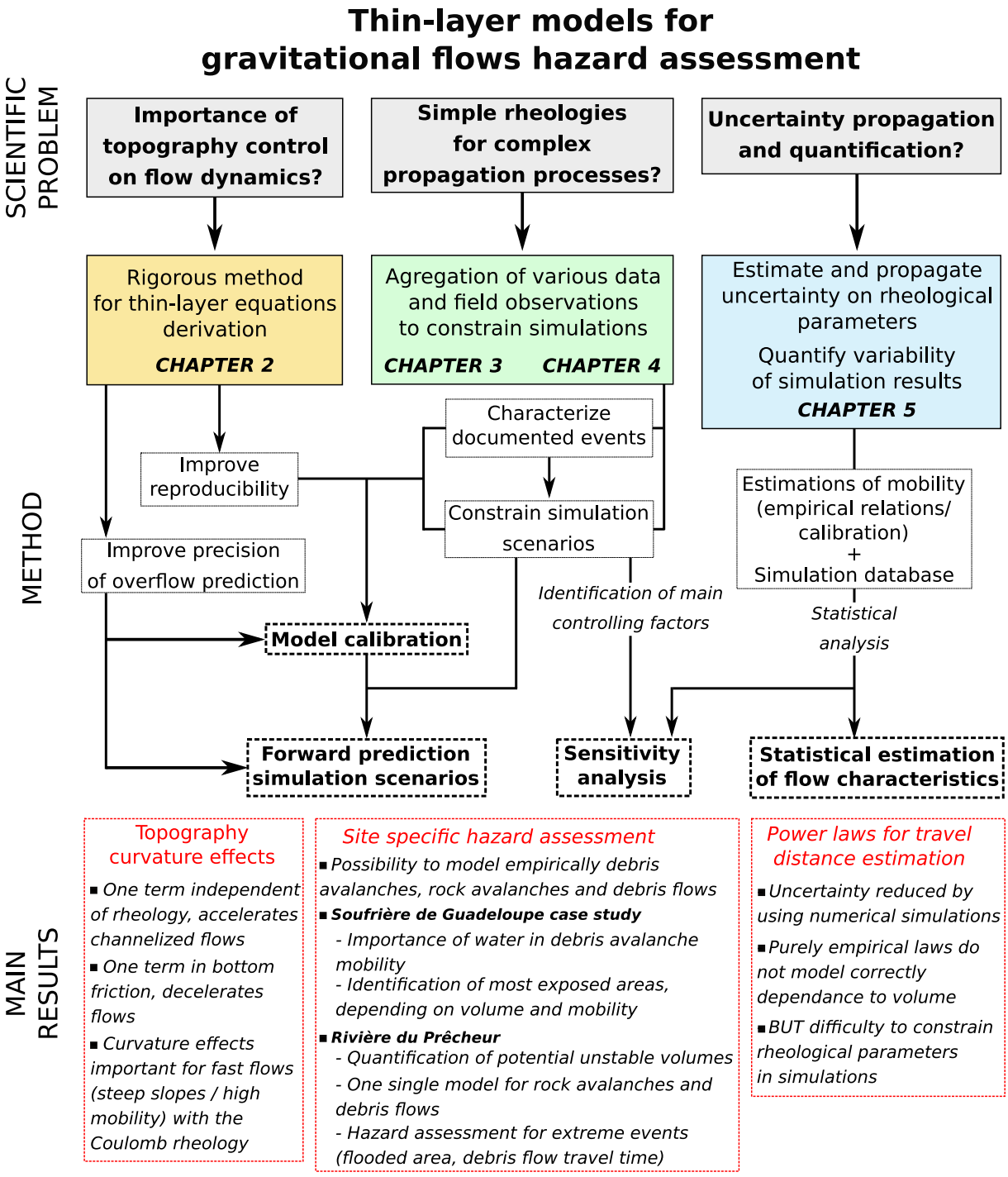

Figure 6.1: Summary of scientific questions, methods and results of the thesis.

Dans ce travail, nous avons estimé la possibilité d'utiliser des modèles d'écoulement en couche mince pour l'évaluation des aléas gravitaires. Nous utilisons pour cela le code numérique SHALTOP avec un nombre limité de paramètres rhéologiques (un ou deux), ce qui simplifie son utilisation opérationnelle. Les paramètres rhéologiques sont calibrés en reproduisant des événements passés : le code est donc utilisé de manière empirique. Toutefois, il inclue une description rigoureuse des interactions géométriques entre l'écoulement et la topographie. Cela permet une modélisation plus fine du contrôle de la topographie sur la dynamique de l'écoulement. La question est donc : dans quelle mesure SHALTOP peut-il être utilisé de manière empirique pour étudier les écoulements gravitaires et quantifier les aléas associés ?

Notre travail se structure autour de trois axes de recherches qui sont illustrés dans la Figure 6.1. Tout d'abord, nous avons analysé l'importance d'une dérivation mathématique rigoureuse des équations, même pour des lois rhéologiques simples. C'est en effet nécessaire pour modéliser correctement les interactions géométriques entre l'écoulement et la topographie, et en particulier la courbure de la topographie. Comme nous l'avons montré dans le Chapitre 2, les équations d'écoulement en couche mince doivent inclure, si elles sont correctes, deux termes de courbure. Le premier est indépendant de la rhéologie et assure que la vitesse de l'écoulement reste bien tangente à la topographie. En particulier, ce terme tend à maintenir les écoulements chenalisés au fond du chenal, et donc accélère ces écoulements. Le deuxième terme de courbure apparaît dans l'expression de la pression au fond de l'écoulement et, en général, ralentit l'écoulement quand une rhéologie frictionnelle est utilisée. En comparant des simulations où les termes de courbures sont exacts à des simulations où ils sont négligés ou approximés, nous avons montré que les effets de courbures sont particulièrement importants pour les écoulements rapides (sur des pentes importantes ou avec de faibles angles de friction avec la rhéologie de Coulomb). Une description incorrecte de la courbure peut ainsi induire une sous-estimation de la vitesse des écoulement chenalisés. Au contraire, enlever la courbure des rhéologies frictionnelles conduit à sur-estimer drastiquement la distance de parcours. Ainsi, les termes de courbure sont importants pour la calibration des modèles : ils assurent que les paramètres rhéologiques obtenus ne proviennent pas d'une mauvaise description de la topographie et peuvent être utilisés dans d'autres contextes topographiques. Une bonne description de la courbure de la topographie est également primordiale pour estimer avec plus de précision les débordements, ce qui est évidemment important pour l'évaluation des aléas.

Après avoir montré la robustesse mathématique de SHALTOP, nous avons montré qu'il peut reproduire, même avec des rhéologies simples, des avalanches de débris et de roches, et des laves torrentielles. Il peut aussi quantifier les aléas associés. Pour y arriver, nous avons dû collecter une grande variété de données (relevés topographiques, mesures géophysiques, observations géomorphologiques, enregistrements sismiques,...) pour définir les scénarios de simulation, calibrer les paramètres rhéologiques et modéliser des scénarios prospectifs. Dans le Chapitre 3, nous avons étudié des avalanches de débris sur la Soufrière de Guadeloupe. La calibration du modèle a mis en évidence la mobilité importante des avalanches sans doute due à l'intégration d'eau dans les matériaux. En testant différentes géométries d'effondrement et différents paramètres rhéologiques, nous avons aussi montré que la ville de Basse-Terre, à 6 km du volcan, n'est menacée qu'en cas de déstabilisations massives et très mobiles. A l'inverse, la périphérie de la ville de Saint-Claude, plus proche du volcan, est également exposée pour des plus petits volumes. Dans le Chapitre 4 nous avons considéré un cas plus complexe, avec l'enchaînement d'une avalanche de roches et d'une lave torrentielle, par remobilisation des dépôts. Dans ce cas, notre d'approche est d'autant plus empirique, car les équations de SHALTOP ne modélisent pas, en théorie, des écoulements bi-phasiques. Néanmoins, SHALTOP parvient à reproduire les caractéristiques principales d'événements extrêmes. Nous avons donc pu identifier les zones les plus exposées aux débordements et estimer les temps de parcours pour un scénario prospectif.

Dans le cas de la Soufrière de Guadeloupe et de la rivière du Prêcheur, même si les simulations

donnent des informations précieuses sur les écoulement gravitaires, elles ne peuvent pas être utilisées directement pour établir des cartes d'aléas quantifiant l'incertitude. En effet, les résultats des simulations sont trop détaillés spatialement et temporellement pour permettre simplement la propagation et la quantification l'incertitude. Cette intégration de l'incertitude est néanmoins un point majeur dans la perspective d'utiliser les modèles d'écoulement en couche mince de manière opérationnelle, pour de l'analyse d'aléa. Dans le Chapitre 5, nous avons donc abordé cette question dans un cadre relativement simplifié : l'estimation de la distance de parcours en fonction du volume déstabilisé. Pour un site d'étude donné, cette estimation est réalisée en analysant avec des outils statistiques une base de données de simulations (pour des volumes et paramètres rhéologiques variés). En calibrant ou en estimant empiriquement les paramètres rhéologiques, nous avons ainsi obtenu une loi puissance, reliant la distance parcourue au volume déstabilisé. En nous basant sur trois cas d'étude, nous avons montré qu'une telle méthode permet de réduire les incertitudes d'estimation par rapport à des méthodes purement empiriques. Nous avons aussi mis en évidence que l'utilisation de simulations numériques permet de mieux modéliser la dépendance entre la distance de parcours et le volume. Toutefois, la détermination des paramètres rhéologiques aboutissant à ces relations reste incertaine, en particulier quand la calibration n'est pas possible.

Nos résultats suggèrent trois pistes de recherches. Tout d'abord, nous avons montré l'importance d'une description fine de la topographie, mais seulement dans le cas simplifié d'une dérivation hydro-statique, avec une friction basale. Une telle description de la topographie reste néanmoins à développer pour des rhéologies plus complexes. Ensuite, bien que nous ayons pu utiliser une grande variété de données pour contraindre nos simulations (en particulier dans le cas du Prêcheur), l'acquisition et le traitement de mesures complémentaires permettraient une caractérisation plus systématique des écoulements gravitaires. Il serait alors possible d'évaluer de manière plus quantitative, avec des outils statistiques, la correspondance entre les simulations et les observations. Ainsi, la mesure systématique des débits et ou des hauteurs des lahars de la rivière du Prêcheur seraient des données précieuses pour calibrer le modèle. Il serait alors possible d'utiliser les simulations pour améliorer la surveillance en estimant, avec les simulations, des relations donnant par exemple le temps de parcours en fonction de la hauteur du lahar.

Pour finir, notons que nous avons utilisé des modèles statistiques relativement simples pour agréger et simplifier les résultats des simulations. Les lois puissances déduites sont faciles à implémenter et à utiliser pour l'estimation d'aléa. Toutefois, elles ne sont pas suffisantes pour spatialiser l'incertitude, dans la perspective d'établir des cartes d'aléas intégrant l'incertitude sur les paramètres des simulations et sur la position et/ou la géométrie des masses initiales. Les méta-modèles pourraient être utilisés à cette fin, même si leur mise en oeuvre est complexe. Ce sont des modèles statistiques déduits d'expériences numériques : leur construction demande un temps de calcul important et un nombre significatifs de simulations (typiquement, plusieurs milliers), mais leur utilisation pour estimer les résultats d'une simulation non réalisée initialement est, en théorie, rapide. En ce sens, nos lois puissances donnant la distance de parcours en fonction du volume et du coefficient de friction au Chapitre 5 peuvent être vues comme des méta-modèles très simples. Des modèles plus complexes pourraient être utilisés pour estimer spatialement les vitesses ou débits maximums, ou même les contour des zones impactées. Une autre piste intéressante d'utilisation est la mise à jour en temps réel de cartes d'aléas (ou du moins des caractéristiques clés des écoulement gravitaires dans les zones menacées) en fonction des informations disponibles à un instant donné pour caractériser l'aléa. Dans le cas de la rivière du Prêcheur, ces informations pourraient être la hauteur de la rivière dans sa partie amont, ou l'estimation du stock de matériaux remobilisables au pied de la falaise Samperre.

Nomenclature

ΔL	Travel distance of landslide along topography
$\Delta L'$	Horizontal travel distance of landslide
δ	Basal friction angle
$\dot{\gamma}$	Shear rate
μ	Basal friction coefficient
μ_H	Heim's ratio
μ_{eff}	Effective friction coefficient
ν	Kinematic viscosity
σ	Stress tensor
σ'	Deviatoric stress tensor
$\tan(\phi)$	Internal friction coefficient
τ_y	Yield stress
θ	Slope steepest angle
$\vec{\mathcal{V}}$	Depth-averaged velocity of the material layer
$\vec{g}$	Gravity field
$\vec{n}$	Unit vector othonormal to topography
$\vec{n}'$	Unit vector orthonormal to material layer surface
$\vec{U}$	Velocity parametrization in the cartesian frame
$\vec{V}$	Velocity parametrization in the topography frame
ξ	Turbulence coefficient
$c = \cos(\theta)$	Cosine of the slope angle
d	Grain diameter
H	Drop height of landslide
h	Height of material layer, in the direction normal to the topography
H_0	Maximum initial thickness of landslide

I Inertial number

$k_{act/pass}$ Earth pressure coefficients

p Pressure field

u_1 Velocity in the direction tangent top the topography

$Z = b(X, Y)$ Parametrization of the topography

List of Figures

List of Tables

Bibliography

Aaron, J. and S. McDougall (2019). "Rock Avalanche Mobility: The Role of Path Material". en. In: *Engineering Geology*, S0013795218319240. ISSN: 00137952. DOI: 10.1016/j.enggeo.2019.05.003 (cit. on pp. 6, 199).

Alejano, L. R., I. Gómez-Márquez, and R. Martínez-Alegría (2010). "Analysis of a Complex Toppling-Circular Slope Failure". en. In: *Engineering Geology* 114.1-2, pp. 93–104. ISSN: 00137952. DOI: 10.1016/j.enggeo.2010.03.005 (cit. on p. 1).

Alexander, D. E. (2002). *Principles of Emergency Planning and Management*. en. Oxford University Press. ISBN: 978-0-19-521838-1 (cit. on pp. ix, xiv).

Allstadt, K. (2013). "Extracting Source Characteristics and Dynamics of the August 2010 Mount Meager Landslide from Broadband Seismograms". en. In: *Journal of Geophysical Research: Earth Surface* 118.3, pp. 1472–1490. ISSN: 2169-9011. DOI: 10.1002/jgrf.20110 (cit. on p. 2).

Ancey, C. (1994). "Modélisation des avalanches denses Approches théorique et numérique". fr. In: *La Houille Blanche* 5-6, pp. 25–39. ISSN: 0018-6368, 1958-5551. DOI: 10.1051/lhb/1994058 (cit. on p. 30).

Andreotti, B., Y. Forterre, and O. Pouliquen (2013). *Granular Media: Between Fluid and Solid*. en. Cambridge: Cambridge University Press. ISBN: 978-1-139-54100-8. DOI: 10.1017/CBO9781139541008 (cit. on p. 11).

Aniel-Quiroga, I. et al. (2018). *Tsunami Hazard Assessment and Scenarios Database for the Tsunami Warning System for the Coast of Oman*. en. Preprint. Sea, Ocean and Coastal Hazards. DOI: 10.5194/nhess-2018-221 (cit. on p. 202).

Anthony, R. E. et al. (2018). "Measuring Mountain River Discharge Using Seismographs Emplaced Within the Hyporheic Zone". en. In: *Journal of Geophysical Research: Earth Surface* 123.2, pp. 210–228. ISSN: 2169-9011. DOI: 10.1002/2017JF004295 (cit. on p. 167).

Apuani, T. et al. (2005). "Stability of a Collapsing Volcano (Stromboli, Italy): Limit Equilibrium Analysis and Numerical Modelling". In: *Journal of Volcanology and Geothermal Research*. The Tectonics and Physics of Volcanoes 144.1, pp. 191–210. ISSN: 0377-0273. DOI: 10.1016/j.jvolgeores.2004.11.028 (cit. on p. 102).

Arattano, M. and L. Marchi (2008). "Systems and Sensors for Debris-Flow Monitoring and Warning". In: *Sensors (Basel, Switzerland)* 8.4, pp. 2436–2452. ISSN: 1424-8220 (cit. on p. 163).

Armanini, A., L. Fraccarollo, and G. Rosatti (2009). "Two-Dimensional Simulation of Debris Flows in Erodible Channels". en. In: *Computers & Geosciences*. Modelling and Simulation of Dangerous Phenomena for Hazard Mapping 35.5, pp. 993–1006. ISSN: 0098-3004. DOI: 10.1016/j.cageo.2007.11.008 (cit. on p. 31).

Aubaud, C. et al. (2013). "A Review of Historical Lahars, Floods, and Landslides in the Precheur River Catchment (Montagne Pelee Volcano, Martinique Island, Lesser Antilles)". en. In: *Bulletin de la Societe Geologique de France* 184.1-2, pp. 137–154. ISSN: 0037-9409. DOI: 10.2113/gssgfbull.184.1-2.137 (cit. on pp. 50, 124, 128, 132, 134, 137, 138, 164–166, 180).

Baker, J. L., T. Barker, and J. M. N. T. Gray (2016). "A Two-Dimensional Depth-Averaged Mu(I)-Rheology for Dense Granular Avalanches". en. In: *Journal of Fluid Mechanics* 787,

pp. 367–395. ISSN: 0022-1120, 1469-7645. DOI: 10.1017/jfm.2015.684 (cit. on pp. 19, 20, 57, 77).

Bardou, E. et al. (2003). "Classification of Debris-Flow Deposits for Hazard Assessment in Alpine Areas". en. In: *Debris-Flow Hazards Mitigation : Mechanics, Prediction and Assessment*. Rickenmann & Chen. Vol. 2. Millpress, p. 11. ISBN: 09 77017 78 X (cit. on pp. 138, 139, 264).

Barré de Saint-Venant, A.-J.-C. (1871). "Théorie Du Mouvement Non Permanent Des Eaux, Avec Application Aux Crues Des Rivières et à l'introduction Des Marées Dans Leur Lit". In: *Comptes rendus hebdomadaires des séances de l'Académie des sciences* LXXIII. Ed. by Académie des sciences. ISSN: 0001-4036 (cit. on pp. 11, 30, 33).

Bartelt, P., O. Buser, and K. Platzer (2007). "Starving Avalanches: Frictional Mechanisms at the Tails of Finite-Sized Mass Movements". en. In: *Geophysical Research Letters* 34.20. ISSN: 1944-8007. DOI: 10.1029/2007GL031352 (cit. on p. 161).

Beguería, S. et al. (2009). "A GIS-Based Numerical Model for Simulating the Kinematics of Mud and Debris Flows over Complex Terrain". en. In: *Natural Hazards and Earth System Science* 9.6, pp. 1897–1909. ISSN: 1684-9981. DOI: 10.5194/nhess-9-1897-2009 (cit. on pp. 12, 31).

Bel, C. et al. (2015). "Monitoring Debris Flow Propagation in Steep Erodible Channels". en. In: *Engineering Geology for Society and Territory - Volume 3*. Ed. by G. Lollino et al. Cham: Springer International Publishing, pp. 103–107. ISBN: 978-3-319-09054-2. DOI: 10.1007/978-3-319-09054-2_20 (cit. on p. 6).

Bel, C. et al. (2017). "Rainfall Control of Debris-Flow Triggering in the Réal Torrent, Southern French Prealps". en. In: *Geomorphology*. SEDIMENT DYNAMICS IN ALPINE BASINS 291, pp. 17–32. ISSN: 0169-555X. DOI: 10.1016/j.geomorph.2016.04.004 (cit. on p. 166).

Benjamin, J., N. J. Rosser, and M. J. Brain (2020). "Emergent Characteristics of Rockfall Inventories Captured at a Regional Scale". en. In: *Earth Surface Processes and Landforms* 45.12, pp. 2773–2787. ISSN: 1096-9837. DOI: 10.1002/esp.4929 (cit. on p. 1).

Benko, B. and D. Stead (1998). "The Frank Slide: A Reexamination of the Failure Mechanism". en. In: 35, p. 13 (cit. on pp. 179, 180).

Berger, M. J. et al. (2011). "The GeoClaw Software for Depth-Averaged Flows with Adaptive Refinement". en. In: *Advances in Water Resources* 34.9, pp. 1195–1206. ISSN: 03091708. DOI: 10.1016/j.advwatres.2011.02.016 (cit. on pp. 31, 33).

Berti, M. and A. Simoni (2005). "Experimental Evidences and Numerical Modelling of Debris Flow Initiated by Channel Runoff". en. In: *Landslides* 2.3, pp. 171–182. ISSN: 1612-5118. DOI: 10.1007/s10346-005-0062-4 (cit. on p. 166).

Berti, M. and A. Simoni (2014). "DFLOWZ: A Free Program to Evaluate the Area Potentially Inundated by a Debris Flow". en. In: *Computers & Geosciences* 67, pp. 14–23. ISSN: 0098-3004. DOI: 10.1016/j.cageo.2014.02.002 (cit. on p. 10).

Blahůt, J. et al. (2019). "A Comprehensive Global Database of Giant Landslides on Volcanic Islands". en. In: *Landslides*. ISSN: 1612-510X, 1612-5118. DOI: 10.1007/s10346-019-01275-8 (cit. on p. 5).

Boichu, M., B. Villemant, and G. Boudon (2011). "Degassing at La Soufrière de Guadeloupe Volcano (Lesser Antilles) since the Last Eruptive Crisis in 1975–77: Result of a Shallow Magma Intrusion?" In: *Journal of Volcanology and Geothermal Research* 203.3, pp. 102–112. ISSN: 0377-0273. DOI: 10.1016/j.jvolgeores.2011.04.007 (cit. on p. 98).

Bolton, M. D. (1986). "The Strength and Dilatancy of Sands". en. In: *Géotechnique* 36.1, pp. 65–78. ISSN: 0016-8505, 1751-7656. DOI: 10.1680/geot.1986.36.1.65 (cit. on p. 161).

Borthwick, A. G. L. and R. W. Barber (1992). "River and Reservoir Flow Modelling Using the Transformed Shallow Water Equations". en. In: *International Journal for Numerical Methods in Fluids* 14.10, pp. 1193–1217. ISSN: 1097-0363. DOI: 10.1002/fld.1650141005 (cit. on p. 60).

Bouchut, F. et al. (2008). "On New Erosion Models of Savage–Hutter Type for Avalanches". en. In: *Acta Mechanica* 199.1-4, pp. 181–208. ISSN: 0001-5970, 1619-6937. DOI: 10.1007/s00707-007-0534-9 (cit. on pp. 9, 12, 30, 162).

Bouchut, F. et al. (2015). "A Two-Phase Shallow Debris Flow Model with Energy Balance". en. In: *ESAIM: Mathematical Modelling and Numerical Analysis* 49.1, pp. 101–140. ISSN: 0764-583X, 1290-3841. DOI: 10.1051/m2an/2014026 (cit. on pp. 12, 30, 124, 177).

Bouchut, F. and M. Westdickenberg (2004). "Gravity Driven Shallow Water Models for Arbitrary Topography". In: *Communications in Mathematical Sciences* 2.3, pp. 359–389 (cit. on pp. 12–15, 23, 30–34, 36, 37, 41, 42, 75–80, 106, 124, 146, 178, 183).

Bouchut, F. et al. (2003). "A New Model of Saint Venant and Savage–Hutter Type for Gravity Driven Shallow Water Flows". en. In: *Comptes Rendus Mathematique* 336.6, pp. 531–536. ISSN: 1631073X. DOI: 10.1016/S1631-073X(03)00117-1 (cit. on pp. 30, 34, 106, 124, 146).

Bouchut, F. et al. (2016). "A Two-Phase Two-Layer Model for Fluidized Granular Flows with Dilatancy Effects". en. In: *Journal of Fluid Mechanics* 801, pp. 166–221. ISSN: 0022-1120, 1469-7645. DOI: 10.1017/jfm.2016.417 (cit. on pp. 8, 12, 30, 124, 177).

Boudon, G. (1988). *Carte Géologique Du Massif Volcanique de La Soufrière (Département de La Guadeloupe, Petites Antilles).* (Cit. on p. 98).

Boudon, G. et al. (2005). "Volcanic Hazard Atlas of the Lesser Antilles : Martinique". In: *Volcanic Hazard Atlas of the Lesser Antilles*. Ed. by J. Lindsay et al. University of the West Indies, Seismic Research Unit, Trinidad and IAVCEI, pp. 126–145 (cit. on p. 125).

Boudon, G. et al. (2007). "Volcano Flank Instability in the Lesser Antilles Arc: Diversity of Scale, Processes, and Temporal Recurrence". en. In: *Journal of Geophysical Research* 112.B8. ISSN: 0148-0227. DOI: 10.1029/2006JB004674 (cit. on pp. 53, 98, 102, 132).

Boudon, G. et al. (2008). "A New Scenario for the Last Magmatic Eruption of La Soufrière of Guadeloupe (Lesser Antilles) in 1530 A.D. Evidence from Stratigraphy Radiocarbon Dating and Magmatic Evolution of Erupted Products". In: *Journal of Volcanology and Geothermal Research*. Evaluating Explosive Eruption Risk at European Volcanoes 178.3, pp. 474–490. ISSN: 0377-0273. DOI: 10.1016/j.jvolgeores.2008.03.006 (cit. on pp. 98, 100, 106, 107, 116, 261).

Bout, B. et al. (2018). "Integration of Two-Phase Solid Fluid Equations in a Catchment Model for Flashfloods, Debris Flows and Shallow Slope Failures". en. In: *Environmental Modelling & Software* 105, pp. 1–16. ISSN: 13648152. DOI: 10.1016/j.envsoft.2018.03.017 (cit. on p. 162).

Bouysse, P., D. Westercamp, and P. Andreieff (1990). *The Lesser Antilles Island Arc*. en. Ed. by J. Moore and A. Mascle. Vol. 110. Proceedings of the Ocean Drilling Program. Ocean Drilling Program. DOI: 10.2973/odp.proc.sr.110.1990 (cit. on p. 98).

Bowman, L. J. and K. B. Henquinet (2015). "Disaster Risk Reduction and Resettlement Efforts at San Vicente (Chichontepec) Volcano, El Salvador: Toward Understanding Social and Geophysical Vulnerability". en. In: *Journal of Applied Volcanology* 4.1, p. 14. ISSN: 2191-5040. DOI: 10.1186/s13617-015-0031-0 (cit. on p. 166).

Brideau, M.-A. et al. (2019). "Field Characterisation and Numerical Modelling of Debris Avalanche Runout on Vancouver Island, British Columbia, Canada". en. In: *Landslides* 16.5, pp. 875–891. ISSN: 1612-510X, 1612-5118. DOI: 10.1007/s10346-019-01141-7 (cit. on pp. 9, 177, 199).

Brothelande, E. et al. (2014). "Fluid Circulation Pattern inside La Soufrière Volcano (Guadeloupe) Inferred from Combined Electrical Resistivity Tomography, Self-Potential, Soil Temperature and Diffuse Degassing Measurements". In: *Journal of Volcanology and Geothermal Research* 288, pp. 105–122. ISSN: 0377-0273. DOI: 10.1016/j.jvolgeores.2014.10.007 (cit. on pp. 100, 103, 115).

Brunet, M. et al. (2017). "Numerical Simulation of the 30–45 Ka Debris Avalanche Flow of Montagne Pelée Volcano, Martinique: From Volcano Flank Collapse to Submarine Emplace-

ment". en. In: *Natural Hazards* 87.2, pp. 1189–1222. ISSN: 0921-030X, 1573-0840. DOI: 10.1007/s11069-017-2815-5 (cit. on pp. xi, xvi, 12, 37, 106, 113, 132, 146).

Burtin, A. et al. (2008). "Spectral Analysis of Seismic Noise Induced by Rivers: A New Tool to Monitor Spatiotemporal Changes in Stream Hydrodynamics". en. In: *Journal of Geophysical Research* 113.B5, B05301. ISSN: 0148-0227. DOI: 10.1029/2007JB005034 (cit. on p. 167).

Calder, E. S. et al. (2005). "Probabilistic Analysis of Rockfall Frequencies during an Andesite Lava Dome Eruption: The Soufrière Hills Volcano, Montserrat". en. In: *Geophysical Research Letters* 32.16. ISSN: 1944-8007. DOI: 10.1029/2005GL023594 (cit. on p. 1).

Cassar, C., M. Nicolas, and O. Pouliquen (2005). "Submarine Granular Flows down Inclined Planes". In: *Physics of Fluids* 17.10, p. 103301. ISSN: 1070-6631. DOI: 10.1063/1.2069864 (cit. on p. 7).

Chen, R., M. Lin, and H. Chen (1995). "Mechanism of Initiation of Debris Flow". en. In: *Urban Disaster Mitigation: The Role of Engineering and Technology*. Elsevier, pp. 231–243. ISBN: 978-0-08-041920-6. DOI: 10.1016/B978-008041920-6/50024-5 (cit. on p. 161).

Christen, M., J. Kowalski, and P. Bartelt (2010). "RAMMS: Numerical Simulation of Dense Snow Avalanches in Three-Dimensional Terrain". en. In: *Cold Regions Science and Technology* 63.1-2, pp. 1–14. ISSN: 0165232X. DOI: 10.1016/j.coldregions.2010.04.005 (cit. on pp. 12, 17, 30, 31, 34, 78, 103, 255).

Christen, M. et al. (2012). "Integral Hazard Managment Using a Unified Software Environment". en. In: *12th Congress INTERPRAEVENT 2012*. Grenoble, France, p. 10 (cit. on pp. 12, 30, 103).

Churuksaeva, V. and A. Starchenko (2015). "Mathematical Modeling of a River Stream Based on a Shallow Water Approach". en. In: *Procedia Computer Science* 66, pp. 200–209. ISSN: 18770509. DOI: 10.1016/j.procs.2015.11.024 (cit. on p. 60).

Clouard, V., J.-E. Athanase, and C. Aubaud (2013). "Physical Characteristics and Triggering Mechanisms of the 2009-2010 Landslide Crisis at Montagne Pelee Volcano, Martinique: Implication for Erosional Processes and Debris-Flow Hazards". en. In: *Bulletin de la Societe Geologique de France* 184.1-2, pp. 155–164. ISSN: 0037-9409. DOI: 10.2113/gssgfbull.184.1-2.155 (cit. on pp. 50, 124, 128, 132, 133, 142, 143, 149, 161, 179, 180, 210).

Cole, S. E. et al. (2009). "Seismic Signals of Snow-Slurry Lahars in Motion: 25 September 2007, Mt Ruapehu, New Zealand". en. In: *Geophysical Research Letters* 36.9. ISSN: 1944-8007. DOI: 10.1029/2009GL038030 (cit. on p. 137).

Corominas, J. et al. (2014). "Recommendations for the Quantitative Analysis of Landslide Risk". en. In: *Bulletin of Engineering Geology and the Environment* 73.2, pp. 209–263. ISSN: 1435-9537. DOI: 10.1007/s10064-013-0538-8 (cit. on pp. ix, x, xiv, xv, 9, 10, 177).

Corominas, J. (1996). "The Angle of Reach as a Mobility Index for Small and Large Landslides". en. In: *Canadian Geotechnical Journal* 33.2, pp. 260–271. ISSN: 0008-3674, 1208-6010. DOI: 10.1139/t96-005 (cit. on pp. 9, 177, 178, 183, 196, 197, 268).

Coussot, P. and C. Ancey (1999). "Rheophysical Classification of Concentrated Suspensions and Granular Pastes". en. In: *Physical Review E* 59.4, pp. 4445–4457. ISSN: 1063-651X, 1095-3787. DOI: 10.1103/PhysRevE.59.4445 (cit. on p. 7).

Coussot, P., A. I. Leonov, and J. M. Piau (1993). "Rheology of Concentrated Dispersed Systems in a Low Molecular Weight Matrix". en. In: *Journal of Non-Newtonian Fluid Mechanics* 46.2, pp. 179–217. ISSN: 0377-0257. DOI: 10.1016/0377-0257(93)85046-D (cit. on pp. 8, 140).

Coussot, P. and M. Meunier (1996). "Recognition, Classification and Mechanical Description of Debris Flows". In: *Earth-Science Reviews* 40.3-4, pp. 209–227. DOI: 10.1016/0012-8252(95)00065-8 (cit. on pp. 4–8, 124, 255).

Coutant, O. et al. (2012). "Joint Inversion of P-Wave Velocity and Density, Application to La Soufrière of Guadeloupe Hydrothermal System". en. In: *Geophysical Journal International* 191.2, pp. 723–742. ISSN: 1365-246X. DOI: 10.1111/j.1365-246X.2012.05644.x (cit. on p. 100).

Crittenden, K. and K. S. Rodolfo (2002). "Bacolor Town and Pinatubo Volcano, Philippines: Coping with Recurrent Lahar Disaster". In: *The Archaeology of Natural Disasters*. One World Archaeology Series, Routledge, London (cit. on p. 166).

Cruden, D. M. (1991). "A Simple Definition of a Landslide". en. In: *Bulletin of the International Association of Engineering Geology - Bulletin de l'Association Internationale de Géologie de l'Ingénieur* 43.1, pp. 27–29. ISSN: 1435-9537. DOI: 10.1007/BF02590167 (cit. on p. 1).

Cruden, D. and D. Varnes (1996). "Landslide Types and Processes". In: *Landslides : Investigation and Mitigation*. Special Report 247. Transportation research board, US National Research Council, pp. 36–75 (cit. on pp. 2, 4).

Davies, T. R. H. (1982). "Spreading of Rock Avalanche Debris by Mechanical Fluidization". en. In: *Rock mechanics* 15.1, pp. 9–24. ISSN: 1434-453X. DOI: 10.1007/BF01239474 (cit. on p. 5).

de Lange, S. et al. (2020). "Debris-Flow Generated Tsunamis and Their Dependence on Debris-Flow Dynamics". en. In: *Coastal Engineering* 157, p. 103623. ISSN: 03783839. DOI: 10.1016/j.coastaleng.2019.103623 (cit. on p. 164).

Delaney, K. B. and S. G. Evans (2014). "The 1997 Mount Munday Landslide (British Columbia) and the Behaviour of Rock Avalanches on Glacier Surfaces". en. In: *Landslides* 11.6, pp. 1019–1036. ISSN: 1612-510X, 1612-5118. DOI: 10.1007/s10346-013-0456-7 (cit. on p. 6).

Delannay, R. et al. (2017). "Granular and Particle-Laden Flows: From Laboratory Experiments to Field Observations". en. In: *Journal of Physics D: Applied Physics* 50.5, p. 053001. ISSN: 0022-3727, 1361-6463. DOI: 10.1088/1361-6463/50/5/053001 (cit. on pp. x, 5, 7, 9, 11, 25, 28, 30, 53).

Delgado-Sánchez, J. M. et al. (2019). "A Two-Layer Shallow Flow Model with Two Axes of Integration, Well-Balanced Discretization and Application to Submarine Avalanches". en. In: *Journal of Computational Physics* 406, p. 109186. ISSN: 0021-9991. DOI: 10.1016/j.jcp.2019.109186 (cit. on p. 60).

Denlinger, R. P. and R. M. Iverson (2004). "Granular Avalanches across Irregular Three-Dimensional Terrain: 1. Theory and Computation:" en. In: *Journal of Geophysical Research: Earth Surface* 109.F1. ISSN: 01480227. DOI: 10.1029/2003JF000085 (cit. on pp. 17, 57).

Desrues, M., P. Lacroix, and O. Brenguier (2019). "Satellite Pre-Failure Detection and In Situ Monitoring of the Landslide of the Tunnel Du Chambon, French Alps". en. In: *Geosciences* 9.7, p. 313. DOI: 10.3390/geosciences9070313 (cit. on pp. ix, xiv).

Dikau, R. et al., eds. (1996). *Landslide Recognition: Identification, Movement and Causes*. en-fr. Wiley. New York (cit. on p. 4).

Dressler, R. F. (1978). "New Nonlinear Shallow-Flow Equations with Curvature". In: *Journal of Hydraulic Research* 16.3, pp. 205–222. ISSN: 0022-1686. DOI: 10.1080/00221687809499617 (cit. on p. 11).

Dumaisnil, C. et al. (2010). "Hydraulic, Physical and Rheological Characteristics of Rain-Triggered Lahars at Semeru Volcano, Indonesia". en. In: *Earth Surface Processes and Landforms* 35.13, pp. 1573–1590. ISSN: 01979337. DOI: 10.1002/esp.2003 (cit. on pp. 138–140, 264).

Durán, O., B. Andreotti, and P. Claudin (2012). "Numerical Simulation of Turbulent Sediment Transport, from Bed Load to Saltation". In: *Physics of Fluids* 24.10, p. 103306. ISSN: 1070-6631. DOI: 10.1063/1.4757662 (cit. on p. 11).

Durand, V. et al. (2018). "On the Link Between External Forcings and Slope Instabilities in the Piton de La Fournaise Summit Crater, Reunion Island". en. In: *Journal of Geophysical Research: Earth Surface* 123.10, pp. 2422–2442. ISSN: 21699003. DOI: 10.1029/2017JF004507 (cit. on pp. 1, 5, 132, 147, 161).

Echos, L. (2015). "Lourde facture pour les routes détruites par les éboulements". fr. In: *Les Echos* (cit. on pp. ix, xiv).

Edwards, A. N. et al. (2017). "Formation of Levees, Troughs and Elevated Channels by Avalanches on Erodible Slopes". en. In: *Journal of Fluid Mechanics* 823, pp. 278–315. ISSN: 0022-1120, 1469-7645. DOI: 10.1017/jfm.2017.309 (cit. on pp. 16, 21).

Elverhøi, A. et al. (2000). "On the Dynamics of Subaqueous Debris Flows". In: *Oceanography* 13.3, pp. 109–117. ISSN: 10428275. DOI: 10.5670/oceanog.2000.20 (cit. on p. 164).

Endo, K. et al. (1989). "The 1984 Collapse and Debris Avalanche Deposits of Ontake Volcano, Central Japan". en. In: *Volcanic Hazards*. Ed. by J. H. Latter. IAVCEI Proceedings in Volcanology. Springer Berlin Heidelberg, pp. 210–229. ISBN: 978-3-642-73759-6 (cit. on p. 106).

Evans, S. and O. Hungr (1993). "The Assessment of Rockfall Hazard at the Base of Talus Slopes". In: *Canadian Geotechnical Journal* 30.4, pp. 620–636. ISSN: 0008-3674. DOI: 10.1139/t93-054 (cit. on pp. 10, 11).

Fan, X. et al. (2019). "Earthquake-Induced Chains of Geologic Hazards: Patterns, Mechanisms, and Impacts". en. In: *Reviews of Geophysics*, 2018RG000626. ISSN: 8755-1209, 1944-9208. DOI: 10.1029/2018RG000626 (cit. on pp. ix, xiv).

Fannin, R. J. and M. P. Wise (2001). "An Empirical-Statistical Model for Debris Flow Travel Distance". In: *Canadian Geotechnical Journal* 38.5, pp. 982–994. ISSN: 0008-3674. DOI: 10.1139/t01-030 (cit. on p. 10).

Favreau, P. et al. (2010). "Numerical Modeling of Landquakes: Landslides and Seismic Waves". en. In: *Geophysical Research Letters* 37.15, p. L15305. ISSN: 00948276. DOI: 10.1029/2010GL043512 (cit. on pp. xi, xvi, 12, 23, 37, 124, 146).

Fell, R. et al. (2008). "Guidelines for Landslide Susceptibility, Hazard and Risk Zoning for Land-Use Planning: Commentary". In: *Engineering Geology* 102.3-4, pp. 99–111. DOI: 10.1016/j.enggeo.2008.03.014 (cit. on pp. ix, xiv, 9).

Fernández-Nieto, E. D. et al. (2016). "A Multilayer Shallow Model for Dry Granular Flows with the -Rheology: Application to Granular Collapse on Erodible Beds". en. In: *Journal of Fluid Mechanics* 798, pp. 643–681. ISSN: 0022-1120, 1469-7645. DOI: 10.1017/jfm.2016.333 (cit. on p. 12).

Fernández-Nieto, E. et al. (2008). "A New Savage–Hutter Type Model for Submarine Avalanches and Generated Tsunami". en. In: *Journal of Computational Physics* 227.16, pp. 7720–7754. ISSN: 00219991. DOI: 10.1016/j.jcp.2008.04.039 (cit. on pp. 94, 97).

Fernández-Nieto, E. et al. (2018). "2D Granular Flows with the Mu(I) Rheology and Side Walls Friction: A Well-Balanced Multilayer Discretization". en. In: *Journal of Computational Physics* 356, pp. 192–219. ISSN: 00219991. DOI: 10.1016/j.jcp.2017.11.038 (cit. on pp. 12, 20, 30).

Feuillard, M. et al. (1983). "The 1975–1977 Crisis of La Soufriere de Guadeloupe (F.W.I): A Still-Born Magmatic Eruption". In: *Journal of Volcanology and Geothermal Research* 16.3, pp. 317–334. ISSN: 0377-0273. DOI: 10.1016/0377-0273(83)90036-7 (cit. on pp. 98, 100).

Feuillet, N. et al. (2002). "Arc Parallel Extension and Localization of Volcanic Complexes in Guadeloupe, Lesser Antilles". en. In: *Journal of Geophysical Research: Solid Earth* 107.B12, ETG 3-1-ETG 3–29. ISSN: 2156-2202. DOI: 10.1029/2001JB000308 (cit. on p. 102).

Feuillet, N. et al. (2011). "The Mw = 6.3, November 21, 2004, Les Saintes Earthquake (Guadeloupe): Tectonic Setting, Slip Model and Static Stress Changes". In: *Journal of Geophysical Research: Solid Earth* 116.B10. ISSN: 0148-0227. DOI: 10.1029/2011JB008310 (cit. on p. 100).

Finlay, P. J., G. R. Mostyn, and R. Fell (1999). "Landslide Risk Assessment: Prediction of Travel Distance". en. In: *Canadian Geotechnical Journal* 36, p. 7 (cit. on pp. 9, 197).

Fischer, J.-T., J. Kowalski, and S. P. Pudasaini (2012). "Topographic Curvature Effects in Applied Avalanche Modeling". en. In: *Cold Regions Science and Technology* 74-75, pp. 21–30. ISSN: 0165232X. DOI: 10.1016/j.coldregions.2012.01.005 (cit. on pp. 30, 39, 41, 42, 59).

Flageollet, J. C. (1989). *Les mouvements de terrain et leur prévention*. fr. Masson. ISBN: 978-2-225-81577-5 (cit. on p. 4).

Froude, M. J. and D. Petley (2018). "Global Fatal Landslide Occurrence from 2004 to 2016". en. In: *Natural Hazards and Earth System Sciences* 18.8, pp. 2161–2181. ISSN: 1684-9981. DOI: 10.5194/nhess-18-2161-2018 (cit. on pp. ix, xiv, 30).

Garres-Díaz, J. et al. (2020). "Multilayer Models for Shallow Two-Phase Debris Flows with Dilatancy Effects". en. In: *Journal of Computational Physics* 419, p. 109699. ISSN: 00219991. DOI: 10.1016/j.jcp.2020.109699 (cit. on p. 30).

GDR MiDi (2004). "On Dense Granular Flows". In: *The European Physical Journal E* 14.4, pp. 341–365 (cit. on pp. 17, 57).

GEO (1996). *Report on the Fei Tsui Road Landslide of August 1995, Volume 2*. Findings of the Landslide Investigation. Geotechnical Engineering office, Hong-Kong (cit. on pp. 179, 180).

GEO (2011). *Guidelines on the Assessment of Debris Mobility for Channelised Debris Flows*. Technical Guidance Note 29. Geotechnical ENgineering office, Hong-Kong (cit. on pp. 12, 30).

George, D. L. and R. M. Iverson (2014). "A Depth-Averaged Debris-Flow Model That Includes the Effects of Evolving Dilatancy. II. Numerical Predictions and Experimental Tests". en. In: *Proceedings of the Royal Society A: Mathematical, Physical and Engineering Sciences* 470.2170, p. 20130820. ISSN: 1364-5021, 1471-2946. DOI: 10.1098/rspa.2013.0820 (cit. on pp. 31, 41, 164).

Germa, A. et al. (2011). "The K–Ar Cassignol–Gillot Technique Applied to Western Martinique Lavas: A Record of Lesser Antilles Arc Activity from 2Ma to Mount Pelée Volcanism". en. In: *Quaternary Geochronology* 6.3-4, pp. 341–355. ISSN: 18711014. DOI: 10.1016/j.quageo.2011.02.001 (cit. on p. 132).

Girolami, L. et al. (2012). "A Three-Dimensional Discrete-Grain Model for the Simulation of Dam-Break Rectangular Collapses: Comparison between Numerical Results and Experiments". en. In: *Granular Matter* 14.3, pp. 381–392. ISSN: 1434-5021, 1434-7636. DOI: 10.1007/s10035-012-0342-3 (cit. on p. 11).

Glade, T. and M. J. Crozier (2005). "A Review of Scale Dependency in Landslide Hazard and Risk Analysis". en. In: *Landslide Hazard and Risk*. John Wiley & Sons, Ltd. Chap. 3, pp. 75–138. ISBN: 978-0-470-01265-9. DOI: 10.1002/9780470012659.ch3 (cit. on pp. ix, xiv, 9).

Glicken, H. (1996). *Rockslide-Debris Avalanche of May 18, 1980, Mount St. Helens Volcano, Washington*. USGS Numbered Series 96-677. U.S. Geological Survey, p. 98. DOI: 10.3133/ofr96677 (cit. on p. 5).

González-Vida, J. M. et al. (2018). *The Lituya Bay Landslide-Generated Mega-Tsunami. Numericalsimulation and Sensitivity Analysis*. en. Preprint. Sea, Ocean and Coastal Hazards. DOI: 10.5194/nhess-2018-224 (cit. on pp. 94, 97).

Gray, J. M. N. T. and A. N. Edwards (2014). "A Depth-Averaged -Rheology for Shallow Granular Free-Surface Flows". en. In: *Journal of Fluid Mechanics* 755, pp. 503–534. ISSN: 0022-1120, 1469-7645. DOI: 10.1017/jfm.2014.450 (cit. on pp. 18, 19, 57).

Gray, J. M. N. T. and K. Hutter (1998). "Physik Granularer Lawinen". en. In: *Physik Journal* 54.1, pp. 37–43. ISSN: 1521-3722. DOI: 10.1002/phbl.19980540110 (cit. on p. 42).

Gray, J. M. N. T., Y.-C. Tai, and S. Noelle (2003). "Shock Waves, Dead Zones and Particle-Free Regions in Rapid Granular Free-Surface Flows". en. In: *Journal of Fluid Mechanics* 491, pp. 161–181. ISSN: 00221120, 14697645. DOI: 10.1017/S0022112003005317 (cit. on pp. 17, 57).

Gray, J., M. Wieland, and K. Hutter (1999). "Gravity-Driven Free Surface Flow of Granular Avalanches over Complex Basal Topography". In: *Proceedings of the Royal Society of London A: Mathematical, Physical and Engineering Sciences* 455, pp. 1841–1874 (cit. on pp. 17, 30, 41, 57, 79).

Greve, R. and K. Hutter (1993). "Motion of a Granular Avalanche in a Convex and Concave Curved Chute: Experiments and Theoretical Predictions". In: *Philosophical Transactions: Physical Sciences and Engineering* 342.1666, pp. 573–600. ISSN: 0962-8428 (cit. on p. 30).

Gruber, U. and P. Bartelt (2007). "Snow Avalanche Hazard Modelling of Large Areas Using Shallow Water Numerical Methods and GIS". en. In: *Environmental Modelling & Software*. Modelling, Computer-Assisted Simulations, and Mapping of Dangerous Phenomena for Hazard Assessment 22.10, pp. 1472–1481. ISSN: 1364-8152. DOI: 10.1016/j.envsoft.2007.01.001 (cit. on p. 59).

Guerricchio, A. et al. (2012). "Landslide hazard connected to deep seated gravitational slope deformations and prolonged rainfall: Maierato landslide case history". it. In: *Rendiconti online della societa geologica italiana* 21/2012 (cit. on p. 1).

Guthrie, R. H. et al. (2012). "The 6 August 2010 Mount Meager Rock Slide-Debris Flow, Coast Mountains, British Columbia: Characteristics, Dynamics, and Implications for Hazard and Risk Assessment". English. In: *Natural Hazards and Earth System Sciences* 12.5, pp. 1277–1294. ISSN: 1561-8633. DOI: 10.5194/nhess-12-1277-2012 (cit. on pp. 2, 53).

Hannion, Y. and J. Hamman (2018). *Glissement de terrain à Venteuil (51)*. fr. Tech. rep. RP-67930-FR. BRGM, p. 24 (cit. on pp. ix, xiv).

Harnett, C. E. et al. (2019). "Presentation and Analysis of a Worldwide Database for Lava Dome Collapse Events: The Global Archive of Dome Instabilities (GLADIS)". en. In: *Bulletin of Volcanology* 81.3, p. 16. ISSN: 0258-8900, 1432-0819. DOI: 10.1007/s00445-019-1276-y (cit. on p. 100).

Hathout, M. et al. (2019). "Expert Judgments Calibration and Combination for Assessment of River Levee Failure Probability". en. In: *Reliability Engineering & System Safety* 188, pp. 377–392. ISSN: 0951-8320. DOI: 10.1016/j.ress.2019.03.019 (cit. on p. 202).

Heim, A. (1932). *Bergsturz und Menschenleben*. de. Fretz & Wasmuth (cit. on pp. 5, 9, 108, 109).

Hibert, C. et al. (2011). "Slope Instabilities in Dolomieu Crater, Réunion Island: From Seismic Signals to Rockfall Characteristics". en. In: *Journal of Geophysical Research* 116.F4. ISSN: 0148-0227. DOI: 10.1029/2011JF002038 (cit. on pp. 5, 77, 132).

Hibert, C. et al. (2014). "Automated Identification, Location, and Volume Estimation of Rockfalls at Piton de La Fournaise Volcano". en. In: *Journal of Geophysical Research: Earth Surface* 119.5, pp. 1082–1105. ISSN: 21699003. DOI: 10.1002/2013JF002970 (cit. on pp. 1, 2, 161).

Highland, L. M. and P. Bobrowsky (2008). *The Landslide Handbook—A Guide to Understanding Landslides*. U.S. Geological Survey Circular 1325. Reston, Virginia: USGS, p. 129 (cit. on pp. 3, 4, 255).

Hincks, T. K. et al. (2014). "Retrospective Analysis of Uncertain Eruption Precursors at La Soufrière Volcano, Guadeloupe, 1975–77: Volcanic Hazard Assessment Using a Bayesian Belief Network Approach". en. In: *Journal of Applied Volcanology* 3.1, p. 3. ISSN: 2191-5040. DOI: 10.1186/2191-5040-3-3 (cit. on pp. 98, 102).

Hirn, A. et al. (1987). "Shallow Seismicity at Montagne Pelée Volcano, Martinique, Lesser Antilles". en. In: *Bulletin of Volcanology* 49.6, pp. 723–728. ISSN: 1432-0819. DOI: 10.1007/BF01079823 (cit. on p. 125).

Hoblitt, R. P. et al. (1998). *Volcano Hazards from Mount Rainier, Washington, Revised 1998*. Tech. rep. 98-428. U.S. Dept. of the Interior, U.S. Geological Survey ;Information Services, [distributor], DOI: 10.3133/ofr98428 (cit. on p. 9).

Hong, M., S. Jeong, and J. Kim (2019). "A Combined Method for Modeling the Triggering and Propagation of Debris Flows". en. In: *Landslides*. ISSN: 1612-5118. DOI: 10.1007/s10346-019-01294-5 (cit. on p. 162).

Horton, P. et al. (2013). "Flow-R, a Model for Susceptibility Mapping of Debris Flows and Other Gravitational Hazards at a Regional Scale". en. In: *Natural Hazards and Earth System Sciences* 13.4, pp. 869–885. ISSN: 1684-9981. DOI: 10.5194/nhess-13-869-2013 (cit. on pp. 10, 177).

Hsu, K. J. (1975). *Catastrophic Debris Streams (Sturzstroms) Generated by Rockfalls*. en. Geological Society of America Bulletin (cit. on pp. 6, 9, 108).

Hu, K.-h., L. Pu, and X.-k. Wang (2016). "Experimental Study of Entrainment Behavior of Debris Flow over Channel Inflexion Points". en. In: *Journal of Mountain Science* 13.6, pp. 971–984. ISSN: 1672-6316, 1993-0321. DOI: 10.1007/s11629-015-3749-6 (cit. on p. 163).

Hu, M. et al. (2015). "Three-Dimensional Run-out Analysis and Prediction of Flow-like Landslides Using Smoothed Particle Hydrodynamics". en. In: *Environmental Earth Sciences* 73.4, pp. 1629–1640. ISSN: 1866-6280, 1866-6299. DOI: 10.1007/s12665-014-3513-1 (cit. on pp. 11, 177).

Hungr, O., J. Corominas, and E. Eberhardt (2005a). "Estimating Landslide Motion Mechanism, Travel Distance and Velocity". In: *Landslide risk management* 1, pp. 99–128 (cit. on pp. 10, 11, 177).

Hungr, O. (1995). "A Model for the Runout Analysis of Rapid Flow Slides, Debris Flows, and Avalanches". en. In: *Canadian Geotechnical Journal* 32.4, pp. 610–623. ISSN: 0008-3674, 1208-6010. DOI: 10.1139/t95-063 (cit. on pp. 12, 30, 57).

Hungr, O. and S. G. Evans (1996). "Rock Avalanche Run out Prediction Using a Dynamic Model". In: *Proceedings of the 7th Int. Symp. Landslides*. Vol. 1. Trondheim, Norway, pp. 233–238 (cit. on p. 199).

Hungr, O., S. Leroueil, and L. Picarelli (2014). "The Varnes Classification of Landslide Types, an Update". en. In: *Landslides* 11.2, pp. 167–194. ISSN: 1612-510X, 1612-5118. DOI: 10.1007/s10346-013-0436-y (cit. on pp. 1, 2, 4–6, 30, 100).

Hungr, O. and S. McDougall (2009). "Two Numerical Models for Landslide Dynamic Analysis". en. In: *Computers & Geosciences* 35.5, pp. 978–992. ISSN: 00983004. DOI: 10.1016/j.cageo.2007.12.003 (cit. on p. 103).

Hungr, O., N. Morgenstern, and H. Wong (2007). "Review of Benchmarking Exercise on Landslide Debris Runout and Mobility Modelling". In: *Proceedingd of The 2007 International Forum on Landdslide Disaster Management*. Ho & Li. ISBN: 978-962-7619-30-7 (cit. on pp. xi, xvi, 12, 32, 38, 58, 124, 146, 184).

Hungr, O. et al., eds. (2005b). *Landslide Risk Management*. en. CRC Press. ISBN: 978-1-4398-3371-1 (cit. on p. 30).

Hürlimann, M., J. O. Garcia-Piera, and A. Ledesma (2000). "Causes and Mobility of Large Volcanic Landslides: Application to Tenerife, Canary Islands". In: *Journal of Volcanology and Geothermal Research* 103.1, pp. 121–134. ISSN: 0377-0273. DOI: 10.1016/S0377-0273(00)00219-5 (cit. on p. 102).

Hussin, H. Y. et al. (2012). "Parameterization of a Numerical 2-D Debris Flow Model with Entrainment: A Case Study of the Faucon Catchment, Southern French Alps". en. In: *Natural Hazards and Earth System Science* 12.10, pp. 3075–3090. ISSN: 1684-9981. DOI: 10.5194/nhess-12-3075-2012 (cit. on p. 178).

Hutchinson, J. N. (1988). "General Report: Morphological and Geotechnical Parameters of Landslides in Relation to Geology and Hydrogeology". In: *Proceedings of the 5th International Symposium on Landslides*. Lausanne: A A Balkema, pp. 3–35. DOI: 10.1016/0148-9062(89)90310-0 (cit. on p. 4).

Hutter, K. et al. (1993). "Two-Dimensional Spreading of a Granular Avalanche down an Inclined Plane Part I. Theory". en. In: *Acta Mechanica* 100.1-2, pp. 37–68. ISSN: 0001-5970, 1619-6937. DOI: 10.1007/BF01176861 (cit. on p. 17).

Hutter, K. and T. Koch (1991). "Motion of a Granular Avalanche in an Exponentially Curved Chute: Experiments and Theoretical Predictions". en. In: *Philosophical Transactions of the Royal Society of London. Series A: Physical and Engineering Sciences* 334.1633, pp. 93–138. ISSN: 0962-8428, 2054-0299. DOI: 10.1098/rsta.1991.0004 (cit. on p. 30).

INSEE (2020). *Comparateur de Territoire, Commune Du Prêcheur (97219)*. https://www.insee.fr/fr/statistiques/1405599?geo=COM-97219 (cit. on p. 125).

Ionescu, I. R. et al. (2015). "Viscoplastic Modeling of Granular Column Collapse with Pressure-Dependent Rheology". en. In: *Journal of Non-Newtonian Fluid Mechanics* 219, pp. 1–18. ISSN: 03770257. DOI: 10.1016/j.jnnfm.2015.02.006 (cit. on pp. 11, 57).

Iverson, R. M. (2003). "The Debris-Flow Rheology Myth". In: *3rd International Conference on Debris-Flow Hazards Mitigation: Mechanics, Prediction, and Assessment*. Vol. 1, pp. 303–314 (cit. on pp. 8, 57).

Iverson, R. M. (1997). "The Physics of Debris Flows". en. In: *Reviews of Geophysics* 35.3, pp. 245–296. ISSN: 87551209. DOI: 10.1029/97RG00426 (cit. on p. 161).

Iverson, R. M. (2012). "Elementary Theory of Bed-Sediment Entrainment by Debris Flows and Avalanches". en. In: *Journal of Geophysical Research: Earth Surface* 117.F3, n/a–n/a. ISSN: 01480227. DOI: 10.1029/2011JF002189 (cit. on pp. 8, 9, 12, 30, 124, 162, 163).

Iverson, R. M. (2014). "Debris Flows: Behaviour and Hazard Assessment". en. In: *Geology Today* 30.1, pp. 15–20. ISSN: 02666979. DOI: 10.1111/gto.12037 (cit. on pp. 161, 162, 177).

Iverson, R. M. and R. P. Denlinger (2001). "Flow of Variably Fluidized Granular Masses across Three-Dimensional Terrain: 1. Coulomb Mixture Theory". en. In: *Journal of Geophysical Research: Solid Earth* 106.B1, pp. 537–552. ISSN: 01480227. DOI: 10.1029/2000JB900329 (cit. on pp. 17, 30, 57, 177).

Iverson, R. M. and D. L. George (2014). "A Depth-Averaged Debris-Flow Model That Includes the Effects of Evolving Dilatancy. I. Physical Basis". en. In: *Proceedings of the Royal Society A: Mathematical, Physical and Engineering Sciences* 470.2170, p. 20130819. ISSN: 1364-5021, 1471-2946. DOI: 10.1098/rspa.2013.0819 (cit. on pp. 12, 30, 31, 34, 124, 164, 255).

Iverson, R. M., D. L. George, and M. Logan (2016). "Debris Flow Runup on Vertical Barriers and Adverse Slopes: Debris Flow Runup". en. In: *Journal of Geophysical Research: Earth Surface* 121.12, pp. 2333–2357. ISSN: 21699003. DOI: 10.1002/2016JF003933 (cit. on p. 59).

Iverson, R. M., M. Logan, and R. P. Denlinger (2004). "Granular Avalanches across Irregular Three-Dimensional Terrain: 2. Experimental Tests". en. In: *Journal of Geophysical Research: Earth Surface* 109.F1. ISSN: 2156-2202. DOI: 10.1029/2003JF000084 (cit. on pp. 58, 73, 260).

Iverson, R. M. and C. Ouyang (2015). "Entrainment of Bed Material by Earth-Surface Mass Flows: Review and Reformulation of Depth-Integrated Theory". en. In: *Reviews of Geophysics* 53.1, pp. 27–58. ISSN: 1944-9208. DOI: 10.1002/2013RG000447 (cit. on p. 9).

Iverson, R. M., S. P. Schilling, and J. W. Vallance (1998). "Objective Delineation of Lahar-Inundation Hazard Zones". en. In: *GSA Bulletin* 110.8, pp. 972–984. ISSN: 0016-7606. DOI: 10.1130/0016-7606(1998)110<0972:ODOLIH>2.3.CO;2 (cit. on p. 10).

Iverson, R. M. et al. (2011). "Positive Feedback and Momentum Growth during Debris-Flow Entrainment of Wet Bed Sediment". en. In: *Nature Geoscience* 4.2, pp. 116–121. ISSN: 1752-0908. DOI: 10.1038/ngeo1040 (cit. on pp. 6, 8, 9, 162).

Jaboyedoff, M. and V. Labiouse (2003). "Preliminary Assessment of Rockfall Hazard Based on GIS Data". In: *10th International Congresson Rock Mechanics ISRM 2003 – Technology Roadmap for Rockmechanics,* Johannesburgh, South Africa, pp. 575–578 (cit. on p. 10).

Johnson, B. C., C. S. Campbell, and H. J. Melosh (2016). "The Reduction of Friction in Long Runout Landslides as an Emergent Phenomenon". en. In: *Journal of Geophysical Research: Earth Surface* 121.5, pp. 881–889. ISSN: 2169-9011. DOI: 10.1002/2015JF003751 (cit. on pp. 6, 161).

Jones, R., V. Manville, and D. Andrade (2015). "Probabilistic Analysis of Rain-Triggered Lahar Initiation at Tungurahua Volcano". en. In: *Bulletin of Volcanology* 77.8, p. 68. ISSN: 1432-0819. DOI: 10.1007/s00445-015-0946-7 (cit. on p. 137).

Jop, P., Y. Forterre, and O. Pouliquen (2006). "A Constitutive Law for Dense Granular Flows". en. In: *Nature* 441.7094, pp. 727–730. ISSN: 0028-0836, 1476-4687. DOI: 10.1038/nature04801 (cit. on pp. 17, 18, 57).

Kang, S. and S.-R. Lee (2018). "Debris Flow Susceptibility Assessment Based on an Empirical Approach in the Central Region of South Korea". en. In: *Geomorphology* 308, pp. 1–12. ISSN: 0169-555X. DOI: 10.1016/j.geomorph.2018.01.025 (cit. on p. 10).

Kelfoun, K. and T. H. Druitt (2005). "Numerical Modeling of the Emplacement of Socompa Rock Avalanche, Chile". en. In: *Journal of Geophysical Research* 110.B12. ISSN: 0148-0227. DOI: 10.1029/2005JB003758 (cit. on pp. xii, xviii, 12, 17, 31, 103).

Kelfoun, K. (2011). "Suitability of Simple Rheological Laws for the Numerical Simulation of Dense Pyroclastic Flows and Long-Runout Volcanic Avalanches". en. In: *Journal of Geophysical Research* 116.B8. ISSN: 0148-0227. DOI: 10.1029/2010JB007622 (cit. on p. 40).

Kelfoun, K. et al. (2017). "Simulation of Block-and-Ash Flows and Ash-Cloud Surges of the 2010 Eruption of Merapi Volcano with a Two-Layer Model: MODEL OF THE 2010 ERUPTION OF MERAPI". en. In: *Journal of Geophysical Research: Solid Earth* 122.6, pp. 4277–4292. ISSN: 21699313. DOI: 10.1002/2017JB013981 (cit. on p. 60).

Knebelman, M. S. (1951). "Spaces of Relative Parallelism". In: *Annals of Mathematics* 53.3, pp. 387–399. ISSN: 0003-486X. DOI: 10.2307/1969562 (cit. on p. 37).

Knill, J. (1996). *Report on the Fei Tsui Road Landslide of August 1995, Volume 1*. Independent Review of the Investigation by the Geotechnical Engineering Office. Geotechnical Engineering office, Hong-Kong (cit. on pp. 179, 180).

Koch, T., R. Greve, and K. Hutter (1994). "Unconfined Flow of Granular Avalanches along a Partly Curved Surface. II. Experiments and Numerical Computations". In: *Proceedings: Mathematical and Physical Sciences* 445.1924, pp. 415–435. ISSN: 0962-8444 (cit. on p. 30).

Komorowski, J. .-C. et al. (2008). "Reconstruction and Analysis of Sub-Plinian Tephra Dispersal during the 1530 A.D. Soufrière (Guadeloupe) Eruption: Implications for Scenario Definition and Hazards Assessment". In: *Journal of Volcanology and Geothermal Research*. Evaluating Explosive Eruption Risk at European Volcanoes 178.3, pp. 491–515. ISSN: 0377-0273. DOI: 10.1016/j.jvolgeores.2007.11.022 (cit. on pp. 98, 100).

Komorowski, J.-C. (2008). *Du Volcan Au Pyroclaste: Une Approche Pluridisciplinaire de La Compréhension Des Processus Éruptifs et de l'évaluation Des Aléas*. en. Mémoire d'Habilitation à Diriger La Recherche. Université René Diderot Paris 7 (cit. on pp. 98, 100, 102, 106–108, 113, 116, 261).

Komorowski, J.-C. et al. (2005). "Volcanic Hazard Atlas of the Lesser Antilles : Guadeloupe". In: *Volcanic Hazard Atlas of the Lesser Antilles*. Ed. by J. Lindsay et al. University of the West Indies, Seismic Research Unit, Trinidad and IAVCEI, pp. 65–102 (cit. on pp. 98, 100, 102).

Komorowski, J.-C. et al. (2013). "Paroxysmal Dome Explosion during the Merapi 2010 Eruption: Processes and Facies Relationships of Associated High-Energy Pyroclastic Density Currents". en. In: *Journal of Volcanology and Geothermal Research* 261, pp. 260–294. ISSN: 03770273. DOI: 10.1016/j.jvolgeores.2013.01.007 (cit. on p. 60).

Koo, R. et al. (2018). "Back-Analysis of Geophysical Flows Using Three-Dimensional Runout Model". en. In: *Canadian Geotechnical Journal* 55.8, pp. 1081–1094. ISSN: 0008-3674, 1208-6010. DOI: 10.1139/cgj-2016-0578 (cit. on p. 11).

Korup, O. et al. (2013). "Long-Runout Landslides". en. In: *Treatise on Geomorphology*. Elsevier, pp. 183–199. ISBN: 978-0-08-088522-3. DOI: 10.1016/B978-0-12-374739-6.00164-0 (cit. on pp. 2, 6, 161).

Kraemer, W. and H. Sonnberger (1986). *The Linear Regression Model Under Test*. en. Physica-Verlag Heidelberg. ISBN: 978-3-642-95878-6. DOI: 10.1007/978-3-642-95876-2 (cit. on p. 210).

Kuehnert, J. et al. (2020). "Simulation of Topography Effects on Rockfall-Generated Seismic Signals: Application to Piton de La Fournaise Volcano". en. In: *Journal of Geophysical Research: Solid Earth* 125.10. ISSN: 2169-9313, 2169-9356. DOI: 10.1029/2020JB019874 (cit. on pp. 1, 147).

Kuo, C. Y. et al. (2009). "Simulation of Tsaoling Landslide, Taiwan, Based on Saint Venant Equations over General Topography". In: *Engineering Geology* 104.3, pp. 181–189. ISSN: 0013-7952. DOI: 10.1016/j.enggeo.2008.10.003 (cit. on pp. 106, 113).

Kwan, J. and H. W. Sun (2007). "Benchmarking Exercise on Landslide Mobility Modelling - Runout Analyses Using 3dDMM". en. In: *Proceedings of The 2007 International Forum on Landslide Disaster Management*. Hong Kong: Geotechnical Division, The Hong Kong Institution of Engineers, p. 22 (cit. on p. 31).

Lagrée, P.-Y., L. Staron, and S. Popinet (2011). "The Granular Column Collapse as a Continuum: Validity of a Two-Dimensional Navier–Stokes Model with a Mu(I)-Rheology". en. In: *Journal of Fluid Mechanics* 686, pp. 378–408. ISSN: 0022-1120, 1469-7645. DOI: 10.1017/jfm.2011.335 (cit. on p. 11).

LaHusen, R. (2005). *Acoustic Flow Monitor System - User Manual*. USGS Numbered Series 2002-429. Geological Survey (U.S.) DOI: 10.3133/ofr2002429 (cit. on p. 137).

LaHusen, R. G. (1998). *Detecting Debris Flows Using Ground Vibrations*. USGS Numbered Series 236-96. U.S. Geological Survey, p. 2. DOI: 10.3133/fs23696 (cit. on p. 137).

Laigle, D. and P. Macabies (2010). *Compte rendu de la mission du 14 au 16 décembre 2010*. fr. Tech. rep. Cemagref/ONF-RTM/DIREN, p. 30 (cit. on p. 140).

Lajeunesse, E. et al. (2006). "New Insights on the Runout of Large Landslides in the Valles-Marineris Canyons, Mars". en. In: *Geophysical Research Letters* 33.4, p. L04403. ISSN: 0094-8276. DOI: 10.1029/2005GL025168 (cit. on p. 197).

Lalubie, G. (2013). "Les Lahars et les laves torrentielles historiques aux Antilles françaises : un risque hydro-volcano-géomorphologique majeur". fr. In: *Physio-Géo. Géographie physique et environnement* Volume 7, pp. 83–109. ISSN: 1958-573X. DOI: 10.4000/physio-geo.3479 (cit. on pp. 135, 137, 140).

Larsen, M. C. and G. F. Wieczorek (2006). "Geomorphic Effects of Large Debris Flows and Flash Floods, Northern Venezuela, 1999". en. In: *Zeitschrift für Geomorphologie, Supplementband* 145, p. 26 (cit. on pp. 5, 161).

Lavigne, F. et al. (2000). "Lahars at Merapi Volcano, Central Java: An Overview". en. In: *Journal of Volcanology and Geothermal Research* 100.1, pp. 423–456. ISSN: 0377-0273. DOI: 10.1016/S0377-0273(00)00150-5 (cit. on p. 137).

Law, R. P. H. et al. (2017). "Three-Dimensional Debris Mobility Modelling Coupling Smoothed Particle Hydrodynamics and ArcGIS". en. In: *Proceedings of the 19 Th International Conference on Soil Mechanics and Geotechnical Engineering*. Seoul, p. 4 (cit. on pp. 12, 30, 31).

Le Friant, A. et al. (2003). "Large-Scale Flank Collapse Events during the Activity of Montagne Pelée, Martinique, Lesser Antilles". en. In: *Journal of Geophysical Research: Solid Earth* 108.B1. ISSN: 2156-2202. DOI: 10.1029/2001JB001624 (cit. on p. 132).

Le Friant, A. et al. (2006). "Potential Flank-Collapse of Soufrière Volcano, Guadeloupe, Lesser Antilles? Numerical Simulation and Hazards". en. In: *Natural Hazards* 39.3, pp. 381–393. ISSN: 0921-030X, 1573-0840. DOI: 10.1007/s11069-005-6128-8 (cit. on pp. 102, 106).

Lefebvre-Lepot, A., B. Merlet, and T. N. Nguyen (2015). "An Accurate Method to Include Lubrication Forces in Numerical Simulations of Dense Stokesian Suspensions". en. In: *Journal of Fluid Mechanics* 769, pp. 369–386. ISSN: 0022-1120, 1469-7645. DOI: 10.1017/jfm.2015.101 (cit. on p. 11).

Legendre, Y. (2012). "Reconstruction Fine de l'histoire Éruptive et Scenarii Éruptifs à La Soufrière de Guadeloupe : Vers Un Modèle Intégré de Fonctionnement Du Volcan". Thesis. Paris 7 (cit. on pp. 53, 98, 100, 102, 106–108, 113, 116, 261).

Legros, F. (2002). "The Mobility of Long-Runout Landslides". en. In: *Engineering Geology* 63.3, pp. 301–331. ISSN: 0013-7952. DOI: 10.1016/S0013-7952(01)00090-4 (cit. on pp. 9, 177, 196, 197, 200).

Legros, F. (2006). "Landslide Mobility and the Role of Water". en. In: *Landslides from Massive Rock Slope Failure*. S.G. Evans, G. Scarascia Mugnozza, A. Strom, and R.L. Hermanns.

Vol. 49. NATO Sciences Series, IV. Earth and Environ- Mental Sciences, pp. 233–242 (cit. on p. 6).

Leonardi, A. et al. (2014). "Coupled DEM-LBM Method for the Free-Surface Simulation of Heterogeneous Suspensions". en. In: *Computational Particle Mechanics* 1.1, pp. 3–13. ISSN: 2196-4378, 2196-4386. DOI: 10.1007/s40571-014-0001-z (cit. on pp. 11, 177).

Leroueil, S. et al. (1996). "Geotechnical Characterization of Slope Movements". en. In: *Landslides*, pp. 53–74. ISBN: 978-90-5410-819-1 (cit. on p. 4).

Lesparre, N. et al. (2012). "Density Muon Radiography of La Soufrière of Guadeloupe Volcano: Comparison with Geological, Electrical Resistivity and Gravity Data". In: *Geophysical Journal International* 190.2, pp. 1008–1019. ISSN: 0956-540X. DOI: 10.1111/j.1365-246X.2012.05546.x (cit. on pp. 100, 102, 115).

Lesparre, N. et al. (2014). "Cross-Section Electrical Resistance Tomography of La Soufrière of Guadeloupe Lava Dome". en. In: *Geophysical Journal International* 197.3, pp. 1516–1526. ISSN: 0956-540X. DOI: 10.1093/gji/ggu104 (cit. on pp. 100, 115).

LeVeque, R. J., D. L. George, and M. J. Berger (2011). "Tsunami Modelling with Adaptively Refined Finite Volume Methods". en. In: *Acta Numerica* 20, pp. 211–289. ISSN: 1474-0508, 0962-4929. DOI: 10.1017/S0962492911000043 (cit. on pp. 31, 33).

Levy, C. et al. (2015). "Friction Weakening in Granular Flows Deduced from Seismic Records at the Soufrière Hills Volcano, Montserrat". en. In: *Journal of Geophysical Research: Solid Earth* 120.11, pp. 7536–7557. ISSN: 2169-9356. DOI: 10.1002/2015JB012151 (cit. on pp. xi, xvi, 2, 40, 77, 132, 147).

Li, P., K. Hu, and X. Wang (2018). "Debris Flow Entrainment Rates in Non-Uniform Channels with Convex and Concave Slopes". en. In: *Journal of Hydraulic Research* 56.2, pp. 156–167. ISSN: 0022-1686, 1814-2079. DOI: 10.1080/00221686.2017.1313321 (cit. on p. 163).

Lissak, C., O. Maquaire, and J.-P. Malet (2009). "Role of Hydrological Process in Landslide Occurrence: Villerville-Cricqueboeuf Landslides (Normandy Coast, France)". en. In: *Proceedings of the International Conference on Landslide Processes: From Geomorphologic Mapping to Dynamic Modelling*. Strasbourg: CERG Editions, pp. 175–180 (cit. on p. 1).

Locat, A. et al. (2011). "Progressive Failures in Eastern Canadian and Scandinavian Sensitive Clays". In: *Canadian Geotechnical Journal* 48.11, pp. 1696–1712. ISSN: 0008-3674. DOI: 10.1139/t11-059 (cit. on p. 2).

Lube, G. et al. (2014). "Dynamics of Surges Generated by Hydrothermal Blasts during the 6 August 2012 Te Maari Eruption, Mt. Tongariro, New Zealand". In: *Journal of Volcanology and Geothermal Research* 286, pp. 348–366. ISSN: 0377-0273. DOI: 10.1016/j.jvolgeores.2014.05.010 (cit. on p. 115).

Luca, I., Y. C. Tai, and C. Y. Kuo (2009a). "Non-Cartesian, Topography-Based Avalanche Equations and Approximations of Gravity Driven Flows of Ideal and Viscous Flows". en. In: *Mathematical Models and Methods in Applied Sciences* 19.01, pp. 127–171. ISSN: 0218-2025, 1793-6314. DOI: 10.1142/S0218202509003371 (cit. on pp. 30, 34, 36, 76).

Luca, I. et al. (2009b). "A Hierarchy of Avalanche Models on Arbitrary Topography". en. In: *Acta Mechanica* 205.1-4, pp. 121–149. ISSN: 0001-5970, 1619-6937. DOI: 10.1007/s00707-009-0165-4 (cit. on pp. 13, 57).

Lucas, A. and A. Mangeney (2007). "Mobility and Topographic Effects for Large Valles Marineris Landslides on Mars". en. In: *Geophysical Research Letters* 34.10. ISSN: 0094-8276. DOI: 10.1029/2007GL029835 (cit. on pp. 37, 146, 160).

Lucas, A. (2010). "Dynamique Des Instabilités Gravitaires Par Modélisation et Télédétection: Applications Aux Exemples Martiens". Theses. Institut de physique du globe de paris - IPGP (cit. on pp. 58, 73, 260).

Lucas, A., A. Mangeney, and J. P. Ampuero (2014). "Frictional Velocity-Weakening in Landslides on Earth and on Other Planetary Bodies". In: *Nature Communications* 5. ISSN: 2041-1723.

DOI: 10.1038/ncomms4417 (cit. on pp. 6, 9, 10, 37, 38, 59, 77, 105, 106, 109–111, 113, 117, 124, 146, 156, 160, 161, 177, 178, 183, 184, 196, 197, 199, 200, 262, 263, 267).

Lucas, A. et al. (2007). "Benchmarking Exercises for Granual Flows". In: *The 2007 International Forum on Landslide Disaster Management*. Hong Kong: Ho & Li (cit. on pp. 178, 184).

Lucas, A. et al. (2011). "Influence of the Scar Geometry on Landslide Dynamics and Deposits: Application to Martian Landslides". en. In: *Journal of Geophysical Research* 116.E10. ISSN: 0148-0227. DOI: 10.1029/2011JE003803 (cit. on pp. 37, 113, 142, 200).

Lusso, C. et al. (2017a). "A Free Interface Model for Static/Flowing Dynamics in Thin-Layer Flows of Granular Materials with Yield: Simple Shear Simulations and Comparison with Experiments". en. In: p. 27 (cit. on pp. 8, 162).

Lusso, C. et al. (2017b). "Two-Dimensional Simulation by Regularization of Free Surface Viscoplastic Flows with Drucker–Prager Yield Stress and Application to Granular Collapse". en. In: *Journal of Computational Physics* 333, pp. 387–408. ISSN: 00219991. DOI: 10.1016/j.jcp.2016.12.036 (cit. on p. 11).

Lyu, L. et al. (2017). "The Role of Bank Erosion on the Initiation and Motion of Gully Debris Flows". en. In: *Geomorphology* 285, pp. 137–151. ISSN: 0169-555X. DOI: 10.1016/j.geomorph.2017.02.008 (cit. on p. 163).

Ma, G., J. T. Kirby, and F. Shi (2013). "Numerical Simulation of Tsunami Waves Generated by Deformable Submarine Landslides". en. In: *Ocean Modelling* 69, pp. 146–165. ISSN: 1463-5003. DOI: 10.1016/j.ocemod.2013.07.001 (cit. on p. 60).

Macías, J. et al. (2015). "The Al-Borani Submarine Landslide and Associated Tsunami. A Modelling Approach". en. In: *Marine Geology* 361, pp. 79–95. ISSN: 0025-3227. DOI: 10.1016/j.margeo.2014.12.006 (cit. on pp. 94, 97).

Malet, J.-P. et al. (2002). "Caractérisation rhéologique des coulées de débris et des laves torrentielles du bassin marneux de Barcelonnette". fr. In: *Rhéologie* 1, pp. 17–25 (cit. on p. 77).

Malet, J.-P. (2003). "Les 'glissements de type écoulement' dans les marnes noires des Alpes du Sud. Morphologie, fonctionnement et modélisation hydro-mécanique". fr. PhD thesis. Université Louis Pasteur – Strasbourg I (cit. on pp. 6, 7).

Mangeney, A., P. Heinrich, and R. Roche (2000a). "Analytical Solution for Testing Debris Avalanche Numerical Models". In: *Pure and Applied Geophysics* 157.6-8, pp. 1081–1096. ISSN: 0033-4553, 1420-9136. DOI: 10.1007/s000240050018 (cit. on pp. 160, 177).

Mangeney, A. et al. (2000b). "Modeling of Debris Avalanche and Generated Water Waves: Application to Real and Potential Events in Montserrat". In: *Physics and Chemistry of the Earth, Part A: Solid Earth and Geodesy* 25.9-11, pp. 741–745 (cit. on pp. xii, xviii).

Mangeney, A. et al. (2007a). "Avalanche Mobility Induced by the Presence of an Erodible Bed and Associated Entrainment". en. In: *Geophysical Research Letters* 34.22. ISSN: 0094-8276. DOI: 10.1029/2007GL031348 (cit. on p. 124).

Mangeney, A. et al. (2007b). "Numerical Modeling of Self-Channeling Granular Flows and of Their Levee-Channel Deposits". en. In: *Journal of Geophysical Research* 112.F2. ISSN: 0148-0227. DOI: 10.1029/2006JF000469 (cit. on pp. xi, xvi, 6, 12, 16, 20, 23, 31, 32, 37, 77, 106, 140, 146, 178, 183).

Mangeney, A. et al. (2010). "Erosion and Mobility in Granular Collapse over Sloping Beds". en. In: *Journal of Geophysical Research* 115.F3. ISSN: 0148-0227. DOI: 10.1029/2009JF001462 (cit. on pp. 9, 162).

Mangeney, A. (2011). "Landslide Boost from Entrainment". en. In: *Nature Geoscience* 4.2, pp. 77–78. ISSN: 1752-0908. DOI: 10.1038/ngeo1077 (cit. on p. 9).

Mangeney-Castelnau, A. et al. (2003). "Numerical Modeling of Avalanches Based on Saint Venant Equations Using a Kinetic Scheme". en. In: *Journal of Geophysical Research* 108.B11, p. 2527. ISSN: 0148-0227. DOI: 10.1029/2002JB002024 (cit. on pp. 34, 40, 255).

Mangeney-Castelnau, A. et al. (2005). "On the Use of Saint Venant Equations to Simulate the Spreading of a Granular Mass: Numerical Simulation of Granular Spreading". en. In: *Journal*

of Geophysical Research: Solid Earth 110.B9. ISSN: 01480227. DOI: 10.1029/2004JB003161 (cit. on pp. xi, xvi, 124, 146, 178, 183).

Marcial, S. et al. (1996). "Instrumental Lahar Monitoring at Mount Pinatubo". en. In: *Fire and Mud: Eruptions and Lahars of Mount Pinatubo, Philippines*. C.G. Newhall and R.S. Punongbayan. University of Washington Press, p. 32 (cit. on p. 137).

Marinelli, G. et al. (2015). "Back Analysis of Johnsons Landing 2012 Landslide Using Two Dynamic Analysis Models". en. In: *Engineering Geology for Society and Territory - Volume 2*. Cham: Springer International Publishing, pp. 1267–1270. DOI: 10.1007/978-3-319-09057-3_222 (cit. on p. 10).

Marra, F. et al. (2016). "Space–Time Organization of Debris Flows-Triggering Rainfall and Its Effect on the Identification of the Rainfall Threshold Relationship". en. In: *Journal of Hydrology*. Flash Floods, Hydro-Geomorphic Response and Risk Management 541, pp. 246–255. ISSN: 0022-1694. DOI: 10.1016/j.jhydrol.2015.10.010 (cit. on p. 166).

Marre, A. (1987). "Le mouvement de terrain de Rilly-la-Montagne du 23 août 1986: naissance et évolution". fre. In: *Travaux de l'Institut de Géographie de Reims* 69.1, pp. 95–111. DOI: 10.3406/tigr.1987.1212 (cit. on p. 1).

Martin, N. et al. (2017). "Continuum Viscoplastic Simulation of a Granular Column Collapse on Large Slopes: Mu(I)-Rheology and Lateral Wall Effects". en. In: *Physics of Fluids* 29.1, p. 013301. ISSN: 1070-6631, 1089-7666. DOI: 10.1063/1.4971320 (cit. on p. 11).

Mathieu, L. et al. (2013). "The Structure and Morphology of the Basse Terre Island, Lesser Antilles Volcanic Arc". en. In: *Bulletin of Volcanology* 75.3, p. 700. ISSN: 1432-0819. DOI: 10.1007/s00445-013-0700-y (cit. on p. 102).

Mathon, C. and A. Barras (2010). *Risque d'occurence de Lave Torrentielle Dans La Rivière Du Prêcheur Suite à l'éboulement Du 11 Mai 2010*. Rapport d'expertise BRGM/RP - 58697-FR. BRGM (cit. on pp. 128, 132, 140).

McArdell, B. W. et al. (2003). "Systematic Comparison of Debris-Flow Laws at the Illgraben Torrent, Switzerland". en. In: *Debris-Flow Hazards Mitigation. Mechanics, Prediction, and Assessment. Proc. of the Third Int. Conf. on Debris-Flow Hazards Mitigation*. Davos, Switzerland: Millpress, p. 11 (cit. on p. 77).

McDougall, S. (2017). "2014 Canadian Geotechnical Colloquium: Landslide Runout Analysis — Current Practice and Challenges". en. In: *Canadian Geotechnical Journal* 54.5, pp. 605–620. ISSN: 0008-3674, 1208-6010. DOI: 10.1139/cgj-2016-0104 (cit. on pp. xi, xvi, 6, 22, 38, 124, 177).

McDougall, S. and O. Hungr (2004). "A Model for the Analysis of Rapid Landslide Motion across Three-Dimensional Terrain". en. In: *Canadian Geotechnical Journal* 41.6, pp. 1084–1097. ISSN: 0008-3674, 1208-6010. DOI: 10.1139/t04-052 (cit. on pp. 12, 30, 31).

McDougall, S. and O. Hungr (2005). "Dynamic Modelling of Entrainment in Rapid Landslides". en. In: *Canadian Geotechnical Journal* 42.5, pp. 1437–1448. ISSN: 0008-3674, 1208-6010. DOI: 10.1139/t05-064 (cit. on pp. 8, 162, 177).

McGuire, L. A. et al. (2017). "Debris Flow Initiation by Runoff in a Recently Burned Basin: Is Grain-by-Grain Sediment Bulking or En Masse Failure to Blame?: DEBRIS FLOW INITIATION". en. In: *Geophysical Research Letters* 44.14, pp. 7310–7319. ISSN: 00948276. DOI: 10.1002/2017GL074243 (cit. on p. 162).

Melo, R. and J. L. Zêzere (2017). "Modeling Debris Flow Initiation and Run-out in Recently Burned Areas Using Data-Driven Methods". en. In: *Natural Hazards* 88.3, pp. 1373–1407. ISSN: 1573-0840. DOI: 10.1007/s11069-017-2921-4 (cit. on p. 10).

Mergili, M. et al. (2017). "R.Avaflow v1, an Advanced Open Source Computational Framework for the Propagation and Interaction of Two-Phase Mass Flows". en. In: *Geoscientific Model Development Discussions*, pp. 1–30. ISSN: 1991-962X. DOI: 10.5194/gmd-2016-218 (cit. on pp. 31, 103, 124, 164).

Mergili, M. et al. (2018). "Computational Experiments on the 1962 and 1970 Landslide Events at Huascarán (Peru) with r.Avaflow: Lessons Learned for Predictive Mass Flow Simulations". en. In: *Geomorphology* 322, pp. 15–28. ISSN: 0169-555X. DOI: 10.1016/j.geomorph.2018.08.032 (cit. on pp. 59, 166, 178, 196).

Mergili, M. et al. (2020). "Back Calculation of the 2017 Piz Cengalo–Bondo Landslide Cascade with r.Avaflow: What We Can Do and What We Can Learn". English. In: *Natural Hazards and Earth System Sciences* 20.2, pp. 505–520. ISSN: 1561-8633. DOI: 10.5194/nhess-20-505-2020 (cit. on p. 125).

Meunier, M. (1999). *Les torrents du Nord-Ouest de la Martinique. Hydrologie des crues, érosion, hydraulique et dynamique torrentielles - Collectif*. fr. Cemagref. ISBN: 2-85362-526-5 (cit. on pp. 135, 137).

Meunier, M. (1991). *Eléments d'hydraulique Torrentielle*. Études Montagnes. Dicova, SEMAGREF (cit. on pp. 4, 5).

Meunier, M. (1994). "Les progrès de la connaissance et les méthodes d'étude des phénomènes torrentiels". fr. In: *La Houille Blanche* 3, pp. 25–31. ISSN: 0018-6368, 1958-5551. DOI: 10.1051/lhb/1994039 (cit. on pp. 4, 5).

Mitchell, A. et al. (2019). "Rock Avalanche Runout Prediction Using Stochastic Analysis of a Regional Dataset". en. In: *Landslides*. ISSN: 1612-510X, 1612-5118. DOI: 10.1007/s10346-019-01331-3 (cit. on pp. 9, 10, 59, 178, 183, 196, 197, 199, 268).

Mitchell, A. et al. (2018). "New Empirical-Statistical Tools for the Analysis of Rock Avalanche Runout". en. In: *7th Canadian Geohazards Conference*. Canmore, Alberta, Canada, p. 7 (cit. on p. 177).

Moase, E., A. Strouth, and A. Mitchell (2018). "A Comparison of Different Approaches for Modelling a Fine-Grained Debris Flow at Seton Portage, British Columbia, Canada". en. In: *Hong Kong*, p. 4 (cit. on pp. 12, 30, 166).

Moretti, L. et al. (2020a). "Constraining Landslide Characteristics with Bayesian Inversion of Field and Seismic Data". en. In: *Geophysical Journal International* 221.2, pp. 1341–1348. ISSN: 0956-540X, 1365-246X. DOI: 10.1093/gji/ggaa056 (cit. on pp. xi, xvi, 37, 43, 124, 146, 178).

Moretti, L. et al. (2012). "Numerical Modeling of the Mount Steller Landslide Flow History and of the Generated Long Period Seismic Waves". en. In: *Geophysical Research Letters* 39.16, n/a–n/a. ISSN: 00948276. DOI: 10.1029/2012GL052511 (cit. on pp. 106, 124).

Moretti, L. et al. (2015). "Numerical Modeling of the Mount Meager Landslide Constrained by Its Force History Derived from Seismic Data". en. In: *Journal of Geophysical Research: Solid Earth* 120.4, pp. 2579–2599. ISSN: 21699313. DOI: 10.1002/2014JB011426 (cit. on pp. 12, 23, 37, 43, 45, 106, 113, 124, 146, 160, 178, 184).

Moretti, R. et al. (2018). "The 2018 February-April Unrest Phase at La Soufrière of Guadeloupe (French West Indies) Andesitic Volcano: Deep Magmatic Fluid Transfer into the Hydrothermal System and Dome-Structure Modulation". en. In: *Cities on Volcanoes 10 International Meeting, Naples, Italy, 2-7 September 2018, Abstracts Volume*. IAVCEI, p. 3 (cit. on pp. 98, 102).

Moretti, R. et al. (2020b). "The 2018 Unrest Phase at La Soufrière of Guadeloupe (French West Indies) Andesitic Volcano: Scrutiny of a Failed but Prodromal Phreatic Eruption". en. In: *Journal of Volcanology and Geothermal Research* 393, p. 106769. ISSN: 0377-0273. DOI: 10.1016/j.jvolgeores.2020.106769 (cit. on pp. 98, 102).

Morgan, J. K. and P. J. McGovern (2005). "Discrete Element Simulations of Gravitational Volcanic Deformation: 2. Mechanical Analysis". en. In: *Journal of Geophysical Research* 110.B5, B05403. ISSN: 0148-0227. DOI: 10.1029/2004JB003253 (cit. on p. 102).

Nachbaur, A. et al. (2019). *Caractérisation Géologique et Identification Des Mécanismes d'instabilité de La Falaise Samperre*. Rapport Final RP-68564-FR. BRGM, p. 69 (cit. on pp. 50, 119, 122, 128, 132, 133, 145, 179, 180, 264).

Nakamura, Y. and H. Glicken (1988). "Blast and Debris-Avalanche Deposits of the 1888 Eruption, Bandai Volcano". en. In: *Journal of Geography (Chigaku Zasshi)* 97.4, pp. 309–316. ISSN: 0022-135X, 1884-0884. DOI: 10.5026/jgeography.97.4_309 (cit. on p. 106).

Nicollin, F. et al. (2006). "Electrical Tomography of La Soufrière of Guadeloupe Volcano: Field Experiments, 1D Inversion and Qualitative Interpretation". In: *Earth and Planetary Science Letters* 244.3, pp. 709–724. ISSN: 0012-821X. DOI: 10.1016/j.epsl.2006.02.020 (cit. on p. 100).

Nicollin, F. et al. (2007). "Reply to Comment on "Electrical Tomography of La Soufrière of Guadeloupe Volcano: Field Experiments, 1D Inversion and Qualitative Interpretation" by N. Linde and A. Revil". In: *Earth and Planetary Science Letters* 258.3-4, pp. 623–626. DOI: 10.1016/j.epsl.2007.04.005 (cit. on p. 100).

O'Brien, J. S., P. Y. Julien, and W. T. Fullerton (1993). "Two-Dimensional Water Flood and Mudflow Simulation". In: *Journal of hydraulic engineering* 119.2, pp. 244–261 (cit. on pp. 12, 30, 31, 39, 77).

OVSG-IPGP (2018a). *Bulletin Mensuel de l'activité Volcanique et Sismique de Guadeloupe*. Monthly Public Report 2018-04. Institut de Physique du Globe de Paris, Gourbeyre (cit. on pp. 98, 102).

OVSG-IPGP (2018b). *Bulletin Mensuel de l'activité Volcanique et Sismique de Guadeloupe*. Monthly Public Report 2018-02. Institut de Physique du Globe de Paris, Gourbeyre (cit. on pp. 98, 102).

OVSM-IPGP (2020). *Bulletin Mensuel de l'Observatoire Volcanologique et Sismologique de Martinique*. Tech. rep. 2020-03. IPGP (cit. on p. 128).

Pailha, M. and O. Pouliquen (2009). "A Two-Phase Flow Description of the Initiation of Underwater Granular Avalanches". en. In: *Journal of Fluid Mechanics* 633, pp. 115–135. ISSN: 1469-7645, 0022-1120. DOI: 10.1017/S0022112009007460 (cit. on p. 8).

Pallares, C. et al. (2015). "Geological and Geotechnical Characteristics of Recent Lahar Deposits from El Misti Volcano in the City Area of Arequipa, South Peru". en. In: *Geotechnical and Geological Engineering* 33.3, pp. 641–660. ISSN: 0960-3182, 1573-1529. DOI: 10.1007/s10706-015-9848-x (cit. on p. 138).

Pannet, P. (2018). *Glissement de Terrain Sur La Commune de Festigny (Marne)*. Tech. rep. RP-56395-FR. BRGM (cit. on pp. ix, xiv).

Pannet, P., D. Charles, and L. Guillen (2015). *Glissement de terrain à Boursault (51)*. fr. Tech. rep. RP-64849-FR. BRGM, p. 24 (cit. on pp. ix, xiv).

Papa, M. N. et al. (2013). "Derivation of Critical Rainfall Thresholds for Shallow Landslides as a Tool for Debris Flow Early Warning Systems". English. In: *Hydrology and Earth System Sciences* 17.10, pp. 4095–4107. ISSN: 1027-5606. DOI: 10.5194/hess-17-4095-2013 (cit. on p. 166).

Pastor, M. et al. (2018a). "Review of Benchmarking Exercise on Landslide Runout Analysis 2018". en. In: *Hong Kong*, p. 65 (cit. on pp. xi, xvi, 10, 12, 32, 90, 124, 146).

Pastor, M., T. Blanc, and M. Pastor (2009a). "A Depth-Integrated Viscoplastic Model for Dilatant Saturated Cohesive-Frictional Fluidized Mixtures: Application to Fast Catastrophic Landslides". en. In: *Journal of Non-Newtonian Fluid Mechanics* 158.1-3, pp. 142–153. ISSN: 03770257. DOI: 10.1016/j.jnnfm.2008.07.014 (cit. on pp. 12, 21, 22, 57).

Pastor, M. et al. (2004). "Simple Approximation to Bottom Friction for Bingham Fluid Depth Integrated Models". en. In: *Journal of Hydraulic Engineering* 130.2, pp. 149–155. ISSN: 0733-9429, 1943-7900. DOI: 10.1061/(ASCE)0733-9429(2004)130:2(149) (cit. on pp. 21, 57, 177).

Pastor, M. et al. (2009b). "A Depth-Integrated, Coupled SPH Model for Flow-like Landslides and Related Phenomena". en. In: *International Journal for Numerical and Analytical Methods in Geomechanics* 33.2, pp. 143–172. ISSN: 03639061, 10969853. DOI: 10.1002/nag.705 (cit. on p. 31).

Pastor, M. et al. (2015). "A Viscoplastic Approach to the Behaviour of Fluidized Geomaterials with Application to Fast Landslides". en. In: *Continuum Mechanics and Thermodynamics* 27.1-2, pp. 21–47. ISSN: 0935-1175, 1432-0959. DOI: 10.1007/s00161-013-0326-5 (cit. on p. 77).

Pastor, M. et al. (2018b). "A Two-Phase SPH Model for Debris Flow Propagation". en. In: *International Journal for Numerical and Analytical Methods in Geomechanics* 42.3, pp. 418–448. ISSN: 03639061. DOI: 10.1002/nag.2748 (cit. on pp. 12, 30, 31, 124, 164).

Pastorello, R., T. Michelini, and V. D'Agostino (2017). "On the Criteria to Create a Susceptibility Map to Debris Flow at a Regional Scale Using Flow-R". en. In: *Journal of Mountain Science* 14.4, pp. 621–635. ISSN: 1993-0321. DOI: 10.1007/s11629-016-4077-1 (cit. on p. 10).

Patra, A. et al. (2005). "Parallel Adaptive Numerical Simulation of Dry Avalanches over Natural Terrain". en. In: *Journal of Volcanology and Geothermal Research* 139.1-2, pp. 1–21. ISSN: 03770273. DOI: 10.1016/j.jvolgeores.2004.06.014 (cit. on p. 31).

Peruzzetto, M. et al. (2018a). "Back-Analysis of a Rock Avalanche and a Debris Flow with the SHALTOP Code". en. In: *Proceedings of the Second JTC1 Workshop on Triggering and Propagation of Rapid Flow-like Landslides*. Hong Kong, p. 4 (cit. on pp. 90, 146).

Peruzzetto, M. et al. (2018b). "Analysis of Curvature Effects for Frictional Rheologies in Thin-Layer Depth-Averaged Flow Propagation Models". In: *EGU, Mechanics of Mass Flows, Poster* (cit. on p. 146).

Peruzzetto, M. et al. (2019). "Modeling of Partial Dome Collapse of La Soufrière of Guadeloupe Volcano: Implications for Hazard Assessment and Monitoring". en. In: *Scientific Reports* 9.1, pp. 1–15. ISSN: 2045-2322. DOI: 10.1038/s41598-019-49507-0 (cit. on pp. 6, 10, 12, 37, 53, 56, 71, 124, 146, 160, 166, 178, 197).

Petley, D. (2012). "Global Patterns of Loss of Life from Landslides". en. In: *Geology* 40.10, pp. 927–930. ISSN: 0091-7613. DOI: 10.1130/G33217.1 (cit. on pp. ix, xiv, 30).

Picarelli, L. et al. (2005). "Main Features of Mudslides in Tectonised Highly Fissured Clay Shales". In: DOI: 10.1007/S10346-004-0040-2 (cit. on p. 2).

Pirulli, M., A. Leonardi, and C. Scavia (2018). "Comparison of Depth-Averaged and Full-3D Model for the Benchmarking Exercise on Lanslide Runout". en. In: *Hong Kong*, p. 14 (cit. on p. 60).

Pirulli, M. and A. Mangeney (2008). "Results of Back-Analysis of the Propagation of Rock Avalanches as a Function of the Assumed Rheology". en. In: *Rock Mechanics and Rock Engineering* 41.1, pp. 59–84. ISSN: 0723-2632, 1434-453X. DOI: 10.1007/s00603-007-0143-x (cit. on pp. 45, 124, 199).

Pirulli, M. and M. Pastor (2012). "Numerical Study on the Entrainment of Bed Material into Rapid Landslides". en. In: *Géotechnique* 62.11, pp. 959–972. ISSN: 0016-8505, 1751-7656. DOI: 10.1680/geot.10.P.074 (cit. on pp. 8, 9, 12, 30, 31, 124, 162, 177).

Pirulli, M. (2009). "The Thurwieser Rock Avalanche (Italian Alps): Description and Dynamic Analysis". en. In: *Engineering Geology*. The Mechanics and Velocity of Large Landslides 109.1, pp. 80–92. ISSN: 0013-7952. DOI: 10.1016/j.enggeo.2008.10.007 (cit. on p. 5).

Pirulli, M. et al. (2007). "The Effect of the Earth Pressure Coefficients on the Runout of Granular Material". en. In: *Environmental Modelling & Software* 22.10, pp. 1437–1454. ISSN: 13648152. DOI: 10.1016/j.envsoft.2006.06.006 (cit. on pp. 12, 31, 57).

Pitman, E. B. and L. Le (2005). "A Two-Fluid Model for Avalanche and Debris Flows". en. In: *Philosophical Transactions of the Royal Society A: Mathematical, Physical and Engineering Sciences* 363.1832, pp. 1573–1601. ISSN: 1364-503X, 1471-2962. DOI: 10.1098/rsta.2005.1596 (cit. on p. 31).

Pitman, E. B. et al. (2003). "Computing Granular Avalanches and Landslides". en. In: *Physics of Fluids* 15.12, pp. 3638–3646. ISSN: 1070-6631, 1089-7666. DOI: 10.1063/1.1614253 (cit. on pp. 33, 39).

Pouliquen, O. and Y. Forterre (2002). "Friction Law for Dense Granular Flows: Application to the Motion of a Mass down a Rough Inclined Plane". en. In: *Journal of Fluid Mechanics* 453. ISSN: 0022-1120, 1469-7645. DOI: 10.1017/S0022112001006796 (cit. on pp. 16, 20, 21, 106).

Prime, N., F. Dufour, and F. Darve (2014a). "Unified Model for Geomaterial Solid/Fluid States and the Transition in Between". en. In: *Journal of Engineering Mechanics* 140.6, p. 04014031. ISSN: 0733-9399, 1943-7889. DOI: 10.1061/(ASCE)EM.1943-7889.0000742 (cit. on p. 8).

Prime, N., F. Dufour, and F. Darve (2014b). "Solid-Fluid Transition Modelling in Geomaterials and Application to a Mudflow Interacting with an Obstacle". en. In: *International Journal for Numerical and Analytical Methods in Geomechanics* 38.13, pp. 1341–1361. ISSN: 03639061. DOI: 10.1002/nag.2260 (cit. on pp. 11, 177).

Prochaska, A. B. et al. (2008). "A Study of Methods to Estimate Debris Flow Velocity". en. In: *Landslides* 5.4, pp. 431–444. ISSN: 1612-510X, 1612-5118. DOI: 10.1007/s10346-008-0137-0 (cit. on p. 59).

Procter, J. N. et al. (2014). "Debris Flow Evolution and the Activation of an Explosive Hydrothermal System; Te Maari, Tongariro, New Zealand". In: *Journal of Volcanology and Geothermal Research* 286, pp. 303–316. ISSN: 0377-0273. DOI: 10.1016/j.jvolgeores.2014.07.006 (cit. on p. 115).

Pudasaini, S. P. (2012). "A General Two-phase Debris Flow Model". en. In: *Journal of Geophysical Research: Earth Surface* 117.F3. ISSN: 2156-2202. DOI: 10.1029/2011JF002186 (cit. on pp. 12, 30, 31).

Pudasaini, S. P., W. Eckart, and K. Hutter (2003). "Gravity-Driven Rapid Shear Flows of Dry Granular Masses in Helically Curved and Twisted Channels". en. In: *Mathematical Models and Methods in Applied Sciences* 13.07, pp. 1019–1052. ISSN: 0218-2025, 1793-6314. DOI: 10.1142/S0218202503002805 (cit. on p. 30).

Pudasaini, S. P. and K. Hutter (2003). "Rapid Shear Flows of Dry Granular Masses down Curved and Twisted Channels". en. In: *Journal of Fluid Mechanics* 495, pp. 193–208. ISSN: 00221120, 14697645. DOI: 10.1017/S0022112003006141 (cit. on pp. 30, 41).

Pudasaini, S. P. and M. Mergili (2019). "A Multi-Phase Mass Flow Model". en. In: *Journal of Geophysical Research: Earth Surface* 124.12, pp. 2920–2942. ISSN: 2169-9011. DOI: 10.1029/2019JF005204 (cit. on pp. 57, 124, 164, 177).

Quan Luna, B. et al. (2012). "Analysis of Debris Flow Behavior with a One Dimensional Run-out Model Incorporating Entrainment". en. In: *Engineering Geology*. Integration of Technologies for Landslide Monitoring and Quantitative Hazard Assessment 128, pp. 63–75. ISSN: 0013-7952. DOI: 10.1016/j.enggeo.2011.04.007 (cit. on p. 6).

Quefféléan, Y. (2018a). *Mission d'expertise ONF-RTM Sur Les Lahars Du Prêcheur*. Tech. rep. ONF-RTM (cit. on pp. 50, 119, 122, 128, 133–135, 137, 166, 167, 179).

Quefféléan, Y. (2018b). *Mission ONF/RTM Sur Les Lahars Au Prêcheur*. Fort-de-France (cit. on p. 134).

Rauter, M. and Z. Tukovic (2018). "A Finite Area Scheme for Shallow Granular Flows on Three-Dimensional Surfaces". en. In: *Computers & Fluids* 166, pp. 184–199. ISSN: 00457930. DOI: 10.1016/j.compfluid.2018.02.017. arXiv: 1802.05229 (cit. on pp. 30, 40, 42).

Rauter, M. et al. (2018). "faSavageHutterFOAM 1.0: Depth-Integrated Simulation of Dense Snow Avalanches on Natural Terrain with OpenFOAM". en. In: *Geoscientific Model Development* 11.7, pp. 2923–2939. ISSN: 1991-9603. DOI: 10.5194/gmd-11-2923-2018 (cit. on p. 42).

Reichenbach, P. et al. (2018). "A Review of Statistically-Based Landslide Susceptibility Models". en. In: *Earth-Science Reviews* 180, pp. 60–91. ISSN: 0012-8252. DOI: 10.1016/j.earscirev.2018.03.001 (cit. on p. 9).

Reid, M. E. (2004). "Massive Collapse of Volcano Edifices Triggered by Hydrothermal Pressurization". en. In: *Geology* 32.5, pp. 373–376. ISSN: 0091-7613. DOI: 10.1130/G20300.1 (cit. on p. 102).

Remaître, A. (2006). "Morphologie et Dynamique Des Laves Torrentielles : Applications Aux Torrents Des Terres Noires Du Bassin de Barcelonnette (Alpes Du Sud)". PhD thesis. Université de Caen/Basse-Normandie (cit. on pp. 6, 8).

Remaître, A., J.-P. Malet, and O. Maquaire (2011). "Geomorphology and Kinematics of Debris Flows with High Entrainment Rates: A Case Study in the South French Alps". en. In: *Comptes Rendus Geoscience* 343.11, pp. 777–794. ISSN: 1631-0713. DOI: 10.1016/j.crte.2011.09.007 (cit. on p. 2).

Ricci, J. et al. (2017). "High-Resolution K-Ar Dating of a Complex Magmatic System: The Example of Basse-Terre Island (French West Indies)". en. In: *Journal of Volcanology and Geothermal Research* 345, pp. 142–160. ISSN: 0377-0273. DOI: 10.1016/j.jvolgeores.2017.07.013 (cit. on p. 98).

Rickenmann, D. (1999). "Empirical Relationships for Debris Flows". en. In: *Natural Hazards* 19.1, pp. 47–77 (cit. on pp. 10, 156).

Rohmer, J. and E. Foerster (2011). "Global Sensitivity Analysis of Large-Scale Numerical Landslide Models Based on Gaussian-Process Meta-Modeling". en. In: *Computers & Geosciences* 37.7, pp. 917–927. ISSN: 00983004. DOI: 10.1016/j.cageo.2011.02.020 (cit. on pp. 178, 184).

Rosas-Carbajal, M. et al. (2017). "Three-Dimensional Density Structure of La Soufrière de Guadeloupe Lava Dome from Simultaneous Muon Radiographies and Gravity Data: 3-D MUON TOMOGRAPHY OF LA SOUFRIÈRE". en. In: *Geophysical Research Letters* 44.13, pp. 6743–6751. ISSN: 00948276. DOI: 10.1002/2017GL074285 (cit. on pp. 100, 115).

Rosas-Carbajal, M. et al. (2016). "Volcano Electrical Tomography Unveils Edifice Collapse Hazard Linked to Hydrothermal System Structure and Dynamics". en. In: *Scientific Reports* 6.1. ISSN: 2045-2322. DOI: 10.1038/srep29899 (cit. on pp. 98, 100, 102, 103, 115, 261).

Rosatti, G. and L. Begnudelli (2013). "Two-Dimensional Simulation of Debris Flows over Mobile Bed: Enhancing the TRENT2D Model by Using a Well-Balanced Generalized Roe-Type Solver". en. In: *Computers & Fluids* 71, pp. 179–195. ISSN: 0045-7930. DOI: 10.1016/j.compfluid.2012.10.006 (cit. on pp. 30, 31).

Roth, D. L. et al. (2016). "Bed Load Sediment Transport Inferred from Seismic Signals near a River". en. In: *Journal of Geophysical Research: Earth Surface* 121.4, pp. 725–747. ISSN: 2169-9011. DOI: 10.1002/2015JF003782 (cit. on p. 167).

Roy, G. L. et al. (2019). "Seismic Analysis of the Detachment and Impact Phases of a Rockfall and Application for Estimating Rockfall Volume and Free-Fall Height". en. In: *Journal of Geophysical Research: Earth Surface* 124.11, pp. 2602–2622. ISSN: 2169-9011. DOI: 10.1029/2019JF004999 (cit. on p. 1).

SafeLand (2012). *Landslide Triggering Mechanisms in Europe – Overview and State of the Art*. en. Delivrable 1.1. SafeLand, p. 378 (cit. on p. 4).

Salaün, A. et al. (2011). "Hydrothermal Alteration in Andesitic Volcanoes: Trace Element Redistribution in Active and Ancient Hydrothermal Systems of Guadeloupe (Lesser Antilles)". English. In: *Journal of Geochemical Exploration* 3.111, pp. 59–83. ISSN: 0375-6742. DOI: 10.1016/j.gexplo.2011.06.004 (cit. on p. 100).

Salm, B. (1993). "Flow, Flow Transition and Runout Distances of Flowing Avalanches". In: *Annals of Glaciology* 18 (cit. on pp. 22, 37, 59, 146, 177).

Salm, B. (1967). "On Nonuniform, Steady Flow Flow Avalanching Snow". en. In: *Assemblée Générale de Berne*. Vol. 79. IAHS, Wallingford, Owfordshire, U.K., pp. 19–29 (cit. on p. 30).

Salm, B., A. Burkard, and H. U. Gubler (1990). *Berechnung von Fliesslawinen: eine Anleitung fuer Praktiker mit Beispielen*. German. Weissfluhjoch/Davos: Eidgenössische Institut für Schnee- und Lawinenforschung (cit. on p. 59).

Samper, A. et al. (2009). "Effusive History of the Grande Découverte Volcanic Complex, Southern Basse-Terre (Guadeloupe, French West Indies) from New K–Ar Cassignol–Gillot Ages". en.

In: *Journal of Volcanology and Geothermal Research* 187.1, pp. 117–130. ISSN: 0377-0273. DOI: 10.1016/j.jvolgeores.2009.08.016 (cit. on p. 98).

Sassa, K. (1999). "Introduction". In: *Landslides of the World*. Kyoto University Press (cit. on p. 4).

Savage, S. B. and K. Hutter (1991). "The Dynamics of Avalanches of Granular Materials from Initiation to Runout. Part I: Analysis". In: *Acta Mechanica* 86.1, pp. 201–223 (cit. on pp. 11, 13, 14, 16, 30, 34, 39, 40, 57).

Schaefer, L. N. et al. (2013). "An Integrated Field-Numerical Approach to Assess Slope Stability Hazards at Volcanoes: The Example of Pacaya, Guatemala". en. In: *Bulletin of Volcanology* 75.6, p. 720. ISSN: 1432-0819. DOI: 10.1007/s00445-013-0720-7 (cit. on p. 102).

Scheidl, C., B. W. McArdell, and D. Rickenmann (2015). "Debris-Flow Velocities and Superelevation in a Curved Laboratory Channel". en. In: *Canadian Geotechnical Journal* 52.3, pp. 305–317. ISSN: 0008-3674, 1208-6010. DOI: 10.1139/cgj-2014-0081 (cit. on pp. 58, 59).

Schneider, D. et al. (2010). "Insights into Rock-Ice Avalanche Dynamics by Combined Analysis of Seismic Recordings and a Numerical Avalanche Model". en. In: *Journal of Geophysical Research* 115.F4. ISSN: 0148-0227. DOI: 10.1029/2010JF001734 (cit. on p. 147).

Schumm, S. A. and R. J. Chorley (1964). "The Fall of Threatening Rock". en. In: *American Journal of Science* 262.9, pp. 1041–1054. ISSN: 0002-9599, 1945-452X. DOI: 10.2475/ajs.262.9.1041 (cit. on p. 1).

Scott, K. M., P. T. Pringle, and J. Vallance (1995). *Sedimentology, Behavior, and Hazards of Debris Flows at Mount Rainier, Washington*. Professionnal Paper 1547. Reston, VA: U.S. Geological Survey. DOI: 10.3133/ofr90385 (cit. on p. 6).

Scott, K. M. et al. (2005). "Catastrophic Precipitation-Triggered Lahar at Casita Volcano, Nicaragua: Occurrence, Bulking and Transformation". en. In: *Earth Surface Processes and Landforms* 30.1, pp. 59–79. ISSN: 1096-9837. DOI: 10.1002/esp.1127 (cit. on p. 115).

Seabold, S. and J. Perktold (2010). "Statsmodels: Econometric and Statistical Modeling with Python". In: *Proceedings of the 9th Python in Science Conference* (cit. on pp. 147, 210).

Sharpe, C. F. S. (F. S. (1938). "Landslides and Related Phenomena". English. In: (cit. on p. 1).

Shen, P. et al. (2018). "EDDA 2.0: Integrated Simulation of Debris Flow Initiation and Dynamics Considering Two Initiation Mechanisms". en. In: *Geoscientific Model Development* 11.7, pp. 2841–2856. ISSN: 1991-9603. DOI: 10.5194/gmd-11-2841-2018 (cit. on p. 162).

Sheridan, M. F. (1980). "Pyroclastic Block Flow from the September, 1976, Eruption of La Soufrière Volcano, Guadeloupe". en. In: *Bulletin Volcanologique* 43.2, pp. 397–402. ISSN: 1432-0819. DOI: 10.1007/BF02598040 (cit. on p. 115).

Sibille, L. et al. (2007). "Material Instability in Granular Assemblies from Fundamentally Different Models". en. In: *International Journal for Numerical and Analytical Methods in Geomechanics* 31.3, pp. 457–481. ISSN: 1096-9853. DOI: 10.1002/nag.591 (cit. on p. 8).

Siebert, L., H. Glicken, and T. Ui (1987). "Volcanic Hazards from Bezymianny- and Bandai-Type Eruptions". en. In: *Bulletin of Volcanology* 49.1, pp. 435–459. ISSN: 1432-0819. DOI: 10.1007/BF01046635 (cit. on p. 106).

Sivakumaran, N. S., T. Tingsanchali, and R. J. Hosking (1983). "Steady Shallow Flow over Curved Beds". en. In: *Journal of Fluid Mechanics* 128, pp. 469–487. ISSN: 1469-7645, 0022-1120. DOI: 10.1017/S0022112083000567 (cit. on p. 11).

Sosio, R. and G. B. Crosta (2009). "Rheology of Concentrated Granular Suspensions and Possible Implications for Debris Flow Modeling". en. In: *Water Resources Research* 45.3. ISSN: 00431397. DOI: 10.1029/2008WR006920 (cit. on p. 77).

Sosio, R., G. B. Crosta, and O. Hungr (2012). "Numerical Modeling of Debris Avalanche Propagation from Collapse of Volcanic Edifices". en. In: *Landslides* 9.3, pp. 315–334. ISSN: 1612-510X, 1612-5118. DOI: 10.1007/s10346-011-0302-8 (cit. on pp. xii, xviii, 103, 106).

Staley, D. M. et al. (2017). "Prediction of Spatially Explicit Rainfall Intensity–Duration Thresholds for Post-Fire Debris-Flow Generation in the Western United States". en. In: *Geomor-*

phology 278, pp. 149–162. ISSN: 0169-555X. DOI: 10.1016/j.geomorph.2016.10.019 (cit. on p. 166).

Staron, L. and E. Lajeunesse (2009). "Understanding How Volume Affects the Mobility of Dry Debris Flows". en. In: *Geophysical Research Letters* 36.12. ISSN: 1944-8007. DOI: 10.1029/2009GL038229 (cit. on p. 160).

Strom, A. and K. Abdrakhmatov (2018). "Quantitative Relationships of Central Asian Bedrock Landslide Parameters". en. In: *Rockslides and Rock Avalanches of Central Asia*. Elsevier, pp. 335–347. ISBN: 978-0-12-803204-6. DOI: 10.1016/B978-0-12-803204-6.00010-7 (cit. on pp. 9, 177, 196, 199).

Synolakis, C. E. et al. (2009). "Validation and Verification of Tsunami Numerical Models". en. In: *Tsunami Science Four Years after the 2004 Indian Ocean Tsunami: Part I: Modelling and Hazard Assessment*. Ed. by P. R. Cummins, K. Satake, and L. S. L. Kong. Pageoph Topical Volumes. Basel: Birkhäuser, pp. 2197–2228. ISBN: 978-3-0346-0057-6. DOI: 10.1007/978-3-0346-0057-6_11 (cit. on pp. 94, 97).

Tang, H. et al. (2019). "Developing and Testing Physically Based Triggering Thresholds for Runoff-Generated Debris Flows". en. In: *Geophysical Research Letters* 46.15, pp. 8830–8839. ISSN: 1944-8007. DOI: 10.1029/2019GL083623 (cit. on p. 166).

Thiery, Y. and M. Terrier (2018). "Évaluation de l'aléa glissements de terrain : état de l'art et perspectives pour la cartographie réglementaire en France". fr. In: *Revue Française de Géotechnique* 156, p. 3. ISSN: 0181-0529, 2493-8653. DOI: 10.1051/geotech/2019003 (cit. on pp. xv, 9).

Thiery, Y. et al. (2017). "Landslide Susceptibility Assessment by EPBM (Expert Physically Based Model): Strategy of Calibration in Complex Environment". en. In: *Advancing Culture of Living with Landslides*. Ed. by M. Mikos et al. Cham: Springer International Publishing, pp. 917–926. ISBN: 978-3-319-53498-5. DOI: 10.1007/978-3-319-53498-5_104 (cit. on p. 177).

Thiery, Y. et al. (2020). "Improvement of Landslide Hazard Assessments for Regulatory Zoning in France: STATE–OF–THE-ART Perspectives and Considerations". en. In: *International Journal of Disaster Risk Reduction* 47, p. 101562. ISSN: 2212-4209. DOI: 10.1016/j.ijdrr.2020.101562 (cit. on pp. x, xv).

Thouret, J. .-C. et al. (2020). "Lahars and Debris Flows: Characteristics and Impacts". en. In: *Earth-Science Reviews* 201, p. 103003. ISSN: 0012-8252. DOI: 10.1016/j.earscirev.2019.103003 (cit. on pp. 2, 6, 124).

USGS (2004). *Landslide Types and Processes*. Fact Sheet 2004-3072 (cit. on pp. 2, 255).

Vallance, J. W. and R. M. Iverson (2015). "Lahars and Their Deposits". en. In: *The Encyclopedia of Volcanoes*. Elsevier, pp. 649–664. ISBN: 978-0-12-385938-9. DOI: 10.1016/B978-0-12-385938-9.00037-7 (cit. on pp. 2, 6, 8, 124, 167).

van Wyk de Vries, B. et al. (2001). "A Gravitational Spreading Origin for the Socompa Debris Avalanche". en. In: *Journal of Volcanology and Geothermal Research* 105.3, pp. 225–247. ISSN: 0377-0273. DOI: 10.1016/S0377-0273(00)00252-3 (cit. on p. 2).

Varnes, D. J. (1958). "Landslide Types and Processes". In: *Highway Research Board Special Report* 29 (cit. on pp. 1, 2, 4).

Varnes, D. J. (1978). "Slope Movement Types and Processes". In: *Landslides, Analysis and Control*. Special Reports 176. Transportation research board, National Academy of Sciences, pp. 11–33 (cit. on pp. 1, 2, 4).

Vilajosana, I. et al. (2008). "Rockfall Induced Seismic Signals: Case Study in Montserrat, Catalonia". en. In: *Natural Hazards and Earth System Sciences* 8.4, pp. 805–812. ISSN: 1684-9981. DOI: 10.5194/nhess-8-805-2008 (cit. on p. 147).

Ville, A., F. Lavigne, and F. Gob (2015). *La Dynamique Torrentielle et Sédimentaire Du Rorrent Du Prêcheur Suite Aux Lahars de 2010 (Martinique, Petites Antilles)*. Mémoire de Master 2 Dynarisk. Université Paris 1 Panthéon-Sorbonne (cit. on p. 166).

Villemant, B. et al. (2014). "Evidence for a New Shallow Magma Intrusion at La Soufrière of Guadeloupe (Lesser Antilles): Insights from Long-Term Geochemical Monitoring of Halogen-Rich Hydrothermal Fluids". In: *Journal of Volcanology and Geothermal Research* 285, pp. 247–277. ISSN: 0377-0273. DOI: 10.1016/j.jvolgeores.2014.08.002 (cit. on pp. 98, 100).

Villemant, B. et al. (2005). "The Memory of Volcanic Waters: Shallow Magma Degassing Revealed by Halogen Monitoring in Thermal Springs of La Soufrière Volcano (Guadeloupe, Lesser Antilles)". In: *Earth and Planetary Science Letters* 237.3, pp. 710–728. ISSN: 0012-821X. DOI: 10.1016/j.epsl.2005.05.013 (cit. on p. 98).

Viroulet, S. et al. (2019). "Shedding Dynamics and Mass Exchange by Dry Granular Waves Flowing over Erodible Beds". en. In: *Earth and Planetary Science Letters* 523, p. 115700. ISSN: 0012821X. DOI: 10.1016/j.epsl.2019.07.003 (cit. on p. 162).

Voellmy, A. (1955). "Uber Die Zerstorungskraft von Lawinen." In: *Schweizerische Bauzeitung, Jahrg.* 73, pp. 159–162, 212–217, 246–249, 280–285 (cit. on pp. 22, 37).

Voight, B. (2000). "Structural Stability of Andesite Volcanoes and Lava Domes". en. In: *Philosophical Transactions of the Royal Society of London. Series A: Mathematical, Physical and Engineering Sciences* 358.1770. Ed. by P. Francis, J. Neuberg, and R. S. J. Sparks, pp. 1663–1703. ISSN: 1471-2962. DOI: 10.1098/rsta.2000.0609 (cit. on pp. 100, 102).

Voight, B. and J. Sousa (1994). "Lessons from Ontake-San: A Comparative Analysis of Debris Avalanche Dynamics". In: *Engineering Geology.* Deep-Seated Landslides and Large-Scale Rock Avalanches 38.3, pp. 261–297. ISSN: 0013-7952. DOI: 10.1016/0013-7952(94)90042-6 (cit. on p. 106).

Vries, B. v. W. de, N. Kerle, and D. Petley (2000). "Sector Collapse Forming at Casita Volcano, Nicaragua". en. In: *Geology* 28.2, pp. 167–170. ISSN: 0091-7613. DOI: 10.1130/0091-7613(2000)28<167:SCFACV>2.0.CO;2 (cit. on pp. 100, 115).

Walder, J. S. and P. Watts (2003). "Evaluating Tsunami Hazards From Debris Flows". en. In: *Submarine Mass Movements and Their Consequences: 1st International Symposium.* Ed. by J. Locat, J. Mienert, and L. Boisvert. Advances in Natural and Technological Hazards Research. Dordrecht: Springer Netherlands, pp. 155–162. ISBN: 978-94-010-0093-2. DOI: 10.1007/978-94-010-0093-2_18 (cit. on p. 164).

Wanatowski, D., J. Chu, and W. L. Loke (2010). "Drained Instability of Sand in Plane Strain". en. In: *Canadian Geotechnical Journal* 47.4, pp. 400–412. ISSN: 0008-3674, 1208-6010. DOI: 10.1139/T09-111 (cit. on p. 161).

Wichmann, W. and M. Becht (2005). "Modelling of Geomorphological Processes in an Alpine Catchment". In: *GeoDynamics, Chapter: 12.* Atkinson, Foody, Darby, Wu. CRC Press (cit. on pp. 10, 177).

Wieland, M., J. M. N. T. Gray, and K. Hutter (1999). "Channelized Free-Surface Flow of Cohesionless Granular Avalanches in a Chute with Shallow Lateral Curvature". In: *Journal of Fluid Mechanics* 392, pp. 73–100. ISSN: 00221120. DOI: 10.1017/S0022112099005467 (cit. on p. 30).

Windows-Yule, C. R. K., D. R. Tunuguntla, and D. J. Parker (2016). "Numerical Modelling of Granular Flows: A Reality Check". en. In: *Computational Particle Mechanics* 3.3, pp. 311–332. ISSN: 2196-4378, 2196-4386. DOI: 10.1007/s40571-015-0083-2 (cit. on p. 11).

Wood, S. N. (2017). *Generalized Additive Models : An Introduction with R, Second Edition.* en. Chapman and Hall/CRC. ISBN: 978-1-315-37027-9. DOI: 10.1201/9781315370279 (cit. on p. 202).

Yamada, M. et al. (2018). "Estimation of Dynamic Friction and Movement History of Large Landslides". en. In: *Landslides* 15.10, pp. 1963–1974. ISSN: 1612-510X, 1612-5118. DOI: 10.1007/s10346-018-1002-4 (cit. on pp. 146, 178, 184).

Yavari-Ramshe, S. and B. Ataie-Ashtiani (2016). "Numerical Modeling of Subaerial and Submarine Landslide-Generated Tsunami Waves—Recent Advances and Future Challenges". en. In:

Landslides 13.6, pp. 1325–1368. ISSN: 1612-510X, 1612-5118. DOI: 10.1007/s10346-016-0734-2 (cit. on p. 30).

Yin, Z.-Y. and C. S. Chang (2013). "Stress–Dilatancy Behavior for Sand under Loading and Unloading Conditions". en. In: *International Journal for Numerical and Analytical Methods in Geomechanics* 37.8, pp. 855–870. ISSN: 1096-9853. DOI: 10.1002/nag.1125 (cit. on p. 161).

Zanuttigh, B. and A. Lamberti (2007). "Instability and Surge Development in Debris Flows". en. In: *Reviews of Geophysics* 45.3. ISSN: 1944-9208. DOI: 10.1029/2005RG000175 (cit. on p. 8).

Zhan, W. et al. (2017). "Empirical Prediction for Travel Distance of Channelized Rock Avalanches in the Wenchuan Earthquake Area". en. In: *Natural Hazards and Earth System Sciences* 17.6, pp. 833–844. ISSN: 1684-9981. DOI: 10.5194/nhess-17-833-2017 (cit. on pp. 9, 177).

Zhao, J. and T. Shan (2013). "Coupled CFD–DEM Simulation of Fluid–Particle Interaction in Geomechanics". en. In: *Powder Technology* 239, pp. 248–258. ISSN: 00325910. DOI: 10.1016/j.powtec.2013.02.003 (cit. on p. 11).

Zhao, J. et al. (2014). "Model Space Exploration for Determining Landslide Source History from Long-Period Seismic Data". en. In: *Pure and Applied Geophysics* 172.2, pp. 389–413. ISSN: 0033-4553, 1420-9136. DOI: 10.1007/s00024-014-0852-5 (cit. on p. 113).

Zimmermann, F. et al. (2020). "2D Runout Modelling of Hillslope Debris Flows, Based on Well-Documented Events in Switzerland". en. In: *Geosciences* 10.2, p. 70. DOI: 10.3390/geosciences10020070 (cit. on pp. 146, 199).

Appendix A

Back-analysis of a rock avalanche and a debris flow with the SHALTOP code

Back-analysis of a rock avalanche and a debris flow with the SHALTOP code

M. Peruzzetto
Institut de Physique du Globe, Paris, France / BRGM, Orléans, France

A. Mangeney
Institut de Physique du Globe, Paris, France

G. Grandjean, C. Levy, Y. Thiery
BRGM, Orléans, France

F. Bouchut
Université Paris-Est – Marne-la-Vallée, Marne-laVallée, France

ABSTRACT

For the the second Joint Technichal Committee on Natural Slopes and Landslides (JTC1) Workshop we use the SHALTOP numerical model to simulate the propagation of two past landslides : the 1806 Goldau rock avalanche and one of the 2008 Yu Tung Road debris flow. The Goldau Rock avalanche extent is reproduced with a simple Coulomb friction law. Runout is correctly reproduced with a friction angle of 11° but spreading is over-estimated. The Yu Tung debris flow is simulated with both a Voellmy and a Bingham rheology, and results are fitted to measured front velocities. The Voellmy rheology yields the best results but its parameters (friction angle and turbulence coefficient) can't be precisely constrained. The Bingham rheology fails to model the dynamics of the flow, suggesting more elaborated visco-plastic models (such as Herschel-Bulkley) could be needed. For both landslides we perform convergence analyses. We also investigate the influence of the flow thickness threshold value chosen to determine the deposits extents or the flow front.

INTRODUCTION

1.1 The SHALTOP numercial model

The SHALTOP code models the propagation of homogeneous granular flows over complex topographies (Bouchut & Westdickenberg 2004, Mangeney et al. 2007). In a fixed cartesian frame, the rigourous asymptotic analysis of the hydrostatic Navier-Stokes equations in the thin layer approximation makes it possible to account for the whole topography curvature tensor, extending the classical Savage-Hutter model.

The equation derivation in Bouchut & Westdickenberg 2004 was carried out assuming a Coulomb-type basal friction. It remains valid for friction angles depending on flow thickness and velocity. Thus, it is possible to adapt easily the code to other rheologies.

In the following we note h the flow thickness perpendicular to topography, θ the steepest slope angle, $z(x,y)$ the topography height and H the curvature tensor. Flow velocity $\vec{v}$ is tangent to the topography and parametrized with $u=(u,u_t)$, following :

$$c=\cos(\theta)=1/\sqrt{1+\|\nabla z\|^2},\quad H=c^3\nabla\nabla z,\quad \vec{v}=c(u,\nabla z\cdot u) \tag{1}$$

1.2 Implemented rheologies

To simulate the Goldau rock avalanche we use a simple Coulomb law with a constant friction coefficient $\mu=\tan(\delta)$ (with δ the friction angle). This kind of rheology has proved to reproduce accurately laboratory

experiments and real landslides (Lucas et al. 2007). The basal stress is collinear to the velocity and its norm T is given by :

$$T = c\rho h\mu g\left(1+\frac{uH^{t}u}{gc}\right) \quad (2)$$

with ρ the material density that simplifies in the resulting flow equations and g the gravity field. For the Yu Tung Road event we add a turbulent term ξ to get the Voellmy rheology that is commonly used to model debris flows :

$$T = c\rho h\mu g\left(1+\frac{uH^{t}u}{gc}\right)+\rho g\frac{\|\vec{v}\|^{2}}{\xi} \quad (3)$$

Eventually the Bingham rheology models visco-plastic behaviors, with a yield stress τ under which the flow stops and a dynamic viscosity η :

$$T = \frac{3}{2}\tau+3\eta\frac{\|\vec{v}\|}{h} \quad (4)$$

In this case the material density no longer simplifies in the flow equations. Thus after dividing by ρ , the parameters in SHALTOP for the Bingham rheology become τ/ρ and η/ρ , the kinematic viscosity.

2 METHOD

2.1 Goldau rock avalanche

Simulations of the Goldau rock avalanche were carried out on a regular 320x281 grid, with a 25-meter step, over 200 seconds. Flow thicknesses and velocities were recorded every 10 seconds. From these records we derive the flow maximum thickness on each grid cell, from which we get the flow extent provided a thickness threshold (grid with 1 where the flow passed, 0 otherwise). We test friction angles between 8° and 16° with a 1° step, and thresholds between 0.5 m and 10 m, every 0.5 m. We quantify the relative difference between observations and simulations with the Root Mean Square (RMS) between observed and computed extents.

2.2 Yu Tung Road debris flow

For this case study we were provided a regular 325x88 grid with a 2-meter step. Simulations are run over 70 seconds, with records every 1 second. Provided a profile following the bottom of the ravine, we derive flow thickness sections for each record. After defining a thickness threshold of the flow (varying between 5 cm and 40 cm with a 5 cm step) we can then track the flow front and get both its position and velocity. We compare our simulations with 5 measured front velocities : one near the landslide onset and 4 further downstream. We chose to compute only the relative RMS between the latters and our simulations, the first velocity being always reasonably reproduced regardless of the chosen parameters.

For the Voellmy rheology we took ξ between 200 m/s² and 1350 m/s² with a 50 m/s² step, and δ between 1° and 12° with a 1° step. Simulations were carried out iteratively to analyze only reasonable parameters. A more systematic approach was used for the Bingham rheology, taking τ/ρ between 0 m²/s² and 0.4 m²/s² with a 0.025 m²/s² step and η/ρ between 0.02 m²/s and 0.04 m²/s with a 0.02 m²/s step. A more refine sampling (steps divided by 2) was done around the best fitting parameters (between 0 m²/s² and 0.1 m²/s² for τ/ρ , and between 0.06 m²/s and 0.12 m²/s for η/ρ) .

2.3 Convergence analysis

Using the best fit parameters (with the Voellmy rheology for the Yu Tung Road case), we performed simulations with varying refined grids to analyze the convergence of the algorithm. Topography and initial mass were interpolated with bivariate splines from the data provided. Grid sizes ranged from 160x140 to 2000x1756 for the Goldau rock avalanche and from 160x43 to 2000x542 for the Yu Tung Road debris flow. The finest mesh were used as references to estimate the error.

3 RESULTS

For the Goldau case, the best fitting friction angle changes for thickness thresholds smaller than 3 m (red dots in Figure 1a), then stabilizes to 11° which is coherent with Aaron (2017). Using these parameters we plot the maximum flow thickness and compare it to the the observed extent (Figure 1b). The runout is correct but lateral spreading is too important. This is consistent with the conclusions of Aaron (2017) who infers the source block started sliding before it turned into a rock avalanche.

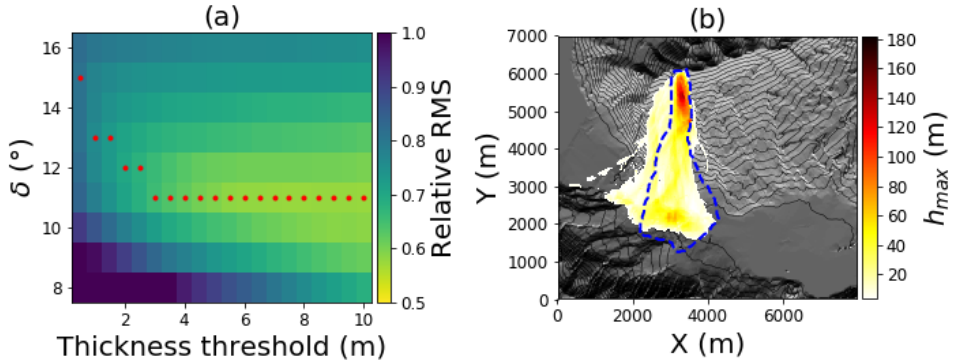

Figure 1 : Simulations of the Goldau rock avalanche with a Coulomb rheology. (a)Relative RMS between simulated and observed extent for various friction angles and thickness thresholds. Red dots show the bet fitting parameter for each thickness threshold. (b) Maximum flow thickness with 11° for δ . The blue dotted line is the observed extent.

Results of the Yu Tung Road back analysis for parameters and thresholds with a relative RMS smaller than 0.4 are presented Figure 2 (a-c) and (d-f) - for the Voellmy rheology and the Bingham rheology respectively. No significant influence of the thickness threshold was highlighted. The Voellmy rheology reproduces accurately the observed velocities, the best fit parameters being 4° for δ and 400 m/s² for ξ with a relative RMS of 0.03. A whole range of parameters however give similar velocity profiles (red dots in Figure 2c), but they do not match the values presented in AECOM (2012) (6° for δ and 300 m/s² for ξ). In comparison, the Bingham rheology yields inconclusive results, with at best a 0.32 relative RMS with 0 m²/s² for τ/ρ and 0.09 m²/s for η/ρ . Other simulations were performed to explore small order of magnitude for τ/ρ , but no significant change in the results were found.

Finally, convergence analysis (Figure 3) confirms the convergence of the algorithm. In both case the estimated error is almost inversely proportional to the number of points along the x-axis, and thus to the space step. Convergence appears to be faster in the Yu Tung Road case. Finer meshes could yield a more robust estimation of the convergence speed, but computing time increases rapidly (1 day and a half for the Yu Tung Road debris flow, more than 2 days for the Goldau Rock avalanche). Besides the interpolation process to generate the topographies can not account for the irregularities of the real topography, hence the finest meshes don't necessarily give more realistic results.

CONCLUSIONS

Our simulation of the Goldau rock avalanche confirms that a simple Coulomb friction law can reproduce quite accurately rock avalanchesdeposits, as previously showned by Lucas et al. (2007). Shallow-water models however fail to model the initiation stage, which in this case may have a significant impact on the propagation. Furthermore, more complex rheologies including turbulence terms seem to be needed to model the dynamics of water-logged flows such as the Yu Tung Road debris flow. In the latter case, the Bingham rheology fails to reproduce observed velocities. Other visco-plastic laws, such as the Herschel-Bulkley law, could be tested.

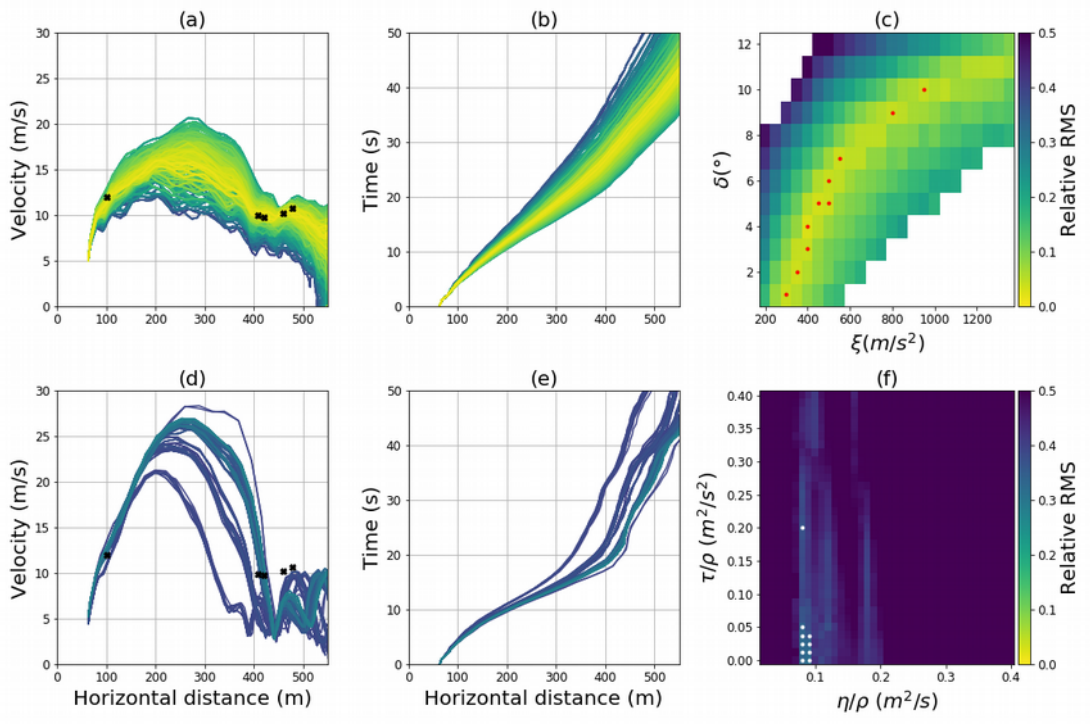

Figure 2 : Simulations of the Yu Tung Road debris flow with a Voellmy rheology (first row, a-c) and a Bingham rheology (second row, d-f). (a,d) Front velocity along profile for parameters and thickness thresholds yielding a relative RMS lower than 0.4. Line colors indicate the relative RMS. Black crosses are observed velocities. (b,e) Flow front position against time. (c,f) Relative RMS averaged over tested thickness thresholds. Points are the 10 smallest RMS

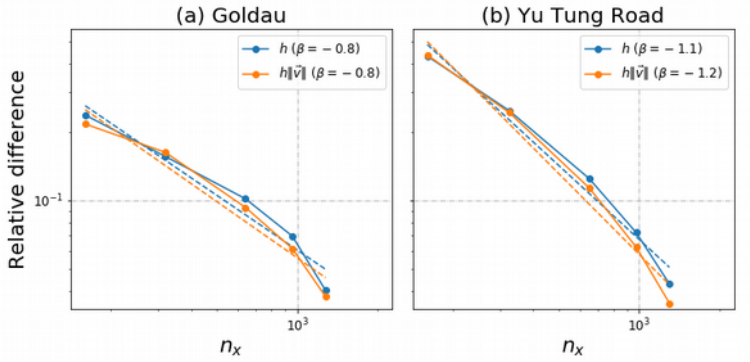

Figure 3 : Convergence analysis for the Goldau (a) and Yu Tung Road (b) simulations, for the thickness h (blue plain line) and the momentum $h\|\vec{v}\|$ (orange plain line). β Is is the slope of the best fiting logarithm fit (dotted lines), and n_x the number of points along the x-axis

REFERENCES

Aaron, J. (2017). Advancement and Calibration of a 3D Numerical Model for Landslide Runout Analysis, *PhD Thesis*. University of British Columbia.

AECOM (2012), Detailes study of the 7 June 2008 landslides on the hillside above Yu Tung Roand, Tung Chung, Geo Report No. 271, The Government of the Hong Kong Special Administrative Region

Bouchut, F. & Westdickenberg M. (2004), Gravity driven shallow water models for arbitrary topography Commun, Math. Sci., 2, 359 – 389.

Lucas, A., Mangeney A., Bouchut F., Bristeau, M.O. & Mège D. (2007). Benchmarking exercises for granular flows. 10.13140/RG.2.1.3945.0088.

Mangeney, A., Bouchut F., Thomas N., Vilotte J.P., & Bristeau M.O. (2007), Numerical modeling of self-channeling granular flows and of their levee-channel deposits, J. Geophys. Res., 112, F02017

Appendix B

Légendes des figures